Stochastic particle transport in disordered media : beyond the Boltzmann equation

Coline Larmier

université PARIS-SACLAY

NNT : 2018SACLS388

Stochastic particle transport in disordered media: beyond the Boltzmann equation

Thèse de doctorat de l'Université Paris-Saclay
préparée à l'Université Paris-Sud

École doctorale n° 576 : Particules, Hadrons, Énergie, Noyau, Instrumentation, Image, Cosmos et Simulation (PHENIICS)
Spécialité de doctorat : Énergie nucléaire

Thèse présentée et soutenue à Saclay, le 15 octobre 2018, par

Coline Larmier

Composition du jury :

M. Grégoire ALLAIRE Professeur, Ecole Polytechnique	Président
M. Anil K. PRINJA Professeur, University of New Mexico (USA)	Rapporteur
M. Raphael VOITURIEZ Directeur de recherche, Paris Sorbonne Université	Rapporteur
Mme Sandra DULLA Professeur, Politecnico di Torino (Italie)	Examinatrice
M. David RIZ Ingénieur-chercheur, CEA/DIF	Examinateur
M. Eric DUMONTEIL Ingénieur-chercheur (HDR), IRSN	Directeur de thèse
M. Alain MAZZOLO Ingénieur-chercheur (HDR), CEA/DEN	Directeur de thèse
M. Andrea ZOIA Ingénieur-chercheur (HDR), CEA/DEN	Encadrant

Thèse de doctorat

Acknowledgments

This PhD thesis has been performed at the Laboratoire de Transport Stochastique et Déterministe (LTSD) within the Service d'Études des réacteurs et de Mathématiques Appliquées (SERMA) at CEA Saclay, from 2015 to 2018. I will start by thanking all of these entities for providing excellent working conditions to PhD students.

I would like to thank Eric Dumonteil and Alain Mazzolo who accepted to be the directors of this thesis. I am deeply indebted to Prof. Anil Prinja and Dr. Raphal Voituriez for acting as referees for my thesis, to Prof. Sandra Dulla and Dr. David Riz for accepting to be part of the examining committee and to Prof. Grégoire Allaire for acting as the president of the PhD committee.

I would like express my deepest gratitude to my advisor Andrea Zoia, who gave me the opportunity to do my PhD under his supervision, showed a wonderful involvement and did an outstanding job in guiding my work through endless scientific discussions. Furthermore, I am also very grateful to Fausto Malvagi for his constant support and his relevant guidance, to François-Xavier Hugot for his precious help concerning the connectivity map, and to Emiliano Masiello for his very nice collaboration for the implementation of a deterministic solver related to Levermore-Pomraning equations.

Then, I would like to thank Anne Nicolas for her encouragement and for her interest in this thesis. I am also grateful to Franck Gabriel, Fausto Malvagi (again), Marc Delpech, Catherine Santucci and Pascal Yvon for having granted me their confidence by supporting my hiring at SERMA, first as a PhD student, then as an engineer-researcher.

Finally, I am indebted to the engineering school of École Centrale Paris for the educational background that I received there as a student.

In addition, I would like to stress that it was very pleasant to share my office with Laurent during these three years, in spite of our incompatible thermoregulation, leading to a considerable waste of energy due to the heating being on full power with open windows...

Il va sans dire que je suis extrêmement reconnaissante envers mes parents et mon frère Kim pour le soutien moral qu'ils n'ont cessé de m'apporter, ainsi que pour l'aide d'ordre logistique qu'ils m'ont fournie en diverses occasions - au hasard, je pense notamment à leur proposition d'assurer la sous-traitance intégrale du buffet.

Bien entendu, je voudrais aussi remercier Guillaume pour son dévouement inconditionnel. En particulier, je le remercie profondément de s'être lancé à la recherche du chaton perdu, allant jusqu'à conduire plus de mille kilomètres pour me ramener l'excellent Bergotte, dont la présence miniature a été infiniment précieuse pour moi durant les derniers mois de thèse.

Enfin, je souhaiterais rendre hommage à ma grand-mère, qui n'a hélas pu assister au dénouement de cette thèse, ainsi qu'à Imma Spoelmann, une personnalité véritablement inspirante.

Contents

Chapter 1

Introduction

Linear particle transport through heterogeneous and disordered media emerges in several applications in nuclear science and engineering, especially in relation to neutron and photon propagation. Examples are widespread and concern for instance:

- the double-heterogeneity of the fuel elements in *pebble-bed* reactors, which contain randomly dispersed micro-spheres of TRISO fuel particles consisting of a fissile material surrounded by a coated ceramic layer of silicon carbide for structural integrity and fission product containment, themselves contained within fuel pebbles made of pyrolytic graphite (which acts as the moderator) and stochastically packed within the vessel [17, 53, 64, 71, 94, 121];
- randomly mixed immiscible materials such as *fluid-vapour mixtures* in boiling water reactors: the behaviour of the water acting as both coolant and moderator in a two-fluid random state must be taken into account in order to properly describe neutron transport [164];
- radiation shielding calculation through *concrete* structures, where the shield effectiveness with respect to the transported particles depends on the random distribution of the components of concrete, such as gravel [66];
- the impact of poison grains for neutron absorbers [33, 125] or Pu grains in MOX fuels [165];
- safety margins evaluation [114, 159, 160, 163], especially for waste storage [161];
- the development of hydrodynamical instabilities at the material interfaces in inertial confinement *fusion pellets* driven by lasers [48, 66, 67, 166, 167];
- and the assessment of re-criticality probability due to the random arrangement of fuel, water and other structural materials resulting from *fuel degradation* after severe accidents [160, 162], such as those occurred at the Three Mile Island unit 2 [18, 47, 50] and at the Fukushima Daiichi power plant [45, 143].

Besides, the spectrum of applications of linear transport within random media is fairly broad and far reaching [24, 75, 147], and concerns also light propagation through turbid media such as sooty air or murky water [27, 57, 74] and engineered optical materials [3, 138, 139], tracer diffusion and charged particle beams in biological tissues with small-scale heterogeneities [111, 116, 149], diffusion through distributed systems of obstacles and absorbing traps [7], radiation trapping in hot atomic vapours [81], and radiative transfer in astrophysics [38, 66], only to name a few.

1.1 Linear particle transport in random media

A *stochastic medium* is such that the material properties at a given point in space are only known statistically [108, 112, 147]. It seems that linear particle transport in stochastic mixtures has been first formulated at the ninth International Conference on Transport Theory (ICTT, Montecatini, Italy, 1985) [66, 105]. This pioneering work by Pomraning and co-workers has been considerably

extended and refined in subsequent years by many authors. The discussion presented in the following sections is closely based on the arguments presented in [66, 108, 112, 126]. For the sake of simplicity, we will focus here our attention to the case of mono-energetic transport in non-multiplying media, in stationary (i.e., time-independent) conditions. However, these hypotheses are not restrictive, as argued in [108, 112, 126].

The stochastic nature of particle transport stems from the materials composing the traversed medium being randomly distributed according to some statistical law. Hence, the total cross section $\Sigma_t(\mathbf{r})$, the differential scattering cross section $\Sigma_s(\mathbf{\Omega}' \to \mathbf{\Omega}, \mathbf{r})$ and the source term $Q(\mathbf{r}, \mathbf{\Omega})$ are in principle random variables [108, 126]. Here $\mathbf{r}$ and $\mathbf{\Omega}$ denote the position and direction variables, respectively. Let us assume that there exists a collection of states $X = \{q\}$: a physical realization of the system under analysis will be denoted by a state q, associated to some stationary probability $\mathcal{P}(q)$, of observing the state q, with the normalization

$$\int_X \mathcal{P}(q)dq = 1. \tag{1.1}$$

To each state q thus correspond the functions $\Sigma_t^{(q)}(\mathbf{r})$, $\Sigma_s^{(q)}(\mathbf{\Omega}' \to \mathbf{\Omega}, \mathbf{r})$ and $Q^{(q)}(\mathbf{r}, \mathbf{\Omega})$ for the material properties [108, 171], and q can be seen as a mapping that associates a material $q(\mathbf{r})$ to each point $\mathbf{r}$.

The ensemble-averaged angular flux is then formally defined as

$$\langle \varphi(\mathbf{r}, \mathbf{\Omega}) \rangle = \int \mathcal{P}(q)\varphi^{(q)}(\mathbf{r}, \mathbf{\Omega})dq, \tag{1.2}$$

where $\varphi^{(q)}(\mathbf{r}, \mathbf{\Omega})$ is the solution of the Boltzmann equation

$$\mathbf{\Omega} \cdot \nabla\varphi^{(q)}(\mathbf{r}, \mathbf{\Omega}) + \Sigma_t^{(q)}(\mathbf{r})\varphi^{(q)}(\mathbf{r}, \mathbf{\Omega}) = \int \Sigma_s^{(q)}(\mathbf{\Omega}' \to \mathbf{\Omega}, \mathbf{r})\varphi^{(q)}(\mathbf{r}, \mathbf{\Omega}')d\mathbf{\Omega}' + Q^{(q)}(\mathbf{r}, \mathbf{\Omega}), \tag{1.3}$$

corresponding to a single realization q, with the appropriate boundary conditions. The physical observable of interest may be more generally some ensemble-averaged functional $\langle F[\varphi] \rangle$ of the particle flux. The key goal of particle transport theory in stochastic media consists in deriving a formalism for the description of the ensemble-averaged angular particle flux $\langle \varphi(\mathbf{r}, \mathbf{\Omega}) \rangle$.

For a finite set of materials $\{\alpha\}$, each associated with non-stochastic source $Q_\alpha(\mathbf{r}, \mathbf{\Omega})$, total cross section $\Sigma_{t,\alpha}(\mathbf{r})$ and scattering transfer law $\Sigma_{s,\alpha}(\mathbf{\Omega}' \to \mathbf{\Omega}, \mathbf{r})$, the ensemble-averaged angular flux can be decomposed as

$$\langle \varphi(\mathbf{r}, \mathbf{\Omega}) \rangle = \sum_\alpha p_\alpha(\mathbf{r}) \langle \varphi_\alpha(\mathbf{r}, \mathbf{\Omega}) \rangle, \tag{1.4}$$

where

$$p_\alpha(\mathbf{r}) = \int_{X_\alpha(\mathbf{r})} \mathcal{P}(q)dq \tag{1.5}$$

is the probability of finding the material α at position $\mathbf{r}$, the subset of states comprising all the states that have material α at position $\mathbf{r}$ being denoted as $X_\alpha(\mathbf{r}) = \{q \in X | q(\mathbf{r}) = \alpha\}$. Observe that the case where the statistical properties of the random materials vary spatially in a continuous fashion and are thus described by stochastic fields has also received intensive research efforts [27, 28, 36, 101, 117, 150, 150]. In the following, however, we will not consider this case and focus exclusively on random media composed of a finite set of random states.

The quantity $\langle \varphi_\alpha(\mathbf{r}, \mathbf{\Omega}) \rangle$, which is often called the material average flux, represents the ensemble-averaged angular flux restricted to those realizations that have material α at position $\mathbf{r}$ [126]:

$$\langle \varphi_\alpha(\mathbf{r}, \mathbf{\Omega}) \rangle = \frac{\int_{X_\alpha(\mathbf{r})} \mathcal{P}(q)\varphi^{(q)}(\mathbf{r}, \mathbf{\Omega})dq}{p_\alpha(\mathbf{r})}. \tag{1.6}$$

Thus, the search for $\langle \varphi(\mathbf{r}, \mathbf{\Omega}) \rangle$ can be decomposed into the search for $\langle \varphi_\alpha(\mathbf{r}, \mathbf{\Omega}) \rangle$ for each material.

Exact solutions for $\langle F[\varphi] \rangle$ can be in principle obtained in the following way: first, a realization of the medium is sampled from the underlying mixing statistics; then, the linear transport equation (1.7) corresponding to this realization is solved by either deterministic or Monte Carlo methods, and the

physical observables of interest $F[\varphi]$ are determined; a sufficiently large collection of realizations is produced; and ensemble averages are finally taken for the physical observables. Reference solutions are very demanding in terms of computational resources, especially if transport is to be solved by Monte Carlo methods in order to preserve the highest possible accuracy in solving the Boltzmann equation. In principle, it would be thus desirable to directly derive a single equation for the ensemble-averaged flux $\langle\varphi\rangle$.

For the sake of clarity, and without loss of generality, in the following we will consider the case of *binary stochastic mixing*, where only two immiscible materials (say α and β) are assumed to be present [108]. Most of the considerations presented here can be in principle extended to the more general case of *n-nary* mixing. Then, by averaging Eq. (1.3) over the set X_α of realizations having material α at $\mathbf{r}$, we obtain the following equation for $\langle\varphi_\alpha(\mathbf{r},\mathbf{\Omega})\rangle$

$$[\mathbf{\Omega}\cdot\nabla+\Sigma_{t,\alpha}]\left(p_\alpha\langle\varphi_\alpha\rangle\right)=p_\alpha\int\Sigma_{s,\alpha}(\mathbf{\Omega}'\to\mathbf{\Omega},\mathbf{r})\langle\varphi_\alpha(\mathbf{r},\mathbf{\Omega}')\rangle d\mathbf{\Omega}'+p_\alpha Q_\alpha+U_{\alpha,\beta}. \tag{1.7}$$

The cross sections $\Sigma_{t,\alpha}$ and $\Sigma_{s,\alpha}$ are those of material α. The quantity

$$U_{\alpha,\beta}=p_{\beta,\alpha}\langle\varphi_{\beta,\alpha}\rangle-p_{\alpha,\beta}\langle\varphi_{\alpha,\beta}\rangle \tag{1.8}$$

represents a coupling term, where

$$p_{i,j}=p_{i,j}(\mathbf{r},\mathbf{\Omega}) \tag{1.9}$$

denotes the probability per unit length of crossing the interface from material i to material j at position $\mathbf{r}$ and direction $\mathbf{\Omega}$. The quantity $\langle\varphi_{i,j}\rangle$, often called the interface average flux, denotes the angular flux averaged over the subset of realizations that have a transition from material i to material j at position $\mathbf{r}$ and in direction $\mathbf{\Omega}$. The equation for the ensemble-averaged flux $\langle\varphi_\beta(\mathbf{r},\mathbf{\Omega})\rangle$ within material β is immediately obtained from Eq. (1.7) by permuting the indexes α and β.

Attempts at establishing similar equations for higher-order moments (for instance, the variance) of the flux have been also proposed, with limited success [113].

Another approach to the derivation of an equation for the ensemble-averaged material flux $\langle\varphi_\alpha(\mathbf{r},\mathbf{\Omega})\rangle$ consists in resorting to the *integral formulation* of the Boltzmann equation. The right hand side of Eq. (1.3) represents the *emission density* of the particles, which is usually denoted by $\chi(\mathbf{r},\mathbf{\Omega})$:

$$\chi(\mathbf{r},\mathbf{\Omega})=Q(\mathbf{r},\mathbf{\Omega})+\int\Sigma_s(\mathbf{\Omega}'\to\mathbf{\Omega},\mathbf{r})\varphi(\mathbf{r},\mathbf{\Omega}')d\mathbf{\Omega}'. \tag{1.10}$$

From Eqs. (1.10) and (1.3), it can be shown that the emission density χ and the angular flux φ are related by the integral (Peierls) equation

$$\varphi(\mathbf{r},\mathbf{\Omega})=\int e^{-\int_0^s\Sigma_t(\mathbf{r}-s'\mathbf{\Omega})ds'}\chi(\mathbf{r}-s\mathbf{\Omega},\mathbf{\Omega})ds. \tag{1.11}$$

By averaging Eq. (1.11) of the subset of states X_α, we are led to the renewal-like equation [106,126,171]

$$\begin{aligned}\langle\varphi_\alpha\rangle=&\,\varphi_0(\mathbf{r}_0,\mathbf{\Omega})e^{-\tau_\alpha(\mathbf{r}_0,\mathbf{r})}R_\alpha(\mathbf{r}_0,\mathbf{r})+\int_0^{s_0}e^{-\tau_\alpha(\mathbf{r}',\mathbf{r})}h_\alpha(\mathbf{r}',\mathbf{r})\langle\bar\varphi_{\beta,\alpha}(\mathbf{r}',\mathbf{\Omega},\mathbf{r})\rangle ds\\&+\int_0^{s_0}e^{-\tau_\alpha(\mathbf{r}',\mathbf{r})}R_\alpha(\mathbf{r}',\mathbf{r})\int\Sigma_{s,\alpha}(\mathbf{\Omega}'\to\mathbf{\Omega},\mathbf{r}')\langle\bar\varphi_{\alpha,\alpha}(\mathbf{r}',\mathbf{\Omega}'\to\mathbf{r})\rangle d\mathbf{\Omega}'ds\\&+\int_0^{s_0}e^{-\tau_\alpha(\mathbf{r}',\mathbf{r})}R_\alpha(\mathbf{r}',\mathbf{r})Q_\alpha(\mathbf{r}',\mathbf{\Omega}).\end{aligned} \tag{1.12}$$

This equation expresses the material average flux $\langle\varphi_\alpha\rangle$ at location $\mathbf{r}$ in terms of new average angular fluxes along the past trajectory in direction $-\mathbf{\Omega}$, i.e., along points at positions $\mathbf{r}'=\mathbf{r}-\mathbf{\Omega}s'$ [106, 108, 171]. The quantity $\mathbf{r}_0$ denotes the boundary or initial point at the origin of the past trajectory, φ_0 is the corresponding initial or boundary value, and $s_0=|\mathbf{r}-\mathbf{r}_0|$. The optical distance along the past trajectory is

$$\tau_\alpha(\mathbf{r}',\mathbf{r})=\int_0^{s'}\Sigma_{t,\alpha}(\mathbf{r}'')ds''. \tag{1.13}$$

The quantity $\langle \bar{\varphi}_{\beta,\alpha}(\mathbf{r}', \mathbf{\Omega}, \mathbf{r}) \rangle$ denotes the ensemble-averaged flux over the subset of states that have the entire trajectory from $\mathbf{r}'$ to $\mathbf{r}$ within material α and change to material β at $\mathbf{r}'$, and the quantity $\langle \bar{\varphi}_{\alpha,\alpha}(\mathbf{r}', \mathbf{\Omega}' \rightarrow \mathbf{r}) \rangle$ denotes the ensemble-averaged flux over the subset of states that have the entire trajectory from $\mathbf{r}'$ to $\mathbf{r}$ within material α [171]. The former is analogous to the interface flux previously introduced, and the latter to the the material flux.

Finally, the quantity $R_\alpha(\mathbf{r}', \mathbf{r})$ represents the conditional probability that the entire trajectory from $\mathbf{r}'$ to $\mathbf{r}$ is within material α, given that $\mathbf{r}$ is in material α, and the quantity

$$h_\alpha(\mathbf{r}', \mathbf{r}) = -\frac{\partial}{\partial s'} R_\alpha(\mathbf{r}', \mathbf{r}) \tag{1.14}$$

is the conditional probability density that the interval from $\mathbf{r}'$ to $\mathbf{r}$ is in α and having changed from material β at $\mathbf{r}'$, given that $\mathbf{r}$ is in material α [126].

1.2 Relation to the material chord length distribution

For both the integro-differential formulation and the integral formulation, Eqs. (1.7) and (1.12), respectively, the ensemble averaged flux $\langle \varphi_\alpha \rangle$ depends on the statistical properties of the traversed medium. This is formally expressed via the probability $p_{\alpha,\beta}(\mathbf{r}, \mathbf{\Omega})$ per unit length of crossing the interface from material α to material β at position $\mathbf{r}$ and direction $\mathbf{\Omega}$ in the case of the integro-differential formulation, and via the conditional probability $R_\alpha(\mathbf{r}', \mathbf{r})$ that the entire trajectory from $\mathbf{r}'$ to $\mathbf{r}$ is within material α, given that $\mathbf{r}$ is in material α, in the case of the integral formulation.

A commonly adopted *hypothesis* concerning the nature of the random media is that the probabilities $p_{\alpha,\beta}(\mathbf{r}, \mathbf{\Omega})$ and $R_\alpha(\mathbf{r}', \mathbf{r})$ do not depend on the position within the medium, which leads to *homogeneous mixing statistics* [108, 126]. This means that all the spatial points within the medium have the same statistical properties, which are then invariant under arbitrary translations. In this case, we have

$$p_{\alpha,\beta}(\mathbf{r}, \mathbf{\Omega}) = p_{\alpha,\beta}(\mathbf{\Omega}) \tag{1.15}$$

and

$$R_\alpha(\mathbf{r}', \mathbf{r}) = R_\alpha(s', \mathbf{\Omega}). \tag{1.16}$$

Consider now a material chunk M_α of the stochastic medium associated to label α, and denote by $f_\alpha(s|\mathbf{\Omega})$ the probability density that the chord $\mathcal{C}$ determined by intersecting an arbitrary line L of orientation $\mathbf{\Omega}$ with the boundaries of the material chunk has a length between s and $s + ds$. The chord $\mathcal{C}$ is formally defined by the intersection $L \cap M_\alpha$ [127]. The probability density $f_\alpha(s|\mathbf{\Omega})$ is normalized, with

$$\int_0^\infty f_\alpha(s|\mathbf{\Omega}) ds = 1. \tag{1.17}$$

By virtue of the homogeneity hypothesis, $f_\alpha(s|\mathbf{\Omega})$ does not depend on the spatial position $\mathbf{r}$. The average linear material size along direction $\mathbf{\Omega}$ follows from the average material chord length

$$\Lambda_\alpha(\mathbf{\Omega}) = \int_0^\infty s f_\alpha(s|\mathbf{\Omega}) ds. \tag{1.18}$$

Assigning the probability density $f_\alpha(s|\mathbf{\Omega})$ is tantamount to saying that the randomness of the medium is entirely described in terms of *homogeneous renewal statistics*, where the probability density of a material change

$$h_\alpha(s|\mathbf{\Omega}) = -\frac{\partial}{\partial s} R_\alpha(s, \mathbf{\Omega}) = \frac{1}{\Lambda_\alpha(\mathbf{\Omega})} \int_s^\infty f_\alpha(s'|\mathbf{\Omega}) ds' \tag{1.19}$$

only depends on the distance s to the interface of material α along the direction $\mathbf{\Omega}$ [106, 108, 126]. The quantity $h_\alpha(s|\mathbf{\Omega})ds$ defines the probability that the distance to the interface from an arbitrary point within material α lies between s and $s + ds$. The probability density $h_\alpha(s|\mathbf{\Omega})$ is also normalized, with

$$\int_0^\infty h_\alpha(s|\mathbf{\Omega}) ds = 1. \tag{1.20}$$

The quantity $R_\alpha(s, \mathbf{\Omega})$ follows from

$$R_\alpha(s, \mathbf{\Omega}) = \int_s^\infty h_\alpha(s'|\mathbf{\Omega})ds' \tag{1.21}$$

and physically represents the probability that the interface along the direction $\mathbf{\Omega}$ from a given point within material α is larger than s.

Finally, for $p_{\alpha,\beta}(\mathbf{\Omega})$ we find

$$p_{\alpha,\beta}(\mathbf{\Omega}) = \frac{p_\alpha}{\Lambda_\alpha(\mathbf{\Omega})} \tag{1.22}$$

and for p_α we obtain

$$p_\alpha = \frac{\Lambda_\alpha(\mathbf{\Omega})}{\Lambda_\alpha(\mathbf{\Omega}) + \Lambda_\beta(\mathbf{\Omega})}, \tag{1.23}$$

where the dependence on $\mathbf{\Omega}$ in the average chord lengths cancels out to yield a direction-independent material probability p_α.

The chord length distribution $f_\alpha(\ell|\mathbf{\Omega})$ has been thoroughly investigated for the case of random inclusions of hard spheres in a background matrix [30, 44, 72, 77, 100, 144], especially in view of its relevance for neutron transport in pebble-bed reactors [17, 31, 32, 53, 64, 71, 94]. For a comprehensive review, see, e.g., [147]. In particular, it has been shown that for homogeneous and isotropic inclusions of poly-dispersed hard spheres in dimension d the average chord length within the background matrix is related to the random medium properties by

$$\Lambda_\alpha = \frac{1-\xi}{\xi}\frac{\kappa_d}{\kappa_{d-1}}\frac{\langle r^d\rangle}{\langle r^{d-1}\rangle}, \tag{1.24}$$

where ξ denotes the packing fraction (i.e., the volume fraction of the space filled by the spheres), $\kappa_d = \pi^{d/2}/\Gamma\left(1+\frac{d}{2}\right)$ is the volume of the unit sphere in dimension d, and $\langle r^n\rangle = \int r^n g(r)dr$ is the n-th moment of the sphere radius, $g(r)$ being the radius distribution [72, 144]. Moreover, accurate Monte Carlo simulations have shown that the associated chord length distribution $f_\alpha(s)$ is nearly exponential, with average provided by Eq. (1.24), and that the accuracy of this approximation improves for increasingly diluted spheres, i.e., small ξ [77, 100], as expected on theoretical grounds [147].

A particularly relevant class of renewal statistics is provided by the *homogeneous Markov mixing* [66, 108], for which the chord length distribution is assumed to be exactly *exponential*, namely,

$$f_\alpha(s|\mathbf{\Omega}) = \rho_\alpha(\mathbf{\Omega})e^{-\rho_\alpha(\mathbf{\Omega})s}, \tag{1.25}$$

where $\rho_\alpha(\mathbf{\Omega}) = 1/\Lambda_\alpha(\mathbf{\Omega})$. For this class of random media, the probability per unit length to cross the interface of material α in direction $\mathbf{\Omega}$ has a Poisson distribution with parameter $\rho_\alpha(\mathbf{\Omega})$ [108]. As such, Markov mixing represents an idealized mathematical description for disordered media, demanding minimal information content [108, 147]. Models satisfying homogeneous Markov mixing were introduced by Pomraning and co-workers for one-dimensional geometries of the rod or slab type, based on a Poisson point process on the line [66, 108]. Extensions to two-dimensional flat or extruded isotropic configurations have been later proposed [48, 65]. The practical realizability of such Markov model having an exponential distribution $f_\alpha(s|\mathbf{\Omega})$ simultaneously in all directions for arbitrary d-dimensional geometry has been an open question for many years [66].

Another fundamental question concerns the robustness of the Markov model, and in particular the impact of the choice of the chord length distribution on the key features of particle transport in random media [66]. The exponential distribution depends only on the parameter $\Lambda_\alpha(\mathbf{\Omega})$, so that the average chord length and the variance are not independent: actually, the variance is simply the square of the average. Hence, one might ask how the transport properties depend on the higher moments of the distribution, and in particular on the variance. Some investigations have been carried out in the framework of renewal theory for generic chord length distributions in one dimension [154, 171].

If the disorder is further assumed to be *isotropic*, the probability of crossing an interface will not depend on $\mathbf{\Omega}$. Observe that the hypothesis of homogeneity is reasonably the only one amenable to meaningful statistical models for the disorder (i.e., models possibly leading to some general results of broad applicability). The hypothesis of isotropy, while often adopted, is not strictly mandatory, and some interesting anisotropy-preserving models can be actually derived as we will show in the following.

1.3 The atomic mix limit

We have thus shown that the characterization of the linear transport within random media is intimately connected to the distribution of the chord lengths within the material chunks. The impact of the randomness of the medium on particle transport clearly depends on the ratio of their two respective characteristic *spatial scales*. The typical size of a particle displacement within the medium is given by the mean free path $1/\Sigma_{t,i}$ for each material i, whereas the typical scale of the randomness of the medium is intuitively given by Λ_i, which yields the average linear size of the chunks containing material i. If the typical particle displacement is much larger than the typical size of the disorder, i.e., if $\Sigma_{t,i}\Lambda_i \ll 1$, then a single particle flight will 'see' a large number of material chunks, and we fall thus within the *atomic mix* regime: for the transport process, we can safely assume that the medium is composed of a homogeneous material, whose properties (including cross sections and sources) are obtained by averaging the properties of each random material, weighted by their respective probability p_i of occurrence [108].

More precisely, it has been shown that under the atomic mix approximation $\Sigma_{t,i}\Lambda_i \ll 1$, the transport equations (1.7) collapse to a single equation for the average flux $\langle\varphi\rangle$, namely,

$$[\mathbf{\Omega}\cdot\nabla + \langle\Sigma_t\rangle]\,\langle\varphi\rangle = \int \langle\Sigma_s(\mathbf{\Omega}'\to\mathbf{\Omega},\mathbf{r})\rangle\langle\varphi(\mathbf{r},\mathbf{\Omega}')\rangle d\mathbf{\Omega}' + \langle Q\rangle + O(\varepsilon), \tag{1.26}$$

where ε is a measure of the smallness of the material chord length Λ_i with respect to the particle mean free path $1/\Sigma_{t,i}$ in material i [108], and the physical properties and the source are averaged over the possible material realizations:

$$\langle\Sigma_t(\mathbf{r})\rangle = p_\alpha\langle\Sigma_{t,\alpha}(\mathbf{r})\rangle + p_\beta\langle\Sigma_{t,\beta}(\mathbf{r})\rangle, \tag{1.27}$$

$$\langle\Sigma_s(\mathbf{\Omega}'\to\mathbf{\Omega},\mathbf{r})\rangle = p_\alpha\langle\Sigma_{s,\alpha}(\mathbf{\Omega}'\to\mathbf{\Omega},\mathbf{r})\rangle + p_\beta\langle\Sigma_{s,\beta}(\mathbf{\Omega}'\to\mathbf{\Omega},\mathbf{r})\rangle, \tag{1.28}$$

and

$$\langle Q(\mathbf{r},\mathbf{\Omega})\rangle = p_\alpha\langle Q_\alpha(\mathbf{r},\mathbf{\Omega})\rangle + p_\beta\langle Q_\beta(\mathbf{r},\mathbf{\Omega})\rangle. \tag{1.29}$$

The atomic mix regime formally corresponds to neglecting disorder-induced spatial correlations, all the terms involving ensemble averages of the kind $\langle\Sigma\varphi\rangle$ being replaced by the product of the averages, namely, $\langle\Sigma\rangle\langle\varphi\rangle$ [108].

In the opposite regime, i.e., for $\Sigma_{t,i}\Lambda_i \gg 1$, the typical particle displacement is much smaller than the typical size of the disorder, so that a single particle flight will typically experience a single material chunk. The intermediate regime, where the two spatial scales are comparable, i.e., $\Sigma_{t,i}\Lambda_i \simeq 1$, will give rise to a non-trivial behavior, whose description will be most easily provided within a probabilistic framework.

1.4 Closure formulas for the transport equations

In the general case of non-vanishing average material chord lengths Λ_i, the set of equations for the ensemble-averaged formulation of the integro-differential version of the transport equation (1.7), whose derivation contains no approximations so far, can be shown to form an *infinite hierarchy*, since the terms $\langle\varphi_\alpha\rangle$ in Eq. (1.8) would involve equations for the conditional averages $\langle\varphi_{\beta,\alpha}\rangle$ and $\langle\varphi_{\alpha,\beta}\rangle$, which in turn would further involve additional conditional averages [108, 171]. The same argument applies to the ensemble-averaged formulation of the integral version of the transport equation (1.12), which contains the conditional averages $\langle\bar{\varphi}_{\beta,\alpha}\rangle$ and $\langle\bar{\varphi}_{\alpha,\alpha}\rangle$ and also leads to an infinite hierarchy of equations involving increasingly more singular statistical averages [171].

For the special case of *collisionless transport* (i.e., in the absence of scattering), it has been shown that for renewal statistics the hierarchy of the integral transport equations (1.12) closes at the second order [126], with the identity

$$\langle\bar{\varphi}_{\beta,\alpha}(\mathbf{r}',\mathbf{\Omega},\mathbf{r})\rangle = \langle\varphi_{\beta,\alpha}(\mathbf{r}',\mathbf{\Omega})\rangle \tag{1.30}$$

between the interface flux along the past trajectory and the local interface flux [107, 126]. For collisionless transport with Markov statistics, it has been further shown that the hierarchy of the integro-differential transport equations (1.7) closes at the first order, with the identity

$$\langle \varphi_{\beta,\alpha}(\mathbf{r},\mathbf{\Omega})\rangle = \langle \varphi_{\beta}(\mathbf{r},\mathbf{\Omega})\rangle \tag{1.31}$$

between the interface flux and the material flux [126].

Unfortunately, such exact closure relations do not exist for the case of non-zero scattering media [108, 118]. Generally speaking, it will be then necessary to truncate the infinite set of equations with some appropriate model leading to a *closure formula*, depending on the underlying mixing statistics. Furthermore, the integro-differential formulation and the integral formulation, while both exact, are not equivalent for transport in stochastic media, so that after introducing a truncation they will possibly yield different results [107, 126].

1.5 The Levermore-Pomraning model

Based on the closure formula valid for collisionless transport with Markov statistics, the celebrated *Levermore-Pomraning model* assumes that the identity

$$\langle \varphi_{\alpha,\beta}\rangle = \langle \varphi_{\alpha}\rangle \tag{1.32}$$

holds also in the presence of scattering for homogeneous Markov mixing [66, 108]. This leads to the truncated integro-differential transport equations

$$\left[\mathbf{\Omega}\cdot\nabla + \Sigma_{t,\alpha}\right](p_\alpha\langle\varphi_\alpha\rangle) = p_\alpha\int \Sigma_{s,\alpha}(\mathbf{\Omega}'\to\mathbf{\Omega},\mathbf{r})\langle\varphi_\alpha(\mathbf{r},\mathbf{\Omega}')\rangle d\mathbf{\Omega}' + p_\alpha Q_\alpha + \frac{p_\beta}{\Lambda_\beta}\langle\varphi_\beta\rangle - \frac{p_\alpha}{\Lambda_\alpha}\langle\varphi_\alpha\rangle. \tag{1.33}$$

The dependence of Λ_i on the direction $\mathbf{\Omega}$ has been omitted, in order to keep notation simple. Equations (1.33), although derived for the case of binary mixing, can be extended more generally to the case of n-nary mixtures. Several generalisations of this model have been later proposed, including higher-order closure schemes [108, 118, 136].

Equations (1.33) form a system of coupled Boltzmann equations, and can thus be solved by standard deterministic methods [1, 11, 171]. In parallel, Monte Carlo algorithms such as the Chord Length Sampling (CLS) have been proposed: the basic idea behind CLS is that the interfaces between the constituents of the stochastic medium are sampled on-the-fly during the particle displacements by drawing the distances s to the following material boundaries from a distribution $f_\alpha(s)$ depending on the mixing statistics. It has been shown that the CLS algorithm formally solves the Levermore-Pomraning model for Markovian binary mixing [122, 123, 167]. Generalization of these Monte Carlo algorithms including partial memory effects due to correlations for particles crossing back and forth between the same materials have been also proposed [167]. Their common feature is that they allow a simpler, albeit approximate, treatment of transport in stochastic mixtures, which might be convenient in practical applications where a trade-off between computational time and precision can be worth considering. Originally formulated for Markov statistics, i.e., exponentially distributed material chords, these models have been largely applied also to random inclusions of disks or spheres into background matrices, with application to pebble-bed and very high temperature gas-cooled reactors [8, 12, 31, 32], where the chord length distribution is known to be approximately exponential only for diluted inclusions [100, 144]. Some methods to mitigate the errors between CLS and the reference solutions have been presented in the context of eigenvalue calculations, e.g., in [68].

1.6 Quenched and annealed disorder

Thus, it appears that two distinct strategies can be adopted in order to describe particle transport in random media [108]. The former, which is based on *quenched disorder* models, leads to exact solutions for the statistical moments of the observables of interest, at the expense of high computational cost.

The latter, which is based on *annealed disorder* models, leads to approximate solutions that might be convenient in practical applications where a trade-off between computational time and precision can be worth considering.

In the *quenched* disorder approach, the random spatial configurations with associated material compositions are first defined based on a probabilistic model. The Boltzmann equation is then solved for each configuration, and the statistical moments (and in principle the full distribution) of the quantities of interest are obtained by taking the ensemble averages with respect to the realizations [108, 109, 114]. The quenched disorder approach leads to reference solutions, because the effects of disorder-induced spatial correlations on particle trajectories are correctly preserved. Analytical results for the ensemble averages demand huge theoretical efforts; considerable progress can be nonetheless achieved by using Monte Carlo methods in order to generate realizations taken from the sought distribution and then using a deterministic or Monte Carlo transport code to solve the transport problem for each sampled configuration.

The goal of the *annealed* disorder approach is to develop effective equations for the ensemble-averaged observables, such as the Levermore-Pomraning model [108]. When particle transport is solved by Monte Carlo simulation, the annealed disorder approach is implemented by introducing disorder-averaged neutron displacement laws that are supposed to 'mimic' the effects of the spatial heterogeneities on particle trajectories, such as in the CLS algorithm [31,32,166,167]. By construction, spatial correlations are neglected by these methods. Since the spatial configuration seen by each particle is regenerated at each particle flight, the CLS corresponds to an annealed disorder model, as opposed to the quenched disorder of the reference solutions, where the spatial configuration is 'frozen' for all the traversing particles.

In order to quantify the accuracy of the various approximate models, comparisons with respect to reference solutions are mandatory. For this purpose, a series of *benchmark problems* have been proposed in the literature. For Markov mixing and renewal statistics, a number of benchmark problems comparing CLS and reference solutions have been proposed [1, 9–11, 171], with focus exclusively on $1d$ geometries, either of the rod or slab type. Flat two-dimensional configurations have received less attention [48, 65, 134]. For the case of randomly dispersed spherical inclusions into background matrices, several benchmark problems have been also examined in two and three dimensions [8, 12, 31, 32]. In the context of eigenvalue problems, intensive research efforts have been devoted so far to the class of stochastic inclusions [20, 43, 54, 68, 69, 94], whereas the case of Markov and renewal mixing has comparatively received less attention, and has been mostly confined to one-dimensional systems [114, 160, 162].

1.7 Plan of this work

In this Thesis, we will investigate linear particle transport in random media, having in mind the applications to reactor physics and in particular the analysis of the re-criticality probability following core degradation. The Thesis is structured in two major parts.

In the first part, we will focus on some *mathematical models* that can be used for the description of random media. Special emphasis will be given to stochastic tessellations, where a domain is partitioned into convex polyhedra by sampling random hyperplanes according to a given probability. Stochastic inclusions of spheres into a matrix will be also briefly introduced.

- In Chapter 2 we will provide the state of the art concerning the key statistical properties of three classes of random tessellations, namely, Poisson, Poisson-Voronoi and Poisson-Box tessellations, and of mono and poly-dispersed spherical inclusions. In particular, we will show that the Poisson tessellations satisfy the Markov property for any dimension d, which allows giving a positive answer to the possibility of explicitly realizing Markov media with exponentially distributed chord lengths in any direction. It has been suggested that such tessellations might be the only stochastic geometries to satisfy the Markov properties [87, 90]. The effects of anisotropy on Poisson geometries are also thoroughly discussed. For each class of random media, the shape of the chord length distribution is recalled and related whenever possible to the statistical features

of the geometry. The distinct features of the chord length distribution for different random geometries are provided.

- A computer code has been developed in order to explicitly construct such geometries by Monte Carlo methods, and the implementation details will be provided in Chapter 3. The chosen algorithms and the global performances of the generator will be analyzed. This generator can be used in order to produce an ensemble of realizations obeying the specific set of probabilities for d-dimensional Poisson, Poisson-Voronoi and Poisson-Box tessellations or spherical inclusions.

- In Chapter 4 we will conclude the first part of the Thesis by performing an exhaustive numerical analysis of the random media introduced in Chapter 2: we will generate large collections of geometry realizations and compute the moments, the correlations and the full distributions of a few relevant observable of interest, such as the chord lengths, the typical volume and surface of a tessellation cell, the number of faces of cell, an so on. The results corresponding to different classes of random geometries will be further compared. This analysis will be carried out with a two-fold aim: on one hand, for the case of very large geometries the comparison between the moments computed by Monte Carlo methods and the exact formulas available for geometries having an infinite extension will allow verifying the correct implementation of the generator. On the other hand, the generator will allow exploring how the observables related to the random geometries behave for finite-size systems, for which exact result do not exist. The full distributions of observables for which only the lower order moments are exactly known will be also computed.

In the second part of this Thesis, we will then assess the general features of *particle transport* within the random media that have been analyzed in the first part of the work. For this purpose, we will consider some benchmark problems that are simple enough so as to allow for a thorough understanding of the effects of the random geometries on particle trajectories and yet retain the key properties of linear transport. Transport calculations will be realized by using the Monte Carlo particle transport code TRIPOLI-4 ®, developed at SERMA.

- In Chapter 5 we will begin by considering the case of quenched transport where the mixing statistics is provided by d-dimensional Poisson tessellations. We will in particular revisit the classical Adams, Lervermore and Pomraning benchmark, originally proposed for single-speed fixed-source transport in one dimension for slab and rod configurations with Markov mixing. Reference solutions will be computed for dimension $d = 1$ (slab), $d = 2$ (extruded) and $d = 3$, based on isotropic Poisson tessellations. At SERMA, the case of two-dimensional Markov geometries has been previously addressed within the framework of the internships of Alice Somaini (transport properties), Thibaut Lepage and Lucie Delaby (geometrical features), under the guidance of Drs. A. Mazzolo and F. Malvagi. To the best of our knowledge, three-dimensional solutions have never been proposed before in the literature. The effect of dimensionality on the computed observables, such as the reflection and transmission coefficients at the boundaries of the domain and the spatial flux within the domain, will be carefully examined.

  Furthermore, we will assess the impact of the chord length distribution on the transport properties: we will introduce a new set of benchmark configurations consisting in void-diffusive and absorption-diffusive three-dimensional random media, and consider several mixing statistics, including isotropic Poisson, Voronoi and Box tessellations. For these classes of renewal distributions, each associated to a different chord length distribution, we will set the average chord length as a control parameter and examine the impact of the higher moments of the chord length on the observables of interest. A crucial point will be the discovery that Box and Poisson tessellations induce very close chord length distributions, which in turn imply very close simulation results for particle transport. This analysis represents an extension to dimension $d = 3$ of the pioneering work carried out in dimension $d = 1$ in order to probe the sensitivity of the transport results to the use of non-exponential distribution of chord lengths [154, 171].

- Eigenvalue problems in quenched disorder will be examined in Chapter 6: we will examine the effects of fuel degradation on the key observables of criticality calculations, namely, the multiplication factor and the kinetics parameters, by assuming that a portion of a fuel assembly is replaced by a random tessellation representing the stochastic material rearrangement following a severe accident. Poisson, Voronoi and Box tessellations will be used, and the impact of the chord length distribution on the obtained results will be evaluated for two benchmark configurations consisting in UOX and MOX assemblies with 17×17 fuel pins. The effects of anisotropy, which can be conveniently introduced in order to model the effects of material stratification, will be also examined by resorting to anisotropic Poisson tessellations: this part of the work has been partly carried out by Alessandro Marinosci, a Master of Science student in Nuclear Engineering at Politecnico di Torino (Italy), who spent a six-month internship at SERMA under the guidance of Dr. A. Zoia and myself. These results provide a generalization to realistic three-dimensional and continuous-energy configurations of the pioneering work performed by Pomraning on eigenvalue problems for Markov mixing in slab and rod configurations [114].

- We will conclude the second part of the Thesis by considering the case of annealed disorder. For this purpose, we will first address the case of the Chord Length Sampling (CLS) algorithm: within the framework of a collaboration with Dr. P. Brantley of the Lawrence Livermore National Laboratory (USA) and Prof. T. Palmer of the Oregon University (USA), we have revisited the Adams, Levermore and Pomraning benchmark by comparing the d-dimensional CLS solutions to the reference solutions previously obtained based on Poisson geometries. The simulation results will be illustrated in Chapter 7. In particular, we will show how the discrepancies between reference and approximated solutions evolve as a function of the system dimensionality. To the best of our knowledge, a similar comparison for Markov mixing has never been attempted before. Finally, in Chapter 7 we propose a new class of improved d-dimensional CLS-like algorithms adapted for Monte Carlo simulations that can include partial memory and better preserve the effects of spatial correlations. The key ingredient will be shown to be the similarity between the chord length distribution in Poisson and Box tessellations. The simulation results for this new class of annealed disorder methods, which we will call Poisson-Box Sampling, will be contrasted to those of CLS and to reference solutions for the configurations of the Adams, Levermore and Pomraning benchmark. For all configurations, the Poisson-Box Sampling will be shown to perform better than the standard CLS and to yield solutions in fairly good agreement with the reference values. Independently and simultaneously, Drs. P. Brantley and G. Zimmerman have developed another improved three-dimensional CLS-like method, named Local Realization Preserving (LRP) algorithm: in the framework of the aforementioned collaboration with Dr. Brantley, a detailed comparison between the Poisson-Box Sampling and the LRP methods is being carried out, and the preliminary results of such investigation will be also presented.

Conclusions will be finally drawn in Chapter 8.

1.8 Relation to published works

Part of the work presented in this manuscript has been published in the following papers:

1. C. Larmier, E. Dumonteil, F. Malvagi, A. Mazzolo, A. Zoia, Finite-size effects and percolation properties of Poisson geometries, Phys. Rev. E **94**, 012130 (2016).

2. C. Larmier, F.-X. Hugot, F. Malvagi, A. Mazzolo, A. Zoia, Benchmark solutions for transport in d-dimensional Markov binary mixtures, J. Quant. Spectrosc. Radiat. Transfer **189**, 133148 (2017).

3. C. Larmier, A. Zoia, F. Malvagi, E. Dumonteil, A. Mazzolo, Monte Carlo particle transport in random media: the effects of mixing statistics, J. Quant. Spectrosc. Radiat. Transfer. **196**, 270-286 (2017).

4. C. Larmier, F.-X. Hugot, F. Malvagi, A. Mazzolo, A. Zoia, in Proceedings of the M&C international conference, Jeju, Korea, April 16-20th 2017.

5. C. Larmier, A. Zoia, F. Malvagi, E. Dumonteil, A. Mazzolo, Neutron multiplication in random media: reactivity and kinetics parameters, Ann. Nucl. Energy **111**, 391-406 (2018).

6. C. Larmier, A. Lam P. Brantley, F. Malvagi, T. Palmer, A. Zoia, Monte Carlo Chord Length Sampling for d-dimensional Markov binary mixtures, J. Quant. Spectrosc. Radiat. Transfer. **204**, 256271 (2018).

7. C. Larmier, A. Zoia, F. Malvagi, E. Dumonteil, A. Mazzolo, Poisson-Box Sampling algorithms for three-dimensional Markov binary mixtures, J. Quant. Spectrosc. Radiat. Transfer. **206**, 70-82 (2018).

8. A. Marinosci, C. Larmier, A. Zoia, Neutron transport in anisotropic random media, Ann. Nucl. Energy **118**, 406-413 (2018).

Moreover, this work has been presented at the following conferences and workshops:

1. 19th Workshop on Stochastic Geometry, Stereology and Image Analysis, Luminy, May 1519, 2017.

2. International Conference on Transport Theory ICTT25, Monterey, California, October 16-20, 2017.

3. Workshop MaNu, Mathématiques pour la neutronique, UPMC, Paris, November 30, 2017.

4. École de recherche en mathématiques pour l'énergie nucléaire, en partenariat avec le GdR MaNu, Roscoff, July 2-6, 2018.

Part I

Analysis of stochastic geometries

Chapter 2

Modeling disordered media by random geometries

2.1 Introduction

In order to pave the way to the description of particle transport through random media, in this Chapter we begin by addressing the key statistical properties of a few classes of stochastic geometries. Random media of interest in reactor physics typically belong to two families: *stochastic inclusions* of fissile chunks within a background matrix [20, 68, 94] and *stochastic tessellations* composed of a collection of fissile and non-fissile volumes obeying a given mixing statistics [108]. In the following we will provide an overview of stochastic inclusions and stochastic tessellations, where the material properties have only a discrete number of random states. Our main focus will be on stochastic tessellations, which will be later used in order to produce reference solutions for particle transport within disordered media.

For all the random media models considered in this work, we will assume a fundamental and natural property of stochastic *homogeneity* (also called spatial stationarity) [87]. A stochastic system is said to be homogeneous if it is stochastically invariant under arbitrary translation. In other words, the construction of the system with respect to an arbitrary point in $\mathbb{R}^d$ is independent of the point chosen. It turns out that little theoretical progress is possible without requiring this assumption. Strictly speaking, stationarity applies to systems having an infinite extension: in practice, we will always consider random media restricted to some finite portion of $\mathbb{R}^d$.

2.1.1 Stochastic inclusions

Stochastic inclusions are a class of probabilistic models where a collection of objects of fixed or random shape are placed at random within a given domain, which is called the background matrix. The objects can or cannot overlap, according to the specific rules of the model. The distribution of the centers of the inclusions as well as the one describing their shape (where needed) are chosen based on physical considerations. Among this class of model, possibly the best-known case is provided by spherical inclusions, where the objects to be positioned within the matrix are spheres of fixed or variable radius.

Stochastic inclusions can be applied to the description of neutron diffusion in pebble-bed reactors, where fissile micro-spheres of constant diameter are randomly dispersed through a graphite matrix, itself arranged within bigger spheres (the pebbles) randomly stacked into the reactor vessel [53, 64, 94]. An illustration is given in Fig. 2.1. Neutron transport in boiling water reactors involves diffusion in a random medium composed of liquid water and vapour, where the vapour bubbles can be described by spheres of varying sizes (because of coalescence and break-up) randomly dispersed through the water [164]. For criticality safety, and in particular for waste storage problems, spherical inclusion models are often used as a convenient approximation when lacking detailed information concerning the shape and position of the dispersed fissile chunks [159, 162].

For our work we will consider in particular spherical inclusions: we will first describe the strategy for the construction of d-dimensional random configurations with fixed and varying radius and detail the statistical properties of the resulting geometries.

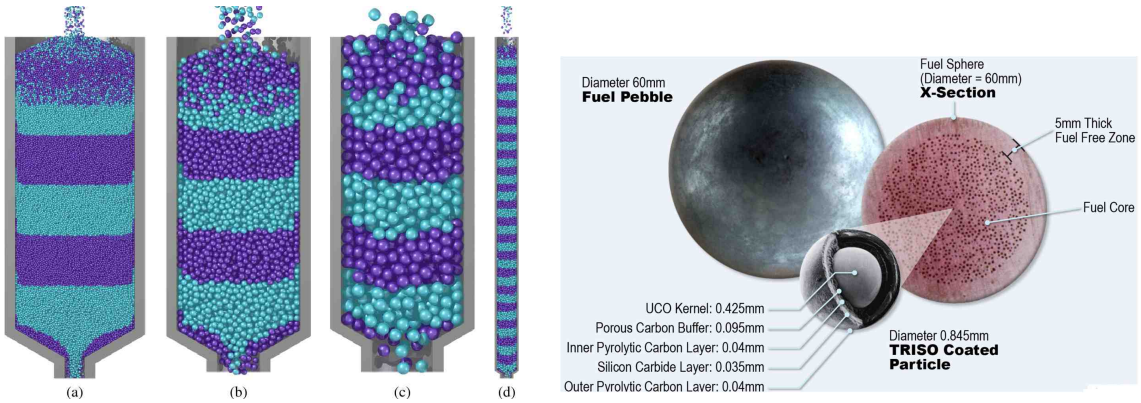

Figure 2.1: Left. Computer-generated random stacks of pebbles for various shapes of the vessel. (a) full-size geometry, (b) 3:1 geometry, (c) 6:1 geometry and (d) tall 6:1 geometry. The snapshots correspond to different levels of drainage. For the first three, approximately 20% of the pebbles having been drained through the container. For the tall 6:1 geometry, roughly the same amount of flow as the 6:1 geometry. Before drainage is initiated, the pebbles are colored in vertical bands, and the deformation of the bands highlights the pattern of flow; the two colors of pebbles are mixed together at the top of each simulation during reinsertion. Image taken from Ref. [121]. Right. Cross section and zoom of a pebble, with fuel kernels dispersed within a graphite matrix. Image taken from `http://fortune.com/2016/02/04/nuclear-startup-x-energy/`.

2.1.2 Stochastic tessellations

There is a vast class of random heterogeneous materials whose microstructure cannot be modelled as a distribution of inclusions or cavities of well-defined shape in a matrix and can be better described by a space-filling random geometry [75, 129, 147].

Consider a disjoint aggregate $\{X_i\}$, $i = 1, 2, \cdots$ of bounded domains in the euclidean space $\mathbb{R}^d$, with $X_i \cap X_j = \emptyset$ for $i \neq j$. The aggregate is space-filling in $\mathbb{R}^d$ if the union of the domains X_i yields the entire space $\mathbb{R}^d$. When the bounded domains are convex and space-filling, the interfaces between domain pairs must be hyperplanes, and the domains X_i must be convex polyhedra. In this case, the aggregate $\{X_i\}$ is a *tessellation* of $\mathbb{R}^d$, and the domains X_i are the cells of the tessellation. Stochastic tessellations are a class of probabilistic models where a given d-dimensional domain is decomposed into random convex polyhedral cells by generating a collection of random hyperplanes in $\mathbb{R}^d$ [24, 75, 85, 127, 129, 147]. Distinct tessellation models use either a direct specification of the random interfaces (i.e., the hyperplanes) between the cells, or a specification of some preliminary random 'framework' that leads via certain rules to a random division of space [87].

Stochastic tessellations might provide a convenient model for the random space-filling arrangement of fuel, water and other structural materials such as those resulting from fuel degradation in Three Mile Island unit 2 [18, 47, 50] and at the Fukushima Daiichi power plant [45, 143]. An illustration is given in Fig. 2.2. Besides, stochastic tessellations are a convenient model to describe, e.g., the turbulent mixtures involving materials of different sizes and shapes that arise due to the hydrodynamical instabilities in inertial confinement fusion targets [48, 67, 166, 167] and crystal aggregates with random nucleation in metallurgy and material science [40, 80]: a comprehensive review can be found, e.g., in [127, 129, 147].

For our work, we will introduce a few significant probabilistic models based on generating random hyper-planes and leading to random tessellations with distinct features: in particular, we will consider the Poisson hyperplane tessellations, the Poisson-Box tessellations (both pertaining to tessellations induced by assigning random rules for the interfaces defining the cells), and the Poisson-Voronoi tessellations (belonging to the class of tessellations induced by assigning a preliminary random framework). Where needed, the subscript or superscript m will denote the class of the stochastic model: $m = \mathcal{P}$ for Poisson tessellations, $m = \mathcal{V}$ for Voronoi tessellations, and $m = \mathcal{B}$ for Box tessellations. For

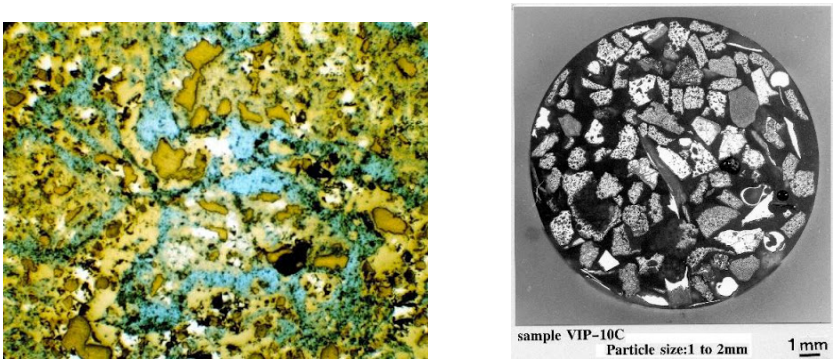

Figure 2.2: Cross sections of corium samples from the Three Mile Island (Reactor number 2) nuclear accident in 1979. Left. The surface of the sample has been oxidized in order to emphasize colors. Green color corresponds to uranium dioxide, whereas brownish part corresponds to metals like zirconium, iron, nickel, melted together. Right. Cross section of a small 1-mm corium grain. Whitish color corresponds to the regions where cladding and uranium melted and mixed. Images taken from `http://www.asahi.com/special/10005/TKY201203050580.html`.

each stochastic model, we will describe the strategy for the construction of d-dimensional tessellations and detail the statistical properties of each stochastic tessellation.

2.2 Stochastic spherical inclusions

A comprehensive review of the fundamental statistical properties of spherical inclusions can be found, e.g., in [147]. The inclusion of randomly dispersed spheres within background matrices has attracted intensive research efforts mainly for applications to pebble-bed and Very High Temperature gas-cooled Reactors (VHTR) [8, 12, 31, 32, 68], especially in the context of eigenvalue problems for neutron transport [20, 43, 54, 68, 69, 94]. Other models of stochastic inclusions with non-spherical shapes have been proposed in order to describe geometrically complex microstructures, concerning, for instance, battery electrodes, fuel cells and solar cells. Some examples of 3D stochastic modeling can be found in [39, 98, 99]. However, we do not consider non-spherical inclusion models in the following.

In this section, we analyze binary random mixtures of two materials (say '0' and '1'), composed of d-dimensional spheres of material 1 randomly placed into a matrix of material 0. The spheres are said to be *hard* when no overlapping is possible. Otherwise, the spheres are said to be *fully penetrable*. For instance, void-filled overlapping spheres surrounded by a scattering material can be used to describe porous media. In the following, we mainly focus on non-overlapping d-dimensional spheres, for dimension $d = 2$ (disks) or $d = 3$ (spheres). Two such models have been mainly proposed: spherical inclusions with *mono-dispersed* radius, meaning that the radius r of the d-dimensional spheres is constant, or *poly-dispersed* radius, meaning that the radius r is randomly sampled from a probability density function $g(r)$ [72, 144, 147]. In the following, both cases will be considered.

For each case, the packing fraction ξ is defined as the volume fraction of the space filled by spheres. The volume fraction of the background matrix is the complementary volume fraction $1 - \xi$. For illustration, some examples of stochastic spherical inclusions are provided in Fig. 2.3, for mono-dispersed or poly-dispersed radius.

2.2.1 Construction of stochastic spherical inclusions

A few algorithms have been proposed in the literature in order to explicit construct spherical inclusions by Monte Carlo methods. In the following, we briefly recall some of the most commonly adopted strategies.

Basic Random Sequential Addition (RSA)

The Random Sequential Addition (RSA) method consists in sequentially introducing random spheres into a box in order to reach the sought packing fraction ξ specified by the model, with the condition that the trial sphere do not overlap those already introduced within the background matrix [156]. An optional constraint is that any sphere overlapping the boundaries is rejected. The position of the sphere is uniformly sampled in the container and the radius randomly sampled from the distribution $g(r)$, for the case of poly-dispersed spheres. The case of mono-dispersed spheres formally corresponds to taking $g(r) = \delta(r - R)$ for some given value R for the radius. In this method, the position of a sphere which has been introduced is fixed, contrary to other algorithms such as those later mentioned in Sec. 2.2.1, where the positions spheres are subsequently adjusted. This algorithm leads to an isotropic random loose packing: indeed, the maximum attainable packing fraction with this method is $\xi \approx 0.38$ for the three-dimensional case [26], and $\xi \approx 0.547$ for the two-dimensional case [35]. For comparison, the packing fraction for a close-packed face-centered cubic lattice is $\xi \approx 0.74$. Further details about three-dimensional RSA sphere packing can be found in [141]. In the following, we assume, without loss of generality, that the container is a box of side L centered in $(0, 0, 0)$.

Algorithm for mono-dispersed spheres. For mono-dispersed three-dimensional spheres of radius R, we want to introduce N spheres in the container, where N is related to ξ by

$$N = \lfloor \frac{3\xi L^3}{4\pi R^3} \rfloor, \tag{2.1}$$

where $\lfloor \cdot \rfloor$ denotes the integer part. Thus, for a constant radius R, the sought parameter ξ is generally not exactly reached, because of round-off effects.

The RSA algorithm for packing N three-dimensional spheres of radius R into the container is the following: initially, there are $k = 0$ spheres in the box. Then, we randomly draw a position (x, y, z) corresponding to the center of the trial sphere. This position is uniformly sampled within the container, such that the sphere does not overlap the boundaries: in other words, x, y and z are sampled from independent uniform distributions $\mathcal{U}[-L/2 + R, L/2 - R]$. Then, we check whether the sphere centered at (x, y, z) with radius R does overlap any of the previous $k-1$ spheres. In the case of overlapping, the sampled sphere is rejected. Otherwise, the trial sphere is added to the list of spheres in the container and the index k is incremented by one. These steps are iterated until the number of spheres in the container reaches $k = N$.

Algorithm for poly-dispersed spheres. For poly-dispersed spheres of random radius r obeying $g(r)$, we start by sequentially sampling the radii r_i of the spheres, until the effective packing fraction resulting from the collection of spheres having radii $r_1, r_2, \cdots, r_N$ is larger than the input parameter ξ. We denote by N the corresponding number of spheres. For the last sphere, the radius r_N can be adjusted such that the effective packing fraction is strictly equal to ξ. Then, we sort the radii in descending order. The purpose of this step is to quickly find a position for the largest spheres.

At this step, there are still $k = 0$ spheres in the box. Then, we randomly sample a position (x, y, z) corresponding to the center of the trial sphere. This position is uniformly sampled within the container, such that the sphere does not overlap the boundaries. We check whether the sphere centered at (x, y, z) with radius r_k does not overlap any of the previous $k - 1$ spheres. In the case of overlapping, this position (x, y, z) is rejected. Otherwise, the trial sphere is accepted, is added to the list of spheres in the container. The counter k is incremented. This step is iterated until the number of spheres in the container reaches $k = N$.

Complexity of the algorithms. For mono or poly-dispersed spheres, the RSA method scales as $\mathcal{O}(N^2)$ with the number N of spheres, since we have to check that all previous spheres do not overlap the trial sphere. This quadratic scaling can lead to very large computational times for configurations where a high packing fraction ξ is sought.

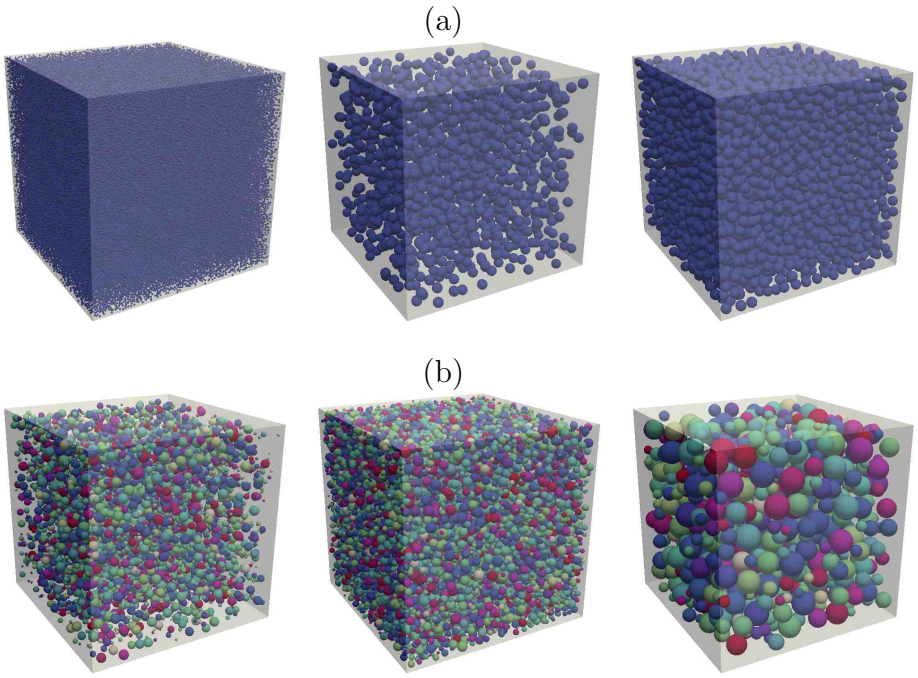

Figure 2.3: Realizations of stochastic spherical inclusions included in a cube of side $L = 10$, with packing fraction ξ. (a) Mono-dispersed radius r: (left) $r = 0.05$ and $\xi = 0.1$; (middle) $r = 0.25$ and $\xi = 0.1$; (right) $r = 0.25$ and $\xi = 0.3$. (b) Poly-dispersed radius r sampled from a random distribution: (left) $r \sim \mathcal{U}[0.05, 0.25]$ and $\xi = 0.1$; (left) $r \sim \mathcal{U}[0.05, 0.25]$ and $\xi = 0.3$; (right) $r \sim \mathcal{U}[0.2, 0.6]$ and $\xi = 0.3$.

Speed-up of the RSA method Fast RSA methods enable to speed-up the basic RSA method by resorting to a fictive meshing of the domain, in order to shorten the computational time spent for the step where we check that the trial sphere does not overlap any other sphere already positioned in the contained. In such methods, instead of checking all previous spheres for overlap, we restrict the research only to nearest-neighbour spheres, by defining a Cartesian mesh with spacing $h = L/n$, where n is the number of cells along each axis. The implementation of such algorithms will be detailed in Chapter 3.

Algorithms for dense packing of spheres

As mentioned above, the basic RSA as well as the fast RSA do not allow reaching packing fractions ξ such as those that might occur for specific applications. For pebble-bed reactors, e.g., the packing fraction is as high as about 0.63 at the center of the vessel [104]. In order to properly model such closely packed systems, a more efficient way of randomly filling space with spheres has to be implemented, ensuring the desired packing fraction. For instance, the ballistic deposition model proposed by Visscher and Bolterlii [155] leads to a sphere packing with a maximum attainable packing fraction $\xi \approx 0.58$. The dynamic algorithm proposed by Jodrey and Tory [46] produces an isotropic random dense packing of spheres up to a packing fraction $\xi \approx 0.649$. In this work, we will not consider these algorithms.

2.2.2 Statistical properties: chord length distribution

In view of particle transport through a random arrangement of spherical inclusions, a particularly relevant observable is the distribution of the chord lengths ℓ determined by the intersection between lines thrown through the geometry and the spheres [127]. In particular, it has been shown that the chord length distribution $\mathcal{P}(\ell)$ plays a prominent role in determining the behaviour of particle trajectories traversing the stochastic tessellation [100, 144]. This can be intuitively understood by considering that the trajectories of particles streaming and colliding through a medium are composed

of a series of straight lines of random length, separated by random reorientations following each collision event: understanding how the geometrical nature of the traversed medium affects the distribution of a straight line with given orientation allows therefore better grasping the effects of the disorder on the particle displacements. In particular, the average chord length through the random geometry can be physically identified with the typical correlation length, i.e., the linear size of the disorder [100,108,144].

For *fully penetrable* spheres, the chord length distribution $\mathcal{P}(\ell_0)$ in the background matrix (material 0) for a line with fixed orientation passing through the random medium has been shown to be exponential [144].

For *hard* spheres, the exact functional form of the chord length distribution across the background matrix for an isotropic random sphere packing is not known, but it has been numerically shown by extensive Monte Carlo simulations that its shape is quasi-exponential. In particular, when the spherical inclusions are sufficiently diluted (i.e., at low packing fractions [1]), the chord length distribution can be described by an exponential function over several decades [100, 144]. The probability density function can be expressed by the approximate formula [144]

$$\mathcal{P}(\ell_0) \approx \frac{\kappa_{d-1}}{\kappa_d} \frac{\xi}{1-\xi} \frac{\langle r^{d-1} \rangle}{\langle r^d \rangle} \exp\left(-\frac{\kappa_{d-1}}{\kappa_d} \frac{\xi}{1-\xi} \frac{\langle r^{d-1} \rangle}{\langle r^d \rangle} \ell_0 \right) \tag{2.2}$$

For the special case $d = 3$, the result has been first established by [30] and reads

$$\mathcal{P}(\ell_0) \approx \frac{3\xi}{4(1-\xi)} \frac{\langle r^2 \rangle}{\langle r^3 \rangle} \exp\left(-\frac{3\xi}{4(1-\xi)} \frac{\langle r^2 \rangle}{\langle r^3 \rangle} \ell_0 \right). \tag{2.3}$$

A remarkable result has been in particular established: for any probability density function $g(r)$ of the sphere radius, the (approximate form of the) chord length distribution across the matrix depends only on the d-th and $(d-1)$-th moments of the radius. From these explicit expressions the average chord length, $\langle \ell_0 \rangle$ immediately follows as

$$\langle \ell_0 \rangle \approx \frac{\kappa_d}{\kappa_{d-1}} \frac{1-\xi}{\xi} \frac{\langle r^d \rangle}{\langle r^{d-1} \rangle} \tag{2.4}$$

In the case of *hard* spheres, the chord length ℓ_1 inside the d-dimensional spheres (material 1) is not exponential. Its distribution can be explicitly computed for a sphere packing with poly-sized radius of probability density function $g(r)$. The probability density function $\mathcal{P}(\ell_1)$ of the chord lengths inside d-dimensional spheres is given by [77]

$$\mathcal{P}(\ell_1) = \begin{cases} \dfrac{\ell_1}{4\langle r \rangle} \displaystyle\int_{\ell_1/2}^{+\infty} \frac{g(r)}{\sqrt{r^2 - (\ell_1/2)^2}} dr & \text{if } d = 2 \\ \dfrac{\ell_1}{2\langle r^2 \rangle} \displaystyle\int_{\ell_1/2}^{+\infty} g(r) dr & \text{if } d = 3. \end{cases} \tag{2.5}$$

In particular, for mono-sized radius ($r = R = \langle r \rangle$), we apply $g(r) = \delta(r - R)$. This yields

$$\mathcal{P}(\ell_1) = \begin{cases} \dfrac{\ell_1}{4R\sqrt{R^2 - (\ell_1/2)^2}} \mathbb{1}_{[0,2R]}(\ell_1) & \text{if } d = 2 \\ \dfrac{\ell_1}{2R^2} \mathbb{1}_{[0,2R]}(\ell_1) & \text{if } d = 3. \end{cases} \tag{2.6}$$

2.3 Poisson tessellations

Poisson geometries are a prominent example of stochastic tessellations: a domain included in a d-dimensional space is partitioned by randomly generated $(d-1)$-dimensional hyperplanes drawn from an underlying Poisson process [75,85,127,129]. A method for the explicit construction of d-dimensional homogeneous and isotropic Poisson tessellations restricted to finite domains has been proposed in the literature [2, 132]. In the following we will detail the algorithm for the construction of Poisson tessellations based on Monte Carlo methods and show that anisotropy can be rather straightforwardly

[1] In this regime, the fully penetrable and hard spheres configurations become indistinguishable.

taken into account. In the following, we will show that Poisson tessellations exactly satisfy the Markov mixing property that is often postulated in the description of random media: a particle traversing the tessellation in a given direction $\mathbf{\Omega}$ will encounter the next material interface after an exponentially distributed length of average $\Lambda(\mathbf{\Omega})$, where $\Lambda(\mathbf{\Omega})$ will be related to a fundamental feature of the Poisson tessellations.

2.3.1 Construction of Poisson tessellations

We illustrate a method for the construction of anisotropic Poisson geometries restricted to a d-dimensional box. Without loss of generality, we assume that the box is centered at the origin. We start by sampling a random number N_H of hyperplanes from a Poisson distribution of intensity $\alpha_d \rho R$, where R is the radius of the d-sphere circumscribed to the box and ρ is the so-called density of the tessellation, carrying the units of an inverse length. The dimension-dependent constant α_d reads

$$\alpha_d = \frac{\Omega_d}{\kappa_{d-1}} = \frac{d\kappa_d}{\kappa_{d-1}}, \tag{2.7}$$

where

$$\Omega_d = \frac{2\pi^{d/2}}{\Gamma\left(\frac{d}{2}\right)} \tag{2.8}$$

is the surface area of the unit d-sphere and

$$\kappa_d = \frac{\pi^{d/2}}{\Gamma\left(1+\frac{d}{2}\right)} \tag{2.9}$$

is the volume of the unit d-sphere. This normalization of the tessellation density is arbitrary and has been chosen so that the correlation length induced by the tessellation (in a sense to be specified later) is simply equal to $1/\rho$ [127]. In particular, for isotropic Poisson tessellations this convention ensures that the mean number of $(d-1)$-hyperplanes intersected by an arbitrary segment of unit length drawn through the tessellation is ρ [127]. Then, we generate the hyperplanes K that will cut the box and thus induce the tessellation. We choose a parameter r uniformly in the interval $[-R, R]$ and additionally sample a unit vector $\mathbf{n}$ from a density $H(\mathbf{n})$ with support in Ω_d^+, i.e., the half-surface of the unit d-sphere. Denoting by $\mathbf{M}$ the point such that $\mathbf{OM} = r\mathbf{n}$, the random plane K will pass trough $\mathbf{M}$ and have normal vector $\mathbf{n}$ (for an illustration, see the scheme in Fig. 2.4). By construction, the hyperplane does intersect the circumscribed d-sphere of radius R but not necessarily the box. The procedure is iterated until N_H random hyperplanes have been generated, which yields homogeneous but (generally) non-isotropic Poisson tessellations [129]. The polyhedra defined by the intersections of such random planes are convex, as mentioned above.

In the following, we first focus on the construction of d-dimensional *isotropic* Poisson tessellations.

1-dimensional Poisson tessellations

In this case, the construction is straightforward. We start by sampling the number N_H of 0-hyperplanes (points) from a Poisson distribution of intensity $2\rho R = \rho L$, which stems from $\alpha_1 = 2$. Then, we uniformly sample N_H random points $x_i, 1 \leq i \leq N_H$ in the interval $[-L/2, L/2]$. Finally, we sort the points x_i in ascending order, in order to obtain an ordered list: $x_0 = -L/2$, x_1, ..., x_{N_H}, $x_{N_H+1} = L/2$. The 1-polyhedra of the corresponding tessellation are the segments $[x_i, x_{i+1}]$, $0 \leq i \leq N_H$.

2-dimensional isotropic Poisson tessellations

We use an iterative approach. At the beginning of the construction, the tessellation is composed by one 2-polyhedron, i.e., the entire square. We start by sampling the number N_H of 1-hyperplanes (lines) from a Poisson distribution of intensity $\pi\rho R = \pi\rho L/\sqrt{2}$, following from $\alpha_2 = \pi$. Then, we sample N_H random lines. The sampling of each random line is done as follows: we choose a parameter

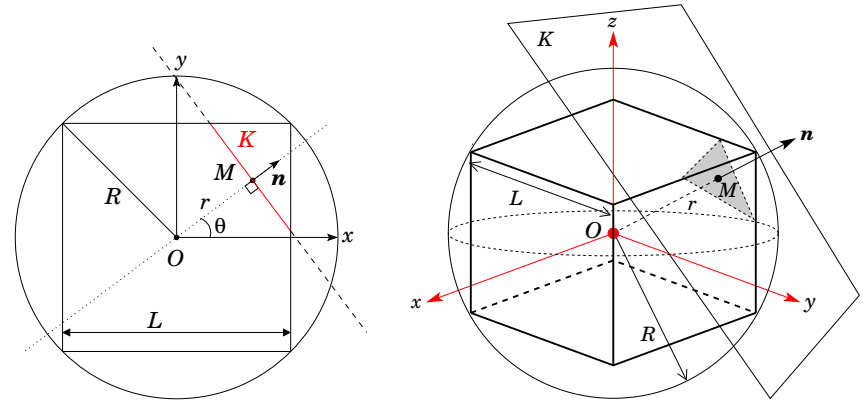

Figure 2.4: Left. Cutting a square in $\mathbb{R}^2$ with a random line. A square of side L is centered in O. The circumscribed circle centered in O has a radius $R = L/\sqrt{2}$. The point $\mathbf{M}$ is defined by $\mathbf{M} = r\mathbf{n}$, where r is uniformly sampled in the interval $[-R, R]$ and $\mathbf{n}$ is a random unit vector sampled from $H(\mathbf{n}) = H(\theta)$, with the components of $\mathbf{n}$ expressed in polar coordinates as: $n_1 = \cos(\theta)$ and $n_2 = \sin(\theta)$. The random line K of equation $n_1 x + n_2 y = r$ is orthogonal to the vector $\mathbf{n}$ and intersects the point $\mathbf{M}$. Right. Cutting a cube in $\mathbb{R}^3$ with a random plane. A cube of side L is centered in O. The circumscribed sphere centered in O has a radius $R = \sqrt{3}L/2$. The point $\mathbf{M}$ is defined by $\mathbf{M} = r\mathbf{n}$, where r is uniformly sampled in the interval $[-R, R]$ and $\mathbf{n}$ is a random unit vector sampled from $H(\mathbf{n})$. The random plane K of equation $n_1 x + n_2 y + n_3 z = r$ is orthogonal to the vector $\mathbf{n}$ and intersects the point $\mathbf{M}$. The components of $\mathbf{n}$ can be expressed in spherical coordinates as: $n_1 = \sin(\theta)\cos(\phi)$, $n_2 = \sin(\theta)\sin(\phi)$, and $n_3 = \cos(\theta)$, where θ is the polar angle (projection onto the z axis), and ϕ is the azimuthal angle (projection onto the $x - y$ plane).

r uniformly in the interval $[-R, R]$ and additionally sample an additional parameter ξ from a uniform distribution in the interval $[0, 1]$. A unit vector $\mathbf{n} = (n_1, n_2)^T$ with components

$$n_1 = \cos(\pi\xi)$$
$$n_2 = \sin(\pi\xi)$$

is generated. The corresponding random line is defined by the equation $n_1 x + n_2 y = r$. For each new random line, we compute the intersections of the line with the polyhedra composing the current tessellation and we update the list of polyhedra of the tessellation. We iterate this step for N_H lines. Some examples of 2-dimensional isotropic Poisson tessellations are provided in Fig. 2.5.

3-dimensional isotropic Poisson tessellations

The approach closely follows the one used for $d = 2$. In order to construct three-dimensional homogeneous and isotropic Poisson tessellations restricted to a box, we use an algorithm recently proposed for finite d-dimensional geometries [2, 132]. At the beginning of the construction, the tessellation is composed by one 3-polyhedron, i.e., the entire cube. We start by sampling the number N_H of 3-hyperplanes (planes) from a Poisson distribution of intensity $4\rho R = 4\sqrt{3}\rho L/2$, following from $\alpha_3 = 4$. Then, we sample N_H random planes. The sampling of each random plane is done as follows: we choose a parameter r uniformly in the interval $[-R, R]$ and additionally sample two additional parameters, namely, ξ_1 and ξ_2, from two independent uniform distributions in the interval $[0, 1]$. A unit vector $\mathbf{n} = (n_1, n_2, n_3)^T$ with components

$$n_1 = 1 - 2\xi_1$$
$$n_2 = \sqrt{1 - n_1^2}\cos(\pi\xi_2)$$
$$n_3 = \sqrt{1 - n_1^2}\sin(\pi\xi_2)$$

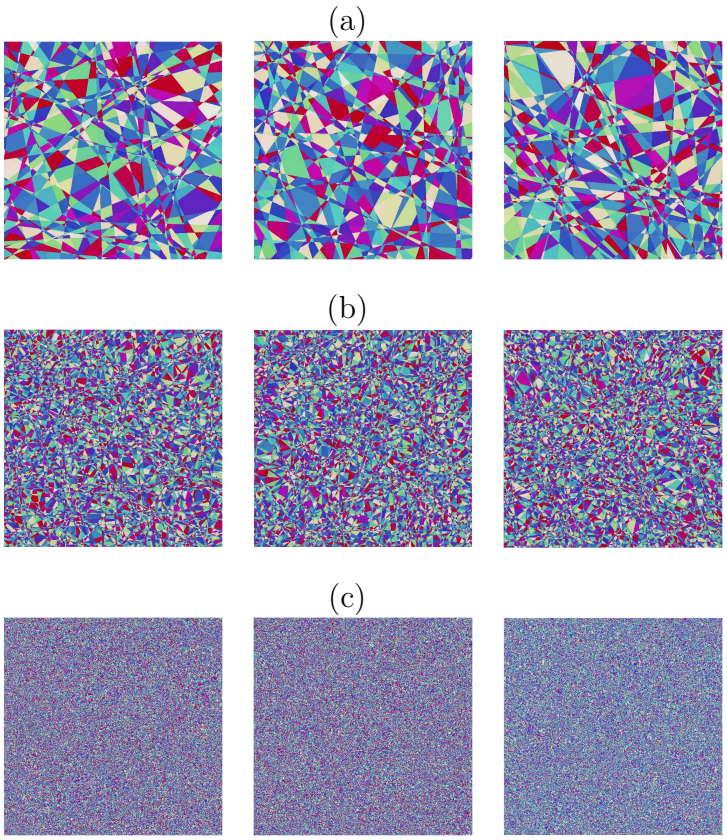

Figure 2.5: Realizations of two-dimensional isotropic Poisson tessellations restricted to a square of side L. For all realizations, we have chosen $\rho = 1$. Top (a): $L = 50$; center (b): $L = 200$; bottom (c): $L = 1000$. For fixed ρ, the average number of random polyhedra increases with increasing L.

is generated. The corresponding random plane is defined by the equation $n_1x + n_2y + n_3z = r$. For each new random plane, we compute the intersections of the plane with the polyhedra composing the current tessellation and we update the list of polyhedra of the tessellation. We iterate this step for N_H planes. Some examples of 3-dimensional isotropic Poisson tessellations are provided in Fig. 2.6.

Anisotropic Poisson tessellations

Anisotropy affects the construction of the tessellations only through the distribution $H(\mathbf{n})$: isotropic Poisson tessellations are obtained as a special case when setting

$$H(\mathbf{n}) = U(\mathbf{n}), \tag{2.10}$$

i.e., the uniform angular distribution over Ω_d^+. Due to geometrical reasons, it is only possible to include anisotropy effects for $d \geq 2$. The density $H(\mathbf{n})$ might admit a finite mass concentrated on a given direction $\mathbf{n}_0$ (a so-called atom), or more generally on a collection of discrete directions $\mathbf{n}_i$, with Dirac delta distributions: the special case where the discrete directions $\mathbf{n}_i$, $i = 1, \cdots, d$, are chosen parallel to the Cartesian axes in dimension d gives rise to the so-called Poisson-Box tessellations [82, 87]. A few examples of realizations corresponding to various angular laws $H(\mathbf{n})$ are illustrated in Fig. 2.7.

2.3.2 Statistical properties of the polyhedral cells

Knowledge of the statistical properties of the polyhedral cells of the stochastic tessellations can be helpful in understanding the behaviour of particle streaming through the geometry. In this framework, the quantities of interest are the volume V_d of a typical cell in dimension d, which characterizes the spatial scale of the random medium, and the surface S_d and the number of faces C_d of a cell, which are

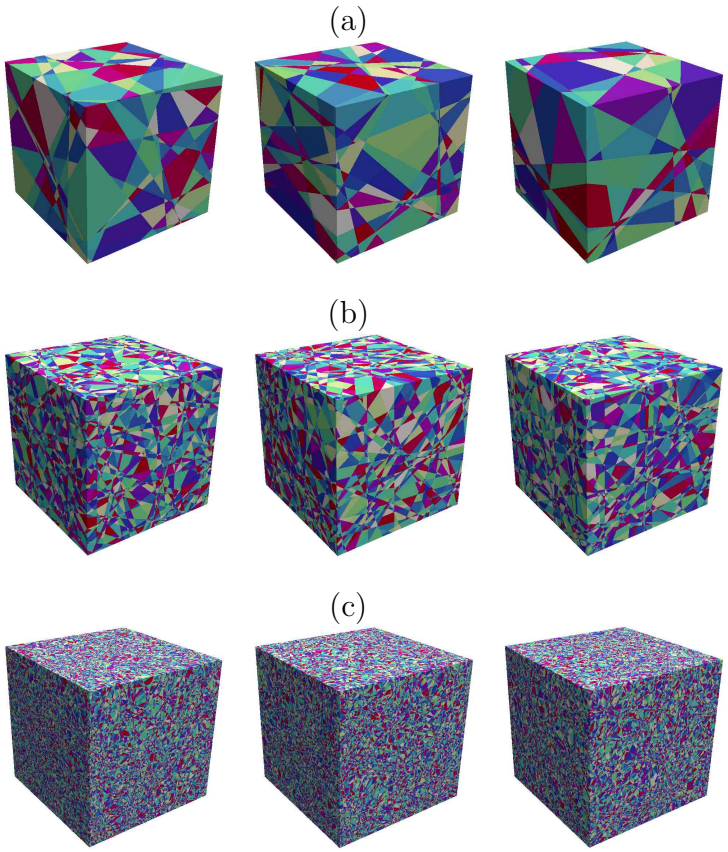

Figure 2.6: Realizations of three-dimensional isotropic Poisson tessellations restricted to a cube of side L. For all realizations, we have chosen $\rho = 1$. Top (a): $L = 10$; center (b): $L = 50$; bottom (c): $L = 200$. For fixed ρ, the average number of random polyhedra increases with increasing L.

related to the connectivity of the medium. The inradius $r_{\mathrm{in},d}$, i.e., the radius of the largest sphere that can be contained in a (convex) polyhedron, and the outradius $r_{\mathrm{out},d}$, i.e., the radius of the smallest sphere enclosing a (convex) polyhedron, can be also useful so as to characterize the shape of the cells (for $d = 1$, the outradius coincides with the inradius).

Such quantities are random variables, whose exact distributions are in most cases unfortunately not known [129]. Nevertheless, analytical expressions have been established for a few low-order moments of the observables, in the limit case of domains having an infinite extension [85, 127, 129]. The case of isotropic Poisson tessellations was first addressed by the pioneering work of Goudsmit for $d = 2$ [41] and later thoroughly explored by Miles first for $d = 2$ and then for higher dimensions in a series of ground-breaking works [82, 85, 87]. Not surprisingly, the derivation of exact results for anisotropic tessellations is even more demanding: the case $d = 2$ was investigated by Miles [82], whereas formulas for higher dimensions were found more recently and are still a subject of active research [129–131].

Isotropic tessellations

For the special case of isotropic Poisson tessellations, the following results have been established for infinite domains [127, 129]. For the volume V_d, we have the moments

$$\langle V_d \rangle = \frac{1}{\kappa_d} \left(\frac{2}{\rho} \right)^d \tag{2.11}$$

and

$$\langle V_d^2 \rangle = \frac{d! \kappa_d^2}{2^d} \langle V_d \rangle^2. \tag{2.12}$$

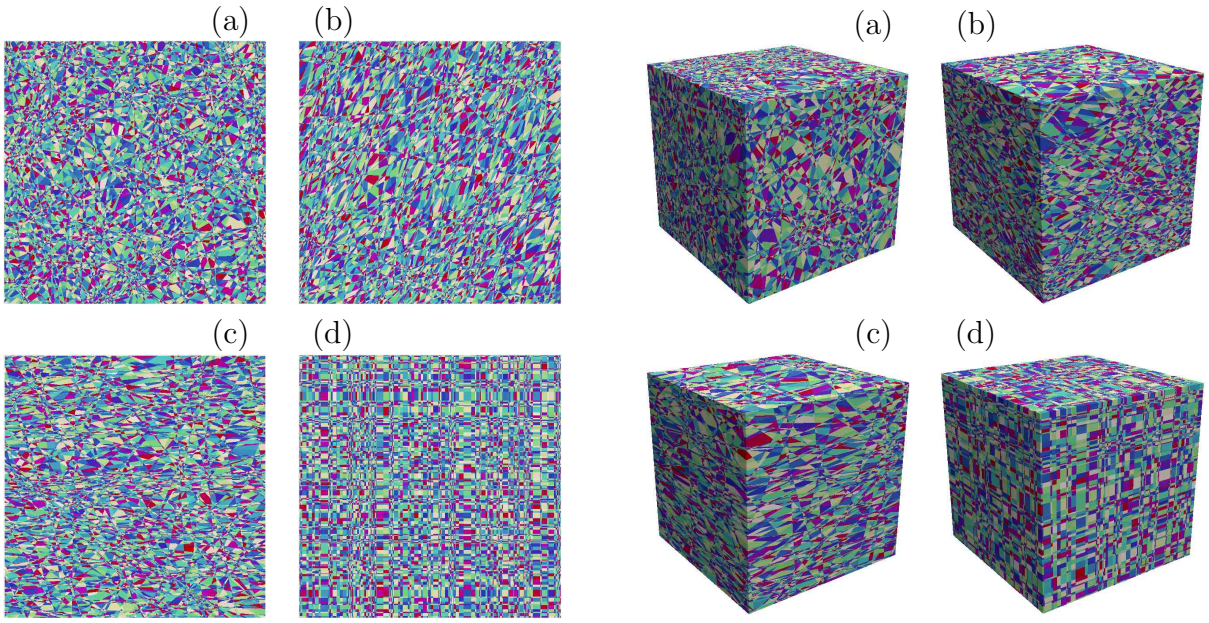

Figure 2.7: Left. Realizations of two-dimensional anisotropic Poisson tessellations restricted to a square of side L, with various angular laws $H(\mathbf{n}) = H(\theta)$, $\theta \in [0, \pi]$. For $d = 2$, $\Omega_2^+ = \pi$. Case a) isotropic distribution, with $H(\theta) = 1/\pi$; b) quadratic distribution, with $H(\theta) = 3\theta^2/\pi^3$; c) symmetric histogram distribution, centered at $\theta = \pi/2$ and having maxima at $\theta = 0$ and $\theta = \pi$; d) box distribution, with $H(\theta) = (1/2)\delta(\theta) + (1/2)\delta(\theta - \pi/2)$. Right. Realizations of three-dimensional anisotropic Poisson tessellations restricted to a cube of side L, with various angular laws $H(\mathbf{n}) = H(\theta, \phi)$. For all realizations, we have chosen $L = 100$ and $\rho = 1$. Case a) isotropic angular distribution ; b) quadratic angular distribution ; c) histogram distribution ; d) box distribution.

The second moment allows computing the coefficient of variation, namely,

$$cv = \sqrt{\frac{\langle V_d^2 \rangle - \langle V_d \rangle^2}{\langle V_d \rangle^2}}, \tag{2.13}$$

which conveys information on the spatial shape of a typical cell [87]. For isotropic Poisson tessellations, from Eq. (2.12) we obtain

$$cv = \sqrt{\frac{d!\kappa_d^2}{2^d} - 1}. \tag{2.14}$$

Furthermore, an elegant recursive formula is known relating the correlations between the surface S_d and the volume to the higher moments of the volume, namely,

$$m\langle V_d^{m-1} S_d \rangle = \alpha_d \rho \langle V_d^m \rangle, \tag{2.15}$$

for $m \geq 1$ [87]. In particular, for $m = 1$ this yields the first moment of S_d, i.e,

$$\langle S_d \rangle = \alpha_d \rho \langle V_d \rangle, \tag{2.16}$$

and for $m = 2$ the correlations

$$\langle V_d S_d \rangle = \frac{\alpha_d \rho}{2} \langle V_d^2 \rangle. \tag{2.17}$$

For the number of faces C_d we have the average

$$\langle C_d \rangle = 2d, \tag{2.18}$$

which does not depend on ρ and is a purely combinatorial result.

Finally, the inradius $r_{\text{in},d}$ has an exponential distribution of parameter $\alpha_d \rho$, and we have in particular

$$\langle r_{\text{in},d} \rangle = \frac{1}{\alpha_d \rho}. \tag{2.19}$$

d	1	2	3
$\langle r_{in,d} \rangle$	$1/2\rho$	$1/\pi\rho$	$1/4\rho$
$\langle V_d \rangle$	$1/\rho$	$4/\pi\rho^2$	$6/\pi\rho^3$
$\langle V_d^2 \rangle$	$2/\rho^2$	$8/\rho^4$	$48/\rho^6$
$\langle S_d \rangle$		$4/\rho$	$24/\pi\rho^2$
$\langle V_d S_d \rangle$		$4\pi/\rho^3$	$96/\rho^5$
$\langle C_d \rangle$	2	4	6
$\langle N_d \rangle$			8
$\langle A_d \rangle$			12
$\langle L_d \rangle$			$12/\rho$
$\langle S_d^2 \rangle$		$(2\pi^2+8)/\rho^2$	$240/\rho^4$
$\langle C_d^2 \rangle$	4	$(\pi^2+24)/2$	$(13\pi^2+336)/12$
$\langle N_d^2 \rangle$			$(13\pi^2+96)/3$
$\langle L_d^2 \rangle$			$24(\pi^2+1)/\rho^2$
$\langle C_d V_d \rangle$		$2\pi/\rho^2$	$4(\pi^2+3)/\pi\rho^3$
$\langle C_d S_d \rangle$		$(\pi^2+8)/\rho$	$(14\pi^2+48)/\pi\rho^2$
$\langle C_d L_d \rangle$			$(5\pi^2+36)/\rho$
$\langle N_d V_d \rangle$			$8\pi/\rho^3$
$\langle N_d S_d \rangle$			$28\pi/\rho^2$
$\langle N_d L_d \rangle$			$(10\pi^2+24)/\rho$
$\langle V_d L_d \rangle$			$24\pi/\rho^4$
$\langle S_d L_d \rangle$			$72\pi/\rho^3$
$\langle V_d^2 S_d \rangle$		$256\pi^2/21\rho^5$	
$\langle V_d^2 C_d \rangle$		$16(8\pi^2-21)/21\rho^4$	
$\langle V_d^3 \rangle$	$6/\rho^3$	$256\pi/7\rho^6$	$1344\pi/\rho^9$

Table 2.1: Exact formulas, as a function of the density parameter ρ and of the dimension d, of the known low-order moments or correlations of polyhedral properties in isotropic Poisson tessellations with an infinite extension: inradius $r_{in,d}$, d-dimensional volume V_d, d-dimensional surface S_d, number of faces C_d, number of vertices N_d, number of edges A_d and total length of edges L_d.

For the outradius $r_{\mathrm{out},d}$, the distribution is not known, and to the best of our knowledge the moments are now known, either, which prevents from using the theoretical ratio $\langle r_{\mathrm{in},d} \rangle / \langle r_{\mathrm{out},d} \rangle$ to extract information of the shape of the cells.

The exact formulas for the moments and the correlations are summarized in Tab. 2.1 as a function of the tessellation density ρ, for $d = 1$, $d = 2$ and $d = 3$.

For isotropic Poisson tessellations, many other results are known for the low-order moments and the correlations of V_d, S_d and C_d [82, 87, 131]. For an exhaustive review, we may refer to, e.g., [129]. Moreover, for $d \geq 3$, the low-order moments and correlations of other polyhedral properties such as the number of vertices for N_d, the number of edges A_d or the total length of edges L_d, have been also derived. The main results are summarized in Tab. 2.1.

Zero-cells of the isotropic tessellations

So far, the statistical properties of the constituents of the isotropic Poisson geometries have been derived by assuming that all of the d-polyhedra have the same statistical weight (for a precise definition, see, e.g., [76,82,85,86]). In other words, each cell of the tessellation contributes equally to the statistical moments.

It is also possible to attribute to each d-polyhedron a statistical weight equal to its d-volume. It can be shown that the statistics of any observable related to the d-polyhedron containing the origin O obeys this latter volume-weighted distribution [85]. This surprising property can be understood by following the heuristic argument proposed by Miles [82]: the origin (or actually any chosen point,

d	1	2	3
$\langle V_d \rangle_0$	$2/\rho$	$2\pi/\rho^2$	$8\pi/\rho^3$
$\langle V_d^2 \rangle_0$	$6/\rho^2$	$64\pi^2/7\rho^4$	$224\pi^2/\rho^6$
$\langle S_d \rangle_0$		π^2/ρ	$16\pi/\rho^2$
$\langle C_d \rangle_0$		$\pi^2/2$	$2(\pi^2+3)/3$
$\langle N_d \rangle_0$			$4\pi^2/3$
$\langle L_d \rangle_0$			$4\pi^2/\rho$

Table 2.2: Moments of the d-polyhedron containing the origin.

since we are considering tessellations having an infinite extension, which are by construction invariant under translation) has greater chances of falling within a larger rather than a smaller volume. In particular, for the moments $\langle X \rangle_0$ of the d-polyhedron containing the origin, the so-called zeros-cell, we formally have

$$\langle X \rangle_0 = \frac{\langle V_d X \rangle}{\langle V_d \rangle}, \tag{2.20}$$

where X denotes an arbitrary observable [85]. The exact formulas for the main observables of the polyhedron containing the origin for isotropic Poisson tessellations are recalled in Tab. 2.2.

Anisotropic tessellations

As expected, the general case of anisotropic Poisson tessellations is much more involved and the obtained formulas generally depend on the angular distribution $H(\mathbf{n})$. For the main polyhedral quantities discussed earlier, the following results have been established for infinite domains [129]. For the volume V_d the first moment obeys

$$\langle V_d \rangle = \frac{d!}{\zeta_d} \left(\frac{2}{\alpha_d \rho} \right)^d, \tag{2.21}$$

where the constant ζ_d depends on the angular distribution $H(\mathbf{n})$ and is defined as

$$\zeta_d = \int_{\Omega_d^+} \cdots \int_{\Omega_d^+} [\mathbf{n}_1, \cdots, \mathbf{n}_d] \, dH(\mathbf{n}_1) \cdots dH(\mathbf{n}_d), \tag{2.22}$$

the integrals being extended over the half-surface of the unit d-sphere. Here the quantity $[\mathbf{n}_1, \cdots, \mathbf{n}_d]$ denotes the d-space determinant [2] of the unit vectors $\mathbf{n}_1, \cdots, \mathbf{n}_d$: for $d = 2$, e.g., it represents the area of the parallelogram spanned by $\mathbf{n}_1$ and $\mathbf{n}_2$; for $d = 3$, it represents the volume of the parallelepiped spanned by $\mathbf{n}_1$, $\mathbf{n}_2$ and $\mathbf{n}_3$ [129]. As a particular case, for isotropic tessellations Eq. (2.22) yields

$$\zeta_d^{\text{iso}} = \frac{d! \kappa_d}{\alpha_d^d}, \tag{2.23}$$

and from Eq. (2.21) we recover Eq. (2.11) for the average volume. The second moment of the volume V_d reads

$$\langle V_d^2 \rangle = \zeta_d \eta_d \kappa_d \langle V_d \rangle^2, \tag{2.24}$$

where the constant η_d also depends on the angular distribution $H(\mathbf{n})$ and is defined as [129]

$$\eta_d = \int_{\Omega_d^+} dU(\mathbf{\Omega}) \left(\int_{\Omega_d^+} |\mathbf{n} \cdot \mathbf{\Omega}| dH(\mathbf{n}) \right)^{-d}. \tag{2.25}$$

From Eq. (2.12) we obtain the coefficient of variation

$$cv = \sqrt{\zeta_d \eta_d \kappa_d - 1}, \tag{2.26}$$

[2] If the determinant is negative, we take the absolute value.

which generalizes Eq. (2.14) to the case of arbitrary $H(\mathbf{n})$ distributions. For isotropic tessellations, Eq. (2.25) yields

$$\eta_d^{\mathrm{iso}} = \left(\frac{\alpha_d}{2}\right)^d. \tag{2.27}$$

Hence, from Eq. (2.24) we recover Eq. (2.12) for the second moment of the volume.

For the surface S_d, the recursive formula given in Eq. (2.15) has been shown to hold for any $H(\mathbf{n})$ [129], so that the first moment of S_d is again related to the average volume by Eq. (2.16) and the correlations between the surface and the volume are again related to the second moment of the volume by Eq. (2.17). Thus, the effect of $H(\mathbf{n})$ is only indirectly conveyed on $\langle S_d \rangle$ and $\langle V_d S_d \rangle$ through the behaviour of $\langle V_d \rangle$ and $\langle V_d^2 \rangle$, respectively.

It is interesting to observe that, although the average volume and surface depend on the angular law $H(\mathbf{n})$ through the function ζ_d, the aspect ratio $\langle V_d \rangle / \langle S_d \rangle$ of the cells does not, and we get

$$\frac{\langle V_d \rangle}{\langle S_d \rangle} = \frac{1}{\alpha_d \rho}, \tag{2.28}$$

depending only on the tessellation density ρ and on the constant α_d.

Finally, for the average number of faces we have again Eq. (2.18), which does not depend on the angular distribution.

The distribution of the inradius $r_{\mathrm{in},d}$ is not affected by the anisotropy of the tessellation, and has again an exponential distribution of parameter $\alpha_d \rho$. For the outradius $r_{\mathrm{out},d}$, no theoretical result is known, to the best of our knowledge. Numerical investigations show however that the average outradius $\langle r_{\mathrm{out},d} \rangle$ depends on $H(\mathbf{n})$, contrary to the average inradius $\langle r_{\mathrm{in},d} \rangle$.

A special case of anisotropic Poisson tessellations corresponds to taking fixed orientations parallel to the orthogonal Cartesian axes in $\mathbb{R}^d$. In the simplest form, each direction is taken with equal probability, which yields a quasi-isotropic stochastic geometry [87]. For these so-called Poisson-Box tessellations, the functions ζ_d and η_d can be computed exactly from Eqs. (2.22) and (2.25), respectively, and yield

$$\zeta_d^{\mathrm{box}} = \frac{d!}{d^d} \tag{2.29}$$

and

$$\eta_d^{\mathrm{box}} = \frac{(2d)^d}{d! \kappa_d}, \tag{2.30}$$

respectively.

Inequalities for anisotropic tessellations

The volume V_d and the surface S_d depend on the anisotropy law $H(\mathbf{n})$. It can be shown that for any sufficiently well-behaved $H(\mathbf{n})$ the quantity ζ_d satisfies

$$\zeta_d \leq \zeta_d^{\mathrm{iso}}, \tag{2.31}$$

which from Eq. (2.21) implies that the average volume attains a minimum for the case of isotropic Poisson tessellations [79, 129], namely,

$$\langle V_d \rangle \geq \langle V_d \rangle^{\mathrm{iso}}. \tag{2.32}$$

More generally, it can be proven that $\langle V_d^m \rangle \geq \langle V_d^m \rangle^{\mathrm{iso}}$ for the moments of any order $m \geq 1$ [79], whence in particular

$$\langle V_d^2 \rangle \geq \langle V_d^2 \rangle^{\mathrm{iso}}. \tag{2.33}$$

Moreover, it has been shown that $\mathrm{cv}^{\mathrm{box}} \leq \mathrm{cv} \leq \mathrm{cv}^{\mathrm{iso}}$ [129].

For S_d, Eq. (2.16) implies that the average surface attains also a minimum for the case of isotropic Poisson tessellations, namely,

$$\langle S_d \rangle \geq \langle S_d \rangle^{\mathrm{iso}}. \tag{2.34}$$

From Eqs. (2.33) and (2.17), we have an analogous inequality for the correlations, namely,

$$\langle V_d S_d \rangle \geq \langle V_d S_d \rangle^{\mathrm{iso}}. \tag{2.35}$$

2.3.3 Chord length distribution

For general anisotropic Poisson tessellations having density ρ and infinite size, an arbitrary line with orientation $\mathbf{\Omega}$ will encounter a number of random hyperplanes per unit length distributed according to a Poisson distribution of density

$$\rho(\mathbf{\Omega}) = \frac{\alpha_d \rho}{2} \int_{\Omega_d^+} |\mathbf{n} \cdot \mathbf{\Omega}| dH(\mathbf{n}), \tag{2.36}$$

depending on the anisotropy law $H(\mathbf{n})$ and on the direction $\mathbf{\Omega}$ [90]. Conversely, the line will be cut by the hyperplanes into segments whose lengths ℓ obey the exponential distribution

$$\mathcal{P}(\ell|\mathbf{\Omega}) = \rho(\mathbf{\Omega}) e^{-\ell\rho(\mathbf{\Omega})}, \tag{2.37}$$

depending on the fixed orientation $\mathbf{\Omega}$. It has been suggested that such tessellations might be the only stochastic geometries to satisfy the Markov properties [87, 90]. We have then a direction-dependent average chord length

$$\Lambda(\mathbf{\Omega}) = \int \ell \mathcal{P}(\ell|\mathbf{\Omega}) d\ell = \frac{1}{\rho(\mathbf{\Omega})}. \tag{2.38}$$

For the special case of isotropic tessellations, Eq. (2.36) yields

$$\int_{\Omega_d^+} |\mathbf{n} \cdot \mathbf{\Omega}| dU(\mathbf{n}) = \frac{2}{\alpha_d}, \tag{2.39}$$

so that

$$\mathcal{P}(\ell|\mathbf{\Omega}) = \rho e^{-\ell\rho}, \tag{2.40}$$

for any orientation $\mathbf{\Omega}$. The average chord length reads then $\Lambda(\mathbf{\Omega}) = \int \ell \mathcal{P}(\ell|\mathbf{\Omega}) d\ell = 1/\rho$.

2.3.4 Random line sections and the Cauchy formula

We will now examine the case where the lines crossing the tessellations are random. To be more precise, we will consider the ensemble $\mathcal{T}$ of independent and identically distributed *homogeneous and isotropic* random lines [3].

[3] In dimension $d = 2$, a line section of a bounded domain $X \subset \mathbb{R}^2$ satisfying the homogeneity and isotropy property can be obtained as follows. Consider the disk S containing X and with the smallest possible radius. Take then an isotropic direction $\mathbf{\Omega}$ emanating from the center of S. Take a random point whose position z is uniformly distributed on the diameter of S in direction $\mathbf{\Omega}$. Construct now the line passing through z and orthogonal to $\mathbf{\Omega}$. If the line intersects the domain X, this is an acceptable line section satisfying the properties above; if not, repeat the whole procedure until a new line hits X.

In dimension $d = 3$, a line section of a bounded domain $X \subset \mathbb{R}^3$ satisfying the homogeneity and isotropy property can be obtained by first constructing a plane section. Consider the sphere S containing X and with the smallest possible radius. Take then an isotropic direction $\mathbf{\Omega}$ emanating from the center of S. Take a random point whose position z is uniformly distributed on the diameter of S in direction $\mathbf{\Omega}$. Construct now the plane passing through z and orthogonal to $\mathbf{\Omega}$. If the plane intersects the domain X, this is a plane section of X satisfying homogeneity and isotropy; if not, repeat the whole procedure until a new plane hits X. Once the plane section is obtained, the procedure for line sections in $d = 2$ can be applied: it can be shown that an homogeneous and isotropic line section of an homogeneous and isotropic plane section of X is actually an homogeneous and isotropic line section of X in $d = 3$.

Other procedures exist for homogeneous and isotropic line sections in dimension d that do not require rejection methods [25]. This can be achieved, e.g., by first choosing a point $\mathbf{P}$ uniformly on the surface of $X \subset \mathbb{R}^d$ and then sampling lines passing through $\mathbf{P}$ and with direction $\mathbf{\Omega}$ satisfying an isotropic incident flux with respect to the normal $\mathbf{n}$ entering the surface of X at point $\mathbf{P}$. This condition imposes the measure [25, 127]

$$\alpha_d \frac{d\mathbf{\Omega}}{\Omega_d} \frac{dS_d(X)}{S_d(X)} (\mathbf{\Omega} \cdot \mathbf{n}). \tag{2.41}$$

The term $\cos\theta = \mathbf{\Omega} \cdot \mathbf{n}$ implies that in polar coordinates trajectories starting on the surface must enter the domain X with $\theta = \arcsin(2s - 1)$ in two dimensions and $\theta = 1/2 \arccos(1 - 2s)$ in three dimensions, s being uniformly distributed in $(0, 1]$ [78, 78].

The probability that a line drawn from the ensemble $\mathcal{T}$ hits a sub-domain $Y \subset X$ of a bounded domain X in $\mathbb{R}^d$ is given by

$$P(\mathcal{T} \cap Y \neq 0) = \frac{S_d(Y)}{S_d(X)}, \tag{2.42}$$

where $S_d(A)$ denotes the surface of a domain A in $\mathbb{R}^d$ [88]. Furthermore, conditionally to hitting Y, such lines are homogeneous and isotropic through Y. This result is independent of the position and orientation of the sub-domain Y within X. Let us denote by ℓ the random line sections induced on Y.

The Cauchy theorem (also called Crofton second theorem) states that the ensemble average $\mathbb{E}[\ell]$ of the random line sections through Y satisfies

$$\mathbb{E}[\ell] = \alpha_d \frac{V_d(Y)}{S_d(Y)}, \tag{2.43}$$

where $V_d(A)$ denotes the volume of a domain A in $\mathbb{R}^d$, provided that lines are homogeneous and isotropic [88, 90]. In other words, the average line section $\mathbb{E}[\ell]$ through Y depends only on the ratio between the volume and the surface of Y, regardless of the specific details of the shape of the domain, up to the dimension-dependent constant α_d. This is a special case of a broader set of stereological formulas derived by Miles for the projection of a body (or a collection of bodies) onto random s-dimensional flats in $\mathbb{R}^d$ [88–90].

Consider then a disjoint aggregate of convex domains $\{X_i\} \subset X$, $i = 1, 2, \cdots, Q$, in $\mathbb{R}^d$. From Eqs. (2.42) and (2.43), the average line section through the aggregate reads

$$\mathbb{E}[\sum_{j=1}^{q} \ell_j] = \alpha_d \sum_{i=1}^{Q} \frac{V_d(X_i)}{S_d(X)} \tag{2.44}$$

where ℓ_j, $j = 1, \cdots, q$ are the line sections of the non void intersections $\mathcal{T} \cap X_j$ between the lines and the domains composing the aggregate [88]. The number q of such intersections is itself random, with expected value

$$\mathbb{E}[q] = \sum_{i=1}^{Q} \frac{S_d(X_i)}{S_d(X)}. \tag{2.45}$$

By formally taking the ratio between Eqs. (2.44) and (2.45), the average line section for the domains composing the aggregate $\{X_i\}$ can be estimated by

$$\lambda_c \equiv \frac{\mathbb{E}[\sum_{j=1}^{q} \ell_j]}{\mathbb{E}[q]} = \alpha_d \frac{\sum_{i=1}^{Q} V_d(X_i)}{\sum_{i=1}^{Q} S_d(X_i)}. \tag{2.46}$$

Suppose now that the aggregate described above is a Poisson stochastic tessellation in $\mathbb{R}^d$, whose cells are disjoint, space-filling polyhedra. By taking ergodic averages over the constituents of the geometries [88, 90], in the limit of infinite size for the average volume of a cell we have

$$\lim_{Q\to\infty} \frac{1}{Q} \sum_{i=1}^{Q} V_d(X_i) \to \langle V_d \rangle = \frac{d!}{\zeta_d} \left(\frac{2}{\alpha_d \rho} \right)^d, \tag{2.47}$$

and for the average surface of a cell we have

$$\lim_{Q\to\infty} \frac{1}{Q} \sum_{i=1}^{Q} S_d(X_i) \to \langle S_d \rangle = \alpha_d \rho \langle V_d \rangle. \tag{2.48}$$

Finally, combining Eqs. (2.46), (2.47) and (2.48), the average chord length Λ_c through the cells of the tessellation induced by the random lines $\mathcal{T}$ can be estimated from

$$\Lambda_c \equiv \lim_{Q\to\infty} \lambda_c \to \alpha_d \frac{\langle V_d \rangle}{\langle S_d \rangle} = \frac{1}{\rho}. \tag{2.49}$$

provided that the lines are uniformly and isotropically distributed [88].

This remarkable result show that under these hypotheses the average chord length Λ_c for anisotropic Poisson tessellations of infinite size is simply equal to the inverse of the tessellation density ρ, and does not depend on the anisotropy law $H(\mathbf{n})$, although $V_d(X_i)$ and $S_d(X_i)$ separately depend on $H(\mathbf{n})$. Observe that the definition in Eq. (2.49) formally corresponds to taking

$$\frac{1}{\Lambda_c} = \int_{\Omega_d^+} \rho(\mathbf{\Omega}) dU(\mathbf{\Omega}) = \rho, \tag{2.50}$$

i.e., averaging the Poisson density $\rho(\mathbf{\Omega})$ as in Eq. (2.36) over the uniform angular distribution $U(\mathbf{\Omega})$. Observe that in general

$$\Lambda_c \neq \int_{\Omega_d^+} \Lambda(\mathbf{\Omega}) dU(\mathbf{\Omega}), \tag{2.51}$$

unless the tessellation is isotropic, in which case $\Lambda_c = \Lambda = 1/\rho$.

2.4 Poisson-Box tessellations

Poisson-Box tessellations form a class of anisotropic stochastic geometries composed of rectangular boxes with random sides. For the case of three-dimensional Poisson Box tessellations (as proposed by [87]), a domain $X \in \mathbb{R}^3$ is randomly partitioned by *i*) randomly generated planes orthogonal to the x-axis, through a Poisson process of intensity ρ_x; *ii*) randomly generated planes orthogonal to the y-axis, through a Poisson process of intensity ρ_y; *iii*) randomly generated planes orthogonal to the z-axis, through a Poisson process of intensity ρ_z. In the following, we will assume that the three parameters are equal, namely, $\rho_x = \rho_y = \rho_z = \rho_{\mathcal{B}}$. Such Poisson-Box tessellations are statistically equivalent to a special case of anisotropic Poisson tessellations, constructed with the following anisotropy law

$$H(\mathbf{n}) = \frac{\mathbf{1}}{\mathbf{3}} \left[\delta(\mathbf{n} = (\mathbf{1}, \mathbf{0}, \mathbf{0})^{\mathbf{T}}) + \delta(\mathbf{n} = (\mathbf{0}, \mathbf{1}, \mathbf{0})^{\mathbf{T}}) + \delta(\mathbf{n} = (\mathbf{0}, \mathbf{0}, \mathbf{1})^{\mathbf{T}}) \right] \tag{2.52}$$

and with a tessellation density

$$\rho = \frac{3}{2} \rho_{\mathcal{B}}. \tag{2.53}$$

2.4.1 Construction of Box tessellations

In order to tessellate a domain $X \in \mathbb{R}^3$, where X is a cube of side L centered in O, the construction algorithm is the following: we start by sampling a random number N_x from a Poisson distribution of parameter $\rho_{\mathcal{B}} L$. Then, we sample N_x points uniformly on the segment $[-L/2, L/2]$. For each point of this set, we cut the geometry with the plane orthogonal to the x-axis and passing through this point. We repeat this process for the y-axis and the z-axis. For the sake of conciseness, we will denote by Box tessellations these Poisson-Box tessellations. Some examples of Box tessellations are provided in Fig. 2.8.

2.4.2 Statistical properties of polyhedral cells

The first-order moments of the typical polyhedral cells of d-dimensional Box tessellations of infinite extension are

$$\langle V_d \rangle = \frac{1}{{\rho_{\mathcal{B}}}^d} \tag{2.54}$$

for the d-dimensional volume and

$$\langle S_d \rangle = \frac{2d}{{\rho_{\mathcal{B}}}^{d-1}} \tag{2.55}$$

for the d-dimensional surface.

In particular, for $d = 3$, the average volume is given by

$$\langle V_3 \rangle = \frac{1}{\rho_{\mathcal{B}}^3} \tag{2.56}$$

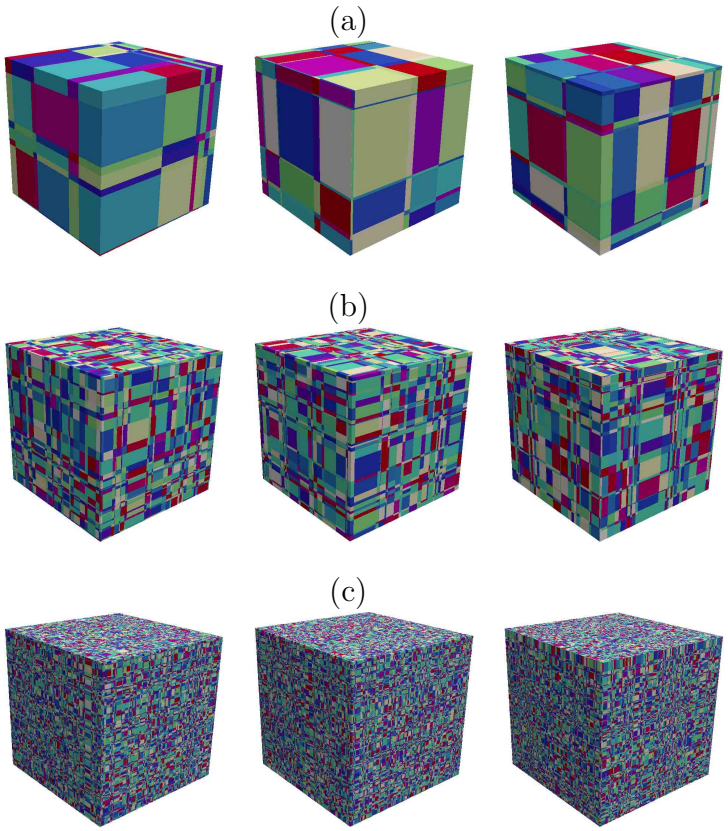

Figure 2.8: Realizations of three-dimensional Box tessellations restricted to a cube of side L. For all realizations, we have chosen $\rho_{\mathcal{B}} = 2/3$. Top (a): $L = 10$; center (b): $L = 50$; bottom (c): $L = 200$. For fixed $\rho_{\mathcal{B}}$, the average number of random polyhedra increases with increasing L.

and the average total surface $\langle S_3 \rangle$ by

$$\langle S_3 \rangle = \frac{6}{\rho_{\mathcal{B}}^2}. \tag{2.57}$$

In addition, the average total length of edges $\langle L_3 \rangle$ is given by

$$\langle L_3 \rangle = \frac{12}{\rho_{\mathcal{B}}}. \tag{2.58}$$

Moreover, the k-th order moment of the volume $\langle V_3^k \rangle$ in three-dimensional Box tessellations of infinite extension is known [87]. Since the random seeds for the tessellations are points obeying a Poisson distribution with parameter $\rho_{\mathcal{B}}$, the inter-particle distances are exponentially distributed with parameter $1/\rho_{\mathcal{B}}$. Hence, the k-th order moment of the inter-particle distances (i.e., the edges of the random boxes) will be $k!/\rho_{\mathcal{B}}^k$. For the volume we have then

$$\langle V_3^k \rangle = \frac{(k!)^3}{\rho_{\mathcal{B}}^{3k}}. \tag{2.59}$$

Equations (2.56) and (2.57) can be equivalently obtained by computing the average volume given by Eq. (2.21) and the average surface given by Eq (2.28) for anisotropic Poisson tessellations with ρ defined as in Eq. (2.53), with ζ_d and η_d from Eqs. (2.29) and (2.30), respectively.

2.4.3 Chord length distribution

In Sec. 2.3.3, we have seen that for general anisotropic Poisson tessellations having density ρ, anisotropy law $H(\mathbf{n})$ and infinite size, an arbitrary line with orientation $\mathbf{\Omega} = (\omega_x, \omega_y, \omega_z)^T$ will encounter a number of random hyperplanes per unit length distributed according to a Poisson distribution whose intensity

$\rho(\mathbf{\Omega})$ is given by Eq. 2.36. In order to infer the chord length statistics for Box tessellations we can use the fact that such tessellations are a special case of anisotropic Poisson tessellations.

We consider the case of three-dimensional Box tessellations of density $\rho_{\mathcal{B}}$, constructed as anisotropic Poisson tessellations with ρ defined as in Eq. 2.53 and $H(\mathbf{n})$ defined as in Eq. 2.52. For three-dimensional Box tessellations, Eqs. 2.7, 2.36, 2.53 and 2.52 yield

$$\rho_{\mathcal{B}}(\mathbf{\Omega}) = \rho_{\mathcal{B}}(|\omega_x| + |\omega_y| + |\omega_z|). \tag{2.60}$$

From Eq. 2.37, the line of orientation $\mathbf{\Omega}$ will be cut by the hyperplanes into segments whose lengths ℓ obey the exponential distribution

$$\mathcal{P}^{\mathcal{B}}(\ell|\mathbf{\Omega}) = \rho_{\mathcal{B}}(|\omega_x| + |\omega_y| + |\omega_z|)e^{-\ell\rho_{\mathcal{B}}(|\omega_x|+|\omega_y|+|\omega_z|)}. \tag{2.61}$$

We will now examine the case where the lines are randomly distributed. Consider a Box tessellation and an ensemble $\mathcal{T}$ of homogeneous and isotropic random lines as previously defined. The considerations stemming from the Cauchy formula presented for anisotropic Poisson tessellations clearly apply also for the Box tessellations. Then, according to Eqs. 2.49 and 2.53, the average chord length Λ_c through the cells of the Box tessellation induced by the random lines $\mathcal{T}$ reads [88]

$$\Lambda_c = \alpha_d \frac{\langle V_d \rangle}{\langle S_d \rangle} = \frac{2}{d\rho_{\mathcal{B}}}. \tag{2.62}$$

Observe that from Eq. (2.60) we can perform the explicit integration

$$\int_{\Omega_d^+} \rho_{\mathcal{B}}(\mathbf{\Omega}) dU(\mathbf{\Omega}) = \frac{2d}{\alpha_d}\rho_{\mathcal{B}} = \frac{1}{\Lambda_c}, \tag{2.63}$$

which yields a result coherent with the considerations presented above for the relation between $\rho_{\mathcal{B}}(\mathbf{\Omega})$ and Λ_c.

2.5 Poisson-Voronoi tessellations

Consider a collection of points $\mathbf{X} = \{\mathbf{x_i}\}$ in $\mathbb{R}^d$. The Voronoi tessellation of $\mathbb{R}^d$ with nuclei $\{x_i\}$ is then defined by the cells

$$C_i = \{y \in \mathbb{R}^d : ||x_i - y|| \leq ||x_j - y||; i \neq j\}, \tag{2.64}$$

where $||\cdot||$ is the usual Euclidean distance. This means that the Voronoi cell C_i associated to the nucleus x_i corresponds to the region of points $y \in \mathbb{R}^d$ such that y is closer to the nucleus x_i than to any other nucleus. The Voronoi cells have disjoint interiors and are convex and closed sets. Furthermore, for subsets $A \subset \mathbb{R}^d$, we have a Voronoi tessellation of A which is simply given by the restriction of the Voronoi cells to A.

In the following, we will exclusively focus on Poisson-Voronoi tessellations, which form a subclass of Voronoi geometries where $\mathbf{X} = \mathbf{x_i}$ is assumed to be a homogeneous Poisson point process [40,80,87]. A Poisson process $\mathbf{X}$ defined on $\mathbb{R}^d$ and with intensity measure μ and intensity function ξ satisfies for any bounded region $B \subseteq \mathbb{R}^d$ with $\mu(B) > 0$,

- $N(B)$ is Poisson distributed with mean $\mu(B)$,
- conditional on $N(B)$, the points in $\mathbf{X}_B$ are independent and identically distributed with density proportional to $\xi(u)$, $u \in B$.

For a stationary point process $\mathbf{X}$ such as the homogeneous Poisson point process where $\xi(u) = \xi$ is constant over the domain, the Voronoi cells are bounded and the tessellation is isotropic. Poisson-Voronoi tessellations provide thus a prototype process for isotropic random division of space [127]. In order to avoid confusion with the Poisson tessellations described above, we will mostly refer to Poisson-Voronoi geometries simply as Voronoi tessellations in the following.

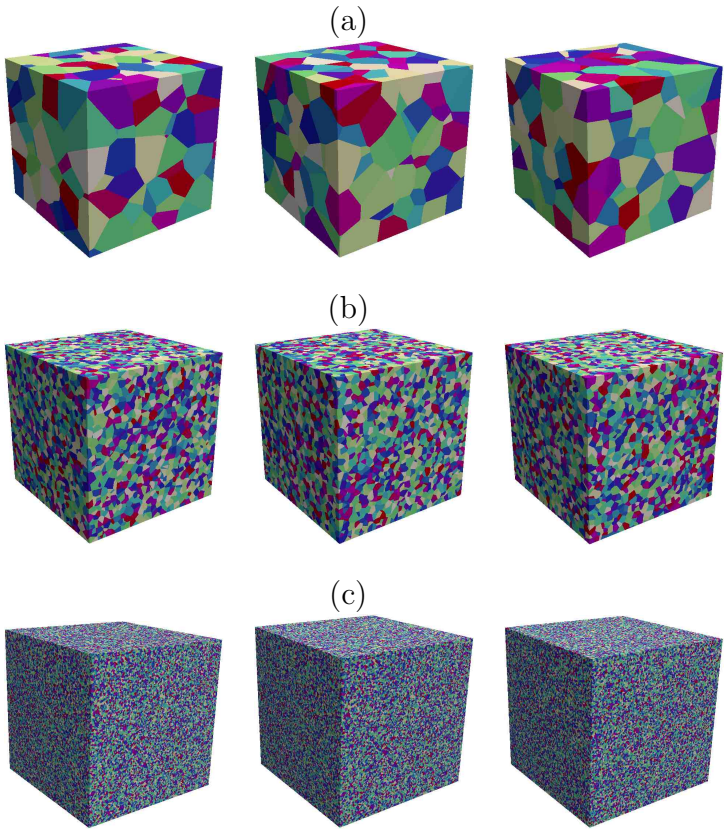

Figure 2.9: Realizations of three-dimensional Voronoi tessellations restricted to a cube of side L. For all realizations, we have chosen $\rho_{\mathcal{V}} \approx 0.6872$. Top (a): $L = 10$; center (b): $L = 50$; bottom (c): $L = 200$. For fixed $\rho_{\mathcal{V}}$, the average number of random polyhedra increases with increasing L.

2.5.1 Construction of Voronoi tessellations

In order to construct d-dimensional Poisson-Voronoi tessellations restricted to $A \subset \mathbb{R}^d$, where A is a d-dimensional box of side L, we use the algorithm proposed in [87]. First, we choose the random number N of nuclei from a Poisson distribution of parameter $(\rho_{\mathcal{V}} L)^d$, where $\rho_{\mathcal{V}}$ characterizes the density of the tessellation and carries the units of an inverse length. Then, N nuclei $x_{i1 \leq x_i \leq N}$ are uniformly sampled in the box $[-L/2, L/2]^d$. Initially, the tessellation is composed of the box itself. We add successively each nucleus to the tessellation, as follows: we compute the corresponding Voronoi cell C_i as the intersection of half-spaces bounded by the mid-planes between the selected nucleus and any other seed of the current tessellation; then, we add this cell to the tessellation and we update the cells truncated by the new cell. This decomposition corresponds to the Green and Sibson algorithm. For illustration, some examples of three-dimensional Voronoi tessellations are provided in Fig. 2.9.

2.5.2 Statistical properties of polyhedral cells

Some first-order moments of the typical polyhedral cells of d-dimensional Voronoi tessellations of infinite extension are known [85]. For instance,

$$\langle V_d \rangle = \frac{1}{\rho_{\mathcal{V}}{}^d} \tag{2.65}$$

for the d-dimensional volume $\langle V_d \rangle$,

$$\langle S_d \rangle = \frac{2\alpha_d \Gamma(2 - \frac{1}{d}) \Gamma(\frac{d}{2} + 1)^{2-1/d} \Gamma(d)}{d\Gamma(\frac{d+1}{2})^2 \Gamma(d - \frac{1}{2}) \rho_{\mathcal{V}}{}^{d-1}} \tag{2.66}$$

for the d-dimensional surface $\langle S_d \rangle$ and

$$\langle N_d \rangle = \frac{2^{d+1}\pi^{(d-1)/2}\Gamma(\frac{d^2+1}{2})\Gamma(\frac{d}{2}+1)^d\Gamma(d)}{d!d\Gamma(\frac{d^2}{2})\Gamma(\frac{d+1}{2})} \tag{2.67}$$

for the number of vertices $\langle N_d \rangle$. In particular, for dimension $d = 3$, this yields

$$\langle V_3 \rangle = \frac{1}{{\rho_{\mathcal{V}}}^3}, \tag{2.68}$$

$$\langle S_3 \rangle = \frac{(256\pi/3)^{\frac{1}{3}}\Gamma\left(\frac{5}{3}\right)}{{\rho_{\mathcal{V}}}^2}, \tag{2.69}$$

and

$$\langle N_3 \rangle = \frac{96\pi^2}{35} \simeq 27.07. \tag{2.70}$$

For three-dimensional Voronoi tessellations, additional moments of the typical polyhedral cells have been derived [80]. For the number of faces $\langle C_3 \rangle$ we have

$$\langle C_3 \rangle = \frac{48\pi^2 + 70}{35} \simeq 15.54, \tag{2.71}$$

for the number of edges $\langle A_3 \rangle$ we have

$$\langle A_3 \rangle = \frac{144\pi^2}{35} \simeq 40.61, \tag{2.72}$$

and finally, for the total length of edges $\langle L_3 \rangle$ we have

$$\langle L_3 \rangle = \frac{(4\pi)^{5/3}\Gamma(\frac{1}{3})}{5 \times 3^{2/3}\rho_{\mathcal{V}}}. \tag{2.73}$$

Moreover, the second-order of the volume $\langle V_3^2 \rangle$ has been obtained by numerical integration [40] and reads

$$\langle V_3^2 \rangle = \frac{1.180}{{\rho_{\mathcal{V}}}^6}. \tag{2.74}$$

2.5.3 Chord length distribution

The chord length distribution for 1-dimensional Voronoi tessellations of infinite extension is exponential, with parameter $1/\rho_{\mathcal{V}}$. For dimension $d > 1$, the chord length distribution is highly non-trivial and has been only recently derived [91, 92]. For a given line of arbitrary direction $\mathbf{\Omega}$ drawn through the tessellation, the probability density function $\mathcal{P}^{\mathcal{V},d}(\ell|\mathbf{\Omega})$ of the chord length ℓ is given by

$$\begin{aligned}\mathcal{P}^{\mathcal{V},d}(\ell|\mathbf{\Omega}) = \varsigma(d)\int_0^{\pi}\int_0^{\pi-\alpha} \ell^{2d-2}\frac{\sin^{2d-3}\alpha\sin^{d-1}\beta}{\sin^{2d-1}(\alpha+\beta)}e^{-\rho_{\mathcal{V}}^d\nu_d(\ell,\alpha,\beta)} \\ \times\left(\rho_{\mathcal{V}}^d d\kappa_d\left(\frac{r\sin\alpha}{\sin(\alpha+\beta)}\right)^d\left(\sum_{i=0}^{\lfloor(d-1)/2\rfloor} b_{d,i}(\beta)\right)^2 - \sum_{i=0}^{\lfloor(d-3)/2\rfloor} c_{d,i}(\beta)\right) d\beta d\,\alpha,\end{aligned} \tag{2.75}$$

where $\varsigma(d)$ is a dimension-dependent constant

$$\varsigma(d) = \frac{d^2(d-1)\pi^{d-1/2}\Gamma(d-\frac{1}{2})\Gamma(\frac{d+1}{2})\rho_{\mathcal{V}}^{2d-1}}{2\Gamma(d)\Gamma(2-\frac{1}{d})\Gamma(\frac{d+2}{2})^{3-1/d}}. \tag{2.76}$$

The quantity $\nu_d(\ell,\alpha,\beta)$ is defined as

$$\nu_d(\ell,\alpha,\beta)) = \kappa_d\ell^d\left(\frac{\sin^d\beta}{\sin^d(\alpha+\beta)}\sum_{i=0}^{\lfloor d/2\rfloor} a_{d,i}(\alpha) + \frac{\sin^d\alpha}{\sin^d(\alpha+\beta)}\sum_{i=0}^{\lfloor d/2\rfloor} a_{d,i}(\beta)\right). \tag{2.77}$$

The coefficients $a_{d,i}(\psi)$ are defined as

$$a_{d,0}(\psi) = \begin{cases} 1 - \dfrac{\psi}{\pi} & \text{if } d \text{ even} \\ \cos^2\left(\dfrac{\psi}{2}\right) & \text{if } d \text{ odd,} \end{cases}$$

$$a_{d,i}(\psi) = \frac{\cos\psi}{2\sqrt{\pi}} \begin{cases} \dfrac{\Gamma(i)}{\Gamma(i+1/2)} \sin^{2i-1}\psi, & d \text{ even} \\ \dfrac{\Gamma(i+1/2)}{\Gamma(i+1)} \sin^{2i}, & d \text{ odd,} \end{cases}$$

for $0 \le i \le \lfloor d/2 \rfloor$; the coefficients $b_{d,i}(\psi)$ are defined as

$$b_{d,0}(\psi) = \begin{cases} \dfrac{(\pi-\psi)\cos\psi + \sin\psi}{\pi}, & d \text{ even} \\ \cos^2\left(\dfrac{\psi}{2}\right), & d \text{ odd} \end{cases}$$

$$b_{d,i}(\psi) = -\frac{1}{4\sqrt{\pi}} \begin{cases} \dfrac{\Gamma(i)}{\Gamma(i+3/2)} \sin^{2i+1}\psi, & d \text{ even} \\ \dfrac{\Gamma(i-1/2)}{\Gamma(i+1)} \sin^{2i}\psi, & d \text{ odd} \end{cases}$$

for $0 \le i \le \lfloor (d-1)/2 \rfloor$; and the coefficients $c_{d,i}(\psi)$ are defined as

$$c_{d,0}(\psi) = \begin{cases} \dfrac{d-1}{\pi}\left[\left(1 - \dfrac{d-2}{d-1}\sin^2\psi\right)(\pi-\psi) + \sin\psi\cos\psi\right], & d \text{ even} \\ \dfrac{1+\cos\psi}{2}\left[1 + (d-2)\cos\psi\right], & d \text{ odd} \end{cases}$$

$$c_{d,i}(\psi) = -\frac{1}{4\sqrt{\pi}} \begin{cases} \dfrac{\Gamma(i)}{\Gamma(i+3/2)}(d-2i-2)\sin^{2i+1}\psi\cos\psi, & d \text{ even} \\ \dfrac{\Gamma(i-1/2)}{\Gamma(i+1)}(d-2i-1)\sin^{2i}\psi\cos\psi, & d \text{ odd} \end{cases}$$

for $0 \le i \le \lfloor (d-3)/2 \rfloor$. Since the Voronoi tessellations defined above are isotropic, the chord length distribution does not depend on the orientation $\mathbf{\Omega}$ of the test line. For illustration, the probability density function of the chord length distribution is provided in Fig. 2.10 for $d = 3$.

The value of the chord length distribution for $\ell = 0$ is given by [92]

$$\begin{aligned} \mathcal{P}^{\mathcal{V},d}(0) &= \frac{d(d-1)\sqrt{\pi}\Gamma(d-\frac{1}{2})\Gamma(\frac{d+1}{2})\Gamma(2-\frac{2}{d})\rho_{\mathcal{V}}}{2\Gamma(d)\Gamma(2-\frac{1}{d})\Gamma(\frac{d+2}{2})^{1+1/d}} \\ &\times \left(2(d-1)\int_0^{\pi} \sin^{d-2}\alpha \left(\sum_{i=0}^{\lfloor (d-1)/2 \rfloor} b_{d,i}(\alpha)\right)^2 d\alpha - \sqrt{\pi}\frac{\Gamma((d+1)/2)}{\Gamma((d+2)/2)}\right) \end{aligned} \tag{2.78}$$

In particular, for $d = 3$ the value of the probability density of the chord length distribution for $\ell = 0$ is [91]

$$\mathcal{P}^{\mathcal{V},3}(0) = \frac{\Gamma(\frac{1}{6})\rho_{\mathcal{V}}}{5 \times 3^{1/3} \times \pi^{1/6}}. \tag{2.79}$$

The average chord length $\Lambda(\mathbf{\Omega})$ in d-dimensional Voronoi tessellations is given by [91, 92]

$$\Lambda(\mathbf{\Omega}) = \int \ell \mathcal{P}^{\mathcal{V},d}(\ell|\mathbf{\Omega}) d\ell = \Lambda = \frac{d\Gamma(\frac{d+1}{2})^2\Gamma(d-\frac{1}{2})}{2\Gamma(2-\frac{1}{d})\Gamma(\frac{d}{2}+1)^{2-1/d}\Gamma(d)\rho_{\mathcal{V}}}, \tag{2.80}$$

independent of the direction $\mathbf{\Omega}$. In particular, for $d = 3$, this yields [91]

$$\Lambda = \frac{1}{(\frac{4\pi}{3})^{\frac{1}{3}}\Gamma\left(\frac{5}{3}\right)\rho_{\mathcal{V}}}. \tag{2.81}$$

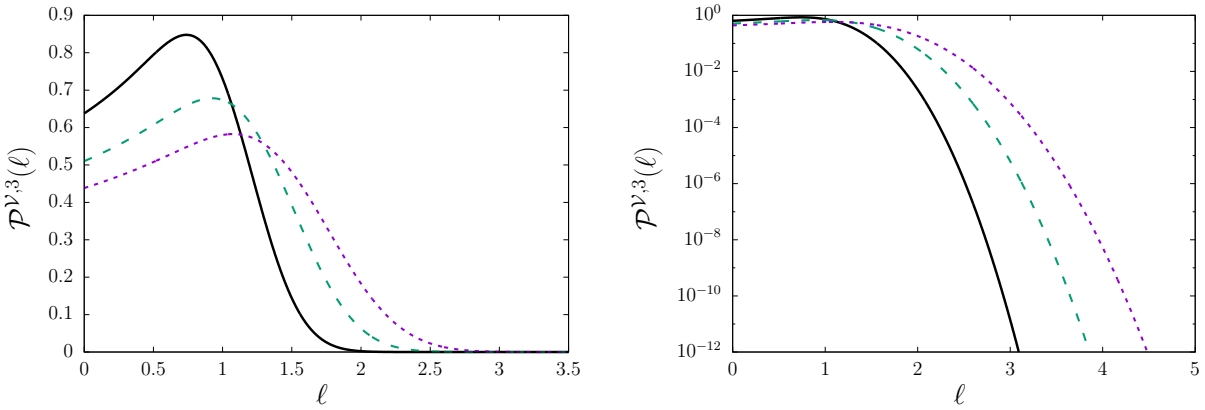

Figure 2.10: Left. The probability density function $\mathcal{P}^{\mathcal{V},3}(\ell)$ of the chord length distribution of three-dimensional Voronoi tessellations, obtained by using Eq. (2.75), as a function of the density parameter $\rho_{\mathcal{V}} = 1$: the solid black line corresponds to $\rho_{\mathcal{V}} = 1$, the dashed green line to $\rho_{\mathcal{V}} = 0.8$ and the dotted violet line to $\rho_{\mathcal{V}} = (4\pi/3)^{-1/3}\Gamma\left(\frac{5}{3}\right)^{-1} \simeq 0.687182$. Right. The same, in log-linear scale.

We conclude by examining the case where the lines are randomly distributed. Consider a Voronoi tessellation and an ensemble $\mathcal{T}$ of homogeneous and isotropic random lines as previously defined. The Cauchy formula applies also for the Voronoi tessellations. Then, the average chord length Λ_c through the cells of the Voronoi tessellation induced by the random lines $\mathcal{T}$ reads [88]

$$\Lambda_c = \alpha_d \frac{\langle V_d \rangle}{\langle S_d \rangle} = \frac{d\Gamma(\frac{d+1}{2})^2\Gamma(d-\frac{1}{2})}{2\Gamma(2-\frac{1}{d})\Gamma(\frac{d}{2}+1)^{2-1/d}\Gamma(d)\rho_{\mathcal{V}}}. \tag{2.82}$$

It is interesting to remark that in this case the average correlation length Λ_c as computed by the Cauchy formula coincides with the average chord length Λ obtained from the chord length distribution as in Eq. (2.80), which is a consequence of the isotropy and homogeneity of the Voronoi tessellations.

2.6 Comparison of the tessellation models

We have shown that the tessellations models described above display rather different features concerning the polyhedral features and the chord length distributions. In particular, the average chord length $\Lambda(\mathbf{\Omega})$ is clearly non-trivially model-dependent. However, a remarkable and universal property stems from the application of the Cauchy formula, which relates the average correlation length Λ_c to purely geometrical quantities, namely, the average volume $\langle V \rangle$ of a random polyhedron and its average surface $\langle S \rangle$, provided that the lines are drawn uniformly and isotropically [127]. Moreover, we have shown that the aspect ratio $\langle V \rangle / \langle S \rangle$ is simply related to the tessellation density, up to a dimension-dependent constant that depends on the chosen model. This means that setting the tessellation density is tantamount to setting the average correlation length Λ_c, which in turns is equivalent to setting the aspect ratio $\langle V \rangle / \langle S \rangle$ of the tessellation cells.

In view of *comparing the effects* of the underlying mixing statistics $m = \mathcal{P}$, $\mathcal{V}$ or $\mathcal{B}$ on particle transport in random media, a mandatory requirement is to determine a criterion on whose basis the tessellations can be considered statistically 'equivalent' with respect to some physical property. A natural choice consists in taking the same average correlation length Λ_c for all the tessellations, which intuitively allows having the same typical scale of disorder in the random medium, to be compared with the typical cross section of the particles traversing the medium [108]. Correspondingly, we have a *constraint* on the densities ρ, $\rho_{\mathcal{V}}$ and $\rho_{\mathcal{B}}$ of the tessellations, which must now satisfy

$$\frac{1}{\rho} = \frac{2}{3\rho_{\mathcal{B}}} = \frac{1}{(\frac{4\pi}{3})^{\frac{1}{3}}\Gamma\left(\frac{5}{3}\right)\rho_{\mathcal{V}}}. \tag{2.83}$$

m	$\mathcal{P}$	$\mathcal{B}$	$\mathcal{V}$
$\langle V_3 \rangle$	$6/\pi\rho^3$	${1/\rho_{\mathcal{B}}}^3$	${1/\rho_{\mathcal{V}}}^3$
$\langle S_3 \rangle$	$24/\pi\rho^2$	${6/\rho_{\mathcal{B}}}^2$	$(256\pi/3)^{\frac{1}{3}}\Gamma\left(\frac{5}{3}\right)/{\rho_{\mathcal{V}}}^2$
$\langle C_3 \rangle$	6	6	$(48\pi^2+70)/35$
$\langle A_3 \rangle$	12	6	$144\pi^2/35$
$\langle N_3 \rangle$	8	8	$96\pi^2/35$
$\langle L_3 \rangle$	$12/\rho$	$12/\rho_{\mathcal{B}}$	$(4\pi)^{5/3}\Gamma(\frac{1}{3})/(5\times 3^{2/3}\rho_{\mathcal{V}})$
Λ_c	$1/\rho$	$2/3\rho_{\mathcal{B}}$	$1/\left((\frac{4\pi}{3})^{\frac{1}{3}}\Gamma\left(\frac{5}{3}\right)\rho_{\mathcal{V}}\right)$

Table 2.3: Exact formulas for the average volume $\langle V_3 \rangle$, the average surface $\langle S_3 \rangle$, the average number of faces $\langle C_3 \rangle$ and the average correlation length Λ_c in infinite tessellations, for different mixing statistics m. Expressions are taken from [87, 127].

In practice, one is often led to simulate tessellations restricted to some bounded regions of linear size L: finite-size effects typically emerge, and the relation (2.83) would not be strictly valid. Indeed, in finite geometries the average correlation length $\Lambda_c(L)$ differs from the corresponding ideal Λ_c for infinite tessellations. However, although a large L is typically required in order for $\Lambda_c(L)$ to converge to the asymptotic value Λ_c, the variability of $\Lambda_c(L)$ between tessellations vanishes even before convergence to the asymptotic limit is achieved, as we will illustrate in Chapter 4. For the sake of simplicity, we will thus neglect such finite-size effects and use Eq. (2.83) to calibrate the model parameters.

It is important to realize that the use of Λ_c as a tool to make the tessellation models 'equivalent' with respect to particle transport implies that other polyhedral features (which also depend on the tessellation densities) will be different: exact formulas are recalled in Tab. 2.3. In principle, it would be possible to calibrate the tessellation models based on different criteria, such as equal average cell volumes, for instance. However, due to the relevance of the average correlation length for particle transport properties, in the following we will assume that all the tested tessellations share the same Λ_c.

2.7 Assigning material properties: colored tessellations

So far, we have addressed the statistical properties of d-dimensional Poisson, Box and Voronoi tessellations based on the assumption that all polyhedra share the same physical properties, i.e., the medium is homogeneous. In many applications, the polyhedra emerging from a random tessellation are actually characterized by different physical properties, which for the sake of simplicity can be assumed to be piece-wise constant over each cell. Such stochastic mixtures can be then formally described by assigning a distinct 'label' i (also called 'color') to each polyhedron of the geometry, with a given probability p_i. A widely studied model is that of *stochastic binary mixtures*, where only two labels are allowed, say 'red' and 'blue', with associated complementary probabilities p and $1-p$, respectively [108].

Stochastic mixtures are realized by resorting to the following procedure: first, a random geometry is constructed by resorting to the algorithms detailed in Secs. 2.3.1, 2.4.1 and 2.5.1. Then, the corresponding coloured geometry is immediately obtained by assigning to each polyhedron a label with a given probability. Adjacent polyhedra sharing the same label are finally merged. For the specific case of binary stochastic mixtures, the merging procedure gives rise to (generally) non-convex red and blue *clusters*, each composed of a random number of convex polyhedra. For illustration, some examples of binary stochastic mixtures based on coloured Poisson tessellations are provided in Figs. 2.11 and 2.12 by Monte Carlo simulation, for different values of ρ and p, in dimension $d=2$ and $d=3$, respectively.

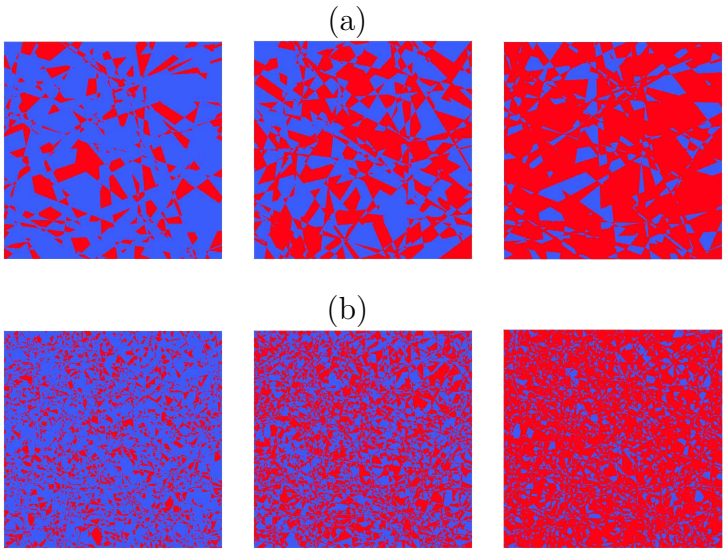

Figure 2.11: Realizations of coloured two-dimensional isotropic Poisson geometries restricted to a square of side L, for different values of density ρ and probability p of assigning the label α. Red corresponds to the label α and blue to the label β. For all realizations, we have chosen $L = 1$. Top (a): $\rho = 50$; bottom (b): $\rho = 200$. Left: $p = 0.25$, middle: $p = 0.5$; right: $p = 0.75$.

2.7.1 Chord length across colored clusters

After assigning colors to stochastic geometries, we can analyze the chord length $\ell_i(\mathbf{\Omega})$ across clusters with label i, for lines with orientation $\mathbf{\Omega}$. If the probability density $\mathcal{P}(\ell|\mathbf{\Omega})$ of having a chord length ℓ through a cell of the tessellation is known, the probability density $\mathcal{P}(\ell_i|\mathbf{\Omega})$ of having a chord length ℓ_i though a cluster with label i can be obtained as follows. If p_i is the probability of a cell to be assigned the label i, the probability that exactly k adjacent cells share the same label [4] is

$$\mathcal{P}(k) = p_i^{k-1}(1 - p_i). \tag{2.84}$$

We can write then

$$\mathcal{P}(\ell_i|\mathbf{\Omega}) = \sum_k \mathcal{P}(\ell_i|\mathbf{\Omega}; k)\mathcal{P}(k), \tag{2.85}$$

where $\mathcal{P}(\ell_i|\mathbf{\Omega}; k)$ is the probability density of having a length ℓ_i if the cluster contains exactly k cells in the direction $\mathbf{\Omega}$. Now, the length ℓ_i conditioned to k cells will satisfy

$$\ell_i(\mathbf{\Omega}) = \sum_{j=0}^{k} x_j(\mathbf{\Omega}) \tag{2.86}$$

where each $x_j(\mathbf{\Omega})$ obeys $\mathcal{P}(x|\mathbf{\Omega})$. Thus, it follows that $\mathcal{P}(\ell_i|\mathbf{\Omega}; k)$ is the k-fold convolution of $\mathcal{P}(\ell|\mathbf{\Omega})$.

For the case of Poisson tessellations, $\mathcal{P}(\ell|\mathbf{\Omega})$ is an exponential distribution of parameter $\rho(\mathbf{\Omega})$, so that $\mathcal{P}(\ell_i|\mathbf{\Omega}; k)$ can be computed explicitly and reads

$$\mathcal{P}(\ell_i|\mathbf{\Omega}; k) = \frac{\rho(\mathbf{\Omega})^k}{\Gamma(k)} \ell_i^{k-1} e^{-\rho(\mathbf{\Omega})\ell_i}, \tag{2.87}$$

i.e., a Gamma distribution of parameters $\rho(\mathbf{\Omega})$ and k. We have then

$$\mathcal{P}(\ell_i|\mathbf{\Omega}) = \sum_k \mathcal{P}(\ell_i|\mathbf{\Omega}; k)\mathcal{P}(k) = \sum_k p_i^{k-1}(1 - p_i) \frac{\rho(\mathbf{\Omega})^k}{\Gamma(k)} \ell_i^{k-1} e^{-\rho(\mathbf{\Omega})\ell_i} = \rho(\mathbf{\Omega})(1 - p_i) e^{-\rho(\mathbf{\Omega})(1-p_i)\ell_i}. \tag{2.88}$$

[4] Here we are actually considering the probability of having k adjacent cells sharing the same label, conditioned to the fact that the starting cell has also the same label.

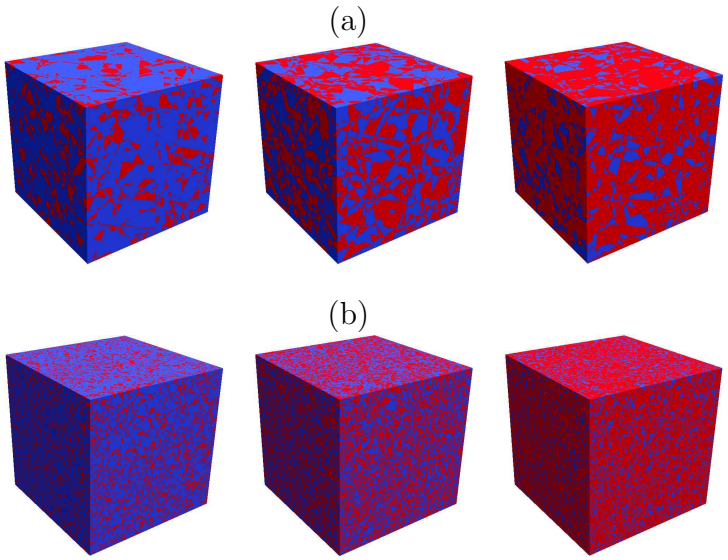

Figure 2.12: Realizations of coloured three-dimensional isotropic Poisson geometries restricted to a cube of side L, for different values of density ρ and probability p of assigning the label α. Red corresponds to the label α and blue to the label β. For all realizations, we have chosen $L = 1$. Top (a): $\rho = 10$; bottom (b): $\rho = 50$. Left: $p = 0.25$; middle: $p = 0.5$; right: $p = 0.75$.

This means that for Poisson tessellations the chord length distribution for a cluster with label i is an exponential distribution with rescaled parameter $\rho_i(\mathbf{\Omega}) = \rho(\mathbf{\Omega})(1-p)$. We can finally define the average chord length for colored clusters, namely,

$$\Lambda_i(\mathbf{\Omega}) = \frac{1}{\rho_i(\mathbf{\Omega})} = \frac{\Lambda(\mathbf{\Omega})}{1-p_i}. \tag{2.89}$$

For Voronoi tessellations, Eq. (2.85) still holds true. However, in view of the very involved functional form of the probability density for the chord length within a single cell (see Eq. (2.75)) exact expressions for the distribution of the chord length within a cluster seem hardly achievable. Nonetheless, observe that independently of the shape of the distribution the expression for the average chord length is still given by

$$\Lambda_i(\mathbf{\Omega}) = \sum_{k=0}^{+\infty} p_i^k \Lambda(\mathbf{\Omega}) = \frac{\Lambda(\mathbf{\Omega})}{1-p_i} \tag{2.90}$$

for any underlying tessellation model. This property of the average chord length across clusters with composition i stems from the binary random sampling of colored labels during the coloring procedure [48]. Similarly, we can formally define the average correlation length for colored tessellations as

$$\Lambda_{c,i} = \frac{\Lambda_c}{1-p_i}. \tag{2.91}$$

2.7.2 Percolation properties in colored tessellations

Let us now consider binary mixtures, without loss of generality. By increasing the coloring probability p, the size of the red clusters also increases. For infinite geometries, the percolation threshold p_c is defined as the probability of assigning a red label to each d-polyhedron above which there exists a giant connected cluster, i.e., an ensemble of connected red d-polyhedra spanning the entire geometry [135]. The percolation probability $\mathcal{P}_C(p)$, i.e., the probability that there exists such a connected percolating cluster, has thus a step behaviour as a function of the colouring probability p, i.e., $\mathcal{P}_C(p) = 0$ for $p < p_c$, and $\mathcal{P}_C(p) = 1$ for $p > p_c$. The same argument applies also to the blue clusters: in particular, depending on the kind of underlying stochastic geometry and on the dimension d, there might exist a range of probabilities p for which both coloured clusters can simultaneously percolate. Actually,

for any finite L, there exists a finite probability that a percolating cluster (i.e. a cluster hitting two opposites borders) exists below $p = p_c$, due to finite-size effects. For illustration, some examples of percolating and non-percolating two-dimensional Poisson geometries are given in Fig.2.13.

Percolation theory has been intensively investigated for the case of regular lattices [135]. Although less is comparatively known for percolation in stochastic geometries, remarkable results have been nonetheless obtained in recent years for, e.g., Voronoi and Delaunay tessellations in two dimensions [4, 6, 97], whose analysis demands great ingenuity (see, e.g., [22, 23, 49]). The percolation threshold of three-dimensional Voronoi tessellations has also been numerically estimated to be $p_c = 0.1453 \pm 2.10^{-3}$ [52]. Furthermore, the percolation threshold of a three-dimensional Box tessellation can be mapped to that of a cubic network, which has been widely studied and numerically estimated to be $p_c = 0.3116077 \pm 4.10^{-7}$ [29]. In the following, we will focus on the case of d-dimensional isotropic Poisson geometries, with special emphasis on the transition occurring at $p = p_c$.

For Poisson geometries, the case $d = 1$ is straightforward and can be solved analytically: $\mathcal{P}_C(p)$ simply coincides with the probability that all the segments composing the Poisson geometry on the line are coloured in red. For any finite L, this happens with probability

$$\mathcal{P}_C(p|L) = pe^{-(1-p)\rho L}. \tag{2.92}$$

It is easy to understand that for $d = 1$ we have $p_c = 1$. For very large $L \to \infty$, $\mathcal{P}_C(p|L)$ converges to a step function, with $\mathcal{P}_C(p) = 1$ for $p = p_c$ and $\mathcal{P}_C(p) = 0$ otherwise. This behaviour is analogous to that of percolation on one-dimensional lattices [135].

To the best of our knowledge, exact results for the percolation probability for Poisson geometries in $d > 1$ are not known. The percolation threshold can be numerically estimated by determining p_c at finite L and extrapolating the results to the limit behaviour for $L \to \infty$. The percolation properties of two-dimensional isotropic Poisson geometries have been first addressed in [65], where the percolation threshold p_c was numerically estimated to be $p_c \simeq 0.586 \pm 10^{-3}$ by Monte Carlo simulation. This means that p_c for Poisson geometries in $d = 2$ is quite close to the percolation threshold of two-dimensional regular square lattices, which reads $p_c^{\text{square}} \simeq 0.5927$ [96]. The comparison with respect to regular square lattices might nonetheless appear somewhat artificial, since the features of the constituents of Poisson geometries have broad statistical distributions around their average values. In particular, the typical 2-polyhedron of infinite Poisson geometries, while having the same average number of sides as a square (see Tab. 2.1), does not share the same aspect ratio, which is a measure of the connectivity of the geometry components: for the 2-polyhedron we have $\langle V_2 \rangle / \langle S_2 \rangle = 1/\pi$ for $\rho = 1$, whereas for a square of side u we have $\langle V_2 \rangle / \langle S_2 \rangle = u/4$, which for u equal to the average side of the 2-polyhedron, namely $u = \langle S_2 \rangle / \langle C_2 \rangle = 1$, yields $\langle V_2 \rangle / \langle S_2 \rangle = 1/4$. In Sec. 4, we will focus on the case of three-dimensional isotropic Poisson geometries.

Two other quantities of interest for percolating clusters are the *average cluster size* and the so-called *strength of the percolating cluster*. For percolation on lattices, the average cluster size $S(p)$ is defined by

$$S(p) = \sum_s s w_s, \tag{2.93}$$

where w_s is the probability that the cluster to which a red site belongs contains s sites, and the sum is restricted to sites belonging to non-percolating clusters [135]. Now, $w_s \propto s n_s(p)$, where $n_s(p)$ is the number of clusters of size s per lattice site, which means that $S(p) \propto \sum_s s^2 n_s(p)$ [135]. Close to the percolation threshold, $S(p)$ is known to behave as $S(p) \propto |p - p_c|^{-\gamma}$ for infinite lattices, where γ is a dimension-dependent critical exponent that does not depend on the specific lattice type [135]. For finite lattices of linear size L, the behaviour of $S(p|L)$ close to $p \to p_c^-$ is dominated by finite-size effects, with a scaling $S(p|L) \propto L^{\gamma/\nu}$, where ν is another dimension-dependent critical exponent that does not depend on the specific lattice type [135]. In order to adapt the definition in Eq. (2.93) to the calculation of average cluster size of the stochastic tessellations, we can either compute the sum by weighting each d-polyhedron composing a non-percolating cluster by its volume, or by attributing to each constituent an equal unit weight. The former choice seems more appropriate on physical grounds.

For percolation on lattices, the strength $P(p)$ is defined as the probability that an arbitrary site belongs to the percolating cluster [135]. Close to the percolation threshold, for infinite lattices $P(p)$ is

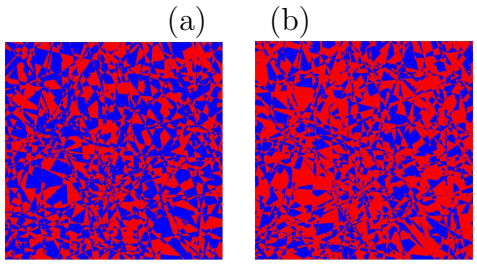

Figure 2.13: Percolating and non-percolating realizations of two-dimensional coloured isotropic Poisson tessellations restricted to a square of side $L = 100$ and density $\rho = 1$ with probability p of assigning a red label. Case (a), $p = 0.5$. The system does not percolate: no red cluster spans the geometry. Case (b), $p = 0.6$. The system percolates since a red cluster spans the geometry.

known to behave as $P(p) \propto (p-p_c)^{\beta}$ when $p \to p_c^+$, where β is a dimension-dependent critical exponent that does not depend on the specific lattice type [135]. For finite lattices of linear size L, the behaviour of $P(p|L)$ close to $p = p_c$ is dominated by finite-size effects, with a scaling $P(p|L) \propto L^{-\beta/\nu}$ [135]. The strength of percolating stochastic tessellations can be again computed by either weighting each d-polyhedron composing the percolating cluster by its volume, or by attributing to each constituent an equal unit weight.

Chapter 3

Development of a Monte Carlo random media generator

Stochastic geometries such as those introduced above are very complex objects, and there is little hope of obtaining close-form results for their key features. In most cases, as discussed earlier, even the simplest distributions associated to their polyhedral cells are unknown, and knowledge of the moments is most often limited to low orders. For instance, the most important distribution for the stochastic tessellations is that of the volume of the cells: this function is unknown for all the models previously introduced.

Numerical investigation based on Monte Carlo methods for the explicit construction of the stochastic geometries and the subsequent analysis of their statistical properties is therefore mandatory. This is even more so in view of the possibility of using these stochastic geometries for the analysis of particle transport in random media: we will need to instantiate a large ensemble of geometries, apply the coloring procedure in order to assign material properties, solve the transport equation in each configuration and finally take ensemble averages with respect to the realizations and/or compute the full distribution of the transport-related physical observables of interest.

In the following, we will describe the *software* that has been developed in this work in order to numerically produce random media and perform the analysis of their statistical features. For this purpose, we have developed an object-oriented C++ code, based on Monte Carlo sampling methods, devoted to the construction of

- three-dimensional spherical inclusions,
- d-dimensional isotropic Poisson tessellations,
- three-dimensional Box tessellations,
- three-dimensional Voronoi tessellations.

The code has a two-fold aim: analyzing the statistical properties of random geometries in order to investigate the behaviour of the physical observables of interest, and generating geometrical configurations and material compositions compatible with the Monte Carlo particle transport code TRIPOLI-4 ® [21] developed at SERMA, in view of investigating the effects of random media on linear transport. In the following, we will refer to this tool as the random media *generator*. For the sake of simplicity, we will focus on geometries restricted to a d-dimensional box.

To initialize the generator, the following inputs have to be provided: the dimension d (for Poisson geometries), the size L of the system (side length of the box) and additional parameters:

- for spherical inclusions, the packing fraction ξ and the description of the radius distribution $g(r)$;
- for tessellations, the arbitrary density of the tessellation, denoted by ρ, $\rho_{\mathcal{B}}$ or $\rho_{\mathcal{V}}$ as defined in Sec. 2.3.1, 2.4.1 and 2.5.1, respectively.

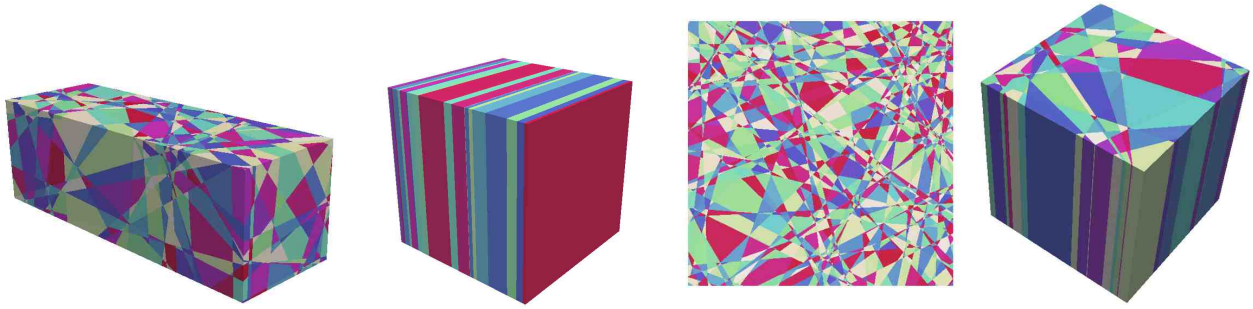

Figure 3.1: From left to right. Example of a parallelepiped with isotropic Poisson tessellation; realization of a 1-dimensional Poisson geometry extended into slab; realization of a 2-dimensional Poisson geometry; realization of a 2-dimensional extruded Poisson geometry..

It is also possible to tessellate a parallelepiped, as shown in Fig. 3.1: in this case, the parameters L_x, L_y and L_z have to be provided instead of L. Each time the class constructor is called, a new object corresponding to a random geometry is created, based on the algorithms described above. For instance, for Poisson tessellations a method tessellates the box with a random number of planes depending on the density of the tessellation, according to the algorithm described in Sec. 2.3.1. An instance of the class contains the geometry, which means information about the hyper-planes of the tessellation, information about cells and information about the neighborhood (the connectivity of the tessellation: two cells are considered as neighbors if they share a face).

3.1 Storage of the geometry

The geometry is stored with the following format:

- for three-dimensional mono-dispersed spherical inclusions: the radius $\langle r \rangle = R$ and a vector of $3d$-points (P_i) for the centers of the spheres;
- for three-dimensional poly-dispersed spherical inclusions: a vector of radii (r_i) and a vector of $3d$-points (P_i) for the centers of the spheres;
- for one-dimensional Poisson tessellations: a vector of sorted $1d$-vertices $(x_i)_{0 \leq i \leq N+1}$ introduced in the geometry (including the two boundaries $x_0 = -L/2$ and $x_N = L/2$). The 1-polyhedra and the corresponding neighborhood are implicit, since in this representation the 1-polyhedron i is the segment $[x_i, x_i + 1]$ and has for neighbors the 1-polyhedra $i - 1$ and $i + 1$;
- for two-dimensional Poisson tessellations: a vector of the lines defining the geometry (including the boundaries of the domain), a vector of $2d$-vertices, a vector of edges and a vector of 2-polyhedra. The object corresponding to an edge contains two vertices (accessed by reference) and is also linked to a line (accessed by reference). The object corresponding to a 2-polyhedron contains a vector of edges (accessed by reference) and a vector of neighbors (accessed by reference);
- for three-dimensional Poisson tessellations: a vector of the planes defining the geometry (including the boundaries of the domain), a vector of $3d$-vertices, a vector of faces and a vector of 3-polyhedra. The object corresponding to a face is a vector of ordered vertices (accessed by reference) and is also linked to a plane (accessed by reference). The object corresponding to a polyhedron is a list of faces (accessed by reference) and a vector of neighbors;
- for three-dimensional Box tessellations: a vector of sorted points $(x_i)_{0 \leq i \leq N_x+1}$ from the Poisson point process on the x-axis (with additional points $x_0 = -L_x/2$ and $x_{N_x+1} = L_x/2$), a vector of sorted points $(y_i)_{0 \leq i \leq N_y+1}$ from the Poisson point process on the y-axis (with additional points $y_0 = -L_y/2$ and $y_{N_y+1} = L_y/2$) and a vector of sorted points $(z_i)_{0 \leq i \leq N_z+1}$ from the

Poisson point process on the z-axis (with additional points $z_0 = -L_z/2$ and $z_{N_z+1} = L_z/2$). The 3-polyhedra composing the tessellation and the neighborhood map are implicit;

- for three-dimensional Voronoi tessellations: a vector of nuclei $(P_i)_{1 \leq i \leq N}$ introduced in the geometry and a vector of 3-polyhedra. The object corresponding to a 3-polyhedron is a vector of neighbors. The planes supporting the faces of the polyhedron i are not stored but can easily be computed as the mid-planes between the nucleus P_i and the nuclei of the neighbors of the polyhedron i.

For the cases $d = 1$ and $d = 2$, an option is available in the code in order to generate extruded geometries based on rod ($d = 1$) or plane ($d = 2$) configurations. Indeed, for real-world applications, three-dimensional geometries are needed. Furthermore, having in mind the possibility of performing particle transport in stochastic tessellations, the Monte Carlo code TRIPOLI-4 ® also requires three-dimensional geometries. That is why we have also implemented:

- *slab* geometries based on $d = 1$ tessellations: the $1d$ rod geometry is extended along the y- and z-axis. For an illustration, see Fig. 3.1;

- *extruded* geometries based on $d = 2$ tessellations: the $2d$ plane geometry is extended along the z-axis. For an illustration, see Fig. 3.1.

This option is used for methods producing the output files related to visualization or export tessellations into a format compatible with the transport code TRIPOLI-4 ®.

3.2 Coloration of the tessellations

Once the tessellation has been built, a method enables to assign color labels to the geometry, i.e., to assign each polyhedron a colored label with a probability p and a blue label with complementary probability $1-p$, where p is a parameter provided to this method. A given geometry can be un-colored and re-colored as many times as needed, for statistical analysis.

Optionally, an additional method enables to aggregate the adjacent polyhedra sharing the same color into clusters. For this purpose, we use the neighborhood map of the polyhedra of the tessellation produced during the construction of the geometry and we resort to the Breadth-First Search algorithm in order to traverse all polyhedra of the tessellation. We create the first red cluster as follows. Initially, the cluster is empty. We start by taking a list containing all red polyhedra of the tessellation and we select the first element of this list. Then, we add this element to the ongoing cluster, we attribute a flag to this element as 'done' and we use the connectivity map to get the corresponding neighbors. Each neighbouring polyhedron which is red and not 'done' is added to the queue. Then, for each element of the queue, we add it to the ongoing cluster, we 'flag' it as 'done' and we add to the queue all neighbors of this element which are red and not 'done'. We iterate this step until the queue is empty, which means that the cluster has been constituted. In order to create the second red cluster, we repeat the whole process by using a list containing all red polyhedra of the tessellation which are not 'done'. We keep on aggregating red clusters until all red polyhedra of the tessellation are marked as 'done'.

3.3 Visualization

The generator can produce output files for the visualization of the created geometries: for a given geometry, a method of the code based on

- a tetrahedral decomposition of the polyhedra, for the tessellations;

- a discretization of the spheres, for the spherical inclusion,

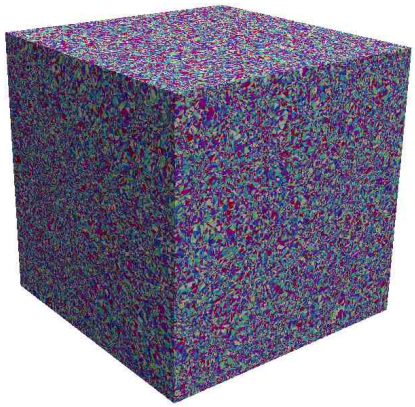

Figure 3.2: Realization of a very dense three-dimensional Poisson geometry, with parameters $L = 370$, $\rho = 1$, leading to about 3×10^7 polyhedra.

writes a datafile describing the geometry within the framework of the `VTk` specifications. Such output files are directly readable by the ParaView ® software. Thus, it is possible for the user to visualize the geometries generated by our computer code, in dimension $d = 1$ (slab), $d = 2$ (plane or extruded) or $d = 3$. The random generator and the visualization tool have been tested for tessellations containing up to thirty millions polyhedra: for illustration, see Fig. 3.2. Two additional options are available for visualization: the user can specify whether un-colored geometries are needed (in which case all cells are colored differently, to increase readability) or colored geometries (in which case the cells are colored depending on their label).

3.4 Statistical properties

For each realized geometry, several properties are computed by the code for statistical analysis, among which:

- the volumic ratio of the spheres in the geometry (for spherical inclusions),
- the number of polyhedra (for tessellations),
- the volume V_i, surface S_i, inradius R_i, etc., of the polyhedron i (for tessellations),
- the volume, surface, inradius, etc., averaged over the whole geometry (for tessellations),
- the number of planes intersected by a random unit length (for tessellations),
- the distribution and the moments of the chord length, as obtained by throwing lines through the geometry: each line is decomposed into a set of chords by the spherical inclusions or the random hyper-planes of the tessellation.

For the case of colored tessellations, additional observables are computed if requested, among which:

- the number of colored clusters,
- the volume of the colored clusters,
- the presence of a percolating cluster.

Further details will be provided in Sec. 4.

3.5 Output files for TRIPOLI-4 ®

It is possible to export the obtained geometry into a format compatible with the geometry input of the Monte Carlo code TRIPOLI-4 ®. For any geometry, a method of the generator allows producing the following input files:

- a file describing the geometry in a surface-based format, associated to the TRIPOLI-4 ® keyword `GEOMETRY`,
- a file describing the material composition of each volume, associated to the TRIPOLI-4 ® keyword `GEOCOMP`,
- a file describing the boundary conditions, if needed, associated to the TRIPOLI-4 ® keyword `BOUNDARY`,
- a file describing the neighborhood (connectivity) map.

These files are directly readable by TRIPOLI-4 ®. The first three files are actually printed as command blocks for a TRIPOLI-4 ® input file. The last one is to be used inside the command block `GEOMETRY`, when the optional keyword `CONNECTIVITY_MAP` is requested by the user.

The *connectivity map* is produced by the random geometry generator by exploiting the relation between the indexes of the cells (polyhedra for tessellations, spheres and boxes for spherical inclusions). Then, this information can be fed to TRIPOLI-4 ® so that the transported particles during geometrical tracking will know which volume they will enter, and by which face, for any current volume, which is expected to considerably accelerate the particle tracking routines, especially for geometries containing a huge number of volumes: a discussion about speed-up due to the connectivity map on the particle transport is provided in Sec. 3.7.

In the following we provide an example of a set of output files created by the generator. We consider a single random Poisson geometry, with parameters $d = 3$, $L = 3$, $\rho = 1$ and $p = 0.2$. The file providing the geometry is written as:

```
GEOMETRIE
 TITRE Example of a 3-dimensional Poisson geometry
 HASH_TABLE
  SURF 1 PLAN 0 0 1 -1.5
  SURF 2 PLAN 0 0 1 1.5
  SURF 3 PLAN 0 1 0 1.5
  SURF 4 PLAN 0 1 0 -1.5
  SURF 5 PLAN 1 0 0 1.5
  SURF 6 PLAN 1 0 0 -1.5
  SURF 7 PLAN 0.332526 -0.0296187 0.942629 -1.11687
  SURF 8 PLAN 0.221761 -0.796614 -0.562342 0.784656
  SURF 9 PLAN 0.595543 -0.467957 -0.652951 -1.79604
  SURF 10 PLAN 0.578349 -0.748902 0.323509 2.15322
  SURF 11 PLAN 0.314375 -0.830398 0.460009 0.622084
  SURF 12 PLAN 0.59591 0.656393 0.462644 2.05206
  SURF 13 PLAN 0.609976 -0.349675 0.711096 0.431487
  SURF 14 PLAN 0.755992 0.350264 0.552984 1.7478
  VOLU 1 EQUA PLUS 3 3 7 8 MOINS 2 1 6  FINV
  VOLU 2 EQUA PLUS 3 2 3 9 MOINS 1 6  FINV
  VOLU 3 EQUA PLUS 2 7 11 MOINS 4 1 4 6 8  FINV
  VOLU 4 EQUA PLUS 3 5 11 13 MOINS 5 1 4 6 7 8  FINV
  VOLU 5 EQUA PLUS 6 2 3 5 8 11 13 MOINS 4 1 6 7 9  FINV
  VOLU 6 EQUA PLUS 1 5 MOINS 3 4 8 10  FINV
  VOLU 7 EQUA PLUS 3 2 5 8 MOINS 2 4 10  FINV
```

```
  VOLU 8 EQUA PLUS 1 7 MOINS 3 1 4 11  FINV
  VOLU 9 EQUA PLUS 2 5 13 MOINS 6 1 4 6 7 8 11  FINV
  VOLU 10 EQUA PLUS 3 2 8 13 MOINS 3 4 6 11  FINV
  VOLU 11 EQUA PLUS 3 2 3 5 MOINS 1 12  FINV
  VOLU 12 EQUA PLUS 2 5 11 MOINS 2 8 13  FINV
  VOLU 13 EQUA PLUS 6 2 3 5 8 11 14 MOINS 1 13  FINV
  VOLU 14 EQUA PLUS 2 5 10 MOINS 4 4 8 11 13  FINV
  VOLU 15 EQUA PLUS 5 2 5 8 10 14 MOINS 4 4 6 11 13  FINV
  VOLU 16 EQUA PLUS 5 2 3 5 11 12 MOINS 1 14  FINV
  VOLU 17 EQUA PLUS 2 2 5 MOINS 2 11 14  FINV
  CONNECTIVITY_MAP /address/map_file
FING
```

Note that the produced tessellation description for TRIPOLI-4 ® is naturally well-suited for the surface-based format. The optional keyword `HASH_TABLE` is strongly suggested for large geometries (more than 10^3 polyhedra), in order to optimize the data structure during the construction phase at the code initialization.

The neighbourhood map is introduced by the keyword `CONNECTIVITY_MAP`, which has to be followed by the address of the file containing the map (which is also produced by the random geometry generator). For this example, the map file reads as:

```
1 2 5 3
2 1 5
3 3 4 1 8
4 4 3 5 9 12
5 5 1 4 2 10 13
6 2 7 14
7 2 6 15
8 2 9 3
9 4 8 10 4 14
10 3 9 5 15
11 1 16
12 3 13 14 4
13 4 12 15 5 16
14 4 15 6 12 9
15 5 14 7 13 10 17
16 3 17 11 13
17 2 16 15
```

In the connectivity map, each line provides the indexes to the neighbors of the polyhedron whose index is given in the first column. At any given line, the second column gives the number of neighbors. The additional columns give the list of neighbors of the considered polyhedron. For instance, we can deduce from this map that the polyhedron of index 9 has 4 neighbors, whose identifiers are: 8, 10, 4 and 14. Similarly as for the keyword `HASH_TABLE`, the use of the connectivity map (although in principle optional) is strongly recommended for large geometries, and might lead to a significant reduction of the simulation time.

The file describing the composition of each volume of the geometry is generated by the generator, provided that the coloring process has been requested by the user. The corresponding file will be for instance:

```
GEOMCOMP
    BLUE  14 5 6 8 9 10 12 13 15 16 17 18 19 20 21
    RED  3 7 11 14
FIN_GEOMCOMP
```

A file describing the boundary conditions can also be generated, when needed. In this example, we want to apply reflection (Neumann) boundary conditions on the planes $y = L/2$, $y = -L/2$, $z = L/2$ and $z = -L/2$. correspondingly, we obtain the following output file:

```
LIMIT
        30
        1 REFLEXION 1
        1 REFLEXION 3
        2 REFLEXION 2
        2 REFLEXION 3
        3 REFLEXION 1
        3 REFLEXION 4
        4 REFLEXION 1
        4 REFLEXION 4
        5 REFLEXION 1
        5 REFLEXION 2
        5 REFLEXION 3
        6 REFLEXION 4
        7 REFLEXION 2
        7 REFLEXION 4
        8 REFLEXION 1
        8 REFLEXION 4
        9 REFLEXION 1
        9 REFLEXION 4
        10 REFLEXION 2
        10 REFLEXION 4
        11 REFLEXION 2
        11 REFLEXION 3
        13 REFLEXION 2
        13 REFLEXION 3
        14 REFLEXION 4
        15 REFLEXION 2
        15 REFLEXION 4
        16 REFLEXION 2
        16 REFLEXION 3
        17 REFLEXION 2
FIN_LIMIT
```

With these output files, we can then create a TRIPOLI-4 ® dataset. The TRIPOLI-4 ® visualization tool T4G [51] enables to visualize two-dimensional sections of the input geometry to be used for particle transport. In order to check the consistency of the geometry as produced based on the output files coming from the random geometry generator, we can compare the T4G representation and the one directly provided by Paraview ®, for a given section. For instance, for the example illustrate here, we might choose a plane section taken at $x = 0.5$. Although the data come from different frameworks (surface-based geometry for T4G, and tetrahedral decomposition for Paraview ®), we can easily verify that the two geometric representations are consistent with each other, as illustrated in Fig. 3.3.

3.6 Computer time for the construction

We have performed extensive tests in order to estimate the time required for the construction of the random geometries. In the following we provide some details concerning the algorithms and their respective computational burden, and we propose possible optimizations. We begin by analyzing the case of spherical inclusions.

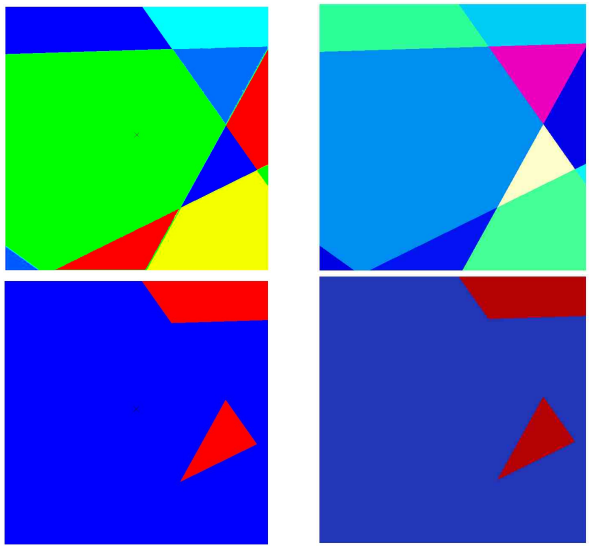

Figure 3.3: Comparison of the cut at $x = 0.5$, for a realization of a three-dimensional Poisson geometry between two visualization tools: `T4G` for the TRIPOLI-4 ® input file (left) and Paraview ® for the object created by the random geometry generator (right). At the top (respectively, bottom), we visualize the un-colored (respectively, colored) geometry.

3.6.1 Spherical inclusions

Fast RSA methods

Fast RSA methods enable to speed-up the basic RSA method by resorting to mesh superposed to the domain, in order to shorten the computational time spent for the step where we check that the trial sphere does not overlap any other sphere already positioned in the contained. For such methods, instead of checking all previous spheres for overlap, we restrict the search only to nearest-neighbour spheres, by defining a Cartesian mesh with spacing $h = L/n$, where n is the number of cells along each axis.

Mono-dispersed radius. A fast RSA method has been proposed in literature for mono-dispersed radius [19]. In this method, it is assumed that $h \leq 2R/\sqrt{3}$, i.e., $n \geq \lfloor \sqrt{3}L/2r \rfloor + 1$. Thus, each mesh cell contains at most one sphere center and only $m = \lfloor 2R/h \rfloor + 1$ neighbouring cells need to be checked in the $\pm x$, $\pm y$, $\pm z$ directions. During the construction, we need to update a list of empty mesh cells and a list of sphere centers contained within each mesh cell. According to [19], this improved method is expected to scale as $\mathcal{O}(N)$ rather than $\mathcal{O}(N^2)$ with respect to the number of spheres, at least on the investigated range of values for N, up to 1.6×10^4 spheres. Nevertheless, the list of empty boxes has a length proportional to N and the removal of one element in this list occurring for each introduction of a sphere has a complexity (N), whence an expected complexity (N^2) for the whole algorithm for large N. The fast RSA algorithm has been implemented in our computer code.

We have investigated and tested a new algorithm, also based on a meshing of the space. In this approach, we assume that $h \geq 2r$, i.e., $n \leq \lfloor L/2r \rfloor$, which ensures that at most one neighbouring cell in the $\pm x$, $\pm y$, $\pm z$ directions from the box cell containing the center of the sphere has to be checked. During the construction, we need to update a list of sphere centers contained within each mesh cell. As in the standard RSA method for mono-dispersed spheres, we compute the number of spheres N to be introduced. At this step, there are $k = 0$ spheres in the box. Then, we randomly select a position (x, y, z) uniformly sampled within the container, such that the sphere centered in (x, y, z) does not overlap the boundaries. We identify a list of neighbouring mesh cells which could contain spheres overlapping the sphere of center (x, y, z). Then, we check whether the sphere centered at (x, y, z) does overlap any of the other spheres contained in the mesh cells identified at the previous step. In case of overlapping, this sphere is rejected. Otherwise, the trial sphere is added to the list of spheres in the container and the counter k is incremented. Furthermore, we assign the trial sphere to the mesh

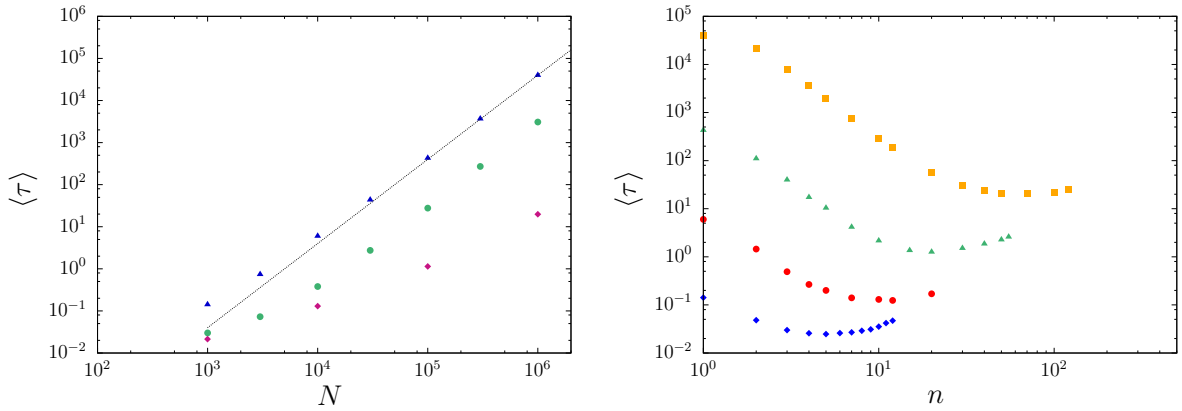

Figure 3.4: Left. Average computer time $\langle\tau\rangle$ for the construction of three-dimensional mono-dispersed spherical inclusions (without overlap of the spheres) as a function of the number of spheres N introduced in the geometry and of the used algorithm. For each configuration, we have generated spherical inclusions in a box of side $L = 100$ with a fixed packing fraction $\xi = 0.3$; the radius $r = r(N)$ is chosen such that $4\pi N r^3/L^3 = \xi$. Blue triangles correspond to results obtained with the basic RSA, green circles to results obtained with the Fast-RSA and red diamonds to the best results (as a function of the number of meshes n along each axis: see also Fig. 3.4 (right)) obtained with our algorithm. The scaling law N^2 is displayed for reference as a dashed line. Right. Average computer time $\langle\tau\rangle$ for the construction of three-dimensional mono-dispersed spherical inclusions (without overlap of the spheres) with the algorithm described in 3.6.1 as a function of the number of meshes n along each axis, for several values of the number of spheres N introduced in the geometry. For each configuration, we have generated spherical inclusions in a box of side $L = 100$ with a fixed packing fraction $\xi = 0.3$; the radius $r = r(N)$ is chosen such that $4\pi N r^3/L^3 = \xi$. Blue diamonds correspond to $N = 10^3$, red circles to $N = 10^4$, green triangles to $N = 10^5$ and orange squares to $N = 10^6$.

cell containing its center. This step is iterated until the number of spheres in the container reaches $k = N$. This algorithm has been also implemented in our computer code. The average number of spheres in each cell is N/n^3, and the number of cells is n^3. If n is too small, we have too many spheres in each mesh cell and the loop over the spheres on the neighbouring cells becomes expensive. If n is too large, the number of spheres per mesh cell is less than one, but the number of cells to manage is huge compared to the gain stemming from the reduction of the number of spheres per cell. An optimum has to be found, in order to have a few spheres per cell and a number of cells small enough. When the number of spheres N is large, the expected complexity is also $\mathcal{O}(N^2)$ but, similarly as for the Fast-RSA, this computationally expensive regime is expected to be reached later than in the case of the standard RSA.

The performance of the basic RSA, the Fast-RSA and our fast algorithm will be discussed in 3.6.1 together the corresponding simulation results for the computer time.

Poly-dispersed radius. For poly-dispersed radii, we need to slightly adapt the methods described above for mono-dispersed radii. Concerning the Fast-RSA, since the radius of spheres can be *a priori* arbitrarily small, taking h such that $h \leq 2r/\sqrt{3}$ for each sphere of radius r is not convenient. For our algorithm, since the radius of spheres can be *a priori* arbitrarily large, taking h such that $h \geq 2r$ for each sphere of radius r is not convenient, either. However, it is possible to take a mesh with an arbitrary spacing $h = L/n$ and to update the list of spheres contained in each mesh box (whether the center is contained in this box or not) during the construction.

The fast algorithm for poly-dispersed radii is the following: as in the basic RSA method for poly-dispersed spheres, we start by sampling sequentially the radii r_i of spheres until the effective packing fraction is larger than the sought parameter ξ. We denote by N the corresponding number of spheres. For the last sphere, the radius r_N is imposed such that the effective packing fraction is strictly equal

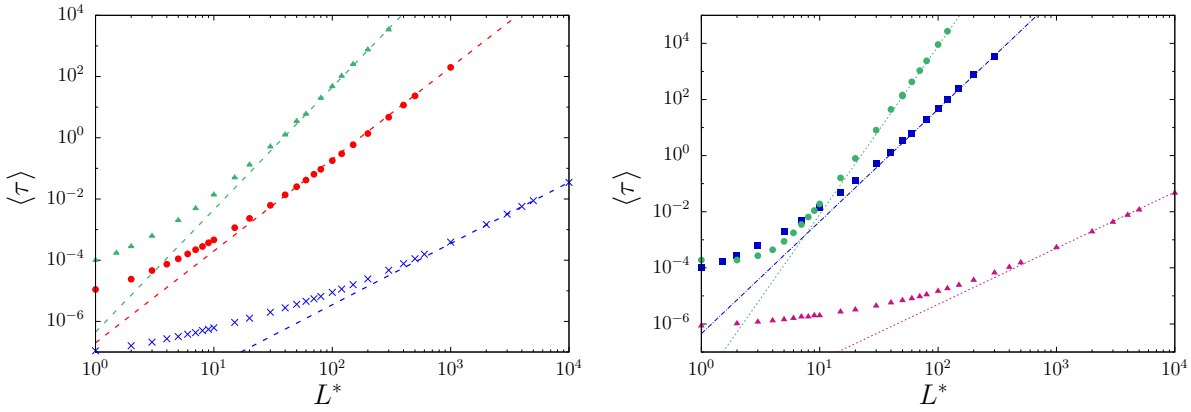

Figure 3.5: Left. Average computer time $\langle\tau\rangle$ for the basic construction (without speed-up) of d-dimensional isotropic Poisson tessellations with our random generator, as a function of the system size L and of the dimension d. Symbols correspond to Monte Carlo results, for $\rho = 1$. Blue crosses correspond to $d = 1$, red circles to $d = 2$ and green triangles to $d = 3$. Dashed lines correspond to scaling laws $(\rho L)^{d+1}$. Right. Average computer time $\langle\tau\rangle$ for the basic construction of three-dimensional isotropic Poisson tessellations, Voronoi tessellations and Box tessellations, as a function of the dimensionless system size $L^* = L/\Lambda_c$. Symbols correspond to Monte Carlo results, for $\Lambda_c = 1$, i.e. $\rho = 1$, $\rho_{\mathcal{B}} = 2/3$ and $\rho_{\mathcal{V}} \approx 0.6872$. Blue squares correspond to Poisson tessellations (without speed-up), red triangles to Box tessellations and green circles to Voronoi tessellations.

to ξ. Then, we sort the radii in descending order. At this step, there are $k = 0$ spheres in the box. Then, we randomly select a position (x, y, z) uniformly sampled within the container, such that the sphere does not overlap the boundaries. We identify a list of mesh cells spanned by the sphere of center (x, y, z) with radius r_k. Then, we check whether the sphere centered at (x, y, z) with radius R does overlap any of the other spheres contained in the mesh cells identified at the previous step. In case of overlapping, this sphere is rejected. Otherwise, the trial sphere is added to the list of spheres in the container and the counter k is incremented. Furthermore, we assign the trial sphere to each spanned mesh cell. This step is iterated until the number of spheres in the container reaches $k = N$.

Performances of RSA methods

In this section, we focus on spherical inclusions with constant radius. The average computer time $\langle\tau\rangle$ needed for the construction of three-dimensional spherical inclusions (with fixed packing fraction $\xi = 0.3$) as a function of the number of spheres N introduced is provided in Fig. 3.4 (left) for the following algorithms: basic RSA, Fast-RSA (as given in [19]) and our fast algorithm described in Sec. 3.6.1. For our method, the displayed result corresponds to the best computer time obtained by varying the parameter n defined above. We can see that the basic RSA method scales as $\mathcal{O}(N^2)$, as expected. Fast-RSA performs better than basic RSA with a speed-up (with respect to the basic RSA) close to 10 for a number of spheres between 10^4 and 10^6. Moreover, our fast algorithm performs systematically better than the Fast-RSA method: the speed-up (with respect to the basic RSA) of this fast algorithm can indeed attain 10^3 for $N = 10^6$ spheres.

Figure 3.4 (right) displays the computer time $\langle\tau\rangle$ needed for the construction of three-dimensional spherical inclusions with our fast algorithm, as a function of the parameter n, for different values of the number of spheres N. For each value of N, n is chosen in the range of values between 1 (the case corresponding to basic RSA) and $n_{\max}(N) = \lfloor L/2r(N) \rfloor$. As expected, the computer time decreases first with increasing n, then attains a minimum $n^*(N)$ depending on N, and finally increases with increasing n.

3.6.2 Tessellations

We consider then the case of stochastic tessellations.

Computer time without speed-up

The average computer time $\langle\tau\rangle$ needed for the construction of d-dimensional isotropic Poisson tessellations as a function of the dimensionless system size ρL and of the dimension d is provided in Fig. 3.5 (left). The computer time scales as $(\rho L)^{d+1}$, whereas the number of cells of the tessellation scales as $(\rho L)^d$ (further considerations will be provided in Sec. 4). In the construction algorithm given in Secs. 2.3.1, 2.4.1 and 2.5.1, we loop over N_H hyperplanes, with N_H linearly proportional to L, and for each hyperplane we loop over all polyhedra of the previous step to check whether they are cut by the new sampled hyperplane: this explains the scaling of the complexity as $\mathcal{O}((\rho L)^{d+1})$.

The average computer time $\langle\tau\rangle$ needed for the construction of three-dimensional Poisson, Voronoi and Box tessellations as a function of the dimensionless system size $L^* = L/\Lambda_c$ is provided in Fig. 3.5 (right). Without any specific speed-up, the computer time scales as $(L^*)^4$ for Poisson tessellations, $(L^*)^6$ for Voronoi tessellations and L^2 for Box tessellations. Voronoi tessellations are constructed with the Green and Sibson algorithm, whose complexity is $\mathcal{O}(N_p^2)$, where N_p denotes the number of polyhedra and scales as $(L^*)^3$. Therefore, the scaling $(L^*)^6$ is coherent for Voronoi tessellations. For Box tessellations, the scaling $(L^*)^2$ corresponds to the quadratic complexity of the sort operation performed on the points (whose number scales as L^*) on each axis.

Such computer times are rather long, especially for three-dimensional Voronoi and Poisson tessellations with a large dimensionless system size. It is therefore convenient to develop some strategies in order to speed-up the algorithms for the construction of these random tessellations.

Computer time with speed-up

In order to reduce the computer time needed for the construction of tessellations, a possible method is to superpose to the domain a Cartesian mesh with spacing $h = L/n$, where L is the size of the box and n is the number of cells along each axis.

For Poisson tessellations without speed-up, for each new plane added to the tessellation we must check whether all previous elements (e.g., vertices, edges, faces and polyedra for $d = 3$) of the tessellations are i) above or below the plane (for the vertices) and ii) cut by this plane (for the other elements). A mesh enables to shorten this very expensive step, by restricting the search only on elements contained in mesh cells which are cut by the considered plane. Fig. 3.6 (left) shows the computer time obtained for three-dimensional Poisson tessellations with this implementation as a function of the parameter n, for different values of the size L of the domain. For each size L, the computer time decreases with increasing n, then it attains a minimum for $n^*(L)$ depending on L, and finally increases with increasing n. Moreover, for each L, the computer time scales as n^3 for large n: in this regime, the handling of the mesh cells dominates, because the number of mesh cells becomes as large as (or larger than) the tessellation complexity. The speed-up factor obtained by taking the best score with respect to the computer time without optimization increases with increasing domain size, so the meshing feature is particularly relevant for geometries with a high complexity. For large enough domains, this method enables to reach a speed-up of about 6 for the computer time.

For the construction of Voronoi tessellations with the Green and Sibson algorithm, the introduction of any seed requires a loop over all previous seeds in order to update the neighborood map. This expensive step leads to a quadratic complexity with respect to the expected number of polyhedra. A mesh enables to restrict the research to the mesh cell containing the new seed and to the neighboring mesh cells. Fig. 3.6 (right) shows the computer time obtained for three-dimensional Voronoi tessellations as a function of the parameter n, for different values of the size L of the domain. This method enables a gain of several orders of magnitude for the computer time.

For d-dimensional Poisson tessellations, we have tested another method allowing a considerable reduction in the computer time needed for the construction. In the basic implementation of the construction, for each new plane all points of the current tessellation are checked (either 'above' or

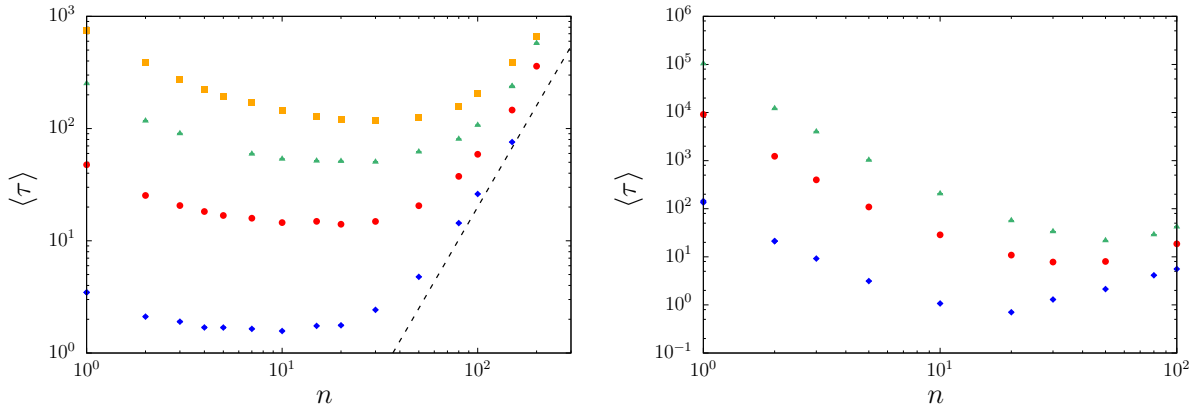

Figure 3.6: (Left) Average computer time $\langle\tau\rangle$ for the construction of three-dimensional isotropic Poisson tessellations with a fictive mesh, as a function of the parameter n such the spacing is $h = L/n$ along each axis, for different values of the system size L. Symbols correspond to Monte Carlo results, for $\rho = 1$. Blue diamonds correspond to $L = 50$, red circles to $L = 100$, green triangles to $L = 150$ and orange squares to $L = 200$. (Right) Average computer time $\langle\tau\rangle$ for the construction of three-dimensional Voronoi tessellations with a fictive mesh, as a function of the parameter n such the spacing is $h = L/n$ along each axis, for different values of the system size L. Symbols correspond to Monte Carlo results, for $\rho_{\mathcal{V}} = 0.6872$. Blue diamonds correspond to $L = 50$, red circles to $L = 100$, green triangles to $L = 150$.

'below' the plane), then all edges (either 'cut' or 'not cut'), then all faces (either 'cut' or 'not cut') and finally all polyhedra (either 'cut' or 'not cut'). As explained in Sec. 3.1, the storage of the geometry corresponds to a descending hierarchy, which means that each constituent knows which sub-elements it contains but does not know in which upper elements it is contained. Thus, for $d = 3$, the edge contains the indexes of the points forming this edge, the face contains the indexes of the edges forming this face and the polyhedron contains the indexes of the faces forming this polyhedron. We have improved this framework with lists describing the ascending hierarchy: one list provides for each edge the list of faces containing it, and one list provides for each face the list of polyhedra containing it. Therefore, since a face which is cut necessarily contains cut edges, we know which faces will be cut from the list of the cut edges. Similarly, since a polyhedron which is cut necessarily contains cut faces, we know which polyhedra will be cut from the list of the cut faces. We reduce therefore the loop on the faces and the polyhedra. The average computer time obtained with this method is shown in Fig. 3.7 (left) for dimension $d = 2$ and $d = 3$. The obtained results are very satisfying and show that this improvement performs better than the mesh.

Finally, it is also possible to combine the meshing of the domain (in order to reduce the loop over points and edges) and the ascending hierarchy (in order to keep the targeting on cut faces and cut polyhedra) for Poisson tessellations: we have implemented this option for $d = 3$. However, the corresponding results are not totally satisfying in terms of speed-up with respect to the algorithm with ascending hierarchy and without meshing. This implementation provides nonetheless an additional speed-up in some cases: for small geometries ($L < 200$), the effect on the reduction of the loop over the points and the edges is not relevant; for large geometries, a speed-up has been observed for some values of the number of meshes n along each axis, but a slowing-down is also possible if n is not in the optimal range. The observed slowing-down (with respect to the optimized algorithm without meshing) could be due to some memory effects occurring due to the storage of additional lists, leading to some instabilities in terms of computer time. This optimization should be therefore used with caution for the choice of n. Fig. 3.7 (right) displays the obtained results with this optimization as a function of n for $L = 200$. For $L = 300$, the average computer time with the optimized algorithm without meshing is $\langle\tau\rangle = 396$ seconds, while the combination of the ascending hierarchy and a meshing with $n = 10$ performs better, with an average computer time $\langle\tau\rangle = 332$ seconds, which corresponds to a gain of 16%.

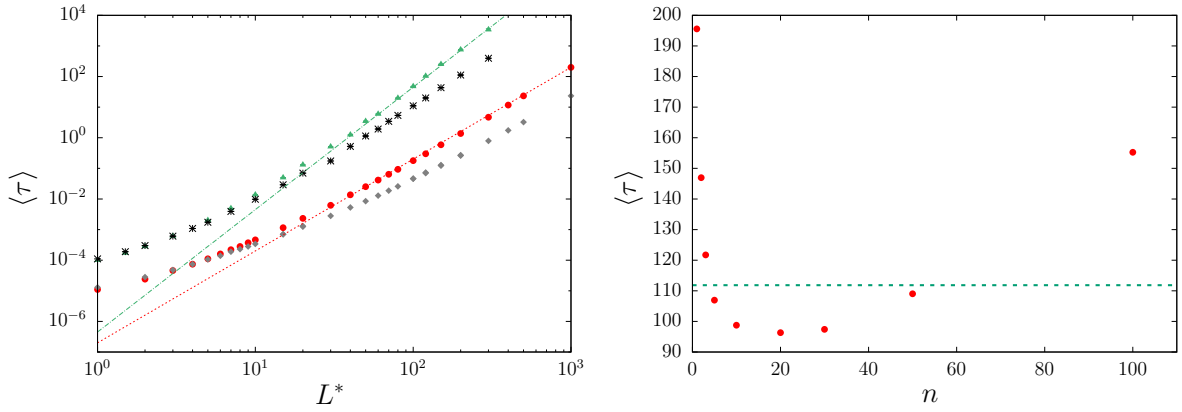

Figure 3.7: Left. Average computer time $\langle\tau\rangle$ for the construction of d-dimensional isotropic Poisson tessellations with our random generator, as a function of the system size L, of the dimension d and of the used algorithm: basic construction or construction with ascending hierarchy. Symbols correspond to Monte Carlo results, for $\rho = 1$. Red circles to $d = 2$ without speed-up, green triangles to $d = 3$ without speed-up, grey diamonds to $d = 2$ with speed-up, black crosses to $d = 3$ with speed-up. Dashed lines correspond to scaling laws $(\rho L)^{d+1}$. Right. Average computer time $\langle\tau\rangle$ for the construction of three-dimensional isotropic Poisson tessellations with ascending hierarchy combined with a fictive mesh, as a function of the parameter n such the spacing is $h = L/n$ along each axis, for the system size $L = 200$. Red symbols correspond to Monte Carlo results obtained with this implementation, for $\rho = 1$. To provide a comparison, the horizontal dashed line corresponds to the average time obtained for $L = 200$ and $\rho = 1$ with the ascending hierarchy and without meshing. For $5 \leq n \leq 50$, the combined method shows a speed-up with respect to the optimized method without meshing. For $n < 5$ or $n > 50$, the combined method is slower than the optimized method without meshing: the managing of mesh cells induces a over-head.

3.7 Optimization of particle tracking in random geometries

Once the geometries have been produced, they can be exported as output files for the Monte Carlo transport code TRIPOLI-4 ®. In Sec. 3.6 we have detailed the strategies that can be applied in order to reduce the computer time devoted to the construction of these geometries. For particle transport through these geometries, it is also useful to develop specific methods enabling to speed-up the tracking of the particles in the presence of a large number of volumes per geometry. We will come back to the issue of particle transport in random media in later Chapters: here we will provide some general considerations concerning the optimization method that we have used in order to accelerate the particle tracking routines in the presence of 'large' random geometries.

3.7.1 Spherical inclusions

For random spherical inclusions, the particle transport in geometries with a large number N of spheres (typically, $N \geq 10^4$) without specific treatments induces a very high computational burden due to the tracking of the particles between the background material and the spheres. Indeed, whenever a particle is in the matrix background, the transport code needs to perform a loop over N spheres to find the next interface. These steps are particularly expensive. That is why it is convenient to speed-up the tracking with a spatial Cartesian mesh (with spacing $h = L/n$) of the box combined with a neighborhood map, in order to restrict the research to spheres of the mesh cell containing the considered particle. We have implemented a method in our generator to mesh the geometry after the construction: we may note that the meshing is not necessarily the same as the one used for the construction. Then, the output files describing the geometry for TRIPOLI-4 ®(see also Sec. 3.5) are

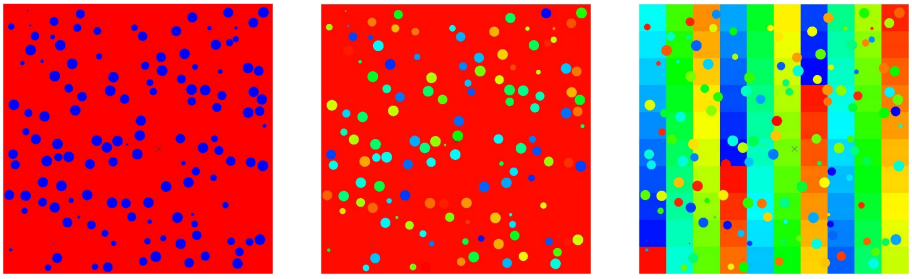

Figure 3.8: Cut at $x = 0.5$, for a realization of a three-dimensional random geometry with mono-dispersed spherical inclusions with the visualization tool `T4G`, from the TRIPOLI-4 ® input file: (left) colored geometry (colors correspond to the composition associated to each volume); (middle) uncolored geometry without spatial meshing; (right) uncolored geometry with $n = 10$ spatial meshes along each axis.

produced by taking into account the mesh, and the neighborhood map is modified accordingly. A realization of a random geometry with mono-dispersed inclusions, with or without mesh, is provided in Fig. 3.8.

In order to estimate the impact of the meshing on the computer time for the particle transport, we have performed simulations on the Monte Carlo transport code TRIPOLI-4 ®with the output files taking into account the Cartesian mesh of the domain, for several values of n. For this purpose, we have used a very simple transport problem corresponding to a criticality calculation (which will be entirely revisited in Chapter 6). In this case, we consider mono-kinetic transport in random spherical inclusions within a box of side $L = 10$ with reflective boundary conditions. For the sake of simplicity, the composition of the spheres and of the background matrix are chosen to be identical: both materials are characterized by a total cross section $\Sigma_{t,0} = \Sigma_{t,1} = 2$, a scattering cross section $\Sigma_{s,0} = \Sigma_{s,1} = 1$, a fissile cross section $\Sigma_{f,0} = \Sigma_{f,1} = 0.5$ and an average number of secondary particles at fission events equal to $\nu_0 = \nu_1 = 2.5$. For each geometry, we have computed the multiplication factor k_{eff}. For each case, we have performed the transport simulation with 10^3 particles and 10^3 generations. The simulation results for the computer time obtained with this method are displayed in Fig. 3.9 as a function of the number of meshes, for several number of spheres N introduced in the geometry. As expected, the mesh speeds-up the transport simulation by several orders of magnitude with respect to the transport simulation without mesh (corresponding to $n = 1$): the gain amounts to 10^3 for $N = 10^5$ spheres and more for $N = 10^6$ spheres. The behaviour as a function of n is similar to that observed in Fig. 3.4 (right) for the construction with a superposed mesh.

3.7.2 Tessellations

The knowledge of the connectivity map (that we have produced during the construction) is expected to considerably speed-up the tracking in random tessellations with a large number of polyhedra. Without connectivity map, the Monte Carlo code will perform a loop over all polyhedra for each calculation of the next crossed interface. This search will be on the contrary restricted to the neighboring polyhedra only in the presence of the connectivity map. The average number of neighbors is equal to 6 for Poisson and Box tessellations and to 15.54 for Voronoi tessellations. Thus, the speed-up is expected to be very interesting for particle transport in geometries with a large number of volumes ($N_p > 10^4$) and for a physical configuration such that the particle transport is dominated by the calculation of the next interface, i.e., with a weak average number of collisions with respect to the number of interface crossings. This happens when $\Lambda_c < 1/\Sigma_t$. In order to estimate the impact of the connectivity map on the computer time for particle transport, we have performed TRIPOLI-4 ®simulations with and without the map. For this investigation, we have focused on three-dimensional Poisson tessellations only. We consider binary mixtures, with $p = 0.3$ for material α and $1 - p$ for material β. For the sake of simplicity, α and β are chosen to be equal.

We consider again the criticality problem tested in Sec. 3.7.1. The simulation results are displayed

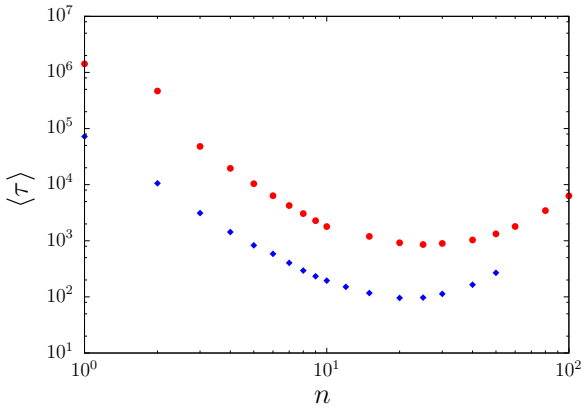

Figure 3.9: Average computer time $\langle\tau\rangle$ for the particle transport in three-dimensional monodispersed spherical inclusions with a spatial meshing as a function of the number of meshes n along each axis, for several values of the number of spheres N introduced in the geometry. For each configuration, we have considered spherical inclusions in a box of side $L = 10$ with a fixed packing fraction $\xi = 0.1$; the radius $r = r(N)$ is chosen such that $4\pi N r^3/L^3 = \xi$. Blue diamonds correspond to $N = 10^5$, red circles to $N = 10^6$.

in Fig. 3.10, as a function of the number of polyhedra N_p. The speed-up is about 30 for large N_p, which shows the improvement induced by the connectivity map for complex tessellations. As expected, the gain for 'small' geometries (less than 10^4 polyhedra) is negligible. The same behaviour is observed for other tessellations (Box, Voronoi) and for other dimensions d.

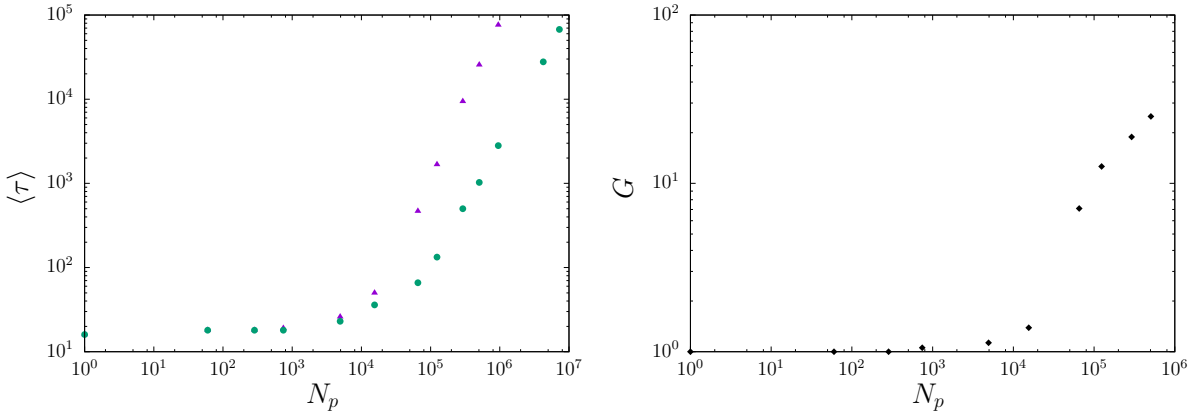

Figure 3.10: (Left) Average computer time $\langle\tau\rangle$ for the particle transport in three-dimensional isotropic Poisson tessellations as a function of the number of polyhedra N_p, without connectivity map (purple triangles) and with connectivity map (green circles), for $\rho = 1$. (Right) Relative gain factor for the computer time thanks to the connectivity map, as a function of the number of polyhedra N_p.

Chapter 4

Analysis of the statistical properties of random tessellations

In the previous Chapter we have recalled the key statistical properties of stochastic tessellations belonging to three relevant classes. As observed, the exact distributions for the physical observables are mostly unknown [127]. Although a number of exact results have been established for the (typically low-order) moments of the observables and for their correlations, at least in the limit case of domains having an infinite extension [24,127,133], numerical analysis is thus mandatory. Monte Carlo simulation offers a unique tool for the investigation of the statistical features of stochastic geometries.

In particular, by resorting to our computer code, based on the explicit construction algorithms provided described in the previous Chapter, in this Chapter we will *i*) investigate the convergence of the moments and distributions of arbitrary physical observables associated to finite-size tessellations towards their known limit behaviour (if any) for infinite tessellations, and *ii*) numerically explore the scaling of the moments and the distributions for which exact asymptotic results are not yet available.

We will start by considering the case of isotropic d-dimensional Poisson tessellations, in view of their relevance for transport problems. We will the perform a comparative analysis of the three classes of random geometries introduced in the previous Chapter, namely, Poisson, Voronoi and Box tessellations. Finally, we will examine the case of anisotropic Poisson tessellations. For the sake of completeness, the key properties of spherical inclusions have been also evaluated and are reported at the end of the Chapter, to be contrasted to those of random tessellations.

4.1 d-dimensional isotropic Poisson tessellations

4.1.1 Number of polyhedra

To begin with, we will first analyse the growth of the number N_p of polyhedra in d-dimensional isotropic Poisson geometries as a function of the linear size L of the domain, for a given value of the tessellation density ρ. In the following, we will always assume that $\rho = 1$, unless otherwise specified (with both ρ and L expressed in arbitrary units). The quantity N_p provides a measure of the *complexity* of the resulting geometries, i.e., the number of cells composing the tessellations. The simulation findings for the average number $\langle N_p|L\rangle$ of d-polyhedra (at finite L) and the dispersion factor, i.e., the ratio $\sigma[N_p|L]/\langle N_p|L\rangle$, σ denoting the standard deviation, are illustrated in Fig. 4.1. For large L, we find an asymptotic scaling law $\langle N_p|L\rangle \sim L^d$: the complexity of the random geometries increases with system size and dimension (Fig. 4.1, left), as expected. This means that the computational cost to generate a realization of a Poisson geometry is also an increasing function of the system size and of the dimension. As for the dispersion factor, an asymptotic scaling law $\sigma[N_p|L]/\langle N_p|L\rangle \sim 1/\sqrt{L}$ is found for large L, independent of the dimension (Fig. 4.1, right): for large systems, the distribution of N_p will be then peaked around the average value $\langle N_p|L\rangle$. For $d = 1$, the exact solution can be easily computed: for each realization, the random number N_p of polyhedra is given by $N_p = N_H + 1$, where N_H follows a Poisson distribution with intensity ρL, according to the construction algorithm given in Sec. 2.3.1.

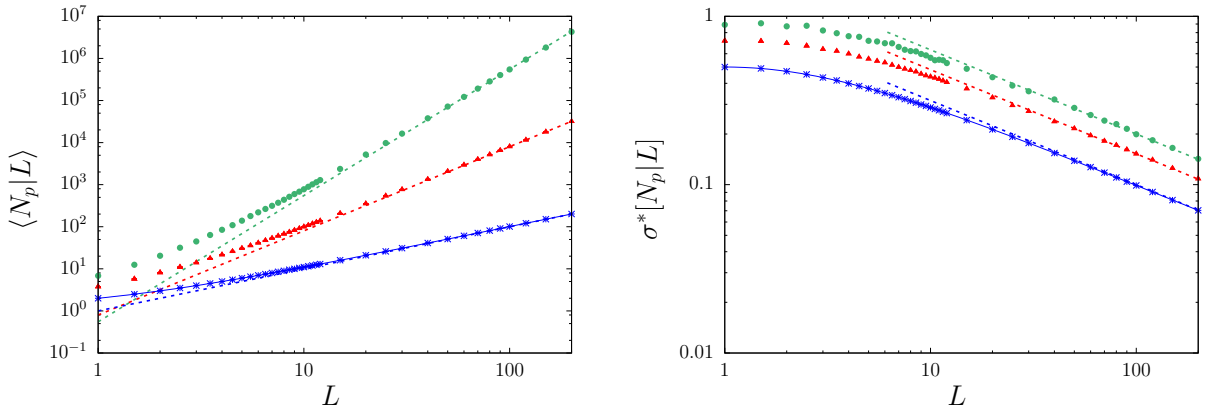

Figure 4.1: The average number $\langle N_p|L\rangle$ of d-polyhedra in d-dimensional isotropic Poisson geometries (left) and the dispersion factor $\sigma^*[N_p|L] = \sigma[N_p|L]/\langle N_p|L\rangle$ (right) as a function of the linear size L of the domain and of the dimension d. For all sizes L we have generated $M = 10^6$ realizations for $d = 1$, $M = 5 \times 10^4$ realizations for $d = 2$ and $M = 5 \times 10^3$ realizations for $d = 3$. Simulation were performed with $\rho = 1$. Symbols correspond to the Monte Carlo simulation results: blue crosses denote $d = 1$, red triangles $d = 2$ and green circles $d = 3$. The scaling laws L^d (left) and $1/\sqrt{L}$ (right) are displayed for reference with dashed lines. For $d = 1$, the exact solutions, given by Eqs. 4.1 and 4.2, are plotted with a blue solid line.

This yields, for $d = 1$

$$\langle N_p|L\rangle = \rho L + 1, \tag{4.1}$$

and

$$\sigma[N_p|L] = \sqrt{\rho L}. \tag{4.2}$$

4.1.2 Stereological properties

We have numerically computed by Monte Carlo simulation the probability of the number of intersections for an arbitrary segment of unit length and the probability density of the chords as a function of the linear size L of the domain and for different dimensions d.

Number of intersections for a segment of unit length

For each realization, a test segment of unit length is sampled by uniformly choosing a point and a direction, and the number of intersections N_i with the polyhedra composing the tessellation are determined. As shown in Fig. 4.2 (left), the distribution of the number of intersections quickly converges to the limit Poisson distribution $\mathcal{P}(N_i)$ of intensity ρ as a function of L, which most probably stems from the unit test segment being only weakly affected by finite-size effects (i.e., by the polyhedra that are cut by the boundaries of the box). Finite-size effects are appreciable only for large values of the number of intersections N_i, which in turn occur with small probability. The asymptotic average number of intersections per unit length for $L \to \infty$ yields $\langle N_i\rangle = \rho$ for any d: the Monte Carlo simulation results obtained for a large $L = 200$ are compared to the theoretical formulas in Tab. 4.1, with the same simulation parameters as above.

Chord lengths

In order to investigate the statistical properties of chord lengths traversing the d-dimensional Poisson tessellations, a line with arbitrary orientation is drawn. The intersections of the line with the polyhedra of the geometry (restricted to a box) are then computed, and the resulting segment lengths are recorded. For $d > 1$, this procedure is repeated for a large number N_L of lines having the same orientation. The whole procedure is iterated for a large number of geometries, in order to get the

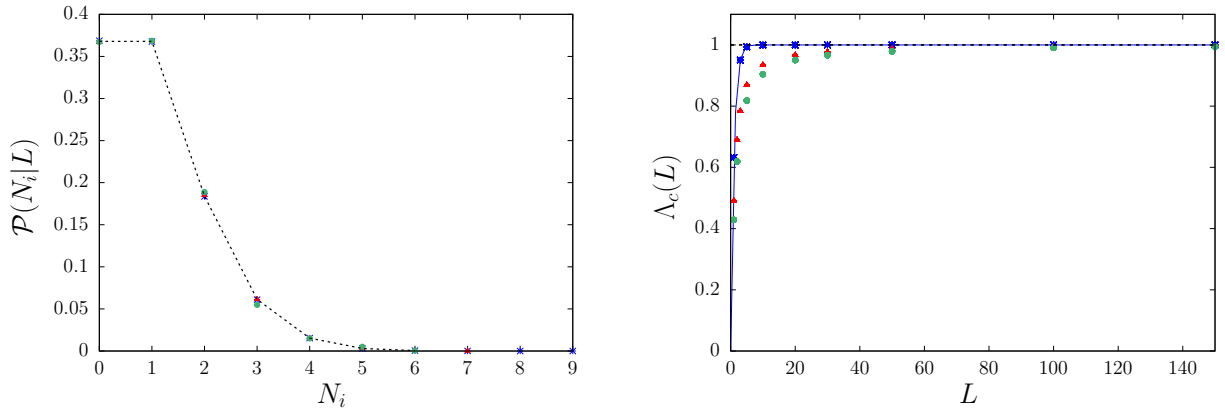

Figure 4.2: Left. The probability density $\mathcal{P}(N_i|L)$ of the number of intersections for a unit segment for d-dimensional isotropic Poisson tessellations with $L = 200$. For all sizes L we have generated $M = 10^6$ realizations for $d = 1$, $M = 5 \times 10^4$ realizations for $d = 2$ and $M = 5 \times 10^3$ realizations for $d = 3$. Simulations were performed with $\rho = 1$. Symbols correspond to the Monte Carlo simulation results: blue crosses denote $d = 1$, red triangles $d = 2$ and green circles $d = 3$. The dotted line corresponds to the limit Poisson distribution with intensity ρ. Right. The correlation length $\Lambda_c(L)$ as a function of the dimension d and of the linear size L of the domain for d-dimensional isotropic Poisson tessellations. We have generated $M = 10^3$ realizations with $\rho = 1$ and irradiated the box with $N_L = 100$ lines per realization. Symbols correspond to the Monte Carlo simulation results, blue crosses denote $d = 1$, red triangles $d = 2$ and green circles $d = 3$. The asymptotic average correlation length $\Lambda_c = 1/\rho$ is displayed as a black dashed line for reference.

d	$\langle N_i \rangle$	Theoretical value	Monte Carlo
1	ρ	1	0.998 ± 0.001
2	ρ	1	1.003 ± 0.005
3	ρ	1	1.02 ± 0.02

Table 4.1: The average number of intersections $\langle N_i \rangle$ in d-dimensional isotropic Poisson tessellations. Monte Carlo simulation results are obtained with $L = 200$ and $\rho = 1$ for any dimension d.

appropriate statistics. Due to the isotropy of the tessellations, the asymptotic distributions for infinite L do not depend on the line direction $\mathbf{\Omega}$, so that the explicit dependence on $\mathbf{\Omega}$ will be dropped, in order to keep notation simple.

The convergence of the correlation length $\Lambda_c(L)$ as a function of the box side L is provided in Fig. 4.2 (right); the rate of convergence appears to be weakly dependent on the dimension d. The numerical results for the chord length distribution $\mathcal{P}(\ell|L)$ at finite L are illustrated in Figs. 4.3 and 4.4. For small L, finite-size effects are apparent in the chord length density: this is due to the fact that the longest line that can be drawn across a box of linear size L is $\sqrt{d}L$, which thus induces a cut-off on the distribution (see in particular Fig. 4.3). For $\rho L \gg 1$, the finite-size effects due to the cut-off fade away and the probability densities eventually converge to the expected exponential distribution of mean $\Lambda = 1/\rho$.

The case $d = 1$ can be treated analytically and might thus provide a rough idea of the approach to the limit case. For any finite L, the distribution of the chord lengths for $d = 1$ is

$$\mathcal{P}(\ell|L) = \rho e^{-\rho\ell} \mathbb{1}_{\ell<L} + e^{-\rho L} \delta(\ell - L), \tag{4.3}$$

$\mathbb{1}_J$ being the indicator function of the domain J. The moments of order m of the chord length ℓ for finite L thus yield

$$\langle \ell^m | L \rangle = \frac{\Gamma(m+1)}{\rho^m} - \frac{\Gamma_{m+1}(\rho L)}{\rho^m} + e^{-\rho L} L^m, \tag{4.4}$$

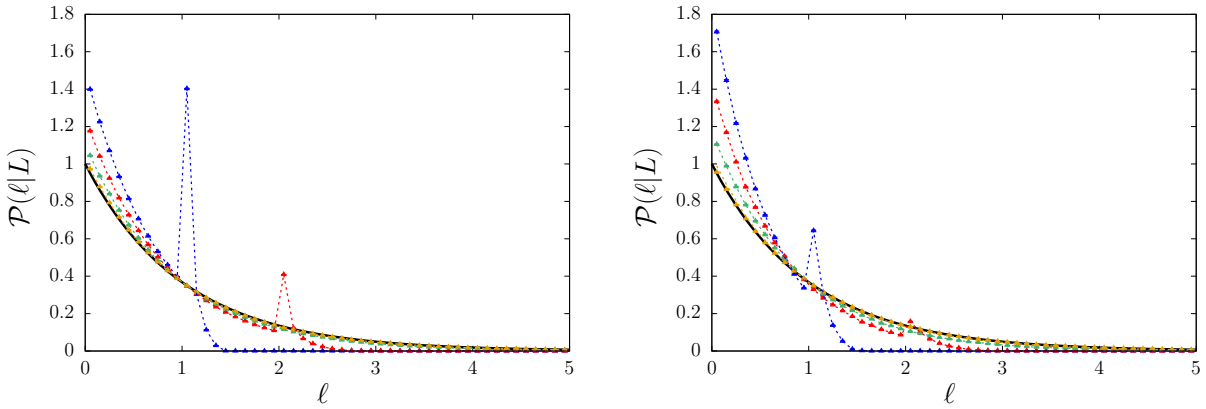

Figure 4.3: The probability densities $\mathcal{P}(\ell|L)$ of the chord length as a function of the linear size L of the domain for $d = 2$ (left) and for $d = 3$ (right). We have generated $M = 10^3$ realizations with $\rho = 1$ and computed the chord length distribution by irradiating the box with $N_L = 100$ lines per realization. Symbols correspond to the Monte Carlo simulation results, with lines added to guide the eye: blue triangles denote $L = 1$, red triangles $L = 2$, green circles $L = 5$, and orange triangles $L = 200$. The asymptotic exponential distribution given in Eq. 2.40 is displayed as a black dashed line for reference.

d	Λ_c	Theoretical value	Monte Carlo
1	$1/\rho$	1	$1.00011 \pm 7 \times 10^{-5}$
2	$1/\rho$	1	$0.9952 \pm 3 \times 10^{-4}$
3	$1/\rho$	1	$0.9940 \pm 8 \times 10^{-4}$

Table 4.2: The average correlation lengths Λ_c in d-dimensional isotropic Poisson tessellations. Monte Carlo simulation results are obtained with $L = 150$ and $\rho = 1$ for any dimension d.

where $\Gamma_a(x)$ is the incomplete Gamma function [103]. In the limit case $L \to \infty$, we have $\langle \ell^m \rangle = \Gamma(m+1)/\rho^m$, so that for the convergence rate we obtain

$$\frac{\langle \ell^m | L \rangle}{\langle \ell^m \rangle} = 1 - \frac{\Gamma_{m+1}(\rho L) - e^{-\rho L}(\rho L)^m}{\Gamma(m+1)}, \tag{4.5}$$

which for large $\rho L \gg 1$ gives

$$\frac{\langle \ell^m | L \rangle}{\langle \ell^m \rangle} \simeq 1 - \frac{(\rho L)^{m-1} e^{-\rho L}}{\Gamma(m+1)}. \tag{4.6}$$

Thus, the average chord length ($m = 1$) converges exponentially fast to the limit behaviour, whereas the higher moments ($m \geq 2$) converge sub-exponentially with power-law corrections. For $d > 1$, the cut-off is less abrupt, but the distributions $\mathcal{P}(\ell|L)$ still show a peak at $\ell = L$, and vanish for $\ell > L\sqrt{d}$. The asymptotic average chord lengths for $L \to \infty$ yield $\langle \ell \rangle = 1/\rho$ for any d: the Monte Carlo simulation results obtained for a large $L = 200$ are compared to the theoretical formulas in Tab. 4.2.

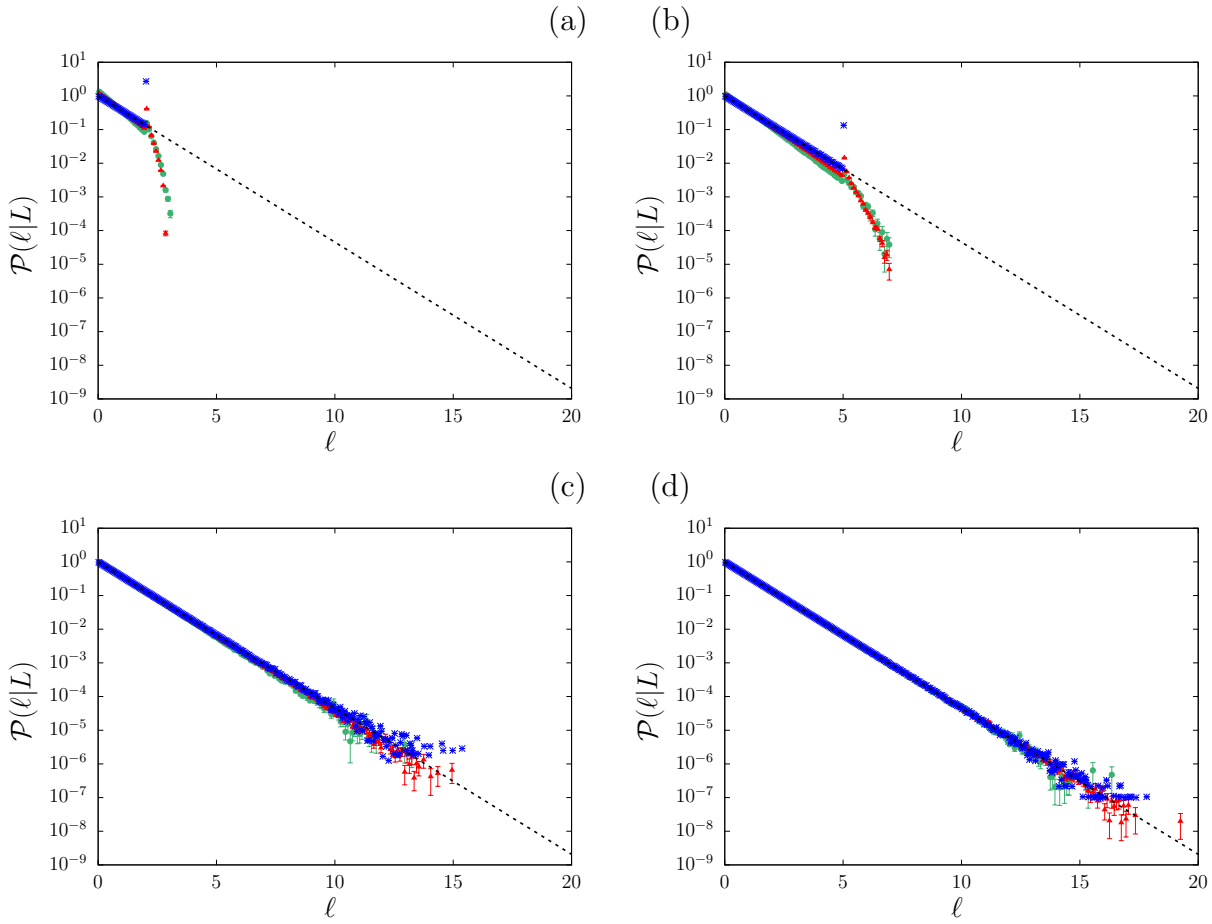

Figure 4.4: The probability densities $\mathcal{P}(\ell|L)$ of the chord length as a function of the dimension d and of the linear size L of the domain for d-dimensional isotropic Poisson tessellations. We have generated $M = 10^6$ realizations for $d = 1$, $M = 5 \times 10^4$ realizations for $d = 2$ and $M = 5 \times 10^3$ realizations for $d = 3$. We have computed the chord length distribution by irradiating the box with $N_L = 100$ lines per realization for $d > 1$. Simulation results have been obtained with $\rho = 1$. Symbols correspond to the Monte Carlo simulation results: blue crosses denote $d = 1$, red triangles $d = 2$ and green circles $d = 3$. The cases illustrated here are as follows: (a) $L = 2$; (b) $L = 5$; (c) $L = 20$; (d) $L = 200$. The asymptotic exponential distribution given in Eq. 2.40 is displayed as a black dashed line for reference.

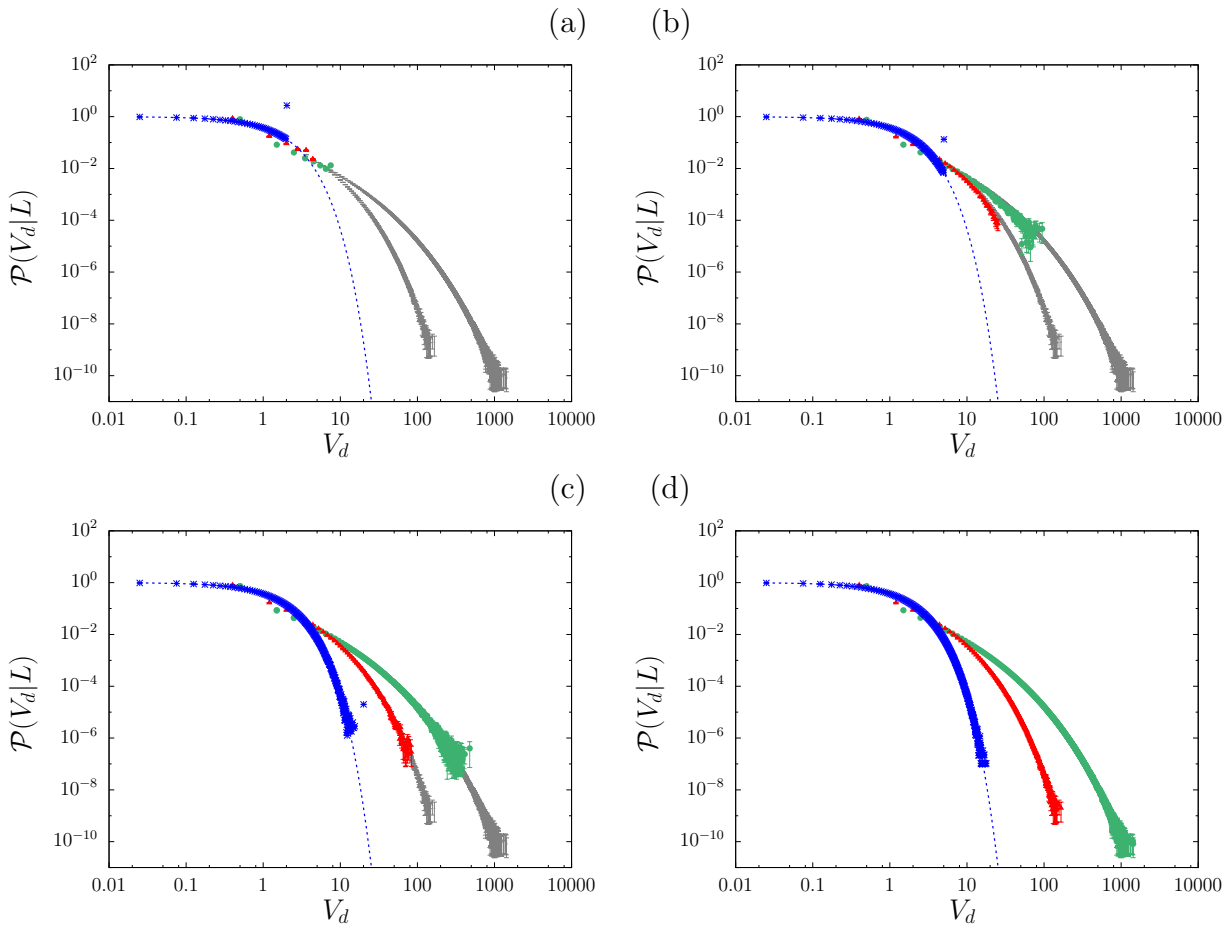

Figure 4.5: The probability densities $\mathcal{P}(V_d|L)$ of the d-volume in d-dimensional isotropic Poisson geometries as a function of the dimension d and of the linear size L of the domain. We have generated $M = 10^6$ realizations for $d = 1$, $M = 5 \times 10^4$ realizations for $d = 2$ and $M = 5 \times 10^3$ realizations for $d = 3$. Simulation results have been obtained with $\rho = 1$. Symbols correspond to the Monte Carlo simulation results: blue crosses denote $d = 1$, red triangles $d = 2$ and green circles $d = 3$. The cases illustrated here are as follows: (a) $L = 2$; (b) $L = 5$; (c) $L = 20$; (d) $L = 200$.

4.1.3 Polyhedral features

Volume

One of the most important physical observables related to the stochastic geometries is the distribution $\mathcal{P}(V_d)$ of the d-volumes V_d of the polyhedra. For $d = 1$, this distribution coincides with that of the chord lengths $\mathcal{P}(\ell)$, which means that the approach to the limit case of infinite domains follows from the same arguments as above. Unfortunately, the functional form of the distribution $\mathcal{P}(V_d)$ is not known for $d > 1$ [86, 87, 127]. We have thus resorted to Monte Carlo simulation so as to assess the impact of the domain size L and of the dimension d on $\mathcal{P}(V_d|L)$ for finite L. The numerical findings are shown in Fig. 4.5. It is apparent that for $L \gg 1$ the distributions $\mathcal{P}(V_d|L)$ approach an asymptotic shape. The rate of convergence as a function of L decreases with increasing d, which is expected on physical grounds because the complexity of the geometries grows as $\sim L^d$. The tails of $\mathcal{P}(V_d)$ for large values of the argument V_d also depend on d: for $d = 1$, $\mathcal{P}(V_d) \sim \exp(-\rho V_d)$, whereas for $d > 1$ the tail appears to be increasingly slower as a function of d. Due to poor statistics for very large values of V_d, we are not able to precisely characterize the asymptotic decay of $\mathcal{P}(V_d)$. It seems however that for $d > 1$ the tail is not purely exponential, and that power law corrections might thus appear. The convergence of the average volume $\langle V_d|L\rangle$ as a function of of the linear size L of the domain and of the dimension d is illustrated in Fig. 4.6 (left).

m	d	$\langle V_d^m \rangle$	Theoretical value	Monte Carlo
	1	$1/\rho$	1	$1.00011 \pm 7 \times 10^{-5}$
1	2	$4/\pi\rho^2$	1.27324	$1.2728 \pm 6 \times 10^{-4}$
	3	$6/\pi\rho^3$	1.90986	1.907 ± 0.004
	1	$2/\rho^2$	2	$2.0007 \pm 3 \times 10^{-4}$
2	2	$8/\rho^4$	8	$7.993 \pm 8 \times 10^{-3}$
	3	$48/\rho^6$	48	47.8 ± 0.2
	1	$6/\rho^3$	6	$6.004 \pm 2 \times 10^{-3}$
3	2	$256\pi/7\rho^6$	114.893	114.7 ± 0.2
	3	$1344\pi/\rho^9$	4222.3	4193 ± 28

Table 4.3: The moments $\langle V_d^m \rangle$ of the d-volume in d-dimensional isotropic Poisson tessellations. Monte Carlo simulation results are obtained with $L = 200$ and $\rho = 1$ for any dimension d.

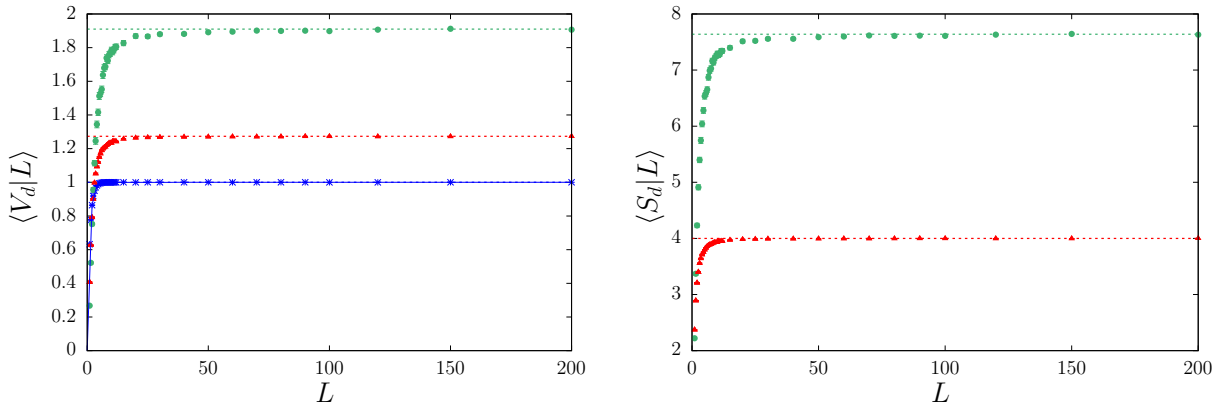

Figure 4.6: First-order moments of the volume and surface of the typical polyhedron as a function of the linear size L of the domain and of the dimension d, for d-dimensional isotropic Poisson geometries. Left: the average d-dimensional volume $\langle V_d|L \rangle$; right: the average d-dimensional surface $\langle S_d|L \rangle$ for $d > 1$. For each case, simulation results have been obtained with $\rho = 1$. We have generated $M = 10^6$ realizations for $d = 1$, $M = 5 \times 10^4$ realizations for $d = 2$ and $M = 5 \times 10^3$ realizations for $d = 3$. Symbols correspond to the Monte Carlo simulation results: blue crosses denote $d = 1$, red triangles $d = 2$ and green circles $d = 3$. Dotted lines correspond to the asymptotic moment given in Tab. 2.1.

Surface

The analysis of the d-surfaces S_d of the d-polyhedra is also of utmost importance, in that it provides information on the interfaces between the constituents of the geometry (see for instance the considerations in [87]). We have then computed the first few moments $\langle S_d^m \rangle$ of the d-surfaces by Monte Carlo simulation. Results are recalled in Tab. 4.4, where we compare the numerical findings for large $L = 200$ to the exact formulas for infinite domains. The analysis of the impact of the domain size L and of the dimension d on the probability densities $\mathcal{P}(S_d|L)$ is provided in Fig. 4.7. The convergence of the average surface $\langle S_d|L \rangle$ as a function of of the linear size L of the domain and of the dimension d is illustrated in Fig. 4.6 (right).

Number of faces

We denote by C_d the number of faces of the tessellation cells, which is related to the connectivity of the random geometry. The exact first-order and second-order moments of C_d have been assessed by Monte Carlo methods as a function of the linear size L of the domain and of the dimension d: simulation results are given in Tab. 4.5, and the analysis of convergence is illustrated in Fig. 4.8. The functional form of the distributions of the number of faces $\mathcal{P}(C_d)$ is not known. We have thus resorted

	$\langle S_d^m \rangle$	Theoretical value	Monte Carlo
$\langle S_2 \rangle$	$4/\rho$	4	3.999 ± 10^{-3}
$\langle S_2^2 \rangle$	$(2\pi^2+8)/\rho^2$	27.7392	$27.73 \pm 2 \times 10^{-2}$
$\langle S_3 \rangle$	$24/\pi\rho^2$	7.63944	7.63 ± 10^{-2}
$\langle S_3^2 \rangle$	$240/\rho^4$	240	239.4 ± 0.7

Table 4.4: The moments $\langle S_d^m \rangle$ of the d-surface of the d-polyhedra. Monte Carlo simulation results are obtained with $L = 200$ and $\rho = 1$ for any dimension d.

	Formula	Theoretical value	Monte Carlo
$\langle C_2 \rangle$	4	4	4 ± 0
$\langle C_2^2 \rangle$	$(\pi^2+24)/2$	16.9348	$16.9347 \pm 5 \times 10^{-5}$
$\langle C_3 \rangle$	6	6	$6 \pm 7 \times 10^{-8}$
$\langle C_3^2 \rangle$	$(13\pi^2+336)/12$	38.6921	$38.6921 \pm 9 \times 10^{-5}$

Table 4.5: Moments of the number of faces C_d for d-dimensional Poisson geometries. Monte Carlo simulation results are obtained with $L = 200$ and $\rho = 1$.

to Monte Carlo simulation so as to estimate the impact of the domain size L and of the dimension d on $\mathcal{P}(C_d|L)$ for finite L. The numerical findings are shown in Fig. 4.8: they may support future theoretical investigations. It is reasonable to think that the convergence is attained rather fast, since $\mathcal{P}(C_d|L)$ can not be distinguished between $L = 10$ and $L = 200$.

Correlations

For the sake of completeness, we report also the Monte Carlo calculations corresponding to correlations between surfaces and volumes, which might be of interest in the characterization of the shape of the cells. Simulation findings are compared to analytical results from [76, 86, 87, 127] in Tabs. 4.6.

Other polyhedral features

For isotropic Poisson tessellations, lower-order moments and correlations are known for many other observables. Moreover, for the case of the inradius the full distribution is known. We have carefully checked the convergence of all these quantities as a function of dimension and system size: simulation results are reported in Appendix A.

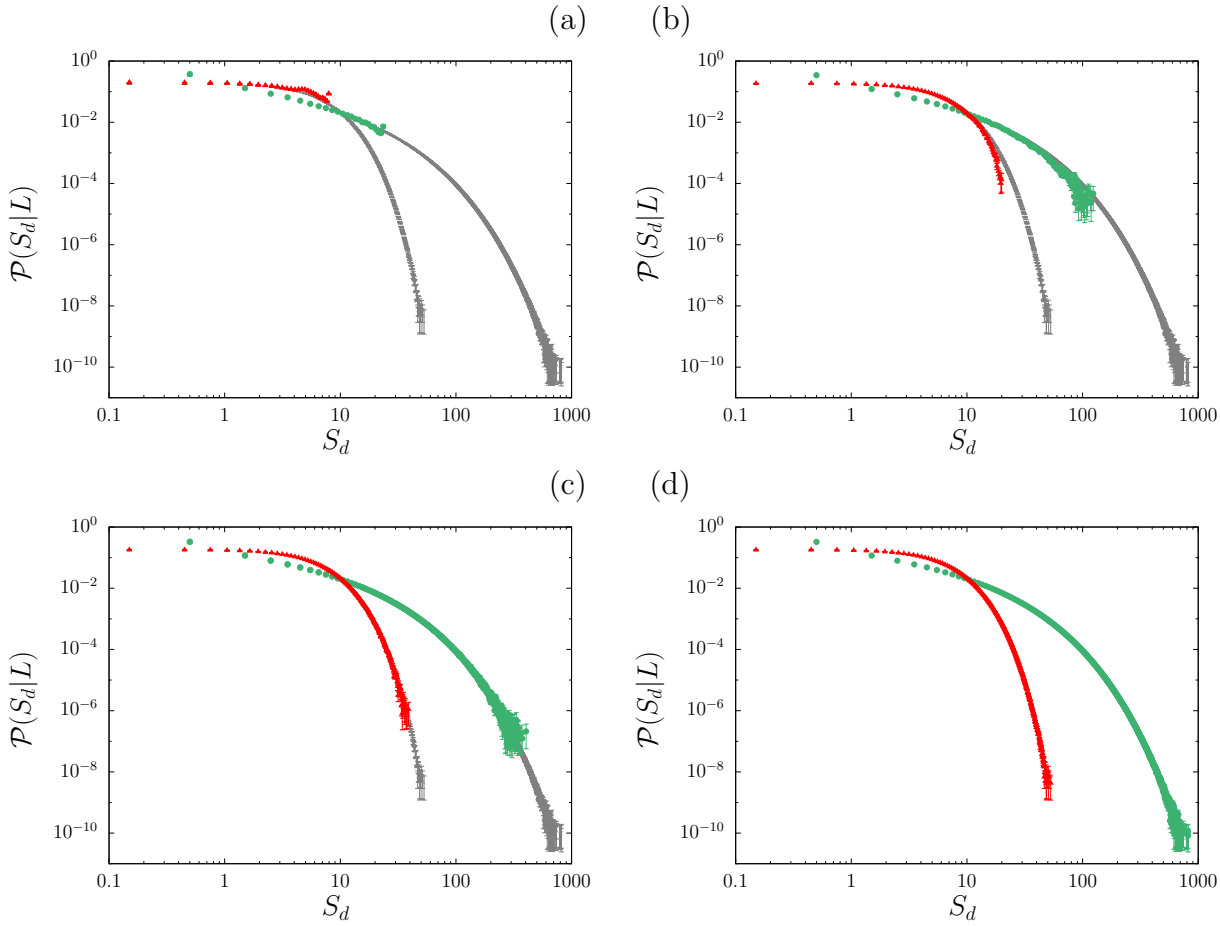

Figure 4.7: The probability densities $\mathcal{P}(S_d|L)$ of the d-surface in d-dimensional isotropic Poisson geometries as a function of the dimension d and of the linear size L of the domain. We have generated $M = 5 \times 10^4$ realizations for $d = 2$ and $M = 5 \times 10^3$ realizations for $d = 3$. Simulation results have been obtained with $\rho = 1$. Symbols correspond to the Monte Carlo simulation results: red triangles $d = 2$ and green circles $d = 3$. The cases illustrated here are as follows: (a) $L = 2$; (b) $L = 5$; (c) $L = 20$; (d) $L = 200$.

	Formula	Theoretical value	Monte Carlo
$\langle S_2 V_2 \rangle$	$4\pi/\rho^3$	12.57	$12.559 \pm 9 \times 10^{-3}$
$\langle S_3 V_3 \rangle$	$96/\rho^5$	96	95.7 ± 0.3

Table 4.6: Correlations of surfaces and volumes in d-dimensional Poisson geometries. Monte Carlo simulation results are obtained with $L = 200$ and $\rho = 1$.

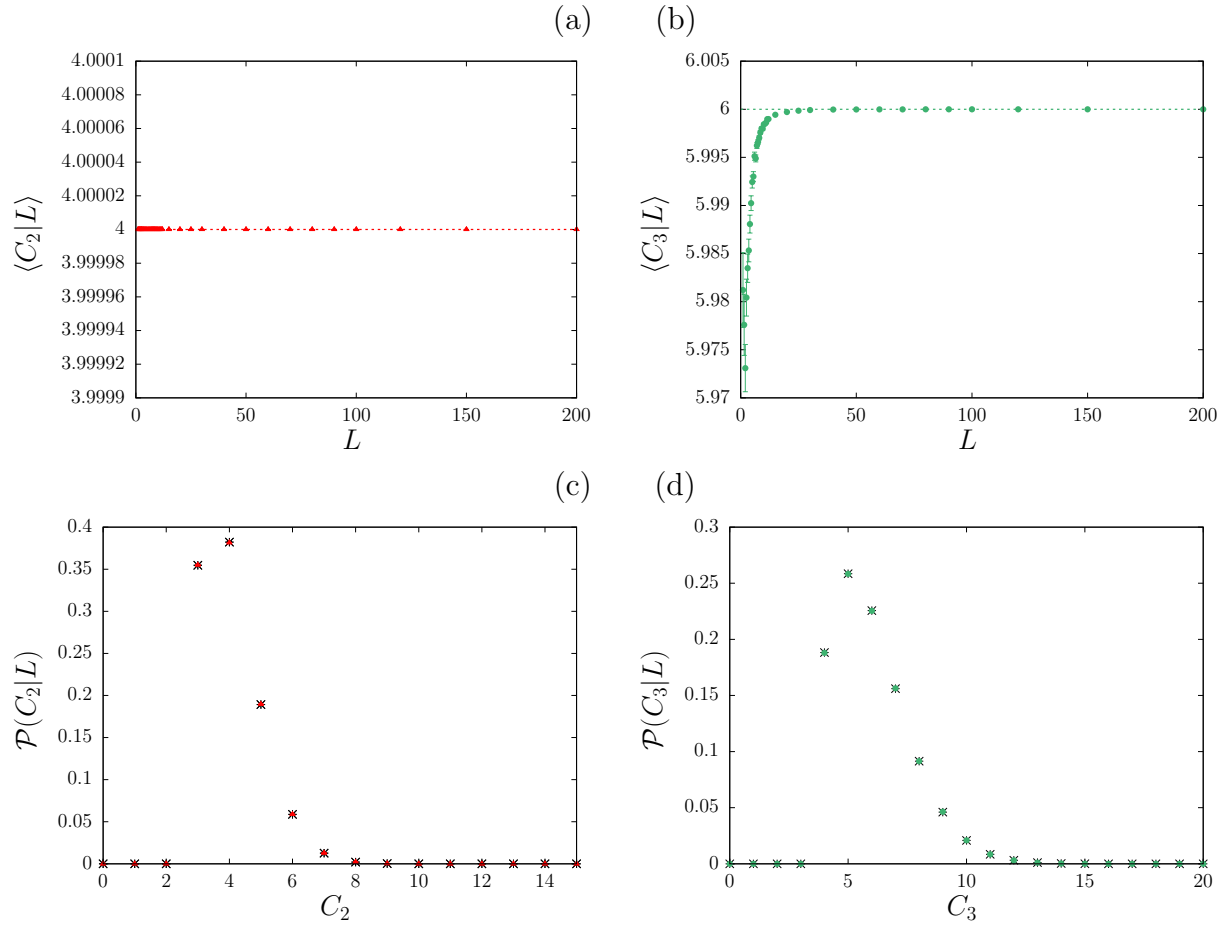

Figure 4.8: (a-b). The first-order moments of the number of faces in d-dimensional Poisson tessellations as a function of the linear size L of the domain. The cases are as follows: (a) the average number of faces $\langle C_2|L\rangle$ for $d = 2$, (b) the average number of faces $\langle C_3|L\rangle$ for $d = 3$. For each case, symbols correspond to the Monte Carlo simulation results: red triangles denote $d = 2$ and green circles $d = 3$. Simulation results have been obtained with $\rho = 1$. We have generated $M = 5 \times 10^4$ realizations for $d = 2$ and $M = 5 \times 10^3$ realizations for $d = 3$. (c-d). The probability densities of the number of faces, for different values of the linear size L of the domain. The cases are as follows: (c) the probability density of the number of faces $\mathcal{P}(C_2|L)$ for $d = 2$, (d) the probability density of the number of faces $\mathcal{P}(C_3|L)$ for $d = 3$. For each case, symbols correspond to the Monte Carlo simulation results: for $d = 2$, black crosses denote $L = 10$ and red triangles $L = 200$, for $d = 3$ black crosses denote $L = 10$ and green circles $L = 200$. Simulation results have been obtained with $\rho = 1$. We have generated $M = 5 \times 10^4$ realizations for $d = 2$ and $M = 5 \times 10^3$ realizations for $d = 3$.

4.1.4 Properties of colored Poisson tessellations

Volumic ratio in coloured geometries

We will now address d-dimensional colored isotropic Poisson tessellations. Without loss of generality, we consider binary mixtures: each polyhedron is assigned a label 'α' with probability p_α and the complementary label with probability $1-p_\alpha$. For tessellations of finite size L, an observable of utmost importance is the volumic ratio $p_\alpha(L)$ for clusters of label α. It is important to note that, for a single geometrical realization, the volumic ratio of color α in the tessellation is not rigorously equal to p_α, because of finite-size effects. In this respect, the lack of a strict constraint on the preservation of the mass associated to each material is a limitation of the modelling approach based on colored stochastic tessellations. However, we expect the finite-size effects to progressively fade away with increasing the size of the tessellation and to become negligible for tessellations large enough: in order to assess this statement, we need to estimate the dispersion of the volumic ratio.

For this purpose, we have computed the average volumic fraction $\langle p_\alpha|L\rangle$ for clusters of label α as a function of the linear size L of the domain and of the dimension d, for different values of p_α. The comparison with the theoretical behaviour p_α is shown in Fig. 4.9 (left). In order to emphasize the role of finite-size effects, in Fig. 4.9 (right) we show the corresponding standard deviation $\sigma[p_\alpha|L]$ induced by the dispersion of the geometry realizations: the deviation with respect to the ideal case decreases with increasing L, as expected. Moreover, the standard deviation decreases with increasing dimension d.

Chord length distributions across coloured clusters

In coloured geometries, the distribution of the chord lengths cut by the $(d-1)$-hyperplanes can be quite naturally conditioned to the colour of the d-polyhedra. In the following we assume that the label α is assigned with probability $p_\alpha = p$. In Sec. 2.7.1 we have seen that for domains of infinite size the chord lengths ℓ_α across clusters of label α obey

$$\mathcal{P}(\ell_\alpha) = \rho(1-p)e^{-\rho(1-p)\ell_\alpha}, \tag{4.7}$$

which can be interpreted as a generalization of the Markov property holding for un-coloured Poisson geometries [65]. Since the underlying tessellations are isotropic, the chord length distribution does not depend on the orientation $\mathbf{\Omega}$ of the test line.

We have numerically computed the full distribution of the colored chord lengths by resorting to Monte Carlo methods. Similarly as for the chord length in un-coloured geometries, we have obtained these results by drawing an arbitrary line with fixed orientation through the geometry. Monte Carlo simulation results corresponding to the probability density function $\mathcal{P}(\ell_\alpha|L)$ of the chord length across material are illustrated in Fig.4.10 for different values of the probability p, for different values of the linear size L of the domain and for any dimension d: for large $\rho L \gg 1$, the obtained probability densities of the chord lengths conditioned to red polyhedra asymptotically converge to the expected exponential density given in Eq. (4.7). A cut-off of the distribution around $\sqrt{d}L$ because of finite-size effects is observed. The finite-size effects are particularly apparent when the coloring probability p (and thus the asymptotic average chord length) is large, as expected. For the same number of geometrical realizations M and the same number of lines N_L thrown across the geometries, the statistics worsens when p is small: this is due to the fact that the lines thrown through the tessellation have smaller chance to traverse clusters of composition α when p is small.

The average correlation length $\Lambda_{c,\alpha}$ in material α has been also computed as a function of L, for different values of p: numerical findings are reported in Fig. 4.11 and compared to the exact result $\Lambda_\alpha = 1/((1-p)\rho)$ for $\rho = 1$.

Percolation threshold

We will now consider the percolation properties of the red clusters in the geometry. In Sec. 2.7.2 we have defined the percolation threshold p_c: for infinite tessellations, the probability that there exists

a connected percolating cluster has a step behaviour as a function of the colouring probability p, i.e., $\mathcal{P}_C(p) = 0$ for $p < p_c$, and $\mathcal{P}_C(p) = 1$ for $p > p_c$. However, for any finite L, there exists a finite probability that a percolating cluster (i.e., a cluster hitting two opposites borders) may appear below $p = p_c$, due to finite-size effects. We have numerically computed the probability $\mathcal{P}_C(p|L)$ in three-dimensional Poisson geometries by Monte Carlo methods. For each p, we have generated a large number of geometrical realizations and correspondingly determined whether there existed at least one percolating cluster. For this purpose, we have resorted to the Breadth-First Search algorithm in order to explore all polyhedra of the tessellation until a percolating cluster is found.

Simulation results for the probability $\mathcal{P}_C(p|L)$ in three-dimensional isotropic Poisson geometries are shown in Fig. 4.12 as a function of p, for various system sizes L. As L increases, the shape of $\mathcal{P}_C(p|L)$ converges to a step function. Based on the Monte Carlo results, we were able to estimate a confidence interval for the percolation threshold, which lies close to $p_c = 0.290 \pm 7 \times 10^{-3}$. As expected, p_c decreases as dimension increases, since the probability that a red cluster can make its way through the blue clusters (acting as obstacles) and eventually reach the opposite side of the box also increases with dimension. For comparison, our estimate of p_c for Poisson geometries lies close to the percolation threshold for three-dimensional regular cubic lattices, which reads $p_c^{cube} \simeq 0.3116$ [42]. This difference might again be explained by noting that the typical 3-polyhedron of infinite Poisson geometries has the same number of vertices ($N_3 = 8$), edges ($A_3 = 12$) and faces ($C_3 = 6$) as a cube (see Tab. 2.1), but it does not share the same aspect ratio. The 3-polyhedron has $\langle V_3 \rangle / \langle S_3 \rangle = 1/4$ for $\rho = 1$, whereas for a cube we have $u/6 = 1/6$ by assuming an average side $u = l_3/A_3 = 1$. For $d = 3$, the estimated p_c for Poisson geometries is also very close to that of continuum percolation models based on spheres, whose threshold reads $p_c^{sphere} \simeq 0.2895$ [145]; this is not true for $d = 2$, where the threshold for continuum percolation models based on disks yields $p_c^{disk} \simeq 0.676339$ [146].

Average cluster size

For percolation on lattices, the average cluster size $S(p)$ of the non-percolating clusters has been defined in Eq. (2.93). Close to the percolation threshold, $S(p)$ is known to behave as $S(p) \propto |p - p_c|^{-\gamma}$ for infinite lattices, where γ is a dimension-dependent critical exponent that does not depend on the specific lattice type [135]. For finite lattices of linear size L, the behaviour of $S(p|L)$ close to $p \to p_c^-$ is dominated by finite-size effects, with a scaling $S(p|L) \propto L^{\gamma/\nu}$, where ν is another dimension-dependent critical exponent that does not depend on the specific lattice type [135].

In order to adapt the definition in Eq. (2.93) to the calculation of average cluster size of the Poisson geometries, we have chosen to compute the sum by weighting each d-polyhedron composing a non-percolating cluster by its volume. Based on this definition, we have thus computed the quantity $S(p|L)$ by Monte Carlo simulation: numerical results are shown in Fig. 4.13 as a function of the colouring probability p and of the system size L. The shape of $S(p|L)$ is similar to that obtained for percolation on regular lattices (see, for instance, [135]), and displays in particular a divergence for p close to the percolation threshold. Far from the value of p_c estimated above, the curves $S(p|L)$ do not depend on the system size, provided that L is large. For $p \gg p_c$, $S(p|L) \to 0$. For $p \to 0$, numerical evidence shows that $S(p|L) \to \langle V_3 \rangle_0$, which is coherent with the volume-weighted average that we have introduced in order to compute the mean cluster size.

Close to p_c, $S(p|L)$ suffers from strong finite-size effects, which are coherent with the behaviour of $S(p|L)$ for regular lattices. For large L, the scaling of $S(p|L)$ as a function of $p - p_c^*$, where p_c^* is our best estimate for the percolation threshold, namely, $p_c^* = 0.290$, shows a power law behaviour with an exponent that is compatible with the universal critical exponent $\gamma = 1.793$ for dimension $d = 3$ [135].

Strength of the percolating cluster

We conclude our investigation of the percolation properties by addressing the behaviour of the so-called strength $P(p)$, which for percolation on lattices is defined as the probability that an arbitrary site belongs to the percolating cluster [135]. The strength of Poisson geometries can be again computed by either weighting each d-polyhedron composing the percolating cluster by its volume, or by attributing to each constituent an equal unit weight. Monte Carlo simulation results of $P(p|L)$ corresponding to

weighting each polyhedron by its volume are shown in Fig. 4.13 (left), as a function of the colouring probability p and of the system size L. Analogously as in the case of $S(p|L)$, the shape of the strength $P(p|L)$ is also similar to that obtained for percolation on regular lattices [135]. Far from the value of p_c estimated above, the curves $P(p|L)$ do not depend on the system size, provided that L is large. In particular, for $p \gg p_c$ the entire geometry will be coloured in red, so that we obtain a linear scaling $P(p|L) \propto p$ for the probability of belonging to the percolating cluster. For $p \ll p_c$, $P(p|L)$ falls off rapidly to zero. Close to p_c, $P(p|L)$ displays strong finite-size effects, which are again coherent with the behaviour of $P(p|L)$ for regular lattices. Fig. 4.13 (right) shows the scaling of $P(p|L)$ as a function of $p - p_c^*$ for different values of the system size. As L increases, $P(p|L)$ displays a power law behaviour with an exponent that is compatible with the universal critical exponent $\beta = 0.4181$ for dimension $d = 3$ [135].

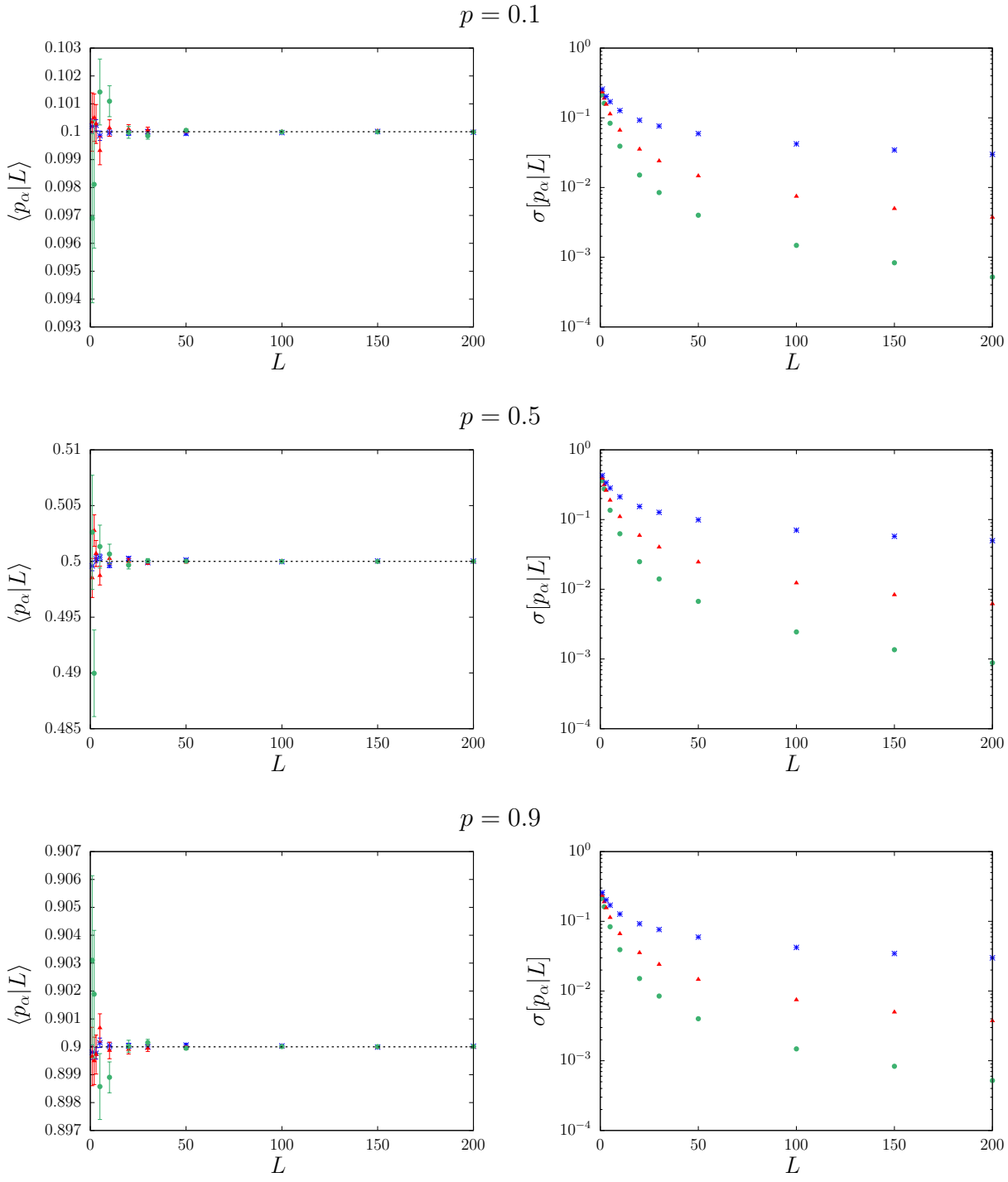

Figure 4.9: Volumic ratio through clusters of composition α in d-dimensional isotropic Poisson tessellations. Left. The average volumic fraction $\langle p_\alpha | L \rangle$ through clusters of composition α as a function of the linear size L for any dimension d. Dotted lines correspond to the asymptotic moment p_α. Right. The standard deviation $\sigma[p_\alpha | L]$ on volumic fraction through clusters of composition α as a function of the linear size L for any dimension d. we have generated $M = 10^6$ realizations for $d = 1$, $M = 5 \times 10^4$ realizations for $d = 2$ and $M = 5 \times 10^3$ realizations for $d = 3$. Simulation results have been obtained with $\rho = 1$ and $p = 0.1$ (top), $p = 0.5$ (middle) and $p = 0.9$ (bottom). Symbols correspond to the Monte Carlo simulation results: blue crosses denote $d = 1$, red triangles $d = 2$ and green circles $d = 3$.

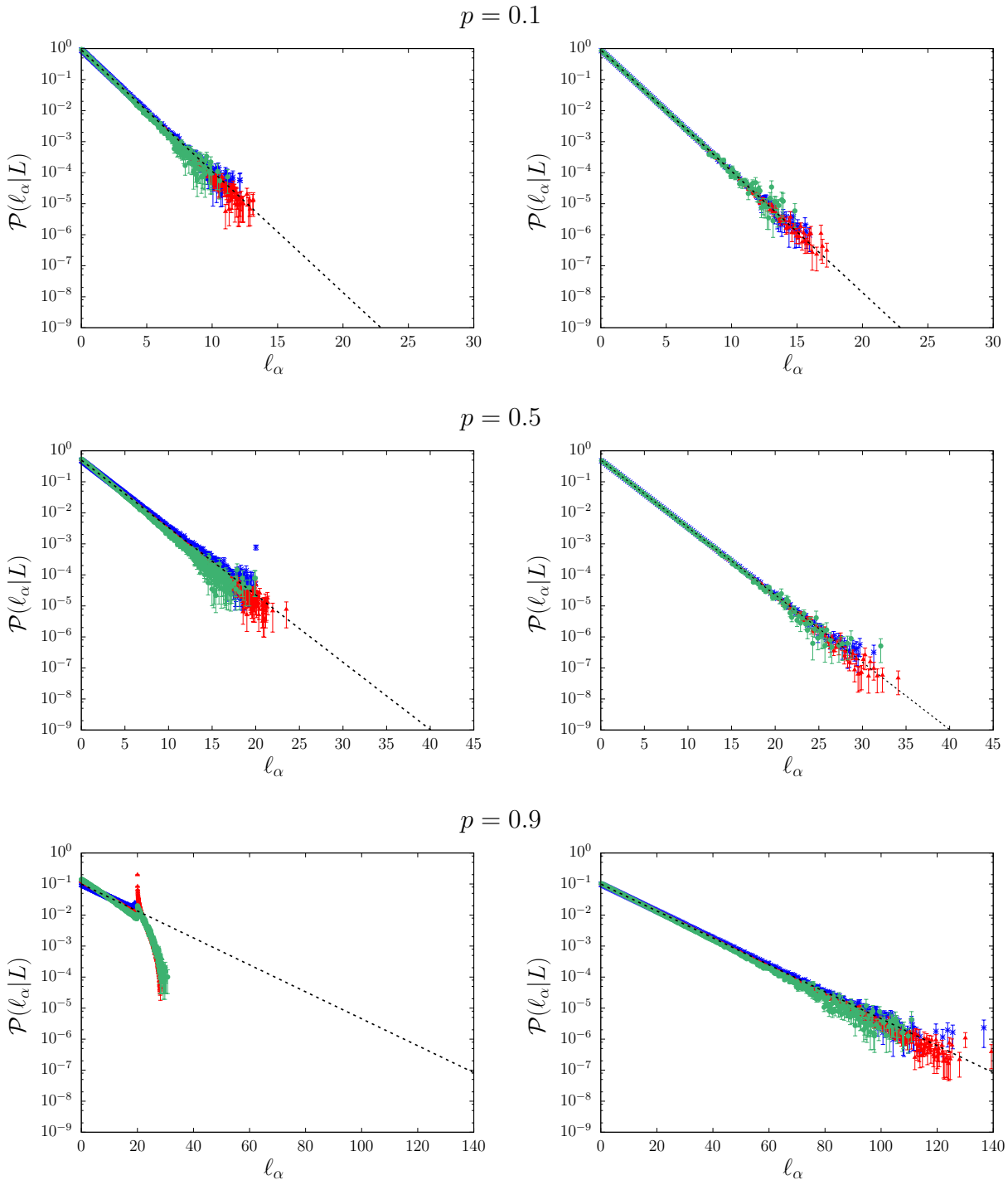

Figure 4.10: The probability densities of the correlation length $\mathcal{P}(\ell_{c,\alpha}|L)$ through clusters of composition α in d-dimensional isotropic Poisson tessellations, as a function of d, for different values of L and of p. Symbols correspond to the Monte Carlo simulation results: blue squares denote $d = 1$, red triangles $d = 1$ and green circles $d = 3$. Simulation results have been obtained with $\rho = 1$, $L = 20$ (left), $L = 150$ (right), $p = 0.1$ (top), $p = 0.5$ (middle) and $p = 0.9$ (bottom). The asymptotic exponential density given by Eq. (4.7) is displayed as a black dashed line. We have generated $M = 5 \times 10^3$ realizations.

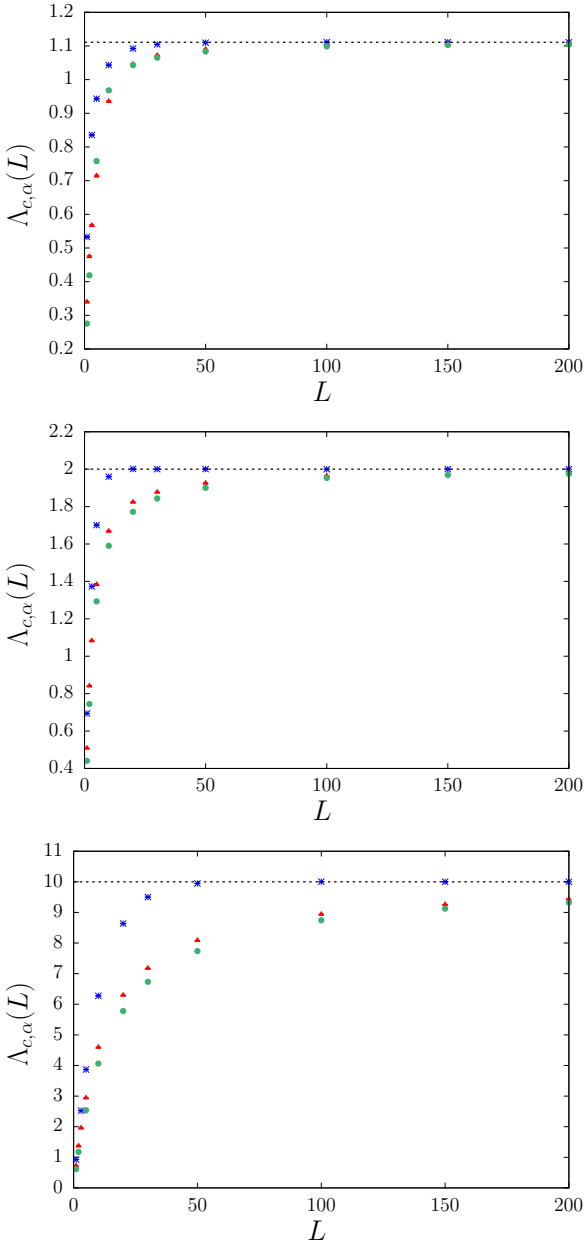

Figure 4.11: The average correlation length $\Lambda_{c,\alpha}(L)$ in d-dimensional isotropic Poisson tessellations as a function of the linear size L for any dimension d, for different values of p. We have generated $M = 10^6$ realizations for $d = 1$, $M = 5 \times 10^4$ realizations for $d = 2$ and $M = 5 \times 10^3$ realizations for $d = 3$. Simulation results have been obtained with $\rho = 1$ and $p = 0.1$ (top), $p = 0.5$ (middle) and $p = 0.9$ (bottom). Symbols correspond to the Monte Carlo simulation results: blue crosses denote $d = 1$, red triangles $d = 2$ and green circles $d = 3$.

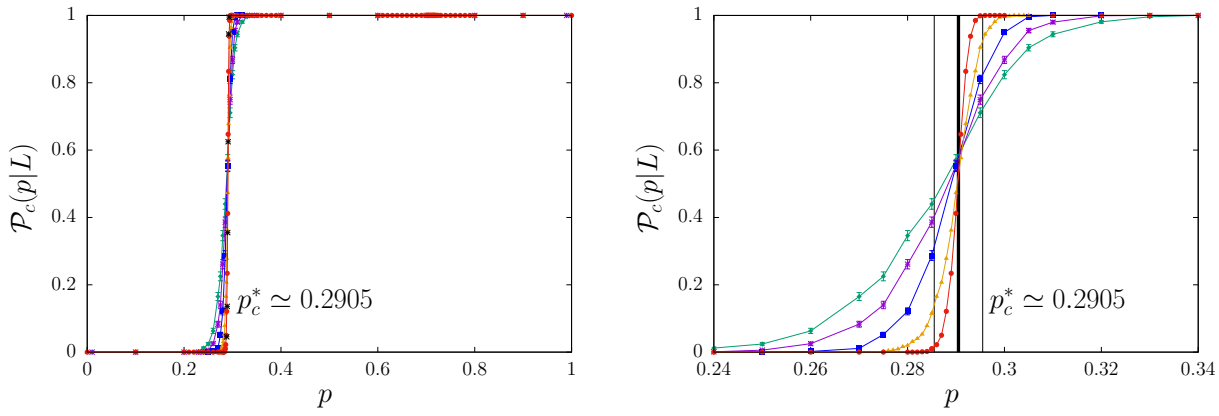

Figure 4.12: Estimation of the percolation threshold for three-dimensional isotropic Poisson tessellations. Left. Monte Carlo simulation of the percolation probability $\mathcal{P}_C(p|L)$ as a function of the colouring probability p and of the linear size L of the domain. Right. Zoom around $p = 0.29$. Green diamonds represent $L = 30$, purple crosses $L = 40$, blue squares $L = 60$, orange triangles $L = 100$ and red circles $L = 200$. Curves have been added to guide the eye. The estimated p_c is displayed as a dashed line, with confidence error bars drawn as thinner dashed lines. Simulation results have been obtained with $\rho = 1$. For all sizes L we have generated $M = 10^3$ realizations.

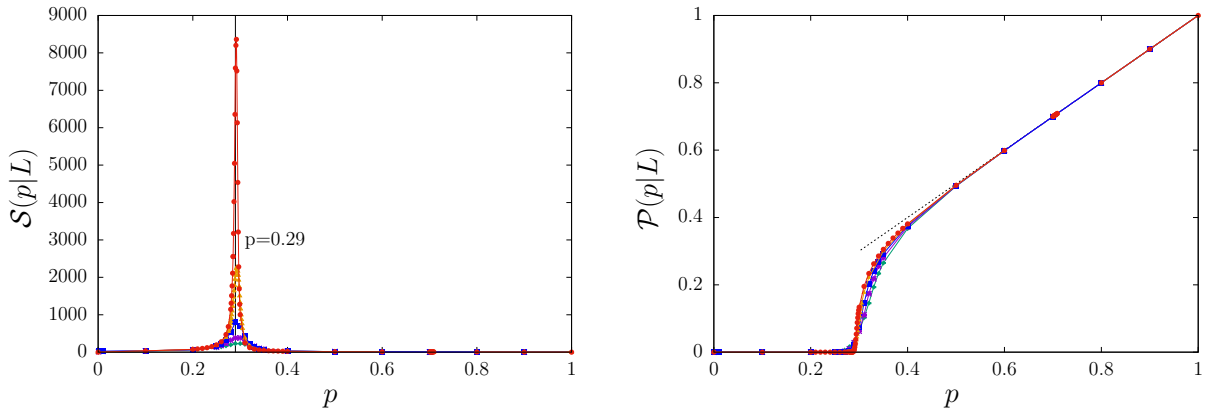

Figure 4.13: Left. The average cluster size $S(p|L)$ as a function of the colouring probability p and of the system size L. Close to $p_c^* = 0.290$, $S(p) \propto |p - p_c|^{-\gamma}$, with $\gamma = 1.793$. Symbols correspond to Monte Carlo results: green diamonds represent $L = 30$, purple crosses $L = 40$, blue squares $L = 60$, orange triangles $L = 100$ and red circles $L = 200$. Right. The percolation strength $P(p|L)$ as a function of the colouring probability p and of the system size L. Close to p_c^*, $P(p) \propto (p - p_c)^\beta$, with $\beta = 0.4181$. For all sizes L we have generated $M = 10^3$ realizations. Symbols correspond to Monte Carlo results: green diamonds represent $L = 30$, purple crosses $L = 40$, blue squares $L = 60$, orange triangles $L = 100$ and red circles $L = 200$. For all sizes L we have generated $M = 10^3$ realizations with $\rho = 1$.

4.2 Comparison of $3d$ tessellation models

In order to compare the statistical features of the three tessellation models introduced in the previous Chapter, a mandatory requirement is to determine a criterion on whose basis the tessellations can be considered statistically 'equivalent' with respect to some physical property. An important point is that Poisson, Voronoi and Box tessellations depend on a single free parameter, namely the tessellation density (which is simply related to the average correlation length Λ_c of the tessellation), plus the coloring probability p.

It is quite natural to set Λ_c to be the same for all the tessellation models to be compared. The coloring probability p is therefore also taken to be identical for all tessellations, so that the average correlation length through clusters pertaining to a given color is again the same for the different models. It is important to stress that this assumption is not unique: for instance, we could have taken the average cell volumes to be the same. However, it has been shown that Λ_c is the single tessellation parameter that has the strongest influence on particle transport [108]. Moreover, as shown in Sec. 2.3.4, the correlation length as following from the Cauchy formula is also related to the ratio between the average volume and of the average surface of the typical tessellation cell: in this respect, setting Λ_c is a means of setting also the typical aspect ratio (volume over surface) of the underlying geometrical structure of the random medium.

Since Λ_c depends on the tessellation density, we have thus a constraint on $\rho = \rho_{\mathcal{P}}$, $\rho_{\mathcal{V}}$ and $\rho_{\mathcal{B}}$, which must now satisfy

$$\frac{1}{\Lambda_c} = \rho_{\mathcal{P}} = \frac{3}{2}\rho_{\mathcal{B}} = \left(\frac{4\pi}{3}\right)^{\frac{1}{3}} \Gamma\left(\frac{5}{3}\right) \rho_{\mathcal{V}}. \tag{4.8}$$

In practice, one is often lead to simulate tessellations restricted to some bounded regions of linear size L: finite-size effects typically emerge, and the relation (4.8) would not be strictly valid. Indeed, in finite geometries the average correlation length differs from the asymptotic value. However, although a large L is typically required in order for the average correlation length to converge to the asymptotic value Λ_c, the variability between tessellations vanishes even before convergence to the asymptotic limit is achieved, as illustrated later (see Fig. 4.17). For the sake of simplicity, we will thus neglect such finite-size effects and use Eq. (4.8) to calibrate the model parameters. Most of the results presented in the following will concern the case of dimension $d = 3$.

4.2.1 Number of polyhedra

The number N_p of polyhedra composing a tessellation provides a measure of the complexity of the resulting geometries. We will analyse the growth of this quantity in Poisson, Voronoi and Box tessellations as a function of the size L of the domain. In the case of Voronoi tessellations, we know from Sec. 2.5.1 that N_p coincides with the number of seeds N_S, following a Poisson distribution of intensity $(\rho_{\mathcal{V}} L)^3$. For the special case $N_S = 0$, we have chosen to take $Np = 1$. Therefore, $N_p = \min(N_S, 1)$. This yields

$$\langle N_p | L \rangle_{\mathcal{V}} = (\rho_{\mathcal{V}} L)^3 + e^{-(\rho_{\mathcal{V}} L)^3} \tag{4.9}$$

and the corresponding standard deviation

$$\sigma[N_p|L]_{\mathcal{V}} = (\rho_{\mathcal{V}} L)^3 (1 - 2e^{-(\rho_{\mathcal{V}} L)^3}) + e^{-(\rho_{\mathcal{V}} L)^3}(1 - e^{-(\rho_{\mathcal{V}} L)^3}) \tag{4.10}$$

Furthermore, the number N_p in the case of Box tessellations is also known: according to the construction detailed in Sec. 2.4, $N_p = (X_1+1)(X_2+1)(X_3+1)$ where X_1, $X2$ and $X3$ are independent and identically distributed and follow a Poisson distribution of intensity $\rho_{\mathcal{B}} L$. We can easily compute the mean

$$\langle N_p | L \rangle_{\mathcal{B}} = (\rho_{\mathcal{B}} L + 1)^3 \tag{4.11}$$

and the standard deviation

$$\sigma[N_p|L]_{\mathcal{B}} = \sqrt{(1 + 3\rho_{\mathcal{B}} L + (\rho_{\mathcal{B}} L)^2)^3 - (1 + \rho_{\mathcal{B}} L)^6}. \tag{4.12}$$

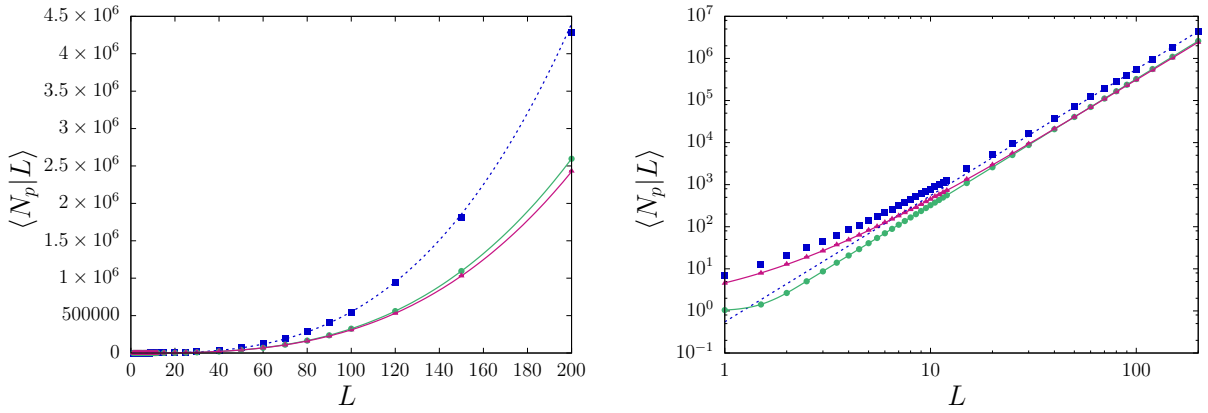

Figure 4.14: Left. The average number $\langle N_p|L\rangle$ of polyhedra composing the tessellation, as a function of the size L of the domain and of the mixing statistics m. The scaling law L^3 is displayed for reference with dashed for Poisson tessellations; the green solid line corresponds to the exact formula for Voronoi tessellations given by Eq.(4.9); the red solid line to corresponds the exact formula for Box tessellations given by Eq. (4.11). Symbols correspond to the Monte Carlo simulation results, with dashed lines added to guide the eye: blue squares denote $m = \mathcal{P}$, green circles $m = \mathcal{V}$, and red triangles $m = \mathcal{B}$. Simulation results have been obtained with $\Lambda = 1$. For all sizes L we have generated $M = 5 \times 10^3$ realizations for $d = 3$.

m	$\langle V_3\rangle$	Theoretical value	Monte Carlo
$\mathcal{P}$	$6/\pi\rho^3$	1.90986	$1.907 \pm 4 \times 10^{-3}$
$\mathcal{B}$	$1/\rho_{\mathcal{B}}^3$	3.375	$3.366 \pm 7 \times 10^{-3}$
$\mathcal{V}$	$1/\rho_{\mathcal{V}}^3$	3.08142	$3.08142 \pm 3 \times 10^{-5}$

Table 4.7: The moment $\langle V_3\rangle$ of the volume as a function of the mixing statistics m. Monte Carlo simulation results are obtained with $L = 200$, $\rho = 1$, $\rho_{\mathcal{B}} = 2/3$ and $\rho_{\mathcal{V}} \simeq 0.6872$. We have generated $M = 5 \times 10^3$ realizations.

The simulation findings for the average number $\langle N_p|L\rangle$ of polyhedra are illustrated in Fig. 4.14. Results concerning the normalized standard deviation $\sigma^*[N_p|L] = \sigma[N_p|L]/\langle N_p|L\rangle$ are given in Fig. 4.15. To begin with, we observe that $\langle N_p|L\rangle$ is smaller for Voronoi and Box tessellations than for Poisson tessellations. However, for large L, we find a common asymptotic scaling law $\langle N_p|L\rangle \sim (L)^3$. The growth of the dispersion $\sigma[N_p|L]$ differs considerably between Voronoi tessellations and the two other models. In the case of Voronoi mixing statistics, we asymptotically find $\sigma[N_p|L] \sim L^{\frac{3}{2}}$, as expected from Eqs. (4.9) and (4.10). For Poisson and Box tessellations, the dispersion is significantly larger, and the asymptotic scaling law becomes $\sigma[N_p|L] \sim L^{\frac{5}{2}}$, which is compatible with Eqs. (4.11) and (4.12). For illustration, the distribution of the number of polyhedra $\mathcal{P}(N_p)$ is displayed in Fig. 4.16. The distribution of N_p is peaked around its average value in Voronoi tessellations, whereas it is more dispersed in Poisson and Box geometries.

4.2.2 Polyhedral features

Volume and surface

We have numerically computed by Monte Carlo simulation the average volume $\langle V_3|L\rangle$ and the average surface $\langle S_3|L\rangle$. The numerical results are illustrated in Fig. 4.17. The average volume as well as the average surface converge towards the expected value for each tessellation (see also Tabs. 4.7-4.8). We have also computed the probability densities of the volume $\mathcal{P}(V_3|L)$ and of the surface $\mathcal{P}(S_3|L)$ in Poisson, Box and Voronoi tessellations as a function of the size L of the domain: the corresponding results are respectively illustrated in Fig. 4.18 and Fig. 4.19. The probability density of the volume in Voronoi tessellations has a distinct behaviour with respect to those of Poisson and Box tessellations

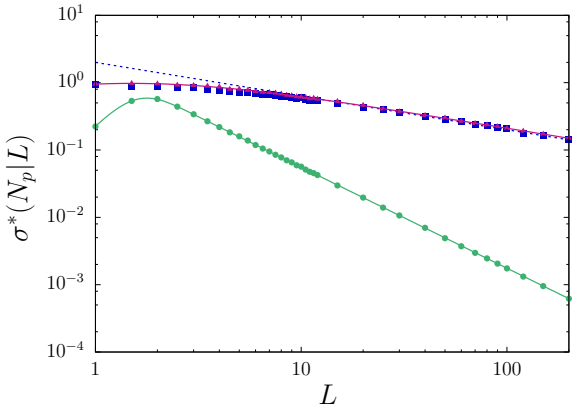

Figure 4.15: The normalized standard deviation $\sigma^*[N_p|L] = \sigma^[N_p|L]/\langle N_p|L\rangle$ of the number of polyhedra composing the tessellation, as a function of the size L of the domain and of the mixing statistics m. The scaling law L^3 is displayed for reference with dashed for Poisson tessellations; the green solid line corresponds to the exact formula for Voronoi tessellations given by Eq.(4.10); the red solid line to corresponds the exact formula for Box tessellations given by Eq.(4.12). Symbols correspond to the Monte Carlo simulation results: blue squares denote $m = \mathcal{P}$, green circles $m = \mathcal{V}$, and red triangles $m = \mathcal{B}$. Simulation results have been obtained with $\Lambda = 1$. For all sizes L we have generated $M = 5 \times 10^3$ realizations for $d = 3$.

m	$\langle S_3\rangle$	Theoretical value	Monte Carlo
$\mathcal{P}$	$24/\pi\rho^2$	7.63944	7.63 ± 10^{-2}
$\mathcal{B}$	$6/\rho_{\mathcal{B}}^2$	13.5	$13.48 \pm 2 \times 10^{-2}$
$\mathcal{V}$	$(256\pi/3)^{\frac{1}{3}}\Gamma\left(\frac{5}{3}\right)/{\rho_{\mathcal{V}}}^2$	12.326	$12.3483 \pm 7 \times 10^{-5}$

Table 4.8: The moment $\langle S_3\rangle$ of the surface as a function of the mixing statistics m. Monte Carlo simulation results are obtained with $L = 200$, $\rho = 1$, $\rho_{\mathcal{B}} = 2/3$ and $\rho_{\mathcal{V}} \simeq 0.6872$. We have generated $M = 5 \times 10^3$ realizations.

that are very similar and show a heavy-tailed distribution. In Voronoi tessellations, the dispersion of the volume is significantly weaker than in Poisson and Box geometries. In particular, the probability to find a volume five times larger than the average is negligible, contrary to Poisson and Box tessellations, where the size of the polyhedra have a significant chance to attain more than one hundred times the average value. The same observations apply also for the probability density of the surface.

Connectivity

The number of faces C_3 of each cell intuitively represents the degree of connectivity of the tessellation. For this observable, Voronoi geometries are expected to have a peculiar behaviour, since the average number of faces amounts to $\langle C_3\rangle \simeq 15.54$ (for infinite domains), which is much larger than the value $\langle C_3\rangle = 6$ for Poisson and Box geometries. In order to verify this behaviour in finite geometries, we have numerically computed by Monte Carlo simulation the average number of faces in Poisson and Voronoi tessellations, as a function of the size L of the domain. For Box tessellations, the number of faces is exactly equal to 6 by construction, without any dispersion. The numerical results are illustrated in Fig. 4.17. The average number of faces converges towards the expected value for each tessellation; nevertheless, Voronoi tessellations require larger L to attain the asymptotic behaviour. In addition, we have numerically computed the distribution of the number of faces $\mathcal{P}(C_3|L)$ for a large $L = 200$: the simulation results are given in Fig. 4.20.

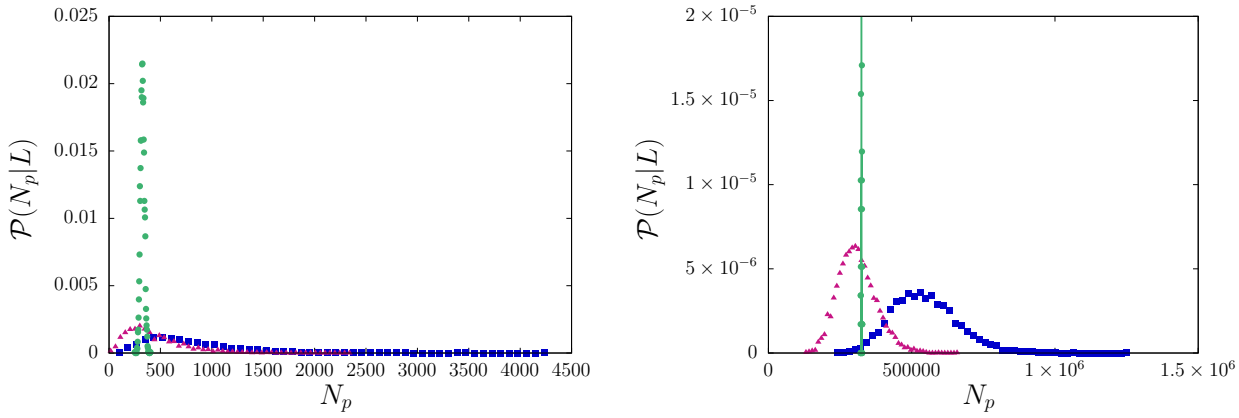

Figure 4.16: The probability density $\mathcal{P}(N_p|L)$ of polyhedra composing the tessellation, as a function of the mixing statistics m, for $L = 10$ (left) and $L = 100$ (right). Symbols correspond to the Monte Carlo simulation results, with dashed lines added to guide the eye: blue squares denote $m = \mathcal{P}$, green circles $m = \mathcal{V}$, and red triangles $m = \mathcal{B}$. Symbols correspond to the Monte Carlo simulation results: blue crosses denote $d = 1$, red triangles $d = 2$ and green circles $d = 3$. Simulation results have been obtained with $\Lambda = 1$. For all sizes L we have generated $M = 5 \times 10^3$ realizations for $d = 3$.

m	$\langle l_3 \rangle$	Theoretical value	Monte Carlo
$\mathcal{P}$	$12/\rho$	12	$11.994 \pm 8 \times 10^{-3}$
$\mathcal{B}$	$12/\rho_{\mathcal{B}}$	18	17.98 ± 0.01
$\mathcal{V}$	$(4\pi)^{5/3}\Gamma(\frac{1}{3})/(5 \times 3^{2/3}\rho_{\mathcal{V}})$	25.4592	$25.3854 \pm 8 \times 10^{-5}$

Table 4.9: The moment $\langle l_3 \rangle$ of the total length of edges as a function of the mixing statistics m. Monte Carlo simulation results are obtained with $L = 200$, $\rho = 1$, $\rho_{\mathcal{B}} = 2/3$ and $\rho_{\mathcal{V}} \simeq 0.6872$. We have generated $M = 5 \times 10^3$ realizations.

4.2.3 Correlation length

We have numerically computed by Monte Carlo simulation the average and the distribution of the correlation length for each tessellation model m. For Voronoi and isotropic Poisson tessellations, the average correlation length coincides with the averaged chord length. For Box tessellations, however, the average chord length depends on the chosen direction of the test line, whereas the average correlation length does not. In order to compare the three tessellation models, it is then convenient to resort to the correlation length. For this purpose, an ensemble of independent and identically distributed *homogeneous and isotropic* random lines [25] has been used. A random tessellation is first generated, and a line satisfying the homogeneity and isotropy property is then drawn according to the prescriptions given in Sec. 2.3.4. The intersections of the line with the cells of the tessellation are computed, and the resulting chord lengths ℓ_c corresponding to homogeneous and isotropic random lines are recorded. This step is repeated for a large number of random lines. Then, a new geometry is generated and the whole procedure is iterated for several geometries, in order to get satisfactory statistics. This yields consistent estimates of the average correlation length Λ_c.

The results for the average correlation length $\Lambda_c(L)$ as a function of the size L of the domain are illustrated in Fig. 4.17 for different tessellation models m. Tab. 4.13 displays the obtained values for the average correlation length $\Lambda_c(L)$ for large L. Monte Carlo simulation results for the correlation length distribution are shown in Fig. 4.21, for $\Lambda_c = 1$ and for several values of L. For small L, finite-size effects are visible in the distributions: indeed, the longest chord that can be drawn across a box of linear size L is $\sqrt{3}L$. For large L, the finite-size effects fade away. In particular, the probability density for Poisson tessellations eventually converges to the expected exponential behaviour. Simulations show that the chord length distributions in Box tessellations and in Poisson tessellations are *very close to*

m	$\langle C_3 \rangle$	Theoretical value	Monte Carlo
$\mathcal{P}$	6	6	$6 \pm 7 \times 10^{-8}$
$\mathcal{B}$	6	6	6 ± 0
$\mathcal{V}$	$(48\pi^2 + 70)/35$	15.54	$15.4091 \pm 2 \times 10^{-5}$

Table 4.10: The moment $\langle C_3 \rangle$ of the number of faces as a function of the mixing statistics m. Monte Carlo simulation results are obtained with $L = 200$, $\rho = 1$, $\rho_{\mathcal{B}} = 2/3$ and $\rho_{\mathcal{V}} \simeq 0.6872$. We have generated $M = 5 \times 10^3$ realizations.

m	$\langle A_3 \rangle$	Theoretical value	Monte Carlo
$\mathcal{P}$	12	12	$12 \pm 2 \times 10^{-7}$
$\mathcal{B}$	12	12	12 ± 0
$\mathcal{V}$	$144\pi^2/35$	40.61	$40.2274 \pm 5 \times 10^{-5}$

Table 4.11: The moment $\langle A_3 \rangle$ of the number of edges as a function of the mixing statistics m. Monte Carlo simulation results are obtained with $L = 200$, $\rho = 1$, $\rho_{\mathcal{B}} = 2/3$ and $\rho_{\mathcal{V}} \simeq 0.6872$. We have generated $M = 5 \times 10^3$ realizations.

each other, a rather surprising fact that is consistent with the observations previously reported in [2]. On the contrary, for Voronoi tessellations the chord length distribution has a distinct non-exponential functional form and for $L \to \infty$ converges to the asymptotic density function given by Eq. (2.75).

A similar investigation can be conducted for $\Lambda_{c,\alpha}(L)$, the correlation length through clusters with material composition α. Numerical findings are displayed in Figs. 4.22-4.23 as a function of p, L and the mixing statistics m, for different values d and L. Theoretical results in the limit of infinite domains are also provided. Finite-size effects are apparent, and their impact increases with increasing Λ_c and p. However, the discrepancy due to mixing statistics is rather weak. The distribution of the chord lengths through material of composition α is illustrated in Fig. 4.24. Here again, the finite-size effects induced by the size of the box vanish for small p and large L.

4.2.4 Volumic ratio in coloured geometries

We have computed the average volumic fraction $\langle p_\alpha | L \rangle$ through clusters of composition α as a function of the linear size L of the domain and of the mixing statistics m, for different values of p_α. The comparison with the theoretical behaviour p_α is shown in Fig. 4.25 (left). In addition, Fig. 4.25 (right) illustrates the corresponding dispersion $\sigma[p_\alpha | L]$ induced by the variability of the geometry realizations: the deviation with respect to the ideal case decreases with increasing L for each mixing statistics m (as was the case of Poisson tessellations). Moreover, the standard deviation is clearly weaker for Voronoi tessellations. This is possibly due to the distribution of the volumes: the distribution of the volume is highly peaked for Voronoi tessellations, whereas the probability densities are heavy-tailed for Poisson and Box tessellations (see Sec. 4.2.2).

m	$\langle N_3 \rangle$	Theoretical value	Monte Carlo
$\mathcal{P}$	8	8	8 ± 10^{-7}
$\mathcal{B}$	8	8	8 ± 0
$\mathcal{V}$	$96\pi^2/35$	27.07	$26.8183 \pm 3 \times 10^{-5}$

Table 4.12: The moment $\langle N_3 \rangle$ of the number of vertices as a function of the mixing statistics m. Monte Carlo simulation results are obtained with $L = 200$, $\rho = 1$, $\rho_{\mathcal{B}} = 2/3$ and $\rho_{\mathcal{V}} \simeq 0.6872$. We have generated $M = 5 \times 10^3$ realizations.

m	Λ_c	Theoretical value	Monte Carlo
$\mathcal{P}$	$1/\rho$	1	$0.9940 \pm 8 \times 10^{-4}$
$\mathcal{B}$	$2/3\rho_{\mathcal{B}}$	1	$0.9927 \pm 8 \times 10^{-4}$
$\mathcal{V}$	$1/\left((\frac{4\pi}{3})^{\frac{1}{3}} \Gamma\left(\frac{5}{3}\right) \rho_{\mathcal{V}} \right)$	1	$0.99760 \pm 2 \times 10^{-5}$

Table 4.13: The average correlation length Λ_c as a function of the mixing statistics m. Monte Carlo simulation results are obtained with $L = 150$, $\rho = 1$, $\rho_{\mathcal{B}} = 2/3$ and $\rho_{\mathcal{V}} \simeq 0.6872$. We have generated $M = 5 \times 10^3$ realizations.

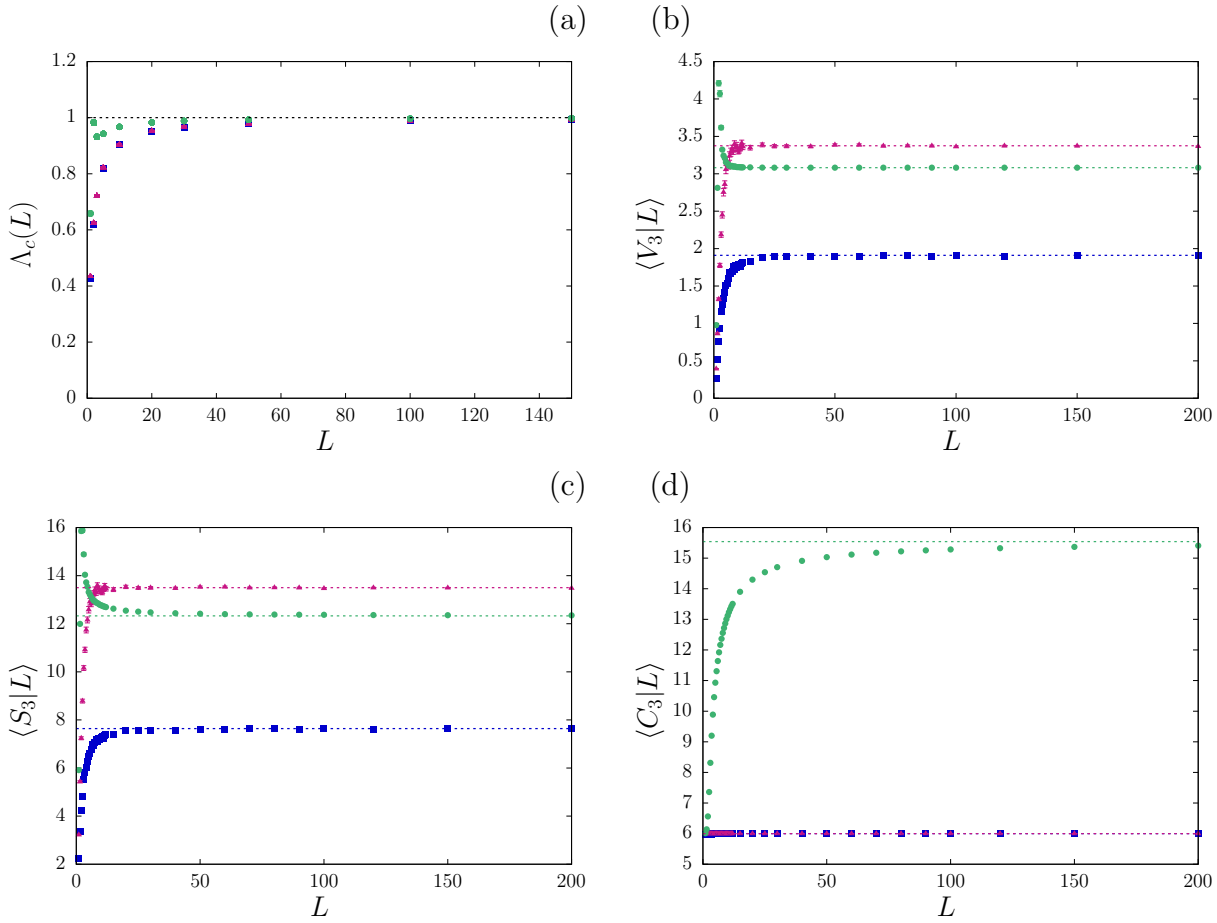

Figure 4.17: The average correlation length $\Lambda_c(L)$ (a), the average volume $\langle V_3|L \rangle$ (b), the average surface $\langle S_3|L \rangle$ (c) and the average number of faces $\langle C_3|L \rangle$ (d) as a function of the linear size L of the domain and of the mixing statistics m. Symbols correspond to the Monte Carlo simulation results: blue squares denote $m = \mathcal{P}$, red triangles $m = \mathcal{B}$ and green circles $m = \mathcal{V}$. Simulation results have been obtained with $\Lambda_c = 1$. For all sizes L we have generated $M = 5 \times 10^3$ realizations. Dashed lines correspond to the exact asymptotic values.

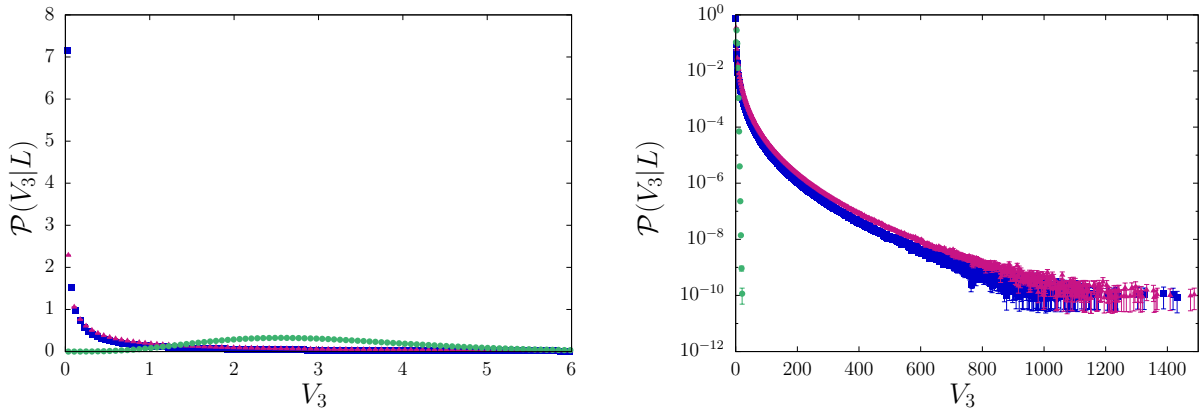

Figure 4.18: Left. The probability densities of the volume of the typical polyhedron $\mathcal{P}(V_3|L)$ as a function of the mixing statistics m, for $L = 200$. Right. Log-linear scale. Symbols correspond to the Monte Carlo simulation results: blue squares denote $m = \mathcal{P}$, red triangles $m = \mathcal{B}$ and green circles $m = \mathcal{V}$. Simulation results have been obtained with $\Lambda = 1$. For all sizes L we have generated $M = 5 \times 10^3$ realizations.

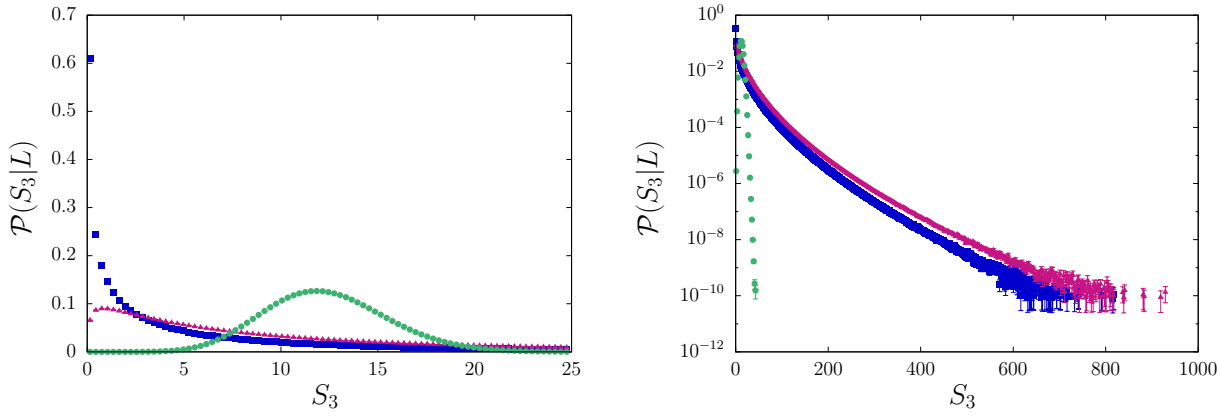

Figure 4.19: Left. The probability densities of the surface of the typical polyhedron $\mathcal{P}(S_3|L)$ as a function of the mixing statistics m, for $L = 200$. Right. Log-linear scale. Symbols correspond to the Monte Carlo simulation results: blue squares denote $m = \mathcal{P}$, red triangles $m = \mathcal{B}$ and green circles $m = \mathcal{V}$. Simulation results have been obtained with $\Lambda = 1$. For all sizes L we have generated $M = 5 \times 10^3$ realizations.

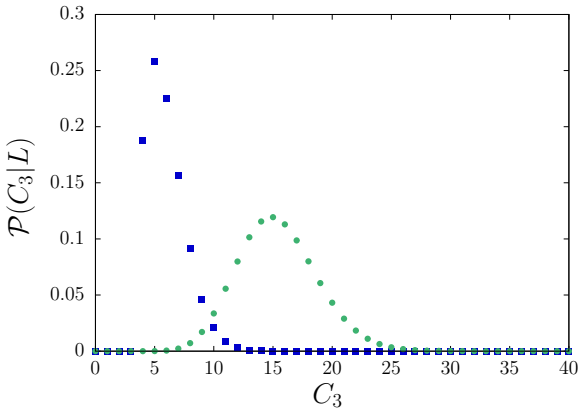

Figure 4.20: The probability densities of the number of faces by polyhedron $\mathcal{P}(C_3|L)$ as a function of the mixing statistics m, for $L = 200$. Symbols correspond to the Monte Carlo simulation results: blue squares denote $m = \mathcal{P}$ and green circles $m = \mathcal{V}$. For Box tessellations, the corresponding probability density function is straighforward: $\mathcal{P}_{\mathcal{B}}(C_3|L) = \delta(C_3 - 6)$. Simulation results have been obtained with $\Lambda_c = 1$. For all sizes L we have generated $M = 5 \times 10^3$ realizations.

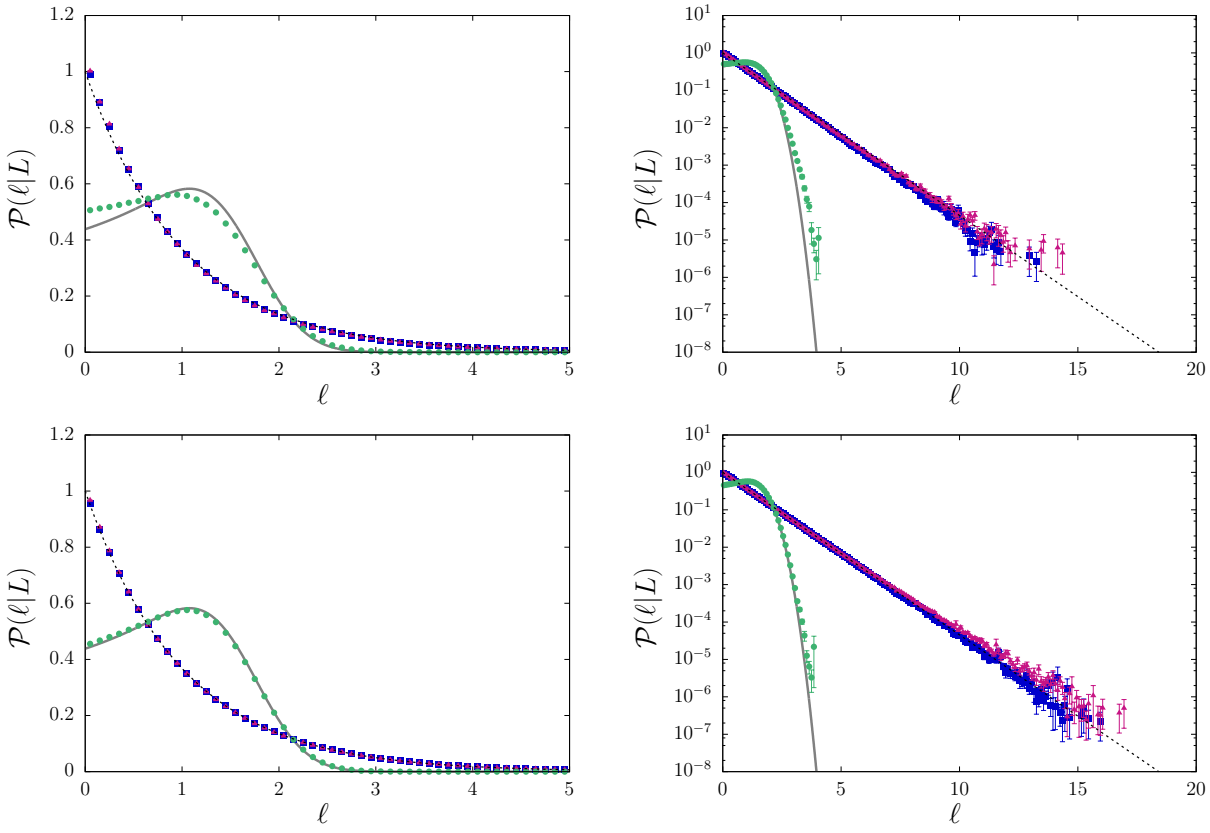

Figure 4.21: Left. The probability densities of the correlation length $\mathcal{P}(\ell_c|L)$ as a function of the mixing statistics m, for $L = 20$ (top) and for $L = 150$ (bottom). Right. Log-linear scale. Symbols correspond to the Monte Carlo simulation results: blue squares denote $m = \mathcal{P}$, red triangles $m = \mathcal{B}$ and green circles $m = \mathcal{V}$. Simulation results have been obtained with $\Lambda = 1$. For all sizes L we have generated $M = 5 \times 10^3$ realizations. For Poisson distribution, the asymptotic exponential density given by Eq. (2.40) is displayed as a black dashed line. The asymptotic probability density for Voronoi tessellations, given by Eq. (2.75), is displayed as a grey solid line.

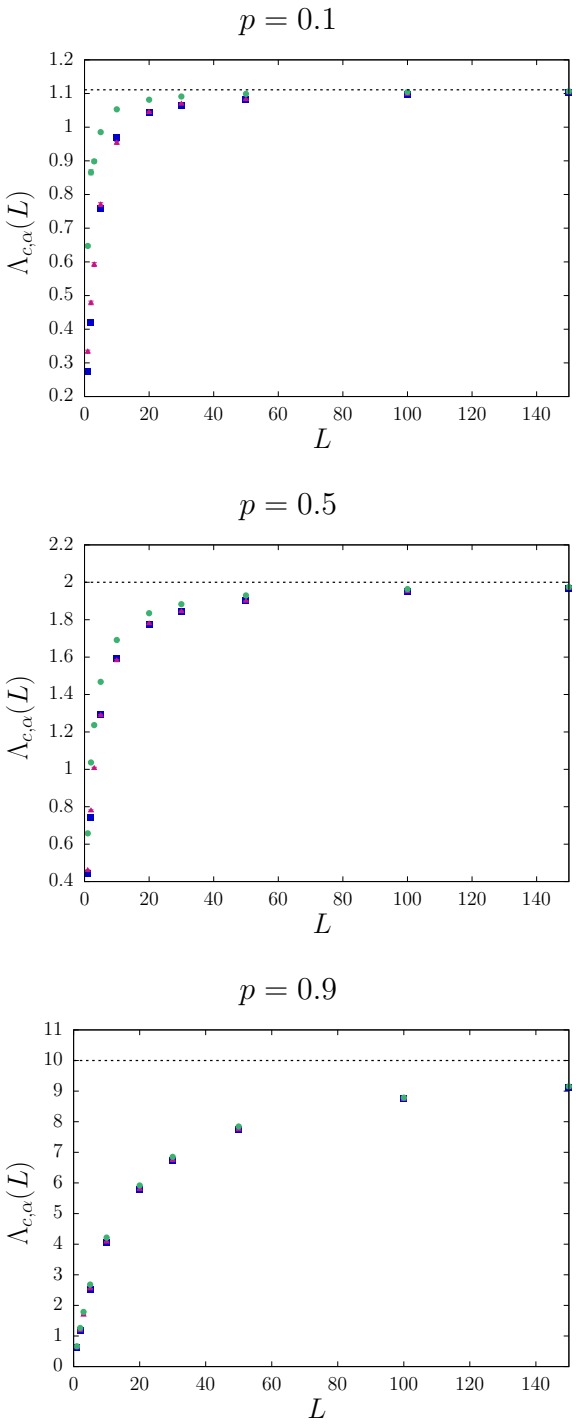

Figure 4.22: The average correlation length $\Lambda_{c,\alpha}(L)$ through clusters of composition α as a function of the linear size L and of the mixing statistics m, for different values of p. Simulation results have been obtained with $\Lambda = 1$ and $p = 0.1$ (top), $p = 0.5$ (middle) and $p = 0.9$ (bottom). Symbols correspond to the Monte Carlo simulation results: blue squares denote $m = \mathcal{P}$, red triangles $m = \mathcal{B}$ and green circles $m = \mathcal{V}$. We have generated $M = 5 \times 10^3$ realizations.

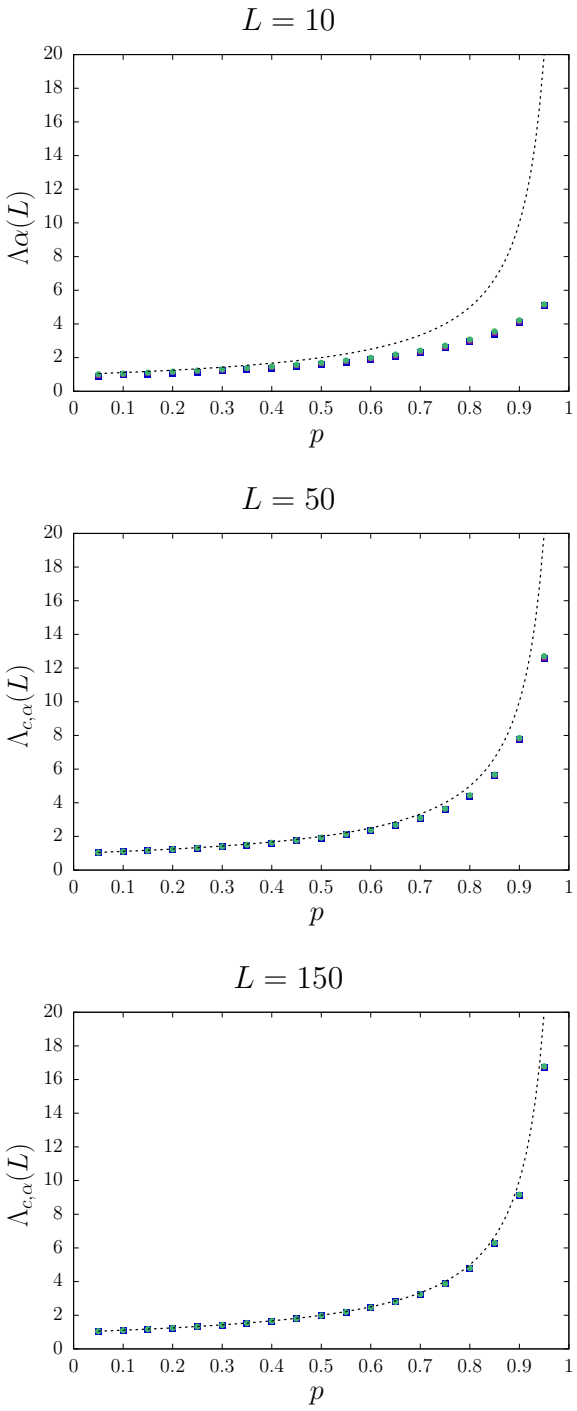

Figure 4.23: The average correlation length $\Lambda_{c,\alpha}(L)$ through clusters of composition α as a function of p and of the mixing statistics m, for different values of L. Simulation results have been obtained with $\Lambda = 1$ and $L = 10$ (top), $L = 50$ (middle) and $L = 150$ (bottom). Symbols correspond to the Monte Carlo simulation results: blue crosses denote $d = 1$, blue squares denote $m = \mathcal{P}$, red triangles $m = \mathcal{B}$ and green circles $m = \mathcal{V}$. We have generated $M = 5 \times 10^3$ realizations.

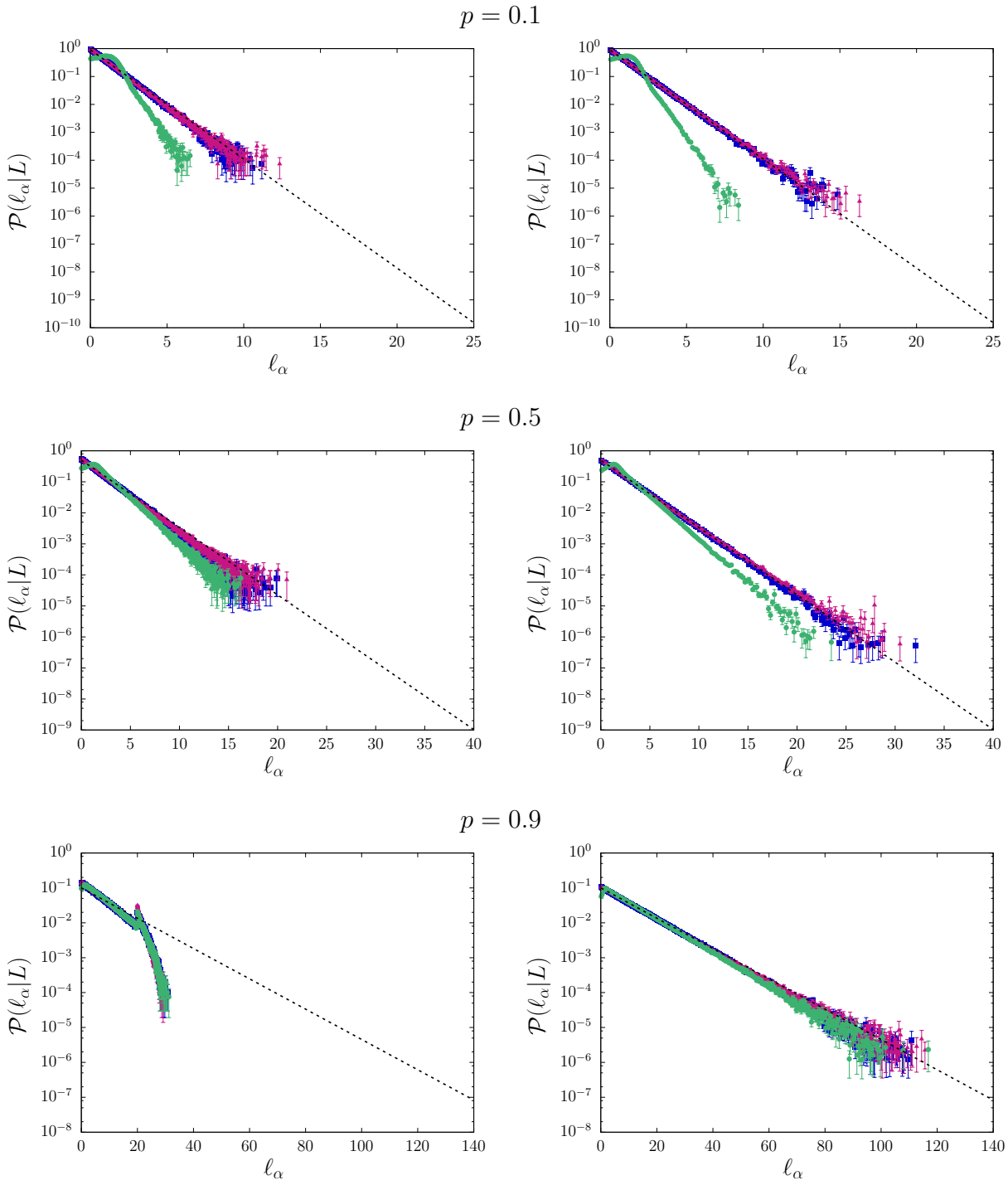

Figure 4.24: The probability densities of the correlation length $\mathcal{P}(\ell_{c,\alpha}|L)$ through clusters of composition α as a function of the mixing statistics m and for different values of L and of p. Symbols correspond to the Monte Carlo simulation results: blue squares denote $m = \mathcal{P}$, red triangles $m = \mathcal{B}$ and green circles $m = \mathcal{V}$. Simulation results have been obtained with $\Lambda = 1$, $L = 20$ (left), $L = 150$ (right), $p = 0.1$ (top), $p = 0.5$ (middle) and $p = 0.9$ (bottom). For Poisson distribution, the asymptotic exponential density given by Eq.(4.7) is displayed as a black dashed line. We have generated $M = 5 \times 10^3$ realizations.

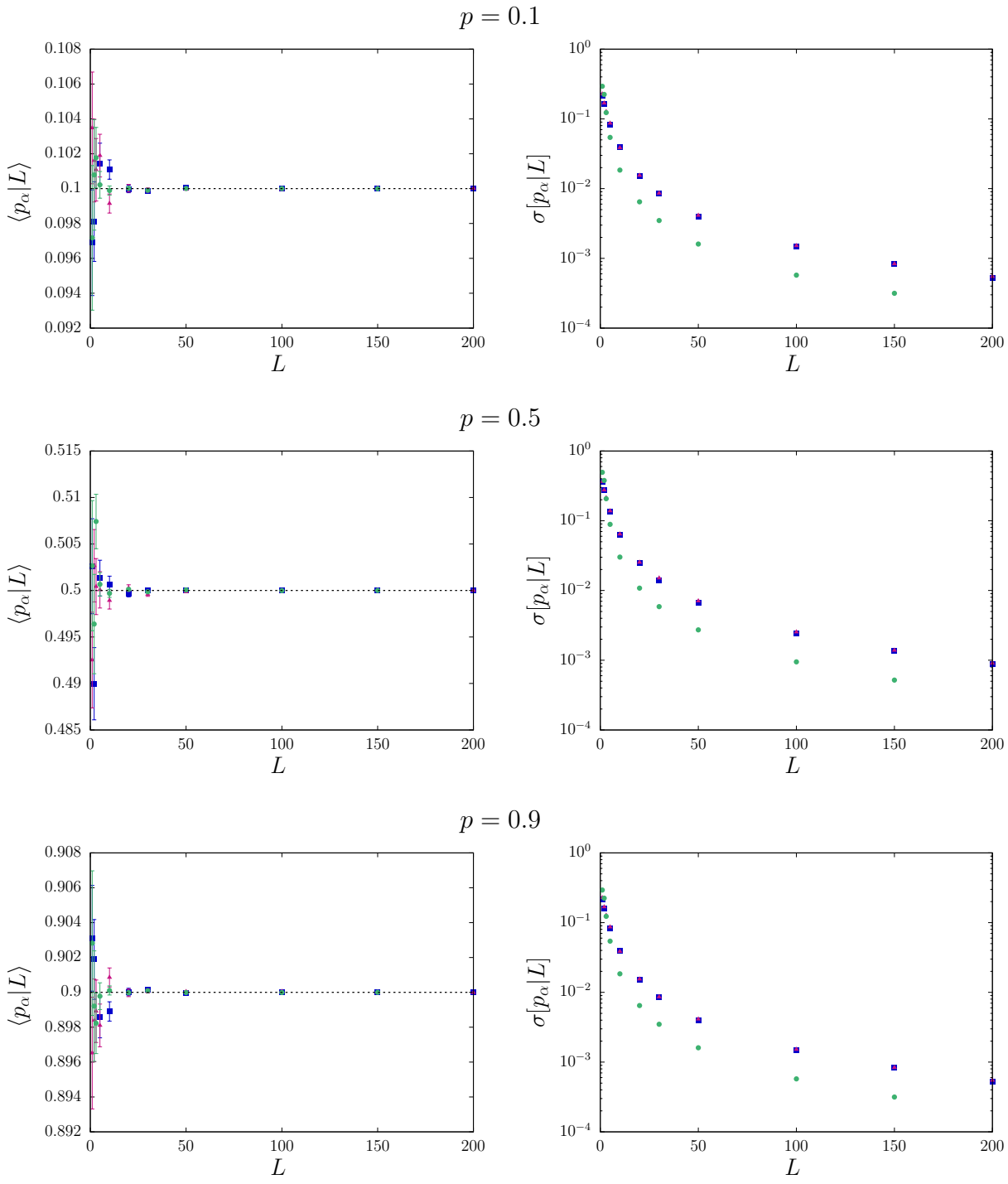

Figure 4.25: Left. The average volumic ratio $\langle p_\alpha|L\rangle$ through clusters of composition α as a function of the mixing statistics m and for different values of L and of p. Dotted lines correspond to the asymptotic moment p_α. Right. The standard deviation $\sigma[p_\alpha|L]$ on volumic fraction through clusters of composition α as a function of the mixing statistics m and for different values of L and of p. Simulation results have been obtained with $\Lambda = 1$ and $p = 0.1$ (top), $p = 0.5$ (middle) and $p = 0.9$ (bottom). Symbols correspond to the Monte Carlo simulation results: blue squares denote $m = \mathcal{P}$, red triangles $m = \mathcal{B}$ and green circles $m = \mathcal{V}$. We have generated $M = 5 \times 10^3$ realizations.

4.3 Impact of anisotropy in Poisson tessellations

We finally consider the case of anisotropic Poisson tessellations. For this purpose, the observables of interest, including the volume and surface of the cells, the number of faces per cell, and the chord length, will be analyzed. In the following, we illustrate some significant examples as a function of the angular law $H(\mathbf{n})$ in dimension $d = 3$, which is relevant for physical applications.

4.3.1 Choice of the angular distributions

In dimension $d = 3$, the direction (unit) vector $\mathbf{n}$ can be characterized by assigning two angles, namely the co-latitude θ and the azimuth ϕ (see Fig. 2.4). We have then $dH(\mathbf{n}) = dH(\theta, \phi)$, or $dH(\mathbf{n}) = dH(\mu, \phi)$ when using the cosine $\mu = \cos(\theta)$. The isotropic distribution in Ω_3^+ yields

$$H_{\rm iso}(\theta, \phi) = \frac{1}{2\pi} \sin(\theta), \tag{4.13}$$

with $0 \leq \theta < \pi$ and $0 \leq \phi < \pi$. In order to probe the effects of the angular distribution, we introduce a few examples of anisotropy laws that might mimic the effects of stratification along the z axis. In other words, we will preferentially sample planes whose normal vector is parallel to the z axis. For the sake of simplicity, we will assume that the distribution $H(\mathbf{n})$ can be factorized with respect to the two variables, and that the distribution of ϕ is uniform (in other words, we preserve the invariance by rotation around the z axis). A quadratic anisotropy can be introduced in the form

$$H_{\rm quadratic}(\mu, \phi) = \frac{3}{2\pi} \mu^2 \text{ for } -1 \leq \mu < 1, \tag{4.14}$$

which has its minimum in $\mu = 0$ and the maxima in $\mu = \pm 1$. A general case that might be of interest for applications is a piece-wise constant distribution, e.g.,

$$H_{\rm histogram}(\mu, \phi) = \frac{1}{A} \times \begin{cases} 80 & \text{for} -1 \leq \mu < -0.95 \\ 4 & \text{for} -0.95 \leq \mu < -0.5 \\ 2 & \text{for} -0.5 \leq \mu < -0.25 \\ 1 & \text{for} -0.25 \leq \mu < 0, \end{cases} \tag{4.15}$$

and symmetric in the range $0 < \mu < 1$, which has maxima around $\mu = \pm 1$. The normalization constant for this example reads $A = 13.1$. More complex functional forms for $H(\mathbf{n})$ can be easily conceived. For the special case of Poisson-Box tessellations with three fixed orientations parallel to the orthogonal Cartesian axes we have

$$H_{\rm box}(\theta, \phi) = \frac{1}{3} \delta(\phi)\, \delta\left(\theta - \frac{\pi}{2}\right) + \frac{1}{3} \delta\left(\phi - \frac{\pi}{2}\right) \delta\left(\theta - \frac{\pi}{2}\right) + \frac{1}{3} \delta(\theta)\, \frac{1}{\pi}. \tag{4.16}$$

For the functional forms of the angular distribution $H(\mathbf{n})$ introduced here, the integrals needed for the constants ζ_3 (see Eq. (2.22)) and η_3 (see Eq. (2.25)) can be easily computed by Monte Carlo sampling, since they are both expressed as expected values over the angular distributions. The functionals to be evaluated are the volume of the parallelepiped spanned by three unit vectors in the case of ζ_3, and the scalar product of two unit vectors in the case of η_3, respectively. In special cases, such as for the isotropic and box distributions, the integrals can be computed analytically. The resulting constants ζ_3 and η_3 are provided in Tab. 4.14. Finally, observe that from Eq. (2.7) we have $\alpha_3 = 4$.

4.3.2 Polyhedral features

In order to explore the statistical features of the cells of the tessellations, we have generated anisotropic Poisson tessellations of a cube of side L. For each angular law $H(\mathbf{n})$ described above, based on our computer code we have generated 5×10^3 realizations for increasing sides L and the same tessellation density $\rho = 1$. The side of the box is varied between $L = 1$ and $L = 200$: we expect that when $L\rho \gg 1$ finite-size effects fade away and the moments of the observables converge to their asymptotic limits

Law $H(\mathbf{n})$	ζ_3	η_3
Isotropic	$\pi/8 \simeq 0.3927$	8
Quadratic	$0.3029 \pm 2 \times 10^{-5}$	$10.2368 \pm 5 \times 10^{-5}$
Box	$2/9 \simeq 0.2222$	$27/\pi \simeq 8.59436$
Histogram	$0.1880 \pm 3 \times 10^{-5}$	$16.597 \pm 2 \times 10^{-5}$

Table 4.14: Numerical values for the constants ζ_3 (see Eq. (2.22)) and η_3 (see Eq. (2.25)), for $d = 3$ and various laws $H(\mathbf{n})$. Integrals have been computed by Monte Carlo sampling for quadratic and histogram laws (whence the error bars) and analytically for isotropic and box laws.

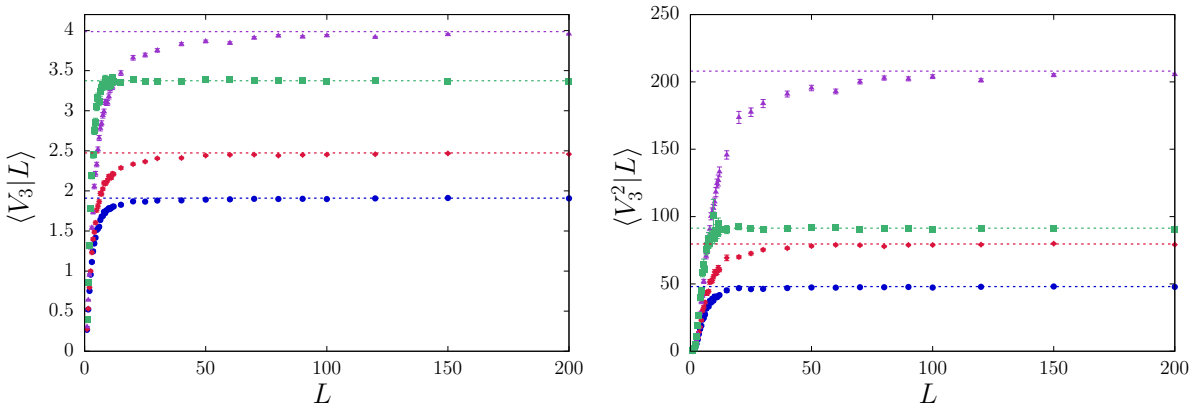

Figure 4.26: Average volume $\langle V_3|L\rangle$ (left) and second moment of the volume $\langle V_3^2|L\rangle$ (right) of the Poisson tessellation cells as a function of the box side L, with various anisotropy laws $H(\mathbf{n})$, for $d = 3$. The tessellation density is $\rho = 1$ for all the angular laws $H(\mathbf{n})$. Symbols denote Monte Carlo simulation results: blue circles correspond to isotropic distribution, red diamonds to quadratic distribution, green squares to box distribution and purple triangles to histogram distribution. Solid lines correspond to the respective limits for infinite Poisson tessellations, as given in Eqs. (2.21) and (2.24), respectively.

corresponding to infinite tessellations. The Monte Carlo simulation results for the average number of faces $\langle C_3\rangle$ of each cell are given in Tab. 4.15 for the largest tested box, i.e., $L = 200$: it is immediately apparent that $\langle C_3\rangle$ does not depend on the angular law $H(\mathbf{n})$, as expected.

The simulation results for the average volume $\langle V_3\rangle$, the second moment $\langle V_3^2\rangle$, the average surface $\langle S_3\rangle$ and the correlations $\langle V_3 S_3\rangle$ between the volume and the surface are given in Tabs. 4.16-4.19, respectively, for $L = 200$. Numerical findings are in good agreement with the theoretical formulas, and the minimum of all these quantities is attained for the case of isotropic tessellations, as predicted by theory. The evolution of these moments as a function of the side L of the box is shown in Figs. 4.26 and 4.27: for small L, finite-size effects are clearly visible; for larger L, the estimated moments converge to their asymptotic limits for infinite tessellations. The rate of convergence to the asymptotic values depends on the anisotropy law $H(\mathbf{n})$: the stronger the anisotropy, the slower the convergence. Isotropic and box tessellations, although converging to different limits, appear to have the nearly same rate of convergence, which stems from box tessellations being quasi-isotropic. Inspection of Fig. 4.26 shows that $\langle V_3\rangle$ and $\langle V_3^2\rangle$ appear to have similar rates of convergence, for a given $H(\mathbf{n})$.

The distribution of the inradius $r_{\text{in},3}$ has been also estimated by Monte Carlo simulation and is provided in Fig. 4.28 (left) for large $L = 200$ and $\rho = 1$. It is immediately apparent that the curves corresponding to different laws $H(\mathbf{n})$ collapse onto the same functional form, which for infinite tessellations is the exponential distribution

$$\mathcal{P}(r_{\text{in},3}) = 4\rho e^{-4\rho r_{\text{in},3}}, \tag{4.17}$$

where we have used $\alpha_3 = 4$. In particular, the average inradius yields $\langle r_{\text{in},3}\rangle = 1/(4\rho)$ for infinite

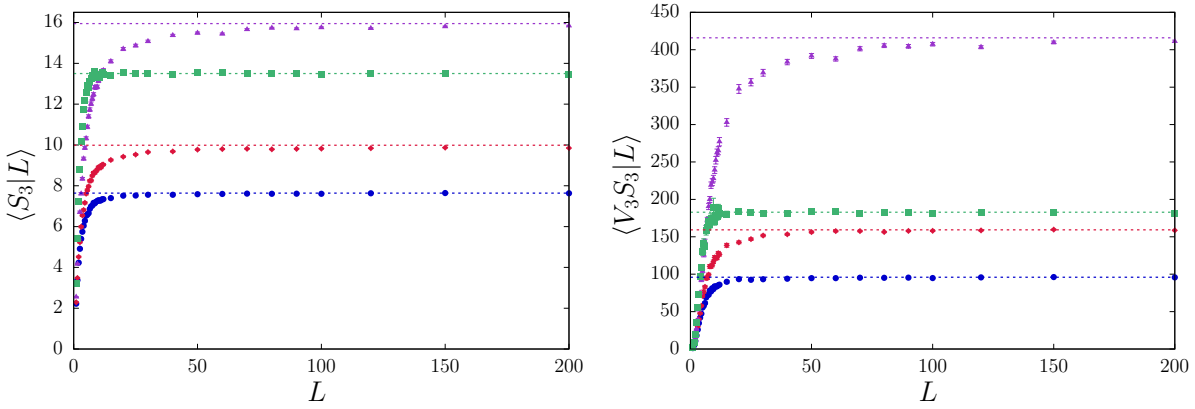

Figure 4.27: Average surface $\langle S_3|L\rangle$ (left) and volume-surface correlations $\langle V_3S_3|L\rangle$ (right) of the Poisson tessellation cells as a function of the box side L, with various anisotropy laws $H(\mathbf{n})$, for $d = 3$. The tessellation density is $\rho = 1$ for all the angular laws $H(\mathbf{n})$. Symbols denote Monte Carlo simulation results: blue circles correspond to isotropic distribution, red diamonds to quadratic distribution, green squares to box distribution and purple triangles to histogram distribution. Solid lines correspond to the respective limits for infinite Poisson tessellations, as given in Eqs. (2.16) and (2.17), respectively.

Law $H(\mathbf{n})$	$\langle C_3\rangle$	Monte Carlo
Isotropic	6	$6 \pm 7 \times 10^{-8}$
Quadratic	6	$6 \pm 9 \times 10^{-8}$
Box	6	6 ± 0
Histogram	6	6 ± 10^{-7}

Table 4.15: Average number of faces $\langle C_3\rangle$ of the Poisson tessellation cells for a box of side $L = 200$, with various anisotropy laws $H(\mathbf{n})$, for $d = 3$. The tessellation density is $\rho = 1$ for all the angular laws $H(\mathbf{n})$. The limit value for infinite Poisson tessellations is $\langle C_3\rangle = 6$ for any $H(\mathbf{n})$.

tessellations. Finite-size effects are negligible, since $\rho L \gg 1$. As mentioned above, to the best of our knowledge the theoretical behaviour of the outradius for infinite tessellations is not known (not even for the simplest case of isotropic tessellations). Monte Carlo simulations show that $\langle r_{\mathrm{out},3}\rangle$ non-trivially depends on the law $H(\mathbf{n})$, contrary to the inradius.

The distribution of the number of faces C_3 has been estimated by Monte Carlo simulation and is displayed in Fig. 4.28 (right) for large $L = 200$ and $\rho = 1$. The curves corresponding to different laws $H(\mathbf{n})$ collapse onto the same functional form, apart from Box tessellations which have a peculiar behaviour: by construction, the number of faces in Box tessellations is equal to 6 for each cell.

4.3.3 Chord lengths

We have estimated the chord length distribution $\mathcal{P}(\ell|\mathbf{\Omega}, L)$ corresponding to lines having a fixed orientation $\mathbf{\Omega}$, for several anisotropy laws $H(\mathbf{n})$. Monte Carlo simulation results are shown in Fig. 4.29 for $L = 150$ and $\rho = 1$. An ensemble of 5×10^3 realizations and 10^3 sample lines for each geometry have been taken for each angular law $H(\mathbf{n})$. Furthermore, Monte Carlo simulation results for the chord length distribution $\mathcal{P}(\ell_\alpha|\mathbf{\Omega}, L)$ through material α are displayed in Fig.4.30. Numerical findings are in good agreement with the exponential density given in Eq. (2.37), which is exact for infinite tessellations. Finite-size effects are negligible, since $L\rho \gg 1$ for these simulations.

The special case of lines that are homogeneously and isotropically distributed has been separately considered. Simulation results for the resulting average correlation length Λ_c are illustrated in Tab. 4.20, where Monte Carlo estimates are compared to the expected theoretical value Λ_c. The

Law $H(\mathbf{n})$	$\langle V_3 \rangle$	Monte Carlo
Isotropic	$6/\pi \simeq 1.90986$	$1.907 \pm 4 \times 10^{-3}$
Quadratic	$\simeq 2.4744$	$2.459 \pm 5 \times 10^{-3}$
Box	$27/8 = 3.375$	$3.366 \pm 7 \times 10^{-3}$
Histogram	$\simeq 3.987$	$3.957 \pm 9 \times 10^{-3}$

Table 4.16: Average volume $\langle V_3 \rangle$ of the Poisson tessellation cells for a box of side $L = 200$, with various anisotropy laws $H(\mathbf{n})$, for $d = 3$. The tessellation density is $\rho = 1$ for all the angular laws $H(\mathbf{n})$. The limit value for infinite Poisson tessellations is given in Eq. (2.21).

Law $H(\mathbf{n})$	$\langle V_3^2 \rangle$	Monte Carlo
Isotropic	48	47.8 ± 0.2
Quadratic	$\simeq 79.6227$	79.2 ± 0.3
Box	$729/8 = 91.125$	90.5 ± 0.4
Histogram	$\simeq 207.9931$	206 ± 1

Table 4.17: Second moment of the volume $\langle V_3^2 \rangle$ of the Poisson tessellation cells for a box of side $L = 200$, with various anisotropy laws $H(\mathbf{n})$, for $d = 3$. The tessellation density is $\rho = 1$ for all the angular laws $H(\mathbf{n})$. The limit value for infinite Poisson tessellations is given in Eq. (2.24).

average correlation length $\Lambda_c(L)$ as a function of the system size L is shown in Fig.4.31(left). Numerical findings confirm that Λ_c does not depend on the anisotropy law $H(\mathbf{n})$ and is simply inversely proportional to the tessellation density ρ, namely, $\Lambda_c = 1/\rho$.

For the purpose of comparison, we have also investigated the estimator

$$\Lambda_c^* \equiv \mathbb{E}\left[\frac{\sum_{j=1}^{q} \ell_j}{q}\right], \tag{4.18}$$

which is to be compared to the estimator introduced in Sec. 2.3.4, namely, $\Lambda_c \equiv \mathbb{E}[\sum_{j=1}^{q} \ell_j]/\mathbb{E}[q]$. The corresponding simulation results for Λ_c^* as a function of L are provided in Fig. 4.31 (right). Generally speaking, we observe that, contrary to Λ_c, this estimator is biased with respect to $1/\rho$: this is particularly visible for the quadratic distribution and for the histogram distribution. These numerical findings are consistent with the analysis provided by Miles [90].

4.4 Spherical inclusions

For the sake of completeness, we conclude this Chapter by investigating the geometrical properties of random spherical inclusions. In particular, we are interested by the chord length distributions through the background matrix and through the spheres. As shown in Chapter 3, we have developed a generator for random spherical inclusions. In the following, we resort to Monte Carlo methods in order to compute the statistical properties of the geometries created by our tool, for the purpose of assessing the behaviour of the chord length distributions and estimating the discrepancy between the simulation results and the theoretical formulas for infinite geometries. Although spherical inclusions are not investigated for the particle transport in this thesis, this preliminary work could be useful for future work, e.g., for a comparison between particle transport in random tessellations and in spherical inclusions.

We have chosen to investigate different radius distributions, with a common average radius $\langle r \rangle = 0.1$: a constant distribution, a uniform distribution between 0 and $R = 2\langle r \rangle$, a linear distribution between 0 and $R = 3\langle r \rangle$ and an exponential distribution of parameter $1/\langle r \rangle$.

Table 4.21 shows the simulation results for the average correlation length Λ_c^0 through the background material and for the average correlation length Λ_c^1 through the spheres. The agreement with the theoretical formulas deduced from Eq. (2.3) and Eq. (2.5) is very satisfying. Figures 4.32 and 4.33, respectively, display the chord length distribution through the background matrix and the chord length

Law $H(\mathbf{n})$	$\langle S_3 \rangle$	Monte Carlo
Isotropic	$24/\pi \simeq 7.63944$	7.63 ± 0.01
Quadratic	$\simeq 9.986$	9.85 ± 0.01
Box	$27/2 = 13.5$	13.48 ± 0.02
Histogram	$\simeq 15.947$	15.84 ± 0.03

Table 4.18: Average surface $\langle S_3 \rangle$ of the Poisson tessellation cells for a box of side $L = 200$, with various anisotropy laws $H(\mathbf{n})$, for $d = 3$. The tessellation density is $\rho = 1$ for all the angular laws $H(\mathbf{n})$. The limit value for infinite Poisson tessellations is given in Eq. (2.16).

Law $H(\mathbf{n})$	$\langle V_3 S_3 \rangle$	Monte Carlo
Isotropic	96	95.7 ± 0.3
Quadratic	$\simeq 159.2455$	158.6 ± 0.6
Box	$729/4 = 182.25$	181.2 ± 0.7
Histogram	$\simeq 415.9862$	411 ± 2

Table 4.19: Volume-surface correlations $\langle V_3 S_3 \rangle$ of the Poisson tessellation cells for a box of side $L = 200$, with various anisotropy laws $H(\mathbf{n})$, for $d = 3$. The tessellation density is $\rho = 1$ for all the angular laws $H(\mathbf{n})$. The limit value for infinite Poisson tessellations is given in Eq. (2.17).

distribution through spheres. For the former, the agreement is rather good but not perfect, as expected: i) the exponential distribution in infinite geometries is itself an approximation, and ii) finite size-effects occur in finite geometries, especially when imposing the condition of non-overlapping the boundaries. The chord length through the background matrix is by construction more affected by this boundary condition. Moreover, these results are consistent with those obtained in [77,100] for similar investigations: the discrepancy with respect to the exponential distribution close to $\ell_0 = 0$ has clearly the same profile as in [77] and seems also compatible with the data reported in [100]. For the chord length distribution in the spheres, the agreement with theoretical formulas is excellent.

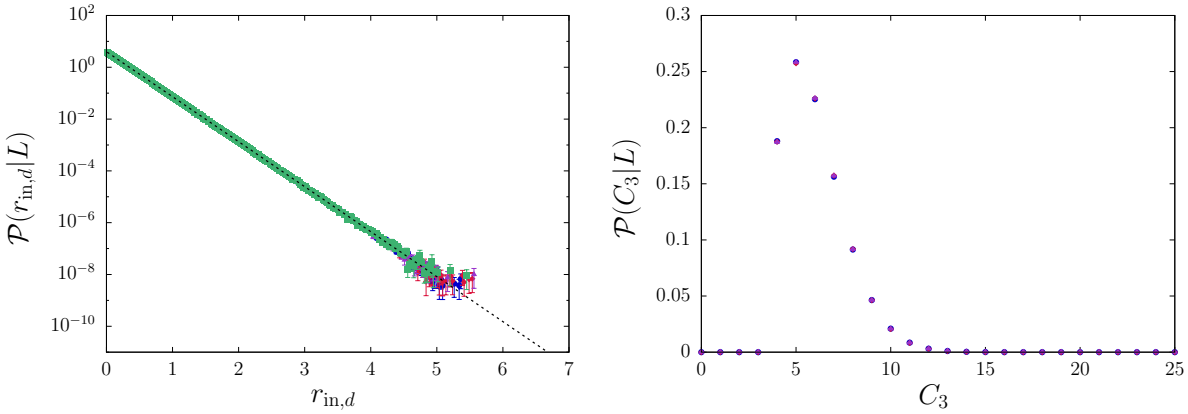

Figure 4.28: Left. Distribution of the in-radius $r_{\mathrm{in},3}$ of the Poisson tessellation cells for a box with side $L = 200$, with various anisotropy laws $H(\mathbf{n})$, for $d = 3$. The tessellation density is $\rho = 1$ for all the angular laws $H(\mathbf{n})$. Symbols denote Monte Carlo simulation results: blue circles correspond to isotropic distribution, red diamonds to quadratic distribution, green squares to box distribution and purple triangles to histogram distribution. The solid line corresponds to the limit distribution for infinite Poisson tessellations, i.e., the exponential density given in Eq. (4.17), independent of $H(\mathbf{n})$. Right. Distribution of the number of faces C_3 of the Poisson tessellation cells for a box with side $L = 200$, with various anisotropy laws $H(\mathbf{n})$, for $d = 3$. The tessellation density is $\rho = 1$ for all the angular laws $H(\mathbf{n})$. Symbols denote Monte Carlo simulation results: blue circles correspond to isotropic distribution, red diamonds to quadratic distribution and purple triangles to histogram distribution. For Box tessellations, C_3 is trivially equal to 6 for each cell.

$H(\mathbf{n})$	Λ_c	Monte Carlo
Isotropic	1	$0.9940 \pm 8 \times 10^{-4}$
Quadratic	1	$0.9937 \pm 8 \times 10^{-4}$
Box	1	$0.9927 \pm 8 \times 10^{-4}$
Histogram	1	$0.9937 \pm 8 \times 10^{-4}$

Table 4.20: Average correlation lengths Λ_c of the Poisson tessellation cells for a box of side $L = 150$, with various anisotropy laws $H(\mathbf{n})$, for $d = 3$. The tessellation density is $\rho = 1$ for all the angular laws $H(\mathbf{n})$. The line orientation is uniform and isotropic. The limit value for infinite Poisson tessellations is $\Lambda_c = 1/\rho$, as in Eq. (2.49).

	$\Lambda_{c,0}$	Monte Carlo	$\Lambda_{c,1}$	Monte Carlo
Constant	1.2	$1.1708 \pm 3 \times 10^{-4}$	0.133333	0.13335 ± 10^{-5}
Uniform	1.8	$1.7484 \pm 4 \times 10^{-4}$	0.2	$0.19999 \pm 2 \times 10^{-5}$
Linear	2.16	$2.0852 \pm 5 \times 10^{-4}$	0.24	$0.24002 \pm 3 \times 10^{-5}$
Exponential	3.6	3.396 ± 10^{-3}	0.4	$0.4000 \pm \times 10^{-4}$

Table 4.21: Average correlation length Λ_c^0 through background material and average correlation length Λ_c^1 through spheres, for three-dimensional spherical inclusions within a box with side L, for several distributions of the radius. The packing fraction is $\xi = 0.1$ and the average radius $\langle r \rangle = 0.1$. We have chosen $L = 80$ for mono-dispersed spheres and $L = 100$ for poly-dispersed spheres. The chord lengths have been computed with 5×10^3 realizations and 10^2 lines per realization.

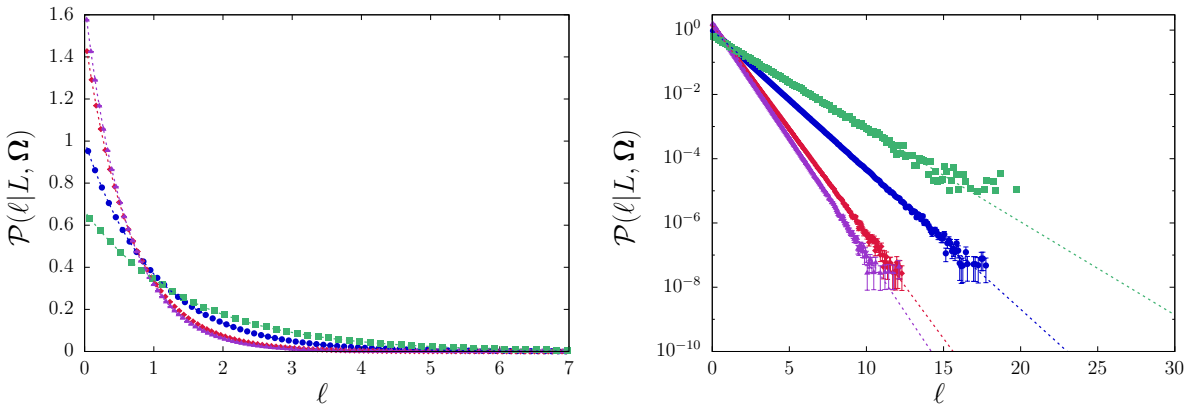

Figure 4.29: Left. Chord length distribution $\mathcal{P}(\ell|\mathbf{\Omega}, L)$ of the Poisson tessellation cells for a box with side $L = 150$, with various anisotropy laws $H(\mathbf{n})$, for $d = 3$. The tessellation density is $\rho = 1$ for all the angular laws $H(\mathbf{n})$. The line orientation is chosen as $\theta = 0$. Symbols denote Monte Carlo simulation results: blue circles correspond to isotropic distribution, red diamonds to quadratic distribution, green squares to box distribution and purple triangles to histogram distribution. The solid lines corresponds to the limit distribution for infinite Poisson tessellations, i.e., the exponential density given in Eq. (2.37), with average $\Lambda(\mathbf{\Omega})$ depending on the orientation $\mathbf{\Omega}$ and on the law $H(\mathbf{n})$ (see Eq. (2.36)). For the isotropic distribution we have $\Lambda(\mathbf{\Omega}) = 1$, for the quadratic distribution $\Lambda(\mathbf{\Omega}) = 2/3$, for the box distribution $\Lambda(\mathbf{\Omega}) = 3/2$, and for the histogram distribution $\Lambda(\mathbf{\Omega}) \simeq 0.62383$. Right. Log-linear scale.

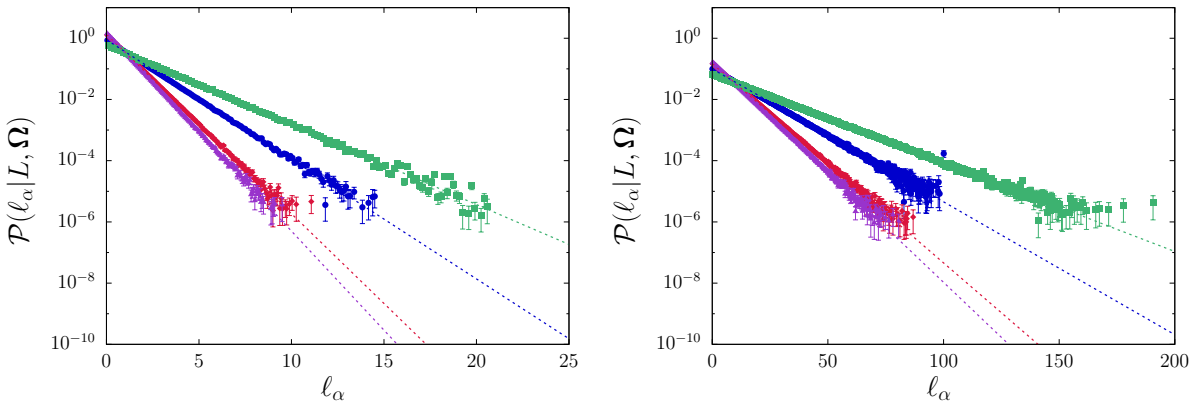

Figure 4.30: Chord length distribution $\mathcal{P}(\ell_\alpha|\mathbf{\Omega}, L)$ through clusters of material α in Poisson tessellations for a box with side $L = 150$, with various anisotropy laws $H(\mathbf{n})$, for $d = 3$, with $p_\alpha = 0.1$ (left) and $p_\alpha = 0.9$ (right). The tessellation density is $\rho = 1$ for all the angular laws $H(\mathbf{n})$. The line orientation is chosen as $\theta = 0$. Symbols denote Monte Carlo simulation results: blue circles correspond to isotropic distribution, red diamonds to quadratic distribution, green squares to box distribution and purple triangles to histogram distribution. The solid lines corresponds to the limit distribution for infinite Poisson tessellations, i.e., the exponential density given in Eq. (2.88), with average $\Lambda_\alpha(\mathbf{\Omega}) = \Lambda(\mathbf{\Omega})/(1 - p_\alpha)$.

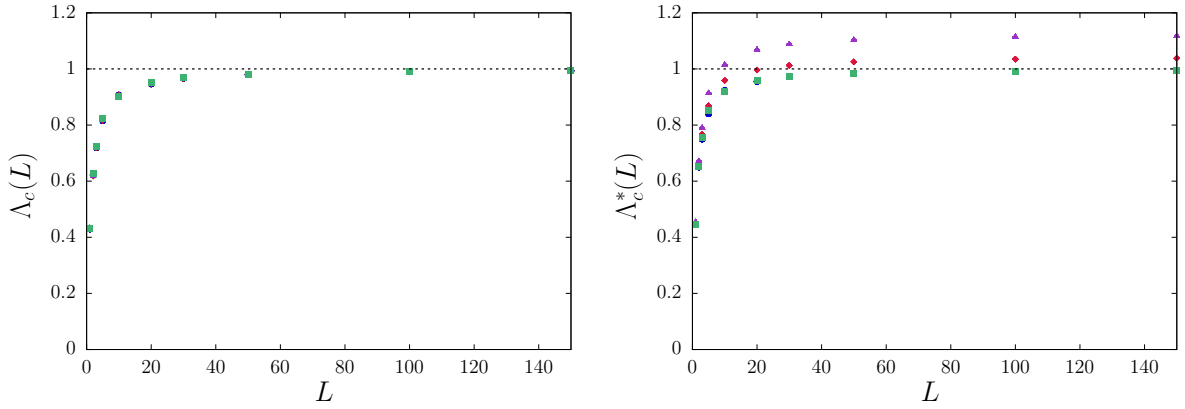

Figure 4.31: Average correlation length Λ_c (left) and estimator Λ_c^* (right) in Poisson tessellation cells for a box of side L, as a function of L, with various anisotropy laws $H(\mathbf{n})$, for $d = 3$. The tessellation density is $\rho = 1$ for all the angular laws $H(\mathbf{n})$. The line orientation is uniform and isotropic. Symbols denote Monte Carlo simulation results: blue circles correspond to isotropic distribution, red diamonds to quadratic distribution, green squares to box distribution and purple triangles to histogram distribution. The limit value for infinite Poisson tessellations is $\Lambda_c = 1/\rho$, as in Eq. (2.49).

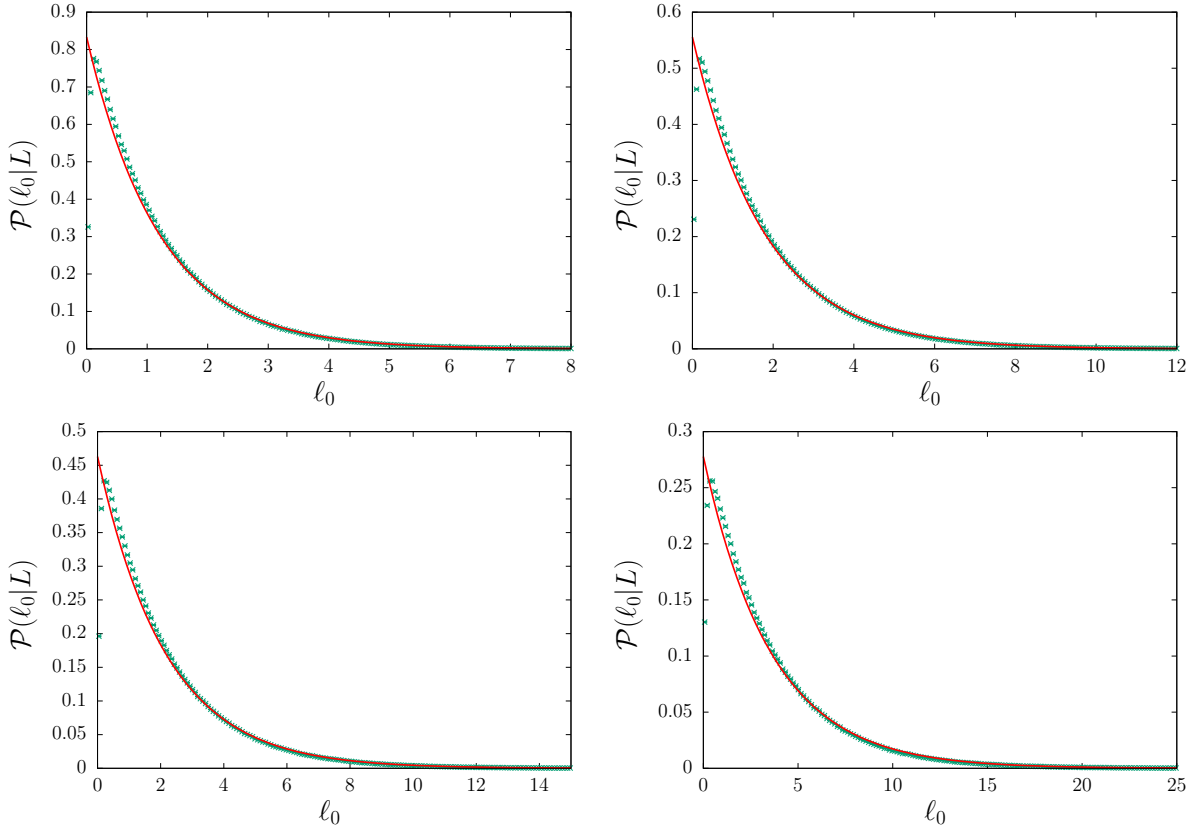

Figure 4.32: Chord length distribution $\mathcal{P}(\ell_0|L)$ through background matrix, for three-dimensional spherical inclusions within a box with side L, for several distributions of the radius. The packing fraction is $\xi = 0.1$ and the average radius $\langle r \rangle = 0.1$. Green crosses denote Monte Carlo simulation results. Solid lines correspond to the (approximate) limit distribution for infinite geometries, i.e., the exponential density given in Eq. (2.3). We have chosen $L = 80$ for mono-dispersed spheres and $L = 100$ for poly-dispersed spheres. The distributions for the radius are the following: (a) constant; (b) uniform; (c) linear; (d) exponential. The chord lengths have been computed with 5×10^3 realizations and 10^2 lines per realization.

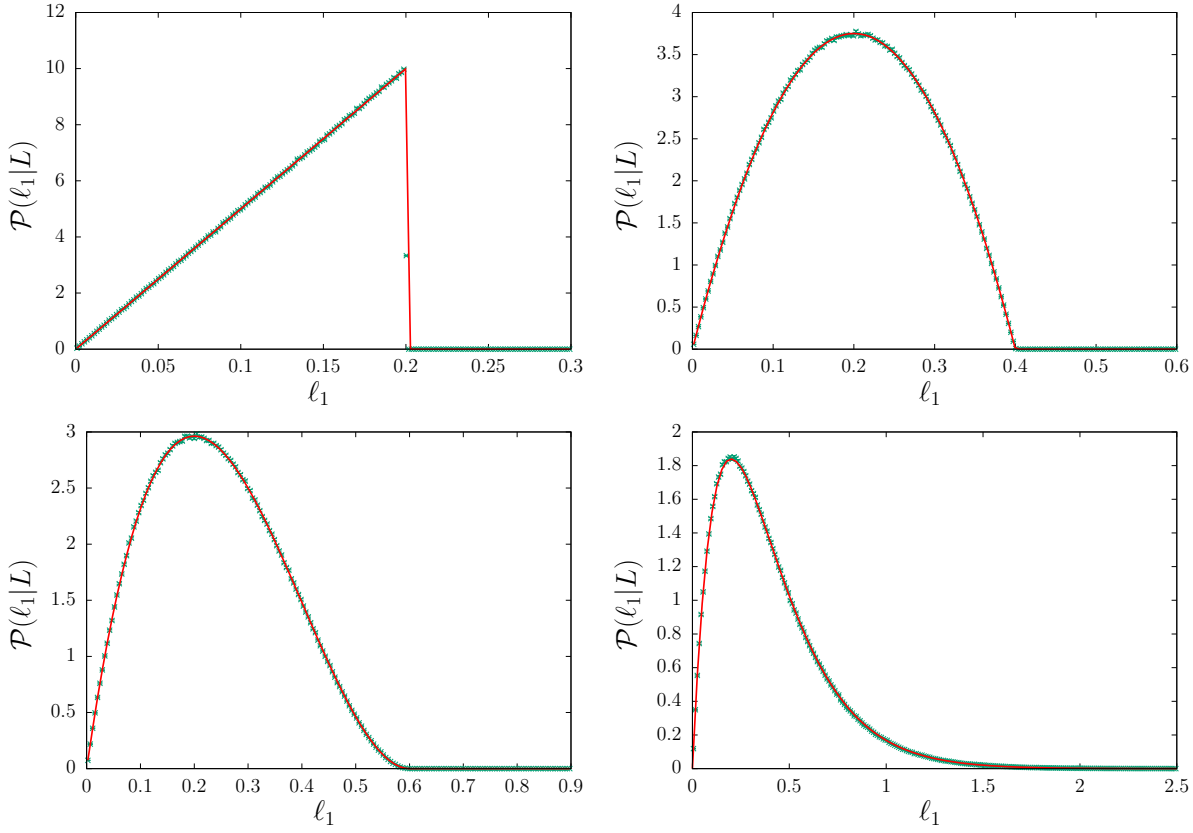

Figure 4.33: Chord length distribution $\mathcal{P}(\ell_1|L)$ through spheres, for three-dimensional spherical inclusions within a box with side L, for several distributions of the radius. The packing fraction is $\xi = 0.1$ and the average radius $\langle r \rangle = 0.1$. Green crosses denote Monte Carlo simulation results. Solid lines correspond to the limit distribution for infinite geometries, i.e., the density given in Eq. (2.5). We have chosen $L = 80$ for mono-dispersed spheres and $L = 100$ for poly-dispersed spheres. The distributions for the radius are the following: (a) constant; (b) uniform; (c) linear; (d) exponential. The chord lengths have been computed with 5×10^3 realizations and 10^2 lines per realization.

Part II

Particle transport in random media

Chapter 5

Fixed-source transport in quenched disorder

5.1 Introduction

As mentioned in Sec. 1.1, the purpose of linear transport theory in stochastic media consists in obtaining the ensemble-averaged angular particle flux $\langle\varphi(\mathbf{r},\mathbf{\Omega})\rangle$, where the average is taken with respect to the physical realizations of the random medium system under analysis. In this Chapter, we will focus on fixed-source stationary, mono-energetic transport in non-multiplying systems with isotropic scattering, which allows more easily grasping the properties of particle propagation in random media without bothering with the complexity of energy dependence, and yet retains the key ingredients of the physical problem of interest. The case of eigenvalue problems will be considered in the next Chapter. In the following, we will focus on the case of binary stochastic media with two immiscible materials, say α and β [108].

The stochastic nature of the medium stems from the materials composing the traversed medium being randomly distributed according to some statistical law. Hence, the total cross section $\Sigma(\mathbf{r})$, the scattering law $\Sigma_s(\mathbf{\Omega}'\rightarrow\mathbf{\Omega},\mathbf{r})$ and the source $Q(\mathbf{r},\mathbf{\Omega})$ are in principle random variables. Each realization will be denoted by a state q, associated to some stationary probability $\mathcal{P}(q)$: the state q is thus associated to the functions $\Sigma^{(q)}(\mathbf{r})$, $\Sigma_s^{(q)}(\mathbf{\Omega}'\rightarrow\mathbf{\Omega},\mathbf{r})$ and $Q^{(q)}(\mathbf{r},\mathbf{\Omega})$ for the material properties [108, 171]. For a given realization q, the angular flux $\varphi^{(q)}(\mathbf{r},\mathbf{\Omega})$ solves the linear Boltzmann equation

$$\mathbf{\Omega}\cdot\nabla\varphi^{(q)}+\Sigma^{(q)}(\mathbf{r})\varphi^{(q)}=\int\Sigma_s^{(q)}(\mathbf{\Omega}'\rightarrow\mathbf{\Omega},\mathbf{r})\varphi^{(q)}(\mathbf{r},\mathbf{\Omega}')d\mathbf{\Omega}'+Q^{(q)}. \tag{5.1}$$

For isotropic scattering, the differential scattering cross section simplifies to

$$\Sigma_s(\mathbf{\Omega}'\rightarrow\mathbf{\Omega},\mathbf{r})=\frac{\Sigma_s(\mathbf{r})}{\Omega_d}, \tag{5.2}$$

where Ω_d is the surface of the unit sphere in dimension d.

The ensemble-averaged angular flux is then formally defined as

$$\langle\varphi(\mathbf{r},\mathbf{\Omega})\rangle=\int\mathcal{P}(q)\varphi^{(q)}(\mathbf{r},\mathbf{\Omega})dq, \tag{5.3}$$

and can be further decomposed as

$$\langle\varphi(\mathbf{r},\mathbf{\Omega})\rangle=\sum_i p_i(\mathbf{r})\langle\varphi_i(\mathbf{r},\mathbf{\Omega})\rangle, \tag{5.4}$$

where $p_i(\mathbf{r})=\int_{X_i}\mathcal{P}(q)dq$ is the probability of finding the material of index i at position $\mathbf{r}$, with the material flux defined as

$$\langle\varphi_i(\mathbf{r},\mathbf{\Omega})\rangle=\int_{X_i}\mathcal{P}(q)\varphi^{(q)}(\mathbf{r},\mathbf{\Omega})dq. \tag{5.5}$$

Starting from this framework, two distinct strategies can be adopted in order to derive a description of $\langle\varphi(\mathbf{r},\mathbf{\Omega})\rangle$, as recalled in Chapter 1. The first, which can be denoted as a *quenched disorder* approach,

consists in deriving exact solutions for $\langle\varphi(\mathbf{r},\mathbf{\Omega})\rangle$ by first generating a collection of material realizations q, obeying some specified distributions $\mathcal{P}(q)$ encoding the statistical properties of the random media, then solving the Boltzmann equation (5.1) for $\varphi^{(q)}(\mathbf{r},\mathbf{\Omega})$ corresponding to each realization q, and finally taking the ensemble average over realizations according to Eq. (5.3). The name 'quenched' is reminiscent of the fact that the configuration (geometry, material compositions and sources) seen by the linear transport process for each realization is 'frozen'. The prominent advantage of this approach is that the obtained solutions $\langle\varphi(\mathbf{r},\mathbf{\Omega})\rangle$ are exact, since all the information concerning disorder-induced spatial correlations is entirely preserved.

Analytical results for the ensemble averages demand huge theoretical efforts, and so far have been obtained only under restrictive hypotheses such as in perturbative approximations [108]. Considerable progress has been achieved by using Monte Carlo methods in order to explicitly generate material realizations q from $\mathcal{P}(q)$ and then using a deterministic or Monte Carlo transport code to solve the transport problem for each sampled configuration. Since a large number of realizations is needed in order to obtain the sought ensemble averages (typically of the order of hundreds or thousands), such reference solutions are very demanding in terms of computational resources, especially if transport is to be solved by Monte Carlo methods so as achieve the highest accuracy in solving the Boltzmann equation.

The second strategy, which can be denoted as a *annealed disorder* approach, consists in deriving a single 'effective' equation for the ensemble-averaged flux $\langle\varphi\rangle$, which would convey all the information concerning the effects of disorder on particle transport via modified displacement or collision kernels. Such an equation could be then solved by deterministic methods, or even by Monte Carlo in case a probabilistic interpretation of the resulting transport operators can be given. However, as shown in Chapter 1, this strategy leads to a hierarchy of coupled equations involving higher-order conditional averages of the flux: unfortunately, the hierarchy cannot be closed, except for very special case such as in the absence of scattering [108]. Closure formulas are thus introduced, in the form of suitable models that allow truncating the infinite hierarchy and finally obtaining a single Boltzmann-like modified transport equation for the average flux. The name 'annealed' is reminiscent that the configuration seen by this modified linear transport process has been pre-averaged in order to come up with a single representative equation: the effects of disorder-induced spatial correlations are thus faded. Higher-order closure schemes can partially overcome this issue by better preserving correlations, at the expense of increased computational cost [108, 136].

In order to assess the accuracy of the various approximate models related to closure formulas, it is therefore mandatory to compute reference solutions for the exact Eqs. (5.3). For this purpose, a series of *benchmark problems* for linear particle transport have been proposed in the literature. The case where the stochastic media consists of randomly dispersed spherical inclusions into background matrices has been extensively studied, and several benchmark problems have been examined in two and three dimensions [8, 12, 31, 32]. For these configurations, it is known that the chord length distribution in the matrix is nearly exponential (provided that the sphere are sufficiently diluted) and the chord length distribution within the spheres can be exactly derived (and is highly non-exponential).

For Markov and renewal statistics, a pioneering work was performed by *Adams, Larsen and Pomraning*, who first proposed a now-classical benchmark problem for transport in stochastic media with Markov mixing in 1989 [1]. As originally formulated, the fiducial quantities for the benchmark where the ensemble-averaged transmission coefficient $\langle T\rangle$ and reflection coefficient $\langle R\rangle$ for a non-stochastic isotropic source located at one end of the geometry. Since then, this benchmark configuration has been updated and extended by including new fiducial quantities such as the ensemble-averaged particle flux $\langle\varphi\rangle$ within the geometry and other kinds of sources [1, 9–11, 171]. In all the examined configurations, the focus was exclusively on $1d$ geometries, either of the rod or slab type. In the case of Markov mixing, a realization simply consists in generating a sequence of exponentially spaced points on a line: the resulting segments or slabs, respectively, define the material chunks of the medium that can be then colored at random by assigning the material properties. Flat two-dimensional configurations with Markov mixing have received less attention [48, 65, 134].

Based on our previous investigation of stochastic tessellations, we are able to explicitly construct realizations of a broad class of random media associated to various chord length distributions, including

Markov (Poisson tessellations) and renewal statistics (Poisson-Voronoi and Poisson-Box tessellations). In this Chapter we will therefore revisit and generalize the benchmark problem by Adams, Larsen and Pomraning (denoted by ALP in the following, for the sake of conciseness), in order to shed new light on the behaviour of reference solutions for linear particle transport in random media. For this purpose, in the following we will:

1. present d-dimensional reference solutions of the ALP benchmark obtained by Monte Carlo particle transport simulations through $1d$ slab, $2d$ extruded and $3d$ Poisson tessellations, and discuss the impact of dimension on the obtained results. To the best of our knowledge, benchmark solutions for transport in $3d$ tessellations have never been addressed before. The dispersion of the physical observables around their average values will be assessed by evaluating their full distributions.

2. further generalize these findings by probing the impact of the underlying mixing statistics on particle transport. The nature of the microscopic disorder is known to subtly affect the path of the travelling particles, so that the observables will eventually depend on the statistical laws describing the shape and the material compositions of the random media [7, 27, 147, 171]. This is especially true in the presence of distributed absorbing traps [7]. For $d = 3$. we will thus consider three different stochastic tessellations, namely, Poisson, Voronoi and Box, and compute the ensemble-averaged reflection and transmission probabilities, as well as the particle flux. Two distinct benchmark configurations will be considered, the former including purely scattering materials and voids, and the latter containing scattering and absorbing materials.

5.2 Methodology

Reference solutions for particle transport in random media can be obtained in the following way: first, a realization of the medium is sampled from the underlying mixing statistics; then, the transport equations corresponding to this realization are solved by either deterministic or Monte Carlo methods, and the physical observables of interest are determined; this procedure is repeated several times so as to create a sufficiently large collection of realizations, and ensemble averages are finally taken for the physical observables (e.g., reflection or transmission coefficients, spatial flux, etc.). The methodology provided in the following applies also to eigenvalue problems, as discussed in Chap. 6.

For a given physical observable $\mathcal{O}$, the benchmark solution is obtained as the ensemble average

$$\langle \mathcal{O} \rangle = \frac{1}{M} \sum_{k=1}^{M} \mathcal{O}_k, \tag{5.6}$$

where $\mathcal{O}_k$ is the Monte Carlo estimate for the observable $\mathcal{O}$ obtained for the k-th realization.

The error affecting the average observable $\langle \mathcal{O} \rangle$ results from two separate contributions, the dispersion

$$\sigma_G^2 = \frac{1}{M} \sum_{k=1}^{M} {\mathcal{O}_k}^2 - \langle \mathcal{O} \rangle^2 \tag{5.7}$$

of the observables exclusively due to the stochastic nature of the geometries and of the material compositions, and

$$\sigma_{\mathcal{O}}^2 = \frac{1}{M} \sum_{k=1}^{M} \sigma_{\mathcal{O}_k}^2, \tag{5.8}$$

which is an estimate of the variance due to the stochastic nature of the Monte Carlo method for the particle transport, $\sigma_{\mathcal{O}_k}^2$ being the dispersion of a single calculation [31, 32]. The statistical error on $\langle \mathcal{O} \rangle$ is then estimated as

$$\sigma[\langle \mathcal{O} \rangle] = \sqrt{\frac{\sigma_G^2}{M} + \sigma_{\mathcal{O}}^2}. \tag{5.9}$$

Case	$\Sigma_{t,\alpha}$	Λ_α	$\Sigma_{t,\beta}$	Λ_β
1	10/99	99/100	100/11	11/100
2	10/99	99/10	100/11	11/10
3	2/101	101/20	200/101	101/20

Table 5.1: Material parameters for the three cases of the benchmark configurations.

5.3 The ALP benchmark revisited

We will consider a series of benchmark configurations for particle transport through Markov binary mixtures in dimension d, based on the pioneering work by Adams, Larsen and Pomraning [1], recently revisited by Brantley [11]. For this purpose, the stochastic media will be generated by resorting to d-dimensional Poisson random tessellations including $1d$ slab, $2d$ extruded, and full $3d$ configurations. For each realization, particle transport will be performed by resorting to the Monte Carlo simulation. We will compute the particle flux $\langle\varphi\rangle$, the transmission coefficient $\langle T\rangle$ and the reflection coefficient $\langle R\rangle$. The dispersion of the physical observables around their average values will be assessed by evaluating their full distributions. This section is organized as follows. First, we will introduce the benchmark specifications and set up the required notation. In Sec. 5.3.2 we will describe how to generate the material configurations corresponding to homogeneous Markov mixing, by resorting to the colored Poisson tessellations. These configurations will be described in Sec. 5.3.3. Then, in Sec. 5.3.4 we will present our simulation results for the physical observables of interest, and discuss the obtained findings and the impact of the dimension d.

5.3.1 Benchmark specifications

The benchmark specifications for our work are essentially taken from those originally proposed in [1] and [171], and later extended in [9–11,153]. We consider single-speed linear particle transport through a stochastic binary medium with *homogeneous* Markov mixing. The medium is non-multiplying, with isotropic scattering. The geometry consists of a box of side $L = 10$, with reflective boundary conditions on all sides of the box except two opposite faces (say those perpendicular to the x axis), where leakage boundary conditions are imposed: particles that leave the domain through these faces can not re-enter. Lengths are expressed in arbitrary units. In [1] and [171], system sizes $L = 0.1$ and $L = 1$ were also considered, but in this work we will focus on the case $L = 10$, which leads to more physically relevant configurations. Two kinds of non-stochastic sources will be considered: either an imposed normalized incident angular flux on the leakage surface at $x = 0$ (with zero interior sources), or a distributed homogeneous and isotropic normalized interior source (with zero incident angular flux on the leakage surfaces). Following the notation in [11], the benchmark configurations pertaining to the former kind of source will be called *Suite* I, whereas those pertaining to the latter will be called *Suite* II.

The material properties for the Markov mixing are entirely defined by assigning the average chord length for each material $i = \alpha, \beta$, namely Λ_i, which in turn allows deriving the homogeneous probability p_i of finding material i at an arbitrary location within the box, namely

$$p_i = \frac{\Lambda_i}{\Lambda_i + \Lambda_j}. \tag{5.10}$$

Note that the material probability p_i defines the volume fraction for material i. The cross sections for each material will be denoted as customary $\Sigma_{t,i}$ for the total cross section and $\Sigma_{s,i}$ for the scattering cross section. The average number of particles surviving a collision in material i will be denoted by $c_i = \Sigma_{s,i}/\Sigma_{t,i} \leq 1$. The physical parameters for the benchmark configurations are recalled in Tabs. 5.1 and 5.2: three cases (numbered 1, 2 and 3) are considered, each containing three sub-cases (noted a, b and c). The case numbers correspond to permutation of materials, whereas the sub-cases represents varying ratios of c_i for each material.

Sub-case	a	b	c
c_α	0	1	0.9
c_β	1	0	0.9

Table 5.2: Material parameters for the three sub-cases of the benchmark configurations.

Configuration	$\langle\Sigma_s\rangle$
1a, 2a	10/11
1b, 2b	1/11
3a	100/101
3b	1/101
1c, 2c, 3c	9/10

Table 5.3: Ensemble-averaged scattering cross section $\langle\Sigma_s\rangle$ for the benchmark configurations.

The physical observables of interest for the proposed benchmark will be the ensemble-averaged outgoing particle currents $\langle J\rangle$ on the two surfaces with leakage boundary conditions, and the ensemble-averaged scalar particle flux $\langle\varphi(x)\rangle = \langle\int\int\int\varphi(\mathbf{r},\mathbf{\Omega})d\mathbf{\Omega}dydz\rangle$ along $0 \leq x \leq L$. For the *Suite* I configurations, the outgoing particle current on the side opposite to the imposed current source will represent the ensemble-averaged transmission coefficient, namely, $\langle T\rangle = \langle J_{x=L}\rangle$, whereas the outgoing particle current on the side of the current source will represent the ensemble-averaged reflection coefficient, namely, $\langle R\rangle = \langle J_{x=0}\rangle$. For the *Suite* II configurations, the outgoing currents on opposite faces are expected to be equal (within statistical fluctuations), for symmetry reasons. In this case, we also introduce the average leakage current $\langle J_{\text{ave}}\rangle = \langle(T+R)/2\rangle$. Observe that the flux $\langle\varphi\rangle$ integrated over the box has a physical interpretation: actually, the integral flux is equal to the average length $\langle\ell_V\rangle$ travelled by the particles within the geometry: see, e.g., the considerations in [78, 93]. Since we are considering single-speed transport, $\langle\varphi\rangle$ is thus also proportional to the residence time spent by the particles in the box. In the absence of absorption, the residence time would be identified with the first passage time from the source to the leakage boundaries.

For the sake of completeness, we have also considered the so-called *atomic mix* model [108], where one assumes that the statistical disorder can be approximated by simply taking a full homogenization of the physical properties based on the ensemble-averaged cross sections. This would formally correspond to assuming that the average chord length within the medium is vanishing small. The atomic mix approximation is known to be valid when the chunks of each material are optically thin, i.e., $\Sigma_{t,i}\Lambda_i \ll 1$ for $i = \alpha, \beta$ [108]. For each case, we compute the corresponding ensemble-averaged scattering cross section $\langle\Sigma_s\rangle$ and ensemble-averaged absorbing cross section $\langle\Sigma_a\rangle$ as follows

$$\langle\Sigma_s\rangle = p_\alpha\Sigma_{s,\alpha} + (1-p_\alpha)\Sigma_{s,\beta} \tag{5.11}$$

and

$$\langle\Sigma_a\rangle = p_\alpha\Sigma_{a,\alpha} + (1-p_\alpha)\Sigma_{a,\beta}. \tag{5.12}$$

The ensemble-averaged scattering cross sections $\langle\Sigma_s\rangle$ corresponding to the atomic mix model are provided in Tab. 5.3. The ensemble-averaged total cross section $\langle\Sigma\rangle = p_\alpha\Sigma_{t,\alpha} + p_\beta\Sigma_{t,\beta}$ for all cases and sub-cases of the benchmark is $\langle\Sigma_t\rangle = 1$.

5.3.2 Construction of the corresponding stochastic geometries

Binary Markov mixtures required for the benchmark specifications are obtained as follows: first, a d-dimensional Poisson tessellation is constructed as described in Sec 2.3.1, restricted to a box of side $L = 10$ and with a density parameter ρ. Then, each polyhedron of the geometry is assigned a material

Case	ρ	p_α
1	1000/99	0.9
2	100/99	0.9
3	40/101	0.5

Table 5.4: Parameters for the colored Poisson geometries corresponding to the three cases of the benchmark configurations.

composition by formally attributing a distinct 'label' (also called 'color'), say 'α' or 'β', with associated complementary probabilities p_α and $p_\beta = 1 - p_\alpha$.

The average chord length Λ_α through clusters with composition α is related to the average chord length Λ of the tessellation cells via

$$\Lambda = (1 - p_\alpha)\Lambda_\alpha, \tag{5.13}$$

and for Λ_β we similarly have

$$\Lambda = p_\alpha \Lambda_\beta. \tag{5.14}$$

This yields $1/\Lambda_\alpha + 1/\Lambda_\beta = 1/\Lambda$, and we recover

$$p_\alpha = \frac{\Lambda}{\Lambda_\beta} = \frac{\Lambda_\alpha}{\Lambda_\alpha + \Lambda_\beta}. \tag{5.15}$$

Thus, based on the formulas above, and using $\rho = 1/\Lambda$, the parameters of the colored Poisson geometries corresponding to the benchmark specifications provided in Tab. 5.1 are easily derived. Their values are recalled in Tab. 5.4.

For the purpose of illustration, examples of realizations of Poisson geometries for the benchmark configurations are displayed in Fig. 5.1 for the $1d$ slab tessellations, in Fig. 5.2 for the $2d$ extruded tessellations, and in Fig. 5.3 for the $3d$ tessellations. The impact of varying the average chord length Λ and the volumetric fractions p_α is apparent.

5.3.3 Analysis of the benchmark configurations

Among the benchmark configurations, case 1 displays the largest fragmentation, since the material chord lengths Λ_α and Λ_β are both much smaller than the linear size L of the box (see Tab. 5.1). This is mirrored in a small correlation length $\Lambda \simeq 0.1$, and a very large number of d-polyhedra $\langle N_p | L \rangle$ composing the tessellation (see Tab. 5.5). The volume fractions are $p_\alpha = 0.9$ and $p_\beta = 0.1$, respectively, so that it is much more probable to cross material α than material β: chunks of material β are small and well mixed within material α. For case $1a$, material α is purely absorbing, but with a small cross section, whereas material β is purely scattering, and is opaque due to its large cross section: in this case, a typical realization will consist in small chunks of opaque material dispersed in larger chunks of an almost transparent material. In the atomic mixing approximation, case $1a$ is mainly scattering.

Case $1b$ is the opposite of case $1a$, with material α being now purely scattering, and material β being purely absorbing. A typical realization will then consist in small absorbing chunks, with a large cross section, dispersed in larger chunks of an almost transparent material. In the atomic mixing approximation, case $1b$ is mainly absorbing.

For case $1c$, the materials have $c_i \neq 1$, so that the chunks have intermediate properties between absorption and scattering.

The features of case 2 are such that the total cross sections and the volume fractions are the same as in case 1, but with larger mean chord lengths Λ_α and Λ_β (see Tab. 5.1). Correspondingly, the correlation length $\Lambda \simeq 1$ is ten times larger than that of case 1, which leads to a considerably lower number of d-polyhedra $\langle N_p | L \rangle$ with respect to case 1 (see Tab. 5.5). The chunks of material α are rather large, whereas those of material β are smaller. The volume fractions are the same as those of case 1, and so are the total cross sections. The scattering and absorbing cross sections for all the sub-cases are then equal to those of case 1.

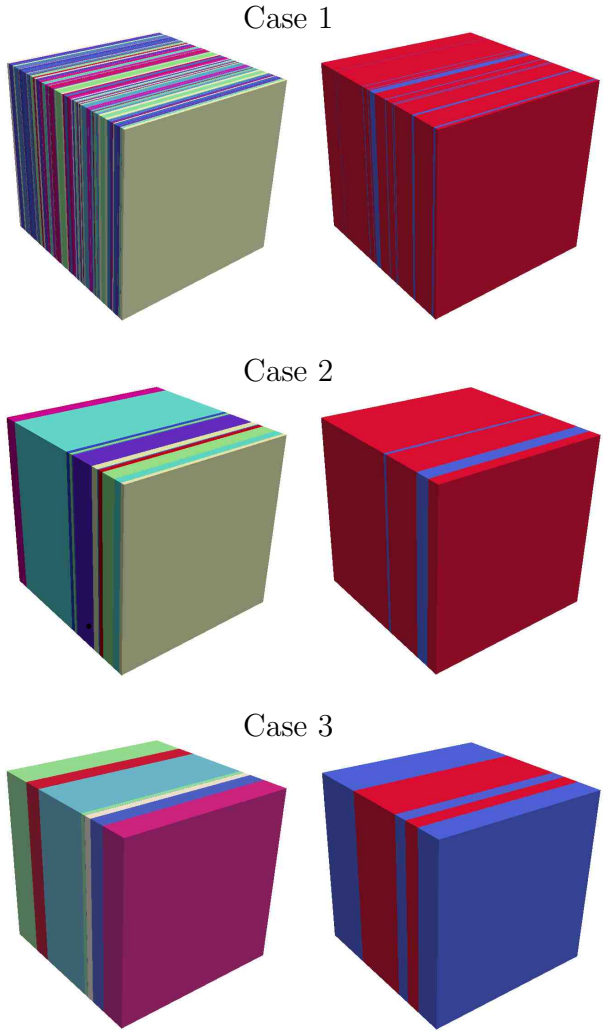

Figure 5.1: Examples of realizations of Poisson geometries corresponding to the benchmark specifications for the $1d$ slab tessellations, before (left) and after (right) attributing the material label. Red denotes label α and blue denotes label β. The corresponding parameters ρ and p_α are provided in Tab.5.4.

For case 3, materials α and β share the same mean chord length, and their respective volume fractions are also equal, i.e., $p_\alpha = p_\beta = 0.5$ (see Tab. 5.1). Chunks are larger than for case 2, with a correlation length $\Lambda \simeq 2.5$, and the number of d-polyhedra $\langle N_p|L\rangle$ is thus lower than for case 2 (see Tab. 5.5). A typical realization in $d = 1$ will be therefore dominated by a single material, which means that the entire box will be typically either colored in red or in blue, but this effect fades away with increasing dimension, as apparent from Fig. 5.2 for the $2d$ extruded tessellations and from Fig. 5.3 for the $3d$ tessellations. The total cross sections of α and β are smaller than those of case 1 and 2, with different scattering and absorbing cross sections for each sub-case.

In case $3a$, material α is purely absorbing, with a small cross section, whereas material β is purely scattering, with a large cross section. In case $3b$, the role of the absorbing and scattering material are inverted, as before. For case $3c$, both materials are partly absorbing and reflecting, and the global cross sections are the same of cases $1c$ and $2c$.

5.3.4 Monte Carlo simulation results

Simulation parameters

The reference solutions for the ensemble-averaged scalar particle flux $\langle\varphi(x)\rangle$ and the currents $\langle R\rangle$ and $\langle T\rangle$ have been computed as follows. For each benchmark case and sub-case, a large number M

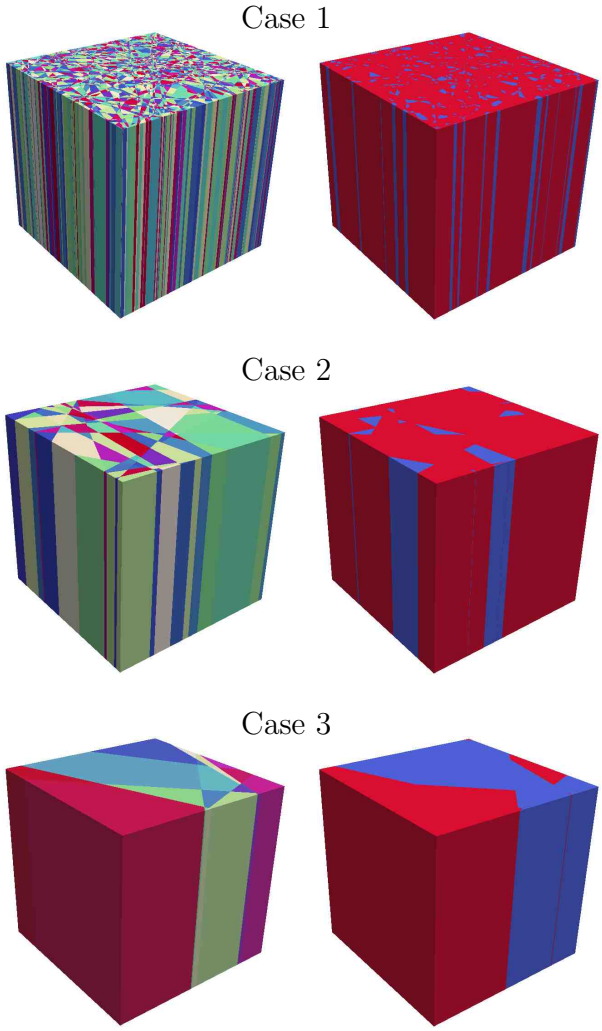

Figure 5.2: Examples of realizations of Poisson geometries corresponding to the benchmark specifications for the $2d$ extruded tessellations, before (left) and after (right) attributing the material label. Red denotes label α and blue denotes label β. The corresponding parameters ρ and p_α are provided in Tab.5.4.

of geometries has been generated, and the material properties have been attributed to each volume as described above. Then, for each realization k of the ensemble, linear particle transport has been simulated by resorting to the production Monte Carlo code TRIPOLI-4 ®, developed at CEA [21]. TRIPOLI-4 ® is a general-purpose stochastic transport code capable of simulating the propagation of neutral and charged particles with continuous-energy cross sections in arbitrary geometries. In order to comply with the benchmark specifications, constant cross sections adapted to mono-energetic transport and isotropic angular distributions have been prepared. Specifically, currents R_k and T_k at a given surface are estimated by summing the statistical weights of the particles crossing that surface. Scalar fluxes $\varphi_k(x)$ have been recorded by resorting to the standard track length estimator over a pre-defined spatial grid containing 10^2 uniformly spaced meshes along the x-axis. The number of simulated particle histories per configuration is 10^6. Finally, we compute the average value of each observable as explained in Sec. 5.2.

Depending on the chord lengths and on the volumetric fractions, the physical observables might display a larger or smaller dispersion around their average values. In order to assess the impact of such dispersion, we have also computed the full distributions of T and R based on the available realizations.

The number M of realizations that have been used for the Monte Carlo simulations has been chosen as follows. For $1d$ slab tessellations, we have taken $M = 4 \times 10^4$ for sub-cases $1b$; $M = 5 \times 10^4$ for sub-cases $2b$; and $M = 10^5$ for sub-cases $3b$. Otherwise, we have used $M = 5 \times 10^4$ for sub-case $2a$ of the *suite* II, and $M = 10^4$ for the remaining cases and sub-cases. For the $2d$ extruded tessellations,

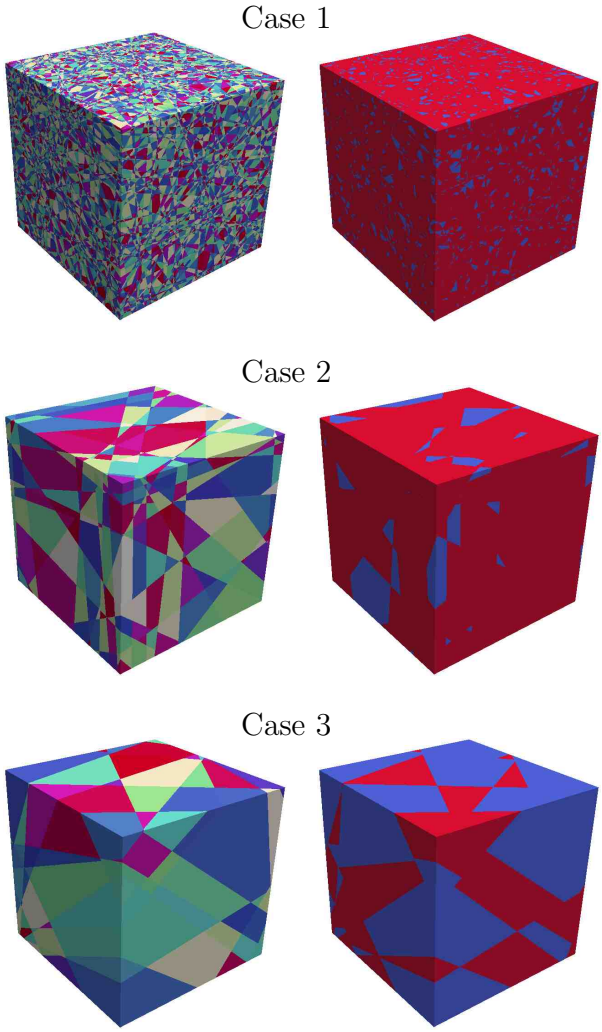

Figure 5.3: Examples of realizations of Poisson geometries corresponding to the benchmark specifications for the $3d$ tessellations, before (left) and after (right) attributing the material label. Red denotes label α and blue denotes label β. The corresponding parameters ρ and p_α are provided in Tab.5.4.

we have taken $M = 2 \times 10^4$ for the sub-cases $2b$ and $M = 5 \times 10^4$ for the sub-cases $3b$. Otherwise, we have used the same number of realizations as in [59], namely, $M = 4 \times 10^3$. Finally, for the $3d$ tessellations we have taken $M = 2 \times 10^4$ for the sub-case $2b$ of the *suite* II; $M = 5 \times 10^3$ for all the other sub-cases of case 2; $M = 5 \times 10^4$ for the sub-case $3b$ of the *suite* II; and $M = 10^4$ for all the other sub-cases of case 3. For all remaining cases and sub-cases, we have used the same number of realizations as in [59], namely, $M = 10^3$.

As a general remark, increasing the dimension d implies an increasing computational burden (each realization takes longer both for generation and for Monte Carlo transport), but also a better statistical mixing (a single realization is more representative of the 'typical' random behaviour). Moreover, since Poisson tessellations have ergodic properties [85, 87], tessellations with smaller average chord length Λ require a lower number of realizations to achieve statistically stable ensemble averages, again at the expenses of an increased computational cost.

Concerning particle transport, it is important to stress that for the simulations discussed here we have largely benefited from a feature that has been recently implemented in the code TRIPOLI-4 ®, namely the possibility of reading pre-computed *connectivity maps* for the volumes composing the geometry. During the generation of the Poisson tessellations, care has been taken so as to store the indexes of the neighbouring volumes for each realization, which means that during the geometrical tracking a particle will have to find the following crossed volume in a list that might be considerably smaller than the total number of random volumes composing the box (depending on the features of

the random geometry). To provide an example, a typical realization of a $3d$ geometry for case 1 will be composed of $\sim 10^5$ volumes, whereas the typical number of neighbours for each volume will of the order of ~ 10. When fed to the transport code, such connectivity maps allow thus for considerable speed-ups for the most fragmented geometries, up to one hundred.

Computer time

Transport calculations have been run on a cluster based at CEA, with Intel Xeon E5-2680 V2 2.8 GHz processors. An overview of the average computer time $\langle t \rangle$ for each benchmark configuration is provided in Tabs. 5.6 and 5.7. Dispersions $\sigma[t]$ are also given. While an increasing trend for $\langle t \rangle$ as a function of dimension is clearly apparent, subtle effects due to correlation lengths and volume fractions for the material compositions come also into play, and strongly influence the average computer time. For some configurations, the dispersion $\sigma[t]$ may become very large, and even be comparable to the average $\langle t \rangle$. Atomic mixing simulations are based on a single homogenized realization, and the dispersion is thus trivially zero.

Transmission, reflection and integral flux

The simulation results for the ensemble-averaged transmission coefficient $\langle T \rangle$, the reflection coefficient $\langle R \rangle$ and the integral flux $\langle \varphi \rangle = \langle \int \int \varphi(\mathbf{r}, \mathbf{\Omega}) d\mathbf{\Omega} d\mathbf{r} \rangle$ are provided in Tabs. 5.8 to 5.13 for all the benchmark configurations, for both *Suite* I and *Suite* II conditions. For the sake of conciseness, for *Suite* II we denote by $\langle T \rangle$ the leakage current at $x = L$ and by $\langle R \rangle$ the leakage current at $x = 0$. For the case of *Suite* II, R and T are equivalent within statistical fluctuations, as expected. Atomic mixing results have been also given for reference. For each Monte Carlo transport simulation, the error on the estimated observable was significantly lower than 1%.

The computed values for the $1d$ slab configurations and the atomic mixing approximation are in excellent agreement (typically to two or three digits) with those previously reported in [1, 9–11, 171], and allow concluding that our choice for the benchmark specifications is coherent. For all examined cases, the atomic mixing approximation generally yields poor results as compared with the benchmark solutions, and in some cases the discrepancy can add up to several orders of magnitude. In addition, the atomic mixing solutions for several cases are strictly identical, since the ensemble-averaged total and scattering cross sections are identical by design. Concerning the benchmark solutions in dimension $d = 1, 2$ and 3, the impact of dimension on the transmission and reflection coefficient is stronger between $d = 1$ and $d = 2$ than between $d = 2$ and $d = 3$, as expected on physical grounds, and has a large variability between cases (from less than 1% for case $1b$ in *Suite* I, to almost 100% for case $2b$ in *Suite* II). For *Suite* I configurations, the reflection coefficient $\langle R \rangle$ in $d = 1$ is always larger than those in $d = 2, 3$. The transmission coefficient $\langle T \rangle$ is also generally larger, apart from cases $1a$, $1c$, and $3a$, where it is smaller. For *Suite* II configurations, the leakage coefficient in $d = 1$ is generally larger than in $d = 2, 3$, apart from case $1a$, where it is smaller, and case $3a$, where it is almost constant with respect to dimension.

Distributions of transmission and reflection coefficients

In order to better apprehend the variability of the transmission and reflection coefficients (or the average leakage current $J_{\text{ave}} = (T + R)/2$ in *Suite* II) around their average values, we have also computed their full distributions based on the available realizations in the generated ensembles. The resulting normalized histograms are illustrated in Figs. 5.4 to 5.9. As a general consideration, the dispersion of the observables decreases with increasing dimension: the mixing is increasingly efficient and the distribution is more peaked around the average, which is expected on physical grounds. However, even for $d = 3$ it is apparent that several configurations display highly non-symmetrical shapes, and possible cut-offs due to finite-size effects. Especially in $d = 1$, bi-modality may also arise for cases 2 and 3, which is due to the aforementioned effect of random geometries being entirely filled with either material α or β: the peaks observed in the distributions correspond to the values of the transmission or reflection coefficient associated to a fully red or fully blue realization. For the $1d$

Case	d	$\langle N_p \vert L \rangle$	$\Lambda(L)$	Λ	$\Lambda_\alpha(L)$	Λ_α	$\Lambda_\beta(L)$	Λ_β
1	1	102.1 ± 0.1	0.0990 ± 0.0001	0.099	0.985 ± 0.004	0.99	0.1098 ± 0.0004	0.11
	2	8206 ± 20	0.0988 ± 0.0003	0.099	0.944 ± 0.007	0.99	0.1058 ± 0.0009	0.11
	3	565646 ± 3586	0.0963 ± 0.0006	0.099	0.90 ± 0.02	0.99	0.098 ± 0.002	0.11
2	1	11.14 ± 0.03	0.987 ± 0.004	0.99	6.22 ± 0.03	9.9	0.695 ± 0.009	1.1
	2	101.4 ± 0.7	0.942 ± 0.007	0.99	5.00 ± 0.05	9.9	0.57 ± 0.01	1.1
	3	817 ± 15	0.93 ± 0.02	0.99	4.4 ± 0.1	9.9	0.50 ± 0.02	1.1
3	1	4.98 ± 0.02	2.48 ± 0.02	2.525	3.63 ± 0.03	5.05	3.70 ± 0.03	5.05
	2	21.2 ± 0.2	2.22 ± 0.02	2.525	2.96 ± 0.04	5.05	3.03 ± 0.04	5.05
	3	86 ± 2	2.07 ± 0.05	2.525	2.68 ± 0.09	5.05	2.53 ± 0.08	5.05

Table 5.5: Statistical properties of the Poisson tessellations used for the benchmark configurations, as a function of the dimension d. The quantity $\langle N_p \vert L \rangle$ denotes the average number of d-polyhedra composing the tessellation, $\Lambda(L)$ is the average correlation length measured by Monte Carlo ray tracing, and $\Lambda_\alpha(L)$ and $\Lambda_\beta(L)$ are the average chord lengths for material α and β, respectively, measured by Monte Carlo ray tracing. The corresponding expected theoretical values for infinite-size tessellations are denoted by Λ, Λ_α and Λ_β.

	Case:	1a	1b	1c	2a	2b	2c	3a	3b	3c
Atomic mixing	$\langle t \rangle$	122	41	65	67	40	66	117	39	66
$d = 1$	$\langle t \rangle$	112	66	107	91	59	71	135	42	66
	$\sigma[t]$	11	22	21	63	14	7	54	6	6
$d = 2$	$\langle t \rangle$	166	72	165	88	58	102	135	56	68
	$\sigma[t]$	9	4	28	26	7	30	39	17	5
$d = 3$	$\langle t \rangle$	3853	1752	4395	89	68	95	135	50	70
	$\sigma[t]$	790	347	1411	14	18	25	30	15	4

Table 5.6: Simulation times t for the benchmark configurations, expressed in seconds. The cases of *suite* I.

slab tessellations, the variances of the transmission and reflection coefficient have been numerically computed in [1]: the values obtained in our simulations are in excellent agreement with those previously reported.

Spatial flux

The spatial profiles of the ensemble-averaged scalar flux $\langle \varphi(x) \rangle = \langle \int \int \int \varphi(\mathbf{r}, \mathbf{\Omega}) d\mathbf{\Omega} dy dz \rangle$ are reported in Figs. 5.10 to 5.12. In TRIPOLI-4 ®, we estimate $\langle \varphi(x) \rangle$ by recording the flux within the spatial grid and by dividing the obtained result by the volume of each mesh. The corresponding data sets are available from the authors upon request. Consistently with the findings concerning the integral observables, the atomic mixing approximation usually leads to poor results as compared with the benchmark solutions for the spatial profiles. The spatial profiles for the atomic mixing approximation and for the $1d$ slab tessellations are in good agreement with those reported in [11]. As a general remark, the scalar flux in $d = 1$ is systematically larger than that in $d = 2$, which in turn is larger than that in $d = 3$. Some exceptions are nonetheless apparent, such as for instance in cases $1a$ for the *Suite* I configuration and $1c$ for the *Suite* II configuration. The impact of dimension on the benchmark solutions depends on the geometry and material configurations, and might vary between a few percent as in case $1a$ for both *Suite* I and *Suite* II, up to 100% or more in case $3b$ for *Suite* II.

	Case:	1a	1b	1c	2a	2b	2c	3a	3b	3c
Atomic mixing	$\langle t \rangle$	49	11	47	46	9	43	139	8	43
$d = 1$	$\langle t \rangle$	100	38	103	105	30	41	190	14	41
	$\sigma[t]$	25	12	21	263	11	8	166	5	8
$d = 2$	$\langle t \rangle$	513	449	512	80	30	52	170	13	44
	$\sigma[t]$	90	82	77	69	5	12	116	3	6
$d = 3$	$\langle t \rangle$	79359	75578	77662	117	85	97	166	17	50
	$\sigma[t]$	23219	21140	22162	40	33	30	83	5	7

Table 5.7: Simulation times t for the benchmark configurations, expressed in seconds. The cases of *suite* II.

Case		Atomic mixing	$1d$	$2d$	$3d$
1a	$\langle R \rangle$	$0.4954 \pm 5 \times 10^{-4}$	0.437 ± 0.002	$0.4060 \pm 6 \times 10^{-4}$	$0.4091 \pm 5 \times 10^{-4}$
	$\langle T \rangle$	$0.00474 \pm 7 \times 10^{-5}$	$0.0148 \pm 2 \times 10^{-4}$	0.0173 ± 10^{-4}	0.0163 ± 10^{-4}
	$\langle \varphi \rangle$	5.501 ± 0.007	6.10 ± 0.01	6.365 ± 0.008	6.328 ± 0.007
1b	$\langle R \rangle$	0.0193 ± 10^{-4}	$0.0845 \pm 4 \times 10^{-4}$	$0.0454 \pm 2 \times 10^{-4}$	$0.0377 \pm 2 \times 10^{-4}$
	$\langle T \rangle$	$1.2 \times 10^{-5} \pm 3 \times 10^{-6}$	$0.00164 \pm 7 \times 10^{-5}$	$0.00108 \pm 3 \times 10^{-5}$	$0.00085 \pm 3 \times 10^{-5}$
	$\langle \varphi \rangle$	1.079 ± 0.001	2.90 ± 0.01	2.163 ± 0.005	1.918 ± 0.003
1c	$\langle R \rangle$	$0.4780 \pm 5 \times 10^{-4}$	$0.4767 \pm 5 \times 10^{-4}$	$0.4078 \pm 5 \times 10^{-4}$	$0.4059 \pm 5 \times 10^{-4}$
	$\langle T \rangle$	$0.00390 \pm 7 \times 10^{-5}$	$0.0159 \pm 3 \times 10^{-4}$	0.0179 ± 10^{-4}	0.0164 ± 10^{-4}
	$\langle \varphi \rangle$	5.184 ± 0.006	6.97 ± 0.03	6.52 ± 0.01	6.303 ± 0.008

Table 5.8: Ensemble-averaged observables for the benchmark configurations: *suite* I - case 1.

Case		Atomic mixing	$1d$	$2d$	$3d$
2a	$\langle R \rangle$	$0.4954 \pm 5 \times 10^{-4}$	0.239 ± 0.003	0.226 ± 0.002	0.225 ± 0.001
	$\langle T \rangle$	$0.00474 \pm 7 \times 10^{-5}$	$0.0973 \pm 9 \times 10^{-4}$	$0.0969 \pm 7 \times 10^{-4}$	$0.0937 \pm 4 \times 10^{-4}$
	$\langle \varphi \rangle$	5.501 ± 0.007	7.64 ± 0.02	7.59 ± 0.02	7.57 ± 0.01
2b	$\langle R \rangle$	0.0193 ± 10^{-4}	$0.2866 \pm 8 \times 10^{-4}$	$0.1980 \pm 8 \times 10^{-4}$	$0.1616 \pm 8 \times 10^{-4}$
	$\langle T \rangle$	$1.2 \times 10^{-5} \pm 3 \times 10^{-6}$	0.194 ± 0.001	$0.1465 \pm 9 \times 10^{-4}$	$0.1194 \pm 9 \times 10^{-4}$
	$\langle \varphi \rangle$	1.079 ± 0.001	11.69 ± 0.04	9.11 ± 0.03	7.77 ± 0.03
2c	$\langle R \rangle$	$0.4780 \pm 5 \times 10^{-4}$	$0.4334 \pm 8 \times 10^{-4}$	$0.3677 \pm 6 \times 10^{-4}$	$0.3457 \pm 5 \times 10^{-4}$
	$\langle T \rangle$	$0.00390 \pm 7 \times 10^{-5}$	0.184 ± 0.002	0.179 ± 0.002	$0.1651 \pm 9 \times 10^{-4}$
	$\langle \varphi \rangle$	5.184 ± 0.006	12.51 ± 0.06	11.46 ± 0.05	10.76 ± 0.03

Table 5.9: Ensemble-averaged observables for the benchmark configurations: *suite* I - case 2.

Case		Atomic mixing	$1d$	$2d$	$3d$
3a	$\langle R \rangle$	$0.7856 \pm 4 \times 10^{-4}$	0.692 ± 0.003	0.680 ± 0.003	0.675 ± 0.001
	$\langle T \rangle$	$0.0670 \pm 2 \times 10^{-4}$	0.163 ± 0.002	0.168 ± 0.002	$0.1692 \pm 9 \times 10^{-4}$
	$\langle \varphi \rangle$	14.89 ± 0.02	16.44 ± 0.05	16.46 ± 0.05	16.38 ± 0.03
3b	$\langle R \rangle$	$0.00206 \pm 5 \times 10^{-5}$	$0.0361 \pm 2 \times 10^{-4}$	$0.0217 \pm 2 \times 10^{-4}$	$0.0165 \pm 2 \times 10^{-4}$
	$\langle T \rangle$	$6 \times 10^{-6} \pm 2 \times 10^{-6}$	$0.0760 \pm 7 \times 10^{-4}$	$0.0568 \pm 6 \times 10^{-4}$	$0.0457 \pm 9 \times 10^{-4}$
	$\langle \varphi \rangle$	1.008 ± 0.001	5.16 ± 0.02	4.00 ± 0.02	3.47 ± 0.03
3c	$\langle R \rangle$	$0.4780 \pm 5 \times 10^{-4}$	0.445 ± 0.001	0.411 ± 0.001	$0.3979 \pm 7 \times 10^{-4}$
	$\langle T \rangle$	$0.00390 \pm 7 \times 10^{-5}$	0.104 ± 0.002	0.094 ± 0.002	0.086 ± 0.001
	$\langle \varphi \rangle$	5.184 ± 0.006	9.00 ± 0.07	8.30 ± 0.07	7.89 ± 0.03

Table 5.10: Ensemble-averaged observables for the benchmark configurations: *suite* I - Case 3.

Case		Atomic mixing	$1d$	$2d$	$3d$
1a	$\langle J_{\text{ave}} \rangle$	$0.1373 \pm 3 \times 10^{-4}$	$0.1525 \pm 3 \times 10^{-4}$	$0.1592 \pm 3 \times 10^{-4}$	$0.1583 \pm 3 \times 10^{-4}$
	$\langle \varphi \rangle$	7.978 ± 0.008	7.70 ± 0.01	7.512 ± 0.008	7.530 ± 0.008
1b	$\langle J_{\text{ave}} \rangle$	0.0270 ± 10^{-4}	$0.0724 \pm 3 \times 10^{-4}$	$0.0542 \pm 2 \times 10^{-4}$	$0.0481 \pm 2 \times 10^{-4}$
	$\langle \varphi \rangle$	1.040 ± 0.001	3.735 ± 0.009	2.182 ± 0.003	1.808 ± 0.003
1c	$\langle J_{\text{ave}} \rangle$	$0.1295 \pm 2 \times 10^{-4}$	$0.1742 \pm 7 \times 10^{-4}$	$0.1630 \pm 3 \times 10^{-4}$	$0.1577 \pm 3 \times 10^{-4}$
	$\langle \varphi \rangle$	7.408 ± 0.008	9.62 ± 0.03	7.77 ± 0.01	7.455 ± 0.008

Table 5.11: Ensemble-averaged observables for the benchmark configurations: *suite* II - case 1.

Case		Atomic mixing	$1d$	$2d$	$3d$
2a	$\langle J_{\text{ave}} \rangle$	$0.1373 \pm 3 \times 10^{-4}$	$0.1904 \pm 3 \times 10^{-4}$	$0.1898 \pm 3 \times 10^{-4}$	$0.1892 \pm 3 \times 10^{-4}$
	$\langle \varphi \rangle$	7.978 ± 0.008	8.29 ± 0.03	7.46 ± 0.03	7.27 ± 0.01
2b	$\langle J_{\text{ave}} \rangle$	0.0270 ± 10^{-4}	$0.2918 \pm 8 \times 10^{-4}$	$0.2274 \pm 6 \times 10^{-4}$	$0.1931 \pm 4 \times 10^{-4}$
	$\langle \varphi \rangle$	1.040 ± 0.001	10.75 ± 0.02	7.97 ± 0.02	6.54 ± 0.01
2c	$\langle J_{\text{ave}} \rangle$	$0.1295 \pm 2 \times 10^{-4}$	0.312 ± 0.001	0.286 ± 0.001	$0.2688 \pm 6 \times 10^{-4}$
	$\langle \varphi \rangle$	7.408 ± 0.008	11.92 ± 0.03	10.39 ± 0.03	9.55 ± 0.02

Table 5.12: Ensemble-averaged observables for the benchmark configurations: *suite* II - case 2.

Case		Atomic mixing	$1d$	$2d$	$3d$
3a	$\langle J_{\text{ave}} \rangle$	$0.3716 \pm 3 \times 10^{-4}$	$0.4112 \pm 6 \times 10^{-4}$	$0.4115 \pm 6 \times 10^{-4}$	$0.4098 \pm 4 \times 10^{-4}$
	$\langle \varphi \rangle$	25.88 ± 0.03	27.3 ± 0.2	24.3 ± 0.2	22.82 ± 0.07
3b	$\langle J_{\text{ave}} \rangle$	0.0252 ± 10^{-4}	$0.1294 \pm 5 \times 10^{-4}$	$0.1003 \pm 4 \times 10^{-4}$	$0.0868 \pm 3 \times 10^{-4}$
	$\langle \varphi \rangle$	0.958 ± 0.001	5.93 ± 0.02	3.75 ± 0.02	2.98 ± 0.01
3c	$\langle J_{\text{ave}} \rangle$	$0.1295 \pm 2 \times 10^{-4}$	0.225 ± 0.001	0.207 ± 0.001	$0.1974 \pm 7 \times 10^{-4}$
	$\langle \varphi \rangle$	7.408 ± 0.008	10.56 ± 0.05	8.78 ± 0.05	8.15 ± 0.02

Table 5.13: Ensemble-averaged observables for the benchmark configurations: *suite* II - case 3.

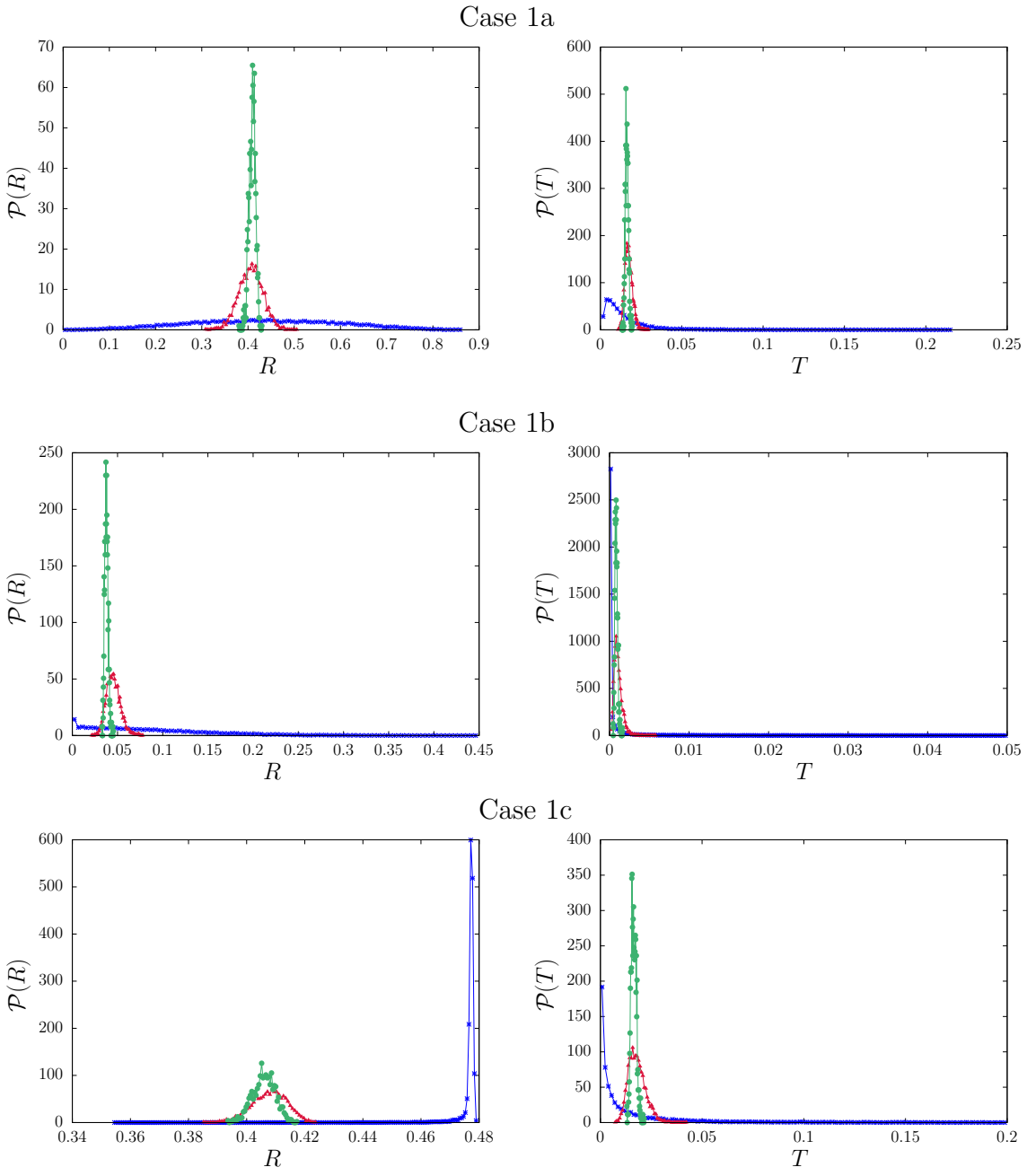

Figure 5.4: Left column: normalized distributions $\mathcal{P}(R)$ of the reflection coefficients R; right column: normalized distributions $\mathcal{P}(T)$ of the transmission coefficients T. *Suite* I configurations, case 1. Blue crosses represent the $1d$ slab tessellations, red triangles the $2d$ extruded tessellations, and green circles the $3d$ tessellations.

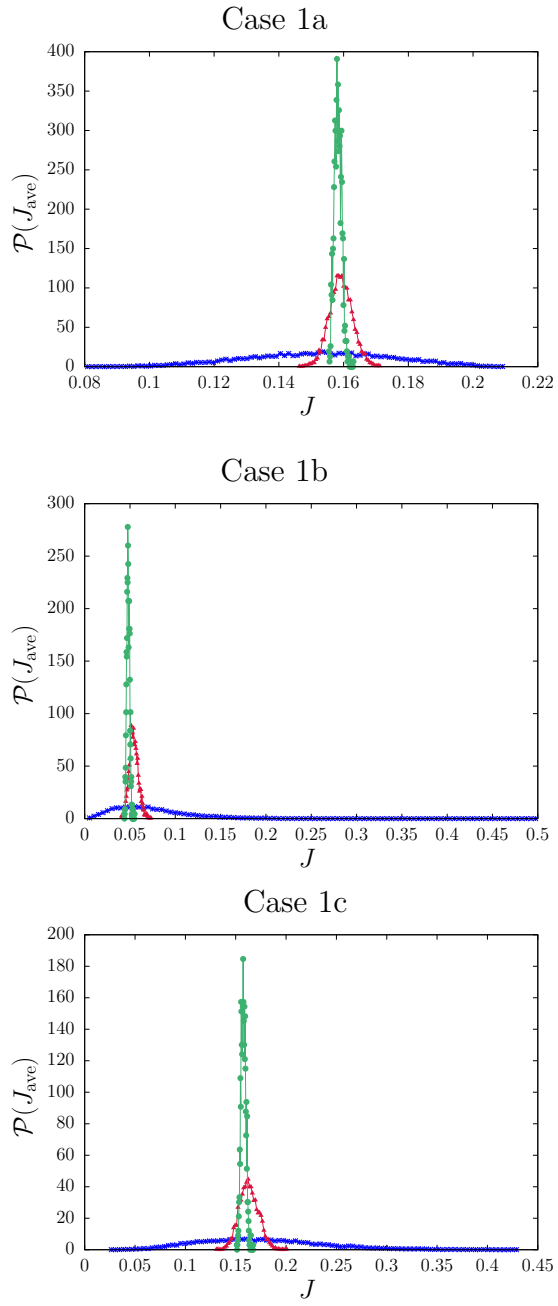

Figure 5.5: Normalized distributions $\mathcal{P}(J_{\rm ave})$ of the average leakage current $J_{\rm ave} = (T + R)/2$ for *suite* II configurations, case 1. Blue crosses represent the $1d$ slab tessellations, red triangles the $2d$ extruded tessellations, and green circles the $3d$ tessellations.

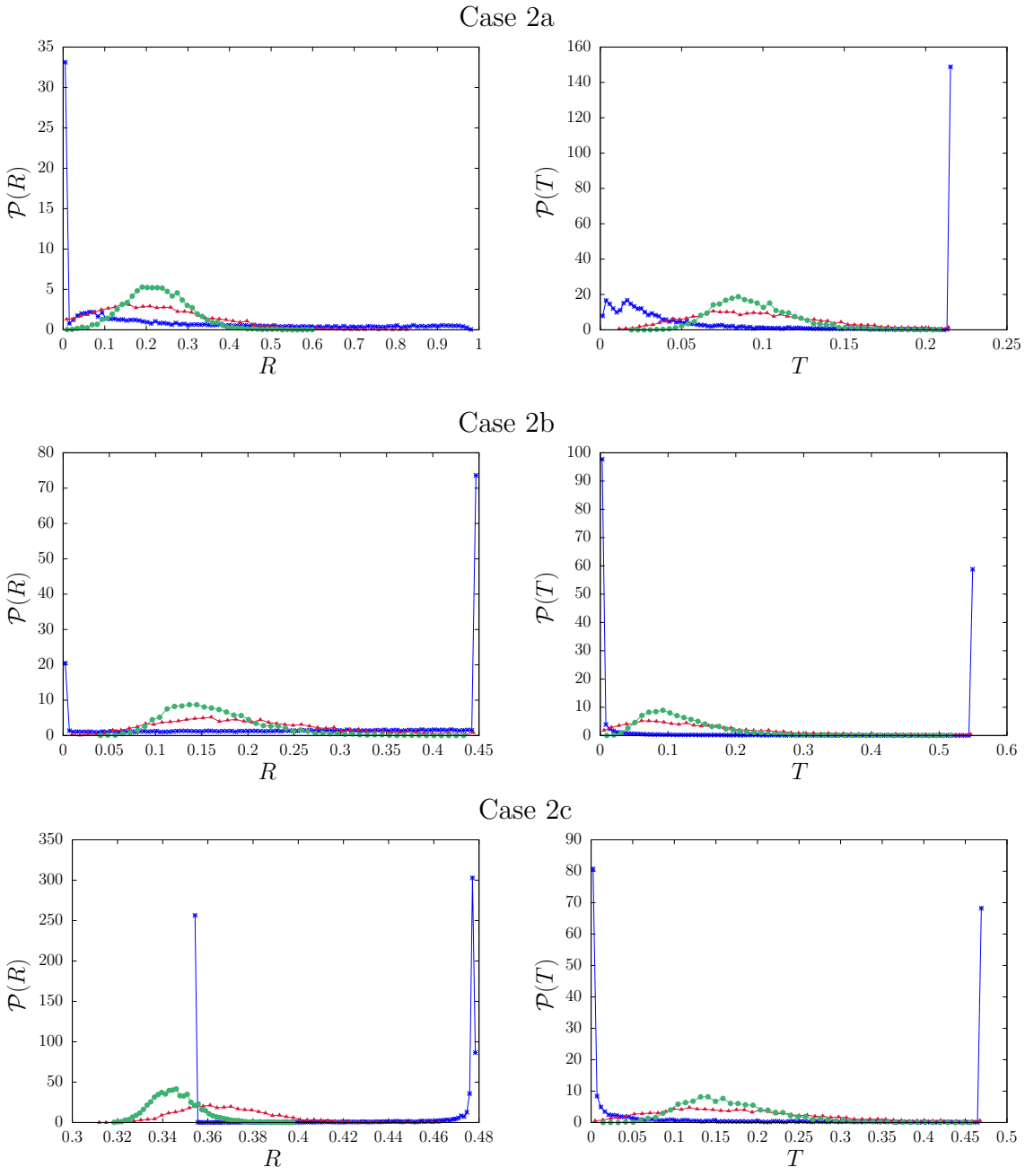

Figure 5.6: Left column: normalized distributions $\mathcal{P}(R)$ of the reflection coefficients R; right column: normalized distributions $\mathcal{P}(T)$ of the transmission coefficients T. *Suite* I configurations, case 2. Blue crosses represent the $1d$ slab tessellations, red triangles the $2d$ extruded tessellations, and green circles the $3d$ tessellations.

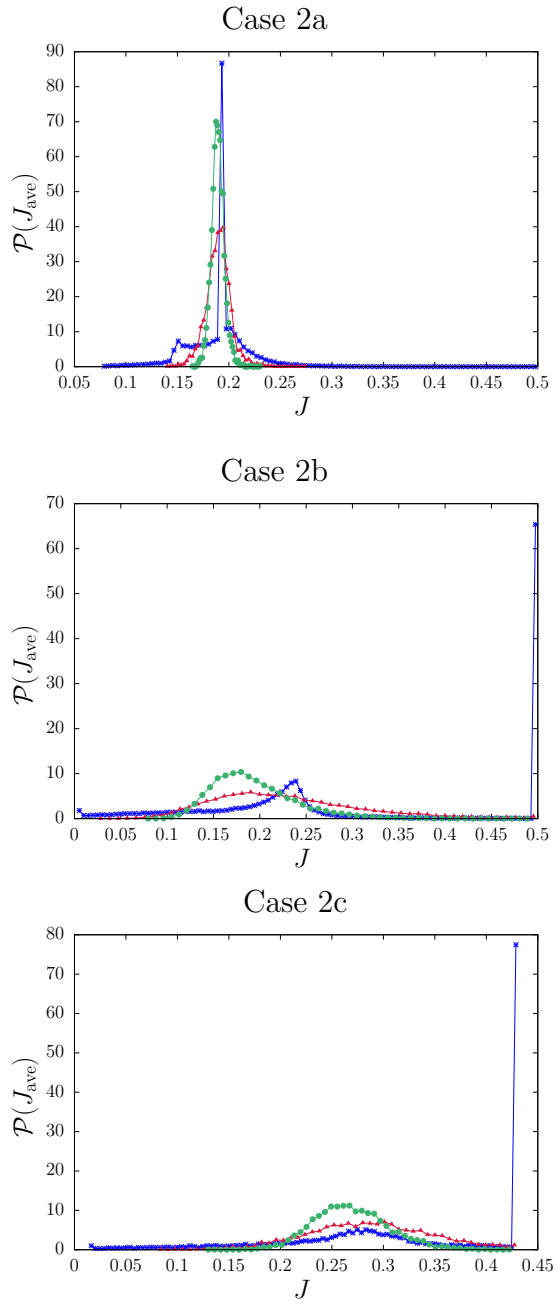

Figure 5.7: Normalized distributions $\mathcal{P}(J_{\rm ave})$ of the average leakage current $J_{\rm ave} = (T + R)/2$ for *suite* II configurations, case 2. Blue crosses represent the $1d$ slab tessellations, red triangles the $2d$ extruded tessellations, and green circles the $3d$ tessellations.

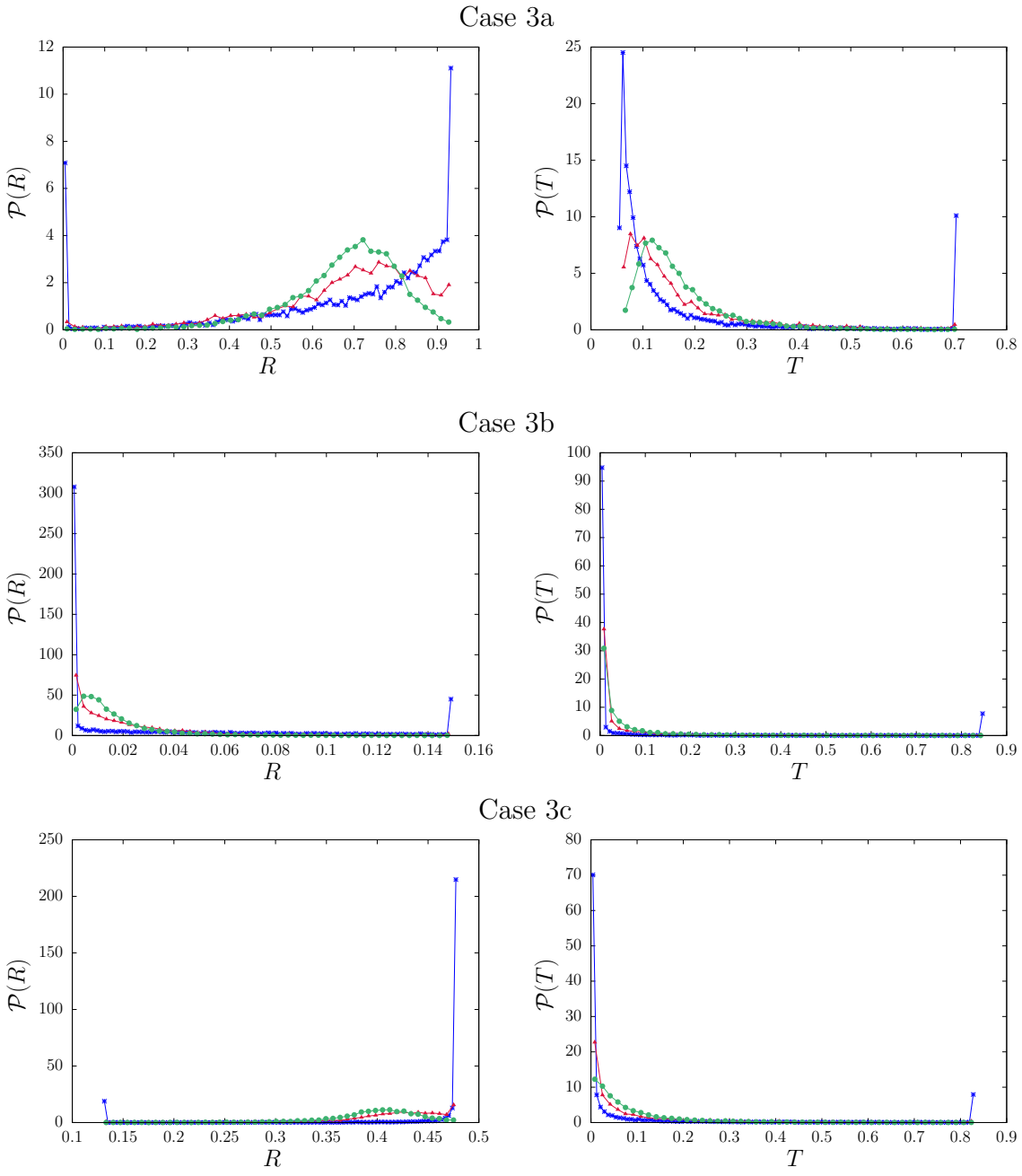

Figure 5.8: Left column: normalized distributions $\mathcal{P}(R)$ of the reflection coefficients R; right column: normalized distributions $\mathcal{P}(T)$ of the transmission coefficients T. *Suite* I configurations, case 3. Blue crosses represent the $1d$ slab tessellations, red triangles the $2d$ extruded tessellations, and green circles the $3d$ tessellations.

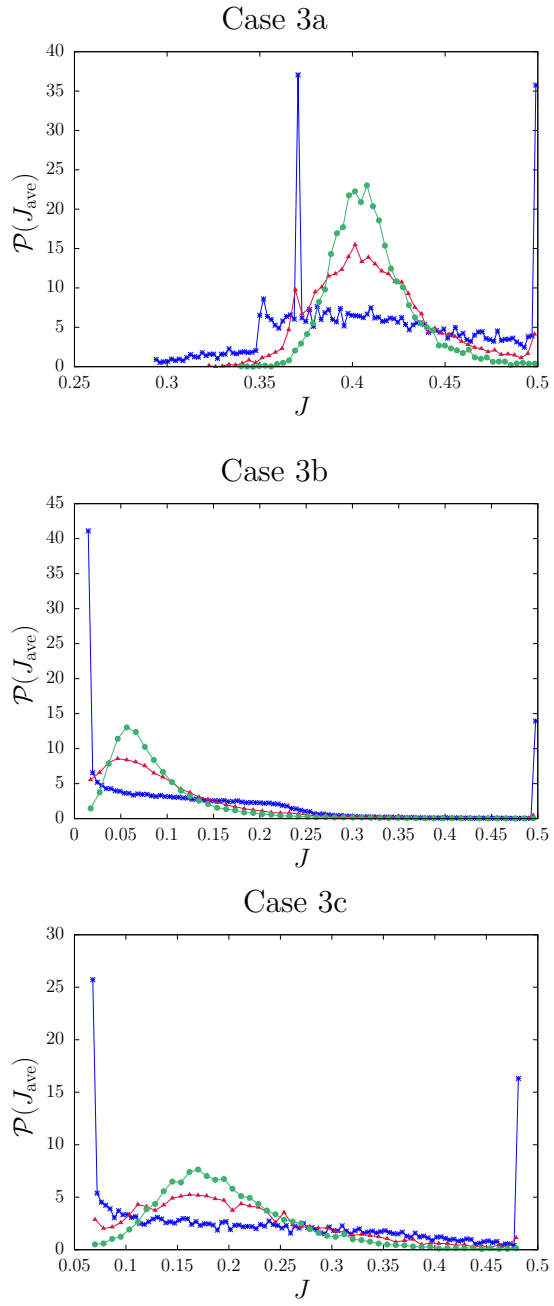

Figure 5.9: Normalized distributions $\mathcal{P}(J_{\rm ave})$ of the average leakage current $J_{\rm ave} = (T + R)/2$ for *suite* II configurations, case 3. Blue crosses represent the $1d$ slab tessellations, red triangles the $2d$ extruded tessellations, and green circles the $3d$ tessellations.

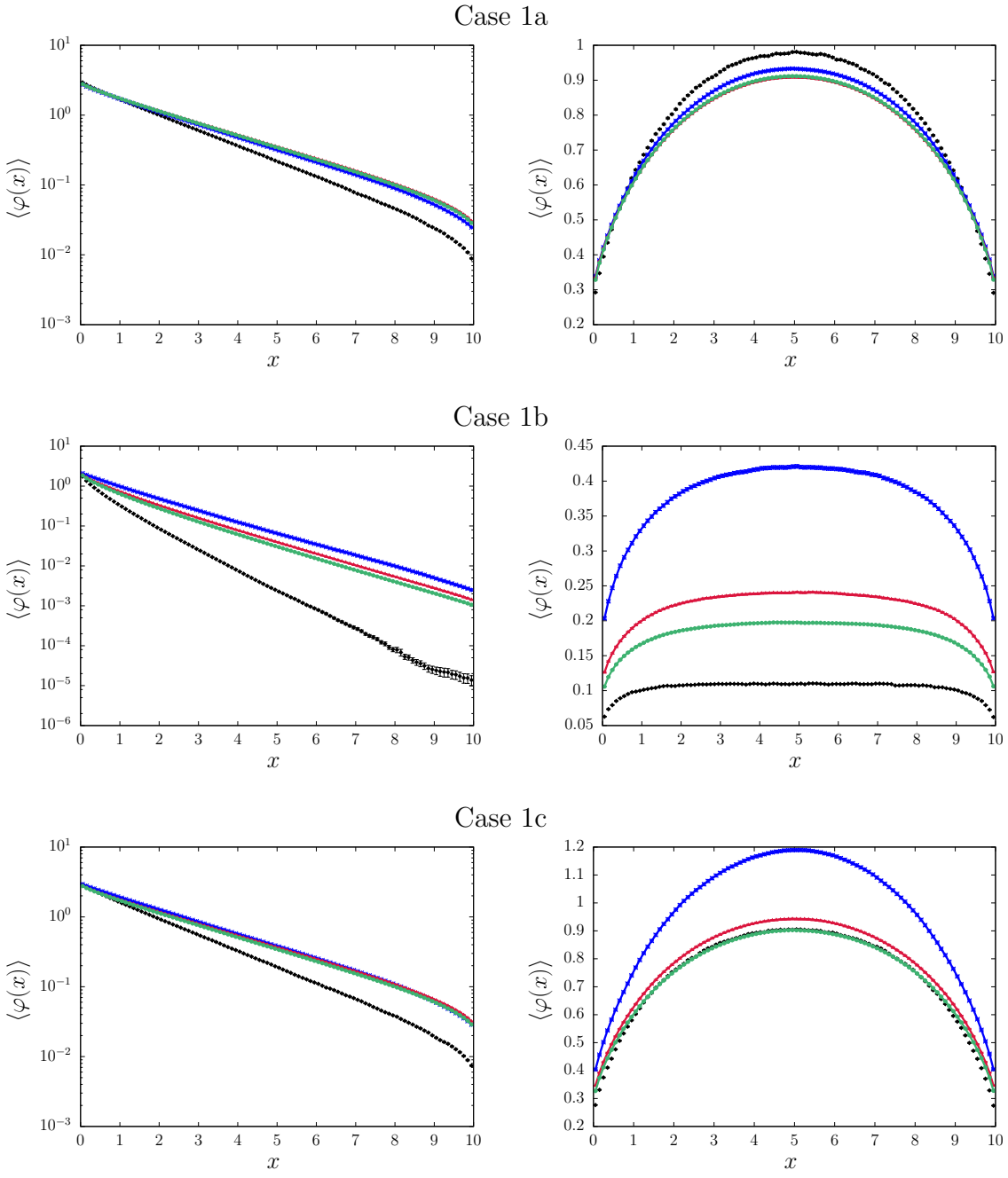

Figure 5.10: Ensemble-averaged spatial scalar flux for the benchmark configurations: Case 1. Left column: *Suite* I configurations; right column: *Suite* II configurations. Black diamonds represent the atomic mixing approximation, blue crosses the $1d$ slab tessellations, red triangles the $2d$ extruded tessellations, and green circles the $3d$ tessellations.

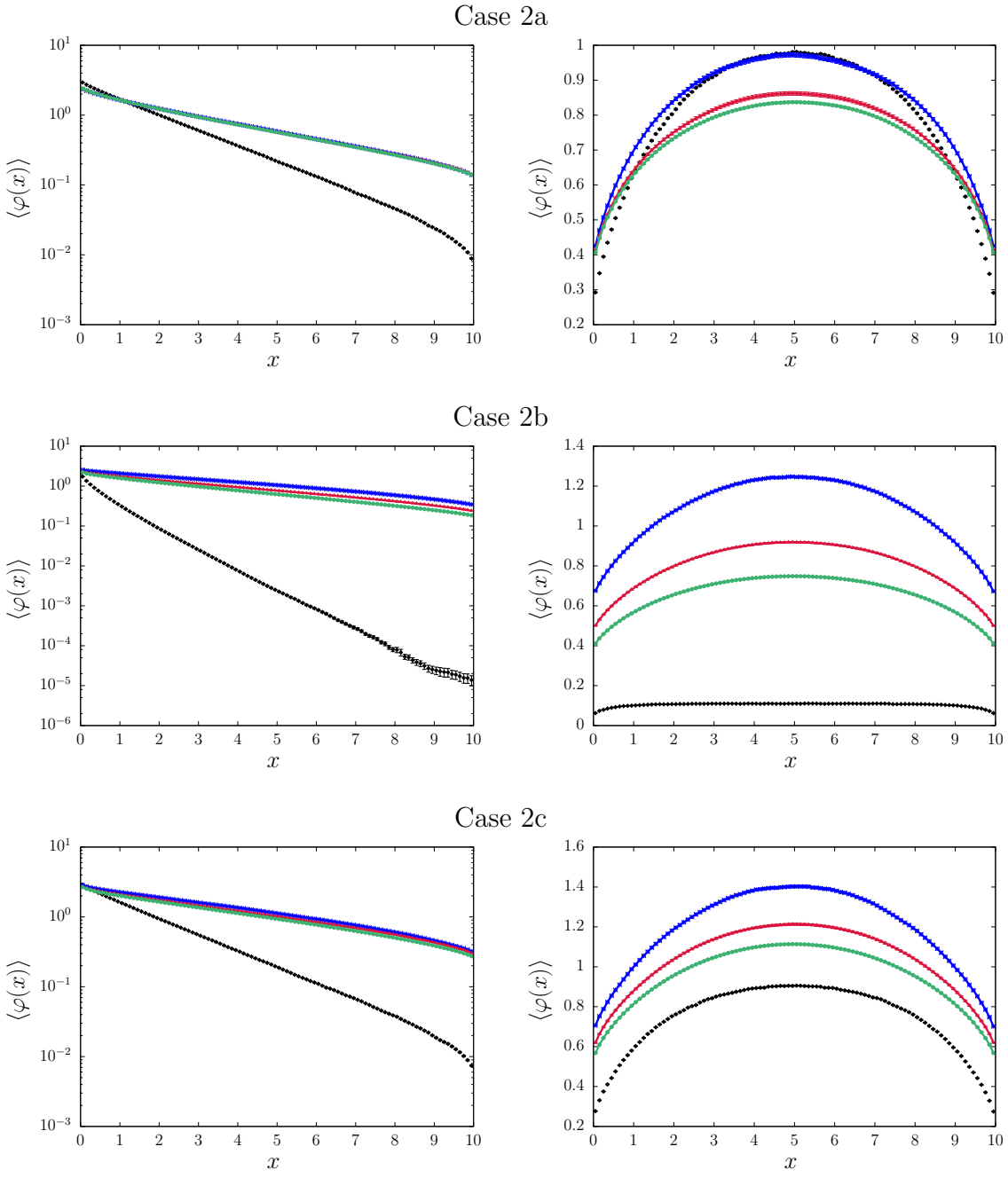

Figure 5.11: Ensemble-averaged spatial scalar flux for the benchmark configurations: Case 2. Left column: *Suite* I configurations; right column: *Suite* II configurations. Black diamonds represent the atomic mixing approximation, blue crosses the $1d$ slab tessellations, red triangles the $2d$ extruded tessellations, and green circles the $3d$ tessellations.

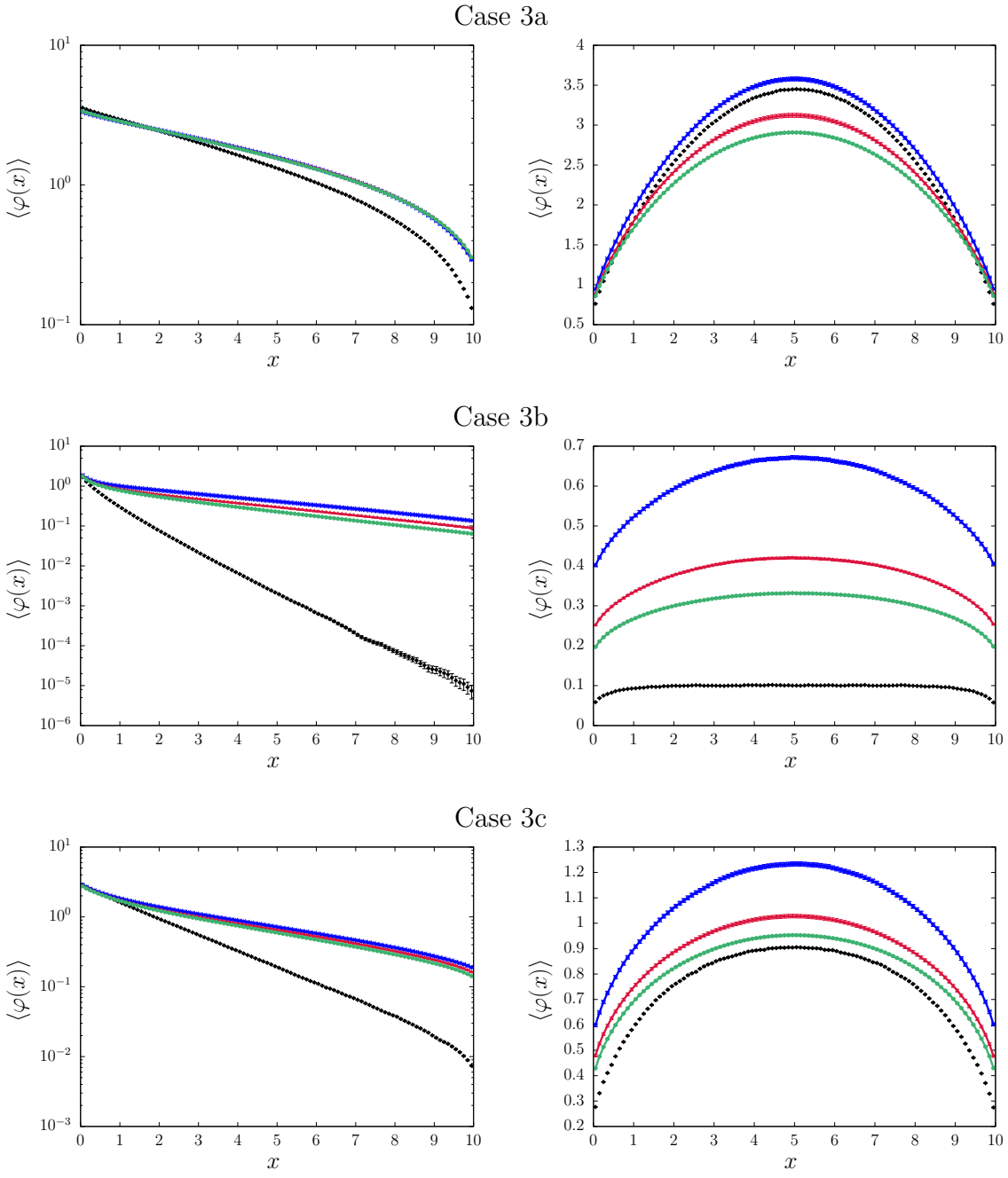

Figure 5.12: Ensemble-averaged spatial scalar flux for the benchmark configurations: Case 3. Left column: *Suite* I configurations; right column: *Suite* II configurations. Black diamonds represent the atomic mixing approximation, blue crosses the $1d$ slab tessellations, red triangles the $2d$ extruded tessellations, and green circles the $3d$ tessellations.

Case	$\Sigma_{s,\alpha}$	$\Sigma_{a,\alpha}$	$\Sigma_{s,\beta}$	$\Sigma_{a,\beta}$
$1a$	0	0	1	0
$1b$	0	0	10	0
$2a$	0	10	1	0
$2b$	0	10	10	0

Table 5.14: Material parameters for the two cases $1, 2$ of benchmark configurations and the two sub-cases a, b.

5.4 The effects of mixing statistics

In Chapter 2, we have introduced several models of random media based on stochastic tessellations, namely homogeneous and isotropic Poisson tessellations (denoted by $m = \mathcal{P}$), Voronoi tessellations (denoted by $m = \mathcal{V}$), and Box tessellations (denoted by $m = \mathcal{B}$). In order to investigate the effects of such mixing statistics on particle transport, we will now introduce new benchmark specifications, partially inspired from the ALP benchmark [1]. This section is organized as follows. In Sec. 5.4.1 we will describe two benchmark configurations. In Sec. 5.4.2 we will provide reference solutions by using the TRIPOLI-4 ® Monte Carlo code, and discuss how mixing statistics affects ensemble-averaged observables.

5.4.1 Benchmark specifications

We propose two benchmark configurations for single-speed linear particle transport through binary mixtures in dimension $d = 3$. For both configurations we set the same geometry and source specifications. The geometry consists of a box of side $L = 10$, with the same boundary conditions as in the d-dimensional generalization of the ALP benchmark introduced above. We will apply a normalized incident angular flux on the leakage surface at $x = 0$ (with zero interior sources).

In benchmark case 1, material α is void, and material β is purely scattering; in benchmark case 2, material α is purely absorbing, and material β is purely scattering. The former case could represent for instance neutron transport in water-vapour mixtures or photon propagation through turbid media, the probability p determining the fraction of voids. The latter case could represent for instance neutron diffusion in the presence of randomly distributed traps, such as Boron or Gadolinium grains, the probability p determining the fraction of absorbers.

The material compositions for the two benchmarks are provided in Tab. 5.14. For each case, we consider two sub-cases a and b by varying the scattering macroscopic cross sections: we set a scattering cross section $\Sigma_{s,\beta} = 1$ for cases $1a$ and $2a$, and $\Sigma_{s,\beta} = 10$ for cases $1b$ and $2b$. The absorbing cross section for material β is zero for all cases and sub-cases. For material α, we set $\Sigma_{a,\alpha} = 10$ for case $2a$ and $2b$ (absorber), and $\Sigma_{a,\alpha} = 0$ elsewhere. Scattering is assumed to be isotropic.

Similarly as in the case of the previous benchmark, the fiducial quantities are the ensemble-averaged reflection probability $\langle R \rangle$ on the face where the incident flux is imposed, the ensemble-averaged transmission probability $\langle T \rangle$ on the opposite face, and the ensemble-averaged scalar particle flux $\langle \varphi \rangle$ within the box.

The construction of the Poisson, Voronoi and Box tessellations has been detailed in Sec. 2.3.1, 2.5.1 and 2.4.1, respectively. For each tessellation we examine three average correlation lengths: $\Lambda_c = 1$, $\Lambda_c = 0.5$ and $\Lambda_c = 0.1$; and seven probabilities of assigning a label α: $p = 0.05$, $p = 0.15$, $p = 0.30$, $p = 0.50$, $p = 0.70$, $p = 0.85$ and $p = 0.95$. The tessellation densities $\rho_{\mathcal{P}}$, $\rho_{\mathcal{V}}$ and $\rho_{\mathcal{B}}$ can be easily derived based on Eq. (2.83) and are recalled in Tab. 5.15. For illustration, examples of realizations of Poisson, Voronoi and Box tessellations for the benchmark configurations are displayed in Figs. 5.13 and Fig. 5.14. For the sake of completeness, we have also considered the so-called atomic mix model.

Λ_c	$\rho_{\mathcal{P}}$	$\rho_{\mathcal{V}}$	$\rho_{\mathcal{B}}$
1	1	0.6872	0.66667
0.5	2	1.3744	1.33333
0.1	10	6.872	6.66667

Table 5.15: Parameters $\rho_{\mathcal{P}}$, $\rho_{\mathcal{V}}$ and $\rho_{\mathcal{B}}$ chosen for the benchmark configurations, as a function of the average correlation length Λ_c.

5.4.2 Monte Carlo simulation results

Simulation parameters

The reference solutions for the probabilities $\langle R \rangle$ and $\langle T \rangle$ and the ensemble-averaged scalar particle flux $\langle \varphi(x) \rangle$ have been computed as described for the previous benchmark. The number of simulated particle histories per configuration is 10^6. The number M of realizations used for the Monte Carlo simulations has been chosen as follows. For configurations with $\Lambda_c = 1$ we have performed 10^3 realizations; for $\Lambda_c = 0.5$ we have taken 8×10^2 realizations; and for $\Lambda_c = 0.1$ we have taken 2×10^2 realizations. Similarly as for Poisson tessellations, Voronoi and Box tessellations also share ergodic properties [85, 87]: smaller average correlation lengths Λ_c require a lower number of realizations to achieve statistically stable ensemble averages.

Computer time

The average computer time of a transport simulation increases significantly for decreasing average correlation length Λ_c of the tessellation, as shown Tab. 5.16. For the calculations discussed here we have again used the pre-computed connectivity maps, with considerable speed-ups for the most fragmented geometries. Transport calculations have been run on the same computer cluster as above. The average computer time t for case $1a$ with $p = 0.05$ is displayed in Tab. 5.16 as a function of the mixing statistics m and of the average correlation length Λ_c of the tessellation. It is apparent that t increases with the complexity of the system, i.e., the number of polyhedra composing the tessellation. Nevertheless, this is not true for geometries with higher Λ_c: simulations in Voronoi tessellations are longer than those in Poisson and Box tessellations, in spite of a lower number of polyhedra. This is likely due to the larger average number of faces in Voronoi geometries, which slows down particle tracking. For geometries composed of a large number of polyhedra, the complexity of the system outweighs this effect. Moreover, the dispersion on the simulation time seems correlated to the dispersion on the number of polyhedra: thus, this dispersion may become very large, and even be comparable to the average t, for Poisson tessellations. Atomic mix simulations have no associated dispersion.

Reflection, transmission and integral flux

The statistical properties of the random media adopted for the benchmark configurations, including the average chord length through colored clusters, have been determined by Monte Carlo simulation and are displayed in Fig. 5.15, which allows probing finite-size effects.

Concerning transport-related observables, the simulation results for the ensemble-averaged reflection probability $\langle R \rangle$, the transmission probability $\langle T \rangle$ and the integral flux $\langle \varphi \rangle = \langle \int \int \varphi(\mathbf{r}, \mathbf{\Omega}) d\mathbf{\Omega} d\mathbf{r} \rangle$ are provided in Figs. 5.16 and 5.17 for all the benchmark configurations, as a function of p, m and Λ_c. Atomic mix results are also provided for reference.

To begin with, we analyse the behaviour of these observables as a function of p. For case 1, the transmission probability increases with the void fraction p. For large values of p, the medium is mainly composed of voids, which enhances transmission because particle trajectories are not hindered by collisions. When p decreases, the proportion of scattering material increases and so does the probability for a particle to scatter, change direction and leak from the face where the source is

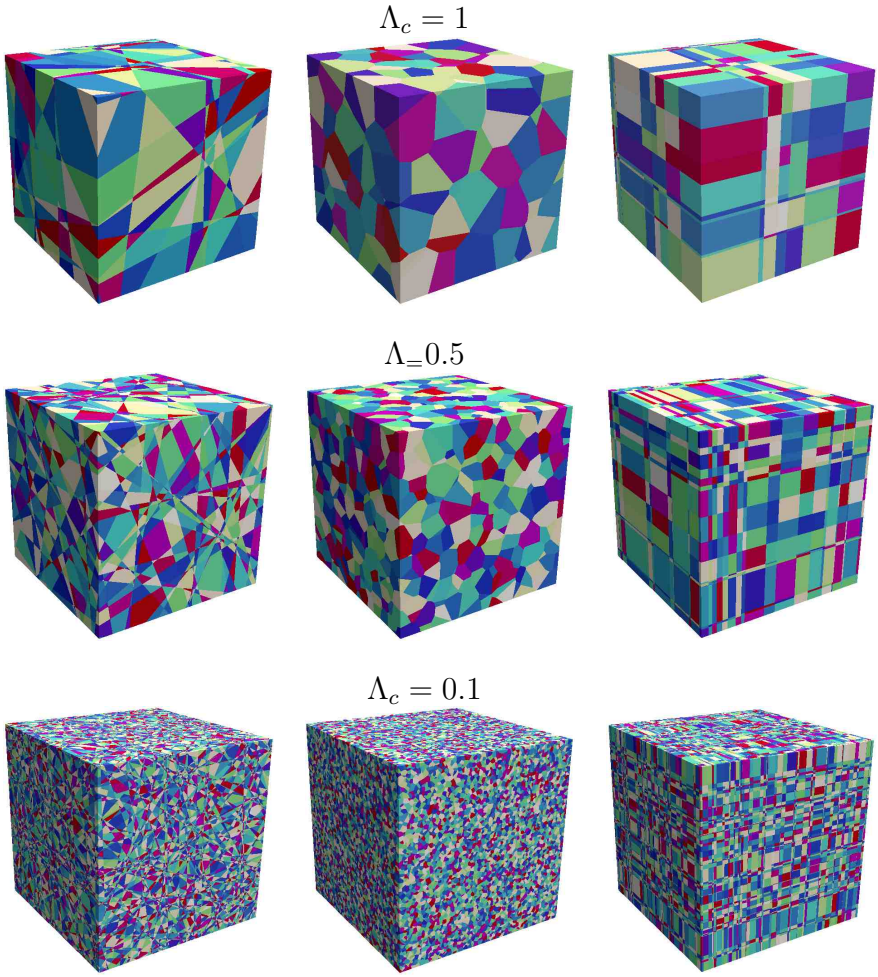

Figure 5.13: Examples of realizations of tessellations corresponding to the benchmark specifications before attributing the material label, for $\Lambda_c = 1$ (top), $\Lambda_c = 0.5$ (center) and $\Lambda_c = 0.1$ (bottom). The size of the cube is $L = 10$. Left: Poisson tessellations; middle: Voronoi tessellations; right: Voronoi tessellations.

imposed. Symmetrically, the reflection probability decreases with p: this is expected on physical grounds, since for case 1 we have $\langle T\rangle + \langle R\rangle = 1$ from particle conservation. Percolation of the void fraction appear to play no significant role for the configurations considered here: the variation of $\langle T\rangle$ and $\langle R\rangle$ with respect to p is smooth and no threshold effects at $p = p_c$ are apparent. The void fraction p has no impact on the integral flux for case 1. Actually, as stated above, $\langle\varphi\rangle = \langle\ell_V\rangle$, and from Cauchy formula for one-speed random walks in purely scattering domains we have

$$\langle\ell_V\rangle = 4\frac{V}{S_{leak}} \tag{5.16}$$

where S_{leak} is the surface area of the boundaries where leakage conditions are applied [78, 93]. This formula, which can be understood as a non-trivial generalization of Cauchy formula applying to the average chord lengths [78], holds true provided that particles enter the domain uniformly and isotropically, which is ensured here by the source that we have chosen and by symmetry considerations. Hence, the flux $\langle\varphi\rangle$ depends exclusively on the ratio of purely geometrical quantities, namely, $\langle\varphi\rangle = 4V/S_{leak}$, which for our benchmark yields $\langle\varphi\rangle = 20$.

For case 2, reflection, transmission and integral flux all decrease with increasing absorber fraction p. This is also expected on physical grounds: the larger is p, the smaller is the survival probability of particles and the shorter is the average residence time within the box (and hence the integral flux). Although Eq. (5.16) can be generalized to include also absorbing media (and even multiplication), the resulting formula will depend on the specific features of the travelling particles and will not have a universal character [78, 93].

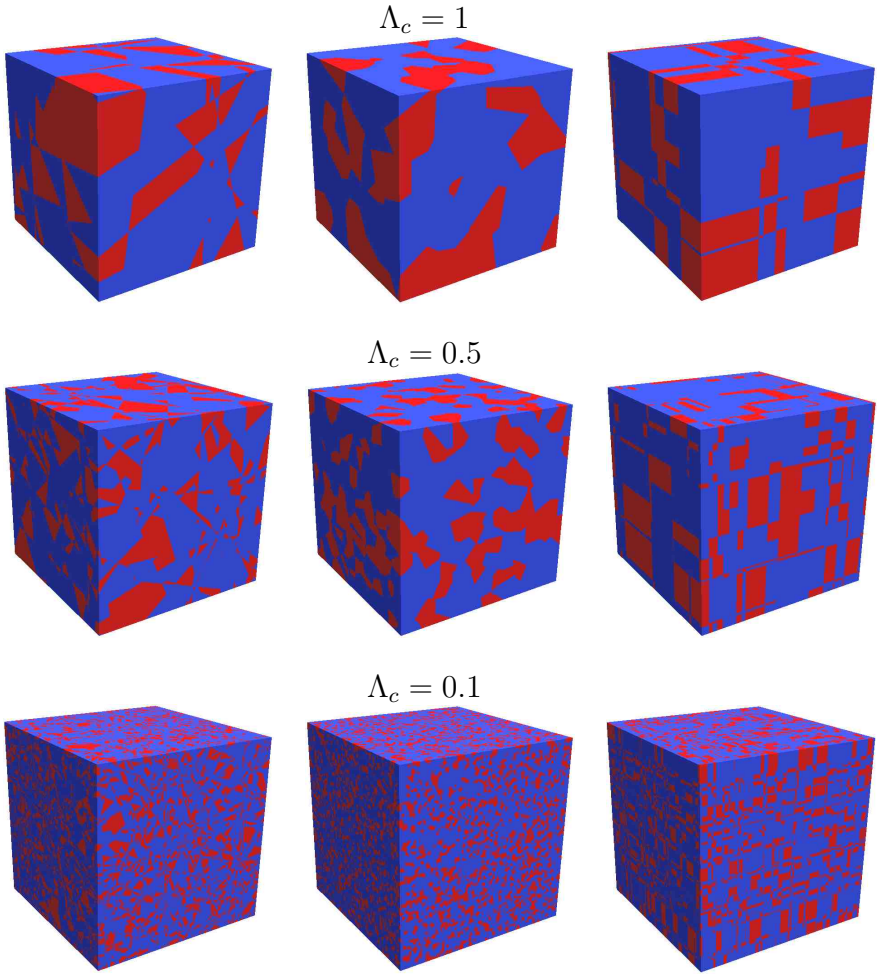

Figure 5.14: Examples of realizations of tessellations corresponding to the benchmark specifications after attributing the material label, with probability $p = 0.3$ of assigning the label α, for $\Lambda_c = 1$ (top), $\Lambda_c = 0.5$ (center) and $\Lambda_c = 0.1$ (bottom). The size of the cube is $L = 10$. Left: Poisson tessellations; middle: Voronoi tessellations; right: Voronoi tessellations.

The impact of the average chord length on $\langle T \rangle$, $\langle R \rangle$ and $\langle \varphi \rangle$ is clearly visible in Figs. 5.16 and 5.17. As a general consideration, for any mixing statistics, the respective observables become closer to those of the atomic mix as Λ_c decreases. These results suggest a convergence towards atomic mix when Λ_c tends to zero, i.e., for high fragmentation. However, in most cases, this convergence is not fully achieved for the range of parameters explored here. The atomic mix approximation is indeed supposed to be valid only when the chunks of different materials are optically thin, and this condition is typically not verified for our configurations (see Tabs. 5.15 and 5.14). Nonetheless, we notice one exception in case 2*b*, for large absorber fractions in the range $0.7 < p < 1$, where the relative positions of the reflection curves corresponding to tessellations are inverted with respect to those corresponding to atomic mix. In such configurations, stochastic geometries with small Λ_c will induce low reflection probabilities and will further enhance the discrepancy with respect to the atomic mix case. This non-trivial behaviour, which stems from finite-size and interface effects dominating the transport process, has been previously observed for the benchmark considered above, under similar conditions, i.e., small chunks of scattering material surrounded by an absorbing medium. The threshold behaviour of $\langle R \rangle$ at $p > 0.7$ might be subtly related to the percolation of the scattering material.

For cases 1*a* and 1*b*, the transmission probability increases with Λ_c: larger void chunks enhance transmission. The reflection probability is complementary to transmission and shows the opposite trend. For case 2*a* and 2*b*, the transmission probability increases again with Λ_c, and so do the reflection probability and the integral flux. Therefore, the absorption probability $\langle A \rangle = 1 - \langle R \rangle - \langle T \rangle$ for case 2 decreases with increasing Λ_c (see Fig. 5.17).

m	Λ_c	$\langle N_p \vert L\rangle$	$\sigma[N_p \vert L]$	$\langle t\rangle$	$\sigma[t]$
AM				145	0
$\mathcal{P}$	1	784	448	176	8
	0.5	5278	2316	217	14
	0.1	561163	117382	7705	2062
$\mathcal{V}$	1	325	17	185	2
	0.5	2596	51	258	4
	0.1	324557	563	2511	208
$\mathcal{B}$	1	473	285	169	7
	0.5	2975	1344	200	11
	0.1	309264	66029	2212	552

Table 5.16: Complexity of the tessellations used for the benchmark configurations, as a function of the mixing statistics m (AM stands for atomic mix) and of the average correlation length Λ_c of the tessellation, for a domain of linear size $L = 10$. $\langle N_p|L\rangle$ denotes the average number of polyhedra composing the tessellation, whereas $\langle t\rangle$ denotes the average computer time (expressed in seconds) for a transport simulation of the benchmark configuration $1a$, with $p = 0.05$.

Let us now consider the relevance of scattering cross sections $\Sigma_{s,\beta}$. For both case 1 and 2, the reflection probability increases when increasing $\Sigma_{s,\beta}$, whereas the transmission probability decreases. For case 2, the resulting absorption probability $\langle A\rangle = 1 - \langle R\rangle - \langle T\rangle$ decreases with $\Sigma_{s,\beta}$. Moreover, larger values of $\Sigma_{s,\beta}$ enhance the discrepancies between results corresponding to different tessellations, as a function of Λ_c: this is apparent when comparing case $1a$ to case $1b$, or case $2a$ to case $2b$. For given parameters m and Λ_c, the discrepancy with respect to atomic mix depends on both p and $\Sigma_{s,\beta}$: this is maximal for large values of p in case 1 and, conversely, for small values of p in case 2.

For case 2, where scattering is in competition with absorption, particles are all the more likely to avoid absorbing regions as the chunks of scattering materials (of linear scale Λ/p) are large compared to the scattering mean free path $1/\Sigma_{s,\beta}$. If the size of scattering chunks is small compared to the scattering mean free path, particles have little or no chance of survival, because they will most often cross an absorbing region. Moreover, $\langle R\rangle$ and $\langle T\rangle$ increase with decreasing p and increasing Λ_c. When the chunks of scattering material are large, the stochastic tessellations typically contain clusters composed of scattering material spanning the geometry, forming 'safe corridors' for the particles. Simulation findings suggest that a small scattering mean free path does reduce the effect of absorption, but only with respect to reflection probability: particles have a greater chance of coming back to the starting boundary when the chunks of scattering material are large compared to the scattering mean free path. On the contrary, the transmission probability is only weakly affected, which shows that for the chosen benchmark configurations of case 2 transport is dominated by the behaviour close to the starting boundary.

Generally speaking, the impact of the mixing statistics m is weaker than that of the other parameters of the benchmarks. This is not entirely surprising, since we have chosen the respective tessellation densities so to have the same Λ_c, and transport properties will mostly depend on the average chord length of the traversed polyhedra. Such behaviour might be of utmost importance when the choice of the mixing statistics is part of the unknowns in modelling random media. For Poisson and Box tessellations, the simulation results for all physical observables are *always in excellent agreement*, which suggests that these mixing statistics are almost equivalent for the chosen configurations. On the contrary, results for Voronoi tessellations have a distinct behaviour, and for most cases these tessellations show systematic discrepancies with respect to those of Poisson or Box geometries, particularly in cases $2a$ and $2b$ for $\langle T\rangle$ and $\langle\varphi\rangle$. These findings are coherent with the peculiar nature of the Voronoi mixing statistics, as illustrated in the previous Chapters: differences in the chord length distribution and in

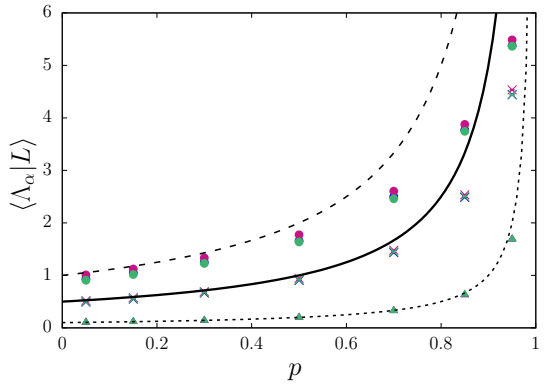

Figure 5.15: The average correlation length $\Lambda_{c,\alpha}(L)$ through clusters of composition α, as a function of the probability p of assigning the label 'α', of the mixing statistics m, and of the average correlation length Λ_c, for a domain of linear size $L = 10$. Symbols correspond to the Monte Carlo simulation results: blue symbols are chosen for $m = \mathcal{P}$, green for $m = \mathcal{V}$, and red for $m = \mathcal{B}$. Circles denote $\Lambda_c = 1$, crosses $\Lambda_c = 0.5$, and triangles $\Lambda_c = 0.1$. In order to provide a reference, the asymptotic function $\Lambda_{c,\alpha} = \Lambda_c/(1-p)$ is displayed for $\Lambda_c = 1$ (dashed line), $\Lambda_c = 0.5$ (continuous line) and $\Lambda_c = 0.1$ (dotted line).

the aspect ratio of the underlying stochastic geometries will induce small but appreciable differences in the transport-related observables.

Integral flux distribution

In order to better assess the variability of the integral flux φ (i.e., of the time spent by the particles in the box) around its average value, we have also computed its full distribution, based on the available realizations in the generated ensembles. The resulting normalized histograms are illustrated in Figs. 5.18 for different values of Λ_c and 5.19 for different values of p and different mixing statistics m.

As a general remark, the dispersion of the integral flux decreases with decreasing Λ_c, when the other parameters are fixed (see Fig. 5.18, where we illustrate an example corresponding to case 1*a* and 1*b*): the ensemble averages become increasingly efficient and the average values become more representative of the full distribution, which is expected on physical grounds. The same behaviour has been observed for the reflection and transmission probabilities, in any configuration, and for all mixing statistics. Moreover, numerical results show that Poisson and Box tessellations have a very close distribution for the integral flux, and that the dispersion around the average is smaller for Voronoi tessellations than for the other tessellations (see Fig. 5.19).

For case 1, all configurations share the same average integral flux. However, the dispersion of φ around the average value depends on the probability p and on the scattering cross section $\Sigma_{s,\beta}$ (see Fig. 5.19), and this not universal. For this case, the impact of p is clearly apparent: for small values of p (chunks of void surrounded by scattering material), the distribution is rather peaked on the average value, whereas, for large values of p (chunks of scattering material surrounded by void), the dispersion is more spread out. The influence of the scattering cross section $\Sigma_{s,\beta}s$ is also visible when comparing cases 1*a* and 1*b*: the dispersion increases with increasing $\Sigma_{s,\beta}$.

Spatial flux

The spatial profiles of the ensemble-averaged scalar flux $\langle \varphi(x) \rangle = \langle \int\int\int \varphi(\mathbf{r}, \mathbf{\Omega}) d\mathbf{\Omega} dy dz \rangle$ along the coordinate x are reported in Figs. 5.20 and 5.21 for case 1 and in Figs. 5.22 and 5.23 for case 2. In TRIPOLI-4 ®, we estimate $\langle \varphi(x) \rangle$ by recording the path lengths within the spatial grid defined above and by dividing the obtained result by the volume of each mesh.

Consistently with the findings concerning the scalar observables, the impact of Λ_c on the spatial profile of the scalar flux is clearly visible (see Figs. 5.20 and 5.22). The lower Λ_c, the closer is the

associated spatial flux profile to the results of the atomic mix. As for the transmission and reflection probabilities, the impact of Λ_c depends on the probability p and on the scattering cross section $\Sigma_{s,\beta}$. The discrepancy between the atomic mix and stochastic tessellations increases with p for case 1 and decreases with p for case 2; furthermore, the discrepancy systematically increases with increasing $\Sigma_{s,\beta}$.

Mixing statistics m plays also a role, but again its effect is weaker with respect to the other benchmark parameters, as illustrated in Figs. 5.21 and 5.23. For each benchmark configuration, we observe an excellent agreement between Poisson tessellations and Box tessellations. On the contrary, spatial profiles associated with Voronoi tessellations agree with those of the other tessellations for case 1, but show a distinct behaviour for case 2.

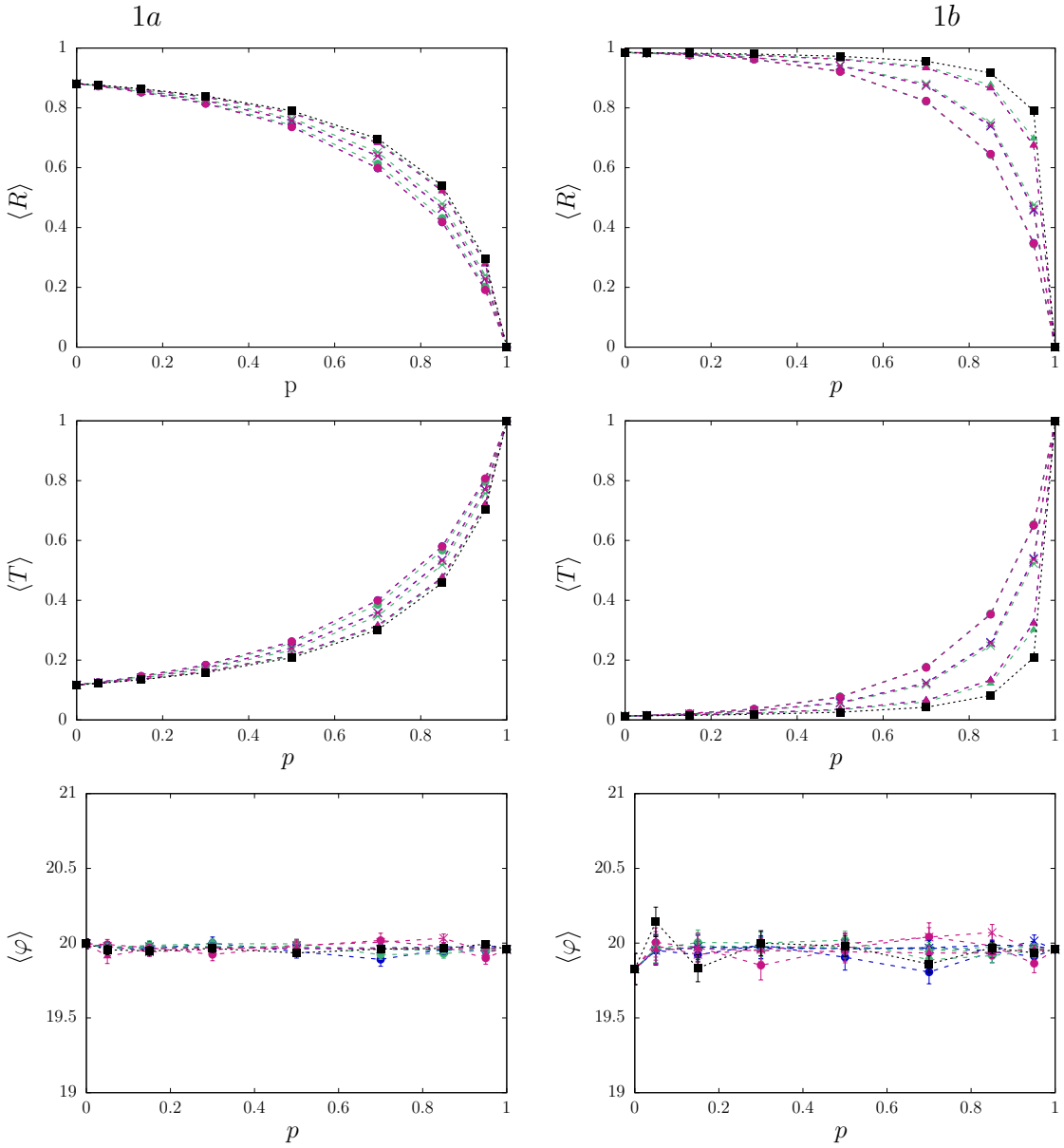

Figure 5.16: Monte Carlo results for the benchmark configurations: cases $1a$ (left) and $1b$ (right). Reflection probability $\langle R \rangle$ (top), transmission probability $\langle T \rangle$ (center) and scalar flux $\langle \varphi \rangle$ (bottom), as a function of p, for different mixing statistics m and different values of Λ_c. Black squares represent the atomic mix approximation. Blue symbols denote $m = \mathcal{P}$, green symbols $m = \mathcal{V}$ and red symbols $m = \mathcal{B}$. Circles denote $\Lambda_c = 1$, crosses $\Lambda_c = 0.5$ and triangles $\Lambda_c = 0.1$. Dashed lines have been added to guide the eye.

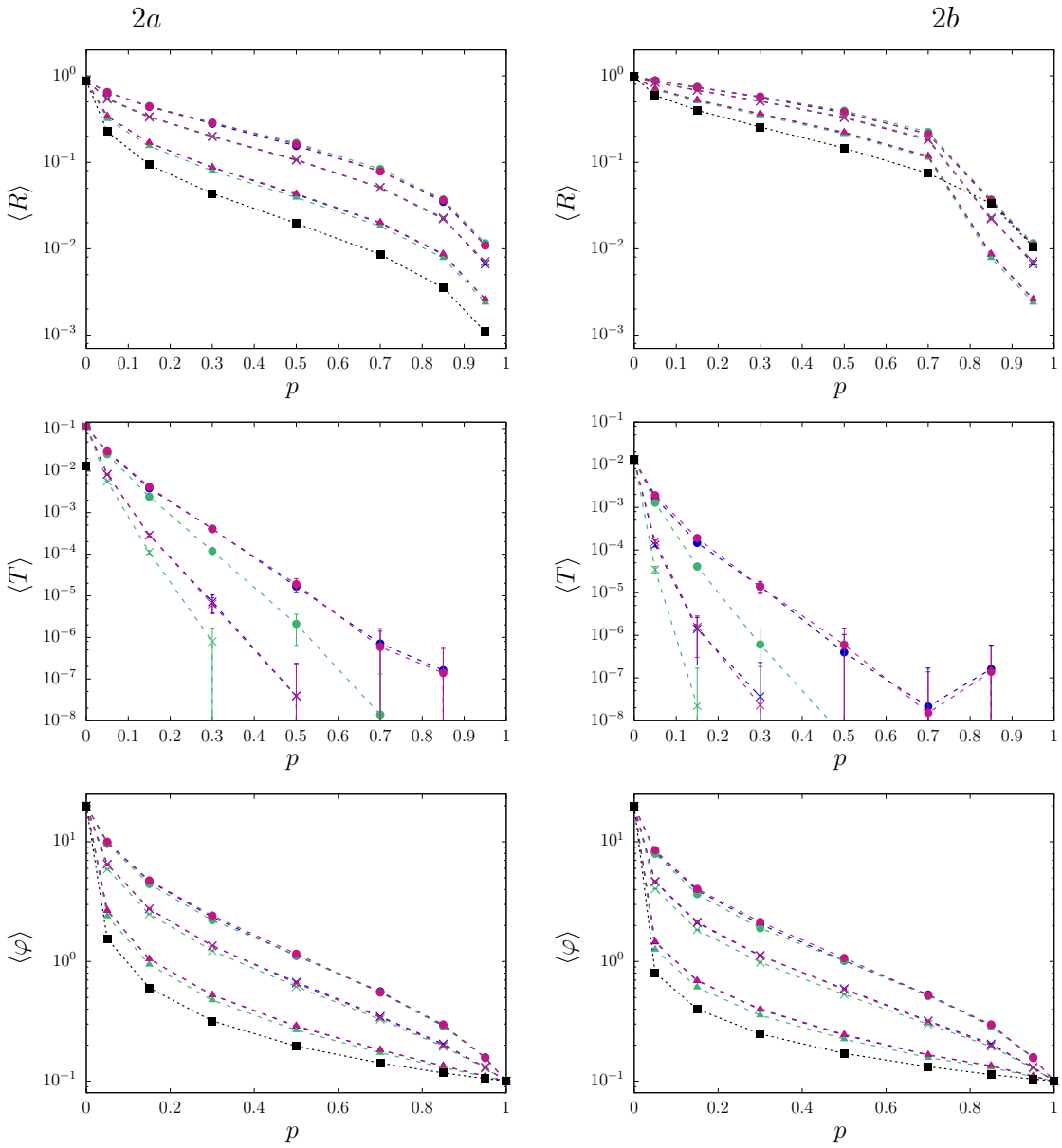

Figure 5.17: Monte Carlo results for the benchmark configurations: cases $2a$ (left) and $2b$ (right). Reflection probability $\langle R \rangle$ (top), transmission probability $\langle T \rangle$ (center) and scalar flux $\langle \varphi \rangle$ (bottom), as a function of p, for different mixing statistics m and different values of Λ_c. Black squares represent the atomic mix approximation. Blue symbols denote $m = \mathcal{P}$, green symbols $m = \mathcal{V}$ and red symbols $m = \mathcal{B}$. Circles denote $\Lambda_c = 1$, crosses $\Lambda_c = 0.5$ and triangles $\Lambda_c = 0.1$. Dashed lines have been added to guide the eye.

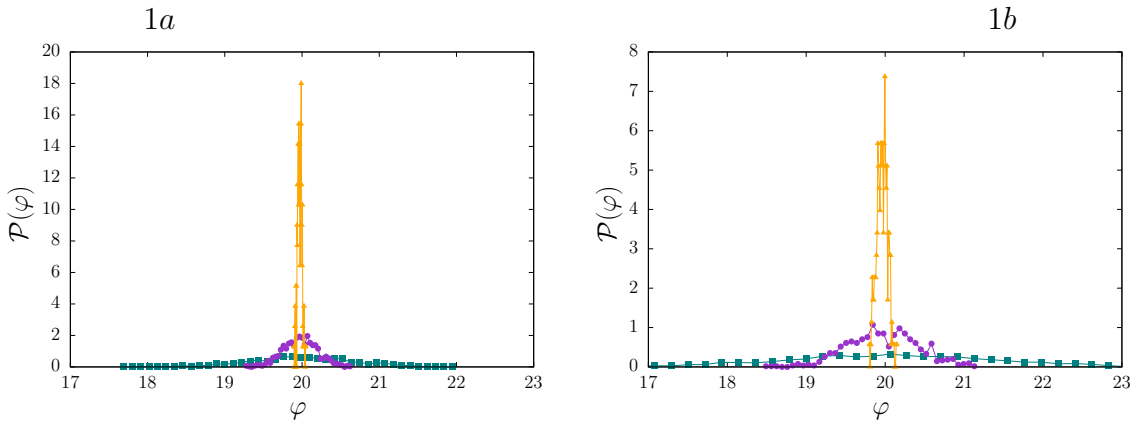

Figure 5.18: Normalized distributions $\mathcal{P}(\varphi)$ of the scalar flux φ, for the benchmark configurations $1a$ (left) and $1b$ (right), for $m = \mathcal{V}$ and for $p = 0.5$. Dark green squares denote $\Lambda_c = 1$, violet circles $\Lambda_c = 0.5$ and orange triangles $\Lambda_c = 0.1$.

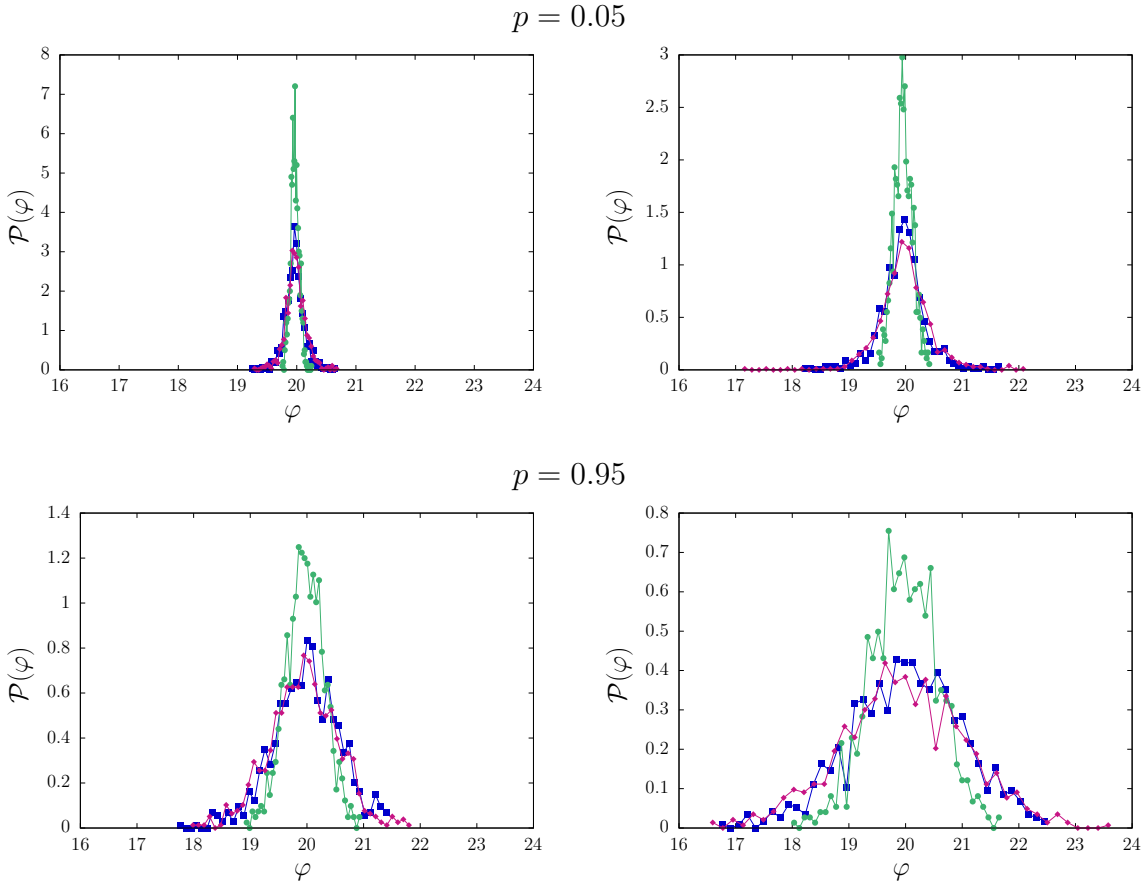

Figure 5.19: Normalized distributions $\mathcal{P}(\varphi)$ of the scalar flux φ, for the benchmark configurations $1a$ (left) and $1b$ (right), for $\Lambda_c = 0.5$. Top: $p = 0.05$; bottom $p = 0.95$. Blue squares denote $m = \mathcal{P}$, green circles $m = \mathcal{V}$ and red diamonds $m = \mathcal{B}$.

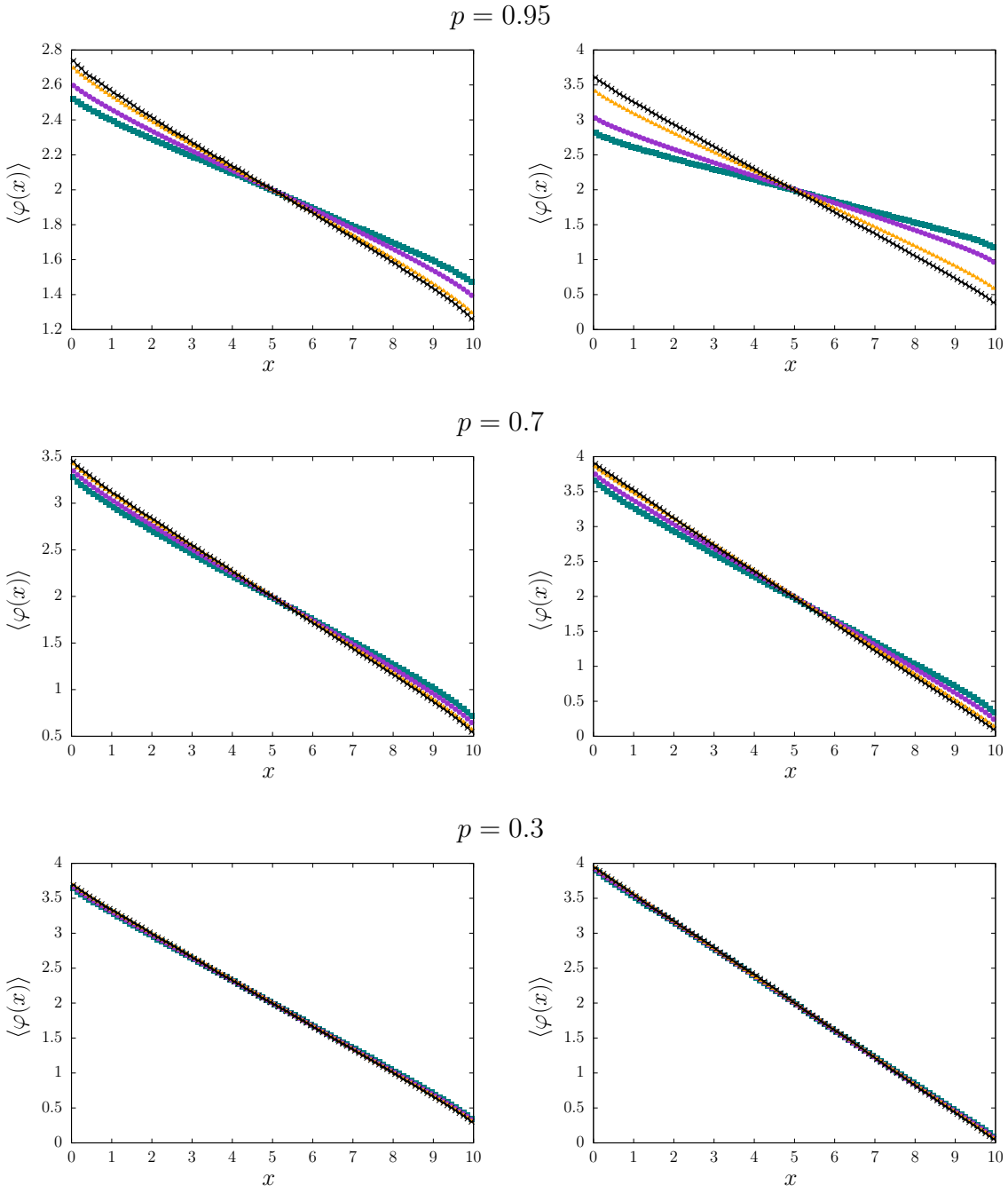

Figure 5.20: Ensemble-averaged spatial scalar flux for Poisson tessellations ($m = \mathcal{P}$), for the benchmark configurations: cases 1a (left) and 1b (right). Top: $p = 0.95$; center$p = 0.7$; bottom: $p = 0.3$. Black crosses denote the atomic mix approximation, dark green squares $\Lambda_c = 1$, violet circles $\Lambda_c = 0.5$ and orange triangles $\Lambda_c = 0.1$.

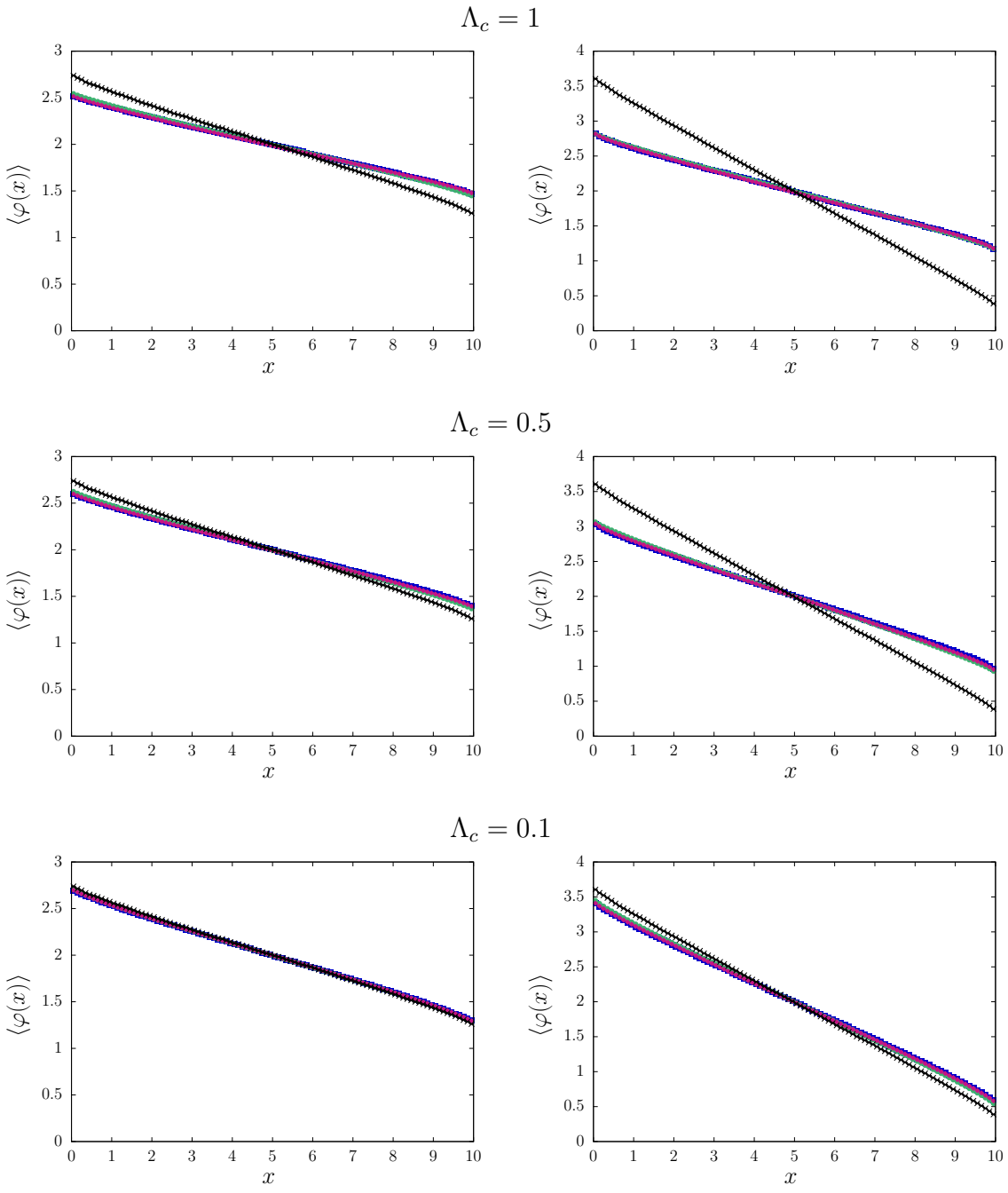

Figure 5.21: Ensemble-averaged spatial scalar flux, for the benchmark configurations: cases $1a$ (left) and $1b$ (right), with $p = 0.95$. Top: $\Lambda_c = 1$; center: $\Lambda_c = 0.5$; bottom: $\Lambda_c = 0.1$. Black crosses denote the atomic mix approximation, blue squares $m = \mathcal{P}$, green circles $m = \mathcal{V}$ and red diamonds $m = \mathcal{B}$.

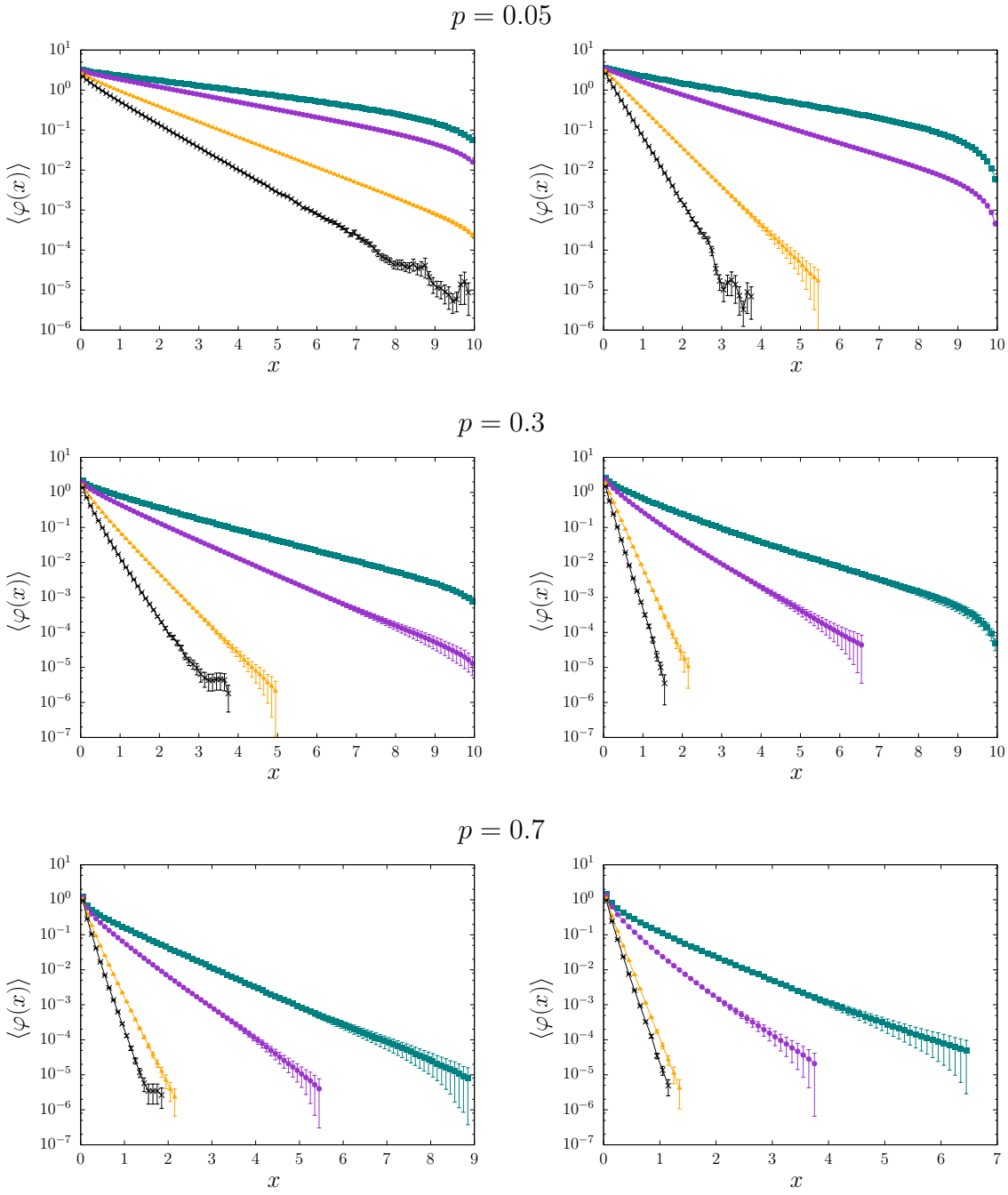

Figure 5.22: Ensemble-averaged spatial scalar flux for Poisson tessellations ($m = \mathcal{P}$), for the benchmark configurations: cases $2a$ (left) and $2b$ (right). Top: $p = 0.05$; center: $p = 0.3$; bottom: $p = 0.7$. Black crosses denote the atomic mix approximation, dark green squares $\Lambda_c = 1$, violet circles $\Lambda_c = 0.5$ and orange triangles $\Lambda_c = 0.1$.

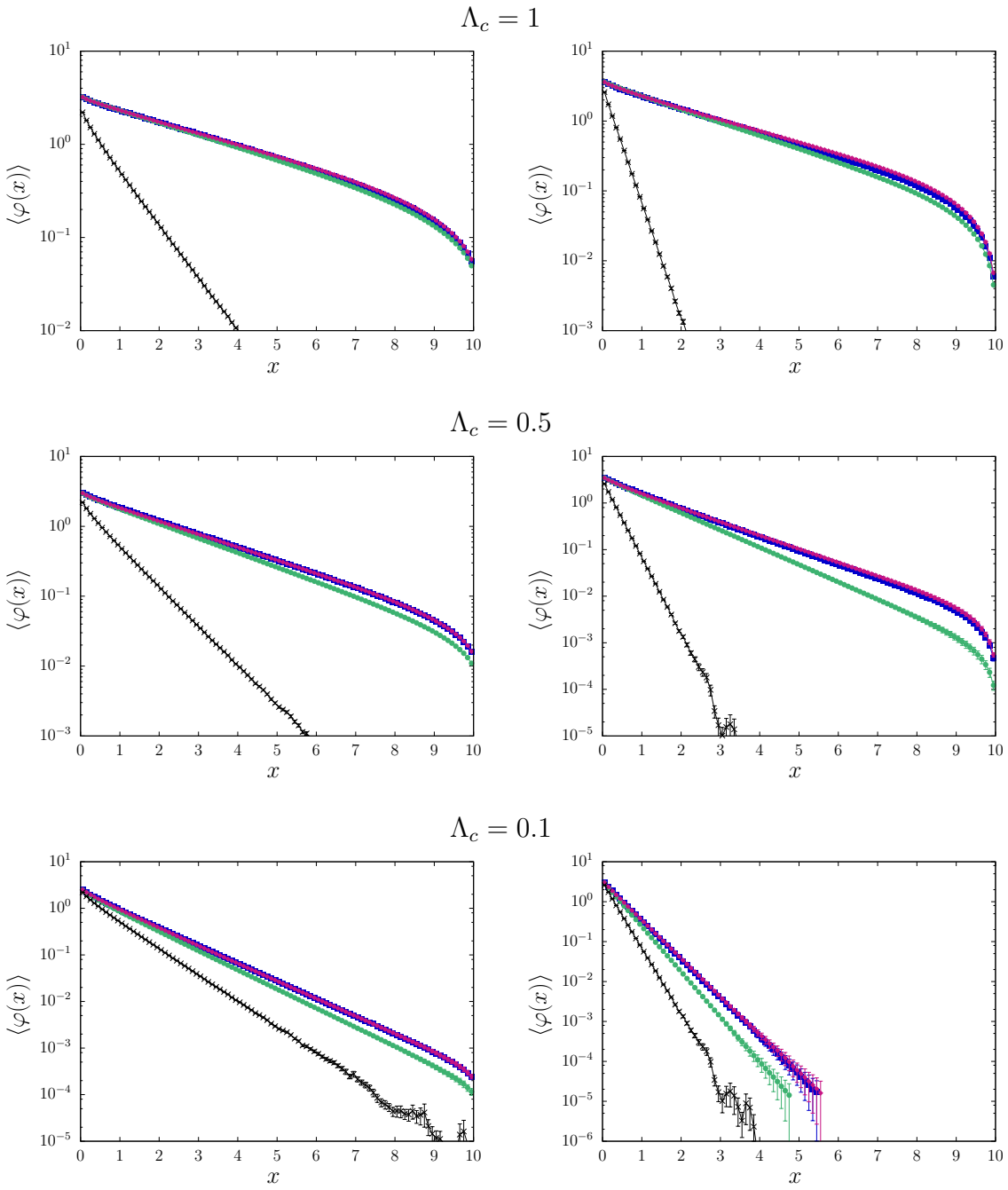

Figure 5.23: Ensemble-averaged spatial scalar flux, for the benchmark configurations: cases $2a$ (left) and $2b$ (right), with $p = 0.05$. Top: $\Lambda_c = 1$; center: $\Lambda_c = 0.5$; bottom: $\Lambda_c = 0.1$. Black crosses denote the atomic mix approximation, blue squares $m = \mathcal{P}$, green circles $m = \mathcal{V}$ and red diamonds $m = \mathcal{B}$.

5.4.3 Back to the ALP benchmark

In order to verify the conclusions obtained for this new benchmark, we have extended to other mixing statistics (Voronoi, Box) the ALP benchmark concerning binary mixtures in d-dimensional Markov geometries and previously described in Sec. 5.3. In this section, we focus on the three-dimensional case only. A natural choice is therefore to set $\Lambda_{c,\alpha}$ and $\Lambda_{c,\beta}$ to be equal for Poisson, Voronoi and Box tessellations, which ensures that the three colored geometries are 'statistically equivalent'. Thus, for each benchmark case we consider Voronoi and Box tessellations comparable to Poisson tessellations used in this benchmark, whose geometrical parameters are given in Tab.5.4. To this aim, we generate Voronoi and Box tessellations within a box of side $L = 10$ with respective density parameters $\rho_{\mathcal{V}}$ and $\rho_{\mathcal{B}}$ chosen by using Eq. 2.83.

For both additional types of tessellations, we have computed the reference solutions for the probabilities $\langle R\rangle$ and $\langle T\rangle$ (or the average leakage current $\langle J_{\text{ave}}\rangle = \langle (T+R)/2\rangle$ for the *Suite* II configurations) and the ensemble-averaged scalar particle flux $\langle \varphi(x)\rangle$. To this aim, we have used the approach and the Monte Carlo parameters described in Sec.5.3.4.

Reference solutions for each type of mixing statistics are provided in Tabs. 5.17 to 5.19 for the benchmark cases corresponding to *suite* I, and in Tabs. 5.20 to 5.22 for the benchmark cases corresponding to *suite* II, respectively: the ensemble-averaged total scalar flux $\langle \varphi\rangle$, transmission coefficient $\langle T\rangle$, and reflection coefficient $\langle R\rangle$ are displayed for Poisson, Voronoi and Box tessellations. The respective computer times are also provided in the same tables. The ensemble-averaged spatial flux $\langle \varphi(x)\rangle$ is illustrated in Figs. 5.24 to 5.26.

Simulation results for these benchmark configurations basically confirm our previous findings: the physical observables related to particle transport through Box tessellations are very close to those of isotropic Poisson tessellations, which was expected based on their respective chord length distributions being very similar. The agreement between the two sets of results increases by decreasing the average chord length (i.e., for more fragmented tessellations). An exception must be remarked for sub-case 1*b* of *suite* I, in particular for the transmission coefficient $\langle T\rangle$, despite this configuration being highly fragmented. Since this sub-case is composed of absorbing chunks dispersed in a scattering background, the observed discrepancy might be attributed to the effects induced by the shape of the chunks on particle transport (which are different for the two tessellations, as shown in Chap. 4). For the spatial flux profiles, slight differences emerge for the less fragmented configurations, e.g., sub-cases 2*b*, 3*a* and 3*b* of *suite* I.

Furthermore, the results obtained with Voronoi tessellations for most cases show systematic discrepancies with respect to those of Poisson or Box geometries. These findings are coherent with those found in Sec. 5.4.2. In particular, we find large discrepancies between Voronoi tessellations and Poisson tessellations in sub-case 1*b*, corresponding to small absorbing chunks surrounded by a scattering background: this is consistent with the results obtained in similar configurations: case 2 of the previous benchmark for small values of p. The distribution of the chord lengths plays an important role in characterizing the transport properties, which explains why the Voronoi tessellation, whose chord length is significantly different from that of the other mixing statistics, shows a distinct behaviour. We conclude by remarking that Box tessellations yield almost identical results with respect to Poisson tessellations: this is a remarkable feature, in that the realizations of Box geometries are much simpler and could be perhaps adapted for deterministic transport codes.

Case	Algorithm	$\langle R \rangle$	$\langle T \rangle$	$\langle \varphi \rangle$	t_{tot} [s]
1a	Poisson	$0.4091 \pm 5 \times 10^{-4}$	0.0163 ± 10^{-4}	6.328 ± 0.007	3.9×10^6
	Box	$0.4092 \pm 6 \times 10^{-4}$	0.0166 ± 10^{-4}	6.321 ± 0.008	8.5×10^5
	Voronoi	$0.4242 \pm 5 \times 10^{-4}$	0.0132 ± 10^{-4}	6.192 ± 0.007	2.1×10^6
1b	Poisson	$0.0377 \pm 2 \times 10^{-4}$	$0.00085 \pm 3 \times 10^{-5}$	1.918 ± 0.003	1.8×10^6
	Box	$0.0379 \pm 2 \times 10^{-4}$	$0.00102 \pm 3 \times 10^{-5}$	1.925 ± 0.004	3.4×10^5
	Voronoi	$0.0335 \pm 2 \times 10^{-4}$	$0.00040 \pm 2 \times 10^{-5}$	1.716 ± 0.003	1.2×10^6
1c	Poisson	$0.4059 \pm 5 \times 10^{-4}$	0.0164 ± 10^{-4}	6.303 ± 0.008	4.4×10^6
	Box	$0.4062 \pm 5 \times 10^{-4}$	0.0168 ± 10^{-4}	6.306 ± 0.009	8.5×10^5
	Voronoi	$0.4156 \pm 5 \times 10^{-4}$	0.0125 ± 10^{-4}	6.051 ± 0.008	2.1×10^6

Table 5.17: Ensemble-averaged observables and computer time t_{tot} for the benchmark configurations: *suite* I - case 1.

Case	Algorithm	$\langle R \rangle$	$\langle T \rangle$	$\langle \varphi \rangle$	t_{tot} [s]
2a	Poisson	0.225 ± 0.001	$0.0937 \pm 4 \times 10^{-4}$	7.57 ± 0.01	4.4×10^5
	Box	0.228 ± 0.001	$0.0950 \pm 4 \times 10^{-4}$	7.54 ± 0.01	4.3×10^5
	Voronoi	0.2222 ± 0.0008	$0.9256 \pm 4 \times 10^{-4}$	7.602 ± 0.009	4.6×10^5
2b	Poisson	$0.1616 \pm 8 \times 10^{-4}$	$0.1194 \pm 9 \times 10^{-4}$	7.77 ± 0.03	3.4×10^5
	Box	$0.1626 \pm 9 \times 10^{-4}$	$0.1202 \pm 9 \times 10^{-4}$	7.77 ± 0.03	2.9×10^5
	Voronoi	$0.1616 \pm 6 \times 10^{-4}$	$0.1172 \pm 6 \times 10^{-4}$	7.69 ± 0.02	3.2×10^5
2c	Poisson	$0.3457 \pm 5 \times 10^{-4}$	$0.1651 \pm 9 \times 10^{-4}$	10.76 ± 0.03	4.8×10^5
	Box	$0.3474 \pm 5 \times 10^{-4}$	$0.1656 \pm 9 \times 10^{-4}$	10.74 ± 0.03	4.0×10^5
	Voronoi	$0.3351 \pm 5 \times 10^{-4}$	$0.1590 \pm 6 \times 10^{-4}$	10.54 ± 0.02	4.4×10^5

Table 5.18: Ensemble-averaged observables and computer time t_{tot} for the benchmark configurations: *suite* I - case 2.

Case	Algorithm	$\langle R \rangle$	$\langle T \rangle$	$\langle \varphi \rangle$	t_{tot} [s]
3a	Poisson	0.675 ± 0.001	$0.1692 \pm 9 \times 10^{-4}$	16.38 ± 0.03	1.4×10^6
	Box	0.677 ± 0.001	0.168 ± 0.001	16.39 ± 0.03	1.3×10^6
	Voronoi	0.671 ± 0.001	$0.1722 \pm 7 \times 10^{-4}$	16.45 ± 0.03	1.4×10^6
3b	Poisson	$0.0165 \pm 2 \times 10^{-4}$	$0.0457 \pm 9 \times 10^{-4}$	3.47 ± 0.03	5.0×10^5
	Box	$0.0166 \pm 2 \times 10^{-4}$	$0.0462 \pm 9 \times 10^{-4}$	3.44 ± 0.03	4.1×10^5
	Voronoi	$0.0182 \pm 2 \times 10^{-4}$	$0.0482 \pm 6 \times 10^{-4}$	3.68 ± 0.02	4.3×10^5
3c	Poisson	$0.3979 \pm 7 \times 10^{-4}$	0.086 ± 0.001	7.89 ± 0.03	7.0×10^5
	Box	$0.4008 \pm 7 \times 10^{-4}$	0.086 ± 0.001	7.86 ± 0.04	6.9×10^5
	Voronoi	$0.3912 \pm 6 \times 10^{-4}$	$0.0849 \pm 8 \times 10^{-4}$	7.98 ± 0.03	7.0×10^5

Table 5.19: Ensemble-averaged observables and computer time t_{tot} for the benchmark configurations: *suite* I - case 3.

Case	Algorithm	$\langle J_{\text{ave}} \rangle$	$\langle \varphi \rangle$	t_{tot} [s]
1a	Poisson	$0.1583 \pm 3 \times 10^{-4}$	7.530 ± 0.008	7.9×10^7
	Box	$0.1580 \pm 3 \times 10^{-4}$	7.533 ± 0.008	3.6×10^7
	Voronoi	$0.1548 \pm 4 \times 10^{-4}$	7.60 ± 0.01	5.4×10^7
1b	Poisson	$0.0481 \pm 2 \times 10^{-4}$	1.808 ± 0.003	7.4×10^7
	Box	$0.0481 \pm 2 \times 10^{-4}$	1.820 ± 0.003	3.3×10^7
	Voronoi	$0.0430 \pm 2 \times 10^{-4}$	1.619 ± 0.002	9.5×10^7
1c	Poisson	$0.1577 \pm 3 \times 10^{-4}$	7.455 ± 0.008	7.7×10^7
	Box	$0.1576 \pm 3 \times 10^{-4}$	7.470 ± 0.008	3.9×10^7
	Voronoi	$0.1513 \pm 4 \times 10^{-4}$	7.38 ± 0.01	4.8×10^7

Table 5.20: Ensemble-averaged observables and computer time t_{tot} for the benchmark configurations: *suite* II - case 1.

Case	Algorithm	$\langle J_{\text{ave}} \rangle$	$\langle \varphi \rangle$	t_{tot} [s]
2a	Poisson	$0.1892 \pm 3 \times 10^{-4}$	7.27 ± 0.01	5.8×10^5
	Box	$0.1882 \pm 3 \times 10^{-4}$	7.31 ± 0.01	4.4×10^5
	Voronoi	$0.1900 \pm 3 \times 10^{-4}$	7.050 ± 0.008	4.6×10^5
2b	Poisson	$0.1931 \pm 4 \times 10^{-4}$	6.53 ± 0.01	1.7×10^6
	Box	$0.1939 \pm 4 \times 10^{-4}$	6.63 ± 0.01	9.1×10^5
	Voronoi	$0.1927 \pm 3 \times 10^{-4}$	6.357 ± 0.009	1.1×10^6
2c	Poisson	$0.2688 \pm 6 \times 10^{-4}$	9.55 ± 0.02	4.9×10^5
	Box	$0.2680 \pm 6 \times 10^{-4}$	9.62 ± 0.02	3.3×10^5
	Voronoi	$0.2633 \pm 4 \times 10^{-4}$	9.24 ± 0.01	4.1×10^5

Table 5.21: Ensemble-averaged observables and computer time t_{tot} for the benchmark configurations: *suite* II - case 2.

Case	Algorithm	$\langle J_{\text{ave}} \rangle$	$\langle \varphi \rangle$	t_{tot} [s]
3a	Poisson	$0.4098 \pm 4 \times 10^{-4}$	22.82 ± 0.07	1.7×10^6
	Box	$0.4088 \pm 4 \times 10^{-4}$	23.33 ± 0.08	1.6×10^6
	Voronoi	$0.4115 \pm 4 \times 10^{-4}$	21.74 ± 0.06	1.5×10^6
3b	Poisson	$0.0868 \pm 3 \times 10^{-4}$	2.98 ± 0.01	8.7×10^5
	Box	$0.0864 \pm 3 \times 10^{-4}$	3.02 ± 0.01	7.2×10^5
	Voronoi	$0.0931 \pm 3 \times 10^{-4}$	2.997 ± 0.007	6.9×10^5
3c	Poisson	$0.1974 \pm 7 \times 10^{-4}$	8.15 ± 0.02	5.0×10^5
	Box	$0.1956 \pm 7 \times 10^{-4}$	8.24 ± 0.02	4.6×10^5
	Voronoi	$0.1997 \pm 6 \times 10^{-4}$	7.97 ± 0.02	4.7×10^5

Table 5.22: Ensemble-averaged observables and computer time t_{tot} for the benchmark configurations: *suite* II - case 3.

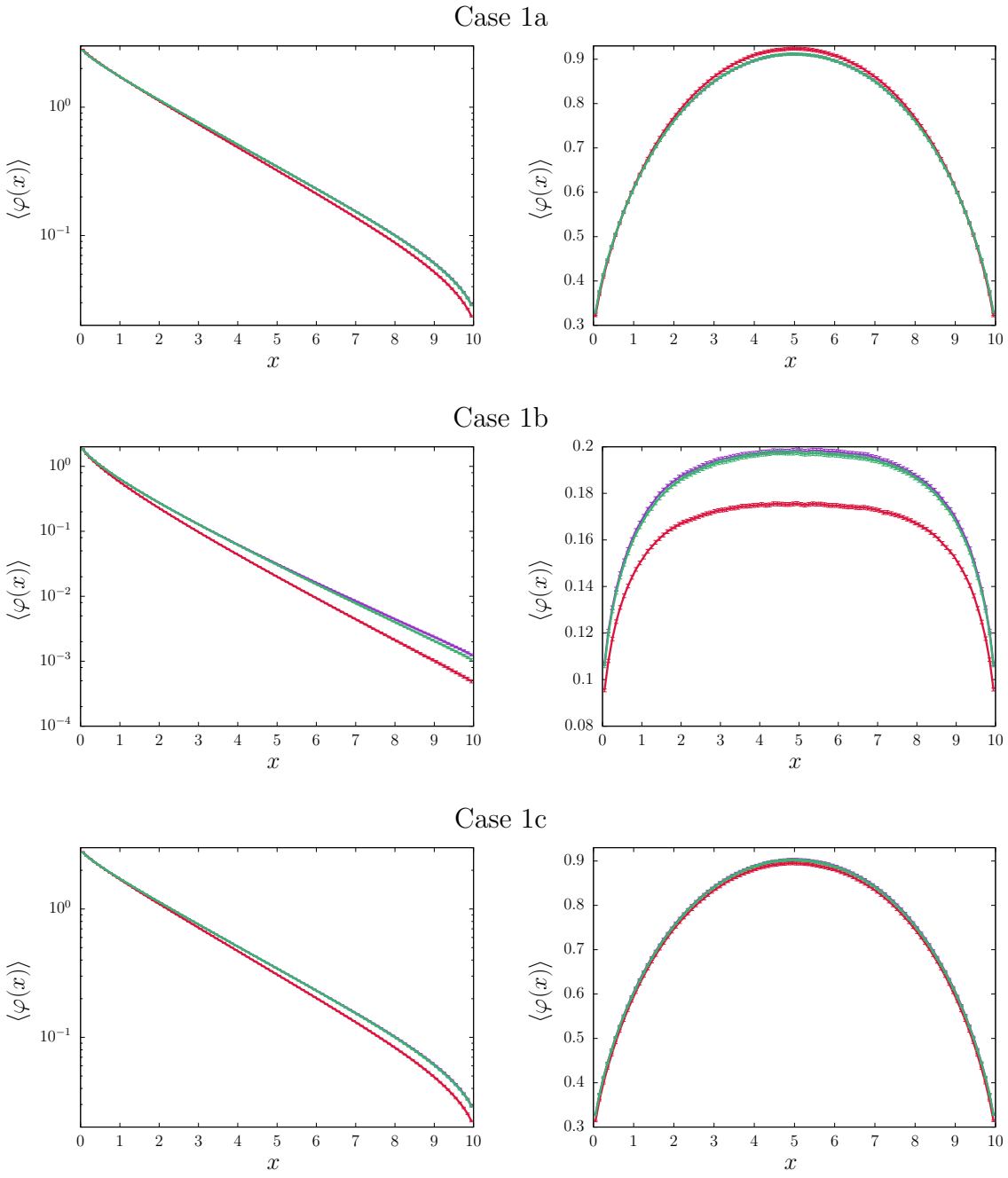

Figure 5.24: Ensemble-averaged spatial scalar flux for the benchmark configurations: Case 1. Left column: *Suite* I configurations; right column: *Suite* II configurations. Solid lines represent the benchmark solutions obtained with the quenched disorder approach: green lines correspond to Poisson tessellations, red lines to Voronoi tessellations and purple lines to Box tessellations.

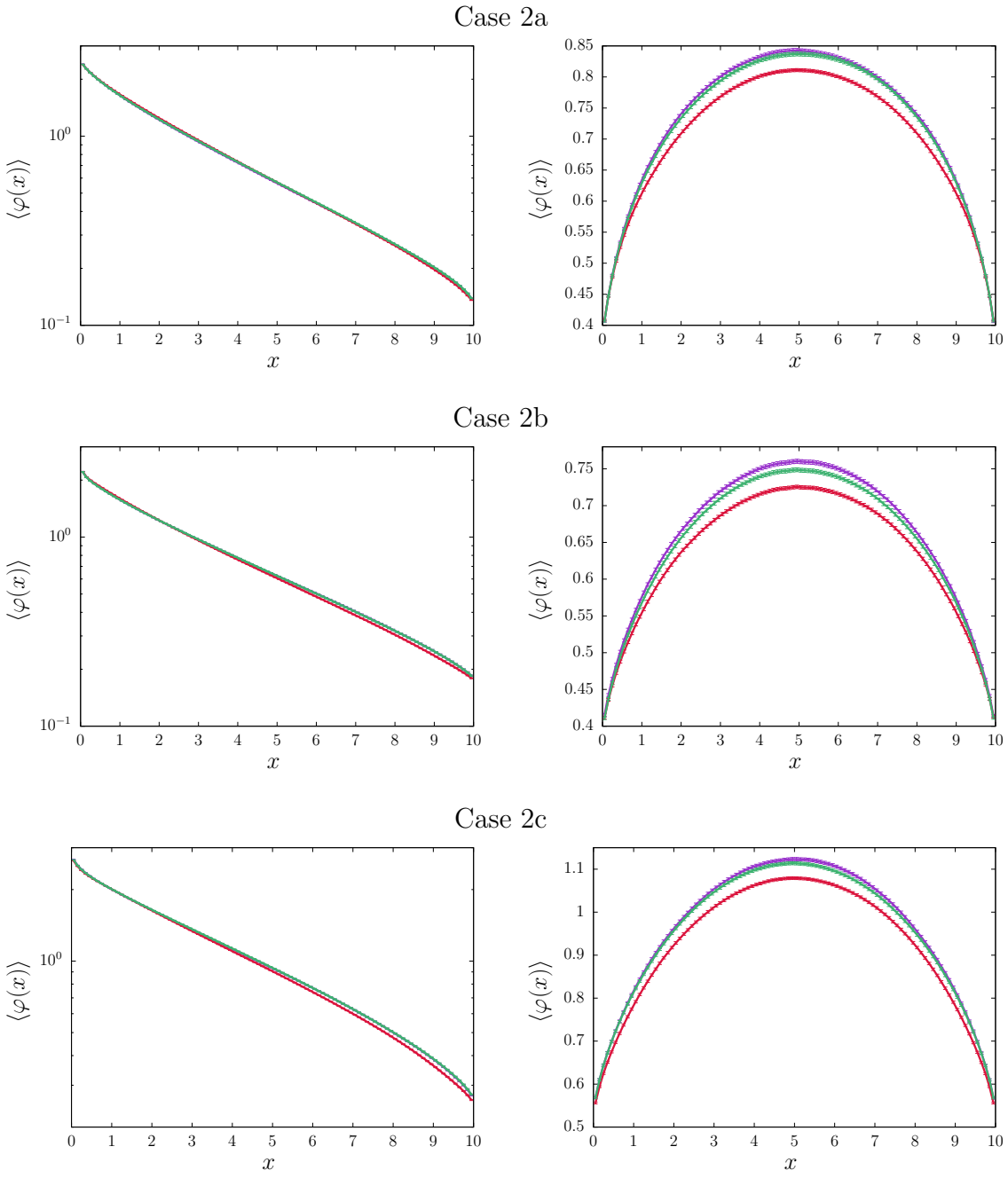

Figure 5.25: Ensemble-averaged spatial scalar flux for the benchmark configurations: Case 2. Left column: *Suite* I configurations; right column: *Suite* II configurations. Solid lines represent the benchmark solutions obtained with the quenched disorder approach: green lines correspond to Poisson tessellations, red lines to Voronoi tessellations and purple lines to Box tessellations.

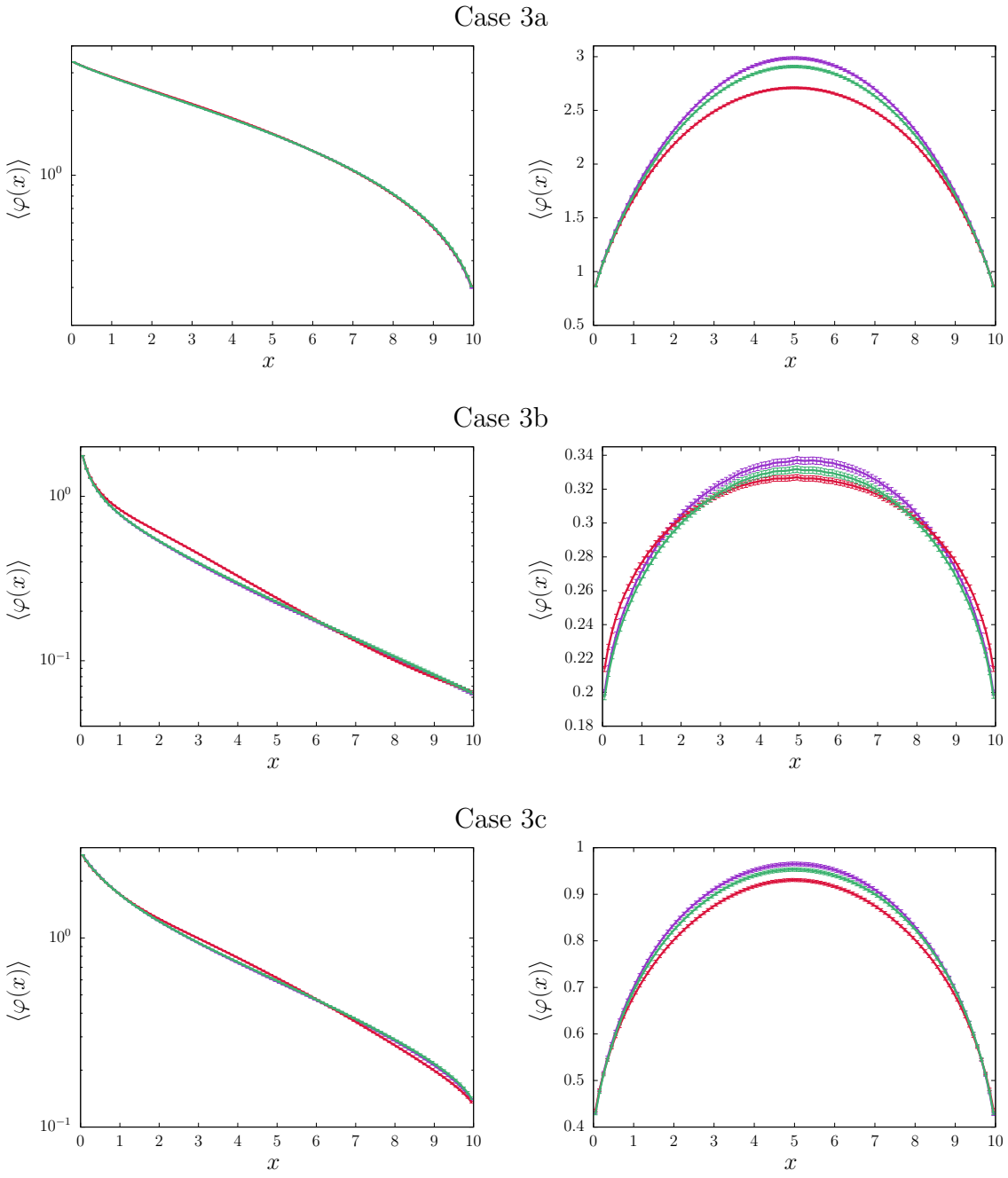

Figure 5.26: Ensemble-averaged spatial scalar flux for the benchmark configurations: Case 3. Left column: *Suite* I configurations; right column: *Suite* II configurations. Solid lines represent the benchmark solutions obtained with the quenched disorder approach: green lines correspond to Poisson tessellations, red lines to Voronoi tessellations and purple lines to Box tessellations.

Chapter 6

Eigenvalue problems in quenched disorder

6.1 Introduction

Consider the stationary neutron transport equation in integro-differential form, namely,

$$\boldsymbol{\Omega}\cdot\nabla_{\mathbf{r}}\varphi+\Sigma_t(\mathbf{r},E)\varphi=\int\int\Sigma_t(\mathbf{r},E')C(\mathbf{r};\boldsymbol{\Omega}',E'\to\boldsymbol{\Omega},E)\varphi(\mathbf{r},\boldsymbol{\Omega}',E')d\boldsymbol{\Omega}'dE'+Q(\mathbf{r},\boldsymbol{\Omega},E),\tag{6.1}$$

where we have explicitly introduced the dependence with respect to the energy E [5]. For a multiplying system with fission, scattering and capture, the collision term can be generally written as

$$\begin{gathered}\Sigma_t(\mathbf{r},E')C(\mathbf{r};\boldsymbol{\Omega}',E'\to\boldsymbol{\Omega},E)=\\ \Sigma_s(\mathbf{r},E')f_s(\boldsymbol{\Omega}',E'\to\boldsymbol{\Omega},E)+\bar{\nu}_f(\mathbf{r},E')\Sigma_f(\mathbf{r},E')\chi_f(\boldsymbol{\Omega}',E'\to\boldsymbol{\Omega},E),\end{gathered}\tag{6.2}$$

where $f_s(\boldsymbol{\Omega}',E'\to\boldsymbol{\Omega},E)$ is the scattering probability distribution function, $\bar{\nu}_f(\mathbf{r},E)$ is the average number of fission neutron emitted at fission, and $\chi_f(\boldsymbol{\Omega},E\to\boldsymbol{\Omega}',E')$ is the associated (normalized) fission spectrum. Neutrons emitted at fission can be either prompt (p) or delayed (d), each having a distinct average number of emitted secondary particles and associated spectrum. Moreover, often fission neutrons are emitted isotropically, and the spectrum is only weakly dependent on the incident neutron energy, in which case we have

$$\begin{gathered}\bar{\nu}_f(\mathbf{r},E')\Sigma_f(\mathbf{r},E')\chi_f(\boldsymbol{\Omega}',E'\to\boldsymbol{\Omega},E)=\\ \bar{\nu}_p(E')\Sigma_f(\mathbf{r},E')\frac{\chi_p(E)}{4\pi}+\sum_j\bar{\nu}_d^j(E')\Sigma_f(\mathbf{r},E')\frac{\chi_d^j(E)}{4\pi},\end{gathered}\tag{6.3}$$

where 4π is the normalization factor of the isotropic distribution and the sum over j runs over the precursor families that decay into delayed neutrons. It is convenient to introduce an operator notation [5] by defining the net disappearance operator $\mathcal{L}$

$$\mathcal{L}\varphi=\boldsymbol{\Omega}\cdot\nabla\varphi+\Sigma_t\varphi-\int\Sigma_s(\mathbf{r},E')f_s(\boldsymbol{\Omega}',E'\to\boldsymbol{\Omega},E)\varphi(\mathbf{r},\boldsymbol{\Omega}',E')dE'd\boldsymbol{\Omega}',\tag{6.4}$$

and the prompt and delayed fission operators

$$\mathcal{F}_p\varphi=\frac{\chi_p(E)}{4\pi}\int\bar{\nu}_p(\mathbf{r},E')\Sigma_f(\mathbf{r},E')\varphi(\mathbf{r},\boldsymbol{\Omega}',E')dE'd\boldsymbol{\Omega}'\tag{6.5}$$

and

$$\mathcal{F}_d^j\varphi=\frac{\chi_d^j(E)}{4\pi}\int\bar{\nu}_d^j(\mathbf{r},E')\Sigma_f(\mathbf{r},E')\varphi(\mathbf{r},\boldsymbol{\Omega}',E')dE'd\boldsymbol{\Omega}',\tag{6.6}$$

respectively. The total fission operator is finally defined as $\mathcal{F}=\mathcal{F}_p+\sum_j\mathcal{F}_d^j$.

We can thus rewrite Eq. (6.1) in compact form as

$$\mathcal{L}\varphi(\mathbf{r},\mathbf{\Omega},E) = \mathcal{F}\varphi(\mathbf{r},\mathbf{\Omega},E) + Q(\mathbf{r},\mathbf{\Omega},E). \tag{6.7}$$

In reactor physics and criticality-safety, a fundamental question is to assess whether Eq. (6.7) admits stationary bounded solutions, which is strictly related to the spectral properties of the Boltzmann operator $\mathcal{B} = \mathcal{F} - \mathcal{L}$. In other words, we would like to determine which is the asymptotic behaviour of the angular neutron flux $\varphi(\mathbf{r},\mathbf{\Omega},E)$ corresponding to an arbitrary source function Q. This calls for an investigation of the eigenvalues and eigenfunctions associated to $\mathcal{B}$. Several forms of such eigenvalue problems exist, although for historical reasons the so-called k-eigenvalue formulation is the most widely used for criticality problems. In this case, one introduces a parameter k and asks whether by dividing the average number of fission neutrons by k a stationary solution is obtained for the homogeneous form of Eq. (6.7) without external sources. This leads to the (generalized) eigenvalue problem

$$\mathcal{L}\varphi_k(\mathbf{r},\mathbf{\Omega},E) = \frac{1}{k}\mathcal{F}\varphi_k(\mathbf{r},\mathbf{\Omega},E), \tag{6.8}$$

where k are the sought eigenvalues and $\varphi_k(\mathbf{r},\mathbf{\Omega},E)$ the corresponding neutron flux eigenfunctions.

Neutron multiplication in *stochastic media* has attracted intense research efforts, in view of many relevant applications emerging in reactor physics and criticality safety. Random media of interest in this context typically belong to two families: stochastic inclusions of fissile chunks within a background matrix, which occur in the design of prismatic and pebble-bed reactors with double heterogeneity fuel [20, 68, 94], and stochastic tessellations composed of a collection of fissile and non-fissile volumes obeying a given mixing statistics [108], such as those resulting from fuel degradation in Three Mile Island unit 2 [18, 47, 50] and at the Fukushima Daiichi power plant [45, 143]. Other applications of random media for criticality safety concern for instance the analysis of the impact of poison grains for neutron absorbers [33] or Pu-rich agglomerates in MOX fuels [165], and safety margins evaluation [114, 159, 160, 163], especially for optimal waste storage [161].

Similarly as for the case of fixed source transport, two distinct strategies can be adopted in order to describe neutron multiplication in random media [108], namely, quenched disorder and annealed disorder. In the quenched disorder approach, the random spatial configurations (with associated material compositions) are first defined based on a probabilistic model. The Boltzmann eigenvalue equation (6.8) is then solved for each configuration, and the statistical moments of the multiplication factor k and of the fundamental eigenfunction φ_k are obtained by taking the ensemble averages with respect to the realizations [108, 109, 114]. The quenched disorder approach leads to reference solutions, because the effects of disorder-induced spatial correlations on neutron trajectories are correctly preserved.

Analytical results for the ensemble averages have been obtained for some special cases, for instance by resorting to perturbation theory, but several simplifications are needed, including mono-energetic (or few-group) transport, isotropic scattering, or diffusion approximation [114, 159–162]. Reference solutions, although computationally expensive, are nonetheless of utmost importance for the validation of approximate, albeit much faster methods, and for the verification of exact formulas. In this respect, Monte Carlo simulation offers a convenient tool for the numerical analysis of eigenvalue problems in stochastic media, in that it allows explicitly generating realizations taken from the sought distribution. A transport code can be then used in order to solve the eigenvalue problem for each sampled configuration.

In the context of eigenvalue problems, intensive research efforts have been devoted so far to the class of stochastic inclusions [20, 43, 54, 68, 69, 94]. In particular, highly sophisticated algorithms have been devised in order to properly take into account boundary effects due to spheres not entirely contained in the medium [43, 54]. Eigenvalue calculations in stochastic tessellations, where the medium is supposed to be partitioned into a collection of random (fissile and non-fissile) volumes obeying a given mixing statistics [108], have been limited so far to one-dimensional configurations of the rod or slab type [114, 160, 162]. Such models might represent, e.g., the accidental positioning of fuel lumps

into moderating material, in the context of criticality safety, or the displacement of control plates in damaged reactor cores.

In order to overcome some of these limitations, in this Chapter we will introduce three-dimensional *stochastic tessellations* as a idealized model to assess the impact of the three-dimensional random fragmentation of fuel elements on the key safety parameters for criticality calculations. In-pile fuel degradation might result from partial core melt-down during severe accidents, with melting, re-solidification and relocation [47, 50], as occurred in the case of the Three Mile Island unit 2 [18]. The effects of such scenario on neutron kinetics are of utmost importance for the evaluation of the re-criticality probability. We will thus analyze the multiplication factor k_{eff}, and the kinetics parameters, namely the effective delayed neutron fraction

$$\beta_{\mathit{eff}} = \frac{\langle \varphi^\dagger \sum_j \mathcal{F}_d^j \varphi \rangle}{\langle \varphi^\dagger \mathcal{F} \varphi \rangle}, \tag{6.9}$$

and the effective neutron generation time [1]

$$\Lambda_{\mathit{eff}} = \frac{\langle \varphi^\dagger \frac{1}{v} \varphi \rangle}{\langle \varphi^\dagger \mathcal{F} \varphi \rangle}, \tag{6.10}$$

where $\langle \cdot \rangle$ denotes integration over the phase space variables and $\varphi^\dagger$ is the adjoint flux (solution to the equation adjoint to Eq. (6.8)), which can be physically interpreted as the neutron importance function [5]. To our best knowledge, the influence of random geometries on kinetics parameters has never been addressed before.

Starting from a reference UOX or MOX assembly with 17×17 fuel pins, we will consider three perturbed configurations having the central pin, 7×7 central pins and the whole 17×17 pins being randomly fragmented. We will assume that the random re-arrangement after melt-down can be described by a Poisson, Voronoi or Box tessellation with ternary mixing statistics [108], accounting for the dispersion of the fuel, the cladding and the moderator, the average linear size of the chunks for each material being a free parameter of the model. For each realization, we will perform criticality calculations by using the Monte Carlo transport code TRIPOLI-4 ® developed at CEA [21], so as to investigate the distribution of k_{eff}, β_{eff} and Λ_{eff} as a function of the model parameters, including the material compositions, the kind of stochastic tessellation, the linear size of the random chunks, and the number of fragmented fuel pins.

In order to better grasp the physical behaviour of these systems without being hindered by the complexity of all the ingredients involved in nuclear accidents, the analysis of assembly configurations that will be carried out in the following is admittedly highly simplified with respect to the realistic description of fuel degradation: for instance, we will focus exclusively on neutron transport, and we will not include the effects due to thermal-hydraulics, thermo-mechanics or the complex physical-chemical reactions occurring in accidental transients [47, 50]. Nonetheless, the proposed methodology is fairly broad and can be applied without any particular restrictions to more sophisticated models.

This Chapter is organized as follows: in Sec 6.2 we will first introduce the benchmark configurations for fuel assemblies with random degradation described by Poisson, Voronoi and Box tessellations. Then, in Sec. 6.3 we will extend our results by taking into account the effects of anisotropy, which is possible induced by material stratification. For this purpose, we will resort to the class of anisotropic Poisson tessellations introduced in Chapter 2.

6.2 A model of assembly with fragmented fuel pins

The stochastic tessellations described in Chapter 2 can be conveniently adopted in order to represent a partially melted fuel assembly, the size of the fuel fragments being determined by the geometry density (which is a free parameter of the model). We propose in the following some benchmark configurations

[1] The symbol $\langle \Lambda_{\mathit{eff}} \rangle$ for the average neutron generation time is not to be confused with Λ_c, which denotes the average correlation length.

Material	Isotopes	Concentration (atoms $\times 10^{24} \times$ cm^{-3})
UOX fuel		
	U235	8.4148×10^{-4}
	U238	2.1625×10^{-2}
	O16	4.4932×10^{-2}
MOX fuel		
	U234	3.9390×10^{-7}
	U235	4.9524×10^{-5}
	U238	2.1683×10^{-2}
	PU238	2.2243×10^{-5}
	PU239	7.0164×10^{-4}
	PU240	2.7138×10^{-4}
	PU241	1.3285×10^{-4}
	PU242	6.6984×10^{-5}
	AM241	1.2978×10^{-5}
	AM242M	2.2569×10^{-10}
	O16	4.5882×10^{-2}
Moderator		
	H1	4.7716×10^{-2}
	O16	2.3858×10^{-2}
	B10	3.9724×10^{-6}
	B11	1.5890×10^{-5}
Cladding		
	ZR90	2.2060×10^{-2}
	ZR91	4.8107×10^{-3}
	ZR92	7.3532×10^{-3}
	ZR94	7.4518×10^{-3}
	ZR96	1.2005×10^{-3}

Table 6.1: Material compositions for the UOX and MOX assemblies used for the benchmark configurations.

that are simple enough to enable a physical interpretation of the effects induced by the presence of random material fragmentation, and yet retain the key ingredients. For the sake of simplicity, we will assume that only three compositions are present, namely the fuel, the cladding and the moderator.

As a reference configuration we will consider an assembly composed of 17×17 square fuel pin-cells of side length $\delta = 1.262082$ cm in the plane O_{xy} and of height $L_z = 10$ cm. Reflective boundary conditions will be imposed on all sides of the assembly. The fuel elements will be entirely either of the UOX or MOX type: the respective material compositions for the fuel, the cladding and the moderator are provided in Tab. 6.1. The proposed compositions correspond to fresh (Beginning Of Life) fuel. The assembly will be assumed to be at a uniform temperature of $T = 300$ K, for conservatism (Doppler effect on reactivity will be reduced).

The partial melting of a collection of fuel pins is then introduced by applying a stochastic ternary mixing model of Poisson, Voronoi or Box type to a central region composed of $n_x \times n_y$ cells. For the sake of simplicity, this region will be assumed to be located at the center of the assembly, with $n_x = n_y = n$, n being odd. The assembly portion corresponding to this region is removed and replaced by a stochastic tessellation. The tessellation is then randomly 'colored' with ternary labels, namely, '$\mathcal{F}$' for fuel, '$\mathcal{C}$' for cladding and '$\mathcal{M}$' for moderator, with corresponding coloring probabilities $p_{\mathcal{F}}$, $p_{\mathcal{C}}$ and $p_{\mathcal{M}}$ chosen so that for each material i the ensemble-averaged volumic ratio $\langle p_i \rangle$ coincides with that of a pin-cell before fragmentation:

$$\begin{aligned} p_{\mathcal{F}} &= \pi R_1^2/\delta^2 \approx 0.335861 \\ p_{\mathcal{C}} &= \pi(R_2^2 - R_1^2)/\delta^2 \approx 0.107943 \\ p_{\mathcal{M}} &= (\delta^2 - \pi R_2^2)/\delta^2 \approx 0.556196. \end{aligned} \tag{6.11}$$

Moreover, in order for the three stochastic tessellation models to yield comparable results with respect to neutron transport, we have set the free parameters of each model (i.e., the geometry densities ρ, $\rho_{\mathcal{V}}$ and $\rho_{\mathcal{B}}$)) so as to have exactly the same average correlation length Λ_c. In-pile and out-of-pile experiments of core degradation show that the fuel fragments after melting are partially mixed with the cladding [47,50]: nonetheless, for the present benchmark we assume that the fuel and the cladding are present in distinct phases. The pin-cells surrounding the perturbed region are left unchanged.

It is important to note that, for a single geometrical realization, the volumic ratio of material i in the tessellation is not rigorously equal to p_i, because of finite-size effects. In this respect, the lack of a strict constraint on the preservation of the mass associated to each material is a limitation of the modelling approach based on colored stochastic tessellations. Indeed, effects attributed to random material rearrangement may be due predominantly to statistical fluctuations in the material mass in each realization, possibly leading to configurations with more material than in the ordered case and less in others. Imposing a rigorous mass-preserving constraint seems to be non-trivial in the context of n-nary statistical mixing models. However, the finite-size effects progressively fade away with increasing fragmentation of the tessellation, and become negligible for tessellations dense enough. This behaviour will be further discussed in Sec. 6.2.3.

For our benchmark model, we have selected three fragmented configurations, each corresponding to a different size for the melted portion of the assembly: in configuration 1, only the central pin-cell is replaced by a ternary mixing ($n = 1$). In configuration 2, we have chosen a portion $n = 7$, i.e., about half of the assembly is fragmented. Finally, in configuration 3, the entire assembly is fragmented ($n = 17$). For illustration, some of the resulting partially melted assemblies are shown in Figs. 6.1 and 6.2.

The physical observables that we would like to determine are the ensemble-averaged multiplication factor $\langle k_{\mathit{eff}} \rangle$, the ensemble-averaged kinetics parameters (namely, the effective neutron generation time $\langle \Lambda_{\mathit{eff}} \rangle$ and the effective delayed neutron fraction $\langle \beta_{\mathit{eff}} \rangle$), as well as and the ensemble-averaged scalar particle flux $\langle \varphi(\mathbf{r}, E) \rangle$ within the assembly.

Our goal is to investigate how these physical observables are affected by the presence of the fragmented fuel pins. For this purpose, we will vary the mixing statistics by separately testing Poisson, Voronoi and Box tessellations, and the average correlation length Λ_c for each tessellation (which basically rules the average size of the material chunks composing the randomized portion of the assembly). In-core experiments have shown that the fragment size may vary between less than a millimetre and several millimetres, depending on the re-solidification speed [18, 47, 50]. Decreasing Λ_c means increasing the density of the tessellations, which implies an increasing computational cost for both the generation of the random geometry, and for the particle transport within the geometry. We have thus a practical limitation to the smallest achievable value of Λ_c. When on the contrary Λ_c becomes comparable to the linear size of the fragmented region, the realization of the ternary mixing are entirely dominated by finite-size effects, the dispersion of the volumic ratio for each material composition becomes relevant. This roughly defines the upper limit for the range of Λ_c that will be considered in the numerical simulations presented in the following.

On the basis of these considerations, we have adapted the range of Λ_c to each configuration: for $n = 1$, we have taken Λ_c from 0.03 cm to 0.5 cm; for $n = 7$, we have taken Λ_c from 0.1 cm to 1.5 cm; and for $n = 17$ we have taken Λ_c from 0.15 cm to 3 cm. Some examples of realizations of Poisson, Voronoi and Box tessellations corresponding to different values of Λ_c are displayed in Fig. 6.2 for the benchmark configuration with $n = 7$.

For any mixing statistics, we will consider also the limit case of $\Lambda_c \to 0$. This corresponds to the so-called 'atomic mix' approximation, where material chunks are assumed to be so fine with respect to the average neutron free path that the stochastic tessellations can be replaced by a homogenized composition where the macroscopic cross sections are obtained by averaging the cross sections of each material weighed by the respective volumic ratios: $P_{\mathcal{F}}$ for the fuel, $P_{\mathcal{M}}$ for the moderator, and $P_{\mathcal{C}}$ for the cladding.

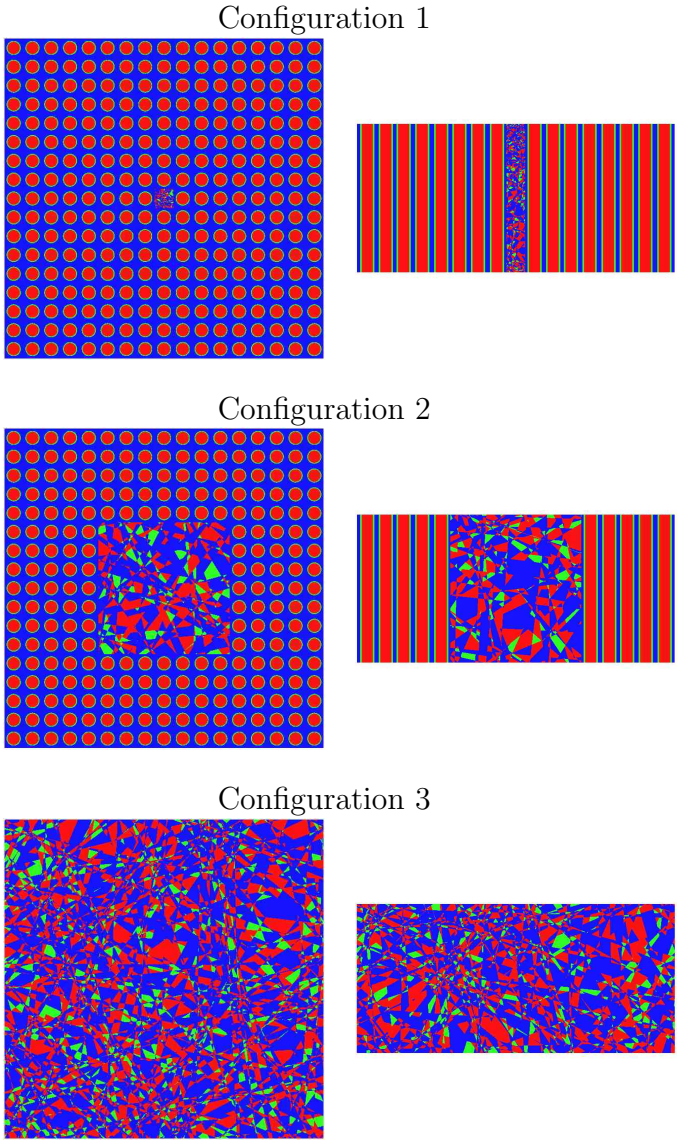

Figure 6.1: Assemblies with Poisson tessellation for the central fuel pins. Top: configuration 1 ($n = 1$), with $\Lambda_c = 0.05$ cm. Center: configuration 2 ($n = 7$), with $\Lambda_c = 0.2$ cm. Bottom: configuration 3 ($n = 17$), with $\Lambda_c = 0.15$ cm. Left column: radial view. Right column: axial view.

6.2.1 Monte Carlo parameters and simulation options

The reference solutions for the ensemble-averaged multiplication factor $\langle k_{\mathit{eff}} \rangle$, kinetics parameters $\langle \Lambda_{\mathit{eff}} \rangle$ and $\langle \beta_{\mathit{eff}} \rangle$, and scalar neutron flux $\langle \varphi(\mathbf{r}, E) \rangle$ have been computed as follows. For each assembly configuration, a large number M of geometries has been generated, and the material properties have been attributed to each volume as described above. Then, for each realization j of the ensemble, eigenvalue calculations have been carried out by using TRIPOLI-4 ® [21]. The number of simulated particle histories per configuration has been chosen so that the statistical error on the computed eigenvalue k_{eff} is smaller than 50 pcm. For a given physical observable $\mathcal{O}$, the benchmark solution is obtained as the ensemble average

$$\langle \mathcal{O} \rangle = \frac{1}{M} \sum_{j=1}^{M} \mathcal{O}_j, \tag{6.12}$$

where $\mathcal{O}_j$ is the Monte Carlo estimate for the observable $\mathcal{O}$ obtained for the j-th realization. Moreover, the error affecting the average observable $\langle \mathcal{O} \rangle$ is computed as detailed in Sec. 5.2. The scalar flux $\varphi_j(\mathbf{r}, E)$ has been recorded by using the standard track length estimator over a pre-defined spatial grid.

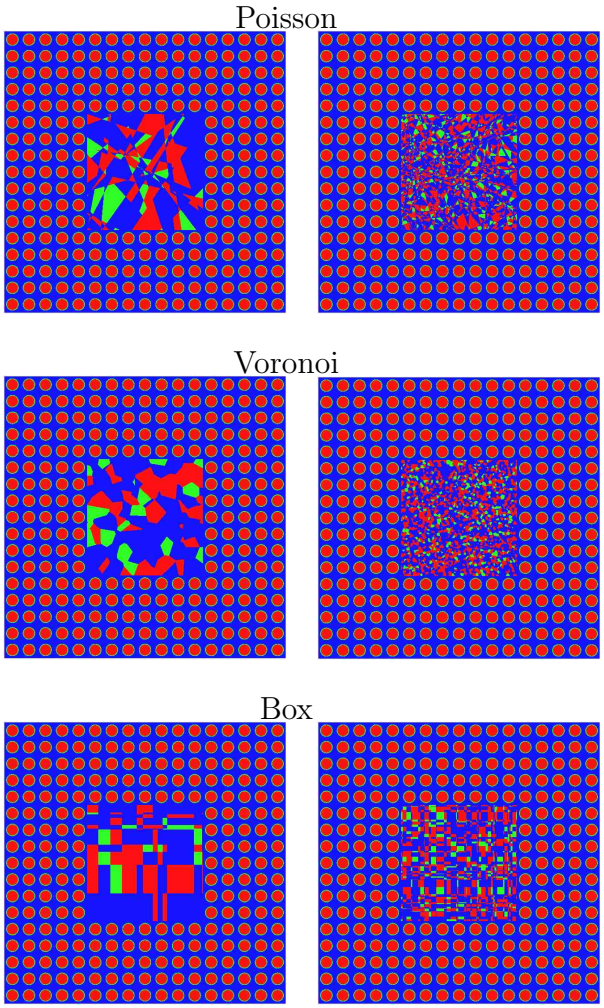

Figure 6.2: Assemblies with stochastic tessellation for the central fuel pins. Radial view of the configuration 2 ($n = 7$), for different mixing statistics and average correlation lengths Λ_c. Top: Poisson tessellation. Center: Voronoi tessellation. Bottom: Box tessellation. Left column: $\Lambda_c = 0.5$ cm. Right column: $\Lambda_c = 0.1$ cm.

Depending on the correlation lengths and on the volumetric fractions, the physical observables might display a larger or smaller dispersion around their average values. In order to assess the impact of such dispersion, we have also computed the full distribution of k_{eff} based on the available realizations. The number of realizations M has been adapted to the configuration (i.e., to the number n of fragmented fuel pins) and to the chosen average correlation length Λ_c. As a general remark, decreasing the average correlation length Λ_c for a given tessellation implies an increasing computational burden (each realization takes longer both for generation and for Monte Carlo transport), but also a better statistical averaging (a single realization is more representative of the 'typical' random behaviour). The parameter M varies between $M = 100$ for, e.g., $n = 1$ and $\Lambda_c = 0.03$ cm, and $M = 3000$ for, e.g., $n = 17$ and $\Lambda_c = 3$ cm.

In TRIPOLI-4 ®, neutrons are simulated in the energy range from 20 MeV to 10^{-5} eV. Particle transport is performed in continuous-energy, and the necessary nuclear data (i.e., point-wise cross-sections, scattering kernels, secondary energy-angle distributions, secondary particle yields, fission spectra, and so on) are read by the code from any evaluation written in ENDF-6 format. For the criticality calculations presented in the following, we have selected the `JEFF-3.1.1` nuclear data library [128]. Concerning probability tables for the unresolved resonance range, TRIPOLI-4 ® adopts the CALENDF code [137]. Thermal data $S(\alpha, \beta)$ for bound hydrogen in water were available in `JEFF-3.1.1` at 296 K. Doppler broadening of elastic scattering differential cross sections has been enforced by using the standard SVT model. The DBRC model for resonant nuclides, although available

in TRIPOLI-4 ® [168], has not been used, since it is not expected to have a major impact on reactivity and kinetics parameters at low temperature.

Concerning kinetics parameters calculations, starting from version `4.10` the Iterated Fission Probability (IFP) method has been implemented in TRIPOLI-4 ® [148] and extensively validated [148,169, 170]. The IFP method allows computing the adjoint flux $\varphi^{\dagger}$ without approximations within regular eigenvalue calculations: as such, the IFP method establishes Monte Carlo simulation as a reference tool for the analysis of effective kinetics parameters, which are key to nuclear reactor safety during transient operation and accidental excursions [56, 95]. In TRIPOLI-4 ®, a superposed-cycles implementation has been chosen for IFP, with an arbitrary number of latent generations M [148]. For all the simulations discussed here, we have chosen $M = 20$.

Similarly as for the case of fixed-source transport, for our simulations we have benefited from the possibility of exploiting pre-computed connectivity maps. It has been recently suggested that replacing the standard track estimator by the Woodcock method would be particularly convenient for particle pursuit through stochastic geometries, since knowledge of the material type at a given point and not of boundary locations would be required [102]: unfortunately, this estimator is not available in TRIPOLI-4 ® at present time.

6.2.2 Simulation results

Complexity and computer time

Before addressing the simulation results for the ensemble-averaged physical observables, we briefly analyse the computational cost of the performed calculations as a function of the complexity of the underlying stochastic tessellations. Eigenvalue calculations have been run on a the same computer cluster as the one adopted for the previous benchmarks. The average number of polyhedra $\langle N_p \rangle$ pertaining to each random geometry increases with decreasing Λ_c, i.e., with increasing fragmentation. The scaling law is fairly independent of the mixing statistics m, and roughly goes as $\langle N_p \rangle \sim 1/\Lambda_c^3$ for any m. The exponent of the scaling law stems from the dimension $d = 3$. The number n of fragmented fuel pins does not affect these results, as expected. The corresponding (ensemble-averaged) computer times for each assembly configuration are reported in Tab. 6.2. Dispersions $\sigma[t]$ are also given. The simulation time increases when increasing the portion of the assembly that is subject to fragmentation. While a decreasing trend for $\langle t \rangle$ as a function of Λ_c is clearly apparent, subtle effects due to correlation lengths and volume fractions for the material compositions come also into play, and strongly influence the average computer time. For some configurations, the dispersion $\sigma[t]$ may become very large, and even be comparable to the average $\langle t \rangle$. The chosen tessellation model visibly affects the computer time. Atomic mix simulations are based on a single homogenized realization.

The multiplication factor

We begin our analysis by considering the behaviour of the multiplication factor $\langle k_{\mathit{eff}} \rangle$, whose evolution is illustrated in Fig. 6.3 for UOX and MOX assemblies with $n = 1$, $n = 7$ and $n = 17$ melted fuel pins, respectively. The computed value $\langle k_{\mathit{eff}} \rangle$ is displayed as a function of increasing correlation length Λ_c, for Poisson, Voronoi and Box tessellations. As detailed above, the error bar on $\langle k_{\mathit{eff}} \rangle$ results from the contribution of the Monte Carlo statistical error (which is of the order of about 50 pcm for all simulations) and the dispersion due to the random realizations. The limit case of atomic mix ($\Lambda_c \to 0$) is also shown. In each figure, the $k_{\mathit{eff},0}$ eigenvalue corresponding to an assembly with intact fuel pins is plotted for reference.

It is interesting to remark that the behaviour of $\langle k_{\mathit{eff}} \rangle$ as a function of Λ_c has been examined in [109, 114] for mono-energetic transport in a rod geometry with Poisson mixing statistics, based on previous work [157, 158]. By resorting to an ingenuous perturbative approach, in [114] it was concluded that $\langle k_{\mathit{eff}} \rangle \geq k_{\mathit{eff},am}$ for $\Lambda_c \to 0$, where $k_{\mathit{eff},am}$ is the eigenvalue corresponding to a (non-stochastic) atomic mix fragmentation. This result surprisingly seems to hold also in the configurations examined here, although we are considering neutron transport in continuous-energy, three-dimensional, highly heterogeneous configurations. This finding is rather intriguing and surely deserves further

			$\Lambda_c = 0.15$ cm	$\Lambda_c = 3$ cm
n	t_{mix}	m	$\langle t \rangle \pm \sigma[t]$	$\langle t \rangle \pm \sigma[t]$
1	3260	$\mathcal{P}$	6170 ± 570	2970 ± 40
		$\mathcal{V}$	4580 ± 110	2940 ± 25
		$\mathcal{B}$	4060 ± 225	2960 ± 30
7	2990	$\mathcal{P}$	18000 ± 3000	2840 ± 60
		$\mathcal{V}$	9200 ± 150	2820 ± 30
		$\mathcal{B}$	7500 ± 1000	2840 ± 40
17	1350	$\mathcal{P}$	48000 ± 16000	2200 ± 200
		$\mathcal{V}$	14000 ± 300	2300 ± 200
		$\mathcal{B}$	16000 ± 3000	2200 ± 200

Table 6.2: Average computer time $\langle t \rangle$ (expressed in seconds) and the corresponding standard deviation $\sigma[t]$ for transport simulations in benchmark configurations $n = 1$, $n = 7$ and $n = 17$ with UOX fuel, as a function of the mixing statistics m, for the minimal and maximal values of the correlation length. The computer time t_{mix} (expressed in seconds) for transport simulations corresponding to atomic mix fuel fragmentation is also displayed. For reference, the computer time for a transport simulation in the UOX assembly with intact fuel pins is equal to 3240 seconds.

investigation. Care should be taken, since the application of expectation operators to the eigenvalue equation might subtly affect the value of $\langle k_{\mathit{eff}} \rangle$ with respect to the deterministic $k_{\mathit{eff},am}$ [109, 114, 157, 158].

In the limit of very large Λ_c, the portion of the assembly affected by the stochastic tessellations would be trivially filled with a single material (fuel, cladding, or moderator), each appearing with its respective coloring probability. In this case, $\langle k_{\mathit{eff}} \rangle$ would be the weighted sum of the multiplication factors of three configurations with the central portion of the assembly replaced by a fuel, cladding or moderator zone, and this value would be typically lower than the reference $k_{\mathit{eff},0}$ pertaining to the unperturbed regular lattice.

Between these two extreme values, for all the stochastic tessellations models $\langle k_{\mathit{eff}} \rangle$ first increases for increasing correlation length Λ_c up to a maximum value, and then decreases for even larger correlation lengths. As shown in Fig. 6.3, this maximum can be in excess or in defect with respect to $k_{\mathit{eff},0}$, depending on the mixing statistics and on the material compositions. Fuel fragmentation would be in principle expected to lower the reactivity of the assemblies, where fuel is arranged in a regular lattice with carefully chosen pitch. However, the lattices are under-moderated, so that local portions of fuel and water that are more reactive than the lattice might appear after fragmentation. In practice, spectral effects related to neutron thermalization in the presence of Uranium vs. Plutonium chunks come also into play, and it turns out that MOX assemblies generally present larger reactivity excursions, with a peak well beyond $k_{\mathit{eff},0}$ for all tessellation models (at least for $n = 7$ and $n = 17$). The redistribution of fissile mass (which is not exactly preserved for a single realization, as observed above) might also contribute to the differences between UOX and MOX assemblies for intermediate correlation lengths. The discrimination of these effects will be left for future work.

As expected on physical grounds, the impact of the stochastic tessellations on the multiplication factor depends on the size of the assembly that has been randomly fragmented. When $n = 1$, the difference between $\langle k_{\mathit{eff}} \rangle$ and the reference $k_{\mathit{eff},0}$ is of the order of 100 pcm, and falls almost within 1σ uncertainty. The major contribution to the dispersion of the multiplication factor stems from the statistical error. In this case, the impact of the specific tessellations models is not appreciable. For UOX assemblies, the average values $\langle k_{\mathit{eff}} \rangle$ lie all slightly above $k_{\mathit{eff},0}$ for any Λ_c, and seem to attain $k_{\mathit{eff},0}$ in the atomic mix limit. For MOX assemblies, the average values $\langle k_{\mathit{eff}} \rangle$ lie all slightly below $k_{\mathit{eff},0}$ for any Λ_c, even in the atomic mix limit.

When $n = 7$, a relevant portion of the fuel pins is fragmented, and the impact of the stochastic

tessellations on the eigenvalue becomes apparent. For both UOX and MOX assemblies, in the atomic mix limit $\langle k_{eff} \rangle$ is well below the reference $k_{eff,0}$ (about 1000 pcm for UOX and 2000 pcm for MOX). The values $\langle k_{eff} \rangle$ computed for Poisson and Box tessellations are almost indistinguishable, which supports our previous analysis. On the contrary, the $\langle k_{eff} \rangle$ obtained for the Voronoi tessellations reach their maximum for a Λ_c larger than in the case of the other two tessellations. The $\langle k_{eff} \rangle$ for Voronoi tessellations lie first below those of the Poisson and Box tessellations; after that $\langle k_{eff} \rangle$ has attained its maximum for the Poisson and Box tessellations, the values corresponding to Voronoi tessellations lie above the others. For the UOX assemblies, the maximum $\langle k_{eff} \rangle$ for Poisson and Box tessellations (for $\Lambda_c \sim 0.5$ cm) is about 300 pcm lower than $k_{eff,0}$, whereas for Voronoi tessellations (for $\Lambda_c \sim 0.7$ cm) is slightly higher. For MOX assemblies, the maxima are attained for larger average correlation lengths ($\Lambda_c \sim 1$ cm for Poisson and Box tessellations and $\Lambda_c \sim 1.6$ cm for Voronoi tessellations) and are largely higher than the reference $k_{eff,0}$ by about 500 pcm.

The behaviour of the case $n = 17$, where the entire collection of fuel pins in the assembly is fragmented, is similar to that of the case $n = 7$. The position of the maxima of $\langle k_{eff} \rangle$ as a function of the average correlation length Λ_c is almost unchanged. The range of excursion of $\langle k_{eff} \rangle$ in the explored domain is nonetheless much larger. The eigenvalue corresponding to the atomic mix limit is lower by about 5000 pcm for the UOX case, and by about 12000 pcm for the MOX case. For UOX, the maxima of $\langle k_{eff} \rangle$ fall below (for Poisson and Box tessellations) or slightly above (for Voronoi tessellations) the reference $k_{eff,0}$. For MOX, the maxima exceed $k_{eff,0}$ by about 2000 pcm for Poisson and Box tessellations, and by about 4000 pcm for Voronoi tessellations.

The delayed neutron fraction

The evolution of the effective delayed neutron fraction $\langle \beta_{eff} \rangle$ is illustrated in Fig. 6.4 for UOX and MOX assemblies with $n = 1$, $n = 7$ and $n = 17$ melted fuel pins, respectively. The computed value $\langle \beta_{eff} \rangle$ is displayed as a function of increasing correlation length Λ_c, for Poisson, Voronoi and Box tessellations. The error bar on $\langle \beta_{eff} \rangle$ is of the order of about 1% of the average, which is comparable with the uncertainty stemming from the IFP calculation for the reference assembly. The limit case of atomic mix ($\Lambda_c \to 0$) is also shown. In each figure, the $\beta_{eff,0}$ value corresponding to an assembly with intact fuel pins is plotted for reference.

For all the assembly configurations, the impact of stochastic tessellations on $\langle \beta_{eff} \rangle$ is only marginal, and in most cases well within error bars. For UOX assemblies we remark nonetheless that the random fragmentation introduces a slight bias on the average value, i.e., $\langle \beta_{eff} \rangle \leq \beta_{eff,0}$, where $\beta_{eff,0}$ is the reference value corresponding to an assembly with intact fuel pins. On the contrary, for MOX assemblies $\langle \beta_{eff} \rangle \simeq \beta_{eff,0}$.

The behaviour of $\langle \beta_{eff} \rangle$ is almost unaffected by the choice of the mixing statistics. Similarly, the average correlation length Λ_c plays no role, and the resulting $\langle \beta_{eff} \rangle$ show a slight increasing trend only for the case $n = 17$. Actually, the effective delayed neutron fraction $\langle \beta_{eff} \rangle$ depends mostly on the volumic fraction of fuel within the assembly, and this quantity is basically flat as a function of Λ_c, as discussed in Sec. 6.2.3.

The neutron generation time

The evolution of the effective neutron generation time $\langle \Lambda_{eff} \rangle$ is illustrated in Figs. 6.5 for UOX and MOX assemblies with $n = 1$, $n = 7$ and $n = 17$ melted fuel pins, respectively. The computed value $\langle \Lambda_{eff} \rangle$ is displayed as a function of increasing average correlation length Λ_c, for Poisson, Voronoi and Box tessellations. The error bar on $\langle \Lambda_{eff} \rangle$ is of the order of about 0.1% of the average, which is comparable with the uncertainty stemming from the IFP calculation for the reference assembly. The limit case of atomic mix ($\Lambda_c \to 0$) is also shown. In each figure, the $\Lambda_{eff,0}$ value corresponding to an assembly with intact fuel pins is plotted for reference.

As expected, in the case $n = 1$ the impact of the stochastic tessellations is small, and the discrepancy between $\langle \Lambda_{eff} \rangle$ and $\Lambda_{eff,0}$ lies within the error bar. For UOX assemblies, the random fragmentation induces $\langle \Lambda_{eff} \rangle \leq \Lambda_{eff,0}$ for any Λ_c, where $\Lambda_{eff,0}$ is the reference value corresponding to an assembly with intact fuel pins. On the contrary, for MOX assemblies $\langle \Lambda_{eff} \rangle \geq \Lambda_{eff,0}$ for any Λ_c.

For the assembly configurations with $n = 7$, the effects of the fuel fragmentation are clearly apparent for $\langle \Lambda_{eff} \rangle$. In the atomic mix limit for small Λ_c, $\langle \Lambda_{eff} \rangle$ lies below $\Lambda_{eff,0}$, and it gradually increases as a function of Λ_c. The ensemble-averaged $\langle \Lambda_{eff} \rangle$ becomes larger than $\Lambda_{eff,0}$ at $\Lambda_c \simeq 0.3$ cm for all mixing statistics. Poisson and Box tessellations yield almost identical results, and the corresponding $\langle \Lambda_{eff} \rangle$ are systematically higher than those from Voronoi tessellations. For UOX assemblies, $\langle \Lambda_{eff} \rangle$ increases by about 10% in the range of Λ_c explored here, whereas for MOX assemblies the increase is of the order of 20% for the same range of Λ_c.

For the case $n = 17$ the behaviour of $\langle \Lambda_{eff} \rangle$ is qualitatively similar to that of $n = 7$, but the excursion range as a function of Λ_c is wider. In particular, for UOX assemblies $\langle \Lambda_{eff} \rangle$ increases by about 300% in the range of Λ_c explored here, whereas for MOX assemblies the increase is of the order of 600% for the same range of Λ_c. As in the previous case, Poisson and Box tessellations yield results for $\langle \Lambda_{eff} \rangle$ that lie systematically higher than those of Voronoi tessellations.

Distribution of the multiplication factor

So far, we have focused on the ensemble-averaged physical observables $\langle k_{eff} \rangle$, $\langle \beta_{eff} \rangle$, and $\langle \Lambda_{eff} \rangle$, and their evolution as a function of the average correlation length for different mixing statistics. In order to fully apprehend the dispersion of the multiplication factors around their average values due to the variability of the random geometry realizations, which is key for criticality safety applications, we have also computed the histograms $\Pi(k_{eff})$. Some representative distributions are displayed in Fig. 6.6 (left) as a function of Λ_c for a Poisson tessellation and in Fig. 6.6 (right) as a function of the mixing statistics for fixed Λ_c.

Fig. 6.6 (left) shows that the shape of the (k_{eff}) distribution is sensitive to the average correlation length: when Λ_c is small, (k_{eff}) is almost Gaussian, with a small dispersion around the average $\langle k_{eff} \rangle$; as Λ_c increases, the dispersion increases, and $\Pi(k_{eff})$ becomes less symmetric (in particular, a long left tail appears for large values of Λ_c).

Fig. 6.6 (right) shows the impact of the mixing statistics on the shape of $\Pi(k_{eff})$, for a given average correlation length Λ_c. It is apparent that the stochastic tessellations affect not only the average values $\langle k_{eff} \rangle$, but also their dispersion. In particular, for the example considered here, The Voronoi tessellation leads to a Gaussian distribution rather peaked around the average value, whereas the Poisson and Box tessellations (whose $\Pi(k_{eff})$ are almost identical) lead to more dispersed and asymmetric distributions, with a long left tail.

Scalar neutron flux

We conclude our analysis by considering the effects of fuel fragmentation on the ensemble-averaged and normalized scalar neutron flux $\langle \varphi(\mathbf{r}, E) \rangle$. For our Monte Carlo simulations, we have defined a 17×17 $x - y$ spatial mesh superposed to the fuel pin-cells, with a single mesh along the z axis. For symmetry reasons, the flux in the reference assemblies should be spatially flat, due to reflective boundary conditions. As for the energy dependence, we have considered a 281 group mesh, covering the entire energy range of the simulation, namely 10^{-5} eV to 20 MeV.

The spatial behaviour of the neutron flux $\langle \varphi(\mathbf{r}) \rangle$ is shown in Fig. 6.7 for $n = 1$ in some representative UOX and MOX assemblies, respectively, and in Fig. 6.8 for $n = 7$ in some representative UOX and MOX assemblies. These curves have been obtained by integrating $\langle \varphi(\mathbf{r}, E) \rangle$ over the entire energy range. The case $n = 17$ leads to a spatially flat neutron flux (the fragmentation is homogeneous and extended to the whole assembly) and will not be shown here. For all the examples discussed here we have considered Poisson stochastic tessellations.

For $n = 1$, the effects of the stochastic tessellations on the spatial shape of the neutron flux are small, and mostly extended to a neighbourhood of the fragmented fuel pin-cell (see Fig. 6.7). The impact is slightly larger for MOX than for UOX assemblies. The sign of the perturbation with respect to the remaining portion of the assembly evolves as a function of Λ: for small Λ_c the ensemble-averaged flux close to the fragmented fuel cell lies below the value for the rest of the assembly, whereas for larger Λ_c the flux close to the fragmented fuel cell lies above. The value of Λ_c for which the ensemble-averaged spatial flux is entirely flat (i.e., the stochastic tessellation has no visible effect on the flux) corresponds

approximately to the average correlation length through a fuel pin. In other words, if the fragmentation of the random geometry is such that neutron trajectories see a homogeneous region whose average behaviour is statistically compatible with the heterogeneous regions of the intact fuel cell, then the neutron flux becomes insensitive to the fragmentation.

When $n = 7$ (Fig. 6.8), the behaviour of the spatial flux is qualitatively similar to the previous case. The amplitude of the perturbations introduced by the stochastic tessellations is larger, and the effect is extended on a larger portion of the assembly. Similarly as for $n = 1$, the MOX assemblies are more sensitive to the perturbation. Again, the sign of the perturbation with respect to the remaining portion of the assembly depends evolves as a function of Λ: for small Λ_c the ensemble-averaged flux close to the fragmented portion of the assembly lies below the value for the rest of the assembly, whereas for larger Λ_c the perturbed flux lies above. As before, there exists a value of Λ_c for which the ensemble-averaged spatial flux is entirely flat.

Concerning the behaviour of the neutron flux with respect to energy, in Fig. 6.9 we show the spatially-integrated and normalized $\langle\varphi(E)\rangle$ for UOX and MOX assemblies. We have chosen the case $n = 17$ with a Poisson stochastic tessellation. The impact of stochastic tessellations on $\langle\varphi(E)\rangle$ is particularly apparent when examining the discrepancies with respect to the reference flux that is obtained for the assemblies with intact fuel pins (see Fig. 6.10), for both UOX and MOX assemblies. The effects on $\langle\varphi(E)\rangle$ vary as a function of Λ. For small Λ, $\langle\varphi(E)\rangle$ lies below the reference flux in the thermal region and above for the epi-thermal and fast regions. For larger Λ, $\langle\varphi(E)\rangle$ lies above the reference flux in the thermal region and below for the epi-thermal and fast regions.

6.2.3 Finite-size effects for the assembly calculations

An investigation of finite-size effects for the stochastic tessellations used above has been carried out for $\Lambda_{c,i}$, the average correlation length through clusters with material composition i. For illustration, in Fig. 6.11 (left) we show the case of the assembly configurations with $n = 17$, where $\Lambda_{c,i}$ is plotted as a function of Λ_c for Poisson tessellations. As Λ_c increases, the value of $\Lambda_{c,i}(L)$ obtained by Monte Carlo simulation progressively deviates from the theoretical behaviour $\Lambda_{c,i} = \Lambda_c/(1 - p_i)$.

We have also computed the average volumic fraction $\langle p_i|L\rangle$ through clusters of composition i, as a function of the average correlation length Λ_c. The comparison with the theoretical behaviour p_i (which is strictly valid only for infinite tessellations) is shown in Fig. 6.11 (right) for an assembly configuration with $n = 17$: the deviation with respect to the ideal case increases with increasing Λ_c, as expected. In order to emphasize the role of finite-size effects, in Fig. 6.11 (right) we have chosen to show the geometry-induced standard deviation σ_G on $p_i(L)$, as given in Eq. (5.7), instead of the uncertainty given by Eq. (5.9).

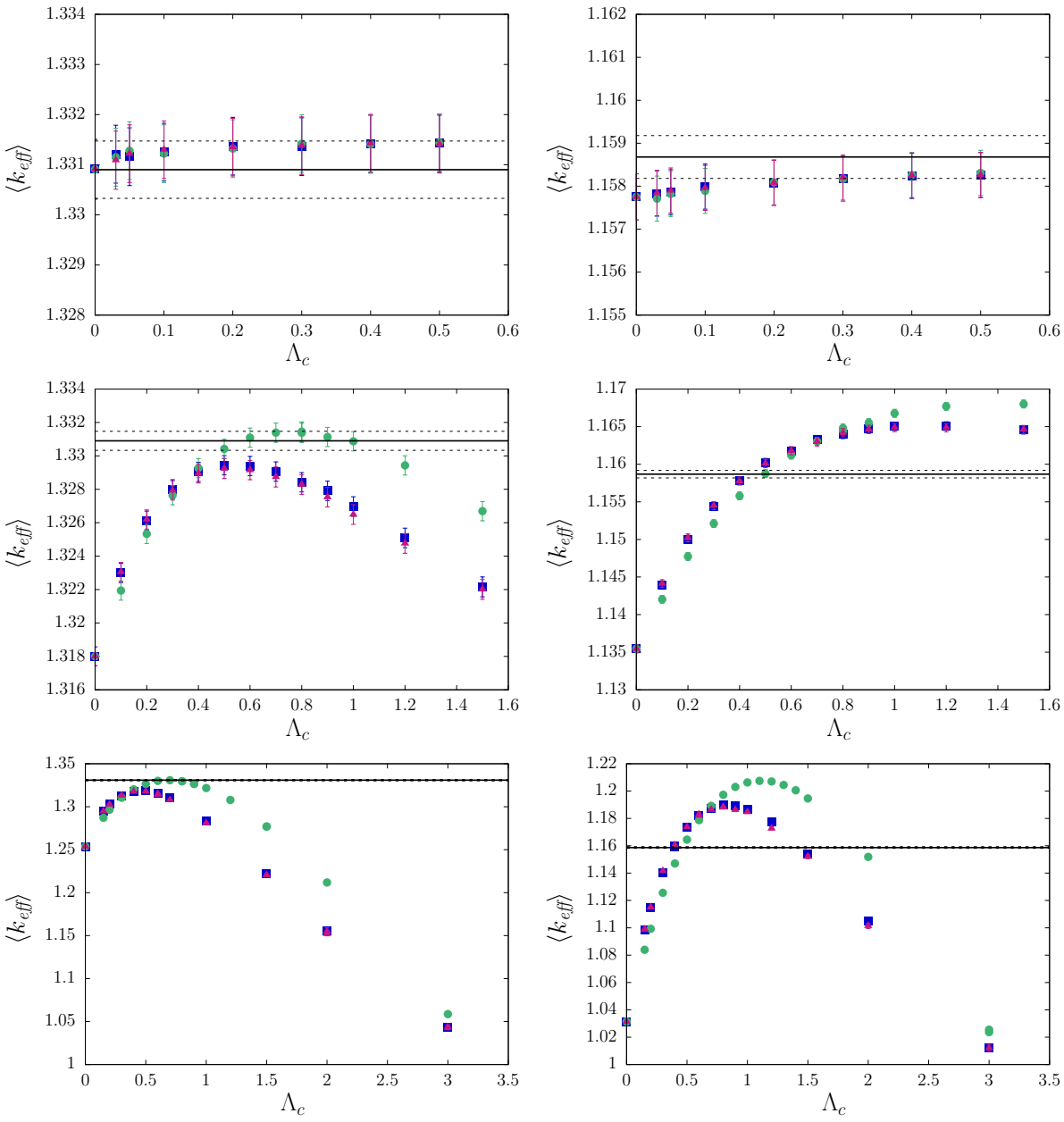

Figure 6.3: Evolution of the ensemble-averaged multiplication factor $\langle k_{eff} \rangle$ as a function of the average correlation length Λ_c, for $n = 1$ (top), $n = 7$ (middle) and $n = 17$ (bottom). Left: UOX assembly. Right: MOX assembly. Blue squares denote the results for Poisson tessellations, red triangles for Box tessellations, and green circles for Voronoi tessellations. The limit case at $\Lambda_c \to 0$ corresponds to the atomic mix model. The black solid line denotes $k_{eff,0}$, the result for the assembly with intact fuel pins, which has been added for reference (dashed lines represent the 1σ statistical uncertainty).

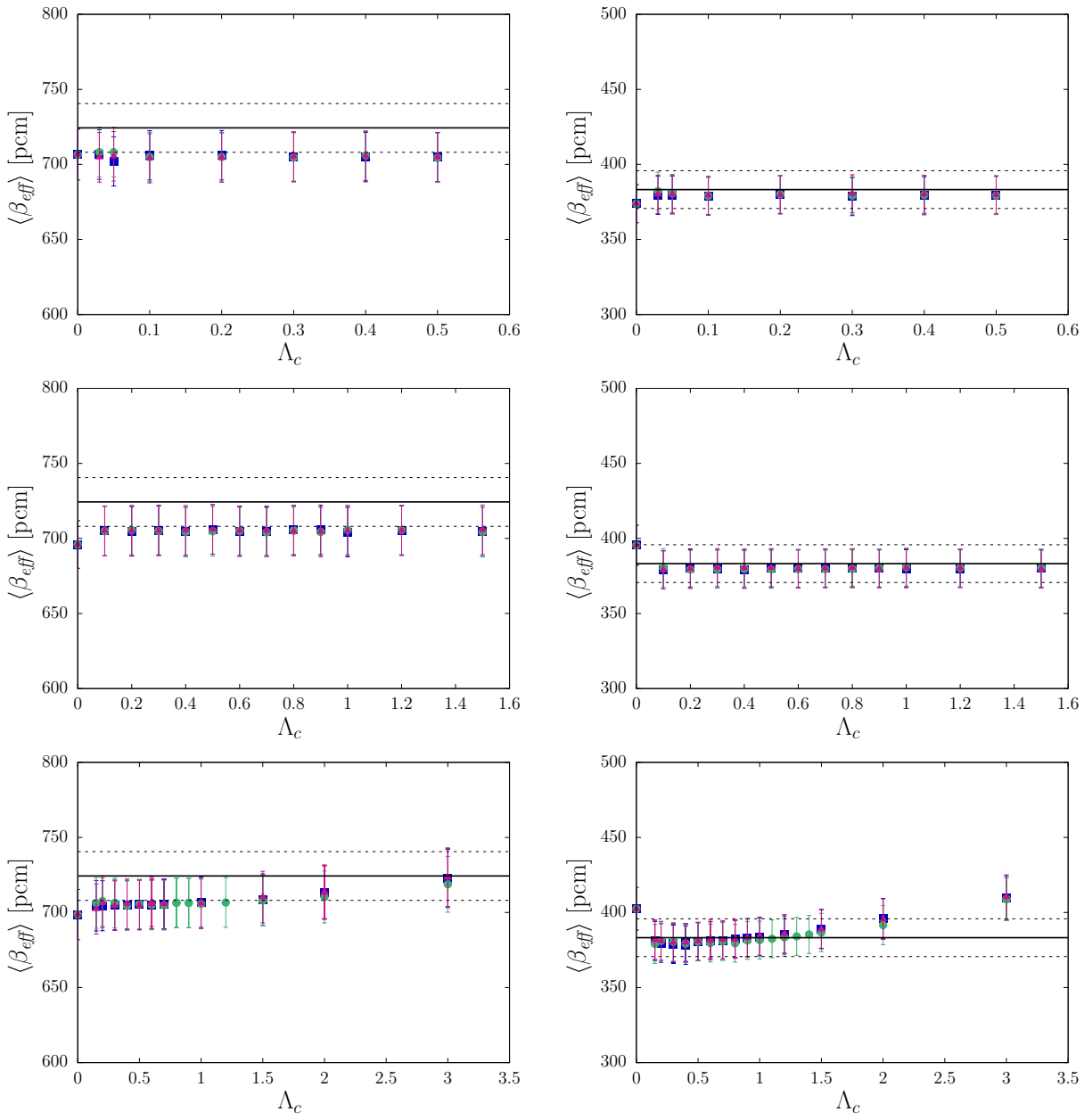

Figure 6.4: Evolution of the ensemble-averaged effective delayed neutron fraction $\langle\beta_{eff}\rangle$ as a function of the average correlation length Λ_c, for $n = 1$ (top), $n = 7$ (middle) and $n = 17$ (bottom). Left: UOX assembly. Right: MOX assembly. Blue squares denote the results for Poisson tessellations, red triangles for Box tessellations, and green circles for Voronoi tessellations. The limit case at $\Lambda_c \to 0$ corresponds to the atomic mix model. The black solid line denotes $\beta_{eff,0}$, the result for the UOX assembly with intact fuel pins, which has been added for reference (dashed lines represent the 1σ statistical uncertainty).

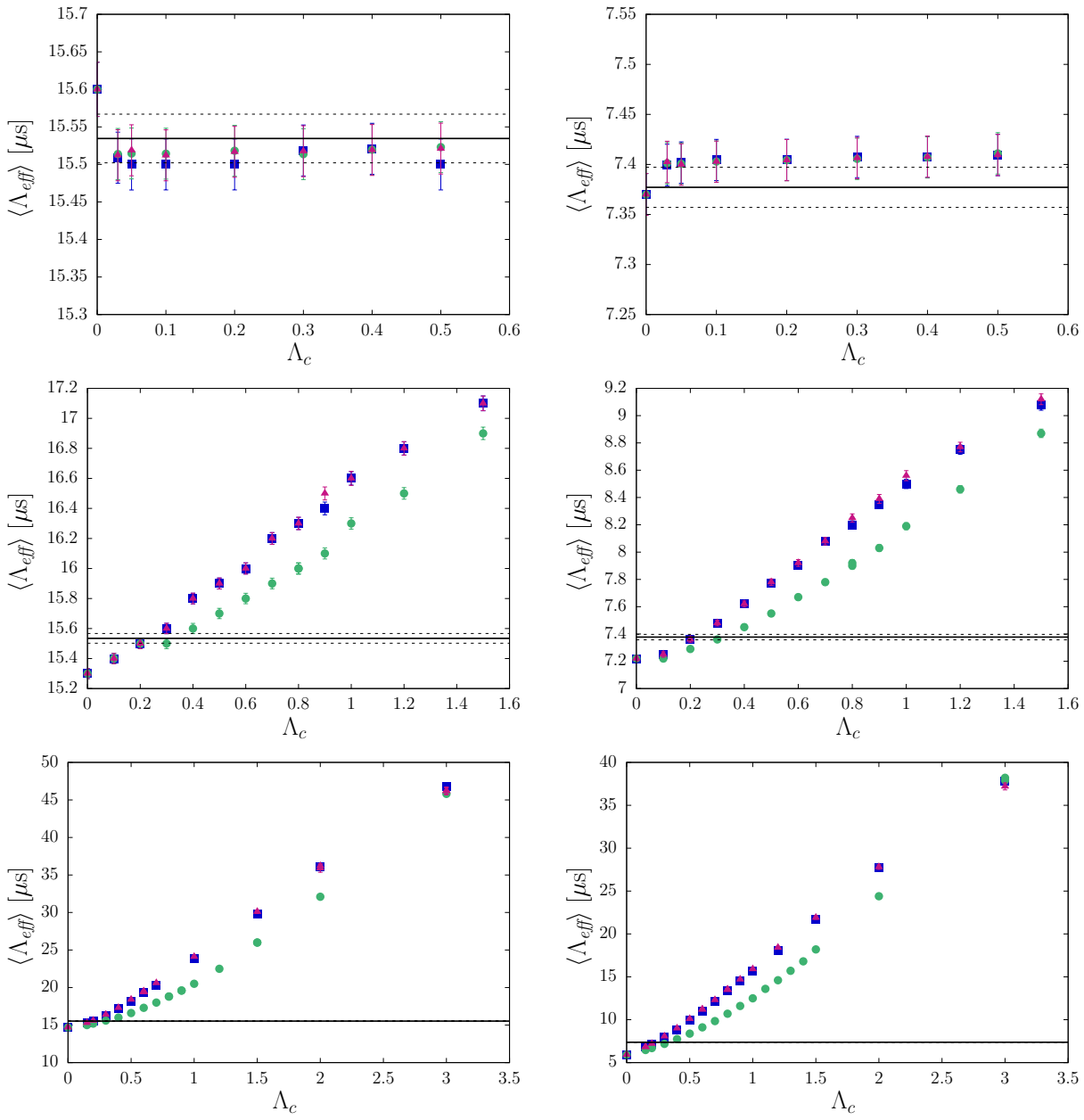

Figure 6.5: Evolution of the ensemble-averaged effective neutron generation time $\langle \Lambda_{eff} \rangle$ as a function of the average correlation length Λ_c, for $n = 1$ (top), $n = 7$ (middle) and $n = 17$ (bottom). Left: UOX assembly. Right: MOX assembly. Blue squares denote the results for Poisson tessellations, red triangles for Box tessellations, and green circles for Voronoi tessellations. The limit case at $\Lambda_c = 0$ corresponds to the atomic mix model. The black solid line denotes $\Lambda_{eff,0}$, the result for the UOX assembly with intact fuel pins, which has been added for reference (dashed lines represent the 1σ statistical uncertainty).

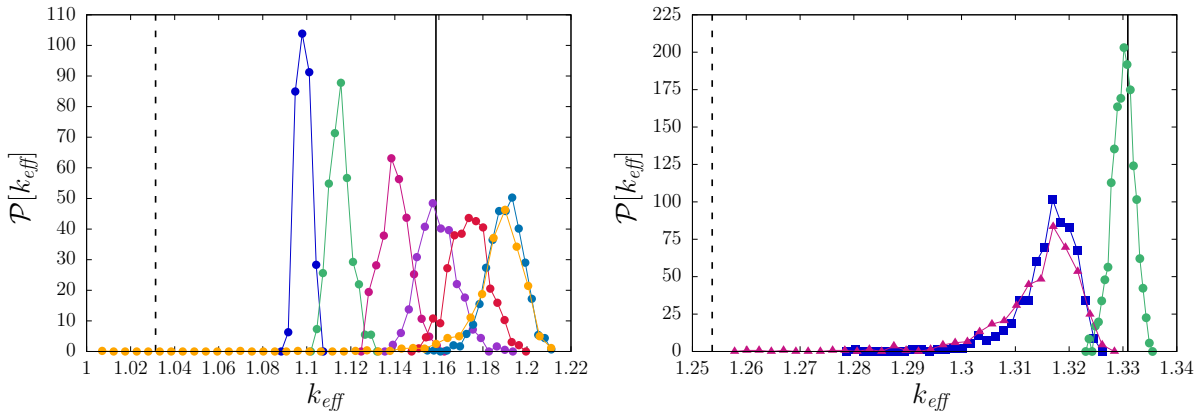

Figure 6.6: Left. Distributions of the multiplication factor k_{eff} as a function of the average correlation length Λ_c for a MOX assembly with $n = 17$. The mixing statistics is a Poisson tessellation. Blue symbols correspond to $\Lambda_c = 0.15$, green symbols to $\Lambda_c = 0.2$, magenta symbols to $\Lambda_c = 0.3$, purple symbols to $\Lambda_c = 0.4$, red symbols to $\Lambda_c = 0.5$, light blue symbols to $\Lambda_c = 0.8$ and orange symbols to $\Lambda_c = 1$. Solid black line corresponds to $k_{eff,0}$ for a MOX assembly with intact fuel pins; dashed black line corresponds to k_{eff} for a MOX assembly with atomic mix. Right. Distributions of the multiplication factor k_{eff} for a UOX assembly with $n = 17$ and different mixing statistics. The average correlation length is $\Lambda_c = 0.6$. Blue symbols correspond to a Poisson stochastic tessellation, green symbols to Voronoi stochastic tessellations and red symbols to Box stochastic tessellations. Solid black line corresponds to $k_{eff,0}$ for a UOX assembly with intact fuel pins; dashed black line corresponds to k_{eff} for a UOX assembly with atomic mix.

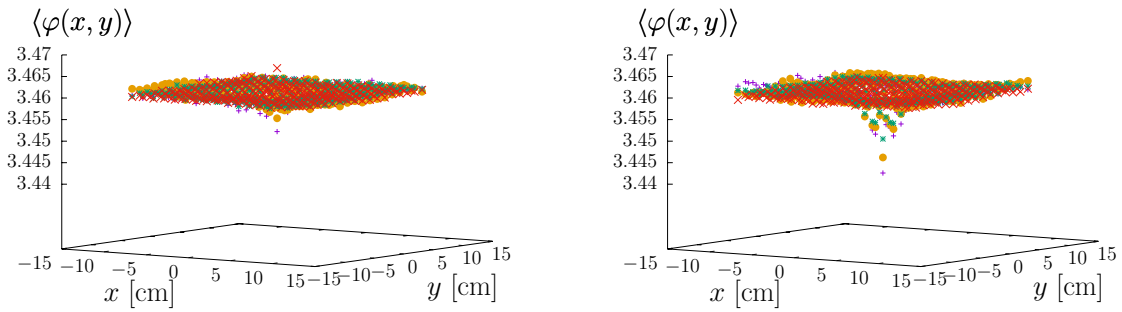

Figure 6.7: Ensemble-averaged spatial flux $\langle\varphi(x,y)\rangle$ (arbitrary units) as a function of the average correlation length Λ_c, with Poisson mixing statistics. Left: UOX assembly with $n = 1$. Purple symbols correspond to $\Lambda_c = 0.03$, orange symbols to $\Lambda_c = 0.05$, green symbols to $\Lambda_c = 0.1$ and red symbols to $\Lambda_c = 0.5$. Right: MOX assembly with $n = 1$. Purple symbols correspond to $\Lambda_c = 0.03$, orange symbols to $\Lambda_c = 0.05$, green symbols to $\Lambda_c = 0.1$ and red symbols to $\Lambda_c = 0.5$.

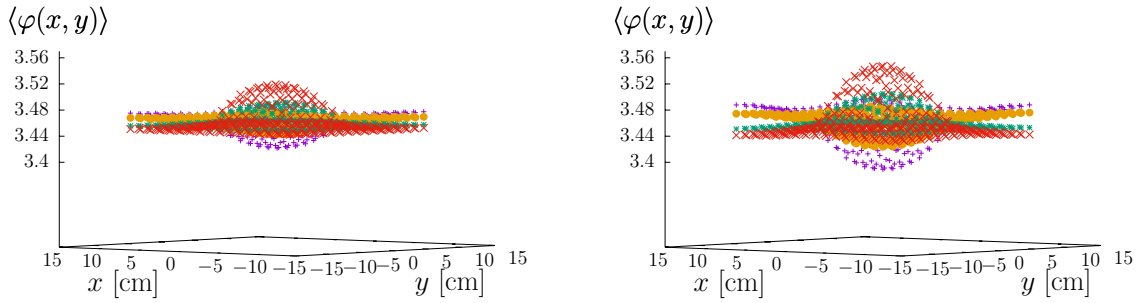

Figure 6.8: Ensemble-averaged spatial flux $\langle\varphi(x,y)\rangle$ (arbitrary units) as a function of the average correlation length Λ_c, with Poisson mixing statistics. Left: UOX assembly with $n = 7$. Purple symbols correspond to $\Lambda_c = 0.1$, orange symbols to $\Lambda_c = 0.2$, green symbols to $\Lambda_c = 0.5$ and red symbols to $\Lambda_c = 0.7$. Right: MOX assembly with $n = 7$. Purple symbols correspond to $\Lambda_c = 0.1$, orange symbols to $\Lambda_c = 0.2$, green symbols to $\Lambda_c = 0.5$ and red symbols to $\Lambda_c = 0.7$.

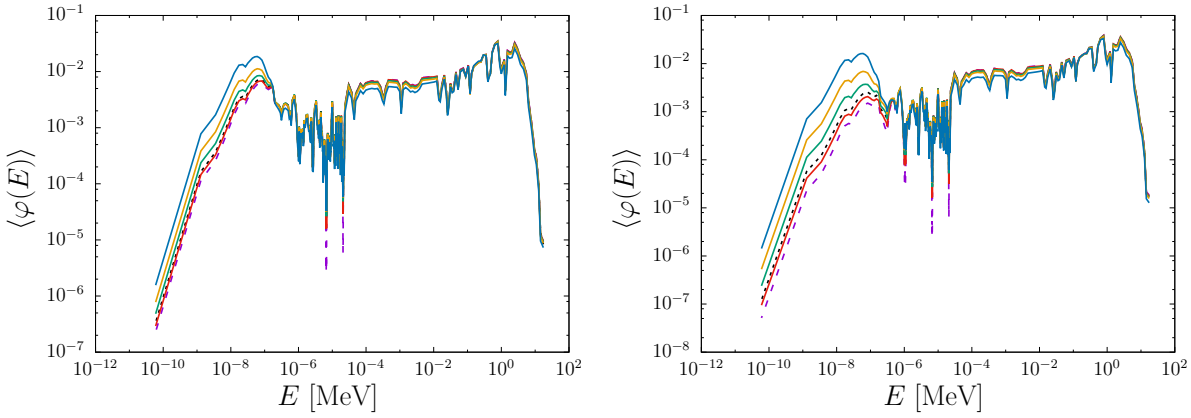

Figure 6.9: Ensemble-averaged spectral flux $\langle\varphi(E)\rangle$ (arbitrary units) as a function of the average correlation length Λ_c, with Poisson mixing statistics. Left: UOX assembly with $n = 17$. Red solid line corresponds to $\Lambda_c = 0.15$, green solid line to $\Lambda_c = 0.5$, orange solid line to $\Lambda_c = 1$ and blue solid line to $\Lambda_c = 3$. Right: MOX assembly with $n = 17$. Red solid line corresponds to $\Lambda_c = 0.15$, green solid line to $\Lambda_c = 0.5$, orange solid line to $\Lambda_c = 1$ and blue solid line to $\Lambda_c = 3$. For both UOX and MOX configurations, the dotted black line corresponds to $\langle\varphi(E)\rangle$ for assemblies with intact fuel pins; the dashed purple line corresponds to $\langle\varphi(E)\rangle$ for assemblies with atomic mix.

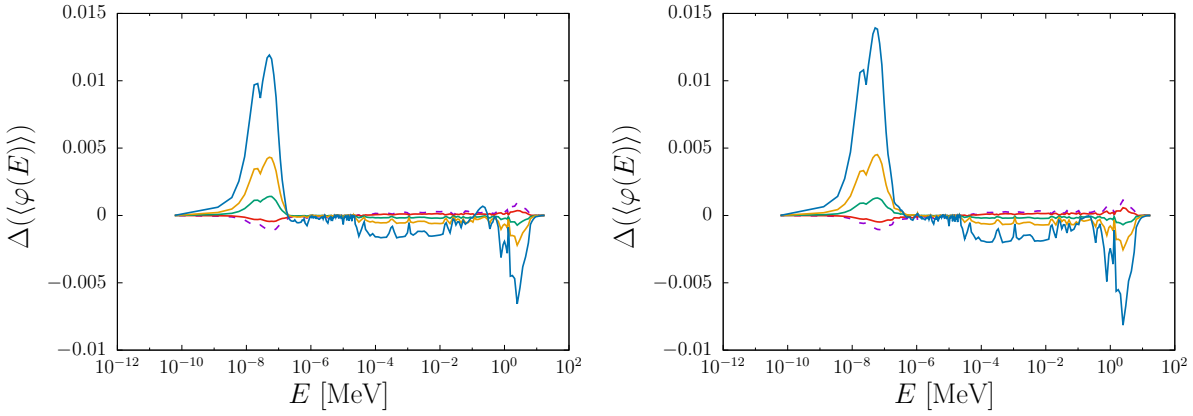

Figure 6.10: Discrepancy $\Delta[\langle\varphi(E)\rangle]$ between the ensemble-averaged spectral flux $\langle\varphi(E)\rangle$ (arbitrary units) as a function of the average correlation length Λ_c and the reference flux, for Poisson mixing statistics. Left: UOX assembly with $n = 17$. Red solid line corresponds to $\Lambda_c = 0.15$, green solid line to $\Lambda_c = 0.5$, orange solid line to $\Lambda_c = 1$ and blue solid line to $\Lambda_c = 3$. Right: MOX assembly with $n = 17$. Red solid line corresponds to $\Lambda_c = 0.15$, green solid line to $\Lambda_c = 0.5$, orange solid line to $\Lambda_c = 1$ and blue solid line to $\Lambda_c = 3$. For both MOX and UOX configurations, the dotted black line corresponds to $\langle\varphi(E)\rangle$ for assemblies with intact fuel pins; the dashed purple line corresponds to $\langle\varphi(E)\rangle$ for assemblies with atomic mix.

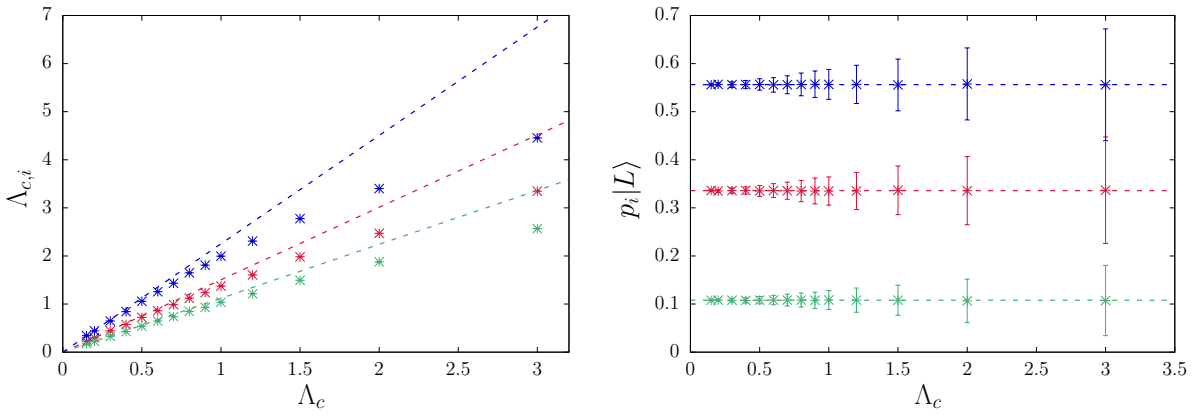

Figure 6.11: Left. Average correlation length $\Lambda_{c,i}(L)$ through clusters of composition i, as a function of Λ_c, for an assembly with $n = 17$. The case of fuel clusters is displayed in red, the case of cladding clusters in green and the case of moderator clusters in blue. Symbols correspond to Monte Carlo simulations. Theoretical values for infinite tessellations are displayed as dashed lines. Right. Average volumic fraction $\langle p_i|L\rangle$ through clusters of composition i, as a function of Λ, for an assembly with $n = 17$. Red symbols denote the fuel fraction, green symbols the cladding fraction and blue symbols the moderator fraction. Symbols correspond to Monte Carlo simulations. Error bars on Monte Carlo results represent the standard deviation σ_G on $p_i(L)$ as given in Eq. (5.7). Theoretical values for infinite tessellations are displayed as dashed lines.

6.3 Including the effects of anisotropy

For real life applications, fuel degradation will generally give rise to anisotropic re-arrangements, possibly due to gravity and other material stratification phenomena [47, 50]. To the best of our knowledge, neutron transport in anisotropic random media has been only considered in relation to the Levermore-Pomraning model [110]. For the sake of simplicity, the stochastic tessellations investigated in the previous section were isotropic (Poisson and Voronoi) or quasi-isotropic (Box). In this Section, we will extend our previous results concerning reference solutions for eigenvalue problems in random media by relaxing the isotropy hypothesis, in order to show how the geometrical properties of the underlying tessellations affect the key safety parameters for eigenvalue problems in stochastic media. For this purpose, we will resort to the anisotropic Poisson tessellations described in Sec. 2.3, and revisit our benchmark model accordingly.

6.3.1 Benchmark specifications

As a reference configuration we will consider the same assembly composed of 17×17 square fuel pin-cells as in the previous Section. In order to describe random material fragmentation, we will assume that the entire fuel lattice is replaced by a Poisson tessellation: the effects of material stratification will be modelled by introducing an anisotropy law $H(\theta, \phi)$ giving rise to planes that are preferentially orthogonal to the z axis. The typical size of the fuel fragments will be imposed by setting the average correlation length Λ_c. The coloring probabilities $p_{\mathcal{F}}$, $p_{\mathcal{C}}$ and $p_{\mathcal{M}} = 1 - p_{\mathcal{F}} - p_{\mathcal{C}}$ are the same as given in Eq. (6.11).

Similarly as done in Sec.6.2, for our benchmark configuration we will investigate the behaviour of the ensemble-averaged multiplication factor $\langle k_{\mathit{eff}} \rangle$ and the ensemble-averaged effective neutron generation time $\langle \Lambda_{\mathit{eff}} \rangle$ and effective delayed neutron fraction $\langle \beta_{\mathit{eff}} \rangle$. The ensemble-averaged scalar particle flux $\langle \varphi(E) \rangle$ within the assembly will be also examined.

In particular, we will quantify the effects of the fuel fragmentation on these observables in terms of both the anisotropy law $H(\mathbf{n})$ and the average correlation length Λ_c. For each Λ_c, we will test the impact of material stratification by varying the law $H(\mathbf{n})$, from isotropic to strongly anisotropic. In particular, we have considered the *quadratic, histogram and box* anisotropy laws introduced in Sec. 4.3.1. The limit case of *slab* tessellations, where the random planes (with exponentially distributed distances) are exactly orthogonal to the z axis, will be also explored for comparison. Some example of realizations corresponding to different anisotropy laws are shown in Fig. 6.12. As for the typical fragment size, in-core experiments suggest that Λ_c might lie in the range from less than a millimetre to several millimetres, depending on the re-solidification speed [18, 47, 50]. For each law $H(\mathbf{n})$ we will then analyse the effects of Λ_c on the observables. For Λ_c comparable to the linear size of the assembly, the tessellations are dominated by finite-size effects, and the dispersion of the volumic ratio for each material composition becomes large.

6.4 Simulation results

The reference solutions for the ensemble-averaged multiplication factor $\langle k_{\mathit{eff}} \rangle$, kinetics parameters $\langle \ell_{\mathit{eff}} \rangle$ and $\langle \beta_{\mathit{eff}} \rangle$, and scalar neutron flux $\langle \varphi(E) \rangle$ are computed by following the same strategy as in Sec 6.2.1. For each assembly configuration, a large number M of geometries is generated, and the material properties are assigned to each volume as described above. The number of simulated particle histories per configuration is given in Sec. 6.2.1. The procedure used in order to obtain the ensemble averages and the associated dispersions has been detailed in Sec. 6.2.1. The physical observables might display a larger or smaller dispersion around their average values depending on the anisotropy laws, on the correlation lengths and on the volumic fractions. The number of realizations M has been chosen based on the average correlation length Λ_c. The parameter M varies between $M = 10^2$ for $\Lambda_c = 0.15$ cm, and $M = 3 \times 10^3$ for $\Lambda_c = 3$ cm.

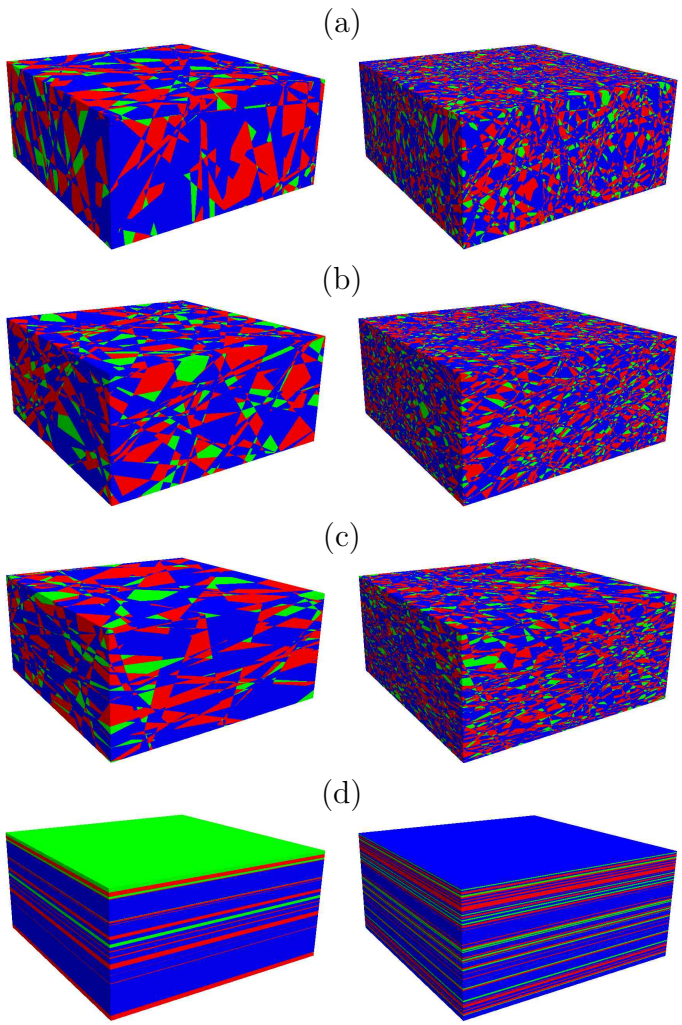

Figure 6.12: Examples of realizations of three-dimensional anisotropic Poisson tessellations as a model of damaged fuel assembly. (a) Isotropic angular distribution. (b) Quadratic angular distribution. (c) Histogram angular distribution. (d) Slab angular distribution. The average correlation length for the three realizations is $\Lambda_c = 0.5$ cm (left) and $\Lambda_c = 0.15$ cm (right). Red corresponds to fuel, green to cladding and blue to moderator.

6.4.1 The average multiplication factor

The behaviour of the ensemble-averaged multiplication factor $\langle k_{\mathit{eff}} \rangle$ is illustrated in Fig. 6.13 for UOX (left) and MOX (right) assemblies. We have determined the evolution of $\langle k_{\mathit{eff}} \rangle$ as a function of the anisotropy laws (quadratic, box, histogram and slab) and of the average correlation length Λ_c. Simulation results corresponding to isotropic Poisson tessellations had been previously examined in Sec. 6.2 and are reported here for comparison. The error bar on $\langle k_{\mathit{eff}} \rangle$ stems from the contribution of the Monte Carlo statistical error (which is of the order of about 50 pcm for all simulations, as mentioned above) and the dispersion due to the random realizations. For reference, the limit case of atomic mix ($\Lambda_c \to 0$) and the $k_{\mathit{eff},0}$ eigenvalue corresponding to an assembly with intact fuel pins are also shown in Fig. 6.13.

Fuel fragmentation has an apparent impact on stochastic tessellations. For both UOX and MOX assemblies, in the atomic mix limit $\langle k_{\mathit{eff}} \rangle$ lies well below the reference $k_{\mathit{eff},0}$ (about 8×10^3 pcm for UOX and 1.2×10^4 pcm for MOX). Close to the atomic mix limit, i.e., $\Lambda_c \to 0$, we can single out two general trends: the behaviour of $\langle k_{\mathit{eff}} \rangle$ as a function of Λ_c is almost independent of the anisotropy law $H(\mathbf{n})$; furthermore, $\langle k_{\mathit{eff}} \rangle \geq k_{\mathit{eff},am}$, where we denote by $k_{\mathit{eff},am}$ the eigenvalue corresponding to the atomic mix limit. The former feature was expected on physical grounds, based on the considerations presented in Sec. 2.3.4: for Λ_c smaller than the neutron mean free path, the distinct details of the angular law $H(\mathbf{n})$ are not detected by the transported particles, and $\langle k_{\mathit{eff}} \rangle$ is almost exclusively affected by the

average correlation length Λ_c, which is independent of $H(\mathbf{n})$. This result stresses the importance of Λ_c as a key property of the Poisson tessellations with respect to particle transport.

For increasing Λ_c, the effects of the anisotropy $H(\mathbf{n})$ on $\langle k_{eff} \rangle$ become apparent: the curve of $\langle k_{eff} \rangle$ as a function of Λ_c gets progressively lower when $H(\mathbf{n})$ is varied from isotropic to strongly anisotropic (the histogram distribution leading to an almost horizontal material stratification in the assembly). The curve of $\langle k_{eff} \rangle$ corresponding to the quadratic anisotropy, which is somehow milder than the histogram distribution, lies in between. The highest $\langle k_{eff} \rangle$ value is attained for an isotropic $H(\mathbf{n})$, which is possibly related to the peculiar inequalities for the polyhedral features of the Poisson tessellation described in Sec. 2.3.2. The values $\langle k_{eff} \rangle$ computed for isotropic and box tessellations are almost indistinguishable, as already noticed in Sec. 6.2: this surprising and important finding stems from the box tessellation being quasi-isotropic. Numerical investigations have actually shown that the chord length distribution for Poisson-Box tessellations is almost identical to that of isotropic Poisson tessellations (see Sec. 4.2.3).

In the limit of very large Λ_c, the stochastic tessellations are trivially filled with a single material (fuel, cladding, or moderator). In this case, $\langle k_{eff} \rangle$ would be the weighted sum of the multiplication factors of three configurations with the assembly replaced by a fuel, cladding or moderator volume, and this value would be typically lower than the reference $k_{eff,0}$ corresponding to the regular lattice (see also Sec. 6.2).

For any anisotropy law $H(\mathbf{n})$, the eigenvalue $\langle k_{eff} \rangle$ as a function of the average correlation length Λ_c attains a maximum, which can be in excess or in defect with respect to $k_{eff,0}$, depending on the mixing statistics and on the material compositions, but only weakly on the angular law $H(\mathbf{n})$. For the UOX assemblies, the maximum $\langle k_{eff} \rangle$ is attained for $\Lambda_c \sim 0.5$ cm (almost independently of $H(\mathbf{n})$), and lies slightly lower than $k_{eff,0}$. For MOX assemblies, the maximum is attained at a larger average correlation length $\Lambda_c \sim 1$ cm, again almost independently of $H(\mathbf{n})$, and is fairly in excess of the reference $k_{eff,0}$. Fuel fragmentation would be expected to lower the reactivity of the assemblies, where fuel is arranged in a regular lattice with optimized pitch. This seems to be the case for UOX compositions, where the tessellation model leads to maxima $\langle k_{eff} \rangle < k_{eff,0}$, independently of the angular law $H(\mathbf{n})$. MOX compositions generally lead to larger reactivity excursions, with maxima well beyond $k_{eff,0}$ for any $H(\mathbf{n})$. As observed above, fissile mass is not rigorously preserved along realizations, and this might further contribute to the discrepancies between UOX and MOX assemblies for intermediate correlation lengths (see also Sec. 6.2).

For both UOX and MOX configurations, the behaviour of $\langle k_{eff} \rangle$ for slab tessellations is distinct with respect to the case of regular anisotropic Poisson tessellations. Slab tessellations formally correspond to degenerate anisotropic Poisson tessellations where a single direction for sampling the random planes is allowed: in the limit of infinite tessellations, this yields polyhedral cells of unbounded volume and surface (contrary to the case of non-degenerate $H(\mathbf{n})$ distributions, for which the polyhedral cells are always bounded, even for infinite tessellations). Nonetheless, the average correlation length Λ_c is well defined and stays finite, which allows comparing slab tessellations to anisotropic Poisson tessellations for a given Λ_c. Moreover, for finite tessellations as those applied to the fragmented assembly model, all polyhedral features of slab tessellations are finite, although cells span the entire geometry. Yet, the peculiar geometrical features of these configurations is mirrored in the resulting properties of the eigenvalues for criticality calculations: in particular, the maximum $\langle k_{eff} \rangle$ eigenvalue is attained for smaller Λ_c (about 0.25 cm for UOX compositions, and 0.5 cm for MOX compositions) and the peak value is lower than in the case of regular anisotropic Poisson tessellations. For MOX assemblies, the maximum corresponding to slab tessellations lies in slight defect of $k_{eff,0}$. These findings are intimately related to the fact that moderator and cladding layers in slab configurations allow for longer neutron excursions in the transversal direction (i.e., without encountering fuel layers) that are forbidden when the polyhedral cells are bounded.

The distribution of the multiplication factor

For criticality safety applications, the dispersion of the multiplication factors around their average values due to the variability of the random geometry realizations is of utmost interest. For this purpose,

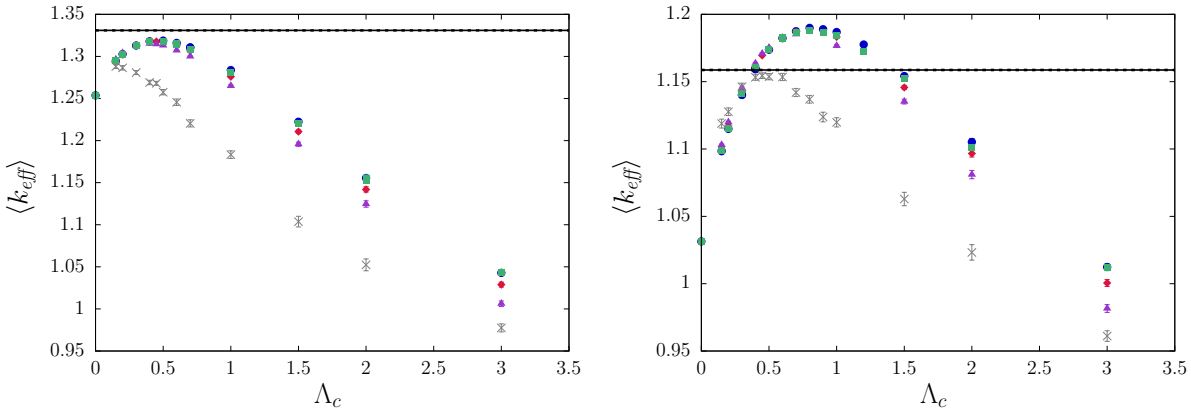

Figure 6.13: Evolution of the ensemble-averaged multiplication factor $\langle k_{eff} \rangle$ as a function of the average correlation length Λ_c and of the anisotropy law $H(\mathbf{n})$. Left: UOX assembly. Right: MOX assembly. Symbols denote Monte Carlo simulation results: blue circles correspond to isotropic distribution, red diamonds to quadratic distribution, purple triangles to histogram distribution, green squares to box distribution and gray crosses to slab distribution. The limit case at $\Lambda_c = 0$ corresponds to the atomic mix model. The black solid line denotes $k_{eff,0}$, the result for the assembly with intact fuel pins, which has been added for reference (dashed lines represent the 1σ statistical uncertainty).

we have also computed the distributions $\mathcal{P}(k_{eff})$. Some representative histograms corresponding to MOX fuel are displayed in Fig. 6.14 as a function of the anisotropy law $H(\mathbf{n})$ for fixed Λ_c (left) or as a function of Λ_c for the same law $H(\mathbf{n})$ (right). In particular, Fig. 6.14 (left) shows that the shape of the $\mathcal{P}(k_{eff})$ distribution is only weakly sensitive to the anisotropy law $H(\mathbf{n})$ for the value of $\Lambda = 1$ cm chosen here. Only the slab tessellation shows a largely different behaviour, as already suggested by the analysis of the average $\langle k_{eff} \rangle$. All the distributions are highly skewed, with a longer tail for lower values of k_{eff}. Figure 6.14 (right) shows the impact of the average correlation length for the case of the histogram anisotropy distribution. It is apparent that Λ_c strongly affects not only the average $\langle k_{eff} \rangle$, but also the dispersion and the skewness of the full distribution $\mathcal{P}(k_{eff})$.

The average kinetics parameters

The evolution of the ensemble-averaged effective delayed neutron fraction $\langle \beta_{eff} \rangle$ is illustrated in Fig. 6.15 for UOX (left) and MOX (right) assemblies. The values $\langle \beta_{eff} \rangle$ obtained by Monte Carlo simulation are displayed as a function of the average correlation length Λ_c, for different anisotropy laws $H(\mathbf{n})$. The isotropic case is taken from Sec. 6.2. The findings corresponding to slab tessellations are shown as well. The limit case corresponding to the atomic mix is also displayed. Moreover, the $\beta_{eff,0}$ value corresponding to an assembly with intact fuel pins is plotted for reference. The impact of stochastic tessellations on $\langle \beta_{eff} \rangle$ is weak, and typically well within error bars. The behaviour of $\langle \beta_{eff} \rangle$ is almost unaffected by the choice of the anisotropy law $H(\mathbf{n})$. The case of slab tessellations yields results that are entirely compatible with those of regular anisotropic tessellations. For UOX assemblies we remark nonetheless that the random fragmentation introduces a slight bias on the average value, i.e., $\langle \beta_{eff} \rangle \leq \beta_{eff,0}$, where $\beta_{eff,0}$ is the reference value corresponding to an assembly with intact fuel pins. On the contrary, for MOX assemblies $\langle \beta_{eff} \rangle \simeq \beta_{eff,0}$. The resulting $\langle \beta_{eff} \rangle$ shows a slight increasing trend with respect to the average correlation length Λ_c. Actually, the effective delayed neutron fraction $\langle \beta_{eff} \rangle$ depends mostly on the volumic fraction of fuel within the assembly, and this quantity only weakly depends on Λ_c and $H(\mathbf{n})$; however, for large Λ_c finite-size effects come into play and affect the distribution of the fissile mass within the assembly (the mass is not exactly preserved by the ternary mixing model, as observed above).

The behaviour of the ensemble-averaged effective neutron generation time $\langle \Lambda_{eff} \rangle$ is illustrated in Fig. 6.16 for UOX (left) and MOX (right) assemblies. The values $\langle \Lambda_{eff} \rangle$ obtained by Monte Carlo

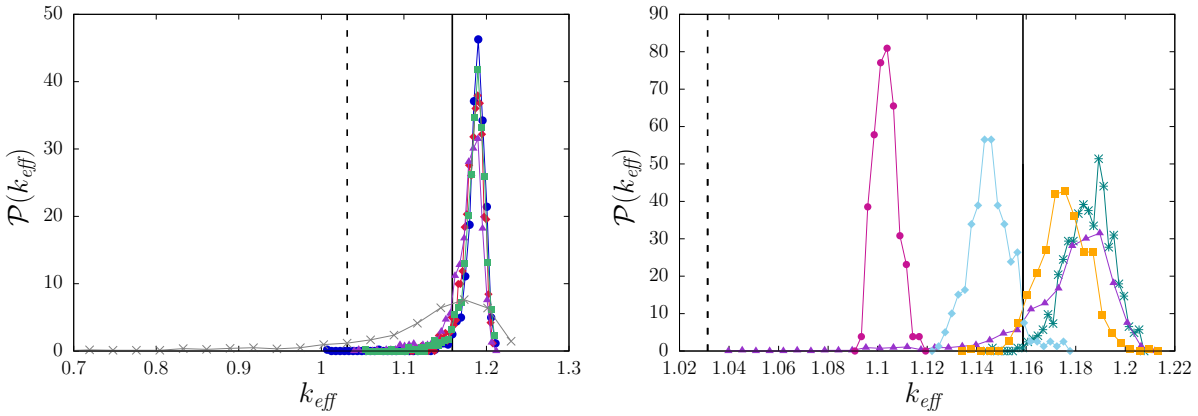

Figure 6.14: Distributions $\mathcal{P}(k_{eff})$ of the multiplication factor k_{eff} for MOX configurations. Left. Impact of the anisotropy law $H(\mathbf{n})$ for fixed Λ_c. Blue circles correspond to isotropic case, red diamonds to quadratic case, purple triangles to histogram case, green squares to box case and gray crosses to slab case, for $\Lambda_c = 1$ cm. Right. Impact of the average correlation length Λ_c for fixed $H(\mathbf{n})$. Magenta circles represent $\Lambda_c = 0.15$ cm, light blue diamonds $\Lambda_c = 0.3$ cm, orange squares $\Lambda_c = 0.5$ cm, dark green crosses $\Lambda_c = 0.7$ cm and purple triangles $\Lambda_c = 1$ cm, for the histogram anisotropy law. The reference values for the case of the intact assembly and for the atomic mix regime are shown as a solid black line and as a dashed black line, respectively.

simulation are displayed as a function of the average correlation length Λ_c, for different anisotropy laws $H(\mathbf{n})$. The isotropic case is taken from Sec. 6.2. The findings corresponding to slab tessellations are shown as well. The limit case corresponding to the atomic mix is also displayed. Moreover, the $\Lambda_{eff,0}$ value corresponding to an assembly with intact fuel pins is plotted for reference. Contrary to the delayed neutron fraction, the effective neutron generation time $\langle \Lambda_{eff} \rangle$ is strongly affected by the fuel fragmentation. In the atomic mix limit for small Λ_c, $\langle \Lambda_{eff} \rangle$ lies slightly below $\Lambda_{eff,0}$, and rapidly increases as a function of Λ_c. In particular, for UOX assemblies $\langle \Lambda_{eff} \rangle$ increases by a factor of 3 in the range of Λ_c explored here, whereas for MOX assemblies $\langle \Lambda_{eff} \rangle$ increases by a factor of 6 for the same range of Λ_c. Enhancing the degree of anisotropy from the isotropic distribution to the histogram distribution increases $\langle \Lambda_{eff} \rangle$, the quadratic law lying in between. Isotropic and box tessellations yield almost identical results. The simulation results corresponding to the slab tessellations are larger than for the regular anisotropic Poisson tessellations: these findings can be explained by the increased lifetime of neutrons in these configurations, the moderator and cladding layers allowing for longer excursions without being absorbed in the transversal directions, i.e, within the material layers.

Analysis of neutron flux

We consider now the effects of fuel fragmentation on the ensemble-averaged and normalized fundamental eigenmode $\langle \varphi(E) \rangle$. We have considered a 281 group mesh, covering the entire energy range of the simulation, namely 10^{-5} eV to 20 MeV. The behaviour of the spatially-integrated and normalized $\langle \varphi(E) \rangle$ for MOX assemblies is shown in Fig. 6.17. For fixed Λ_c, the impact of the anisotropy law is rather weak, as shown in Fig. 6.17 (left), although spectra in tessellations clearly differ from those of the intact assembly and of the atomic mix. On the other hand, for a given anisotropy law $H(\mathbf{n})$, the impact of Λ_c is apparent: for small Λ_c, $\langle \varphi(E) \rangle$ lies slightly below the reference flux (corresponding to the intact assembly) in the thermal region and above for the epi-thermal and fast regions. For larger Λ, $\langle \varphi(E) \rangle$ lies above the reference flux in the thermal region and below for the epi-thermal and fast regions.

Simulation time

For all the configurations examined here, we have recorded the computational cost of the performed calculations as a function of the complexity of the underlying stochastic tessellations. The corresponding

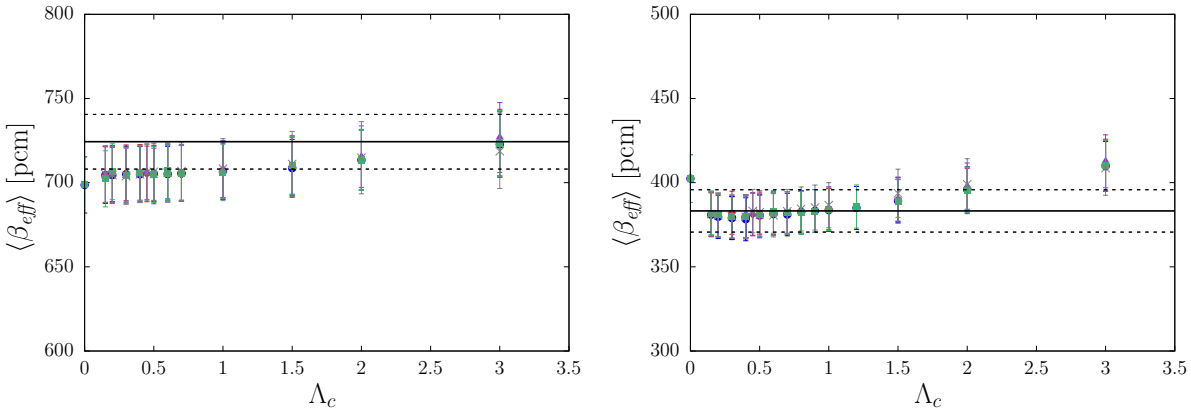

Figure 6.15: Evolution of the ensemble-averaged effective delayed neutron fraction $\langle\beta_{eff}\rangle$ as a function of the average correlation length Λ_c and of the anisotropy law $H(\mathbf{n})$. Left: UOX assembly. Right: MOX assembly. Symbols denote Monte Carlo simulation results: blue circles correspond to isotropic distribution, red diamonds to quadratic distribution, purple triangles to histogram distribution, green squares to box distribution and gray crosses to slab distribution. The limit case at $\Lambda_c \to 0$ corresponds to the atomic mix model. The black solid line denotes $\beta_{eff,0}$, the result for the assembly with intact fuel pins, which has been added for reference (dashed lines represent the 1σ statistical uncertainty).

Fuel	Anisotropy	$\Lambda_c = 0.15$ cm $\langle$t$\rangle \pm \sigma$[t]	$\Lambda_c = 3$ cm $\langle$t$\rangle \pm \sigma$[t]
UOX	Isotropic	48260 ± 16384	2209 ± 192
	Quadratic	33691 ± 7980	2165 ± 210
	Histogram	19407 ± 5560	2185 ± 234
	Box	16451 ± 346	2165 ± 198
	Slab	5864 ± 1737	2643 ± 821
MOX	Isotropic	37628 ± 8146	2052 ± 193
	Quadratic	46726 ± 28523	2687 ± 863
	Histogram	19407 ± 5560	2185 ± 234
	Box	15033 ± 3166	1998 ± 198
	Slab	4031 ± 1318	1962 ± 371

Table 6.3: Average simulation times $\langle t\rangle$ (expressed in seconds) and their dispersions $\sigma[t]$ for UOX and MOX fuels, corresponding to different anisotropy laws $H(\mathbf{n})$, and average correlation lengths Λ_c. For comparison, the simulation time for the atomic mix limit is $t_{mix} \simeq 1350$ s for UOX and $t_{mix} \simeq 1200$ s for MOX.

(ensemble-averaged) computer times for each assembly configuration are reported in Tab. 6.3, together with the associated dispersions $\sigma[t]$. The average simulation time $\langle t\rangle$ globally decreases for increasing Λ_c, as expected. The chosen anisotropy law $H(\mathbf{n})$ also affects the computer time. For large Λ, simulation times are almost independent of the anisotropy law; for small Λ, the shortest simulation times are attained for the slab tessellations. Moreover, subtle effects due to correlation lengths and volume fractions for the material compositions come also into play, and strongly influence the average computer time. For some configurations, the dispersion $\sigma[t]$ may become very large, and even be comparable to the average $\langle t\rangle$. Atomic mix simulations are based on a single homogenized realization.

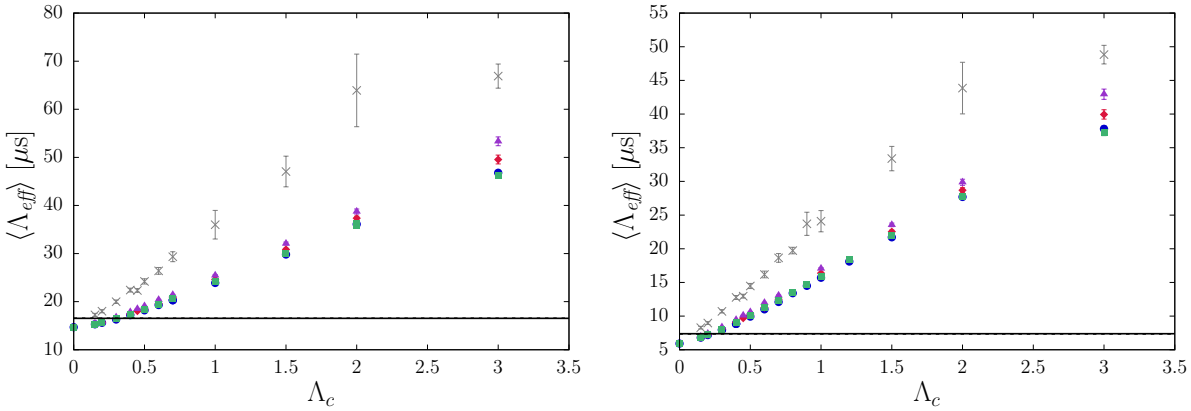

Figure 6.16: Evolution of the ensemble-averaged effective neutron generation time $\langle \Lambda_{eff} \rangle$ as a function of the average correlation length Λ_c and of the anisotropy law $H(\mathbf{n})$. Left: UOX assembly. Right: MOX assembly. Symbols denote Monte Carlo simulation results: blue circles correspond to isotropic distribution, red diamonds to quadratic distribution, purple triangles to histogram distribution, green squares to box distribution and gray crosses to slab distribution. The limit case at $\Lambda_c \to 0$ corresponds to the atomic mix model. The black solid line denotes $\Lambda_{eff,0}$, the result for the UOX assembly with intact fuel pins, which has been added for reference (dashed lines represent the 1σ statistical uncertainty).

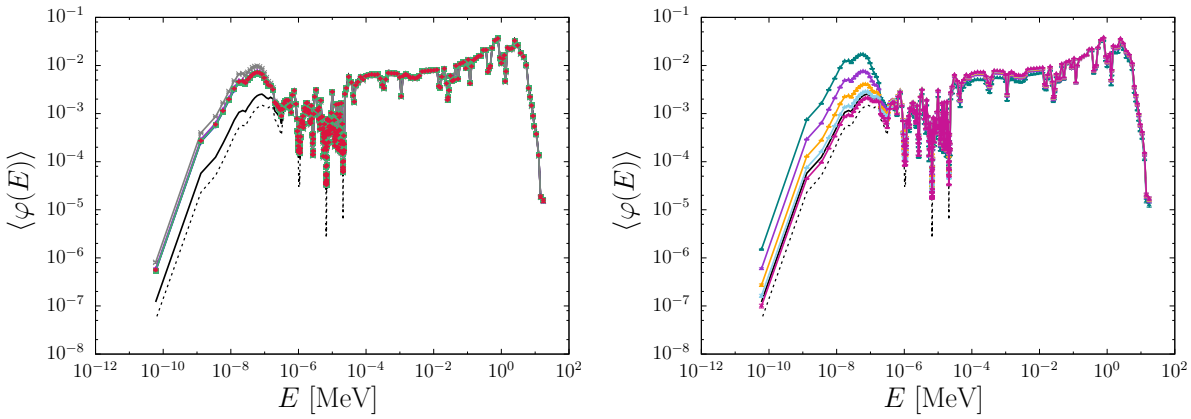

Figure 6.17: Fundamental eigenmode $\langle \varphi(E) \rangle$ for MOX fuel. Left. Impact of the anisotropy law $H(\mathbf{n})$ for fixed Λ_c. Blue circles correspond to isotropic distribution, red diamonds to quadratic distribution, purple triangles to histogram distribution, green squares to box distribution and gray crosses to slab distribution, for $\Lambda_c = 1$ cm. Right. Impact of the average correlation length Λ_c for fixed $H(\mathbf{n})$. Dark green symbols represent results for $\Lambda_c = 3$ cm, purple symbols for $\Lambda_c = 1$ cm, orange symbols for $\Lambda_c = 0.5$ cm, light blue symbols for $\Lambda_c = 0.3$ cm and magenta symbols for $\Lambda_c = 0.15$ cm, for the histogram anisotropy law. The reference spectra for the case of the intact assembly and for the atomic mix regime are shown as a solid black line and as a dashed black curve, respectively.

Chapter 7

Annealed disorder approach

7.1 Introduction

As shown in the previous Chapters, reference solutions for particle transport in quenched disorder are very demanding in terms of computational resources, especially if transport is to be solved by Monte Carlo methods in order to preserve the highest possible accuracy in solving the Boltzmann equation. In principle, it would be thus desirable to directly derive a single equation for the ensemble-averaged flux $\langle\varphi\rangle$. For binary stochastic mixing, where only two immiscible materials (say α and β) are present, the following equation for $\langle\varphi_\alpha(\mathbf{r},\mathbf{\Omega})\rangle$ is obtained:

$$[\mathbf{\Omega}\cdot\nabla+\Sigma_\alpha]\,p_\alpha\langle\varphi_\alpha\rangle=\frac{p_\alpha\Sigma_{s,\alpha}}{\Omega_d}\int\langle\varphi_\alpha(\mathbf{r},\mathbf{\Omega}')\rangle d\mathbf{\Omega}'+p_{\beta,\alpha}\langle\varphi_{\beta,\alpha}\rangle-p_{\alpha,\beta}\langle\varphi_{\alpha,\beta}\rangle+p_\alpha S_\alpha \tag{7.1}$$

where $p_i(\mathbf{r})$ is the probability of finding the material of index i at position $\mathbf{r}$ and $p_{i,j}=p_{i,j}(\mathbf{r},\mathbf{\Omega})$ represents the probability per unit length of crossing the interface from material i to material j in direction $\mathbf{\Omega}$. The quantity $\langle\varphi_{i,j}\rangle$ denotes the angular flux averaged over those realizations where there is a transition from material i to material j at $\mathbf{r}$ and in direction $\mathbf{\Omega}$. Excluding the special case of particle transport in the absence of scattering, Eq. (7.1) leads to an infinite hierarchy for $\langle\varphi_\alpha\rangle$ [108].

In order to explicitly derive the ensemble-averaged flux $\langle\varphi_\alpha\rangle$, it is therefore necessary to introduce a closure formula, which will in general depend on the underlying mixing statistics [108,136,171]. The Levermore-Pomraning model assumes for instance $\langle\varphi_{\alpha,\beta}\rangle=\langle\varphi_\alpha\rangle$, with

$$p_{i,j}(\mathbf{r},\mathbf{\Omega})=\frac{p_i}{\Lambda_i(\mathbf{\Omega})}, \tag{7.2}$$

where $\Lambda_i(\mathbf{\Omega})$ is the mean chord length in material i and direction $\mathbf{\Omega}$ [108], which yields

$$[\mathbf{\Omega}\cdot\nabla+\Sigma_\alpha]\,p_\alpha\langle\varphi_\alpha\rangle=\frac{p_\alpha\Sigma_{s,\alpha}}{\Omega_d}\int\langle\varphi_\alpha(\mathbf{r},\mathbf{\Omega}')\rangle d\mathbf{\Omega}'+p_\alpha S_\alpha+\frac{p_\beta}{\Lambda_\beta}\langle\varphi_\beta\rangle-\frac{p_\alpha}{\Lambda_\alpha}\langle\varphi_\alpha\rangle. \tag{7.3}$$

Several generalisations of this model have been later proposed, including higher-order closure schemes [108, 136]. This approach corresponds to the assumption of annealed *disorder*: particles are assumed to travel in an 'average' medium with modified transport kernels (here represented by the additional creation and disappearance terms that mirror the random transitions between material α and material β) that mimic the effects of disorder on the particle displacements.

In parallel to the derivation of such annealed-disorder equations, a family of Monte Carlo algorithms have been conceived in order to approximate the ensemble-averaged solutions to various degrees of accuracy [31, 32, 167]. Their common feature is that they allow a simpler treatment of transport in stochastic mixtures (typically by neglecting the correlations on particle trajectories induced by the spatial disorder). In this context, a prominent role is played by the so-called Chord Length Sampling (CLS) algorithm, which is supposed to formally solve the Levermore-Pomraning model for Markovian binary mixing [122, 123, 167]. The basic idea behind CLS is that the interfaces between the constituents of the stochastic medium are sampled on-the-fly during the particle displacements by drawing the distances to the following material boundaries from a distribution depending on the

mixing statistics. The free parameters of the CLS model are the average chord length Λ_i through each material and the volume fraction p_i. Since the spatial configuration seen by each particle is regenerated at each particle flight, the CLS corresponds to an annealed disorder model, as opposed to the quenched disorder of the reference solutions, where the spatial configuration is frozen for all the traversing particles. Generalization of these Monte Carlo algorithms including partial memory effects due to correlations for particles crossing back and forth the same materials have been also proposed [167].

In this Chapter, we will compare the CLS simulation results to the reference solutions for the ALP benchmark [1]. The case of $1d$ slab disorder has been considered previously in the literature [1, 9–11, 171] and will be reported here for the sake of completeness. In addition, we will also consider $2d$ extruded and full $3d$ Markov mixing configurations. The physical observables of interest will be the particle flux $\langle\varphi\rangle$, the transmission coefficient $\langle T\rangle$ and the reflection coefficient $\langle R\rangle$: we will examine the discrepancies between reference and CLS simulation results as a function of the benchmark configurations and of the system dimensionality d.

In order to verify the consistency of the proposed results, a *scientific collaboration* has been established with Dr. P. Brantley of the Lawrence Livermore National Laboratory and with Professor T. Palmer of the Oregon University. Within the framework of this collaboration, the CLS calculations have been performed by using two independent Monte Carlo implementations of the CLS algorithm, in TRIPOLI-4 ® [21] and Mercury, the Monte Carlo particle transport code being developed at LLNL [14, 15].

This Chapter is organized as follows: in Sec. 7.2 we will detail the methods and the algorithms that we have adopted in order to produce the CLS results. Simulation findings will be illustrated and discussed in Sec. 7.3.

Then, in Sec. 7.4 we will develop a new class of CLS-like Monte Carlo algorithms for particle transport with annealed disorder, aimed at improving the standard CLS for d-dimensional Markov media, yet keeping the increase in algorithmic complexity to a minimum. Inspiration comes from the observation that the physical observables related to particle transport through quasi-isotropic Poisson tessellations based on Cartesian boxes are almost identical to those computed for isotropic Poisson tessellations, for any dimension d, as shown in the previous Chapters, which confirms the considerations in [2]. This quite remarkable property suggests that the standard CLS algorithm can be extended by replacing the memoryless sampling of material interfaces by the sampling of d-dimensional Cartesian boxes sharing the statistical features of quasi-isotropic Poisson tessellations, so as to mimic the spatial correlations that would be induced by isotropic Poisson tessellations. We will call this class of algorithms Poisson Box Sampling (PBS). Moreover, within the framework of the collaboration with Dr. Brantley, we will additionally implement and test a new algorithm (LRP, for Local Realization Preserving) which is also supposed to better preserve the effects of spatial correlations. These new algorithms will be contrasted with the standard CLS and with the reference solutions for the ALP benchmark: their distinct merits and possible drawbacks will be thoroughly examined.

7.2 Chord Length Sampling

The pioneering work by Zimmerman and Adams [166, 167] in the early 1990s has led to a family of algorithms that go now under the name of Chord Length Sampling methods. In particular, it has been shown that the standard form of the CLS (Algorithm A in [167]) formally solves the Levermore-Pomraning equations, i.e., Eq. (7.3), corresponding to Markov mixing with the approximation that memory of the crossed material interfaces is lost at each particle flight [122, 123].

Algorithm A proceeds as follows [167]: each particle history begins by sampling position, angle and velocity from the specified source, as customary. Moreover, the particle is assigned a supplementary attribute, the material label, which is sampled from the probability p_i. Then we need to compute three distances, denoted respectively ℓ_b, ℓ_c, and ℓ_i. The quantity ℓ_b is the distance to the next physical boundary, along the current direction of the particle. The quantity ℓ_c is the distance to the next collision, which is determined by using the material cross section that has been chosen at

the previous step: if the particle has a material α, e.g., then ℓ_c will be drawn from an exponential distribution of parameter $1/\Sigma_\alpha$. Finally, the quantity ℓ_i is the distance to the next material interface, which is sampled from an exponential distribution with parameter Λ_α, i.e., the average chord length of material α, if the particle has a material label α (whence the name of CLS).

Then, the minimum distance among ℓ_b, ℓ_c and ℓ_i must be selected: if the minimum is ℓ_b, the particle is moved along a straight line until it hits the external boundary; if the minimum is ℓ_c, the particle is moved to the collision point, and the outgoing particle features are selected according to the collision kernel pertaining to the current material label. If the minimum is ℓ_i, the particle is moved to the interface between the two materials, and the material label is switched. If the particle is not absorbed, a new set of distances ℓ_b, ℓ_c and ℓ_i are determined. During the time spent within the random medium, the particle will be thus either colliding within a random chunk, or crossing the interface between two chunks; the particle will ultimately get absorbed in one of the chunks, or escape out of the boundaries of the random medium. The Monte Carlo estimators for the scalar flux and the currents are the same as those for the reference solutions described above.

As observed above, Algorithm A assumes that the particle has no memory of its past history, and in particular the crossed interfaces are immediately forgotten (which is coherent with the closure formula of the Levermore-Pomraning model). In this respect, CLS is an approximation of the exact treatment of disorder-induced spatial correlations (actually, it can be shown that CLS is exact only for pure absorbers). As a result, Algorithm A is expected to be less accurate in the presence of strong scatterers with optically thick mean material chunk length. A thorough discussion of the shortcomings of the CLS approach for $d = 1$ can be found, e.g., in [70].

7.2.1 Slab geometries

For mono-energetic particle transport in slab geometries with isotropic scattering, the Levermore-Pomraning equations read

$$\left(\mu\frac{\partial}{\partial x} + \Sigma_{t,i}\right)(p_i\langle\varphi_i\rangle) = p_i\frac{\Sigma_{s,i}}{2}\int_{-1}^{1} d\mu'\langle\varphi_i(x,\mu')\rangle + p_i Q_i + |\mu|\left(\frac{p_j}{\Lambda_j}\langle\varphi_j\rangle - \frac{p_i}{\Lambda_i}\langle\varphi_i\rangle\right) \tag{7.4}$$

in $0 \le x \le L$ and $-1 \le \mu \le 1$, for material $i = \{\alpha, \beta\}$ and $j \neq i$, where $\langle\varphi_i\rangle = \langle\varphi_i(x,\mu)\rangle$ is the material i angular particle flux for particles at position x with a direction cosine $\mu = \cos(\theta)$ with respect to the x axis and $Q_i = (x,\mu)$ is the angular source associated with material i at spatial location x in direction μ. The cross sections $\Sigma_{t,\alpha}$ and $\Sigma_{s,\alpha}$ are those of material α. Tabs.5.1-5.2 summarize the values used for the ALP benchmark. The source is given by

$$Q_i(x,\mu) = \begin{cases} 0 & \textit{suite} \text{ I}, \\ \dfrac{1}{2L} & \textit{suite} \text{ II}, \end{cases}$$

and the boundary conditions read

$$\langle\varphi_i(0,\mu)\rangle = \begin{cases} 2 & \textit{suite} \text{ I}, \\ 0 & \textit{suite} \text{ II}, \end{cases} \quad \mu > 0$$

and

$$\langle\varphi_i(L,\mu)\rangle = \begin{cases} 0 & \textit{suite} \text{ I}, \\ 0 & \textit{suite} \text{ II}, \end{cases} \quad \mu < 0.$$

Correspondingly, the CLS algorithm that formally solves the Levermore-Pomraning model given by Eq. 7.4 is the following. For *suite* I, the source particle position is set to $x = 0$, and the direction cosine is sampled from

$$\mu = \sqrt{\xi}, \tag{7.5}$$

where ξ is a uniform random number in $[0, 1)$, in order to ensure the isotropic incident flux condition. For *suite* II, the starting position x is sampled uniformly in $[0, L]$, and the direction cosine is sampled uniformly in $[-1, 1]$ in order to ensure the uniform and isotropic source condition. According to the

Levermore-Pomraning prescription, the distance to material interfaces for a particle in material α is sampled from an exponential distribution as follows:

$$d_i = -\frac{\Lambda_\alpha}{|\mu|}\ln(1-\xi), \tag{7.6}$$

where the factor $1/|\mu|$ accounts for the projection of the distance along the x axis. The distance to the next collision is sampled from the exponential distribution of parameter $1/\Sigma_\alpha(x)$, and the distance to the boundary is computed as customary. For isotropic scattering, the cosine direction after collision is sampled uniformly in $[-1,1]$.

7.2.2 Two-dimensional extruded geometries

Assuming again mono-energetic particle transport with isotropic scattering in two-dimensional geometries extruded in the z axis direction, the Levermore-Pomraning equations read

$$\begin{aligned}&\left(\sqrt{1-\mu^2}\cos(\phi)\frac{\partial}{\partial x}+\sqrt{1-\mu^2}\sin(\phi)\frac{\partial}{\partial y}+\Sigma_{t,i}\right)(p_i\langle\varphi_i\rangle)=\\ &p_i\frac{\Sigma_{s,i}}{4\pi}\int_{-1}^{1}d\mu'\int_0^{2\pi}d\phi'\langle\varphi_i(x,y,\mu',\phi')\rangle+p_iQ_i+\sqrt{1-\mu^2}\left(\frac{p_j}{\Lambda_j}\langle\varphi_j\rangle-\frac{p_i}{\Lambda_i}\langle\varphi_i\rangle\right),\end{aligned} \tag{7.7}$$

for material $i=\{\alpha,\beta\}$ and $j\neq i$, where $\langle\varphi_i\rangle=\langle\varphi_i(x,y,\mu,\phi)\rangle$ is the material i angular particle flux for particles at position x,y with a direction cosine $\mu=\cos(\theta)$ with respect to the z axis and a polar angle ϕ with respect to the x axis and $Q_i=(x,y,\mu,\phi))$ is the angular source associated with material i at spatial location x,y in direction μ,ϕ.

The cross sections $\Sigma_{t,\alpha}$ and $\Sigma_{s,\alpha}$ are those of material α. Tabs.5.1-5.2 summarize the values used for the ALP benchmark. The source is given by

$$Q_i(x,y,\mu,\phi)=\begin{cases}0 & \textit{suite} \text{ I},\\ \dfrac{1}{4\pi L^2} & \textit{suite} \text{ II},\end{cases}$$

and the boundary conditions read

$$\langle\varphi_i(0,y,\mu,\phi)\rangle=\begin{cases}4\pi & \textit{suite} \text{ I},\\ 0 & \textit{suite} \text{ II},\end{cases}\quad \mu>0$$

and

$$\langle\varphi_i(L,y,\mu,\phi)\rangle=\begin{cases}0 & \textit{suite} \text{ I},\\ 0 & \textit{suite} \text{ II},\end{cases}\quad \mu<0.$$

The CLS algorithm that formally corresponds to solving the Levermore-Pomraning model given by Eq. 7.7 is the following. For *suite* I, the source particle positions are set to $x=0$ and y taken uniformly in $[0,L]$. Then we sample a direction cosine μ' (with respect to the x axis) from

$$\mu'=\sqrt{\xi} \tag{7.8}$$

where ξ is taken in $[0,1)$, and a polar angle ϕ' (with respect to the y axis) uniform in $[0,2\pi]$. The initial particle direction is

$$\mathbf{\Omega}_0=\left\{\frac{\mu'}{f},\frac{\sqrt{1-\mu'^2}\cos(\phi')}{f}\right\}, \tag{7.9}$$

with

$$f=\sqrt{\mu'^2+(1-\mu'^2)\cos^2(\phi')}, \tag{7.10}$$

in order to ensure the isotropic incident flux condition, and the initial direction cosine μ_0 is defined by

$$\mu_0=\sqrt{1-\mu'^2}\sin(\phi'). \tag{7.11}$$

For *suite* II, the starting positions x, y are sampled uniformly in $[0, L] \times [0, L]$, the direction cosine μ is sampled uniformly in $[-1, 1]$ and the polar angle ϕ is sampled uniformly in $[0, 2\pi]$ in order to ensure the uniform and isotropic source condition, which yields the initial particle direction

$$\mathbf{\Omega}_0 = \{\cos(\phi), \sin(\phi)\}\,. \tag{7.12}$$

According to the Levermore-Pomraning prescription, the distance to material interfaces for a particle in material α is sampled from an exponential distribution as follows:

$$d_i = -\frac{\Lambda_\alpha}{\sqrt{1-\mu^2}} \ln(1-\xi), \tag{7.13}$$

where the factor $1/\sqrt{1-\mu^2}$ again accounts for the projection of the distance on the $x-y$ plane. The distance to the next collision is sampled from the exponential distribution of parameter $1/\Sigma_\alpha(x, y)$, and the distance to the boundary is computed as customary. For isotropic scattering, the cosine direction μ after collision is sampled uniformly in $[-1, 1]$, and the polar angle ϕ is sampled uniformly in $[0, 2\pi]$; the particle direction is then given by

$$\mathbf{\Omega} = \{\cos(\phi), \sin(\phi)\}\,. \tag{7.14}$$

7.2.3 Three-dimensional geometries

The Levermore-Pomraning equations for mono-energetic transport with isotropic scattering in three-dimensional geometries read

$$\left(\sqrt{1-\mu^2}\cos(\phi)\frac{\partial}{\partial x} + \sqrt{1-\mu^2}\sin(\phi)\frac{\partial}{\partial y} + \mu\frac{\partial}{\partial z} + \Sigma_{t,i}\right)(p_i\langle\varphi_i\rangle) =$$
$$p_i\frac{\Sigma_{s,i}}{4\pi}\int_{-1}^{1} d\mu' \int_0^{2\pi} d\phi' \langle\varphi_i(x, y, z, \mu', \phi')\rangle + p_i Q_i + \frac{p_j}{\Lambda_j}\langle\varphi_j\rangle - \frac{p_i}{\Lambda_i}\langle\varphi_i\rangle, \tag{7.15}$$

where $\langle\varphi_i\rangle = \langle\varphi_i(x, y, z, \mu, \phi)\rangle$ is the the material i angular particle flux for particles being at position x, y, z with a direction cosine $\mu = \cos(\theta)$ with respect to the z axis and a polar angle ϕ with respect to the x axis and $Q_i = (x, y, z, \mu, \phi))$ is the angular source associated with material i at spatial location x, y, z in direction μ, ϕ. The source is given by

$$Q_i(x, y, z, \mu, \phi) = \begin{cases} 0 & \textit{suite} \text{ I}, \\ \dfrac{1}{4\pi L^3} & \textit{suite} \text{ II}, \end{cases}$$

and the boundary conditions read

$$\langle\varphi_i(0, y, z, \mu, \phi)\rangle = \begin{cases} 4\pi & \textit{suite} \text{ I}, \\ 0 & \textit{suite} \text{ II}, \end{cases} \quad \mu > 0$$

and

$$\langle\varphi_i(L, y, z, \mu, \phi)\rangle = \begin{cases} 0 & \textit{suite} \text{ I}, \\ 0 & \textit{suite} \text{ II}, \end{cases} \quad \mu < 0.$$

The CLS algorithm that formally corresponds to solving the Levermore-Pomraning model given by Eq. 7.15 is the following. For *suite* I, the source particle positions are set to $x = 0$ and y, z taken uniformly in $[0, L] \times [0, L]$. Then we sample a direction cosine μ' (with respect to the x axis) from

$$\mu' = \sqrt{\xi} \tag{7.16}$$

where ξ is taken in $[0, 1)$, and a polar angle ϕ' (with repect to the y axis) uniform in $[0, 2\pi]$. The initial particle direction is

$$\mathbf{\Omega}_0 = \left\{\mu', \sqrt{1-\mu'^2}\cos(\phi'), \sqrt{1-\mu'^2}\sin(\phi')\right\} \tag{7.17}$$

in order to ensure the isotropic incident flux condition. For *suite* II, the starting positions x, y, z are sampled uniformly in $[0, L] \times [0, L] \times [0, L]$, the direction cosine μ is sampled uniformly in $[-1, 1]$ and the polar angle is sampled uniformly in $[0, 2\pi]$ in order to ensure the uniform and isotropic source condition, which yields the initial particle direction

$$\mathbf{\Omega}_0 = \left\{ \sqrt{1-\mu^2}\cos(\phi), \sqrt{1-\mu^2}\sin(\phi), \mu \right\}. \tag{7.18}$$

According to the Levermore-Pomraning prescription, the distance to material interfaces for a particle in material α is sampled from an exponential distribution as follows:

$$d_i = -\Lambda_\alpha \ln(1-\xi). \tag{7.19}$$

The distance to the next collision is sampled from the exponential distribution of parameter $1/\Sigma_\alpha(x, y, z)$, and the distance to the boundary is computed as customary. For isotropic scattering, the cosine direction μ after collision is sampled uniformly in $[-1, 1]$, and the polar angle ϕ is sampled uniformly in $[0, 2\pi]$; the particle direction is then given by

$$\mathbf{\Omega} = \left\{ \sqrt{1-\mu^2}\cos(\phi), \sqrt{1-\mu^2}\sin(\phi), \mu \right\}. \tag{7.20}$$

7.3 Simulation results

The specifications for the ALP benchmark are taken from [1, 9–11, 171], as recalled in Sec. 5.3.1.

The simulation results for the total scalar flux $\langle\varphi\rangle$, the transmission coefficient $\langle T\rangle$ and the reflection coefficient $\langle R\rangle$ are provided in Tabs. 7.1 to 7.3 for the benchmark cases corresponding to *suite* I, and in Tabs. 7.4 to 7.6 for the benchmark cases corresponding to *suite* II, respectively. The reference solutions have been computed by following the procedure detailed in Sec. 5.3.

The CLS results have been obtained with both TRIPOLI-4 ® and Mercury Monte Carlo codes by following the procedure described in Sec. 7.2. We will denote by $\sigma_{\mathrm{CLS}}[\mathcal{O}]$ the resulting statistical uncertainty associated to each physical observable $\mathcal{O}$. For the TRIPOLI-4 ® CLS simulations of the d-dimensional benchmark configurations we have used 10^9 particle histories. The Monte Carlo Levermore-Pomraning CLS algorithm was previously implemented in Mercury [12] in a manner consistent with the algorithmic descriptions in [11, 167] and Sec. 7.2. The Mercury Levermore-Pomraning implementation has been demonstrated [12] to accurately reproduce the independent one-dimensional slab geometry Monte Carlo Levermore-Pomraning results in [11]. We modelled the three-dimensional benchmark *suites* I and II using the Mercury Levermore-Pomraning CLS implementation with 10^9 particle histories. We obtained results that are generally statistically equivalent to the TRIPOLI-4 ® CLS results to typically within three standard deviations for the reflection and transmission coefficients and the scalar flux distributions (agreement to typically four to five digits). For this work, we will present only the TRIPOLI-4 ® simulation results. Computer times for the reference and CLS solutions are also provided in the same tables: not surprisingly, the CLS approach is much faster than the reference method, since a single transport simulation is needed.

As a general remark, the accuracy of CLS with respect to reference solutions increases with increasing system dimensionality d. This is expected on physical grounds, since the higher d and the smaller is the impact of the spatial correlations: a particle undergoing back-scattering is less likely to cross exactly the same material interface as the one crossed during the previous flight. In other words, the approximations introduced in the CLS algorithm by neglecting spatial correlations will have a weaker effect on particle transport. Nonetheless, simulation results show a few exceptions among the examined configurations. Moreover, the accuracy of CLS also generally improves when increasing the tessellation density, i.e., decreasing the average chord length: configurations pertaining to case 1 globally show a better agreement than those of case 2, and those of case 2 show a better agreement than those of case 3.

The effects of system dimensionality on the discrepancies between CLS and exact solutions are stronger for configurations with smaller average chord lengths. This behaviour is again consistent with the fact that increasing the chord length induces larger chunks of materials, and for chunks that

Case	d	Algorithm	$\langle R \rangle$	$\langle T \rangle$	$\langle \varphi \rangle$	t_{tot} [s]
1a	1	Ref	0.437 ± 0.002	$0.0148 \pm 2 \times 10^{-4}$	6.10 ± 0.01	1.1×10^6
		CLS	$0.37814 \pm 2 \times 10^{-5}$	$0.026403 \pm 5 \times 10^{-6}$	$6.6288 \pm 2 \times 10^{-4}$	2.6×10^3
		Err [%]	-13.49 ± 0.33	78.43 ± 2.35	8.64 ± 0.26	
	2	Ref	$0.4060 \pm 6 \times 10^{-4}$	0.0173 ± 10^{-4}	6.365 ± 0.008	6.5×10^5
		CLS	$0.39001 \pm 2 \times 10^{-5}$	$0.020100 \pm 5 \times 10^{-6}$	$6.5056 \pm 2 \times 10^{-4}$	4.2×10^3
		Err [%]	-3.93 ± 0.15	16.03 ± 0.91	2.21 ± 0.13	
	3	Ref	$0.4091 \pm 5 \times 10^{-4}$	0.0163 ± 10^{-4}	6.328 ± 0.007	3.9×10^6
		CLS	$0.40176 \pm 2 \times 10^{-5}$	$0.017491 \pm 4 \times 10^{-6}$	$6.3933 \pm 2 \times 10^{-4}$	4.6×10^3
		Err [%]	-1.79 ± 0.13	7.53 ± 0.86	1.03 ± 0.12	
1b	1	Ref	$0.0845 \pm 4 \times 10^{-4}$	$0.00164 \pm 7 \times 10^{-5}$	2.90 ± 0.01	2.6×10^6
		CLS	$0.058641 \pm 8 \times 10^{-6}$	0.001545 ± 10^{-6}	$2.7738 \pm 2 \times 10^{-4}$	6.2×10^2
		Err [%]	-30.59 ± 0.36	-5.79 ± 4.23	-4.26 ± 0.40	
	2	Ref	$0.0454 \pm 2 \times 10^{-4}$	$0.00108 \pm 3 \times 10^{-5}$	2.163 ± 0.005	2.9×10^5
		CLS	$0.042346 \pm 6 \times 10^{-6}$	0.001067 ± 10^{-6}	$2.1467 \pm 2 \times 10^{-4}$	9.6×10^2
		Err [%]	-6.70 ± 0.49	-1.04 ± 3.10	-0.78 ± 0.23	
	3	Ref	$0.0377 \pm 2 \times 10^{-4}$	$0.00085 \pm 3 \times 10^{-5}$	1.918 ± 0.003	1.8×10^6
		CLS	$0.036714 \pm 6 \times 10^{-6}$	$0.0008413 \pm 9 \times 10^{-7}$	$1.91440 \pm 6 \times 10^{-5}$	1.0×10^3
		Err [%]	-2.52 ± 0.52	-1.03 ± 3.46	-0.20 ± 0.17	
1c	1	Ref	$0.4767 \pm 5 \times 10^{-4}$	$0.0159 \pm 3 \times 10^{-4}$	6.97 ± 0.03	1.1×10^6
		CLS	0.36953 ± 10^{-5}	$0.023765 \pm 3 \times 10^{-6}$	$6.9137 \pm 2 \times 10^{-4}$	5.6×10^3
		Err [%]	-22.48 ± 0.08	49.14 ± 3.21	-0.82 ± 0.49	
	2	Ref	$0.4078 \pm 5 \times 10^{-4}$	0.0179 ± 10^{-4}	6.52 ± 0.01	6.6×10^5
		CLS	0.38557 ± 10^{-5}	$0.019478 \pm 3 \times 10^{-6}$	$6.4952 \pm 2 \times 10^{-4}$	9.8×10^3
		Err [%]	-5.45 ± 0.12	8.59 ± 0.90	-0.35 ± 0.17	
	3	Ref	$0.4059 \pm 5 \times 10^{-4}$	0.0164 ± 10^{-4}	6.303 ± 0.008	4.4×10^6
		CLS	0.39619 ± 10^{-5}	$0.016992 \pm 2 \times 10^{-6}$	6.2957 ± 10^{-4}	1.1×10^4
		Err [%]	-2.40 ± 0.12	3.62 ± 0.84	-0.12 ± 0.13	

Table 7.1: Ensemble-averaged observables and computer time t_{tot} for the benchmark configurations: *suite* I - case 1.

span a large fraction of the entire geometry the impact of dimensionality must be rather weak: in this regime, particle transport is mostly influenced by the material volume fractions (i.e., the coloring probability).

The behaviour of *suite* II configurations is quite similar to that of *suite* I configurations, and no specific trend due to the source and/or initial conditions can be easily detected.

The spatial scalar flux $\langle \varphi \rangle$ within the box is illustrated in Figs. 7.1 to 7.3 for case 1 to case 3, respectively. The discrepancies between CLS and reference solutions for this observable have the same behaviour as for the scalar quantities described above. The discrepancy decreases with increasing system dimensionality and with decreasing average chord length. For dense geometries (case 1) the effects of dimensionality on the discrepancy are rather strong, and become less appreciable for less dense geometries. The kind of source and/or initial conditions plays again a minor role. This analysis is confirmed by plotting the differences $\Delta[\langle \varphi(x) \rangle]$ between reference and CLS solutions (see Figs. 7.4 to 7.6 for case 1 to case 3, respectively). Since both reference and CLS solutions are affected by a statistical uncertainty, the error bars on $\Delta[\langle \varphi(x) \rangle]$ have been computed by taking the combined variance

$$\sigma[\Delta[\mathcal{O}]] = \sqrt{\sigma^2[\langle \mathcal{O} \rangle] + \sigma^2_{\text{CLS}}[\mathcal{O}]} \tag{7.21}$$

for each observable $\mathcal{O}$.

Case	d	Algorithm	$\langle R \rangle$	$\langle T \rangle$	$\langle \varphi \rangle$	t_{tot} [s]
2a	1	Ref	0.239 ± 0.003	$0.0973 \pm 9 \times 10^{-4}$	7.64 ± 0.02	9.1×10^5
		CLS	0.18051 ± 10^{-5}	0.12841 ± 10^{-5}	7.8140 ± 10^{-4}	2.1×10^3
		Err [%]	-24.46 ± 0.91	32.01 ± 1.26	2.21 ± 0.28	
	2	Ref	0.226 ± 0.002	$0.0969 \pm 7 \times 10^{-4}$	7.59 ± 0.02	3.5×10^5
		CLS	0.18972 ± 10^{-5}	0.11403 ± 10^{-5}	7.7288 ± 10^{-4}	3.0×10^3
		Err [%]	-16.03 ± 0.80	17.70 ± 0.86	1.83 ± 0.20	
	3	Ref	0.225 ± 0.001	$0.0937 \pm 4 \times 10^{-4}$	7.57 ± 0.01	4.4×10^5
		CLS	0.20043 ± 10^{-5}	$0.105624 \pm 9 \times 10^{-6}$	$7.6615 \pm 2 \times 10^{-4}$	3.1×10^3
		Err [%]	-11.08 ± 0.45	12.74 ± 0.54	1.22 ± 0.13	
2b	1	Ref	$0.2866 \pm 8 \times 10^{-4}$	0.194 ± 0.001	11.69 ± 0.04	3.0×10^6
		CLS	0.21827 ± 10^{-5}	0.17938 ± 10^{-5}	$10.7138 \pm 5 \times 10^{-4}$	5.4×10^2
		Err [%]	-23.84 ± 0.22	-7.45 ± 0.56	-8.33 ± 0.28	
	2	Ref	$0.1980 \pm 8 \times 10^{-4}$	$0.1465 \pm 9 \times 10^{-4}$	9.11 ± 0.03	1.0×10^6
		CLS	0.16674 ± 10^{-5}	0.13377 ± 10^{-5}	$8.3763 \pm 4 \times 10^{-4}$	8.8×10^2
		Err [%]	-15.79 ± 0.33	-8.68 ± 0.54	-8.06 ± 0.30	
	3	Ref	$0.1616 \pm 8 \times 10^{-4}$	$0.1194 \pm 9 \times 10^{-4}$	7.77 ± 0.03	3.4×10^5
		CLS	0.14223 ± 10^{-5}	0.10996 ± 10^{-5}	$7.2609 \pm 2 \times 10^{-4}$	9.3×10^2
		Err [%]	-11.99 ± 0.44	-7.91 ± 0.68	-6.50 ± 0.37	
2c	1	Ref	$0.4334 \pm 8 \times 10^{-4}$	0.184 ± 0.002	12.51 ± 0.06	7.1×10^5
		CLS	0.28962 ± 10^{-5}	0.19497 ± 10^{-5}	$11.3443 \pm 4 \times 10^{-4}$	3.3×10^3
		Err [%]	-33.17 ± 0.12	5.83 ± 1.24	-9.35 ± 0.46	
	2	Ref	$0.3677 \pm 6 \times 10^{-4}$	0.179 ± 0.002	11.46 ± 0.05	4.1×10^5
		CLS	0.27853 ± 10^{-5}	0.16713 ± 10^{-5}	$10.1679 \pm 3 \times 10^{-4}$	5.6×10^3
		Err [%]	-24.25 ± 0.12	-6.74 ± 0.82	-11.25 ± 0.39	
	3	Ref	$0.3457 \pm 5 \times 10^{-4}$	$0.1651 \pm 9 \times 10^{-4}$	10.76 ± 0.03	4.8×10^5
		CLS	0.27693 ± 10^{-5}	0.15031 ± 10^{-5}	$9.6048 \pm 2 \times 10^{-4}$	8.9×10^3
		Err [%]	-19.89 ± 0.12	-8.98 ± 0.49	-10.73 ± 0.23	

Table 7.2: Ensemble-averaged observables and computer time t_{tot} for the benchmark configurations: *suite* I - case 2.

Case	d	Algorithm	$\langle R \rangle$	$\langle T \rangle$	$\langle \varphi \rangle$	t_{tot} [s]
3a	1	Ref	0.692 ± 0.003	0.163 ± 0.002	16.44 ± 0.05	1.3×10^6
		CLS	$0.60758 \pm 2 \times 10^{-5}$	0.24037 ± 10^{-5}	$16.3738 \pm 7 \times 10^{-4}$	3.8×10^3
		Err [%]	-12.14 ± 0.34	47.09 ± 1.60	-0.43 ± 0.30	
	2	Ref	0.680 ± 0.003	0.168 ± 0.002	16.46 ± 0.05	5.4×10^5
		CLS	$0.62678 \pm 2 \times 10^{-5}$	0.21473 ± 10^{-5}	$16.3866 \pm 7 \times 10^{-4}$	6.0×10^3
		Err [%]	-7.77 ± 0.40	27.99 ± 1.45	-0.44 ± 0.33	
	3	Ref	0.675 ± 0.001	$0.1692 \pm 9 \times 10^{-4}$	16.38 ± 0.03	1.4×10^6
		CLS	$0.64107 \pm 2 \times 10^{-5}$	0.19957 ± 10^{-5}	$16.3231 \pm 6 \times 10^{-4}$	9.1×10^3
		Err [%]	-5.06 ± 0.20	17.96 ± 0.65	-0.36 ± 0.19	
3b	1	Ref	$0.0361 \pm 2 \times 10^{-4}$	$0.0760 \pm 7 \times 10^{-4}$	5.16 ± 0.02	4.2×10^6
		CLS	$0.024013 \pm 5 \times 10^{-6}$	$0.075671 \pm 8 \times 10^{-6}$	$5.0313 \pm 5 \times 10^{-4}$	3.5×10^2
		Err [%]	-33.50 ± 0.44	-0.37 ± 0.95	-2.48 ± 0.40	
	2	Ref	$0.0217 \pm 2 \times 10^{-4}$	$0.0568 \pm 6 \times 10^{-4}$	4.00 ± 0.02	2.8×10^6
		CLS	$0.015501 \pm 4 \times 10^{-6}$	$0.052503 \pm 7 \times 10^{-6}$	$3.7582 \pm 4 \times 10^{-4}$	5.7×10^2
		Err [%]	-28.55 ± 0.61	-7.51 ± 0.97	-6.03 ± 0.41	
	3	Ref	$0.0165 \pm 2 \times 10^{-4}$	$0.0457 \pm 9 \times 10^{-4}$	3.47 ± 0.03	5.0×10^5
		CLS	$0.012454 \pm 3 \times 10^{-6}$	$0.040345 \pm 6 \times 10^{-6}$	3.2382 ± 10^{-4}	8.0×10^2
		Err [%]	-24.48 ± 0.97	-11.80 ± 1.68	-6.55 ± 0.70	
3c	1	Ref	0.445 ± 0.001	0.104 ± 0.002	9.00 ± 0.07	6.6×10^5
		CLS	0.32613 ± 10^{-5}	$0.119665 \pm 9 \times 10^{-6}$	$8.4702 \pm 6 \times 10^{-4}$	3.4×10^3
		Err [%]	-26.71 ± 0.17	15.11 ± 2.54	-5.91 ± 0.75	
	2	Ref	0.411 ± 0.001	0.094 ± 0.002	8.30 ± 0.07	2.7×10^5
		CLS	0.33767 ± 10^{-5}	$0.094998 \pm 9 \times 10^{-6}$	$7.6579 \pm 5 \times 10^{-4}$	5.6×10^3
		Err [%]	-17.92 ± 0.22	0.72 ± 2.54	-7.72 ± 0.83	
	3	Ref	$0.3979 \pm 7 \times 10^{-4}$	0.086 ± 0.001	7.89 ± 0.03	7.0×10^5
		CLS	0.34652 ± 10^{-5}	$0.080613 \pm 7 \times 10^{-6}$	$7.3217 \pm 2 \times 10^{-4}$	8.8×10^3
		Err [%]	-12.92 ± 0.15	-6.16 ± 1.19	-7.17 ± 0.40	

Table 7.3: Ensemble-averaged observables and computer time t_{tot} for the benchmark configurations: *suite* I - case 3.

Case	d	Algorithm	$\langle L \rangle$	$\langle \varphi \rangle$	t_{tot} [s]
1a	1	Ref	$0.1525 \pm 3 \times 10^{-4}$	7.70 ± 0.01	9.9×10^{5}
		CLS	$0.165716 \pm 8 \times 10^{-6}$	7.3449 ± 10^{-4}	2.6×10^{3}
		Err [%]	8.69 ± 0.24	-4.65 ± 0.14	
	2	Ref	$0.1592 \pm 3 \times 10^{-4}$	7.512 ± 0.008	2.1×10^{6}
		CLS	$0.162634 \pm 8 \times 10^{-6}$	7.4287 ± 10^{-4}	4.6×10^{3}
		Err [%]	2.17 ± 0.17	-1.11 ± 0.10	
	3	Ref	$0.1583 \pm 3 \times 10^{-4}$	7.530 ± 0.008	7.9×10^{7}
		CLS	$0.159828 \pm 8 \times 10^{-6}$	$7.4924 \pm 2 \times 10^{-4}$	5.3×10^{3}
		Err [%]	0.98 ± 0.17	-0.49 ± 0.10	
1b	1	Ref	$0.0724 \pm 3 \times 10^{-4}$	3.735 ± 0.009	1.5×10^{6}
		CLS	$0.069346 \pm 6 \times 10^{-6}$	$3.4898 \pm 2 \times 10^{-4}$	5.8×10^{2}
		Err [%]	-4.28 ± 0.36	-6.55 ± 0.22	
	2	Ref	$0.0542 \pm 2 \times 10^{-4}$	2.182 ± 0.003	1.8×10^{6}
		CLS	$0.053662 \pm 5 \times 10^{-6}$	$2.1468 \pm 2 \times 10^{-4}$	8.9×10^{2}
		Err [%]	-0.92 ± 0.33	-1.63 ± 0.16	
	3	Ref	$0.0481 \pm 2 \times 10^{-4}$	1.808 ± 0.003	7.4×10^{7}
		CLS	$0.047859 \pm 5 \times 10^{-6}$	$1.79609 \pm 6 \times 10^{-5}$	1.0×10^{3}
		Err [%]	-0.42 ± 0.33	-0.63 ± 0.14	
1c	1	Ref	$0.1742 \pm 7 \times 10^{-4}$	9.62 ± 0.03	1.0×10^{6}
		CLS	$0.172845 \pm 7 \times 10^{-6}$	$8.2618 \pm 3 \times 10^{-4}$	6.7×10^{3}
		Err [%]	-0.76 ± 0.38	-14.11 ± 0.22	
	2	Ref	$0.1630 \pm 3 \times 10^{-4}$	7.77 ± 0.01	2.1×10^{6}
		CLS	$0.162379 \pm 6 \times 10^{-6}$	$7.4824 \pm 2 \times 10^{-4}$	1.2×10^{4}
		Err [%]	-0.38 ± 0.18	-3.76 ± 0.12	
	3	Ref	$0.1577 \pm 3 \times 10^{-4}$	7.455 ± 0.008	7.7×10^{7}
		CLS	$0.157383 \pm 6 \times 10^{-6}$	7.3335 ± 10^{-4}	1.4×10^{4}
		Err [%]	-0.19 ± 0.17	-1.63 ± 0.10	

Table 7.4: Ensemble-averaged observables and computer time t_{tot} for the benchmark configurations: *suite* II - case 1.

Case	d	Algorithm	$\langle L \rangle$	$\langle \varphi \rangle$	t_{tot} [s]
2a	1	Ref	$0.1904 \pm 3 \times 10^{-4}$	8.29 ± 0.03	5.3×10^{6}
		CLS	$0.195346 \pm 9 \times 10^{-6}$	$6.8189 \pm 2 \times 10^{-4}$	1.7×10^{3}
		Err [%]	2.57 ± 0.16	-17.70 ± 0.30	
	2	Ref	$0.1898 \pm 3 \times 10^{-4}$	7.46 ± 0.03	3.2×10^{5}
		CLS	$0.193217 \pm 9 \times 10^{-6}$	$6.8517 \pm 2 \times 10^{-4}$	2.8×10^{3}
		Err [%]	1.82 ± 0.18	-8.16 ± 0.33	
	3	Ref	$0.1892 \pm 3 \times 10^{-4}$	7.27 ± 0.01	5.8×10^{5}
		CLS	$0.191527 \pm 9 \times 10^{-6}$	$6.8774 \pm 2 \times 10^{-4}$	3.0×10^{3}
		Err [%]	1.21 ± 0.16	-5.36 ± 0.18	
2b	1	Ref	$0.2918 \pm 8 \times 10^{-4}$	10.75 ± 0.02	1.5×10^{6}
		CLS	0.26783 ± 10^{-5}	$9.8684 \pm 5 \times 10^{-4}$	4.9×10^{2}
		Err [%]	-8.21 ± 0.24	-8.20 ± 0.20	
	2	Ref	$0.2274 \pm 6 \times 10^{-4}$	7.97 ± 0.02	6.1×10^{5}
		CLS	$0.209414 \pm 9 \times 10^{-6}$	$7.2072 \pm 4 \times 10^{-4}$	7.8×10^{2}
		Err [%]	-7.91 ± 0.26	-9.60 ± 0.24	
	3	Ref	$0.1931 \pm 4 \times 10^{-4}$	6.54 ± 0.01	1.7×10^{6}
		CLS	$0.181518 \pm 9 \times 10^{-6}$	$6.0577 \pm 2 \times 10^{-4}$	8.6×10^{2}
		Err [%]	-6.01 ± 0.21	-7.31 ± 0.19	
2c	1	Ref	0.312 ± 0.001	11.92 ± 0.03	4.1×10^{5}
		CLS	$0.283614 \pm 9 \times 10^{-6}$	$10.3022 \pm 4 \times 10^{-4}$	2.8×10^{3}
		Err [%]	-9.09 ± 0.33	-13.56 ± 0.25	
	2	Ref	0.286 ± 0.001	10.39 ± 0.03	2.1×10^{5}
		CLS	$0.254187 \pm 8 \times 10^{-6}$	$8.8967 \pm 3 \times 10^{-4}$	5.2×10^{3}
		Err [%]	-11.26 ± 0.31	-14.35 ± 0.27	
	3	Ref	$0.2688 \pm 6 \times 10^{-4}$	9.55 ± 0.02	4.9×10^{5}
		CLS	$0.240117 \pm 8 \times 10^{-6}$	$8.3498 \pm 2 \times 10^{-4}$	8.4×10^{3}
		Err [%]	-10.69 ± 0.20	-12.58 ± 0.18	

Table 7.5: Ensemble-averaged observables and computer time t_{tot} for the benchmark configurations: *suite* II - case 2.

Case	d	Algorithm	$\langle L \rangle$	$\langle \varphi \rangle$	t_{tot} [s]
3a	1	Ref	$0.4112 \pm 6 \times 10^{-4}$	27.3 ± 0.2	1.9×10^{6}
		CLS	0.40935 ± 10^{-5}	$19.3460 \pm 8 \times 10^{-4}$	4.3×10^{3}
		Err [%]	-0.45 ± 0.15	-29.24 ± 0.39	
	2	Ref	$0.4115 \pm 6 \times 10^{-4}$	24.3 ± 0.2	6.8×10^{5}
		CLS	0.40967 ± 10^{-5}	$19.5145 \pm 7 \times 10^{-4}$	7.4×10^{3}
		Err [%]	-0.44 ± 0.15	-19.64 ± 0.53	
	3	Ref	$0.4098 \pm 4 \times 10^{-4}$	22.82 ± 0.07	1.7×10^{6}
		CLS	0.40807 ± 10^{-5}	$19.7173 \pm 6 \times 10^{-4}$	1.1×10^{4}
		Err [%]	-0.42 ± 0.10	-13.61 ± 0.28	
3b	1	Ref	$0.1294 \pm 5 \times 10^{-4}$	5.93 ± 0.02	1.4×10^{6}
		CLS	$0.125785 \pm 7 \times 10^{-6}$	$5.7673 \pm 6 \times 10^{-4}$	3.1×10^{2}
		Err [%]	-2.80 ± 0.35	-2.82 ± 0.34	
	2	Ref	$0.1003 \pm 4 \times 10^{-4}$	3.75 ± 0.02	6.7×10^{5}
		CLS	$0.093978 \pm 7 \times 10^{-6}$	$3.3419 \pm 4 \times 10^{-4}$	5.2×10^{2}
		Err [%]	-6.26 ± 0.38	-10.88 ± 0.36	
	3	Ref	$0.0868 \pm 3 \times 10^{-4}$	2.98 ± 0.01	8.7×10^{5}
		CLS	$0.080949 \pm 6 \times 10^{-6}$	2.6747 ± 10^{-4}	7.8×10^{2}
		Err [%]	-6.78 ± 0.34	-10.12 ± 0.30	
3c	1	Ref	0.225 ± 0.001	10.56 ± 0.05	4.1×10^{5}
		CLS	$0.211761 \pm 8 \times 10^{-6}$	$9.5120 \pm 6 \times 10^{-4}$	3.8×10^{3}
		Err [%]	-6.02 ± 0.55	-9.92 ± 0.46	
	2	Ref	0.207 ± 0.001	8.78 ± 0.05	1.7×10^{5}
		CLS	$0.191469 \pm 7 \times 10^{-6}$	$7.8470 \pm 5 \times 10^{-4}$	6.7×10^{3}
		Err [%]	-7.54 ± 0.64	-10.68 ± 0.51	
	3	Ref	$0.1974 \pm 7 \times 10^{-4}$	8.15 ± 0.02	5.0×10^{4}
		CLS	$0.183044 \pm 7 \times 10^{-6}$	7.4839 ± 10^{-4}	1.1×10^{4}
		Err [%]	-7.26 ± 0.33	-8.20 ± 0.25	

Table 7.6: Ensemble-averaged observables and computer time t_{tot} for the benchmark configurations: *suite* II - case 3.

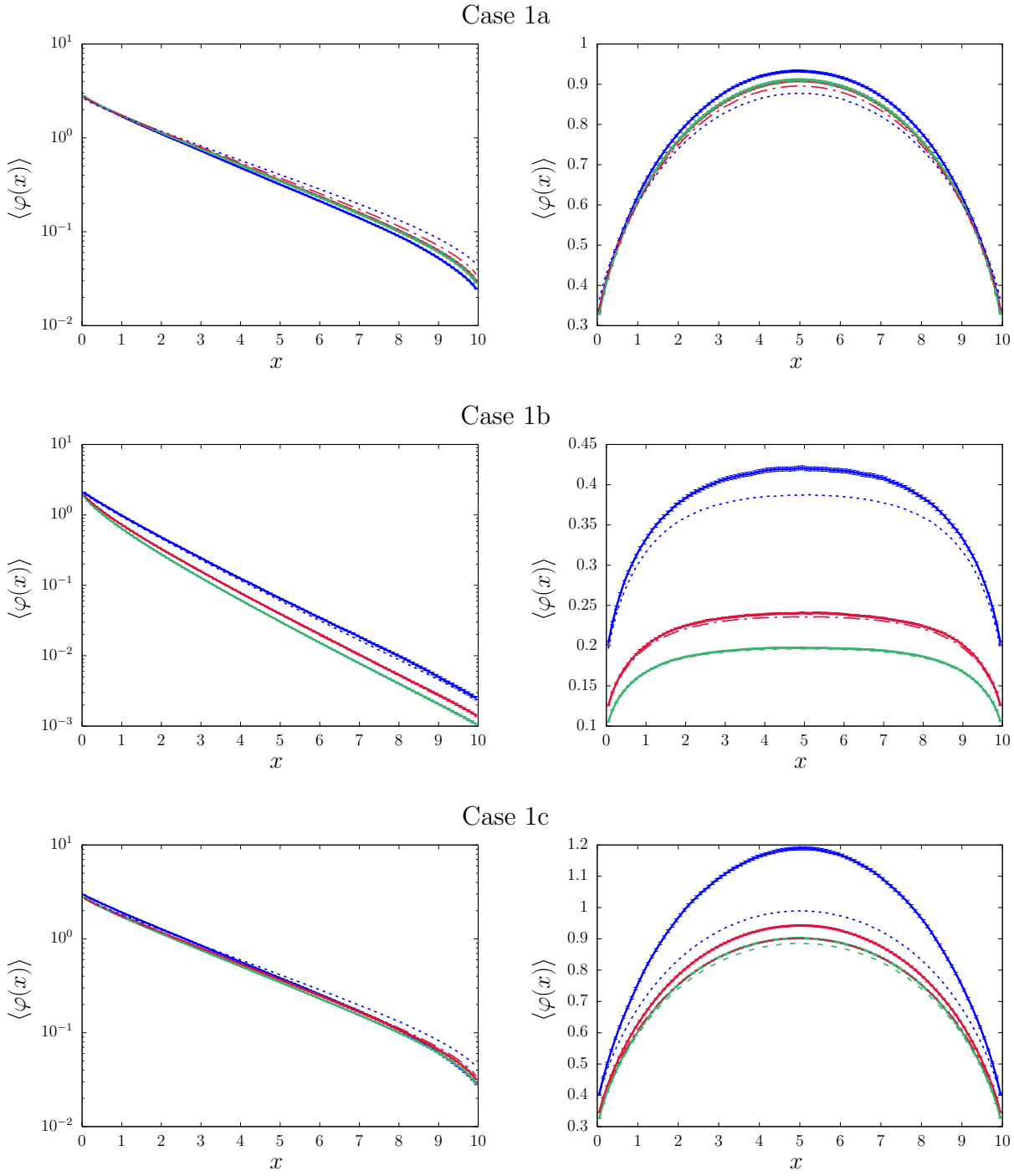

Figure 7.1: Ensemble-averaged spatial scalar flux for the benchmark configurations: Case 1. Left column: *suite* I configurations; right column: *suite* II configurations. Blue lines correspond to $d = 1$, red lines to $d = 2$ and green lines to $d = 3$. Solid lines represent the benchmark solutions (quenched disorder approach), dotted or dashed lines represent the solutions from the Chord Length Sampling algorithm (annealed disorder approach).

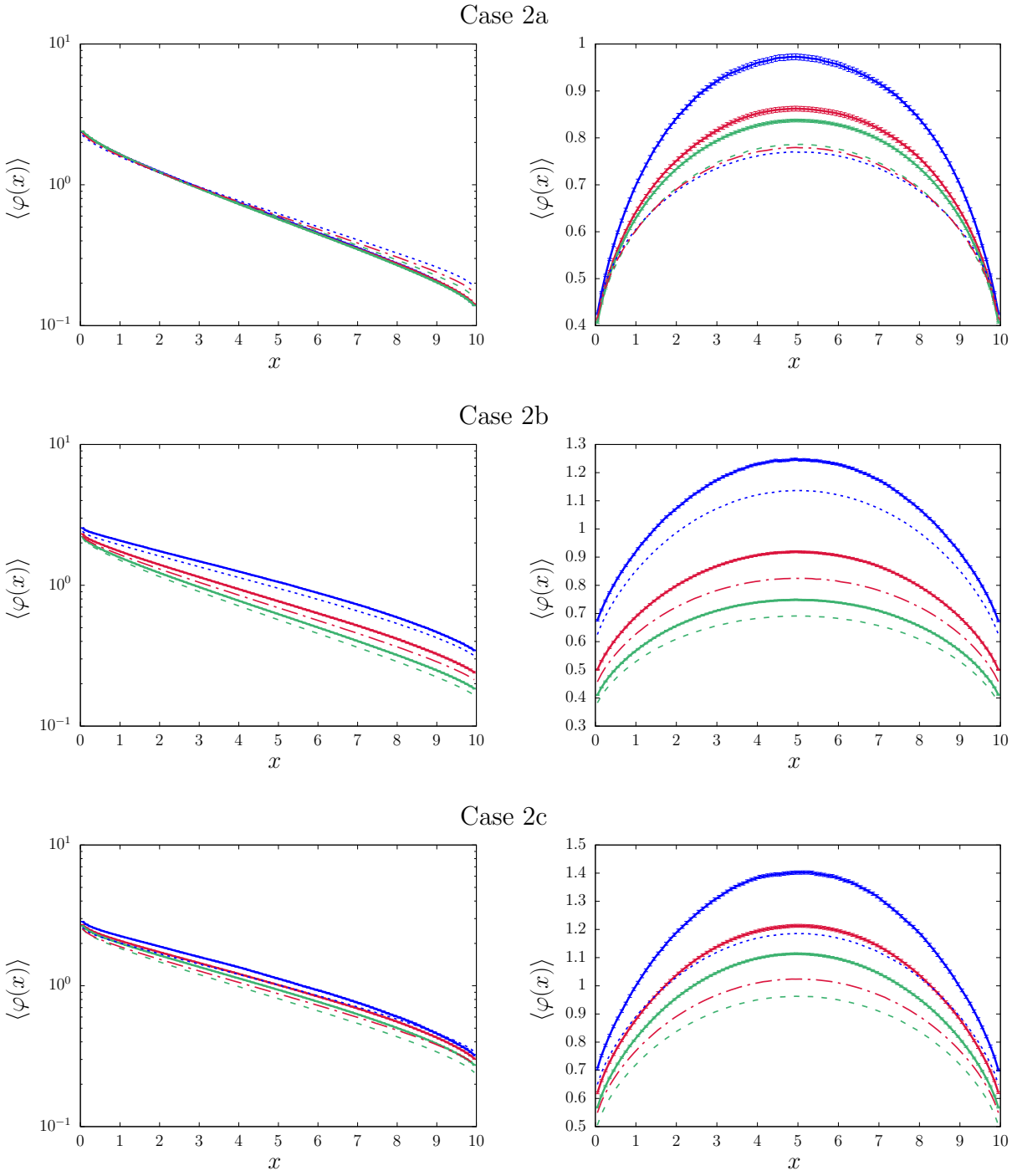

Figure 7.2: Ensemble-averaged spatial scalar flux for the benchmark configurations: Case 2. Left column: *suite* I configurations; right column: *suite* II configurations. Blue lines correspond to $d = 1$, red lines to $d = 2$ and green lines to $d = 3$. Solid lines represent the benchmark solutions (quenched disorder approach), dotted or dashed lines represent the solutions from the Chord Length Sampling algorithm (annealed disorder approach).

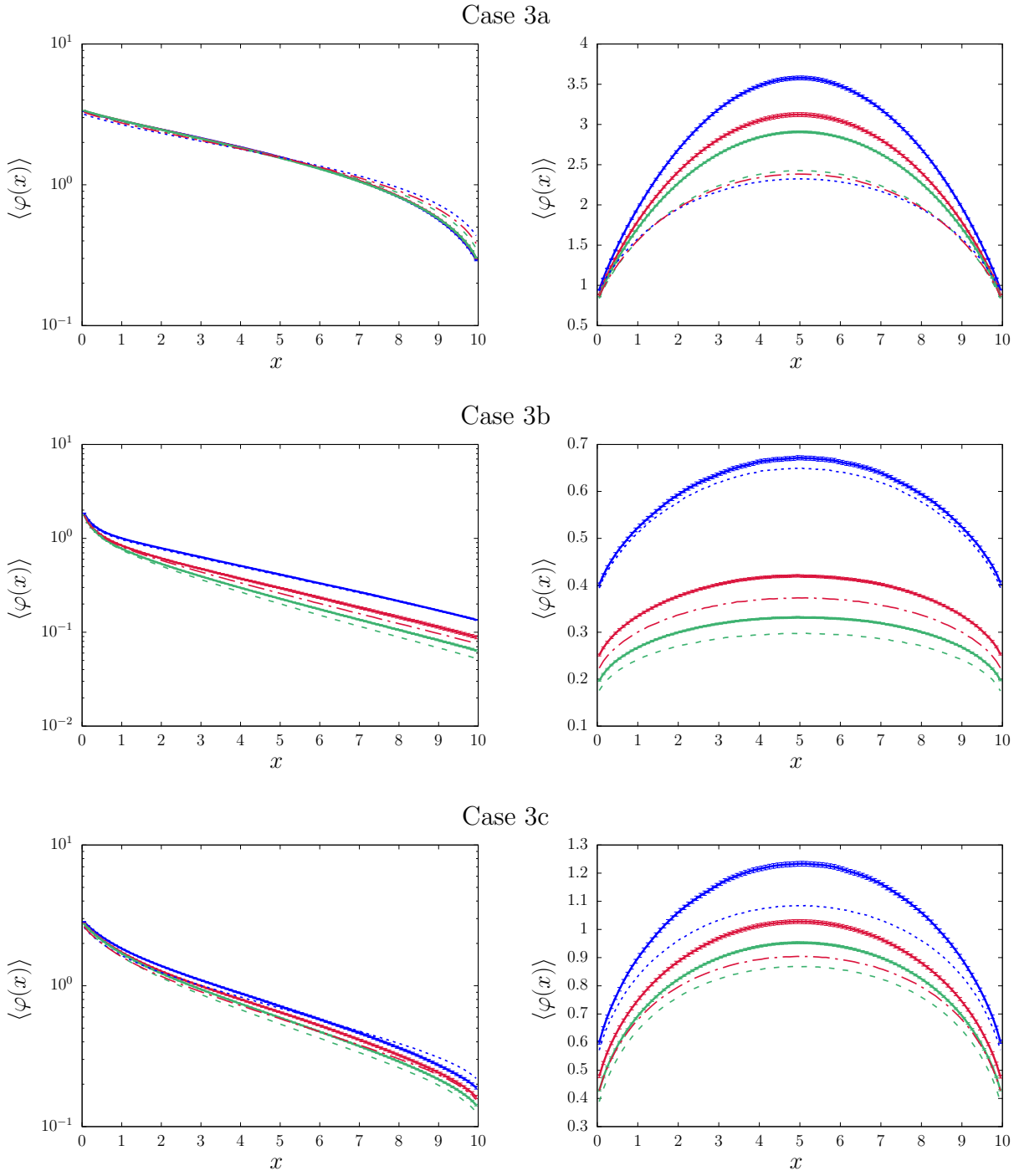

Figure 7.3: Ensemble-averaged spatial scalar flux for the benchmark configurations: Case 3. Left column: *suite* I configurations; right column: *suite* II configurations. Blue lines correspond to $d = 1$, red lines to $d = 2$ and green lines to $d = 3$. Solid lines represent the benchmark solutions (quenched disorder approach), dotted or dashed lines represent the solutions from the Chord Length Sampling algorithm (annealed disorder approach).

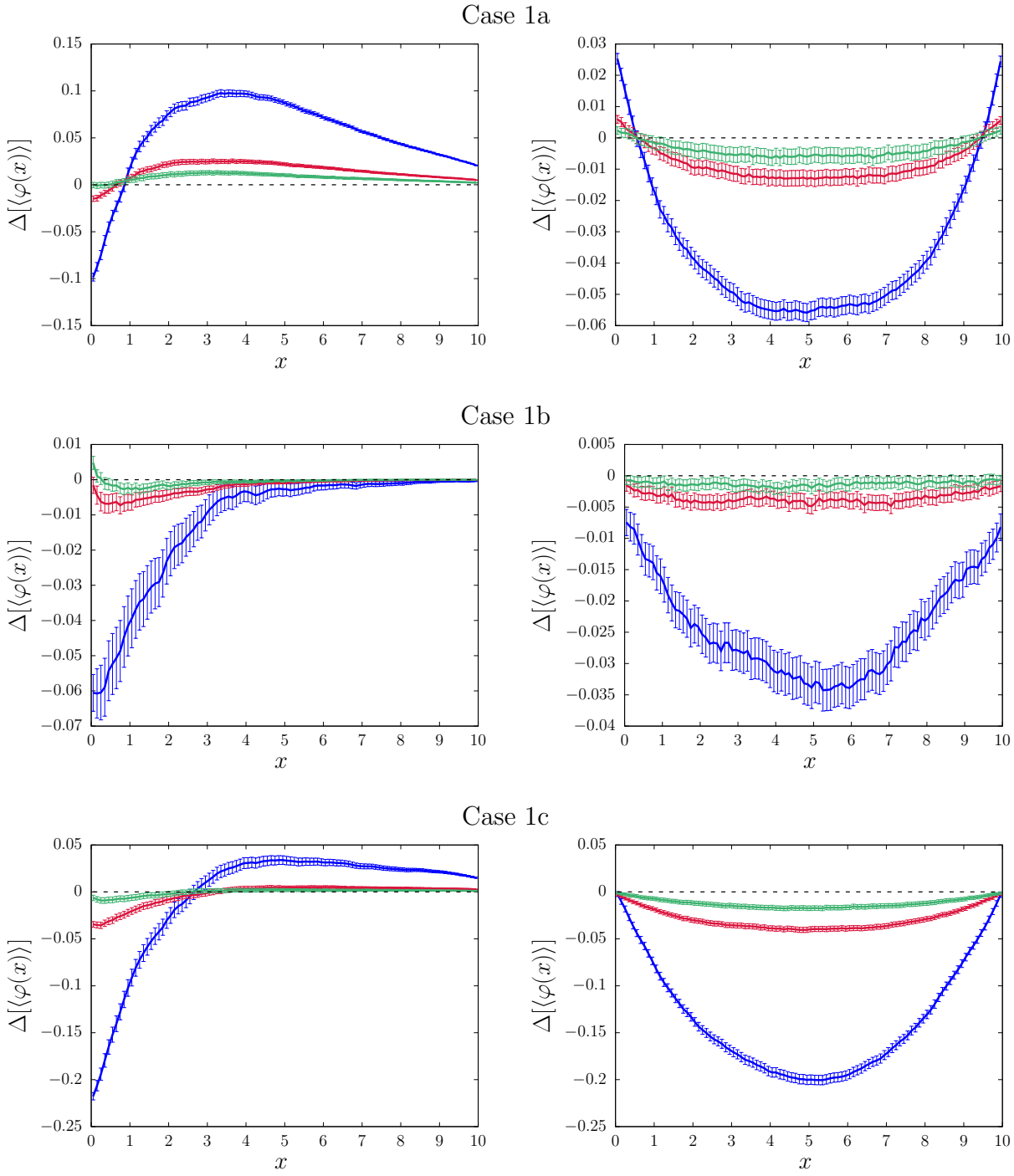

Figure 7.4: Discrepancy $\Delta[\langle\varphi(x)\rangle]$ between the ensemble-averaged spatial flux $\langle\varphi(x)\rangle$ obtained with Poisson tessellations (quenched disorder approach) and that obtained with the Chord Length Sampling algorithm (annealed disorder approach) for the benchmark configurations: Case 1. Left column: *suite* I configurations; right column: *suite* II configurations. Blue lines correspond to $d = 1$, red lines to $d = 2$ and green lines to $d = 3$. Error bars are computed as in Eq. (7.21).

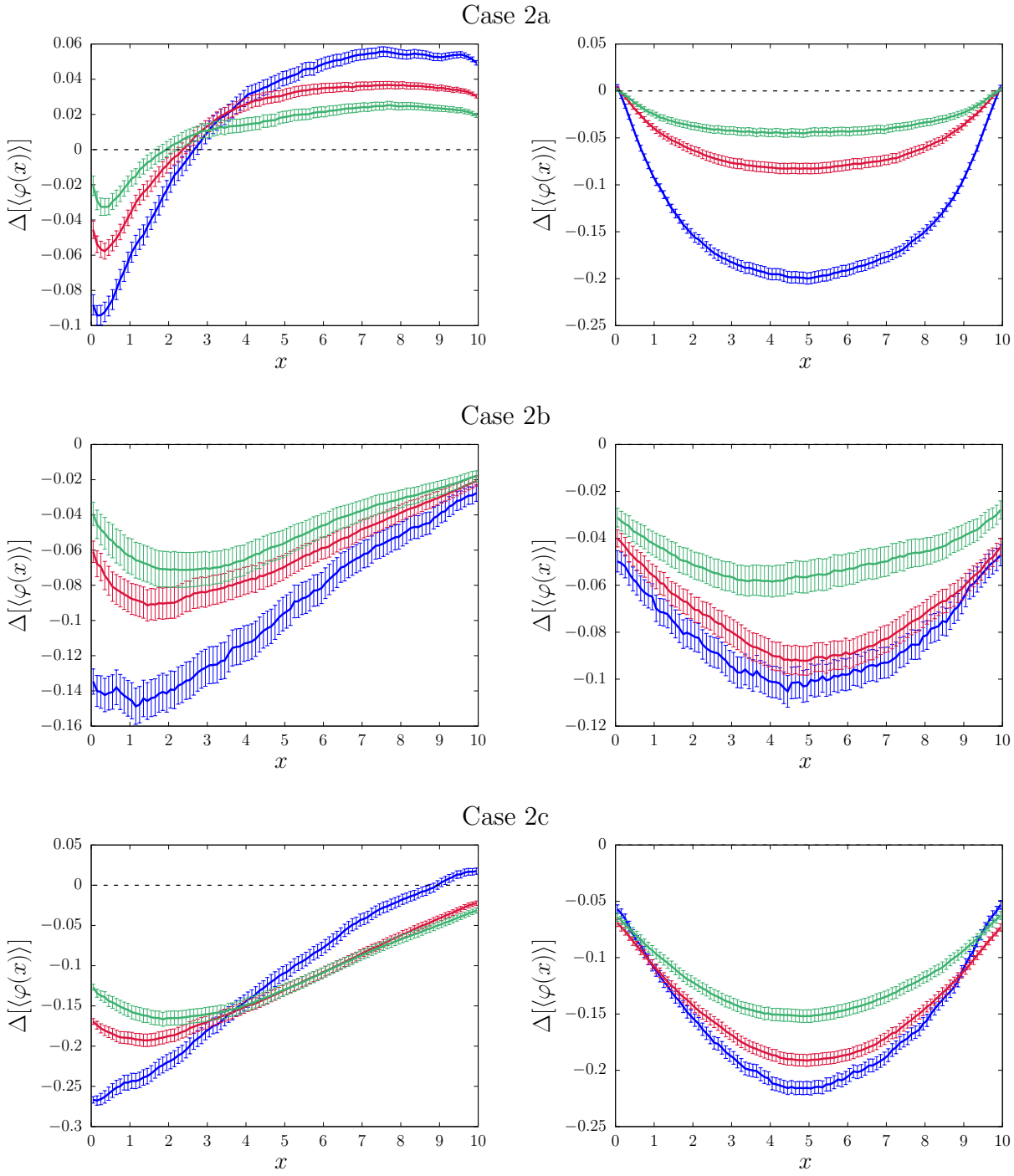

Figure 7.5: Discrepancy $\Delta[\langle\varphi(x)\rangle]$ between the ensemble-averaged spatial flux $\langle\varphi(x)\rangle$ obtained with Poisson tessellations (quenched disorder approach) and that obtained with the Chord Length Sampling algorithm (annealed disorder approach) for the benchmark configurations: Case 2. Left column: *suite* I configurations; right column: *suite* II configurations. Blue lines correspond to $d = 1$, red lines to $d = 2$ and green lines to $d = 3$. Error bars are computed as in Eq. (7.21).

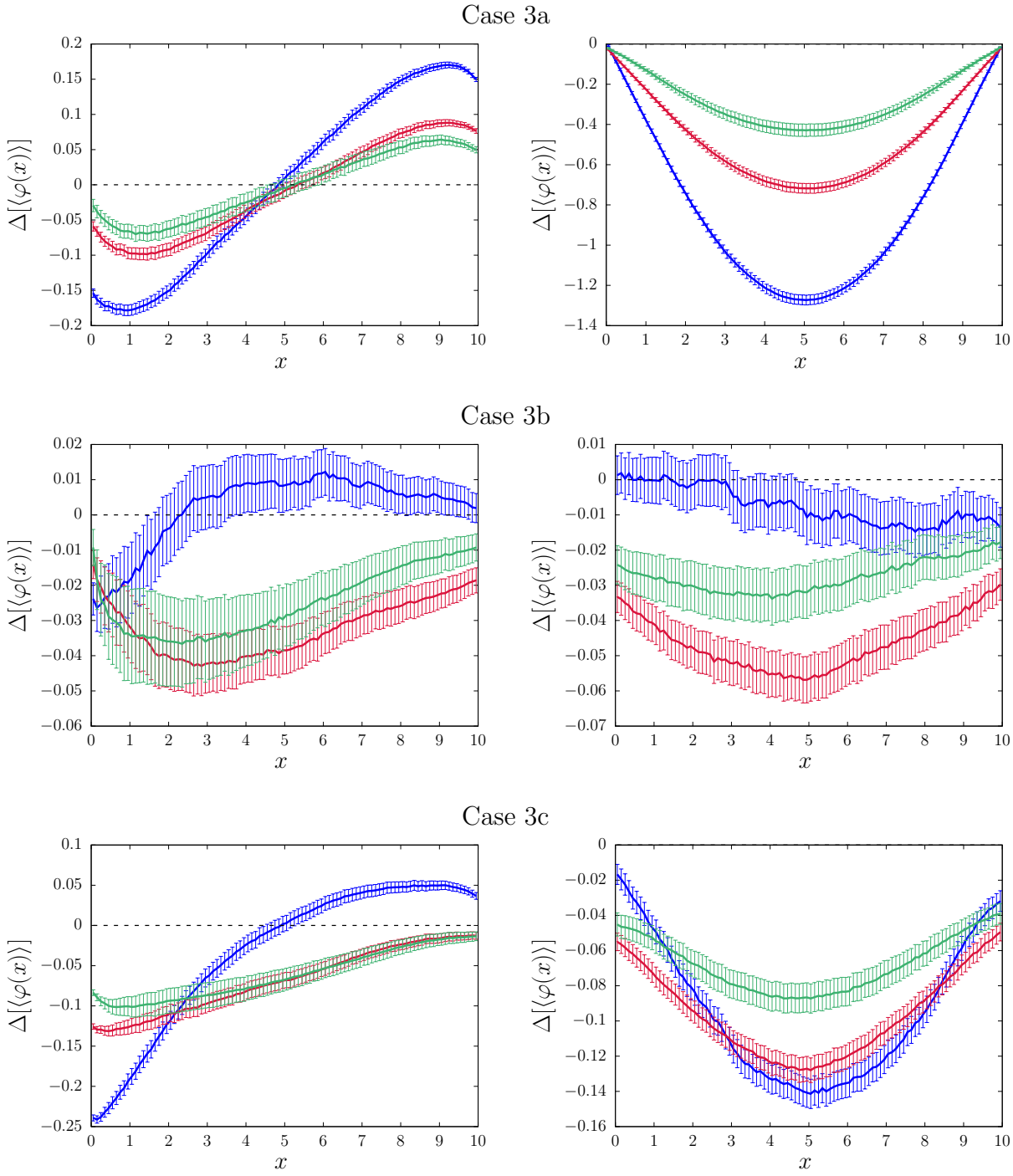

Figure 7.6: Discrepancy $\Delta[\langle\varphi(x)\rangle]$ between the ensemble-averaged spatial flux $\langle\varphi(x)\rangle$ obtained with Poisson tessellations (quenched disorder approach) and that obtained with the Chord Length Sampling algorithm (annealed disorder approach) for the benchmark configurations: Case 3. Left column: *suite* I configurations; right column: *suite* II configurations. Blue lines correspond to $d = 1$, red lines to $d = 2$ and green lines to $d = 3$. Error bars are computed as in Eq. (7.21).

7.4 Improved CLS-like algorithms

The previous considerations have shown that CLS solutions may display discrepancies as compared to reference solutions, whose relevance varies strongly with the system dimensionality, the average chord length and the material volume fraction. For the case of $1d$ slab geometries with Markov mixing, possible improvements to the standard CLS algorithm accounting for partial memory effects for particle trajectories have been detailed [167], and numerical tests have revealed that these corrections contribute to palliating the discrepancies [11], although a generalization to higher dimensions seems hardly feasible with reasonable computational burden [167].

As observed above, Algorithm A assumes that the particle has no memory of its past history, and in particular the crossed interfaces are immediately forgotten (which is consistent with the closure formula of the Levermore-Pomraning model). In this respect, CLS is an approximation of the exact treatment of disorder-induced spatial correlations. In particular, CLS is expected to be less accurate in the presence of strong scatterers with optically thick mean material chunk length: see [11] and Sec.5.3. A thorough discussion of the shortcomings of the CLS approach for $d = 1$ can be found, e.g., in [70].

For the case of $1d$ slab geometries, two improved versions of CLS Algorithm A have been proposed in the literature, by partially taking into account the memory effects induced by the spatial correlations [167]: in the former, called Algorithm B, instead of sampling the material interfaces one at a time a full random slab is generated, and particles do not switch material properties until either the forward or the backward surfaces of the slab are crossed; in the latter, called Algorithm C, a slab is generated as in Algorithm B, and the slab traversed before entering the current one is also kept in memory. The basic idea behind Algorithms B and C is to preserve the shape and the position of the material chunks (thus partially restoring spatial correlations) by generating an additional typical random slab whenever particles cross the material surfaces of the current volume.

As expected, Algorithms B and C have been shown to approximate the reference solutions for Markov mixing in $1d$ more accurately than Algorithm A, at the expense of an increased computational cost [11, 167]. Algorithm B in particular has been extensively tested for the ALP benchmark in slab geometries, and performs better than Algorithm A for all configurations [11]. As observed in [167], it is not trivial to extend Algorithms B and C to higher dimensions: this can be immediately understood by remarking that randomly generating a typical material chunk in dimension three with Markov mixing would correspond to sampling a typical polyhedral cell of the isotropic Poisson tessellations, whose exact distributions for the volume, surface, number of faces, etc., are unfortunately unknown to this day [87, 127]. In dimension one the typical chunk is a slab of exponentially distributed width, which considerably simplifies the computational burden.

7.4.1 Poisson-Box Sampling methods

A possible way to overcome this issue and improve Algorithm A in higher dimensions is however suggested by the numerical findings concerning Box tessellations. Since the chord length distribution of Box tessellations is very close to that of Poisson tessellations, it seems reasonable to extend Algorithm B by generating on-the-fly the typical cells of Box tessellations, i.e., Cartesian boxes with exponentially distributed side lengths. The generalization of Algorithm C would immediately follow by keeping memory of the last visited box. We will call this new class of Monte Carlo algorithms Poisson Box Sampling (PBS), and we will denote by PBS-1 the former (inspired by Algorithm B) and by PBS-2 the latter (inspired by Algorithm C). In view of the aforementioned similarity between quasi-isotropic and isotropic Poisson tessellations, intuitively we expect that PBS methods will preserve the increased accuracy of Algorithms B and C over Algorithm A, yet allowing for a relatively straightforward construction and a fairly minor additional computational burden.

Poisson-Box Sampling 1

By adapting the strategy of CLS, the algorithm for PBS-1 proceeds as follows:

Step 1: initialize each particle history by sampling position, angle and velocity from the specified source. In addition, a random Cartesian box is generated. The box is defined by its material label i and its spatial position, given by the coordinates (x_c, y_c, z_c) of its center and its sides: l_x, l_y and l_z. Three pairs of random numbers, namely, (Δ_x^+, Δ_x^-), (Δ_y^+, Δ_y^-) and (Δ_z^+, Δ_z^-), are sampled from independent exponential distributions of average $3\Lambda/2$. Then, we set the center of the box

$$x_c = x + (\Delta_x^+ - \Delta_x^-)/2, \tag{7.22}$$
$$y_c = y + (\Delta_y^+ - \Delta_y^-)/2, \tag{7.23}$$
$$z_c = z + (\Delta_z^+ - \Delta_z^-)/2, \tag{7.24}$$

and the sides

$$l_x = \Delta_x^+ + \Delta_x^-, \tag{7.25}$$
$$l_y = \Delta_y^+ + \Delta_x^-, \tag{7.26}$$
$$l_z = \Delta_z^+ + \Delta_z^-. \tag{7.27}$$

The material label of the box is sampled according to p_i.

Step 2: we compute three distances: the distance ℓ_b to the next physical boundary, along the current direction of the particle; the distance ℓ_c to collision, which is determined by using the material cross section that has been chosen at the previous step: if the particle is in a box with material label α, e.g., then ℓ_c will be drawn from an exponential distribution of parameter $1/\Sigma_\alpha$; and the distance ℓ_i to the next interface of the current box along the particle direction (the boundaries of the box being easily determined).

Step 3: the minimum distance among ℓ_b, ℓ_c and ℓ_i has to be selected. Then,

- if the minimum is ℓ_b, the particle is moved along a straight line until the external boundary is hit (the direction is updated in the case of reflection);
- if the minimum is ℓ_c, the particle is moved to the collision point, and the outgoing particle features are selected according to the collision kernel pertaining to the current material label;
- if the minimum is ℓ_i, the particle is moved along a straight line until the interface of the current box is hit: a new box is sampled, and the new box becomes the current box. For the sampling of a new box, we begin by drawing a random spacing δ from an exponential distribution with average $3\Lambda/2$. Without loss of generality, if the interface of the current box hit by the particle is perpendicular to the x-axis, we set the following values for the side l_x of the new box and the position x_c of its center: $l_x = \delta$, $x_c = x + l_x\,\Omega_x/|\Omega_x|$, where Ω_x is the particle direction along the x-axis. The other features of the current box, namely, l_y, l_z, y_c and z_c, are left unchanged for the new box (as suggested by the construction of Box tessellations). We would proceed in the same way for the y- and z-axis. Finally, the label of the new box is randomly sampled according to the coloring probability p_i.

Step 4: If the particle has not undergone a capture in the previous step, return to Step 2.

Contrary to Algorithm A, the correlations induced by spatial disorder are partially preserved by the PBS-1 algorithm: indeed, each particle will see the same material properties until the current box is left. Moreover, when a new box is created, its features strongly depend on those of the previous box. This should globally improve the accuracy of PBS-1 with respect to CLS in reproducing the reference solutions for the benchmark. Long-range correlations spanning more than a box (i.e., a linear size of the order of Λ) are nonetheless suppressed, so that we still expect some discrepancies between PBS-1 solutions and those obtained by the quenched disorder approach for either Poisson or Box tessellations.

Poisson-Box Sampling 2

In order to further improve the accuracy of the PBS methods, we propose a second method, inspired by Algorithm C, that will be denoted PBS-2. The strategy is exactly as in the PBS-1 algorithm, the only difference being in the fact that, once a new box has been sampled, the old box is not deleted but is kept in memory (size, position and material label) until a new material interface is selected. If the particle leaves the new box by another interface, the old box is definitively deleted, another box is sampled and the new box becomes the old box. If the selected interface is the one that has been kept in memory, the new box will simply be the old box, and the roles are reversed. This implementation intuitively extends the range of spatial correlations, and is thus supposed to correspondingly enhance the accuracy with respect to reference solutions, at the expense of increasing the computational burden, too.

7.4.2 Local Realization Preserving (LRP) algorithm

Another method to improve Algorithm A in three-dimensional geometries has been recently proposed by Brantley and Zimmerman [16] under the name of Local Realization Preserving (LRP) algorithm. In this this approach, each particle is associated with the distance to material interface in the forward direction of particle travel, denoted ℓ_i^+, and to the distance to material interface in the backward direction of particle travel, denoted ℓ_i^-. After a collision, these quantities are either maintained as-is or switched to account for backscattering, which is expected to increase the accuracy of this algorithm with respect to Chord Length Sampling. The algorithm is the following:

Step 1**:** we initialize each particle history by sampling position, angle and velocity from the specified source. The material identifier j is sampled according to p_j; in addition, we sample ℓ_i^+ and ℓ_i^- from two independent exponential distributions of mean Λ_j.

Step 2**:** we compute three distances: the distance ℓ_b to the next physical boundary, along the current direction of the particle; the distance ℓ_c to collision, which is determined by using the material cross section that has been chosen at the previous step: if the particle is in material α, e.g., then ℓ_c will be drawn from an exponential distribution of mean $1/\Sigma_j$; and the distance ℓ_i to material interface, which is equal to the current value of ℓ_i^+.

Step 3**:** the minimum distance among ℓ_b, ℓ_c and ℓ_i has to be selected. Then,

- if the minimum is ℓ_b, the particle is moved along a straight line until the external boundary is hit (the direction is updated in the case of reflection) and ℓ_i^+ (respectively ℓ_i^-) is decremented (respectively incremented) by ℓ_b.

- if the minimum is ℓ_c, the particle is moved to the collision point, and the outgoing particle features are selected according to the collision kernel pertaining to the current material label. Then, ℓ_i^+ (respectively ℓ_i^-) is decremented (respectively incremented) by ℓ_b. Finally, we compute the cosine μ between the incoming and outgoing directions of the particle; we sample a random number ξ from a uniform distribution $\mathcal{U}[0,1]$; if $\mu < 2\xi - 1$, we switch the values of ℓ_i^+ and ℓ_i^-, otherwise they are maintained: this corresponds to switch ℓ_i^+ and ℓ_i^- with probability $P(\mu) = (1-\mu)/2$. Thus, for μ close to -1, which corresponds to backscattering, the probability to switch the distances to material interfaces is strong, whereas this probability becomes weak for for μ close to 1 (i.e., forward-scattering). This linear probabilistic model preserves the average deflection cosine of the scattering and is expected to (partially) take into account the back-scattering, as explained in [16].

- if the minimum is ℓ_i, the particle is moved to the interface between the two materials, and the material label j is switched; moreover, a new value of ℓ_i^+ is sampled from a exponential distribution of mean Λ_j, while ℓ_i^- is set to zero.

Step 4**:** If the particle has not undergone a capture in the previous step, return to Step 2.

Not differently from PBS, LRP is also an approximate method: it allows better taking into account the effects of back-scattering, but a particle can nonetheless experience different material identifiers at the same location during its history, which is expected to induce discrepancies with respect to reference solutions.

7.4.3 Simulation results for PBS and LRP methods

We consider again the ALP benchmark, with the specifications given in Sec. 5.3.1.

The simulation results corresponding to CLS, PBS and LRP for the total scalar flux $\langle\varphi\rangle$, the transmission coefficient $\langle T\rangle$ and the reflection coefficient $\langle R\rangle$ are provided in Tabs. 7.7 to 7.9 for the benchmark cases corresponding to *suite* I, and in Tabs. 7.10 to 7.12 for the benchmark cases corresponding to *suite* II, respectively. The spatial flux $\langle\varphi(x)\rangle$ is illustrated in Figs. 7.7 to 7.12. For the CLS, PBS and LRP simulations of the benchmark configurations we have used 10^9 particles (10^3 replicas with 10^6 particles per replica), with resulting statistical uncertainties associated to each physical observable $\mathcal{O}$ denoted by $\sigma_{\mathrm{CLS}}[\mathcal{O}]$ and $\sigma_{\mathrm{PBS}}[\mathcal{O}]$, respectively.

Results for the transmission coefficient $\langle T\rangle$ and the reflection coefficient $\langle R\rangle$ obtained with LRP algorithm have already been published in [16], for *suite* I only. Nevertheless, we have reproduced the simulations in order to get the spatial flux and also the results corresponding to *suite* II; therefore, in the following, we display the results that we have obtained.

Generally speaking, the solutions computed with PBS-1 show a better agreement with respect to the reference solutions based on Poisson tessellations than those computed with CLS, and overall remarkably well approximate the benchmark observables. Moreover, as expected from the previous considerations, PBS-2 shows a further enhanced accuracy with respect to PBS-1. A single exception has been detected for sub-case 1*b* of *suite* I, as reported in Tab. 7.7 and in Fig. 7.7. For case 1*b*, material α is purely scattering, and material β is purely absorbing, with a small average chord length Λ. A typical realization will then consist in small absorbing chunks, with a large cross section, dispersed in larger chunks of an almost transparent material. For this configuration, the results of the Box tessellations are slightly different from those of Poisson tessellations, as observed above, for the spatial flux and the transmission coefficient. It turns out that both PBS algorithms provide results that are in excellent agreement with the reference solutions for the Box tessellation, which is consistent with their implementation. However, because of the observed discrepancy between Box and Poisson tessellations for sub-case 1*b*, PBS shows a small bias with respect to Poisson reference solutions. For the same case, CLS displays a better accuracy as compared to Poisson solutions, and this is most probably due to the fact that this algorithm exactly preserves isotropy.

For *suite* I, the accuracy of CLS with respect to reference solutions for $\langle T\rangle$, $\langle R\rangle$ and $\langle\varphi(x)\rangle$ increases with decreasing average chord length Λ, which is coherent with the previous findings in the case of $d = 1$ [11, 167] and $d = 2$ shown in Sec. 7.2. In contrast, the PBS algorithms are less sensitive to Λ. As remarked above, for all the benchmark configurations CLS is least accurate in scattering materials with optically thick chunks, as for case 2*c*; for these cases, PBS yields significantly better results. The CLS and the PBS algorithms generally under-predict the reflection coefficient $\langle R\rangle$, analogously as observed in $d = 1$ [11]. For the transmission coefficient $\langle T\rangle$, the approximate solutions of CLS and PBS lead to an overall over-prediction, with some exceptions for sub-cases *b* and *c* in cases 2 and 3 (corresponding to larger Λ, with the material cross section of α being much smaller than that of β). An explanation for CLS has been given in [11]: optically thick materials can be re-sampled as being optically thin when a particle makes repeated attempts at penetrating them. Adding memory effects might modify this general trend, as shown in the case of PBS-2. The CLS yields the maximum discrepancy for $\langle R\rangle$ (roughly -25% relative error) for case 3*b*, where material α is purely scattering, with a small cross section, whereas material β is purely absorbing, with a large cross section. For this same case, the PBS-2 yields only -4% relative error. For $\langle T\rangle$, the maximum relative error of CLS (roughly 18%) is for case 3*a*, where the roles of materials are inverted with respect to case 3*b*, namely, material α is purely absorbing, with a small cross section, whereas material β is purely scattering,

with a large cross section. For this same case, the PBS-2 yields 8% relative error. The PBS-1 yields a maximum discrepancy for $\langle R \rangle$ (roughly -15% relative error) for case $3b$, i.e., the same as for CLS, and for $\langle T \rangle$ (roughly 15% relative error) for case $3a$, which is again the same as for CLS (excluding the case $1b$ based on the considerations presented above). The PBS-1 is overall more accurate than CLS, although somewhat large errors may appear in some of the configurations. The PBS-2 algorithm is always more accurate than PBS-1. As a general comment, when the CLS is accurate, the PBS methods yield comparable or slightly better results; when the CLS is not accurate, the PBS methods yield largely better results: this observation is coherent with the behaviour of CLS Algorithm B with respect to the CLS Algorithm A in $d = 1$ [11]. As for the scalar flux, the accuracy of CLS and PBS improves with decreasing Λ. The maximum error on $\langle \varphi \rangle$ is for case $2c$ (as in $d = 1$ [11]), whereas for PBS-1 the maximum error is for $2b$. An important remark is that for $d = 3$ both CLS and PBS methods produce physically realistic flux distributions $\langle \varphi(x) \rangle$: this was known for CLS [62] and it is first illustrated here for the PBS methods.

For *suite* II, the errors introduced by the approximate models with respect to the reference solutions are somewhat smaller than for the *suite* I. For the average leakage $\langle J \rangle$, the maximum error for CLS is achieved for case $2c$ (as in $d = 1$ [11]), whereas the maximum error for PBS-1 is for $2b$. Generally speaking, PBS-1 performs better than CLS for $\langle J \rangle$, and PBS-2 better than PBS-1. As for the spatial flux $\langle \varphi(x) \rangle$, CLS is more accurate when the materials are optically thin [11], and this holds true also for the PBS methods. For the flux, the maximum error for CLS is for case $3a$ (the error is considerably reduced for the PBS-2 method), and the accuracy of CLS and PBS improves with decreasing Λ. For $d = 3$ both CLS and PBS methods produce again physically realistic flux distributions $\langle \varphi(x) \rangle$. As a general comment, when the CLS is accurate, the PBS methods yield comparable or slightly better results, similarly as for the *suite* I; when the CLS is not accurate, the PBS methods yield largely better results (this observation is again coherent with the behaviour of CLS Algorithm B with respect to CLS Algorithm A in $d = 1$ [11]).

The analysis of the approximate solutions suggests that the accuracy of CLS overall improves when decreasing the average chord length Λ: configurations pertaining to case 1 globally show a better agreement than those of case 2, and those of case 2 show a better agreement than those of case 3, as pointed out in Sec.7.2. The improved PBS methods are less sensitive to the average chord length Λ and show a satisfactory agreement for all benchmark configurations. For intermediate and large Λ, i.e., case 2 and 3, the impact of boundary conditions (due to the medium being of finite size) comes also into play, and the polyhedra composing the tessellations will be more often truncated by the sides of the box. These effects should be properly taken into account when comparing CLS and PBS solutions to reference results, since the volumic ratio is not preserved in this case [68]: the investigation of these phenomena is left for future work.

Computer times for the CLS and PBS solutions are also provided in Tabs. 7.7 to 7.9: not surprisingly, the approaches based on annealed disorder are much faster than the reference methods, since a single transport simulation is needed. PBS methods, while still much faster than reference solutions, for most configurations take sensibly longer than CLS: this is partly due to the increased complexity of the algorithms, and partly due to the fact that CLS is based on the sampling of the colored chord lengths (corresponding to clusters of polyhedra sharing all the same material label), whereas PBS require the sampling of un-colored boxes one at a time. Nonetheless, keeping in memory a further box amounts to an almost negligible additional computational burden for PBS-2 as opposed to PBS-1.

As a general consideration, the solutions computed with LRP show a better agreement with respect to the reference solutions based on Poisson tessellations than those computed with CLS, and overall remarkably well approximate the benchmark observables. Moreover, the results obtained for the average reflection and transmission coefficients for the *suite* I are compatible with those presented in [16].

Computer times for the LRP solutions are given in Tabs. 7.7 to 7.9. As expected, the computer time is comparable between CLS and LRP method, since both are based on the sampling of colored chords. Moreover, LRP algorithm is faster than PBS methods because of the sampling of un-colored boxes for the latter methods.

Case	Algorithm	$\langle R \rangle$	$\langle T \rangle$	$\langle \varphi \rangle$	t_{tot} [s]
1a	Poisson	$0.4091 \pm 5 \times 10^{-4}$	0.0163 ± 10^{-4}	6.328 ± 0.007	3.9×10^{6}
	Box	$0.4092 \pm 6 \times 10^{-4}$	0.0166 ± 10^{-4}	6.321 ± 0.008	8.5×10^{5}
	CLS	$0.40176 \pm 2 \times 10^{-5}$	$0.017491 \pm 4 \times 10^{-6}$	$6.3933 \pm 2 \times 10^{-4}$	4.6×10^{3}
	Err [%]	-1.79 ± 0.13	7.53 ± 0.86	1.03 ± 0.12	
	PBS-1	$0.40683 \pm 2 \times 10^{-5}$	$0.017030 \pm 4 \times 10^{-6}$	$6.3440 \pm 2 \times 10^{-4}$	1.9×10^{4}
	Err [%]	-0.55 ± 0.13	4.70 ± 0.84	0.25 ± 0.12	
	PBS-2	$0.40760 \pm 2 \times 10^{-5}$	$0.016898 \pm 4 \times 10^{-6}$	$6.3368 \pm 2 \times 10^{-4}$	1.9×10^{4}
	Err [%]	-0.36 ± 0.13	3.88 ± 0.83	0.14 ± 0.12	
	LRP	$0.40607 \pm 2 \times 10^{-5}$	$0.016718 \pm 4 \times 10^{-6}$	$6.3557 \pm 2 \times 10^{-4}$	4.5×10^{3}
	Err [%]	-0.74 ± 0.13	2.78 ± 0.82	0.44 ± 0.12	
1b	Poisson	$0.0377 \pm 2 \times 10^{-4}$	$0.00085 \pm 3 \times 10^{-5}$	1.918 ± 0.003	1.8×10^{6}
	Box	$0.0379 \pm 2 \times 10^{-4}$	$0.00102 \pm 3 \times 10^{-5}$	1.925 ± 0.004	3.4×10^{5}
	CLS	$0.036714 \pm 6 \times 10^{-6}$	$0.0008413 \pm 9 \times 10^{-7}$	$1.91440 \pm 6 \times 10^{-5}$	1.0×10^{3}
	Err [%]	-2.52 ± 0.52	-1.03 ± 3.46	-0.20 ± 0.17	
	PBS-1	$0.036729 \pm 6 \times 10^{-6}$	$0.001025 \pm 1 \times 10^{-6}$	$1.91635 \pm 6 \times 10^{-5}$	5.8×10^{3}
	Err [%]	-2.48 ± 0.52	20.58 ± 4.21	-0.10 ± 0.17	
	PBS-2	$0.037188 \pm 6 \times 10^{-6}$	0.001028 ± 10^{-6}	$1.92029 \pm 6 \times 10^{-5}$	6.0×10^{3}
	Err [%]	-1.26 ± 0.52	20.88 ± 4.23	0.11 ± 0.17	
	LRP	$0.040808 \pm 6 \times 10^{-6}$	0.000895 ± 10^{-6}	1.9450 ± 10^{-4}	1.1×10^{3}
	Err [%]	8.35 ± 0.57	5.34 ± 3.68	1.39 ± 0.17	
1c	Poisson	$0.4059 \pm 5 \times 10^{-4}$	0.0164 ± 10^{-4}	6.303 ± 0.008	4.4×10^{6}
	Box	$0.4062 \pm 5 \times 10^{-4}$	0.0168 ± 10^{-4}	6.306 ± 0.009	8.5×10^{5}
	CLS	0.39619 ± 10^{-5}	$0.016992 \pm 2 \times 10^{-6}$	$6.2957 \pm 2 \times 10^{-4}$	1.1×10^{4}
	Err [%]	-2.40 ± 0.12	3.62 ± 0.84	-0.12 ± 0.13	
	PBS-1	0.40278 ± 10^{-5}	$0.017054 \pm 3 \times 10^{-6}$	$6.3049 \pm 2 \times 10^{-4}$	4.7×10^{4}
	Err [%]	-0.78 ± 0.12	4.00 ± 0.85	0.03 ± 0.13	
	PBS-2	0.40399 ± 10^{-5}	$0.016998 \pm 3 \times 10^{-6}$	$6.3082 \pm 2 \times 10^{-4}$	4.8×10^{4}
	Err [%]	-0.48 ± 0.12	3.66 ± 0.85	0.08 ± 0.13	
	LRP	0.40586 ± 10^{-5}	$0.016951 \pm 3 \times 10^{-6}$	$6.3560 \pm 2 \times 10^{-4}$	1.1×10^{4}
	Err [%]	-0.02 ± 0.12	3.37 ± 0.84	0.84 ± 0.13	

Table 7.7: Ensemble-averaged observables and computer time t_{tot} for the benchmark configurations: *suite* I - case 1.

Case	Algorithm	$\langle R \rangle$	$\langle T \rangle$	$\langle \varphi \rangle$	t_{tot} [s]
2a	Poisson	0.225 ± 0.001	$0.0937 \pm 4 \times 10^{-4}$	7.57 ± 0.01	4.4×10^5
	Box	0.228 ± 0.001	$0.0950 \pm 4 \times 10^{-4}$	7.54 ± 0.01	4.3×10^5
	CLS	0.20043 ± 10^{-5}	$0.105624 \pm 9 \times 10^{-6}$	$7.6615 \pm 2 \times 10^{-4}$	3.1×10^3
	Err [%]	-11.08 ± 0.45	12.74 ± 0.54	1.22 ± 0.13	
	PBS-1	0.22066 ± 10^{-5}	$0.098160 \pm 9 \times 10^{-6}$	$7.5601 \pm 2 \times 10^{-4}$	5.3×10^3
	Err [%]	-2.11 ± 0.50	4.77 ± 0.50	-0.12 ± 0.13	
	PBS-2	0.22365 ± 10^{-5}	$0.097014 \pm 9 \times 10^{-6}$	$7.5504 \pm 2 \times 10^{-4}$	5.3×10^3
	Err [%]	-0.79 ± 0.51	3.55 ± 0.49	-0.25 ± 0.13	
	LRP	0.21049 ± 10^{-5}	$0.100990 \pm 9 \times 10^{-6}$	$7.6464 \pm 2 \times 10^{-4}$	2.9×10^3
	Err [%]	-6.62 ± 0.48	7.79 ± 0.51	1.02 ± 0.13	
2b	Poisson	$0.1616 \pm 8 \times 10^{-4}$	$0.1194 \pm 9 \times 10^{-4}$	7.77 ± 0.03	3.4×10^5
	Box	$0.1626 \pm 9 \times 10^{-4}$	$0.1202 \pm 9 \times 10^{-4}$	7.77 ± 0.03	2.9×10^5
	CLS	0.14223 ± 10^{-5}	0.10996 ± 10^{-5}	$7.2609 \pm 2 \times 10^{-4}$	9.3×10^2
	Err [%]	-11.99 ± 0.44	-7.91 ± 0.68	-6.50 ± 0.37	
	PBS-1	0.14394 ± 10^{-5}	0.11168 ± 10^{-5}	$7.3065 \pm 2 \times 10^{-4}$	3.1×10^3
	Err [%]	-10.94 ± 0.45	-6.48 ± 0.70	-5.92 ± 0.38	
	PBS-2	0.15193 ± 10^{-5}	0.11572 ± 10^{-5}	$7.5152 \pm 2 \times 10^{-4}$	3.2×10^3
	Err [%]	-5.99 ± 0.47	-3.09 ± 0.72	-3.23 ± 0.39	
	LRP	0.17656 ± 10^{-5}	0.12854 ± 10^{-5}	$8.0303 \pm 4 \times 10^{-4}$	9.6×10^2
	Err [%]	9.25 ± 0.55	7.65 ± 0.80	3.40 ± 0.41	
2c	Poisson	$0.3457 \pm 5 \times 10^{-4}$	$0.1651 \pm 9 \times 10^{-4}$	10.76 ± 0.03	4.8×10^5
	Box	$0.3474 \pm 5 \times 10^{-4}$	$0.1656 \pm 9 \times 10^{-4}$	10.74 ± 0.03	4.0×10^5
	CLS	0.27693 ± 10^{-5}	0.15031 ± 10^{-5}	$9.6048 \pm 2 \times 10^{-4}$	8.9×10^3
	Err [%]	-19.89 ± 0.12	-8.98 ± 0.49	-10.73 ± 0.23	
	PBS-1	0.32610 ± 10^{-5}	0.16385 ± 10^{-5}	$10.4372 \pm 2 \times 10^{-4}$	1.0×10^4
	Err [%]	-5.67 ± 0.14	-0.78 ± 0.53	-3.00 ± 0.25	
	PBS-2	0.33558 ± 10^{-5}	0.16586 ± 10^{-5}	$10.6010 \pm 2 \times 10^{-4}$	9.9×10^3
	Err [%]	-2.93 ± 0.14	0.44 ± 0.54	-1.48 ± 0.25	
	LRP	0.34333 ± 10^{-5}	0.17682 ± 10^{-5}	$10.9273 \pm 4 \times 10^{-4}$	4.7×10^3
	Err [%]	-0.68 ± 0.14	7.07 ± 0.57	1.56 ± 0.26	

Table 7.8: Ensemble-averaged observables and computer time t_{tot} for the benchmark configurations: *suite* I - case 2.

Case	Algorithm	$\langle R \rangle$	$\langle T \rangle$	$\langle \varphi \rangle$	t_{tot} [s]
3a	Poisson	0.675 ± 0.001	$0.1692 \pm 9 \times 10^{-4}$	16.38 ± 0.03	1.4×10^{6}
	Box	0.677 ± 0.001	0.168 ± 0.001	16.39 ± 0.03	1.3×10^{6}
	CLS	$0.64107 \pm 2 \times 10^{-5}$	0.19957 ± 10^{-5}	$16.3231 \pm 6 \times 10^{-4}$	9.1×10^{3}
	Err [%]	-5.06 ± 0.20	17.96 ± 0.65	-0.36 ± 0.19	
	PBS-1	$0.64806 \pm 2 \times 10^{-5}$	0.19408 ± 10^{-5}	$16.3182 \pm 6 \times 10^{-4}$	8.1×10^{3}
	Err [%]	-4.02 ± 0.21	14.72 ± 0.64	-0.39 ± 0.19	
	PBS-2	$0.66148 \pm 2 \times 10^{-5}$	0.18226 ± 10^{-5}	$16.3416 \pm 7 \times 10^{-4}$	8.1×10^{3}
	Err [%]	-2.04 ± 0.21	7.73 ± 0.60	-0.25 ± 0.19	
	LRP	$0.65240 \pm 2 \times 10^{-5}$	0.19007 ± 10^{-5}	$16.4803 \pm 8 \times 10^{-4}$	6.0×10^{3}
	Err [%]	-3.38 ± 0.21	12.35 ± 0.62	0.60 ± 0.20	
3b	Poisson	$0.0165 \pm 2 \times 10^{-4}$	$0.0457 \pm 9 \times 10^{-4}$	3.47 ± 0.03	5.0×10^{5}
	Box	$0.0166 \pm 2 \times 10^{-4}$	$0.0462 \pm 9 \times 10^{-4}$	3.44 ± 0.03	4.1×10^{5}
	CLS	$0.012454 \pm 3 \times 10^{-6}$	$0.040345 \pm 6 \times 10^{-6}$	3.2382 ± 10^{-4}	8.0×10^{2}
	Err [%]	-24.48 ± 0.97	-11.80 ± 1.68	-6.55 ± 0.70	
	PBS-1	$0.013974 \pm 4 \times 10^{-6}$	$0.044533 \pm 6 \times 10^{-6}$	3.3178 ± 10^{-4}	1.2×10^{3}
	Err [%]	-15.26 ± 1.09	-2.65 ± 1.86	-4.26 ± 0.71	
	PBS-2	$0.015823 \pm 4 \times 10^{-6}$	$0.047299 \pm 7 \times 10^{-6}$	$3.4216 \pm 2 \times 10^{-4}$	1.2×10^{3}
	Err [%]	-4.05 ± 1.23	3.40 ± 1.97	-1.26 ± 0.74	
	LRP	$0.015743 \pm 4 \times 10^{-6}$	$0.041365 \pm 7 \times 10^{-6}$	$3.2910 \pm 4 \times 10^{-4}$	6.6×10^{2}
	Err [%]	-4.53 ± 1.22	-9.58 ± 1.73	-5.03 ± 0.71	
3c	Poisson	$0.3979 \pm 7 \times 10^{-4}$	0.086 ± 0.001	7.89 ± 0.03	7.0×10^{5}
	Box	$0.4008 \pm 7 \times 10^{-4}$	0.086 ± 0.001	7.86 ± 0.04	6.9×10^{5}
	CLS	0.34652 ± 10^{-5}	$0.080613 \pm 7 \times 10^{-6}$	$7.3217 \pm 2 \times 10^{-4}$	8.8×10^{3}
	Err [%]	-12.92 ± 0.15	-6.16 ± 1.19	-7.17 ± 0.40	
	PBS-1	0.36242 ± 10^{-5}	$0.086946 \pm 8 \times 10^{-6}$	$7.5230 \pm 2 \times 10^{-4}$	7.6×10^{3}
	Err [%]	-8.92 ± 0.15	1.21 ± 1.29	-4.62 ± 0.41	
	PBS-2	0.38437 ± 10^{-5}	$0.089701 \pm 8 \times 10^{-6}$	$7.7650 \pm 2 \times 10^{-4}$	7.2×10^{3}
	Err [%]	-3.41 ± 0.16	4.42 ± 1.33	-1.55 ± 0.42	
	LRP	0.38018 ± 10^{-5}	$0.093849 \pm 8 \times 10^{-6}$	$7.8474 \pm 5 \times 10^{-4}$	5.2×10^{3}
	Err [%]	-4.46 ± 0.16	9.25 ± 1.39	-0.51 ± 0.43	

Table 7.9: Ensemble-averaged observables and computer time t_{tot} for the benchmark configurations: *suite* I - case 3.

Case	Algorithm	$\langle J \rangle$	$\langle \varphi \rangle$	t_{tot} [s]
1a	Poisson	$0.1583 \pm 3 \times 10^{-4}$	7.530 ± 0.008	7.9×10^{7}
	Box	$0.1580 \pm 3 \times 10^{-4}$	7.533 ± 0.008	3.6×10^{7}
	CLS	$0.159828 \pm 8 \times 10^{-6}$	$7.4924 \pm 2 \times 10^{-4}$	5.3×10^{3}
	Err [%]	0.98 ± 0.17	-0.49 ± 0.10	
	PBS-1	$0.158605 \pm 8 \times 10^{-6}$	$7.5218 \pm 2 \times 10^{-4}$	2.3×10^{4}
	Err [%]	0.21 ± 0.17	-0.10 ± 0.10	
	PBS-2	$0.158416 \pm 8 \times 10^{-6}$	$7.5259 \pm 2 \times 10^{-4}$	2.3×10^{4}
	Err [%]	0.09 ± 0.17	-0.05 ± 0.10	
	LRP	$0.158898 \pm 8 \times 10^{-6}$	$7.5171 \pm 2 \times 10^{-4}$	5.3×10^{3}
	Err [%]	0.39 ± 0.17	-0.17 ± 0.10	
1b	Poisson	$0.0481 \pm 2 \times 10^{-4}$	1.808 ± 0.003	7.4×10^{7}
	Box	$0.0481 \pm 2 \times 10^{-4}$	1.820 ± 0.003	3.3×10^{7}
	CLS	$0.047859 \pm 5 \times 10^{-6}$	$1.79609 \pm 6 \times 10^{-5}$	1.0×10^{3}
	Err [%]	-0.42 ± 0.33	-0.63 ± 0.14	
	PBS-1	$0.047910 \pm 5 \times 10^{-6}$	$1.80671 \pm 6 \times 10^{-5}$	5.5×10^{3}
	Err [%]	-0.32 ± 0.33	-0.05 ± 0.14	
	PBS-2	$0.048013 \pm 5 \times 10^{-6}$	$1.81201 \pm 6 \times 10^{-5}$	5.6×10^{3}
	Err [%]	-0.10 ± 0.33	0.25 ± 0.14	
	LRP	$0.048628 \pm 5 \times 10^{-6}$	1.8300 ± 10^{-4}	1.1×10^{3}
	Err [%]	1.18 ± 0.34	1.24 ± 0.14	
1c	Poisson	$0.1577 \pm 3 \times 10^{-4}$	7.455 ± 0.008	7.7×10^{7}
	Box	$0.1576 \pm 3 \times 10^{-4}$	7.470 ± 0.008	3.9×10^{7}
	CLS	$0.157383 \pm 6 \times 10^{-6}$	7.3335 ± 10^{-4}	1.4×10^{4}
	Err [%]	-0.19 ± 0.17	-1.63 ± 0.10	
	PBS-1	$0.157630 \pm 6 \times 10^{-6}$	7.4260 ± 10^{-4}	6.1×10^{4}
	Err [%]	-0.04 ± 0.17	-0.39 ± 0.11	
	PBS-2	$0.157705 \pm 6 \times 10^{-6}$	7.4434 ± 10^{-4}	6.3×10^{4}
	Err [%]	0.01 ± 0.17	-0.15 ± 0.11	
	LRP	$0.158901 \pm 7 \times 10^{-6}$	$7.4808 \pm 2 \times 10^{-4}$	1.4×10^{4}
	Err [%]	0.77 ± 0.17	0.35 ± 0.11	

Table 7.10: Ensemble-averaged observables and computer time t_{tot} for the benchmark configurations: *suite* II - case 1.

Case	Algorithm	$\langle J \rangle$	$\langle \varphi \rangle$	t_{tot} [s]
2a	Poisson	$0.1892 \pm 3 \times 10^{-4}$	7.27 ± 0.01	5.8×10^5
	Box	$0.1882 \pm 3 \times 10^{-4}$	7.31 ± 0.01	4.4×10^5
	CLS	$0.191527 \pm 9 \times 10^{-6}$	$6.8774 \pm 2 \times 10^{-4}$	3.0×10^3
	Err [%]	1.21 ± 0.16	-5.36 ± 0.18	
	PBS-1	$0.189005 \pm 9 \times 10^{-6}$	$7.1825 \pm 2 \times 10^{-4}$	5.7×10^3
	Err [%]	-0.12 ± 0.15	-1.16 ± 0.19	
	PBS-2	$0.188756 \pm 9 \times 10^{-6}$	$7.2490 \pm 2 \times 10^{-4}$	5.9×10^3
	Err [%]	-0.26 ± 0.15	-0.25 ± 0.19	
	LRP	$0.191150 \pm 9 \times 10^{-6}$	$7.3194 \pm 2 \times 10^{-4}$	3.9×10^3
	Err [%]	1.01 ± 0.16	0.72 ± 0.19	
2b	Poisson	$0.1931 \pm 4 \times 10^{-4}$	6.53 ± 0.01	1.7×10^6
	Box	$0.1939 \pm 4 \times 10^{-4}$	6.63 ± 0.01	9.1×10^5
	CLS	$0.181518 \pm 9 \times 10^{-6}$	$6.0577 \pm 2 \times 10^{-4}$	8.6×10^2
	Err [%]	-6.01 ± 0.21	-7.31 ± 0.19	
	PBS-1	$0.182655 \pm 9 \times 10^{-6}$	$6.1625 \pm 2 \times 10^{-4}$	2.8×10^3
	Err [%]	-5.42 ± 0.21	-5.70 ± 0.19	
	PBS-2	$0.187874 \pm 9 \times 10^{-6}$	$6.3690 \pm 2 \times 10^{-4}$	2.9×10^3
	Err [%]	-2.72 ± 0.21	-2.54 ± 0.20	
	LRP	$0.200751 \pm 9 \times 10^{-6}$	$6.6771 \pm 4 \times 10^{-4}$	9.6×10^2
	Err [%]	3.95 ± 0.23	2.17 ± 0.21	
2c	Poisson	$0.2688 \pm 6 \times 10^{-4}$	9.55 ± 0.02	4.9×10^5
	Box	$0.2680 \pm 6 \times 10^{-4}$	9.62 ± 0.02	3.3×10^5
	CLS	$0.240117 \pm 8 \times 10^{-6}$	$8.3498 \pm 2 \times 10^{-4}$	8.4×10^3
	Err [%]	-10.69 ± 0.20	-12.58 ± 0.18	
	PBS-1	$0.260937 \pm 9 \times 10^{-6}$	$9.2561 \pm 2 \times 10^{-4}$	9.8×10^3
	Err [%]	-2.94 ± 0.22	-3.09 ± 0.20	
	PBS-2	$0.265038 \pm 9 \times 10^{-6}$	$9.4484 \pm 2 \times 10^{-4}$	9.7×10^3
	Err [%]	-1.42 ± 0.22	-1.08 ± 0.20	
	LRP	$0.273215 \pm 9 \times 10^{-6}$	$9.5234 \pm 4 \times 10^{-4}$	4.9×10^3
	Err [%]	1.63 ± 0.23	-0.30 ± 0.20	

Table 7.11: Ensemble-averaged observables and computer time t_{tot} for the benchmark configurations: *suite* II - case 2.

Case	Algorithm	$\langle J \rangle$	$\langle \varphi \rangle$	t_{tot} [s]
3a	Poisson	$0.4098 \pm 4 \times 10^{-4}$	22.82 ± 0.07	1.7×10^6
	Box	$0.4088 \pm 4 \times 10^{-4}$	23.33 ± 0.08	1.6×10^6
	CLS	0.40807 ± 10^{-5}	$19.7173 \pm 6 \times 10^{-4}$	1.1×10^4
	Err [%]	-0.42 ± 0.10	-13.61 ± 0.28	
	PBS-1	0.40795 ± 10^{-5}	$20.7792 \pm 7 \times 10^{-4}$	1.0×10^4
	Err [%]	-0.45 ± 0.10	-8.96 ± 0.29	
	PBS-2	0.40856 ± 10^{-5}	$22.0417 \pm 8 \times 10^{-4}$	1.1×10^4
	Err [%]	-0.30 ± 0.10	-3.43 ± 0.31	
	LRP	0.41201 ± 10^{-5}	$22.3400 \pm 9 \times 10^{-4}$	9.0×10^3
	Err [%]	0.54 ± 0.10	-2.12 ± 0.32	
3b	Poisson	$0.0868 \pm 3 \times 10^{-4}$	2.98 ± 0.01	8.7×10^5
	Box	$0.0864 \pm 3 \times 10^{-4}$	3.02 ± 0.01	7.2×10^5
	CLS	$0.080949 \pm 6 \times 10^{-6}$	2.6747 ± 10^{-4}	7.8×10^2
	Err [%]	-6.78 ± 0.34	-10.12 ± 0.30	
	PBS-1	$0.082950 \pm 6 \times 10^{-6}$	$2.8168 \pm 2 \times 10^{-4}$	1.1×10^3
	Err [%]	-4.48 ± 0.35	-5.35 ± 0.32	
	PBS-2	$0.085533 \pm 6 \times 10^{-6}$	$2.9531 \pm 2 \times 10^{-4}$	1.2×10^3
	Err [%]	-1.50 ± 0.36	-0.77 ± 0.34	
	LRP	$0.082285 \pm 6 \times 10^{-6}$	$2.7149 \pm 4 \times 10^{-4}$	7.0×10^2
	Err [%]	-5.24 ± 0.34	-8.78 ± 0.31	
3c	Poisson	$0.1974 \pm 7 \times 10^{-4}$	8.15 ± 0.02	5.0×10^5
	Box	$0.1956 \pm 7 \times 10^{-4}$	8.24 ± 0.02	4.6×10^5
	CLS	$0.183044 \pm 7 \times 10^{-6}$	7.4839 ± 10^{-4}	1.1×10^4
	Err [%]	-7.26 ± 0.33	-8.20 ± 0.25	
	PBS-1	$0.188079 \pm 7 \times 10^{-6}$	$7.7653 \pm 2 \times 10^{-4}$	8.9×10^3
	Err [%]	-4.71 ± 0.34	-4.75 ± 0.26	
	PBS-2	$0.194130 \pm 8 \times 10^{-6}$	$8.0753 \pm 2 \times 10^{-4}$	8.8×10^3
	Err [%]	-1.64 ± 0.36	-0.95 ± 0.27	
	LRP	$0.196205 \pm 7 \times 10^{-6}$	$7.8964 \pm 5 \times 10^{-4}$	6.6×10^3
	Err [%]	-0.59 ± 0.36	-3.14 ± 0.27	

Table 7.12: Ensemble-averaged observables and computer time t_{tot} for the benchmark configurations: *suite* II - case 3.

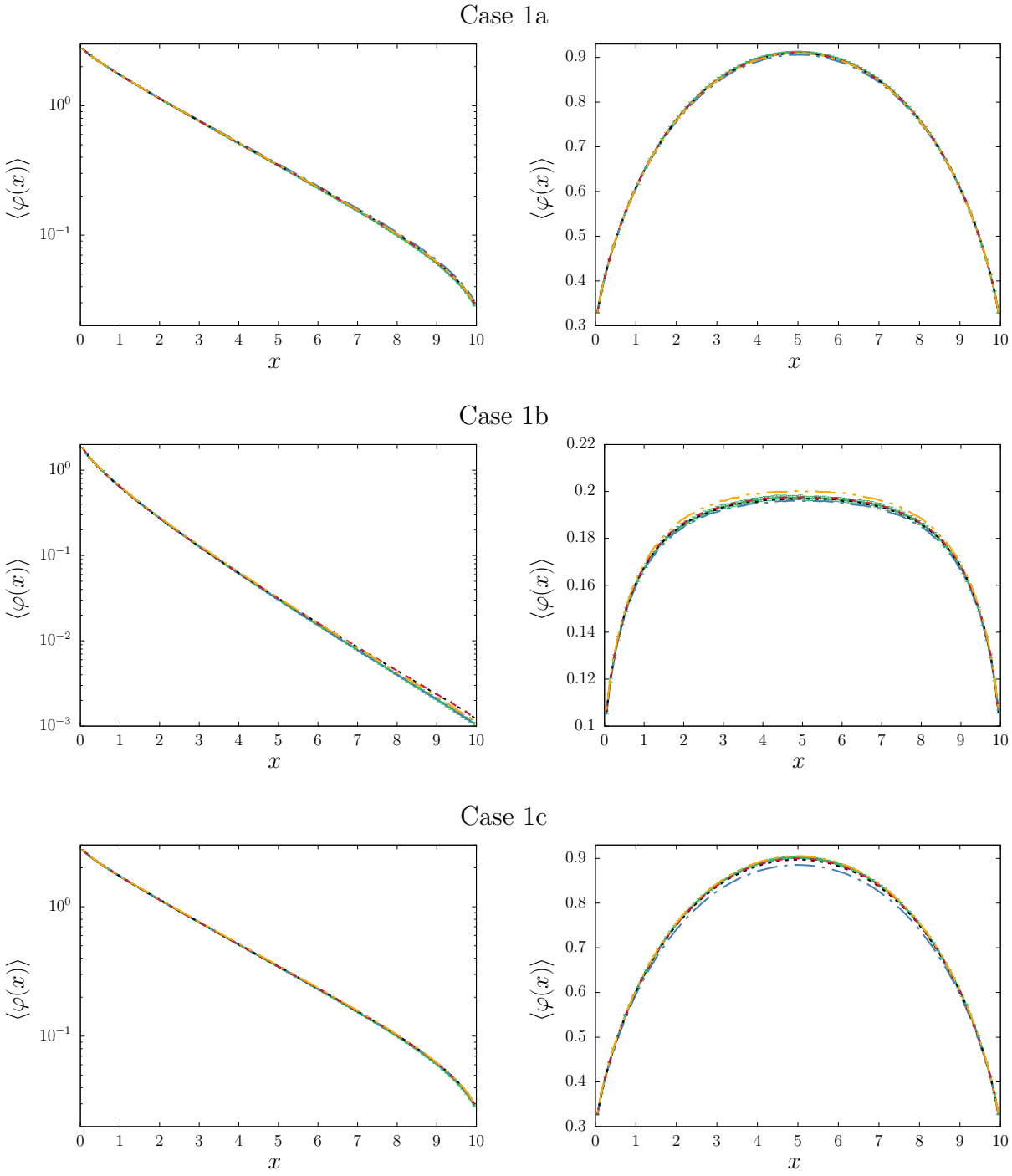

Figure 7.7: Ensemble-averaged spatial scalar flux for the benchmark configurations: Case 1. Left column: *suite* I configurations; right column: *suite* II configurations. Solid green lines represent the benchmark solutions obtained with the quenched disorder approach for Markovian mixtures (Poisson tessellations). Dotted or dashed lines represent the solutions from annealed disorder approach: blue lines correspond to CLS results, black lines to PBS-1 results, red lines to PBS-2 results and orange lines to LRP results.

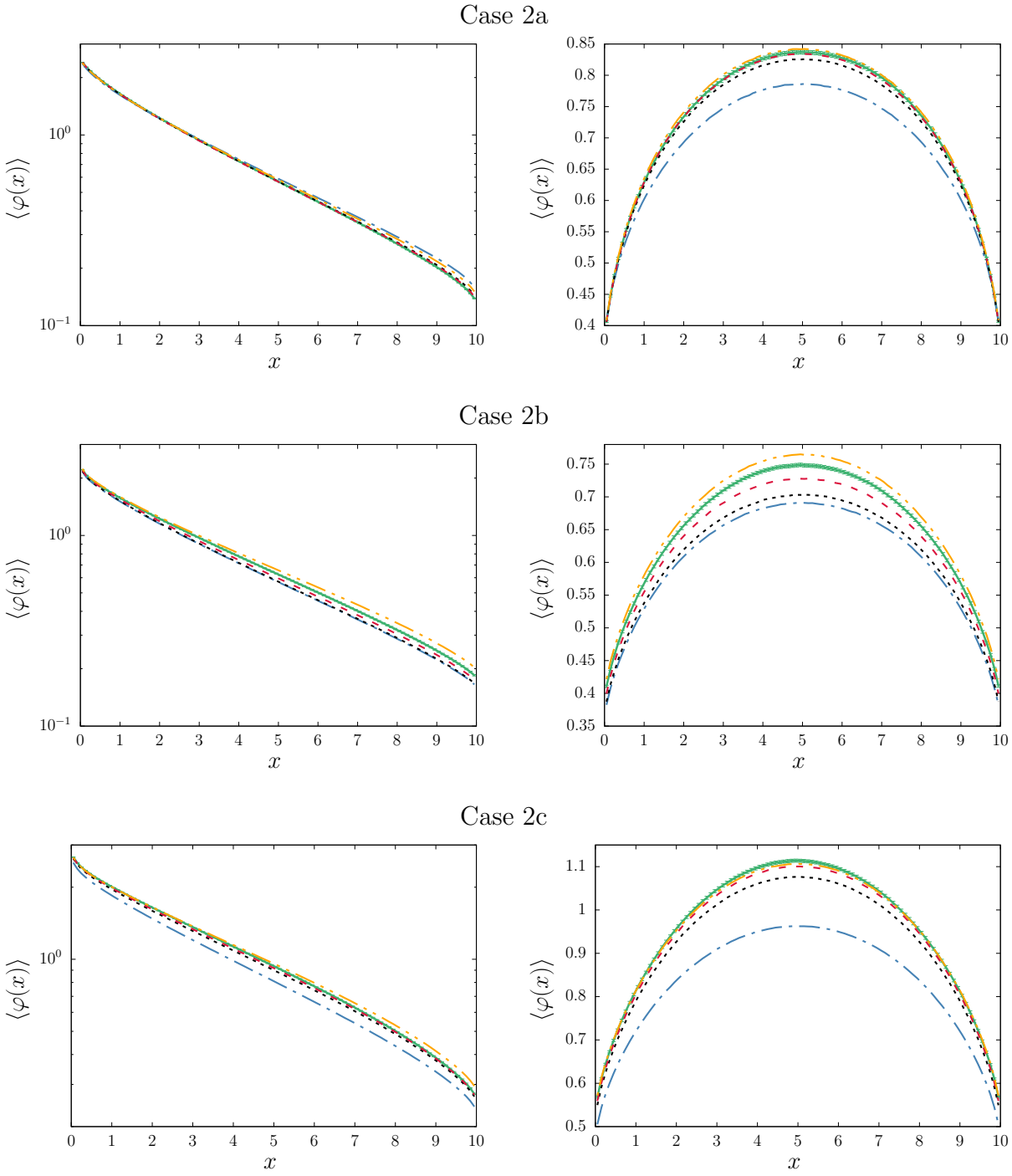

Figure 7.8: Ensemble-averaged spatial scalar flux for the benchmark configurations: Case 2. Left column: *suite* I configurations; right column: *suite* II configurations. Solid green lines represent the benchmark solutions obtained with the quenched disorder approach for Markovian mixtures (Poisson tessellations). Dotted or dashed lines represent the solutions from annealed disorder approach: blue lines correspond to CLS results, black lines to PBS-1 results, red lines to PBS-2 results and orange lines to LRP results.

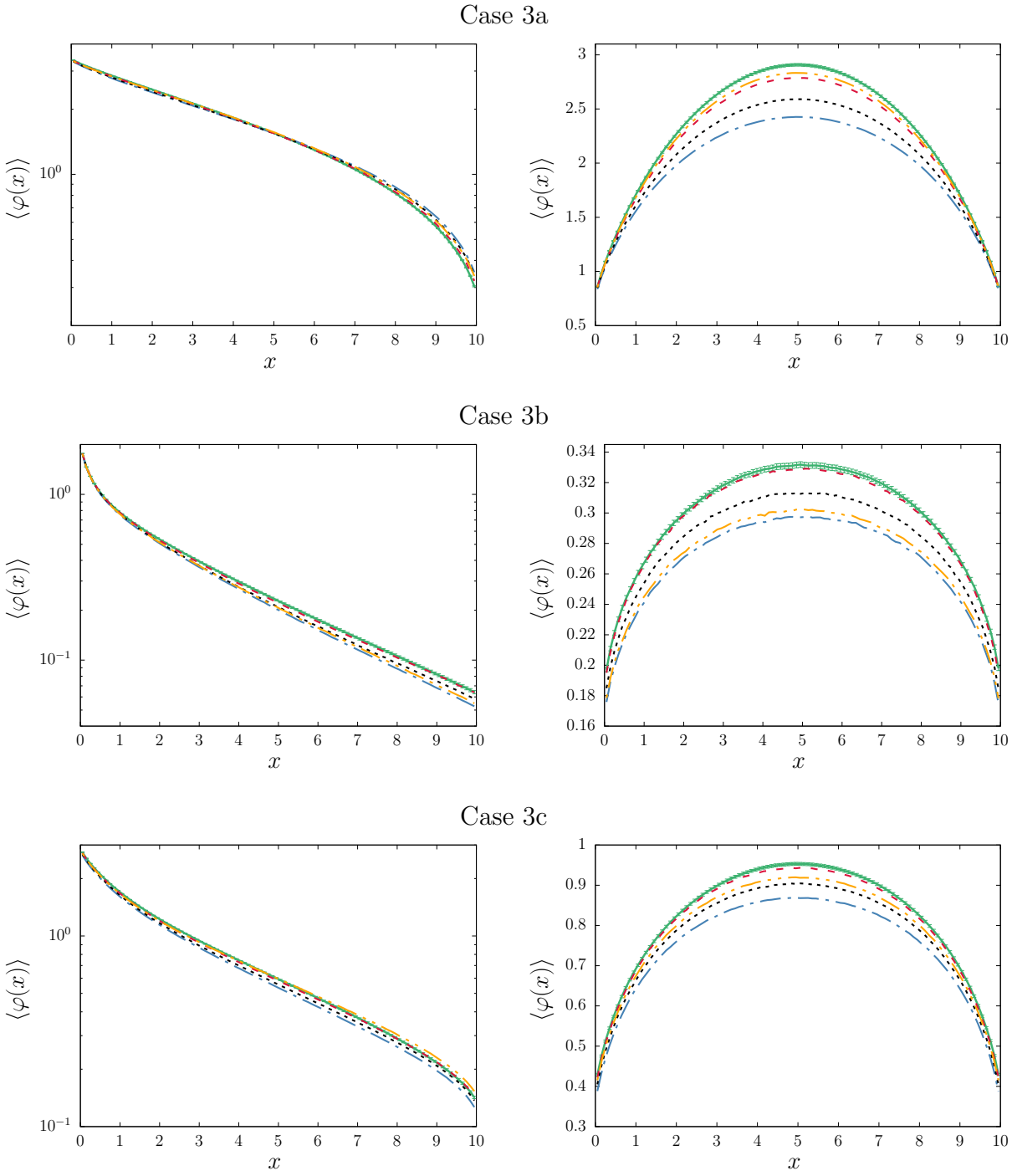

Figure 7.9: Ensemble-averaged spatial scalar flux for the benchmark configurations: Case 3. Left column: *suite* I configurations; right column: *suite* II configurations. Solid green lines represent the benchmark solutions obtained with the quenched disorder approach for Markovian mixtures (Poisson tessellations). Dotted or dashed lines represent the solutions from annealed disorder approach: blue lines correspond to CLS results, black lines to PBS-1 results, red lines to PBS-2 results and orange lines to LRP results.

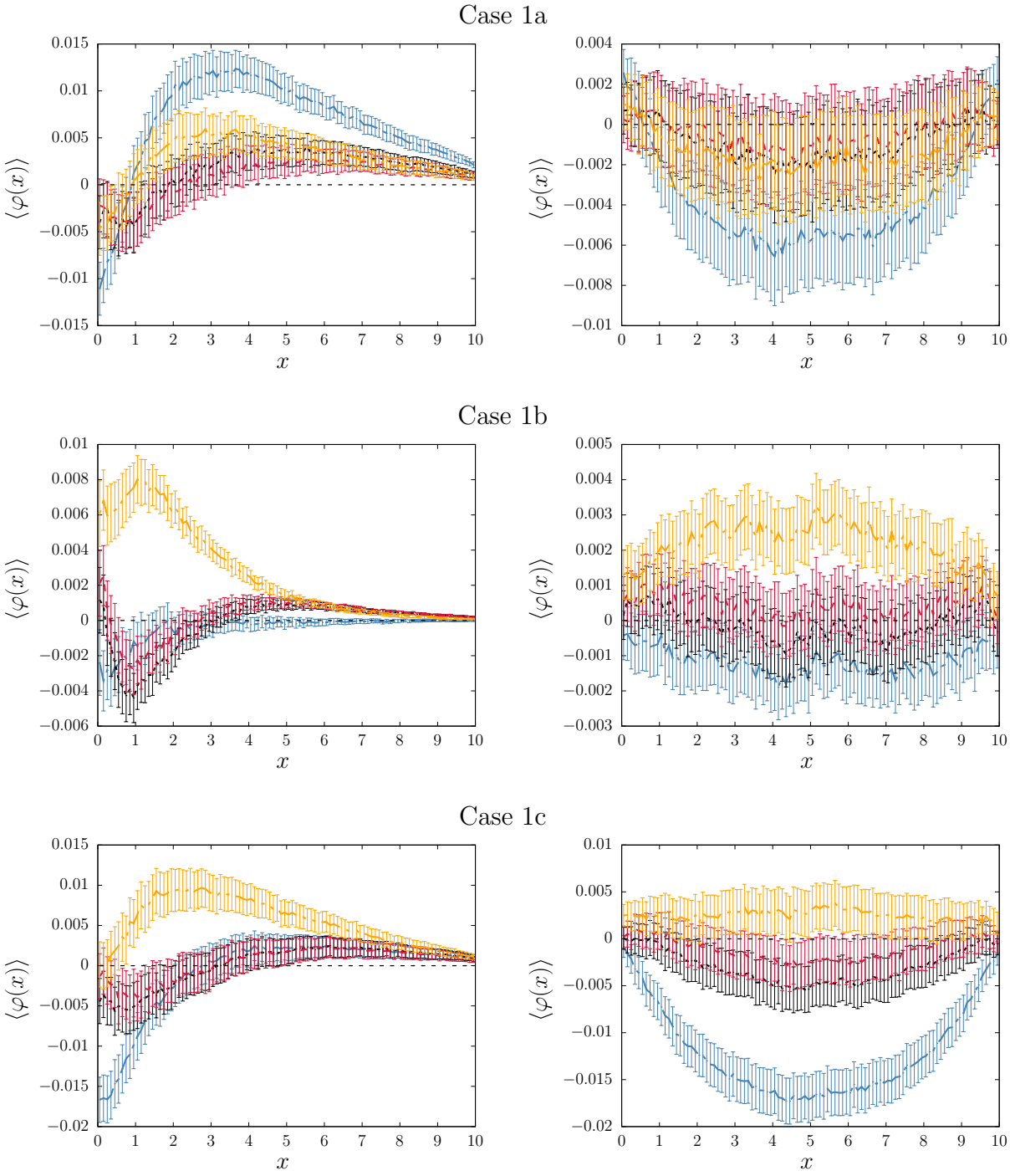

Figure 7.10: Ensemble-averaged spatial scalar flux for the benchmark configurations: Case 1. Left column: *suite* I configurations; right column: *suite* II configurations. Solid green lines represent the benchmark solutions obtained with the quenched disorder approach for Markovian mixtures (Poisson tessellations). Dotted or dashed lines represent the solutions from annealed disorder approach: blue lines correspond to CLS results, black lines to PBS-1 results, red lines to PBS-2 results and orange lines to LRP results.

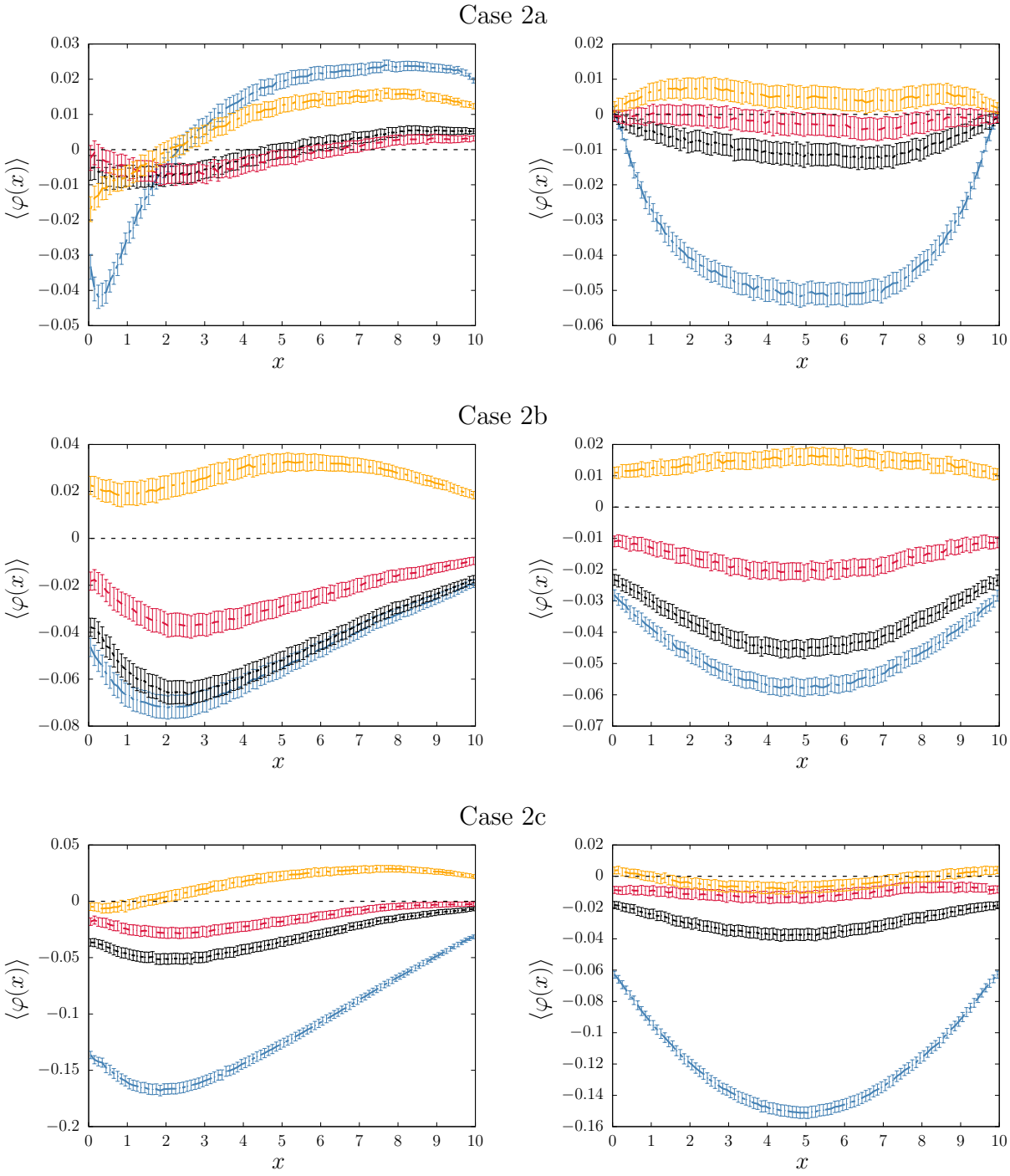

Figure 7.11: Ensemble-averaged spatial scalar flux for the benchmark configurations: Case 2. Left column: *suite* I configurations; right column: *suite* II configurations. Solid green lines represent the benchmark solutions obtained with the quenched disorder approach for Markovian mixtures (Poisson tessellations). Dotted or dashed lines represent the solutions from annealed disorder approach: blue lines correspond to CLS results, black lines to PBS-1 results, red lines to PBS-2 results and orange lines to LRP results.

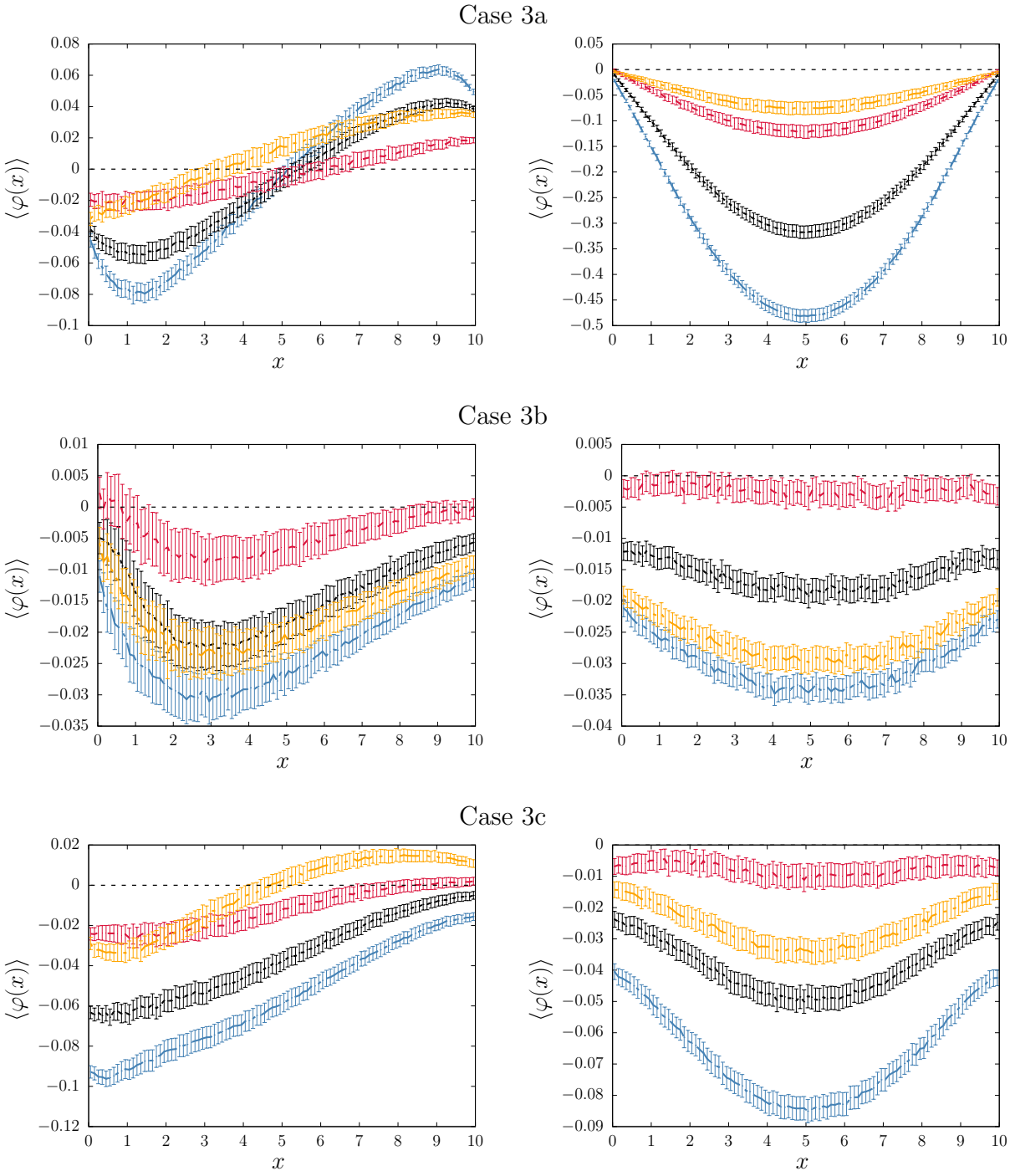

Figure 7.12: Ensemble-averaged spatial scalar flux for the benchmark configurations: Case 3. Left column: *suite* I configurations; right column: *suite* II configurations. Solid green lines represent the benchmark solutions obtained with the quenched disorder approach for Markovian mixtures (Poisson tessellations). Dotted or dashed lines represent the solutions from annealed disorder approach: blue lines correspond to CLS results, black lines to PBS-1 results, red lines to PBS-2 results and orange lines to LRP results.

7.5 Annealed disorder approach for eigenvalue problems

We conclude this Chapter by examining the applicability of the annealed disorder approach to k-eigenvalue problems. For this purpose, we consider particle transport in a domain of infinite size (or restricted to a box of size L with reflective boundary conditions) filled with three-dimensional Markov binary mixtures. We will describe this problem by both the quenched and annealed disorder approach, in order to perform a comparison between the results obtained by these two methods. For the annealed disorder approach, we will investigate several algorithms, namely, CLS, PBS and LRP. In addition, we will provide the solutions of the corresponding Levermore-Pomraning equations for this criticality problem, which are expected to yield results equivalent to the CLS model. For the sake of simplicity, we focus here on mono-kinetic transport.

7.5.1 The Levermore-Pomraning equations for the eigenvalue problem

For a domain of infinite size filled with binary mixtures, the Levermore-Pomraning equations for the criticality problem are given by

$$\begin{cases} \Sigma_{t,\alpha}\langle\varphi_\alpha\rangle = \Sigma_{s,\alpha}\langle\varphi_\alpha\rangle + \dfrac{1}{k_{\text{eff}}}\nu_\alpha\Sigma_{f,\alpha}\langle\varphi_\alpha\rangle + \dfrac{\langle\varphi_\beta\rangle}{\Lambda_\beta} - \dfrac{\langle\varphi_\alpha\rangle}{\Lambda_\alpha} \\ \Sigma_{t,\beta}\langle\varphi_\beta\rangle = \Sigma_{s,\beta}\langle\varphi_\beta\rangle + \dfrac{1}{k_{\text{eff}}}\nu_\beta\Sigma_{f,\beta}\langle\varphi_\beta\rangle + \dfrac{\langle\varphi_\alpha\rangle}{\Lambda_\alpha} - \dfrac{\langle\varphi_\beta\rangle}{\Lambda_\beta} \end{cases}$$

where $\langle\varphi_\alpha\rangle$ and $\langle\varphi_\beta\rangle$ are the total flux in material α and material β, respectively. Without loss of generality, we assume in the following that α is fissile, which means that $\nu_\alpha\Sigma_\alpha > 0$). Then, two cases can be distinguished: if material β is also fissile (i.e., $\nu_\beta\Sigma_\beta > 0$), then $1/k_{\text{eff}}$ is the smallest root of the polynomial

$$P(x) = (\nu_\alpha\nu_\beta\Sigma_{f,\alpha}\Sigma_{f,\beta})\,x^2 - (\nu_\beta\Sigma_{f,\beta}\gamma_\alpha + \nu_\alpha\Sigma_{f,\alpha}\gamma_\beta)\,x + \left(\gamma_\alpha\gamma_\beta - \frac{1}{\Lambda_\alpha\Lambda_\beta}\right)$$

where γ_α is given by

$$\gamma_\alpha = \Sigma_{t,\alpha} - \Sigma_{s,\alpha} + \frac{1}{\Lambda_\alpha},$$

and symmetrically

$$\gamma_\beta = \Sigma_{t,\beta} - \Sigma_{s,\beta} + \frac{1}{\Lambda_\beta}.$$

If the material β is not fissile, then k_{eff} is directly given by

$$k_{\text{eff}} = \frac{\nu_\alpha\Sigma_{f,\alpha}}{\gamma_\alpha - \frac{1}{\Lambda_\alpha\Lambda_\beta}\frac{1}{\gamma_\beta}}, \tag{7.28}$$

with γ_α and γ_β defined as before. In addition, we can single out the special case where material β is purely scattering, i.e., $\Sigma_{t,\beta} = \Sigma_{s,\beta}$. In this case, $\gamma_\beta = 1/\Lambda_\beta$. In this case, any term containing Λ_α or Λ_β vanishes, and we have

$$k_{\text{eff}} = \frac{\nu_\alpha\Sigma_{f,\alpha}}{\Sigma_{t,\alpha} - \Sigma_{s,\alpha}} = k_{\text{eff}}^\alpha, \tag{7.29}$$

where k_{eff}^α corresponds to the effective multiplication factor in an infinite domain with only material α. Thus, in a domain with an infinite extension, if material α is mixed with a purely scattering material β, the value of k_{eff} corresponding to the solution of the Levermore-Pomraning equations does not depend on Λ_c or p_α.

7.5.2 The criticality problem for the annealed algorithms

So far, we have described the CLS, PBS and LRP algorithms for a fixed source transport in non-multiplying media, i.e., without fission. For annealed disorder algorithms, a particle can undergo the following events: crossing of an interface, reflection/leakage (depending on the boundary conditions) or collision. For collision, we will have now to take into account fission. The annealed disorder method can be adapted to k-eigenvalue problems by plugging the general algorithms described in the previous Sections to the classical power iteration algorithm for Monte Carlo criticality calculations. Concerning the particle histories, we use the same routine as in the corresponding annealed algorithm for a fixed source transport problem (including the initialization procedure for the source particles), with the additional modifications if the next event is a collision: in this case, we sample a number n_d of descendant particles as $n_d = \lfloor \xi + \nu_i \Sigma_{f,i}/\Sigma_{t,i} \rangle$, where ξ is a random number from an uniform distribution in $[0,1]$ and where i corresponds to the current material label ($i = \alpha, \beta$). Then, n_d particles are added to the fission sources for the next generation. Similarly as in the classical power iteration, new particles inherit the position where the mother particle has undergone fission, the statistical weight of the mother particle. A new direction is sampled for each new particle. Furthermore, for annealed algorithms, new particles inherit

- for the CLS algorithm: the material label i only;
- for the PBS-1 algorithm: the material label i and additionally the coordinates (x_c, y_x, l_c) of center of the current random box and its dimensions l_x, l_y, l_z;
- for the PBS-2 algorithm: the material label i and additionally the coordinates (x_c, y_x, l_c) of center of the current random box, its dimensions l_x, l_y, l_z and the necessary data for the previous box (center, dimensions and the face by which the mother particle has entered the box);
- for the LRP algorithm: the material label i and additionally the forward distance ℓ_i^+ to the next interface and the backward distance ℓ_i^- to the next interface; for the new particle, these distances are switched with probability $P(\mu) = (1-\mu)/2$, where μ denotes the cosine between the incoming direction of the mother particle and the outgoing direction of the daughter particle.

7.5.3 Simulation results

We will assume the following parameters for the mixing statistics: material α allows scattering with $\Sigma_{s,\alpha} = 0.5$, capture with $\Sigma_{c,\alpha} = 0.25$, and fission with $\Sigma_{f,\alpha} = 0.25$ and $\nu_\alpha = 2.5$. We have then $\Sigma_{t,\alpha} = 1$. Material β allows scattering with $\Sigma_{s,\beta} = 0.95$ and capture with $\Sigma_{c,\beta} = 0.05$. We have then $\Sigma_{t,\beta} = 1$. We have chosen $p_\alpha = 0.3$ for all configurations. This configuration would mimic the behaviour of fuel chunks dispersed in water. Then, we consider several values of the average chord length Λ_c, between 0.05 and 10, in order to investigate several order of magnitudes for the ratio between the total cross section $\Sigma_{t,\alpha} = \Sigma_{t,\beta} = 1$ and the correlation length of the mixture, either through material α, $\Lambda_\alpha = \Lambda_c/(1-p_\alpha)$, or through material β, $\Lambda_\beta = \Lambda_c/p_\alpha$.

We have computed k_{eff} with the following methods: i) by solving the Levermore-Pomraning equations, ii) by performing Monte Carlo simulations with the quenched disorder approach and iii) by performing Monte Carlo simulation with the annealed disorder approach. In order to compute the solution of the Levermore-Pomraning equations for this problem, we have evaluated Eq (7.28) with the parameters given above. For the quenched disorder approach, we have generated $M = 2 \times 10^2$ geometrical realizations of Poisson tessellations within a box of linear size L, with a tessellation density parameter $\rho = 1/\Lambda_c$ and a coloring probability p_α. In order to limit the finite-size effects, we have chosen to take $L = L(\Lambda_c) = 100 * \Lambda_c$ for each value of Λ_c. Then, we have performed a transport simulation with TRIPOLI-4 ®for each geometrical realization, by applying reflective boundary conditions. The parameters for the power iteration are the following: we consider 10^4 particles per cycle and 2×10^3 cycles. For each simulation, the multiplication factor k_{eff} is computed by discarding the 200 first cycles. Finally, we compute the ensemble-average $\langle k_{\text{eff}} \rangle$ over all realizations. For the quenched disorder approach, we have applied the CLS, PBS-1, PBS-2 and LRP algorithms, detailed in Sec. 7.5.2,

in a box of size $L = L(\Lambda_c) = 100\Lambda_c$ with reflective boundary conditions, with parameters Λ_c and p_α for each value of Λ_c. For every Λ_c, we have performed a transport simulation: i) for the CLS, by using the power iteration method with 10^5 particles and 5×10^4 cycles by discarding the 4×10^4 first cycles and ii) for the other algorithms, by using 10^3 independent replicas with 10^5 particles and by recording the local value of k_{eff} for the 2×10^4-th generation.

Fig. 7.13 displays the results obtained for the multiplication factor: analytical solution from the Levermore-Pomraning equations, simulation results with the quenched disorder approach and simulation results with the annealed disorder approach (including CLS, PBS-1, PBS-2 and LRP).

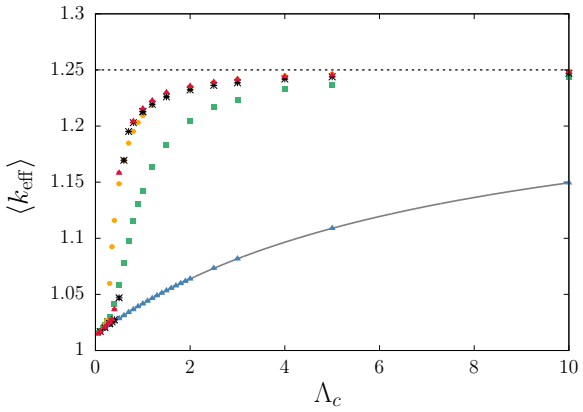

Figure 7.13: Multiplication factor k_{eff} as a function of the correlation length Λ_c. The solid grey line represent the analytical solutions for the Levermore Pomraning equations. Symbols correspond to Monte Carlo results. Green squares correspond to the benchmark solutions obtained with the quenched disorder approach for three-dimensional Markovian mixtures (Poisson tessellations). The other symbols represent the solutions from annealed disorder approach: blue triangles correspond to CLS results, black stars to PBS-1 results, red diamonds to PBS-2 results and orange circles to LRP results.

The agreement between the solutions of the Levermore-Pomraning equations (denoted LP in the following) and the results from CLS algorithm is excellent, as expected. Moreover, PBS-1, PBS-2 and LRP results show a similar behaviour. As a general consideration, the results obtained with the quenched disorder approach are systematically higher than those of LP/CLS results, and systematically lower than those of PBS/LRP results. Furthermore, three regimes can be distinguished as a function of the ratio $r = \Lambda_c \Sigma_t$ of the correlation length over the particle mean free path:

- when $r \ll 1$, all results collapse to the same functional form, with k_{eff} converging to the value of the multiplication factor k_{eff}^{AM} corresponding to the atomic mixing, i.e.,

$$k_{\text{eff}}^{AM} = \frac{p_\alpha \nu_\alpha \Sigma_{f,\alpha}}{p_\alpha \Sigma_{f,\alpha} + p_\alpha \Sigma_{c,\alpha} + (1 - p_\alpha)\Sigma_{c,\beta}} \approx 1.0135135, \tag{7.30}$$

  when Λ_c goes to zero. When the correlation length is smaller than the mean free path of the particle, the particle 'sees' a several material chunks during a flight, which leads to the limit case of the atomic mixing, for Λ_c small enough;

- when $r \simeq 1$, the multiplication factor rises quickly as a function of Λ_c for quenched disorder, PBS and LRP results, while the LP/CLS results increase with a smoother behaviour. In this regime, the sensitivity with respect to Λ_c is very high (apart from the case of LP/CLS): a slight offset possibly leads to large discrepancies between benchmark and annealed results. The discrepancy between benchmark and LP/CLS results increases with increasing Λ_c;

- when $r \gg 1$, the discrepancies between benchmark, PBS and LRP fade away and the curves collapse to

$$k_{\text{eff}}^{\alpha} = \frac{\nu_\alpha \Sigma_{f,\alpha}}{\Sigma_{f,\alpha} + \Sigma_{c,\alpha}} = 1.25, \tag{7.31}$$

where k_{eff}^{α} corresponds to the 'dominant' multiplication factor, i.e., the multiplication factor in an infinite medium with material α only. If the correlation length is very large compared to the migration length, the particles born in the chunks of fissile material α have a weak probability to leak out of this material. Then, the multiplication factor is very close to k_{eff}^{α}. The LP results converge to k_{eff}^{α} also when Λ_c goes to ∞, but with a slower convergence rate.

The accuracy of annealed algorithms is fairly good for $r \ll 1$ (and for $r \gg 1$ for PBS or LRP methods). For the other regimes, the poor agreement between quenched disorder and LP/CLS results is due to the fact that correlations are neglected in the annealed algorithms. Moreover, finite-size effects occur for benchmark solutions. The introduction of correlations with 'improved' annealed algorithms is not totally satisfying, because the discrepancy with respect to the benchmark solutions is still large in the regime $r \simeq 1$, where the sensitivity of the multiplication factor is very high. This poor accuracy can again be explained by correlations effects in the annealed algorithms. The heritage of local geometrical data for new particles seems to be rather difficult to handle and to understand on sound theoretical bases: in view of the importance of annealed algorithms for criticality problems (similar attempts have already been proposed for random spherical inclusions), these preliminary results might inspire future work.

Chapter 8

Conclusions

In this Thesis we have examined linear particle transport in random media, in view of several applications emerging in reactor physics. The first part of the work has concerned the analysis of stochastic geometry models that can be used in order to describe heterogeneous media.

- In Chapter 2 we have provided the state of the art concerning some reference models of random media, including three classes of *random tessellations*, namely, Poisson, Poisson-Voronoi and Poisson-Box tessellations, and mono and poly-dispersed *spherical inclusions*. We have shown that the Poisson tessellations satisfy the Markov property for any dimension d, which allows giving a positive answer to the possibility of explicitly realizing Markov media with exponentially distributed chord lengths in any direction, a long-standing conjecture suggested in [66]. The effects of anisotropy on Poisson geometries have been also analyzed. For each class of random media, the shape of the chord length distribution has been recalled and the average chord length Λ has been related whenever possible to the statistical features of the geometry. The distinct features of the chord length distribution for different random geometries have been provided.

- In Chapter 3 we have then detailed the *computer code* that has been developed in order to explicitly construct such geometries by Monte Carlo methods. The chosen algorithms and the global performances of the generator have been analyzed, and it has been shown that it is possible to generate large tessellations containing up to 10^7 polyhedral cells in reasonable time. The generator can produce an ensemble of realizations obeying the specific set of probabilities for d-dimensional Poisson, Poisson-Voronoi and Poisson-Box tessellations or spherical inclusions.

- In Chapter 4 we have examined the *statistical properties* of stochastic tessellations by resorting to Monte Carlo simulation. First, we have addressed the scaling of the key features of the random d-polyhedra composing the geometry, encompassing the chord lengths, the volume, the surface, the inradius, and so on, as a function of the system size and of the dimension. When possible, we have compared the results of our Monte Carlo simulations for very large systems to the exact findings that are known for infinite tessellations. When exact asymptotic results were not available from literature, we have provided accurate numerical estimates that could support future theoretical advances. Colored random media, where each d-polyhedron is assigned a random label with two possible values, have been also examined. All adjacent polyhedra sharing the same label have been regrouped into possibly non-convex clusters, whose statistical features have been characterized for the case of three-dimensional geometries.

  We have in particular examined the percolation properties of this prototype model of disordered systems: the probability that a cluster spans the entire geometry, the probability that a given polyhedron belongs to a percolating cluster (the so-called strength), and the average cluster size. We have been able to determine the corresponding percolation threshold, namely, $p_c \simeq 0.290 \pm 7 \times 10^{-3}$, which lies close to that of percolation on regular cubic lattices. An analogous result had been previously established for the two-dimensional Poisson geometries, where the percolation threshold had been also found to lie close to that of regular square lattices. The critical exponents associated to the percolation strength and to the average cluster size have

been finally determined, and were found to be compatible with the theoretical values $\beta \simeq 0.4181$ and $\gamma \simeq 1.793$, respectively, that are conjectured to be universal for percolation on lattices.

Future work will be aimed at refining these Monte Carlo estimates. For all the tessellation models considered in this Chapter, we have assumed that the random media are spatially homogeneous, which allows relying on exact formulas for the first few moments of the observables of interest, at least for infinite tessellations. Including non-homogeneity effects would be rather straightforward for our generator: it would be then interesting to compare Monte Carlo simulation results to the highly non-trivial formulas that have been recently established for special cases of non-homogeneous stochastic tessellations [129, 130].

The second part of the work has concerned particle transport in random media, with focus on both fixed-source and eigenvalue problems of interest for radiation shielding and reactor physics and criticality-safety applications.

- In Chapter 5 we have then computed reference solutions for *linear transport in quenched disorder*. In order to establish a proper and easily reproducible framework, we have built our specifications upon the benchmark originally proposed by Adams, Larsen and Pomraning, and recently revisited by Brantley. We have thus considered a box of fixed side, with two free surfaces on opposite sides, and reflecting boundary conditions everywhere else. As a prototype example of stochastic media, we have adopted Markov geometries with binary mixing: such geometries have been numerically implemented by using isotropic (colored) Poisson tessellations. Three kinds of Poisson tessellations have been tested: $1d$ slab tessellations, $2d$ extruded tessellations, and full $3d$ tessellations. To the best of our knowledge, benchmark solutions for $3d$ tessellations with Markov mixing have never been studied before. Material compositions and correlation lengths, as well as source and boundary conditions, have been assigned based on the benchmark specifications, amounting to a total of 18 distinct cases for each dimension. A large number of random geometries and material compositions have been realized. For each realization, mono-energetic linear transport with isotropic scattering and absorption has been simulated by Monte Carlo method. The code TRIPOLI-4 ® developed at CEA has been used for this purpose. The physical observables that have been examined in this work are the reflection and transmission coefficients, and the scalar particle flux, averaged over the ensemble of available realizations. The full distributions of the reflection and transmission coefficients have been also examined, in order to evaluate the impact of correlation lengths and volumetric fractions on the dispersion of these observables around their average values.

  The reference solutions presented in this work might be helpful for the validation of the fast but approximate methods that have been developed over the years so as to describe particle propagation in stochastic media with effective transport kernels, i.e., without having to average over medium realizations. In particular, benchmark solutions for the full $3d$ tessellations are essential to real-world applications. Furthermore, the numerical tools that we have used in this work in order to generate the colored Poisson geometries and to perform the stochastic transport are extremely flexible, and could thus easily accommodate several extensions or improvements of the current benchmark specifications. In particular, we might include anisotropy in the scattering kernels, energy-dependent cross sections and scattering distributions, particle production from fission, different geometrical shapes and arbitrary boundary conditions.

  Furthermore, we have addressed the *impact of the mixing statistics*, i.e., basically the chord length distribution, on particle transport. In this work, we have considered the effects of varying the stochastic tessellation model on the statistical properties of the resulting random media and on the transport-related physical observables, such as the reflection and the transmission probabilities. In order to single out the sensitivity of the simulation results to the various model parameters, we have proposed two benchmark configurations that are simple enough and yet retain the key physical ingredients. In the former, we have considered a binary mixture composed of diffusing materials and voids; in the latter, a binary mixture composed on diffusing and

absorbing materials. The mixing statistics that have been selected for this work are the homogeneous and isotropic Poisson tessellations, the Poisson-Voronoi tessellations, and the Poisson-Box tessellations. For each benchmark configuration we have provided reference solutions by using Monte Carlo simulation via the code TRIPOLI-4 ®. The effects of the underlying mixing statistics, the cross sections, the material compositions and the average chord length of the stochastic geometries have been accurately and extensively assessed by varying each parameter.

The Voronoi tessellation, whose chord length is significantly different from that of the other mixing statistics, shows a distinct behaviour. We have also found that Box tessellations yield almost identical results with respect to Poisson tessellations: this is a remarkable feature, in that the realizations of Box geometries are much simpler and could be perhaps adapted for deterministic transport codes. This analysis represents an extension to dimension $d = 3$ of the pioneering work carried out in dimension $d = 1$ in order to probe the sensitivity of the transport results to the use of non-exponential distribution of chord lengths [154, 171].

- *Eigenvalue problems in quenched disorder* have been examined in Chapter 6: we have proposed a methodology for the analysis of the impact of random geometries in three-dimensional fuel assembly, with application to criticality safety for severe accidents. Based on a random geometry generator that we have recently developed for Poisson, Voronoi and Box tessellations, we were able to create large ensembles of UOX and MOX assembly configurations with varying portions of fragmented fuel cells. These configurations can be read by the Monte Carlo transport code TRIPOLI-4 ®, which has been used to compute the multiplication factor, the adjoint-weighted kinetics parameters, and the scalar neutron flux. The analysis of the resulting ensemble-averaged physical quantities has allowed assessing the impact of stochastic tessellations on the key reactor core parameters.

  In particular, we have determined the evolution of the multiplication factor $\langle k_{eff} \rangle$, the delayed neutron fraction $\langle \beta_{eff} \rangle$, and the mean generation time $\langle \Lambda_{eff} \rangle$ as a function of the mean chord length of the random geometries, which is related to the correlation length of the fragmented portion of the assembly. The effect of varying the mixing statistics has been also examined: while Poisson and Box tessellations yield almost identical results, Voronoi tessellations yield distinct results. These findings show that the three mixing statistics, while sharing the same average chord length by construction, might yet induce subtle effects on neutron transport due to the precise shape of their associated chord length distributions. Generally speaking, MOX assemblies seem more sensitive than UOX assemblies to the perturbations introduced by the stochastic tessellations.

  The impact of *anisotropy* in the random media has been also assessed by using anisotropic Poisson tessellations with varying anisotropy laws and mean correlation lengths Λ_c. The anisotropy law was chosen in order to mimic the effects of stratification on the fuel degradation. When $\Lambda_c \to 0$, the neutron mean free path becomes larger than the typical scale of the fragmentation, and the distinct effects of anisotropy fade away. The maximum excursion of the average multiplication factor $\langle k_{eff} \rangle$ and the minimum excursion of the average effective neutron generation time $\langle \Lambda_{eff} \rangle$ are reached in the case of isotropic tessellations. The special case of Box tessellations, that are quasi-isotropic, leads to transport properties that are almost identical to the isotropic case. Finally, the degenerate case of slab tessellations (leading to material layers that are exactly orthogonal to the z axis) was separately considered, for comparison: it was shown that the transport properties are rather different than in the case of regular anisotropic Poisson tessellations, which can be understood based on the peculiar nature of the slab geometries, where neutrons can travel long distances along the transversal directions without being absorbed.

  Our approach focuses on methodological and conceptual aspects. Stochastic tessellations, despite being convenient model for disordered materials, do not fully qualify for providing an accurate description of reactor safety applications without further proof: in particular, multiphysics feedbacks such as temperature or density variations have been admittedly neglected in our analysis, and one might think of a variety of degraded configurations that cannot be rep-

resented by tessellations. The complex physical-chemistry of the reactions occurring between the fuel and the cladding at high temperature have not been addressed, either. Thus, the conclusions drawn in this paper may not directly apply to real-world problems, such as the assessment of re-criticality probability of out-of-pile deposition of corium debris. Nonetheless, our approach is fairly broad and might be extended to more complex situations. For instance, the same procedure could be applied also to the assessment of re-criticality probability of out-of-pile core degradation leading to the deposition of corium debris. Monte Carlo simulation, which is capable of dealing with arbitrarily shaped geometries, would be particularly useful in this context.

Future work will be also aimed at investigating the behaviour of neutron transport through disordered media in non-stationary conditions. Recent works have actually shown that under certain circumstances, the disorder-averaged neutron decay constant might be positive when $\langle k_{eff} \rangle < 1$ [114, 163], an intriguing result that seems to suggest that information conveyed by $\langle k_{eff} \rangle$ alone is perhaps incomplete.

- *Particle transport in annealed disorder* has been finally addressed in Chapter 7. The so-called Algorithm A of *Chord Length Sampling* method is perhaps the most widely adopted simulation tool to provide approximate solutions, based on the Levermore-Pomraning model for Markovian binary mixing. The interfaces between the constituents of the random medium are sampled on-the-fly during the particle displacements by drawing the distances to the following material boundaries from a distribution depending on the mixing statistics: the correlations on particle trajectories induced by the spatial disorder are thus neglected. Comparisons of CLS solutions with respect to reference results are mandatory in order to quantify the degree of approximations introduced in these models. For Markov mixing, a number of benchmark problems have been proposed in the literature for this purpose, but so far analyses have been conducted in one-dimensional media of the rod or slab type.

  Within the framework of a collaboration with Dr. P. Brantley of the Lawrence Livermore National Laboratory (USA) and Prof. T. Palmer of the Oregon University (USA), we have contrasted CLS simulation results to the reference solutions for the classical benchmark problem proposed by Adams, Larsen and Pomraning. In particular, we have examined the evolution of the particle flux, the transmission coefficient and the reflection coefficient as a function of the benchmark configurations and of the system dimension d. Two main trends have been detected: the accuracy of CLS algorithm with respect to reference solutions generally increases with increasing system dimensionality. Moreover, the accuracy of the CLS algorithm increases for decreasing average chord length, i.e., for denser stochastic tessellations. The impact of dimensionality is particularly relevant for case 1 configurations (which have smaller chord lengths), and progressively diminishes for configurations having larger material chunks. The considerations presented here, although derived strictly speaking for the Adams, Larsen and Pomraning benchmark considered here, seem to be quite general. This work represents a first step towards extensive comparisons between CLS and reference solutions for Markov mixing statistics in higher dimensions. Furthermore, extension of these comparisons to reference solutions for other types of d-dimensional mixing statistics based on spatial tessellations (such as the Poisson-Voronoi model) would be interesting topics for future research.

  In order to go beyond the known limitations of the standard CLS method, we have proposed a *new family of Monte Carlo methods* aimed at approximating ensemble-averaged observables for particle transport in Markov binary mixtures. Several numerical investigations have shown that Algorithm A works reasonably well in most cases, yet discrepancies between CLS and reference solutions may appear due to the fact that Algorithm A neglects the correlations induced by spatial disorder. For the case of one-dimensional slab geometries, two variants of the standard CLS method, namely Algorithm B and Algorithm C, have been proposed in the literature by partially including spatial correlations and memory effects. These algorithms provide an increased accuracy with respect to Algorithm A thanks to the on-the-fly generation of typical

slabs during the particle displacements, but their generalization to higher dimensions appears to be non-trivial. A rigorous generalization in dimension three would for instance demand sampling on-the-fly typical polyhedra from homogeneous and isotropic Poisson tessellations, whose exact statistical distribution are unfortunately unknown.

In order to overcome these issues and derive CLS-like methods capable of taking into account spatial correlations for d-dimensional configurations, we have resorted to the key observation that (quasi-isotropic) Box tessellations based on Cartesian boxes yield chord length distributions and transport-related physical observables that in most cases are barely distinguishable from those coming from isotropic Poisson tessellations. This remarkable feature has inspired a generalization of CLS Algorithms B and C based on sampling on-the-fly random boxes obeying the same statistical properties as for Box tessellations. We have called these family of algorithms *Poisson Box Sampling*, or PBS. We have proposed two variants of PBS: in PBS-1 we generate random d-dimensional boxes, similarly as done in Algorithm B of CLS, and in PBS-2 we additionally keep memory of the last generated box, in full analogy with Algorithm C of CLS. In order to test the performances of these new methods, we have compared PBS simulation results to the reference solutions and CLS solutions for the classical benchmark problem proposed by Adams, Larsen and Pomraning for particle propagation in stochastic media with binary Markov mixing. In particular, we have examined the evolution of the transmission coefficient, the reflection coefficient and the spatial particle flux for the benchmark configurations in dimension $d = 3$.

A preliminary investigation has shown that Poisson and Box tessellations lead to very similar results for all the benchmark configurations, as expected on the basis of previous works, which substantiates our motivation for PBS methods. Overall, the PBS-1 algorithm reproduces reference solutions based on Poisson tessellations more accurately that Algorithm A of CLS, at the expense of an increased computational cost. PBS-2 further increases the accuracy of PBS-1 by including memory effects and thus enhancing the range of spatial correlations that are correctly captured by the algorithm; the additional computational burden required by PBS-2 is almost negligible. PBS always produces physically relevant answers (i.e., observables that are relatively close to the reference solutions) for the transmission and reflection coefficients, and furthermore preserves the correct shape for the spatial flux within the domain. An interesting feature is that PBS methods, and PBS-2 in particular, yield satisfactory results for the entire range of average correlation lengths Λ_c explored in the benchmark configurations, whereas CLS performances typically worsen for increasing Λ_c. *Future research work* will be aimed at testing the performances of PBS methods as applied to other benchmark configurations with Markov mixtures, such as diffusing matrices with void or absorbing chunks, or multiplying systems, in order to gain a deeper understanding of the range of validity of this class of algorithms.

A local realization preserving (LRP) algorithm that extends the standard CLS in a way similar to PBS (i.e., by preserving information about the shape of the traversed polyhedra) has been independently and simultaneously developed at LLNL and tested against reference solutions and CLS Algorithm A [16]: we have then implemented the LRP method and compared it to PBS. Numerical results shown that LRP and PBS have very similar performances in terms of accuracy and simulation time. We conclude by observing that in principle it would possible to propose a lowest-order PBS algorithm that did not include memory effects but that was still based on Box tessellations. In other words, boundaries would be sampled in the three coordinate axes but only in the forward particle direction for each axis. When a particle is scattered, the three boundaries could be sampled again based on the new particle direction (or only those for which the particle was now proceeding in the reverse axial direction). Such zero-order approach does not seem to be relevant, in view of the simplicity of including memory effects in the PBS algorithm, but a comparison against CLS might possibly provide additional information. Investigations of this simplified scheme, and other variations of the PBS, are currently on-going and will be possibly the object of a future extension of the present work.

Appendix A

Additional properties of isotropic Poisson tessellations

For the sake of completeness, in this Appendix we illustrate the Monte Carlo analysis that we have performed on other statistical features of isotropic Poisson geometries that might convey useful information on the behavior of the tessellation cells.

A.1 Inradius and outradius

The *inradius* $r_{\mathrm{in},d}$ is defined as the radius of the largest sphere that can be contained in a (convex) d-dimensional polyhedron, and as such represents a measure of the linear size of the tessellation cells [127]. A illustration of this quantity is provided in Fig. A.1 (left). In Sec. 2.3.2 we have seen that the probability density function of the inradius for isotropic d-dimensional Poisson geometries of infinite size is exponential, namely,

$$\mathcal{P}(r_{\mathrm{in},d}) = \rho\alpha_d e^{-\rho\alpha_d r_{\mathrm{in},d}}, \tag{A.1}$$

where the dimension-dependent constant α_d reads $\alpha_1 = 2$, $\alpha_2 = \pi$, and $\alpha_3 = 4$.

The case $d = 1$ is straightforward, since the inradius simply coincides with the half-length of the 1-polyhedron. Then, Eq. (4.4) yields

$$\langle r_{\mathrm{in},d}^m | L\rangle = \frac{\Gamma(m+1)}{(2\rho)^m} - \frac{\Gamma_{m+1}(2\rho L)}{(2\rho)^m} + e^{-2\rho L} L^m, \tag{A.2}$$

In principle, for $d > 1$, it would be possible to analytically determine the coordinates of the center and the radius of the largest contained sphere, once the equations of the $(d-1)$-hyperplanes defining the d-polyhedron are known [124]. We have however chosen to numerically compute the inradius by resorting to a linear programming algorithm. For a given realization of a Poisson geometry, we select in turn a convex d-polyhedron: this will be formally defined by a set $\mathbf{x} \in \mathbb{R}^d$ such that

$$\mathbf{a}_i^T \mathbf{x} \leq \mathbf{b}_i \;\; (1 \leq i \leq q), \tag{A.3}$$

where q is the number of $(d-1)$-hyperplanes composing the surface of the d-polyhedron. The inradius $r_{\mathrm{in},d}$ can be then computed based on the Chebyshev center $(\mathbf{x}, r_{\mathrm{in},d})$ of the d-polyhedron, which can be found by maximising $r_{\mathrm{in},d}$ with the constraints

$$\forall i \in \{1, 2, ..., q\}, \;\; \mathbf{a}_i^T \mathbf{x} + r_{\mathrm{in},d} ||\mathbf{a}_i|| \leq \mathbf{b}_i \tag{A.4}$$

$$r_{\mathrm{in},d} > 0. \tag{A.5}$$

This maximisation problem can be finally solved by using the simplex method [115].

The results of the Monte Carlo simulation for $\mathcal{P}(r_{\mathrm{in},d})$ are shown in Fig. A.2 as a function of L and d. For any finite L, the numerical distributions suffer from finite-size effects, analogous to those affecting the distributions of the segment lengths ℓ: in particular, a cut-off appears at $r_{\mathrm{in},d} = \sqrt{d}L/2$.

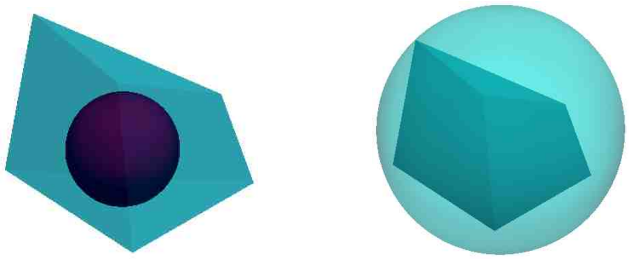

Figure A.1: Left. Illustration of the inradius, i.e. radius of the largest sphere included in a polyhedron. Right. Illustration of the outradius, i.e. radius of the smallest sphere containing a polyhedron.

m	d	$\langle r^m_{\mathrm{in},d}\rangle$	Theoretical value	Monte Carlo
1	1	$1/2\rho$	0.5	$0.50006 \pm 4 \times 10^{-5}$
1	2	$1/\pi\rho$	0.31831	$0.31825 \pm 8 \times 10^{-5}$
1	3	$1/4\rho$	0.25	$0.2499 \pm 2 \times 10^{-4}$
2	1	$1/\rho^2$	1	$1.0004 \pm 2 \times 10^{-4}$
2	2	$2/\pi^2\rho^2$	0.2026	0.2026 ± 10^{-4}
2	3	$1/8\rho^2$	0.125	$0.1249 \pm 2 \times 10^{-4}$

Table A.1: The moments inradius $\langle r^m_{\mathrm{int},d}\rangle$ of the inradius in d-dimensional isotropic Poisson tessellations. Monte Carlo simulation results are obtained with $L = 200$ and $\rho = 1$ for any dimension d.

As $\rho L \gg 1$, finite-size effects fade away and the numerical distributions converge to the expected exponential behaviour. The convergence rate as a function of the system size L is weakly dependent on the dimension d. The asymptotic average inradius for $L \to \infty$ yields $\langle r_{\mathrm{in},d}\rangle = 1/(\alpha_d \rho)$: the Monte Carlo simulation results obtained for a large $L = 200$ are compared to the theoretical formulas in Tab. A.1, with the same simulation parameters as above.

The *outradius* $r_{\mathrm{out},d}$ is defined as the radius of the smallest sphere enclosing a (convex) polyhedron, and can be thus used together with the inradius so as to characterize the shape of the polyhedra (for illustration, see Fig. A.1 (right)). For $d = 1$, the outradius coincides with the inradius. The probability density and the moments of the outradius of Poisson geometries for $d > 1$ are not known. We have then numerically computed the moments of the outradius by resorting to an algorithm recently proposed in [37]. This algorithm implements a pivoting scheme similar to the simplex method for linear programming. It starts with a large d-ball that includes all vertices of the convex d-polyhedron and progressively shrinks it [37]. For reference, the Monte Carlo simulation results for the first few moments of $r_{\mathrm{out},d}$ obtained for a large $L = 200$ are given in Tab. A.2, with the same simulation parameters as above: these numerical findings might inspire future theoretical advances. In addition, Fig. A.3 shows the evolution the average outradius $\langle r_{\mathrm{out},d}|L\rangle$ as a function of the linear size L of the domain and of the dimension d. The probability density function of the outradius for a large L, for any dimension d. is also provided in Fig. A.3.

A.2 Other polyhedral quantities

For the case of isotropic Poisson tessellations, some other polyhedral quantities have been exactly computed for the case $L \to \infty$, so that it is interesting to compare them to numerical simulations. Notation is as follows. For the case of the 2-polyhedron, the number of vertices N_2 and the number of edges A_2 coincide with the number of faces C_2. For the 3-polyhedron, we denote l_3 the total length of edges, N_3 the number of vertices, A_3 the number of edges, respectively. The exact first-order and second-order moments of these physical observables are given in Tab. 2.1. We have assessed these moments by Monte Carlo methods as a function of the linear size L of the domain and of the dimension

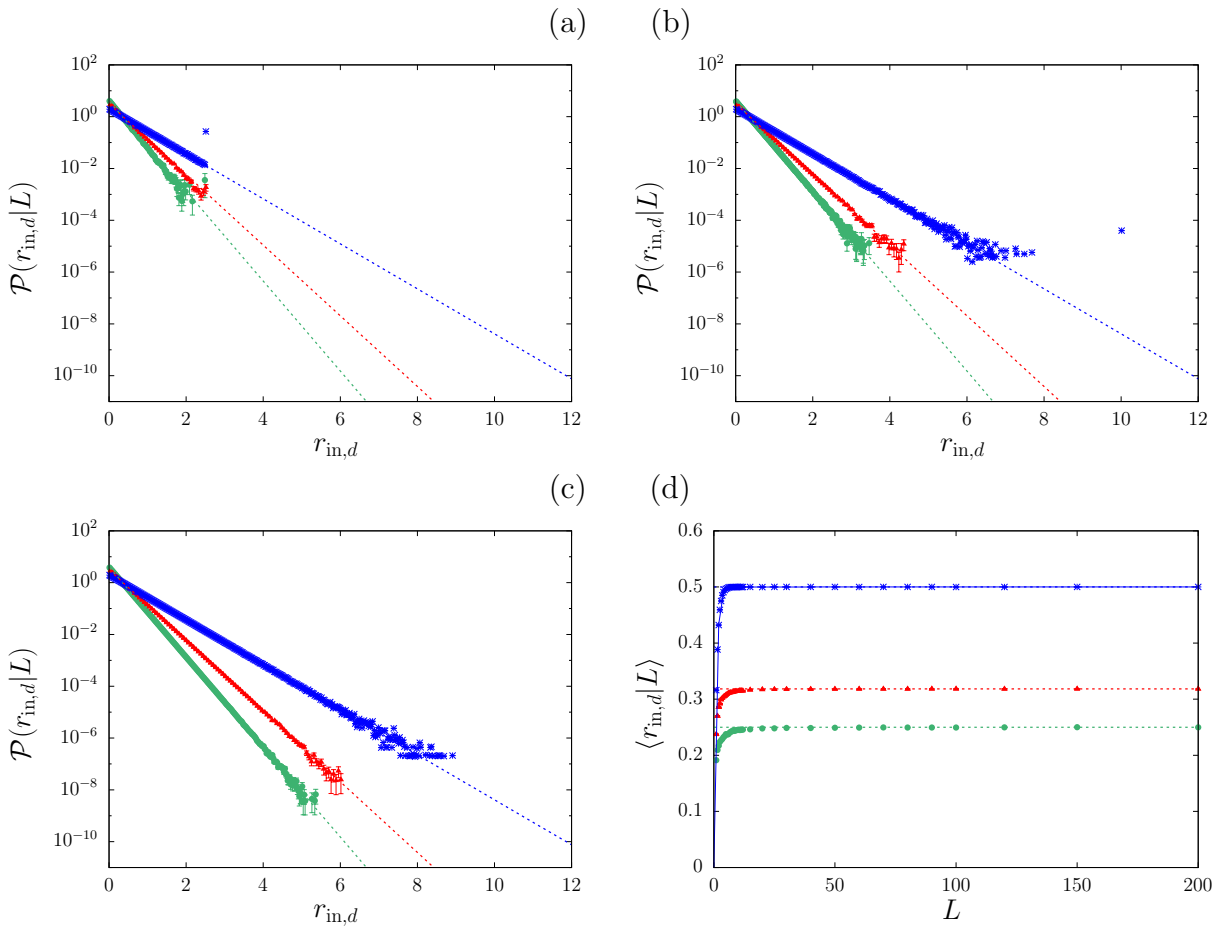

Figure A.2: (a-c). The probability densities $\mathcal{P}(r_{\mathrm{in},d}|L)$ of the inradius in d-dimensional isotropic Poisson geometries as a function of the dimension d and of the linear size L of the domain. We have generated $M = 10^6$ realizations for $d = 1$, $M = 5 \times 10^4$ realizations for $d = 2$ and $M = 5 \times 10^3$ realizations for $d = 3$. Simulation results have been obtained with $\rho = 1$. Symbols correspond to the Monte Carlo simulation results: blue crosses denote $d = 1$, red triangles $d = 2$ and green circles $d = 3$. The cases illustrated here are as follows: (a) $L = 5$; (b) $L = 20$; (c) $L = 200$. (d). Convergence of the average inradius $\langle r_{\mathrm{in},d}|L\rangle$ as a function of the linear size L of the domain and of the dimension d.

d: the results are provided in Figs. A.4, A.5 and A.6. Moreover, Tab. A.3 summarizes the numerical values obtained for large L.

For the case $d = 2$ we have also computed the fraction P_3 of random polygons having 3 sides and the fraction P_4 of polygons having 4 sides. These estimates are also given in Tab. A.3 and are to be compared with the exact results $P_3 = 2 - \pi^2/6$ and

$$P_4 = \pi^2 \log(2) - \frac{1}{3} - \frac{7}{36}\pi^2 - \frac{7}{2}\zeta(3) \tag{A.6}$$

respectively [142], where ζ is the Riemann Zeta function [103].

The functional form of the distributions of the number of edges $\mathcal{P}(A_d)$ (for $d > 2$) and of the the number of vertices $\mathcal{P}(N_d)$ (for $d > 2$) are not known. We have thus resorted to Monte Carlo simulation so as to estimate the impact of the domain size L and of the dimension d on $\mathcal{P}(A_d|L)$ and $\mathcal{P}(N_d|L)$ for finite L. The numerical findings are shown in Fig. A.5 and may support future theoretical investigations. It is reasonable to think that the convergence of each distribution is attained, since $\mathcal{P}(A_d|L)$ and $\mathcal{P}(N_d|L)$ can not be distinguished between $L = 10$ and $L = 200$.

d		Monte Carlo
2	$\langle r_{\mathrm{out},d} \rangle$	$0.8453 \pm 2 \times 10^{-4}$
2	$\langle r^2_{\mathrm{out},d} \rangle$	$1.2318 \pm 6 \times 10^{-4}$
3	$\langle r_{\mathrm{out},d} \rangle$	$1.1524 \pm 8 \times 10^{-4}$
3	$\langle r^2_{\mathrm{out},d} \rangle$	$2.126 \pm 3 \times 10^{-3}$

Table A.2: The moments $\langle r^m_{\mathrm{out},d} \rangle$ of the outradius in d-dimensional isotropic Poisson tessellations. Monte Carlo simulation results are obtained with $L = 200$ and $\rho = 1$ for any dimension d.

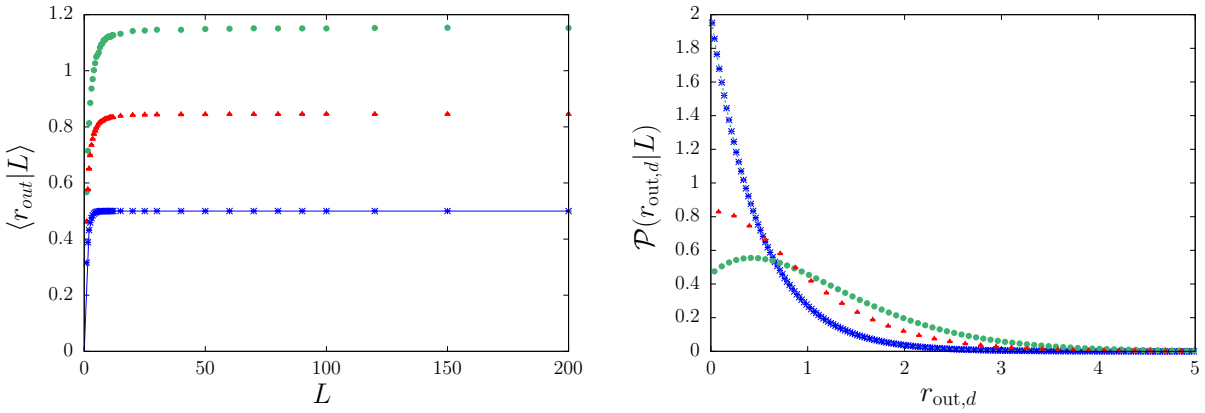

Figure A.3: The outradius in d-dimensional Poisson tessellations. Left. The average outradius $\langle r_{\mathrm{out},d}|L \rangle$ as a function of the dimension d and of the linear size L of the domain. Right. The probability density $\mathcal{P}(r_{\mathrm{out},d}|L)$ as a function of the dimension d, with $L = 200$. We have generated $M = 10^6$ realizations for $d = 1$, $M = 5 \times 10^4$ realizations for $d = 2$ and $M = 5 \times 10^3$ realizations for $d = 3$. Simulation results have been obtained with $\rho = 1$. Symbols correspond to the Monte Carlo simulation results: red triangles $d = 2$ and green circles $d = 3$.

A.3 Correlations

For the sake of completeness, we report the exhaustive Monte Carlo calculations corresponding to the correlations for the physical observables of Poisson geometries of infinite size, in dimension $d = 2$ and $d = 3$. The case of 'typical' d-polyhedra and that of d-polyhedra containing the origin are separately considered. When analytical results are known (from [76, 86, 87, 127]), our Monte Carlo estimates are compared to the exact values. Otherwise, numerical findings are provided for reference. All symbols have been introduced above. The moments and the correlations are reported in Tabs. A.4 - A.7.

A.4 Polyhedra containing the origin

We have carried out an extensive analysis of the features of the d-polyhedra containing the origin: numerical findings for the most relevant quantities are reported in Tab. A.8 for large L and compared to the exact formula provided in Tab. 2.2. For some of the computed quantities, such as the average inradius $\langle r_{\mathrm{in},d} \rangle_0$ or the average outradius $\langle r_{\mathrm{out},d} \rangle_0$, exact results are not available, and our numerical findings may thus support future theoretical investigations.

The average d-volume $\langle V_d \rangle_0$, the average d-surface $\langle S_d \rangle_0$, the average total edge of lengths $\langle l_d \rangle_0$ and the average number of faces $\langle C_d \rangle_0$ of the polyhedron containing the origin as a function of the linear size of the domain L and of the dimension d are provided in Fig. A.7. Similarly as for the properties related to the typical polyhedron, the rate of convergence as a function of L decreases with increasing d. Moreover, the convergence of the d-volume V_d, d-surface S_d and the total edge of lengths l_d is faster for the polyhedron containing the origin than for the typical polyhedron: this was expected, since the size of the polyhedron containing zero is less affected by finite-size effects (i.e., by the polyhedra that

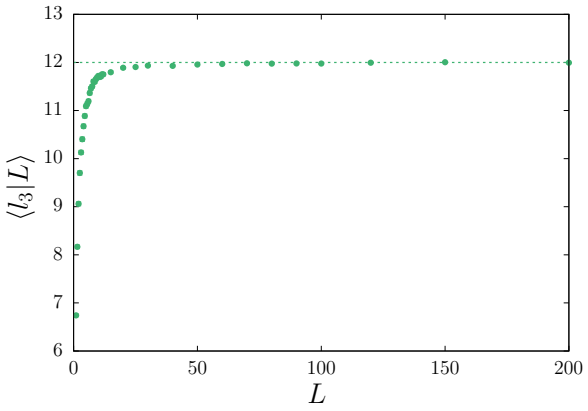

Figure A.4: The average total length of edges $\langle l_3|L\rangle$ as a function of the linear size L of the domain for $d = 3$. Symbols correspond to the Monte Carlo simulation results. Dotted lines correspond to the asymptotic (i.e., $L \to \infty$) moment given in Tab. 2.1.

	Formula	Theoretical value	Monte Carlo
P_3	$2 - \pi^2/6$	0.35507	$0.35505 \pm 1 \times 10^{-5}$
P_4	$\pi^2 \log(2) - \frac{1}{3} - \frac{7}{36}\pi^2 - \frac{7}{2}\zeta(3)$	0.38147	$0.38150 \pm 2 \times 10^{-5}$
$\langle N_3\rangle$	8	8	8 ± 10^{-7}
$\langle N_3^2\rangle$	$(13\pi^2 + 96)/3$	74.7683	$74.7684 \pm 4 \times 10^{-4}$
$\langle A_3\rangle$	12	12	$12 \pm 2 \times 10^{-7}$
$\langle l_3\rangle$	$12/\rho$	12	$11.994 \pm 8 \times 10^{-3}$
$\langle l_3^2\rangle$	$24(\pi^2 + 1)/\rho^2$	260.871	260.6 ± 0.4

Table A.3: Other moments of physical observables related to d-dimensional Poisson geometries: for $d = 2$, probabilities P_i of having a given number of vertices; for $d = 3$, number of edges A_3, number of vertices N_3 and total length of edges l_3. Monte Carlo simulation results are obtained with $L = 200$ and $\rho = 1$.

are cut by the boundaries of the box). Conversely, the convergence of the number of faces C_d is slower for the polyhedron containing the origin than for the typical polyhedron.

The full distribution $\mathcal{P}_0(r_{\text{in},d}|L)$ of the inradius of the d-polyhedron containing the origin has been estimated, and is compared to $\mathcal{P}(r_{\text{in},d}|L)$ for the inradius of a typical polyhedron of the tessellation in Fig. A.8 for $d = 1$ and $d = 3$ and a large system size $L = 200$: it is immediately apparent that $\langle r_{\text{in},d}\rangle_0 > \langle r_{\text{in},d}\rangle$. Moreover, the behaviour of the two distributions for small $r_{\text{in},d}$ is also different: for $L \to \infty$, $\mathcal{P}(r_{\text{in},d}|L)$ attains a finite value for $r_{\text{in},d} \to 0$ due to its exponential shape; on the contrary, our Monte Carlo simulations seem to suggest a power-law scaling $\mathcal{P}_0(r_{\text{in},d}|L) \sim r_{\text{in}}^{\gamma_d}$ for $r_{\text{in},d} \to 0$, with $\gamma_d = 1 + (d-1)/2$.

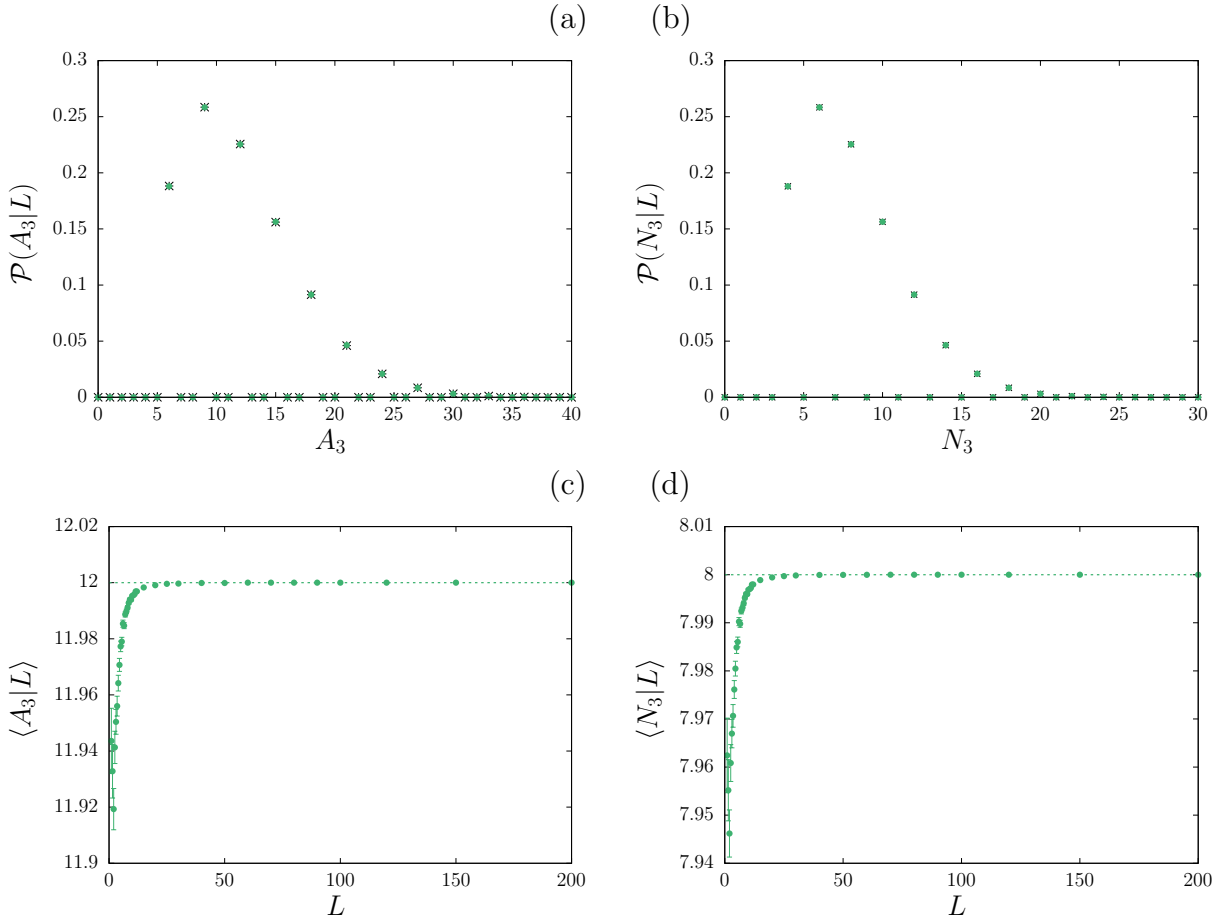

Figure A.5: Edges and vertices in d-dimensional Poisson tessellations as a function of the linear size L of the domain. The cases are as follows: (a) the probability densities of the number of edges $\mathcal{P}(A_3|L)$ for $d = 3$ and (b) the probability density of the number of vertices $\mathcal{P}(N_3|L)$ for $d = 3$. For each case, symbols correspond to the Monte Carlo simulation results: for $d = 2$, black crosses denote $L = 10$ and red triangles $L = 200$, for $d = 3$ black crosses denote $L = 10$ and green circles $L = 200$. Simulation results have been obtained with $\rho = 1$. We have generated $M = 5 \times 10^4$ realizations for $d = 2$ and $M = 5 \times 10^3$ realizations for $d = 3$. Furthermore, (c) is the average number of edges $\langle A_3|L\rangle$ for $d = 3$ and (d) the average number of vertices $\langle N_3|L\rangle$ for $d = 3$. For each case, symbols correspond to the Monte Carlo simulation results: red triangles denote $d = 2$ and green circles $d = 3$. Simulation results have been obtained with $\rho = 1$. We have generated $M = 5 \times 10^4$ realizations for $d = 2$ and $M = 5 \times 10^3$ realizations for $d = 3$.

	Formula	Theoretical value	Monte Carlo
$\langle C_2 S_2\rangle$	$(\pi^2 + 8)/\rho$	17.870	$17.866 \pm 4 \times 10^{-3}$
$\langle C_2 V_2\rangle$	$2\pi/\rho^2$	6.283	$6.281 \pm 3 \times 10^{-3}$
$\langle C_2 V_2^2\rangle$	$16(8\pi^2 - 21)/21\rho^4$	44.16	$44.12 \pm 4 \times 10^{-2}$
$\langle S_2 V_2^2\rangle$	$256\pi^2/21\rho^5$	120.3	120.2 ± 0.2

Table A.4: Moments and correlations of physical observables related to two-dimensional Poisson geometries. Monte Carlo simulation results are obtained with $L = 200$ and $\rho = 1$.

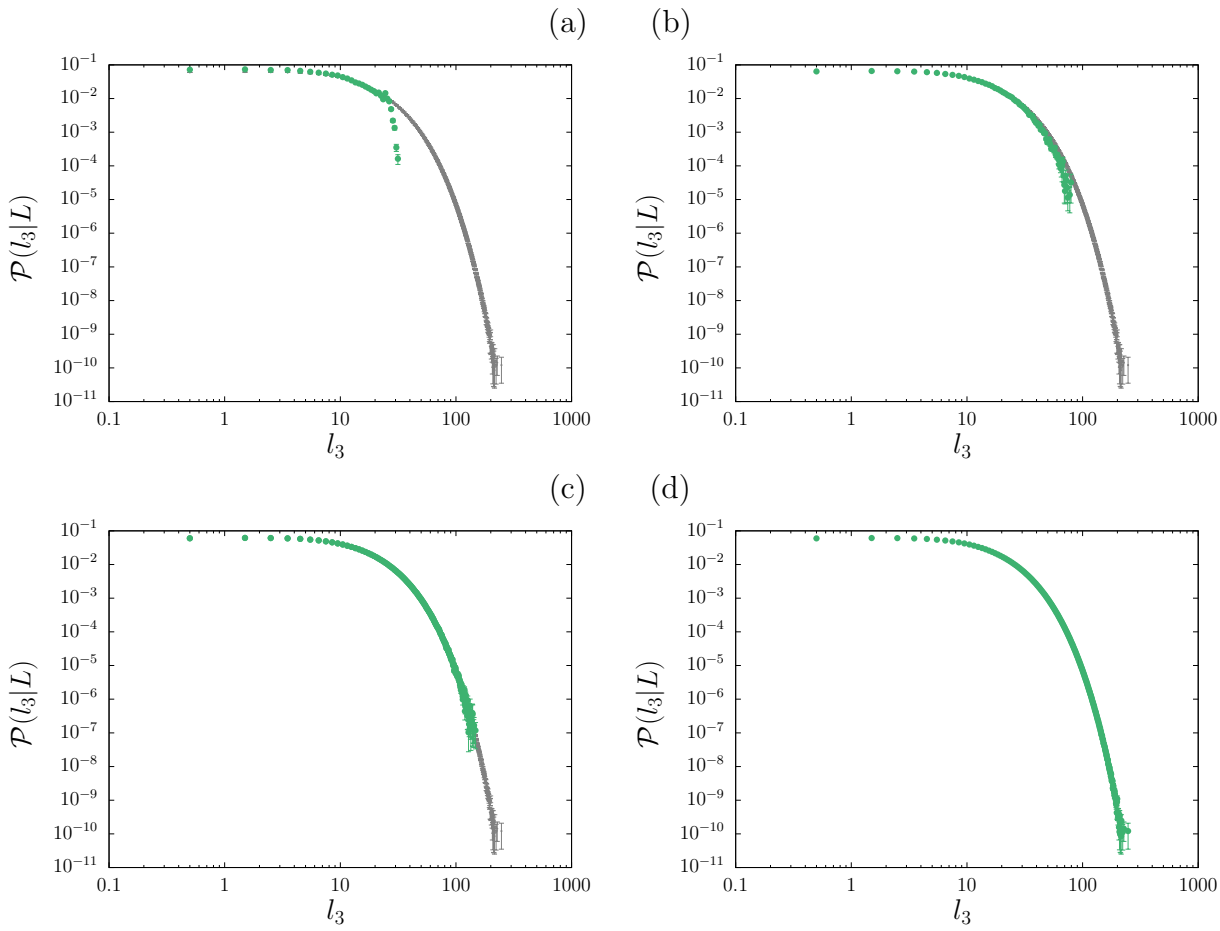

Figure A.6: The probability densities $\mathcal{P}(l_3|L)$ of the total length of edges in three-dimensional isotropic Poisson geometries as a function of the linear size L of the domain. Simulation results have been obtained with $\rho = 1$. Symbols correspond to the Monte Carlo simulation results, obtained with $M = 5 \times 10^3$ realizations. The cases illustrated here are as follows: (a) $L = 2$; (b) $L = 5$; (c) $L = 20$; (d) $L = 200$.

	Formula	Theoretical value	Monte Carlo
$\langle N_3 V_3 \rangle$	$8\pi/\rho^3$	25.13	25.09 ± 0.05
$\langle N_3 S_3 \rangle$	$28\pi/\rho^2$	87.9646	87.9 ± 0.1
$\langle N_3 l_3 \rangle$	$(10\pi^2 + 24)/\rho$	122.696	$122.63 \pm 8 \times 10^{-2}$
$\langle C_3 V_3 \rangle$	$4(\pi^2 + 3)/\pi\rho^3$	16.3861	$16.36 \pm 3 \times 10^{-2}$
$\langle C_3 S_3 \rangle$	$(14\pi^2 + 48)/\pi\rho^2$	59.2612	$59.19 \pm 8 \times 10^{-2}$
$\langle C_3 l_3 \rangle$	$(5\pi^2 + 36)/\rho$	85.348	$85.30 \pm 6 \times 10^{-2}$
$\langle V_3 l_3 \rangle$	$24\pi/\rho^4$	75.3982	75.2 ± 0.2
$\langle S_3 l_3 \rangle$	$72\pi/\rho^3$	226.195	225.8 ± 0.5

Table A.5: Moments and correlations of physical observables related to three-dimensional Poisson geometries. Monte Carlo simulation results are obtained with $L = 200$ and $\rho = 1$.

	Monte Carlo
$\langle C_2 r_{\mathrm{in},d} \rangle$	$1.4552 \pm 4 \times 10^{-4}$
$\langle V_2 r_{\mathrm{in},d} \rangle$	$1.1285 \pm 8 \times 10^{-4}$
$\langle S_2 r_{\mathrm{in},d} \rangle$	2.273 ± 10^{-3}
$\langle C_2 r_{\mathrm{out},d} \rangle$	$3.7593 \pm 9 \times 10^{-4}$
$\langle V_2 r_{\mathrm{out},d} \rangle$	$2.580 \pm 2 \times 10^{-3}$
$\langle S_2 r_{\mathrm{out},d} \rangle$	$5.827 \pm 3 \times 10^{-3}$
$\langle r_{\mathrm{in},d} r_{\mathrm{out},d} \rangle$	$0.4678 \pm 2 \times 10^{-4}$

Table A.6: Moments and correlations of physical observables related to two-dimensional Poisson geometries. Monte Carlo simulation results are obtained with $L = 80$ and $\rho = 1$.

	Monte Carlo
$\langle A_3^2 \rangle$	$168.229 \pm 8 \times 10^{-4}$
$\langle A_3 N_3 \rangle$	$112.153 \pm 5 \times 10^{-4}$
$\langle A_3 C_3 \rangle$	$80.0763 \pm 3 \times 10^{-4}$
$\langle A_3 V_3 \rangle$	$37.63 \pm 8 \times 10^{-2}$
$\langle A_3 S_3 \rangle$	131.80 ± 0.2
$\langle A_3 l_3 \rangle$	183.9 ± 0.1
$\langle N_3 C_3 \rangle$	$53.3842 \pm 2 \times 10^{-4}$
$\langle N_3 r_{\mathrm{in},d} \rangle$	$2.583 \pm 2 \times 10^{-3}$
$\langle A_3 r_{\mathrm{in},d} \rangle$	$3.875 \pm 3 \times 10^{-3}$
$\langle C_3 r_{\mathrm{in},d} \rangle$	1.791 ± 10^{-3}
$\langle V_3 r_{\mathrm{in},d} \rangle$	$1.704 \pm 5 \times 10^{-3}$
$\langle S_3 r_{\mathrm{in},d} \rangle$	4.91 ± 10^{-2}
$\langle l_3 r_{\mathrm{in},d} \rangle$	$5.527 \pm 8 \times 10^{-3}$
$\langle N_3 r_{\mathrm{out},d} \rangle$	$11.127 \pm 8 \times 10^{-3}$
$\langle A_3 r_{\mathrm{out},d} \rangle$	16.69 ± 10^{-2}
$\langle C_3 r_{\mathrm{out},d} \rangle$	$7.868 \pm 5 \times 10^{-3}$
$\langle V_3 r_{\mathrm{out},d} \rangle$	$5.90 \pm 2 \times 10^{-2}$
$\langle S_3 r_{\mathrm{out},d} \rangle$	$19.05 \pm 4 \times 10^{-2}$
$\langle l_3 r_{\mathrm{out},d} \rangle$	$23.07 \pm 3 \times 10^{-2}$
$\langle r_{\mathrm{in},d} r_{\mathrm{out},d} \rangle$	$0.4776 \pm 7 \times 10^{-4}$

Table A.7: Moments and correlations of physical observables related to three-dimensional Poisson geometries. Monte Carlo simulation results are obtained with $L = 200$ and $\rho = 1$.

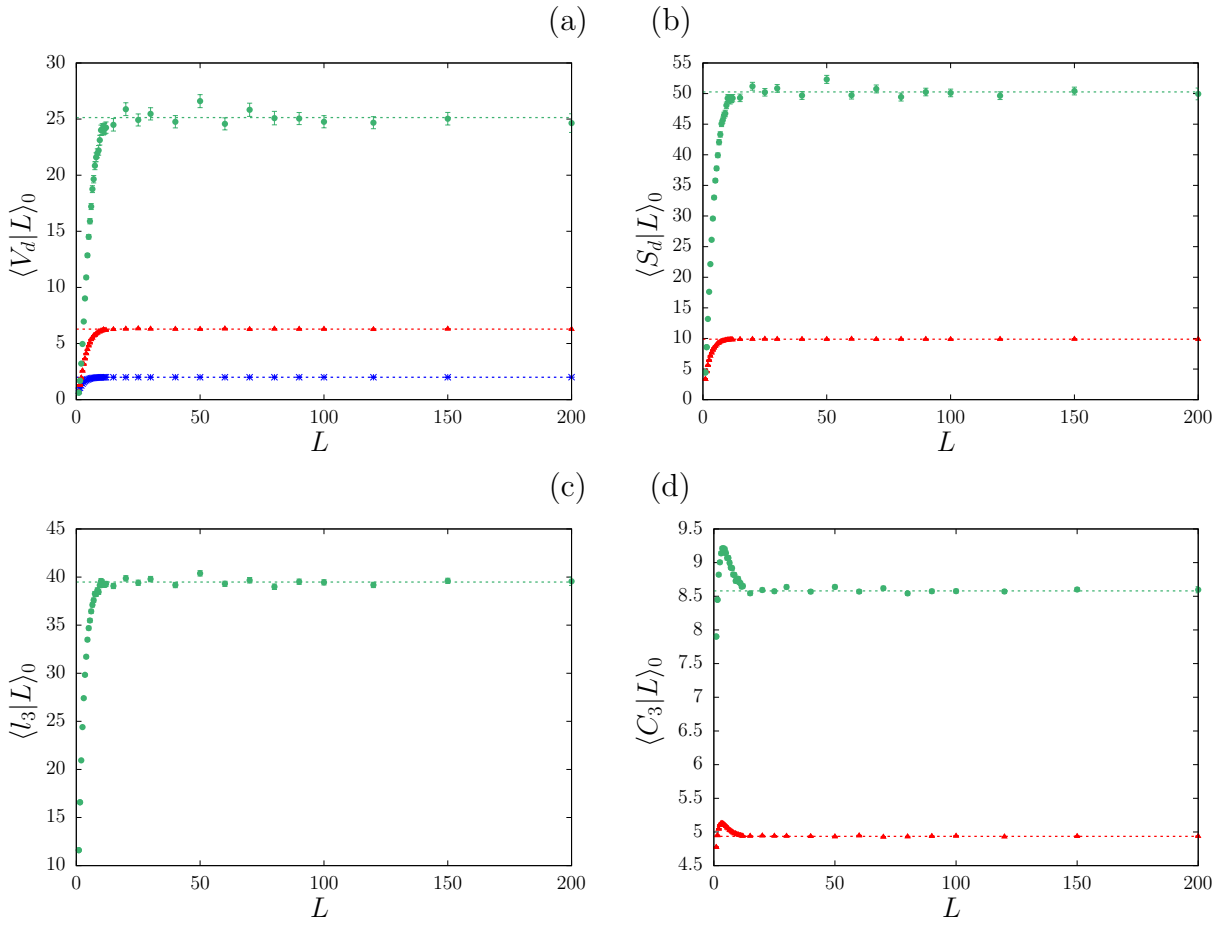

Figure A.7: First-order moments of the properties of the polyhedron containing the origin as a function of the linear size L of the domain and of the dimension d, for d-dimensional isotropic Poisson geometries. The observables illustrated here are as follows: (a) the average d-dimensional volume $\langle V_d|L\rangle_0$, (b) the average d-dimensional surface $\langle S_d|L\rangle_0$ for $d > 1$, (c) the average total length of edges $\langle l_3|L\rangle_0$ for $d = 3$ and (d) the average number of faces $\langle C_d|L\rangle_0$. For each case, we have generated $M = 10^6$ realizations for $d = 1$, $M = 5 \times 10^4$ realizations for $d = 2$ and $M = 5 \times 10^3$ realizations for $d = 3$. Simulation results have been obtained with $\rho = 1$. Symbols correspond to the Monte Carlo simulation results: blue crosses denote $d = 1$, red triangles $d = 2$ and green circles $d = 3$. Dotted lines correspond to the asymptotic (i.e., $L \to \infty$) moment given in Tab. 2.2.

d		Formula	Theoretical value	Monte Carlo
1	$\langle V_1 \rangle_0$	$2/\rho$	2	2.001 ± 10^{-3}
1	$\langle V_1^2 \rangle_0$	$6/\rho^2$	6	$6.006 \pm 9 \times 10^{-3}$
2	$\langle V_2 \rangle_0$	$2\pi/\rho^2$	6.28319	$6.27 \pm 3 \times 10^{-2}$
2	$\langle V_2^2 \rangle_0$	$64\pi^2/7\rho^4$	90.2364	89 ± 1
2	$\langle S_2 \rangle_0$	π^2/ρ	9.8696	$9.86 \pm 2 \times 10^{-2}$
2	$\langle C_2 \rangle_0$	$\pi^2/2$	4.9348	$4.935 \pm 5 \times 10^{-3}$
2	$\langle r_{\mathrm{in},2} \rangle_0$			$0.886 \pm 2 \times 10^{-3}$
2	$\langle r_{\mathrm{out},2} \rangle_0$			$2.026 \pm 5 \times 10^{-2}$
3	$\langle V_3 \rangle_0$	$8\pi/\rho^3$	25.1327	25.8 ± 0.6
3	$\langle V_3^2 \rangle_0$	$224\pi^2/\rho^6$	2210.79	2433 ± 285
3	$\langle S_3 \rangle_0$	$16\pi/\rho^2$	50.2655	51.1 ± 0.7
3	$\langle N_3 \rangle_0$	$4\pi^2/3$	13.1595	13.20 ± 0.06
3	$\langle C_3 \rangle_0$	$2(\pi^2+3)/3$	8.57974	8.60 ± 0.03
3	$\langle l_3 \rangle_0$	$4\pi^2/\rho$	39.4784	39.8 ± 0.3
3	$\langle r_{\mathrm{in},3} \rangle_0$			$0.902 \pm 7 \times 10^{-3}$
3	$\langle r_{\mathrm{out},3} \rangle_0$			$3.11 \pm 2 \times 10^{-2}$

Table A.8: Moments of the d-polyhedron containing the origin for d-dimensional isotropic Poisson tessellations. Monte Carlo simulation results are obtained with $L = 200$ and $\rho = 1$ for any dimension d.

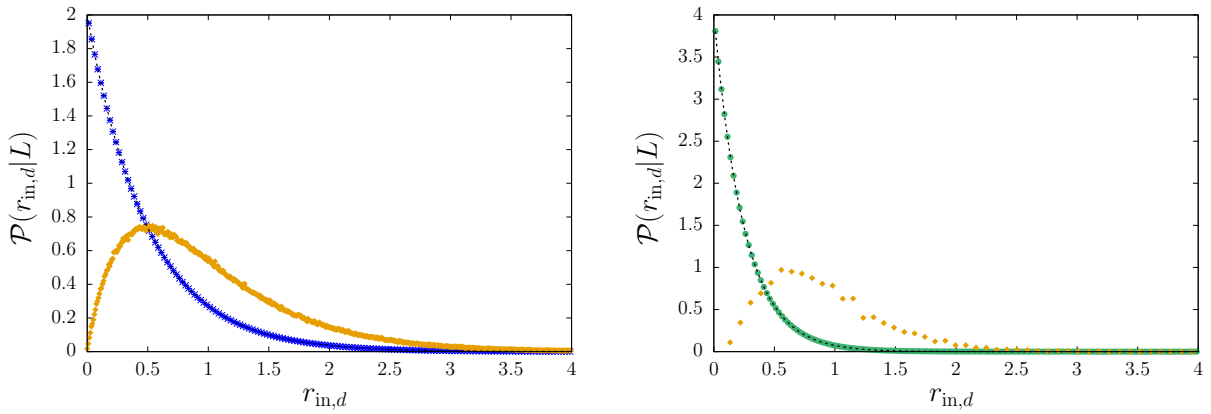

Figure A.8: Comparison between $\mathcal{P}(r_{\mathrm{in},d}|L)$ for a typical polyhedron (green circles) and $\mathcal{P}_0(r_{\mathrm{in},d}|L)$ for the polyhedron containing the origin (orange diamonds) in d-dimensional isotropic Poisson geometries, for $L = 200$. Left: $d = 1$. Right: $d = 3$. The dashed line represents the asymptotic distribution in Eq. (A.1). Symbols correspond to the Monte Carlo simulation results, generated with $M = 10^6$ realizations. Simulation results have been obtained with $\rho = 1$.

Appendix B

Resumé détaillé en français

B.1 Introduction

Dans le contexte de la physique des réacteurs, le transport des neutrons est régi par l'équation de Boltzmann

$$\mathbf{\Omega} \cdot \nabla \varphi(\mathbf{r}, \mathbf{\Omega}) + \Sigma_t(\mathbf{r})\varphi(\mathbf{r}, \mathbf{\Omega}) = \int \Sigma_s(\mathbf{\Omega}' \to \mathbf{\Omega}, \mathbf{r})\varphi(\mathbf{r}, \mathbf{\Omega}')d\mathbf{\Omega}' + Q(\mathbf{r}, \mathbf{\Omega}), \tag{B.1}$$

où $\varphi(\mathbf{r}, \mathbf{\Omega})$, inconnue de l'équation, désigne le flux de neutrons. Concernant la notation, $\mathbf{r}$ et $\mathbf{\Omega}$ correspondent respectivement aux variables de position et de direction. $\Sigma_t(\mathbf{r})$ est la section efficace macroscopique totale, $\Sigma_s(\mathbf{\Omega}' \to \mathbf{\Omega}, \mathbf{r})$ la section efficace macroscopique diffusive et $Q(\mathbf{r}, \mathbf{\Omega})$ le terme de source. Par souci de simplicité, l'équation linéaire de Boltzmann est donnée ici pour du transport monocinétique et en l'absence de fission.

La résolution de l'équation de Boltzmann repose sur des méthodes déterministes ou stochastiques. L'approche stochastique s'appuie sur des codes de transport Monte Carlo, tels que Tripoli-4 ®. Développé par le CEA, ce code est utilisé pour la criticité, la radio-protection et l'instrumentation nucléaire, en simulant les trajectoires aléatoires des neutrons dans la matière. Ces marches aléatoires s'effectuent habituellement dans des milieux parfaitement connus, i.e. $\Sigma_t(\mathbf{r})$, $\Sigma_s(\mathbf{\Omega}' \to \mathbf{\Omega}, \mathbf{r})$ et $Q(\mathbf{r}, \mathbf{\Omega})$ sont des fonctions déterministes.

Cependant, de nombreuses applications liées aux réacteurs nucléaires nécessitent de simuler les parcours des neutrons dans des milieux aléatoires. Les exemples sont nombreux : étude de l'impact de la dispersion de micro-sphères de combustible dans les réacteurs *pebble-beds*, analyse de l'impact de la taille des grains dans les poisons consommables et dans les pastilles des combustibles MOX, analyse de l'impact des variations de densité dans l'eau du modérateur ou le béton, ou encore estimation de la probabilité de re-criticité dans les coeurs de réacteurs en configuration post-accidentelle (corium, in-core ou out-of-core). Dans le cas de milieux aléatoires, les quantités $\Sigma_t(\mathbf{r})$, $\Sigma_s(\mathbf{\Omega}' \to \mathbf{\Omega}, \mathbf{r})$ et $Q(\mathbf{r}, \mathbf{\Omega})$ deviennent des variables aléatoires.

Une hypothèse usuelle concernant les milieux stochastiques est qu'il existe une collection d'états (ou réalisations physiques) $X = \{q\}$, associés à une fonction de densité $\mathcal{P}(q)$. La fonction $q(\mathbf{r})$ attribue à toute position $\mathbf{r}$ une composition physique. L'objectif de la théorie du transport de particules dans les milieux stochastiques est de dériver un formalisme pour la description des moyennes d'ensemble du flux de particules $\langle \varphi(\mathbf{r}, \mathbf{\Omega}) \rangle = \int \mathcal{P}(q)\varphi^{(q)}(\mathbf{r}, \mathbf{\Omega})dq$, où $\varphi^{(q)}$ est solution de l'équation de Boltzmann pour une réalisation q donnée. De façon générale, la solution analytique est inaccessible, néanmoins, il est possible de recourir aux méthodes de Monte Carlo pour les moyennes d'ensemble.

Dans la cadre de ce travail, on s'intéresse aux milieux aléatoires mélangeant un ensemble fini de compositions physiques $\{i\}$, avec des propriétés physiques associées, comme par exemple les sections efficaces macroscopiques totale $\Sigma_{t,i}(\mathbf{r})$ et diffusive $\Sigma_{s,i}(\mathbf{r}, \mathbf{\Omega}' \to \mathbf{\Omega})$ ou la source $Q_i(\mathbf{r}, \mathbf{\Omega})$. On note $p_i(\mathbf{r})$ la probabilité de trouver le matériel i à la position $\mathbf{r}$. On peut décomposer la moyenne d'ensemble du flux sur les flux conditionnés aux matériaux $\langle \varphi_i(\mathbf{r}, \mathbf{\Omega}) \rangle$ pondérés par les probabilités de coloriage, i.e. $\langle \varphi(\mathbf{r}, \mathbf{\Omega}) \rangle = \sum_i p_i(\mathbf{r}) \langle \varphi_i(\mathbf{r}, \mathbf{\Omega}) \rangle$. Dans cette thèse, on se limite au cas des mixtures dites *homogènes*, c'est-à-dire que $p_i(\mathbf{r})$ ne dépend pas de $\mathbf{r}$.

Un cas largement étudié est celui des mixtures binaires, avec seulement deux matériaux α et β. Dans ce cas, sans perte de généralité, on peut écrire une équation de type Boltzmann pour les flux conditionnés aux matériaux $\langle\varphi_\alpha(\mathbf{r},\mathbf{\Omega})\rangle$ and $\langle\varphi_\beta(\mathbf{r},\mathbf{\Omega})\rangle$, avec un terme de couplage $U_{\alpha,\beta}(\mathbf{r},\mathbf{\Omega})$ représentant le désordre :

$$[\mathbf{\Omega}\cdot\nabla+\Sigma_{t,\alpha}]\left(p_\alpha\langle\varphi_\alpha\rangle\right)=p_\alpha\int\Sigma_{s,\alpha}(\mathbf{\Omega}'\rightarrow\mathbf{\Omega},\mathbf{r})\langle\varphi_\alpha(\mathbf{r},\mathbf{\Omega}')\rangle d\mathbf{\Omega}'+p_\alpha Q_\alpha+U_{\alpha,\beta}. \tag{B.2}$$

Malheureusement, le terme de couplage $U_{\alpha,\beta}$ ne dépend pas seulement de la moyenne d'ensemble des flux conditionnés aux matériaux $\langle\varphi_\alpha(\mathbf{r},\mathbf{\Omega})\rangle$ et $\langle\varphi_\beta(\mathbf{r},\mathbf{\Omega})\rangle$ mais aussi des moments supérieurs, ce qui conduit à une hiérarchie infinie d'équations. Dans le cas général, on ne peut donc pas résoudre de manière explicite ce système d'équations sans formule de clôture. En revanche, il est possible de montrer que ce terme de couplage $U_{\alpha,\beta}$ dépend de la distribution de la longueur de corde dans chaque matériau. Ainsi, on s'attend à ce que le désordre soit fortement lié aux propriétés stéréologiques des mixtures aléatoires.

Pour le transport de neutrons dans des milieux désordonnés, deux approches peuvent être distinguées :

- l'approche dite 'désordre figé' : on génère un grand nombre de réalisations de géométries aléatoires suivant un modèle stochastique, grâce à un générateur de géométries stochastiques; pour chaque réalisation géométrique, le transport de particules est simulé dans cette géométrie et les observables de transport associées (réflexion, transmission, flux, facteur de multiplication, etc.) sont enregistrées; on calcule ensuite les moyennes d'ensemble pour chaque observable ainsi que les distributions. Cette approche a l'avantage de fournir des solutions de référence mais comporte un coût computationnel élevé.

- l'approche dite 'désordre homogénéisé' : les lois de déplacement des neutrons dans la matière sont modifiées afin d'introduire des opérateurs de transport 'efficaces' dans l'équation de Boltzmann, afin de représenter le plus fidèlement possible le désordre, au détriment des corrélations induites par la structure géométrique, qui sont perdues dans cette approche : généralement, cette méthode ne fournit donc que de solutions approchées. En revanche, elle ne nécessite qu'une seule simulation de transport, ce qui revient à réduire considérablement le temps de calcul. En outre, cette approche ne nécessite aucun générateur de géométries aléatoires.

B.2 Modélisation du désordre par des géométries stochastiques

Pour les applications liées à la physique des réacteurs, deux principales classes de géométries stochastiques sont généralement considérées : les inclusions sphériques aléatoires, dans lesquelles des objets sont dispersés aléatoirement dans une matrice, et les tessellations aléatoires, dans lesquelles l'espace est partitionné suivant des lois de probabilité. Les inclusions sphériques ayant été déjà largement étudiées, je me suis concentrée dans cette thèse sur la classe des tessellations aléatoires. Nous avons considéré trois modèles de tessellations homogènes :

- les tessellations de Poisson, qui satisfont aux milieux dits 'Markoviens', dans lesquelles la longueur de corde est distribuée exponentiellement ;

- les tessellations Poisson-Voronoi, simplement dites 'Voronoi' dans la suite, très utilisées dans le domaine de la mécanique pour décrire les microstructures ;

- les tessellations dites 'Box', un cas spécial des tessellations de Poisson anisotropes, construites avec des plans orthogonaux aux axes cartésiens, qui définissent des parallélépipèdes de dimensions aléatoires.

Ces trois modèles engendrent une décomposition de l'espace en volumes polyédraux convexes. Cette propriété est cruciale pour le déversement de ces géometries dans des codes de transport. L'algorithme utilisé pour tesseller une boîte d-dimensionnelle de taille L avec un paramètre appelé densité de la tessellation (homogène à l'inverse d'une longueur), est détaillé pour chaque modèle de tessellation :

- Pour les tessellations de Poisson, on procède de façon itérative. Au début de la construction, la tessellation ne compte que la boîte vide. Puis, le nombre d'hyperplans à introduire dans la tessellation est tiré aléatoirement d'une distribution de Poisson dont l'intensité dépend de la dimension, de la taille linéaire L de la boîte et du paramètre de densité ρ. Ensuite, chaque hyperplan est tiré aléatoirement de façon à garantir l'homogénéité de la tessellation. En particulier, le vecteur normal $\mathbf{n}$ de chaque hyperplan obéit à une loi de probabilité $\mathcal{H}(\mathbf{n})$, qui correspond à la la loi d'anisotropie de la tessellation. Lorsque l'hyperplan est tiré, on calcule les intersections de cet hyperplan avec les polyèdres composant la tessellation et on itère jusqu'à atteindre le nombre d'hyperplans tiré préalablement.

- Les tessellations de Voronoi sont obtenues en tirant aléatoirement des points (germes) d'un processus de Poisson homogène d'intensité $\mu = \rho_{\mathcal{V}}^3$ dans la boîte. Puis, une décomposition déterministe est appliquée aux germes pour la construction des cellules de Voronoi. Chaque cellule de Voronoi, associée à un germe, est définie comme la région des points de l'espace tels que ces points sont plus proches du germe considéré que de tout autre germe.

- Les tessellations Box sont obtenues en tirant des points d'un processus de Poisson homogène d'intensité $\rho_{\mathcal{B}}$ sur un axe Cartésien donné. On découpe ensuite l'espace avec les plans orthogaux à l'axe, passant par les points tirés au préalable. Cette étape est répétée sur les $d-1$ axes Cartésiens restants.

D'après la littérature, les propriétés géométriques de ces tessellations sont connues seulement pour un nombre limité d'observables et pour des géométries infinies. On distingue les propriétés polyhédrales (par exemple, relatives au volume, à la surface, au nombre de voisins, etc., typique d'un polyèdre de la tessellation) des propriétés stéréologiques (par exemple, la distribution des cordes). En particulier, un résultat très important concernant la distribution de la longueur de corde dans les géométries de Poisson anisotropes (d'extension infinie) est le suivant : une droite d'orientation $\mathbf{\Omega}$ est découpée en cordes dont la longueur est distribuée exponentiellement avec une moyenne $\Lambda(\mathbf{\Omega})$, qui dépend de $\mathbf{\Omega}$, de la dimension d, de la densité de la tessellation ρ et de la loi d'anisotropie $\mathcal{H}$. Dans le cas spécial des géométries de Poisson isotropes, cette quantité ne dépend plus de $\mathbf{\Omega}$ et devient : $\Lambda(\mathbf{\Omega}) = \Lambda = 1/\rho$. Dans les tessellations de Voronoi, la distribution de la longueur de corde a été dérivée trés récemment. Comme les tessellations de Voronoi sont isotropes, la distribution des cordes ne dépend pas de l'orientation $\mathbf{\Omega}$ des droites. En particulier, il ressort que cette distribution est non exponentielle. Dans les tessellations de Box, la distribution de la longueur de corde est aussi exponentielle suivant une direction $\mathbf{\Omega}$ donnée, comme cas particulier des tessellations de Poisson anisotropes. Si l'on irradie maintenant les tessellations avec des droites distribuées de manière isotrope et uniforme (notion de μ-randomness), la longueur de corde moyenne, notée Λ_c, qui représente physiquement la longueur de corrélation du milieu, peut être calculée en appliquant la formule de Cauchy, en utilisant les formules de littérature pour les premiers moments du volume $\langle V_d \rangle$ des polyèdres et celui de la surface totale $\langle S_d \rangle$ des polyèdres. Ainsi, la quantité Λ_c peut être exprimée, pour chaque modèle de tessellation, en fonction du paramètre de densité correspondant (i.e., ρ, pour Poisson, $\rho_{\mathcal{V}}$ pour Voronoi et $\rho_{\mathcal{B}}$ pour Box). Afin de comparer les différents modèles de tessellations, un choix pertinent est de calibrer les densités des tessellations de manière à obtenir la même longueur de corrélation Λ_c (dans la limite des géométries infinies).

Une fois que les tessellations sont produites, une étape importante est celle dite du *coloriage*, dans laquelle on assigne à chaque polyèdre de la tessellation un label i (correspondant à une composition physique) avec une probabilité p_i. Une observable clé est la longueur de corde dans le matériel i. On

sait que, pour des droites distribuées isotropiquement et uniformément, la moyenne de la longueur de corde dans le matériel i, notée $\Lambda_{c,i}$, est reliée à la longueur de corrélation Λ_c et aux probabilités de coloriage $\{p_i\}$ par la formule suivante : $\Lambda_{c,i} = \Lambda_c/(1-p_i)$. En outre, pour le cas spécifique des tessellations de Poisson, la distribution des cordes colorées est toujours distribuée exponentiellement suivant une direction $\mathbf{\Omega}$ donnée, avec la moyenne : $\Lambda_i(\mathbf{\Omega}) = \Lambda(\mathbf{\Omega})/(1-p_i)$.

On peut ensuite agréger les polyèdres voisins de même composition en *clusters* colorés, généralement non-convexes. Cette étape d'agrégation est facultative pour le transport, puisque le tracking des particules s'effectue dans des volumes convexes. En revanche, elle est nécessaire pour l'étude de propriétés géométriques spécifiques comme celles liées à la percolation, qui représente physiquement une connectivité préférentielle. En particulier, le seuil de percolation de la tessellation correspond à la valeur critique p_c de la probabilité de coloriage du matériel i telle qu'au-delà de ce seuil, il existe presque sûrement un cluster de matériel i traversant toute la géométrie : il est important de noter que ce seuil ne dépend pas du matériel i. Ce seuil n'est défini rigoureusement que pour des géométries infinies, néanmoins il est possible de l'estimer avec des géométries finies de tailles croissantes. Notons qu'aucune estimation du seuil de percolation n'a été proposée jusqu'ici pour les tessellations de Poisson en dimension 3.

B.3 Description du générateur de géométries aléatoires

La première étape de cette thèse a été d'implémenter un code générant différents modèles de géométries aléatoires (tessellations et inclusions sphériques dites 'sans chevauchement'), décrites au chapitre précédent, pour les dimensions $d = 1$, $d = 2$ et $d = 3$. Ce générateur a été codé en langage C++ et prend en entrée la taille L de la boîte englobante ainsi que des paramètres géométriques :

- pour les tessellations : densité de tessellation (ρ, $\rho_{\mathcal{V}}$ ou $\rho_{\mathcal{B}}$ suivant le modèle de tessellation) et probabilités $\{p_i\}$ de coloriage (pour des mélanges n-aires) ;
- pour les inclusions sphériques : ratio volumique ξ occupé par les sphères et distribution du rayon $g(r)$ des sphères.

Chaque type de géométries aléatoires a nécessité un algorithme de construction et une structure de données particulière. L'objectif de ce générateur est double : i) l'investigation des propriétés statistiques géométriques des tessellations, notamment pour l'étude des effets de taille finie ; ii) la production de géométries aléatoires pour réaliser des simulations de transport dans des milieux désordonnés, grâce à l'implémentation d'une interface avec le code de transport Monte Carlo TRIPOLI-4 ®: le générateur peut en effet sortir des fichiers décrivant chaque géométrie, qui sont lisibles par le code de transport.

Nous avons étudié le temps moyen de construction des tessellations en fonction de la taille du système $L^* = L/\Lambda_c$. Nous avons montré que cette quantité va comme $(L^*)^{d+1}$ pour les géométries de Poisson. De plus, le temps de construction va comme $(L^*)^{2d}$ pour Voronoi et $(L^*)^2$ pour Box. Nous avons ensuite montré certaines techniques d'accélération de la construction pour les tessellations de Poisson et Voronoi, ainsi que pour les inclusions sphériques, avec un maillage fictif destiné à restreindre les recherches sur tous les éléments au cours de la construction.

Enfin, nous avons implémenté dans le générateur de géométries aléatoires une méthode permettant de générer une carte de voisinage des polyèdres (dans le cas des tessellations) ou des sphères et de la matrice maillée (dans le cas des inclusions sphériques). Cette carte peut être fournie au code de transport TRIPOLI-4 ®. Nous avons montré que cette carte de voisinage accélère considérablement le tracking des particules durant la simulation de transport, notamment lorsque les géométries sont complexes : typiquement, l'effet de la carte de voisinage devient visible à partir de 10^4 volumes dans la géométrie. Cette accélération s'explique par la réduction de l'étape où la particule quitte un volume : à défaut de carte de voisinage, le code boucle sur tous les volumes de la géométrie afin de trouver le prochain volume du parcours de la particule. Avec la carte de voisinage, cette boucle est restreinte aux seuls voisins du volume courant.

B.4 Etude statistique des géométries aléatoires

En utilisant le générateur de géométries, nous avons étudié la complexité (nombre de polyèdres composant la tessellation) ainsi que les propriétés statistiques polyédrales (volume, surface, nombre de faces, etc. typique d'une cellule) et stéréologiques (distribution de la longueur de corde) pour différentes tessellations. Pour les observables dont il existe des formules exactes pour les tessellations infinies, nous avons caractérisé les effets de taille finie en fonction de la taille du système, de la dimension d, de la loi d'anisotropie (pour les géométries de Poisson) ou du type de tessellation (Poisson, Voronoi ou Box à même longueur de corrélation). Puis, nous avons vérifié la convergence des moments et des distributions vers les formules de la littérature pour des systèmes assez grands. Pour les observables dont le comportement n'est pas connu, même pour des géométries infinies, nous avons estimé numériquement les distributions et moments correspondants. En outre, nous avons montré que pour des droites isotropes et uniformes, la distribution de la longueur de corde dans les tessellations Box est (bien qu'on puisse démontrer qu'elle est non strictement exponentielle grâce au moment d'ordre quatre) quasi similaire à celle dans les tessellations de Poisson (strictement exponentielle), y compris dans la queue de distribution, tandis que la distribution de la longueur de corde pour le Voronoi a un comportement très distinct, comme prévu par la théorie. Enfin, nous avons établi pour la première fois une estimation du seuil de percolation des géométries de Poisson isotropes en dimension 3. Cette étude a fait l'objet d'une publication [1].

B.5 Transport de particles dans du désordre figé pour les problèmes à source fixe

En utilisant l'approche 'désordre homogéisé' détaillée en introduction, nous avons effectué des simulations de transport de particules dans des géométries Markoviennes, i.e. tessellations de Poisson. En guise de première appliaction, nous avons repris un benchmark classique de littérature (proposé par Larsen, Adams et Pomraning en 1989) concernant le transport dans des géométries de Poisson unidimensionnelles et l'avons étendu aux dimensions 2 et 3. Pour cela, nous avons utilisé les géométries de Poisson produites par notre générateur aléatoire et exploité le logiciel TRIPOLI-4 ®pour effectuer des calculs de réflexion, transmission et flux sur chaque réalisation géométrique. En particulier, pour les moyennes d'ensemble des observables cibles, nous avons mis en évidence le fait que les solutions sont d'autant plus proches du régime de l'*atomic mix* (cas du milieu homogène dans lequel toutes les propriétés physiques sont moyennées) que la dimension d est grande et que la longueur de corrélation est petite. De plus, nous avons estimé les distributions des observables et constaté que la dispersion est d'autant plus petite que la dimension d est grande et que la longueur de corrélation est petite. En outre, nous avons montré que pour des longueurs de corrélation suffisamment grandes, des effets pathologiques sont susceptibles d'apparaître, notamment des distributions bimodales pour la dimension 1. Ceci montre que les moyennes d'ensemble ne sont pas toujours représentatives et que, dans certains cas, toute la distribution est nécessaire. Cette étude a fait l'objet d'une publication [2].

Nous avons ensuite estimé l'impact du modèle de tessellation (Poisson, Voronoi ou Box, à longueur de corrélation fixée) sur le transport de neutrons, pour des problèmes à source fixe (poursuite du benchmark d'Adams, Larsen et Pomarning et définition d'un nouveau benchmark dans des milieux non-multipliants). Les résultats suggèrent que les géométries Poisson et Box sont équivalentes pour le transport (probablement en raison de la distribution de longueur de corde très similaire pour ces deux modèles), tandis que les solutions issues du modèle Voronoi se distinguent par un comportement spécifique. Par ailleurs, les tessellations de Voronoi conduisent à des distributions moins dispersées que les deux autres modèles. Ce travail a également fait l'objet d'une publication [3].

B.6 Transport de particles dans du désordre figé pour les problèmes à valeur propre

Nous avons poursuivi l'approche du transport 'désordre figé' pour des milieux multipliants (en résolvant l'équation de Boltzmann à valeur propre, pour chaque réalisation), afin de modéliser un assemblage UOX ou MOX partiellement fondu en faisant l'hypothèse que les éléments de combustible fragmentés suite à un accident avec fusion partielle du coeur peuvent être remplacés par des tessellations aléatoires ternaires, avec les compositions suivantes : fuel (UOX ou MOX), modérateur (eau) et gaine (zinc, principalement). Les probabilitités de coloriage $\{p_i\}$ des tessellations ont été choisies de manière à respecter les ratios volumiques dans une pin-cell intacte.

Nous avons étudié l'impact des géométries aléatoires sur la réactivité (via le facteur de multiplication) et sur les paramètres cinétiques. Ils montrent que le facteur de multiplication moyen dépend fortement de la longueur de corrélation de la tessellation : d'abord, cette observable augmente, avant d'atteindre un maximum puis de diminuer en fonction de la longueur de corrélation. En outre, les résultats issus des tessellations de Poisson et de Box sont quasi identiques, alors que les résultats obtenus avec des tessellations de Voronoi donnent typiquement des facteurs de multiplication plus élevés. Enfin, ce comportement est amplifié en passant du combustible UOX au MOX, le facteur de multiplication moyen pouvant alors dépasser celui de l'assemblage non endommagé. Les résultats de cette étude ont été publiés [4].

Les géométries étudiées étant jusqu'ici isotropes (ou quasi isotropes, pour le cas Box), nous avons étudié l'impact des anisotropies (directions privilégiées) dans le cadre des tessellations de Poisson, pour une application à la modélisation du corium, afin d'estimer l'impact des effets de stratification des matériaux (dus à la gravité) sur le facteur de multiplication. Cette étude a été publiée [7].

B.7 Transport de particles dans du désordre homogénéisé

L'algorithme *Chord Length Sampling* (CLS) s'inscrit dans l'approche 'désordre homogénéisé', présentée en introduction. Il a été démontré que cet algorithme est l'implémentation stochastique du modèle déterministe des équations de Levermore-Pomraning, qui sont obtenues pour des mixtures Markoviennes en appliquant une relation de clôture (strictement valide uniquement pour du transport sans collision) sur le terme de couplage $U_{\alpha,\beta}$ dans le système d'équations pour les flux conditionnés aux matériaux (voir Eq.B.2). On obtient ainsi une expression très simplifiée pour le terme de couplage, qui dépend seulement des longueurs de corde moyennes dans chaque matériau et des probabilités de coloriage : $U_{\alpha,\beta} = \frac{p_\beta}{\Lambda_{c,\beta}}\langle\varphi_\beta\rangle - \frac{p_\alpha}{\Lambda_{c,\alpha}}\langle\varphi_\alpha\rangle$, ce qui conduit à un système d'équations approchées couplées. L'algorithme CLS est un algorithme de transport Monte Carlo classique dans lequel un nouvel événement intervient afin de tenir compte du désordre : le franchissement d'interfaces entre les matériaux. Cet événement est tiré au vol au cours de la simulation : dans le matériau i, la distance à la prochaine interface est tirée d'une distribution exponentielle de moyenne $\Lambda_{c,i} = \Lambda_c/(1-p_i)$.

Nous avons implémenté cet algorithme pour le benchmark de Adams, Larsen et Pomraning en dimension 1, 2 et 3. Les résultats ont été comparés aux solutions de référence correspondantes (obtenues avec les tessellations de Poisson). Les résultats clé sont les suivants : la précision de l'algorithme CLS par rapport aux solutions de référence augmente avec la dimension d (comme conjecturé par Sahni) et décroît avec la longueur de corrélation et avec la section efficace de diffusion des matériaux. Une publication, en collaboration avec le *Lawrence Livermore National Laboratory* (LLNL) et *Oregon University*, détaille les résultats obtenus [5].

L'algorithme CLS est une méthode approchée, d'où la mauvaise précision par rapport aux solutions de référence pour certaines configurations. En effet, on sait que dans cet algorithme, les corrélations sont négligées, i.e. que les particules n'ont pas la mémoire des milieux déjà traversés : les effets dits de

back-scattering ne peuvent donc pas être bien pris en compte. On peut se demander, dès lors, comment améliorer l'algorithme CLS pour augmenter sa précision. En dimension 1, deux versions améliorées du CLS (algorithmes dits 'B' et 'C') ont étés proposées dans la littérature, afin d'inclure des effets supplémentaires de corrélation et de mémoire locale. Nous avons voulu développer de tels algorithmes en dimension d. Nous avons proposé une nouvelle classe de méthodes de type 'désordre homogénéisé', les algorithmes *Poisson-Box Sampling* (PBS). Il s'agit d'ajouter des effets de corrélation et de mémoire pour mieux reproduire le désordre dans des géométries de Poisson, en passant par les tessellations Box, qui présentent des résultats de transport très similaires à ceux issus des tessellations de Poisson. Nous avons implémenté deux algorithmes distincts : dans la première version (PBS-1), on génère au vol des boîtes dont les dimensions sont distribuées exponentiellement de manière à préserver la longueur de corrélation des tessellations de Poisson ; dans la seconde version (PBS-2), on garde en plus en mémoire les caractéristiques de la dernière boîte rencontrée. Nous avons testé ces deux algorithmes sur le benchmark d'Adams, Larsen et Pomraning, pour la dimension 3. De manière générale, la précision des résultats obtenus est bien meilleure que celle de l'algorithme CLS. De plus, l'algorithme PBS-2 est plus performant que la version PBS-1, comme attendu. Une publication présente le détail de ces résultats [6].

B.8 Conclusions

Nous avons implémenté un générateur de géométries aléatoires pour des géométries Markoviennes (notamment en dimension 3), produit pour la première fois des solutions de référence $3d$ pour des problèmes de transport à source fixe et pour des problèmes de criticité dans des géométries aléatoires. Nous avons également obtenu des solutions approchées avec l'algorithme CLS et comparé ces résultats avec les solutions de référence correspondantes, pour la dimension 3. Enfin, nous avons proposé une nouvelle famille d'algorithmes de transport (PBS) avec l'approche 'désordre homogénéisé' et obtenu des résultats très satisfaisants pour des problèmes de transport à source fixe.

B.9 Références

1. C. Larmier, E. Dumonteil, F. Malvagi, A. Mazzolo, A. Zoia, Finite size-effects and percolation properties of Poisson geometries, Physical Review E 94 012130 (2016)

2. C. Larmier, F.-X. Hugot, F. Malvagi, A. Mazzolo, A. Zoia, Benchmark solutions for d-dimensional Markov binary mixtures, JQSRT 189, 133-148 (2017)

3. C. Larmier, A. Zoia, F. Malvagi, E. Dumonteil, A. Mazzolo, Monte Carlo particle transport in random media: Effects of mixing statistics. JQSRT 196, 270-286 (2017)

4. C. Larmier, A. Zoia, F. Malvagi, E. Dumonteil, A. Mazzolo, Reactivity and kinetics parameters for neutron multiplication in random media. Annals of Nuclear Energy 111, 391-406 (2018)

5. C. Larmier, A. Lam, P. Brantley, F. Malvagi, T. Palmer, A. Zoia, Monte Carlo Chord Length Sampling for d-dimensional Markov binary mixtures. JQSRT 204, 256-271 (2018)

6. C. Larmier, A. Zoia, F. Malvagi, E. Dumonteil, A. Mazzolo, Poisson-Box Sampling algorithm for three-dimensional Markov binary mixtures. JQSRT 206, 70-82 (2018).

7. A. Marinosci, C. Larmier, A. Zoia, Neutron transport in anisotropic random media. Annals of Nuclear Energy 118, 406-413 (2018)

Bibliography

[1] M.L. Adams, E.W. Larsen, G.C. Pomraning, J. Quant. Spectrosc. Radiat. Transfer **42**, 253-266 (1989).

[2] A.Yu. Ambos, G.A. Mikhailov, Russ. J. Numer. Anal. Math. Modelling **26**, 263-273 (2011).

[3] P. Barthelemy, J. Bertolotti, D.S. Wiersma, Nature **453**, 495-498 (2009).

[4] A. M. Becker, R. M. Ziff, Phys. Rev. E **80**, 041101 (2009).

[5] G. I. Bell, S. Glasstone, *Nuclear reactor theory* (Van Nostrand Reinhold Company, 1970).

[6] B. Bollobás, O. Riordan, Probab. Theory Relat. Fields **136**, 417-468 (2006).

[7] J.P. Bouchaud, A. Georges, Phys. Rep. **195**, 127-293 (1990).

[8] P.S. Brantley, J.N. Martos, in Proceedings of M&C2011, Rio de Janeiro, Brazil, 2011.

[9] P.S. Brantley, T.S. Palmer, in Proceedings of M&C2009, Saratoga Springs, New York, 2009.

[10] P.S. Brantley, in Proceedings of M&C2009, Saratoga Springs, New York, 2009.

[11] P.S. Brantley, J. Quant. Spectrosc. Radiat. Transfer **112**, 599-618 (2011).

[12] P.S. Brantley, Trans. Am. Nucl. Soc., Anaheim, CA, November 9-13, 2014.

[13] P.S. Brantley, N.A. Gentile, G.B. Zimmerman, in Proceedings of M&C 2017 - Jeju, Korea, 2017.

[14] P.S. Brantley, et al., *Mercury User Guide: Version 5.6*, LLNL-SM-560687 (Modification #12), 2017.

[15] P.S. Brantley et al., in Proceedings of M&C 2017 - Jeju, Korea, 2017.

[16] P.S. Brantley, G.B. Zimmerman, Trans. Am. Nuc. Soc. **117**, 765-768 (2017).

[17] D.J. Behrens, Proc. Phys. Soc. Section A **62**, 607-616 (1949).

[18] J.M. Broughton, P. Kuan, D.A. Petti, E.L. Tolman, Nucl. Techn. **87**, 34-53 (1989).

[19] F.B. Brown, Trans. Am. Nucl. Soc. **94**, 571-573 (2006).

[20] F.B. Brown, W.R. Martin, Ann. Nucl. Energy **31**, 2039-2047 (2004).

[21] E. Brun, et al., Ann. Nucl. Energy **82**, 151-160 (2015).

[22] P. Calka, Adv. Appl. Prob. **35**, 551-562 (2003).

[23] P. Calka, J. Stat.Phys. **132**, 627-647 (2008).

[24] S.N. Chiu, D. Stoyan, W.S. Kendall, J. Mecke, *Stochastic geometry and its applications* (Wiley, New York, USA, 2013).

[25] R. Coleman, J. Appl. Probab. **6**, 430-441 (1969).

[26] D. W. Cooper, Phys. Rev. A. **38**, 522 (1988).

[27] A.B. Davis, A. Marshak, J. Quant. Spectrosc. Radiat. Transfer **84**, 3-34 (2004).

[28] A. Davis, M. Mineev-Weinstein, J. Quant. Spectrosc. Radiat. Transfer **112** 632-645 (2011).

[29] Y. Deng, H.J.W. Blöte, Phys. Rev. E **27**, 016126 (2005).

[30] M. Dixmier, J. Phys. France **39**, 873-895 (1978).

[31] T.J. Donovan, Y. Danon, Nucl. Sci. Eng. **143**, 226-239 (2003).

[32] T.J. Donovan, T.M. Sutton, Y. Danon, in Proceedings of M&C2003, Gatlinburg, TN, 2003.

[33] W.B. Doub, Nucl. Sci. Eng. **10**, 299-307 (1961).

[34] J.J. Duderstadt, W.R. Martin, W.R., *Transport theory* (J. Wiley and sons, New York, 1979).

[35] J. Feder, J. Theor.Biol. **87**, 237 (1980).

[36] E.D. Fichtl, A.K. Prinja, J. Quant. Spectrosc. Radiat. Transfer **112**, 646-659 (2011).

[37] K. Fischer, B. Gärtner, and M. Kutz, in Proc. 11th European Symposium on Algorithms (ESA), 630-641 (2003).

[38] H. Frisch, U. Frisch, in Colloques internationaux du CNRS **250**, 113 (1975).

[39] G. Gaiselmann, M. Neumann, L. Holter, T. Hocker, M. R. Prestat, Comput. Mater. Sci. **67**, 48-62 (2013).

[40] E.N. Gilbert, Ann. Math. Statist. **33**, 958-972 (1962).

[41] S. Goudsmit, Rev. Mod. Phys. **17**, 321 (1945).

[42] P. Grassberger, J. Phys. A **25**, 5867-5888 (1992).

[43] D.P. Griesheimer, D.L., Millman, C.R. Willis, J. Quant. Spectrosc. Radiat. Transfer **112**, 577598 (2010).

[44] D. Guéron, A. Mazzolo, Phys. Rev. E **68**, 066117 (2003).

[45] S. Gunji, K. Tonoike, K. Izawa, H. Sono, Prog. Nuc. Energy **101**, 321-328 (2017).

[46] W. S. Jodrey, E. M. Tory, Nature **239**, 504 (1972).

[47] S. Hagen, P., Hofmann, Nucl. Eng. Design **103**, 85-106 (1987).

[48] O. Haran, D. Shvarts, R., Thieberger, Phys. Rev. E **61**, 6183-6189 (2000).

[49] H. J. Hilhorst, P. Calka, J. Stat.Phys. **132**, 627-647 (2008).

[50] P. Hofmann, J. Nucl. Mat. **270**, 194-211 (1999).

[51] F.-X. Hugot, Y.-K., Lee, Progr. Nuc. Sci. Techn. **2**, 851-854 (2011).

[52] G.R. Jerauld, L.E. Scriven, H.T. Davis, J. Phys. C Solid State Phys. **17**, 3429-3439 (1984).

[53] W. Ji, W.R. Martin, in Proceedings of M&C + SNA 2007, Monterey, USA, 2007.

[54] W. Ji, W.R. Martin, Nucl. Sci. Eng. **169**, 19-39 (2011).

[55] M. G. Kendall, P. A. P.Moran, *Geometrical probability* (Charles Griffin And Company Limited, London, 1963).

[56] B.C. Kiedrowski, F.B. Brown, P.P.H. Wilson, Nucl. Sci. Eng. **68**, 226 (2011).

[57] A.B. Kostinski, R.A. Shaw, J. Fluid Mech. **434**, 389-398 (2001).

[58] C. Larmier, E. Dumonteil, F. Malvagi, A. Mazzolo, A. Zoia, Phys. Rev. E **94**, 012130 (2016).

[59] C. Larmier, F.-X. Hugot, F. Malvagi, A. Mazzolo, A. Zoia, J. Quant. Spectrosc. Radiat. Transfer **189**, 133148 (2017).

[60] C. Larmier, A. Zoia, F. Malvagi, E. Dumonteil, A. Mazzolo, J. Quant. Spectrosc. Radiat. Transfer. **196**, 270-286 (2017).

[61] C. Larmier, A. Zoia, F. Malvagi, E. Dumonteil, A. Mazzolo, Ann. Nucl. Energy **111**, 391-406 (2018).

[62] C. Larmier, A. Lam, P. Brantley, F. Malvagi, T. Palmer, A. Zoia, J. Quant. Spectrosc. Radiat. Transfer. **204**, 256271 (2018).

[63] C. Larmier, A. Zoia, F. Malvagi, E. Dumonteil, A. Mazzolo, J. Quant. Spectrosc. Radiat. Transfer. **206**, 70-82 (2018).

[64] E.W. Larsen, R. Vasques, J. Quant. Spectrosc. Radiat. Transfer. **112**, 619-631 (2011).

[65] T. Lepage, L. Delaby, F. Malvagi, A. Mazzolo, Prog. Nucl. Sci. Techn. **2**, 743-748 (2011).

[66] C.D. Levermore, G.C. Pomraning, D.L. Sanzo, J. Wong, J. Math. Phys. **27**, 2526-2536 (1986).

[67] C.D. Levermore, G.B. Zimmerman, J. Math. Phys. **34**, 4725-4729 (1993).

[68] C. Liang, W. Ji, F.B. Brown, Ann. Nucl. Energy **53**, 140-146 (2013).

[69] C. Liang, W. Ji, Trans. Am. Nucl. Soc. **105**, 495-497 (2011).

[70] C. Liang, W. Ji, Transp. Theory Stat. Phys. **40**, 282-303 (2011).

[71] J. Lieberoth, A. Stojadinovic, Nuc. Sci. Eng. **76**, 336-344 (1980).

[72] B. Lu, S. Torquato, Phys. Rev. A **45**, 992 (1992),

[73] I. Lux, L. Koblinger, *Monte Carlo particle transport methods: Neutron and photon calculations* (CRC Press, Boca Raton, 1991).

[74] F. Malvagi, R.N. Byrne, G.C. Pomraning, R.J.C. Somerville, J. Atm. Sci. **50**, 2146-2158 (1992).

[75] G. Matheron, *Random sets and integral geometry* (Wiley, 1970).

[76] G. Matheron, Adv. Appl. Prob. **4** 508-541 (1972).

[77] A. Mazzolo, B. Roesslinger, Monte Carlo Meth. Appl. **10**, 443-454 (2004).

[78] A. Mazzolo, C. de Mulatier, A. Zoia, J. Math. Phys. **55**, 083308 (2014).

[79] J. Mecke, Adv. Appl. Prob. **27**, 56-62 (1995).

[80] J.L. Meijering, Philips Res. Rep. **8**, 270-290 (1953).

[81] N. Mercadier, W. Guerin, M. Chevrollier, R. Kaiser, Nature Physics **5**, 602-605 (2008).

[82] R. E. Miles, Proc. Nat. Acad. Sci. USA **52**, 901-907 (1964).

[83] R. E. Miles, Proc. Nat. Acad. Sci. USA **52**, 1157-1160 (1964).

[84] R. E. Miles, Adv. Appl. Prob. **1**, 211-237 (1969).

[85] R. E. Miles, Izv. Akad. Nauk. Arm. SSR Ser. Mat. **5**, 263-285 (1970).

[86] R. E. Miles, Adv. Appl. Prob. **3**, 1-43 (1969).

[87] R. E. Miles, Suppl. Adv. Appl. Prob. **4**, 243-266 (1972).

[88] R. E. Miles, J. Microscopy **95**, 181-195 (1972).

[89] R. E. Miles, J. Microscopy **138**, 115-125 (1985).

[90] R. E. Miles, in: Proc. first intl. symp. science on form, 147-155, KTK Scientific Publisher, Tokyo, 1986.

[91] L. Muche, D. Stoyan, J. Appl. Prob. **29**, 467-471 (1992).

[92] L. Muche, J. Appl. Prob. **42**, 48-68 (2010).

[93] C. de Mulatier, A. Mazzolo, A. Zoia, EPL **107**, 30001 (2014).

[94] I. Murata, T. Mori, M. Nakagawa, Nucl. Sci. Eng. **123**, 96-109 (1996).

[95] Y. Nauchi, T. Kameyama, J. Nucl. Sci. Technol. **47**, 977 (2010).

[96] M. E. J. Newman and R. M. Ziff, Phys. Rev. Lett. **85**, 4104-4107 (2000).

[97] R. Neher, K. Mecke, and H. Wagner, J. Stat. Mech. P01011 (2008).

[98] M. Neumann, J. Stanek, O. M. Pecho, L. Holtzer, V. Benes, V. Schmidt, Comput. Mater. Sci. **118**, 353-364 (2016).

[99] M. Neumann, V. Schmidt, in Proc. ECCOMAS Congress, 2016.

[100] G.L. Olson, D.S. Miller, E.W. Larsen, J.E. Morel, J. Quant. Spectrosc. Radiat. Transfer **101**, 269-283 (2006).

[101] A.J. Olson, A. Prinja, B. Franke, EPJ Web of Conferences **153**, 06014 (2017).

[102] A.J. Olson, A.K. Prinja, B.C. Franke, Trans. Am. Nucl. Soc. **111**, 651 (2014).

[103] F.W.J. Olver, D.W. Lozier, R.F. Boisvert, C.W. Clark, *NIST Handbook of mathematical functions* (Cambridge University Press, 2010).

[104] A.M. Ouguag, J.J. Cogliati, J.-L. Kloosterman, in Proceedings of M&C2005, Avignon, France, 2005.

[105] G.C. Pomraning, Transp. Th. Stat. Phys. **15**, 773 (1986).

[106] G.C. Pomraning, J. Quant. Spectrosc. Radiat. Transfer. **42**, 279-293 (1989).

[107] G.C. Pomraning, R. Sanchez, J. Quant. Spectrosc. Radiat. Transfer. **43**, 267-270 (1990).

[108] G.C. Pomraning, *Linear kinetic theory and particle transport in stochastic mixtures* (World Scientific Publishing, NJ, USA, 1991).

[109] G.C. Pomraning, Nucl. Sci. Eng. **108**, 325-330 (1991).

[110] G.C. Pomraning, Ann. Nucl. Energy **19**, 737-763 (1992).

[111] G.C. Pomraning, A.K. Prinja, Transp. Th. Stat. Phys. **24**, 565-590 (1995).

[112] G.C. Pomraning, Adv. Nuc. Sci. Tech. **24**, 47-93 (1996).

[113] G.C. Pomraning, J. Quant. Spectrosc. Radiat. Transfer. **56**, 629-646 (1996).

[114] G.C. Pomraning, Ann. Nucl. Energy **26**, 217-235 (1999).

[115] W. H. Press et al., *Numerical Recipes in C. The Art of Scientific Computing* (Cambridge University Press, Cambridge, 2002).

[116] A.K. Prinja, G.C. Pomraning, Transp. Th. Stat. Phys. **24**, 535-564 (1995).

[117] A.K. Prinja, A. Gonzalez-Aller, Nucl. Sci. Eng. **124**, 89-96 (1996).

[118] A.K. Prinja, Ann. Nucl. Energy **31**, 2005-2016 (2004).

[119] D. Ren, *Topics in integral geometry* (World Scientific, Singapore, 1994).

[120] P. I. Richards, Proc. Nat. Acad. Sci. USA **52**, 1160-1164 (1964).

[121] C.H. Rycroft, A. Dehbie, T. Linde, S. Guntay, Nucl. Eng. Design **265**, 69-84 (2013).

[122] D.C. Sahni, J. Math. Phys. **30**, 1554-1559 (1989).

[123] D.C. Sahni, Ann. Nucl. Energy **16**, 397-408 (1989).

[124] K. K. Sahu, A. K. Lahiri, Phil. Mag. **84**, 1185-1196 (2004).

[125] R. Sanchez, G.C. Pomraning, Ann. Nucl. Energy **18**, 371 (1991).

[126] R. Sanchez, J. Math. Phys. **30**, 2498-2511 (1989).

[127] L.A. Santaló, *Integral geometry and geometric probability* (Addison-Wesley, Reading, MA, USA, 1976).

[128] A. Santamarina, et al., The JEFF-3.1.1 Nuclear Data Library, JEFF Report 22, OECD-NEA Data Bank, 2009.

[129] R. Schneider, W. Weil, *Stochastic and integral geometry* (Springer, Berlin, Germany, 2008).

[130] R. Schneider, *Extremal properties of random mosaics.* In: Bolyai Soc. Math. Studies **24**, 301-330 (Springer, Berlin, 2013).

[131] R. Schneider, J. Math. Anal. Appl. **434**, 1365-1375 (2016).

[132] J. Serra, *Image analysis and mathematical morphology* (Academic Press, London, 1982).

[133] H. Solomon, *Geometric Probability* (SIAM Press, Philadelphia, PA, 1978).

[134] A. Somaini, *Neutron transport in stochastic geometries*, Master Dissertation, Politecnico di Milano, 2014.

[135] D. Stauffer, A. Aharony, *Introduction to percolation theory* (CRC Press, FL, USA, 1994).

[136] B. Su, G.C. Pomraning, J. Quant. Spectrosc. Radiat. Transfer **54**, 779-801 (1995).

[137] J.C. Sublet, CALENDF-2010: User Manual, Rapport CEA-R-6277 (2011).

[138] T. Svensson et al., Phys. Rev. E **87**, 022120 (2013).

[139] T. Svensson et al., Phys. Rev. E **89**, 022141 (2014).

[140] P. Switzer, Ann. Math. Statist. **36**, 1859-1863 (1965).

[141] J. Talbot, P. Scaaf, G. Tarjus, Mol. Phys. **72**, 1397 (1990).

[142] J. C. Tanner, J. App. Probab. **20**, 778-787 (1983).

[143] K. Tonoike, in: Proceedings of GLOBAL 2013, Salt Lake City, Utah, USA, 729-735, 2013.

[144] S. Torquato, B. Lu, Phys. Rev. E., **47**, 2950 (1993).

[145] M. D. Rintoul and S. Torquato, J. Phys. A: Math. Gen. **30**, L585 (1997).

[146] J. Quintanilla, S. Torquato, and R. M. Ziff, J. Phys. A: Math. Gen. **33**, L399-L407 (2000).

[147] S. Torquato, *Random heterogeneous materials: microstructure and macroscopic properties* (Springer-Verlag, New York, USA, 2013).

[148] G. Truchet, P. Leconte, A. Santamarina, F. Damian, E. Brun, A. Zoia, Ann. Nuc. Energy **85**, 17 (2015).

[149] V. Tuchin, *Tissue optics: light scattering methods and instruments for medical diagnosis* (Cardiff, UK, SPIE Press, 2007).

[150] T. Ueki, Nucl. Sci. Eng. **178**, 16-28 (2014).

[151] T. Ueki, J. Nucl. Sci. Tech. **54**, 267-279 (2017).

[152] E. Underwood, *Quantitative Stereology* (Addison-Wesley, 1970).

[153] R. Vasques, *A review of particle transport theory in a binary stochastic medium*, Master Dissertation, Universidade Federal Do Rio Grande Do Sul, 2005.

[154] D. Vanderhaegen, J. Quant. Spectrosc. Radiat. Transfer **39**, 333-337 (1988).

[155] W. H. Visscher, H. Bolterlii, Phys. Rev. A, **32**, 2347 (1985).

[156] B. Widom, J. Chem. Phys. **44**, 3888 (1966).

[157] M.M.R. Williams, Nucl. Sci. Eng. **40**, 144-150 (1970).

[158] M.M.R. Williams, Atomkernenergie **22**, 248 (1974).

[159] M.M.R. Williams, Nucl. Sci. Eng. **136**, 34-58 (2000).

[160] M.M.R. Williams, E.W. Larsen, Nucl. Sci. Eng. **139**, 66-77 (2001).

[161] M.M.R. Williams, Nucl. Sci. Eng. **143**, 1-18 (2003).

[162] M.M.R. Williams, Ann. Nucl. Energy **31**, 1073-1081 (2004).

[163] M.M.R. Williams, Ann. Nucl. Energy **52**, 22-27 (2013).

[164] Q. Wu, S. Kim, M. Ishii, S., Beus, Int. J. Heat Mass Transf. **41**, 1103-1112 (1998).

[165] T. Yamamoto, Ann. Nucl. Energy **37**, 398-405 (2010).

[166] G.B. Zimmerman, Lawrence Livermore National Laboratory Report UCRL-JC-105616 (2010).

[167] G.B. Zimmerman, M.L. Adams, Trans. Am. Nucl. Soc. **66**, 287 (1991).

[168] A. Zoia, E. Brun, J. Jouanne, F. Malvagi, Ann. Nucl. Energy **54**, 218-226 (2012).

[169] A. Zoia, E. Brun, Ann. of Nucl. Energy **90**, 71-82 (2016).

[170] A. Zoia, Y. Nauchi, E. Brun, C. Jouanne, Ann. Nucl. Energy **96**, 377-388 (2016).

[171] O. Zuchuat, R. Sanchez, I. Zmijarevic, F. Malvagi, J. Quant. Spectrosc. Radiat. Transfer **51** 689-722 (1994).

université PARIS-SACLAY | ÉCOLE DOCTORALE PHENIICS

Titre : Transport stochastique de particules dans des matériaux désordonnés : au-delà de l'équation de Boltzmann

Mots clés : Milieux aléatoires, Transport, Tessellations, Monte Carlo, Poisson, Voronoï, Inclusions sphériques

Résumé : Des milieux hétérogènes et désordonnés émergent dans plusieurs applications de la science et de l'ingénierie nucléaires, en particulier en ce qui concerne la propagation des neutrons et des photons. Les exemples sont très répandus et concernent par exemple la double hétérogénéité des éléments combustibles dans les réacteurs à lit de boulets ou l'évaluation de la probabilité de re-criticité suite aux arrangements aléatoires du combusitble résultant d'accidents graves. Dans cette thèse, nous étudierons le transport linéaire de particules dans des milieux aléatoires. Dans la première partie, nous nous concentrerons sur quelques modèles mathématiques qui peuvent être utilisés pour la description de matériaux aléatoires. Une attention particulière sera accordée aux tessellations stochastiques, où un domaine est partitionné en polyèdres convexes en échantillonnant des hyperplans aléatoires selon une probabilité donnée. Les inclusions stochastiques de sphères dans une matrice seront également brièvement introduites. Un code informatique sera développé afin de construire explicitement de telles géométries par des méthodes de Monte Carlo. Dans la deuxième partie, nous évaluerons ensuite les caractéristiques générales du transport de particules dans des milieux aléatoires. Pour ce faire, nous allons considérer quelques benchmarks assez simples pour permettre une compréhension approfondie des effets des géométries aléatoires sur les trajectoires de particules tout en conservant les propriétés clés du transport linéaire. Les calculs de transport seront réalisés en utilisant le code de transport de particules Monte Carlo TRIPOLI-4 ®, développé au SERMA. Les cas de modèles de désordre quenched et annealed seront considérés séparément. Dans le premier, un ensemble de géométries sera généré en utilisant notre code, et le problème de transport sera résolu pour chaque configuration: des moyennes d'ensemble seront alors prises pour les observables d'intérêt. Dans le second cas, un modèle de transport efficace capable de reproduire les effets du désordre dans une seule réalisation sera étudié. Les approximations des modèles annealed seront élucidées, et des améliorations significatives seront proposées. (Un résumé détaillé est donné en Annexe B.)

Title: Stochastic particle transport in disordered media: beyond the Boltzmann equation

Keywords: Random media, Transport, Tessellations, Monte Carlo, Poisson, Voronoi, Spherical inclusions

Abstract: Heterogeneous and disordered media emerges in several applications in nuclear science and engineering, especially in relation to neutron and photon propagation. Examples are widespread and concern for instance the double-heterogeneity of the fuel elements in pebble-bed reactors, or the assessment of re-criticality probability due to the random arrangement of fuel resulting from severe accidents. In this Thesis, we will investigate linear particle transport in random media. In the first part, we will focus on some mathematical models that can be used for the description of random media. Special emphasis will be given to stochastic tessellations, where a domain is partitioned into convex polyhedra by sampling random hyperplanes according to a given probability. Stochastic inclusions of spheres into a matrix will be also briefly introduced. A computer code will be developed in order to explicitly construct such geometries by Monte Carlo methods. In the second part, we will then assess the general features of particle transport within random media. For this purpose, we will consider some benchmark problems that are simple enough so as to allow for a thorough understanding of the effects of the random geometries on particle trajectories and yet retain the key properties of linear transport. Transport calculations will be realized by using the Monte Carlo particle transport code TRIPOLI-4 ®, developed at SERMA. The cases of quenched and annealed disorder models will be separately considered. In the former, an ensemble of geometries will be generated by using our computer code, and the transport problem will be solved for each configuration: ensemble averages will then be taken for the observables of interest. In the latter, effective transport model capable of reproducing the effects of disorder in a single realization will be investigated. The approximations of the annealed disorder models will be elucidated, and significant ameliorations will be proposed.

Université Paris-Saclay
Espace Technologique / Immeuble Discovery
Route de l'Orme aux Merisiers RD 128 / 91190 Saint-Aubin, France